Wiersma, Jelle Pouwel (2021) ***Cave sedimentation processes in the Homo naledi-bearing Rising Star Cave, Cradle of Humankind, South Africa.*** **PhD Thesis, James Cook University.**

Cave sedimentation processes in the *Homo naledi*-bearing Rising Star Cave, Cradle of Humankind, South Africa

Thesis submitted by

Jelle Pouwel Wiersma

April 2021

For the Degree of Doctor of Philosophy
College of Science and Engineering
Department of Earth and Environmental Sciences
James Cook University

Statement of Access

I, the undersigned author of this thesis, understand that James Cook University will make this thesis available for use within the university library and allow access in other approved libraries after this submission. All users consulting this thesis will have to sign the following statement:

In consulting this thesis, I agree not to copy or closely paraphrase it in whole or in part without the written consent of the author; and to make proper public written acknowledgement for any assistance which I have obtained from it.

Beyond this, I do not wish to place any further restrictions on access to this thesis.

Jelle P. Wiersma
April 2021

Declaration

I declare that this thesis is my own work and has not been submitted in any form for another degree or diploma at any university or other institute or tertiary education. Information derived from the published or unpublished work of others has been acknowledged in the text and a list of references is given.

Jelle P. Wiersma
April 2021

Every reasonable effort has been made to gain permission and acknowledge the owners of copyright material. I would be pleased to hear from any copyright owner who has been omitted or incorrectly acknowledged.

Statement on the contributions of others

Nature of Assistance	Contribution	Names & affiliations of co-contributors
Intellectual support	Supervision	Assoc. Prof. Eric Roberts, JCU Prof. Paul Dirks, JCU
	Proposal writing	Assoc. Prof. Eric Roberts, JCU Prof. Paul Dirks, JCU Dr. Lee Berger, UW Dr. Carl Spandler, JCU Dr. Christa Placzek, JCU
	Data analysis	Assoc. Prof. Eric Roberts, JCU Prof. Paul Dirks, JCU Dr. David Grant, MU
	Editorial assistance	Assoc. Prof. Eric Roberts, JCU Prof. Paul Dirks, JCU
Financial support	Research funding Stipend	National Geographic Malapa research grant Lyda Hill Foundation Australian Research Council (ARC), grant number: DP140104282 JCU IPRS
External data collection	MLA	SEM lab at Memorial University, Canada under supervision of Dr. David Grant

Statement of Contribution

Chapter	Publication on which chapter is based	Nature and extent of intellectual input
2	Wiersma, J.P., Dirks, P.H.G.M. and Roberts, E.M.	Roberts contributed to concept developments, fieldwork, data analysis, and provided editorial assistance.
3	Wiersma, J.P., Roberts, E.M., Dirks, P.H.G.M.	Roberts contributed to concept developments, fieldwork, data analysis, and provided editorial assistance.
4	Wiersma, J.P., Roberts, E.M., Dirks, P.H.G.M.	Roberts contributed to concept development, sample collection, data analysis, and provided editorial assistance.
5	Wiersma, J.P., Roberts, E.M. and Dirks, P.H.G.M. (2019). Sedimentology.	Roberts contributed to concept development and idea discussion, sample collection, and provided editorial assistance.

I confirm the candidate's contribution to these papers and consent to the inclusion of these papers in this thesis.

Name: Prof. Eric Roberts

Signature:

Date: April 20, 2021

Statement of Contribution

Chapter	Publication on which chapter is based	Nature and extent of intellectual input
2	Wiersma, J.P., Dirks, P.H.G.M. and Roberts, E.M.	Dirks contributed to concept developments, fieldwork, data analysis, and provided editorial assistance.
3	Wiersma, J.P., Roberts, E.M., Dirks, P.H.G.M.	Dirks contributed to concept developments, fieldwork, data analysis, and provided editorial assistance
4	Wiersma, J.P., Roberts, E.M., Dirks, P.H.G.M.	Dirks contributed to concept developments, data analysis and provided editorial assistance.
5	Wiersma, J.P., Roberts, E.M. and Dirks, P.H.G.M. (2019). Sedimentology.	Dirks contributed to concept development and idea discussion, sample collection, and provided editorial assistance.

I confirm the candidate's contribution to these papers and consent to the inclusion of these papers in this thesis.

Name: Prof. Paul Dirks

Signature:

Date: April 20, 2021

Acknowledgements

Firstly, I like to express my sincere gratitude to both my advisors, Dr. Eric Roberts and Prof. Paul Dirks for providing me with the opportunity to work on the Rising Star Cave project, their continuous support of my Ph.D. study and related research, for their patience, motivation, and mentorship, continuously pushing me to become a better academic. Their guidance helped me during my time of research and writing of this thesis. Besides my advisors, I would like to thank Dr. Lee Berger for his generous support and allowing me access to Rising Star Cave.

My sincere thanks also go to Dr. Marina Elliott and the entire Rising Star caving team: Rick Hunter, Steven Tucker, Mathabela Tsikoane, Maropeng Ramalepa, Nompumelelo "Pume" Hlopbe, and Wayne Crichton for their logistical support, for watching my back from above or wherever you were perched in the cave, and for staying longer than you had to, allowing me to finish my work. I want to extend my gratitude to Dirk van Rooyen and Steven Tucker, for enticing me to ascend into the geologically unexplored chambers above the Postbox. This 'new' locality proved extremely significant and insightful for my research! Thank you all for your company, your help, and some good laughs along the way. I miss you all and I could not have done this work without you. You have made my caving experiences in South Africa very memorable.

Thanks to the JCU geology and EGRU staff, Jan Marten Huizenga, Espen Knudsen, Bob Henderson, James Daniel, Carl Spandler, Ioan Sanislav, Christa Placzek, Kaylene Camuti, and Huiquing (Jeffrey) Huang for their support, fruitful discussions, and help with lab work. I am grateful for Dr. Jan Marten Huizenga, for recruiting me every year to tutor Introductory Geology. I thank Judi Botting, Dot Cunningham, and Elaina Jones for their administrative assistance. Bec Steele, where would the postgraduate students be without you! You are the captain that keeps us sailing. I cannot thank you enough for all your dedication to the students, your tireless hard work and above all, patience, to make our life as a Ph.D. student so much easier. It sure did so for me.

I am fortunate to gratefully acknowledge the support of my friends and fellow postgraduate students: Chris Todd, Robbie Coleman, Helge Behnsen, Jaime Poblete, Alex Parker, Matt van Ryt, Stefanie Mrozek, Paul Slezak, Kelly Heilbronn, Elliott Foley, Pieter Creus,

Truong Le, Leigh Lawrence, Tegan Beveridge, Chris Yule, Jess Robins, Caleb Puszkiewicz, Josh Spence, Grace Manestar, and Michal Wenderlich. Thank you all for your friendship, the stimulating discussions accompanied by copious amounts of caffeine, the rants and great laughs we had over many beers in our office "cell-block" and at Uni Club. I cherish the fun times together during Empire game night, and the many memorable trips to Magnetic "Maggie" Island in the last 3.5 years.

Finally, I acknowledge the people who mean a lot to me, my parents, Ids and Paulien, for showing faith in me and never fail to support my work. Although you hardly understood what I researched on, you were willing to support any decision I made.

I owe thanks to two very special people in my life, my life partner and buddy through thick and thin, Akiko, for your continued and unfailing love, support and understanding during the pursuit of my Ph.D. degree that made the completion of this thesis possible. You were always around at times I thought it was impossible to carry on and helped me keep things in perspective and push me forward. Ganbare! Second, my son Arjen, for enduring my ignorance and the patience you showed me during my research, and I am deeply sorry you had to endure my long absences in your life. Words cannot begin to describe how grateful I am to both of you, for your love and unconditional support. I love you dearly.

Thesis Abstract

Since the discovery of the middle Pleistocene hominin *Homo naledi* in 2013, the Rising Star Cave has become one of the most important fossil hominin-bearing localities in the world. This thesis was conducted in conjunction with ongoing paleoanthropological work and other geological investigations in the cave system. The goal of this project was to contribute to understanding the geological and taphonomical context for the fossil assemblage, focusing on the clastic sediments and depositional processes in the cave. This project involved multiple field seasons mapping and studying the bedrock stratigraphy of the dolomitic Proterozoic-aged Malmani Subgroup in the study area. Here, underground mapping and sampling of clastic sediments in Rising Star Cave, and an exhaustive laboratory-based analysis of these cave sediments was conducted focusing on petrology, geochemistry, grain-size distribution and provenance.

A total of ten unique clastic facies were identified and described within Rising Star Cave and interpreted in terms of their depositional environments. The architecture and sediment distribution in the cave indicates that much of the sediment entered the cave system from a shallow westerly dipping subterranean debris cone with its apex positioned in the Postbox Chamber. Sediments in the cave fine away from this debris cone from proximal coarse clastic alluvial and colluvial facies in the Postbox Chamber to more distal deposited silt-clay-sized facies in the Dinaledi Subsystem. The depositional history of Rising Star Cave shows a complex interplay of multiple episodes of deposition, erosion and reworking of pre-existing sediments that occurred in response to periods of surface flooding, heavy rainfall and neotectonic activity, as well as localized events that took place inside the cave (e.g., roof collapse, autobrecciation). The clastic sediments also preserve stratigraphic fining up patterns, best observed in Dragon's Back Chamber. This fining upward trend occurs as the Upper Bloubank

Spruit continuously migrated in a north-eastern direction, further away from, and ultimately, well below the cave. Overall, the clastic cave sediments share a compositional and textural similarity to those found on the surrounding landscape based on the mineralogical, radio-isotopic, geochemical, and physical properties of the sediments analyzed. They are most similar to sediments present in the Upper Bloubank Spruit riverbed and the strath terraces surrounding the cave.

U-Pb detrital zircon geochronology reveals ten discrete grain age populations, ranging from 3431-238 Ma, linking cave and surface sediments. Results indicate that the surface sediments surrounding and clastic sediments within Rising Star Cave are mostly sourced from the Permian-Jurassic Karoo Supergroup deposits, rather than being exclusively derived from erosion of the host Malmani Subgroup dolomites. No evidence for distal, aeolian-sources (i.e., Kalahari sand) were recorded in the detrital zircon signature, which further implies that the clastic cave and surface sediments are locally sourced from the now mostly eroded Karoo. The sediment budget in the cave constitutes ~95 % allochthonous clastic detrital sediment that consist primarily of medium to fine-grained sand, silt, and clays, various (diagenetic) heavy minerals, and locally abundant intercalations of micromammal fossils. A localized depositional process termed "sedimentary autobrecciation" produces distinctive deposits in parts of the cave where fine-grained facies are present, particularly in the Dinaledi Chamber. Here, clay-rich fine-grained laminated orange-red mud facies on the cave floor, in dissolution pockets, and on chert shelves desiccate in combination with diagenetic alteration (Mg- and Fe-oxide formation) and slumping to form distinctive, unlithified mud clast breccias. The process of autobrecciation in the Rising Star Cave is slow, with first order formation rates estimated to be ~8 x 10^{-4} mm/year. The slow formation of the unlithified mud clast breccia facies sediments and lack of laminated mud facies within these deposits, indicates that conditions in the Dinaledi Chamber were probably stable and dry for at least the last *ca* 300 ka, which excludes *Homo naledi* being actively transported by fluvial mechanisms during the time their remains entered the cave.

This thesis is dedicated to my dearest son—

Arjen Lewis

Table of Contents

Chapters

Appendices of analytical data

Chapters 2 & 3.

Chapter 4.

Appendices of published papers

List of Tables

Chapter 2.

Chapter 3.

Chapter 4.

Chapter 5.

List of Figures

Chapter 1.

Chapter 2.

Chapter 3.

Chapter 4.

Chapter 5.

Thesis Structure

The thesis is structured as a "thesis by publication" and all four data chapters have been prepared for publication in internationally recognized, peer-reviewed journals. Each data chapter presents a unique aspect of the research and is complementary to the other chapters. At the time of submission of this thesis, Chapter 5 is published in Sedimentology (Wiersma et al., 2020; see Appendix 5), Chapter 3 is being prepared for submission in mid-2021, and Chapter 4 has been submitted for review to Quaternary Research. In addition to what is presented in this thesis, the author (Wiersma) has contributed to other published Rising Star Cave studies, involving geochronology and geochemistry, which have resulted in co-authored publications (Dirks et al., 2017 and Robbins et al., 2021) and conference abstracts (Wiersma et al., 2017).

The thesis consists of six chapters: Chapter 1 presents a brief introduction and (geological) background to the Rising Star Cave study; Chapters 2-5 are four individual data chapters that each investigate a separate geological aspect of the cave; and Chapter 6 is a thesis summary, presenting the major findings and conclusions of the study.

In more detail:

Chapter 1 presents the main aims of the project and the structure of the thesis. This chapter additionally provides general background and in depth regional geological information regarding the fossiliferous cave systems within the Cradle of Humankind but focussing primarily on the local geology of the Rising Star Cave system.

Chapter 2 investigates the stratigraphy of the lower Monte Christo Formation and discusses the geomorphic landscape features that surround the cave. This work focuses on the dolomite stratigraphy in which the Rising Star Cave formed. Additionally, Chapter 2 presents a geomorphic reconstruction of the landscape surrounding the cave, reconstructing the role of fluvial migration patterns and timing of opening of Rising Star Cave, presenting information on the different alluvial, alluvial terrace, and colluvial sediments on surface, thus placing temporal constraints on the depositional history of surface cave sediments, including the deposition of the *Homo naledi* fossils. This chapter, when published, will have the following authors: Wiersma, J. P., Dirks, P. H. G. M., and Roberts, E. M. The author contributions are as follows: JPW collected, analysed and interpreted the data, wrote and revised the manuscript. PHGMD provided data interpretation and manuscript edits. EMR provided manuscript edits.

Chapter 3 presents the sedimentology and stratigraphy of Rising Star Cave and provides detailed lithostratigraphic and facies descriptions for the sediments in the investigated chambers in the cave. This work allows to determine the different sediment types and facies that occur in the cave. This chapter, when published, will have the following authors: Wiersma, J. P., Roberts, E. M., Dirks, P. H. G. M., and Robbins, J. L. The author contributions are as follows: JPW designed the experiment, collected, analysed and interpreted the data, wrote and revised the manuscript. EMR provided data interpretation and manuscript edits. PHGMD designed the experiment, provided data interpretation and manuscript edits. JLR provided manuscript edits.

Chapter 4 presents the sediment provenance and sediment budget of Rising Star Cave sediments. This work presents a novel investigation that serves to determine the origin of the clastic cave sediments based on U/Pb detrital zircon analysis. Experimental dissolution of cave-hosting dolomites additionally demonstrates a primarily allochthonous origin of the cave sediments. This chapter has the following authors: Wiersma, J. P., Dirks, P. H. G. M., and Roberts, E. M. The author contributions are as follows: JPW collected, analysed and interpreted the data, wrote and revised the manuscript. PHGMD provided data interpretation and manuscript edits. EMR provided manuscript edits.

Chapter 5 has been published in *Sedimentology* and focuses on the highly localised process of sedimentary autobrecciation in the laminated mud sediments within the Dinaledi Chamber. The process provides direct taphonomical context for the distribution and position of the *Homo naledi* fossils. This chapter builds upon previous work conducted by Dirks et al. (2015). This chapter consists of the following authors: Wiersma, J. P., Dirks, P. H. G. M., and Roberts, E. M. The author contributions are as follows: JPW designed the experiment, collected, analysed and interpreted the data, wrote and revised the manuscript. PHGMD provided data interpretation and manuscript edits. EMR provided geological context from the Dinaledi Chamber, data interpretation and manuscript edits.

Chapter 6 summarizes the main conclusions of the project and makes suggestions for future sedimentologic work on the Rising Star Cave project.

Published thesis chapters and other manuscripts that were published during the Ph.D. are included as appendices at the end of this thesis.

Appendix 1 contains supplementary grain size analysis and sediment type data in support of Chapters 2 and 3.

Appendix 2 contains supplementary detrital zircon spot locations, U-Pb data and Kolmogorov-Smirnov statistical data in support of Chapter 4.

Appendix 3 is the publication, Dirks et al. (2017). The age of *Homo naledi* and associated sediments in the Rising Star cave, South Africa, *elife* 6:e24231.

Appendix 4 is the publication, Wiersma et al. (2020). Formation of mud clast breccias and the process of sedimentary autobrecciation in the hominin-bearing (*Homo naledi*) Rising Star Cave system, South Africa. Sedimentology, 67:2, 897-919.

Appendix 5 is the publication, Robbins et al. (2021). Providing context to the *Homo naledi* fossils: Constraints on the age of sediment deposits in the Rising Star Cave, South Africa, Chemical Geology.

Chapter One

Project Introduction

1.1. Aims of study

The central theme of this research project is to provide geological, sedimentary and taphonomic context for the *Homo naledi* fossils from Rising Star Cave, South Africa. To meet this objective, this study investigates local and cave-wide clastic sediments and sedimentary processes correlated with broader geological and geomorphic processes by implementing various qualitative and quantitative techniques. Cave lithostratigraphy and facies analysis are used in this study to establish a basic sedimentologic framework that allows for the identification of different sediment types and facies associations throughout the investigated cave chambers. Particle size analysis, thin section petrography and scanning electron microscopy studies further refine how sedimentation patterns and clastic detrital sediments are distributed throughout the cave. Mineral liberation analysis (MLA), bulk and clay X-ray diffraction (XRD) and X-ray fluorescence (XRF) geochemistry provide compositional and textural trends for the cave and surface sediments, and additionally recognize the occurrence of highly localized, (bio)geochemical processes in the cave. U-Pb detrital zircon analysis provides insight into sediment provenance and the depositional history of the sediments in the cave linked with those on surface. The interpretation of local geomorphology is critical in understanding the evolution of the landscape that surrounds the cave, and provides temporal constraints on when the cave was open and allowed for sediments and fossils to accumulate. This research has placed the *Homo naledi* fossils and the Rising Star Cave system into a better-defined geologic context.

1.2. General background

Cave systems in the Cradle of Humankind UNESCO World Heritage Site in South Africa (Fig. 1) have long been known to yield spectacular fossil hominins (Dart, 1925; Brain, 1993; Tobias, 2000; Berger et al., 2010; Dirks et al., 2010; Berger et al., 2015; Hawks et al., 2017). The Cradle of Humankind hosts some of the world's most important fossil hominin cave sites, yielding Plio-Pleistocene-aged australopithecines, *Australopithecus sediba*, *Au. africanus*, *Au. robustus*, *Paranthropus robustus*, and early *Homo*, including the recently discovered, *Homo naledi* (Dart, 1925; Brain, 1993; Tobias, 2000; Berger et al., 2010; Dirks et al., 2010; Berger et al., 2015; Hawks et al., 2017). The southern African Pliocene and Pleistocene-aged hominin fossils contain some of our earliest ancestors, as well as more recent closely related taxa and have significantly increased

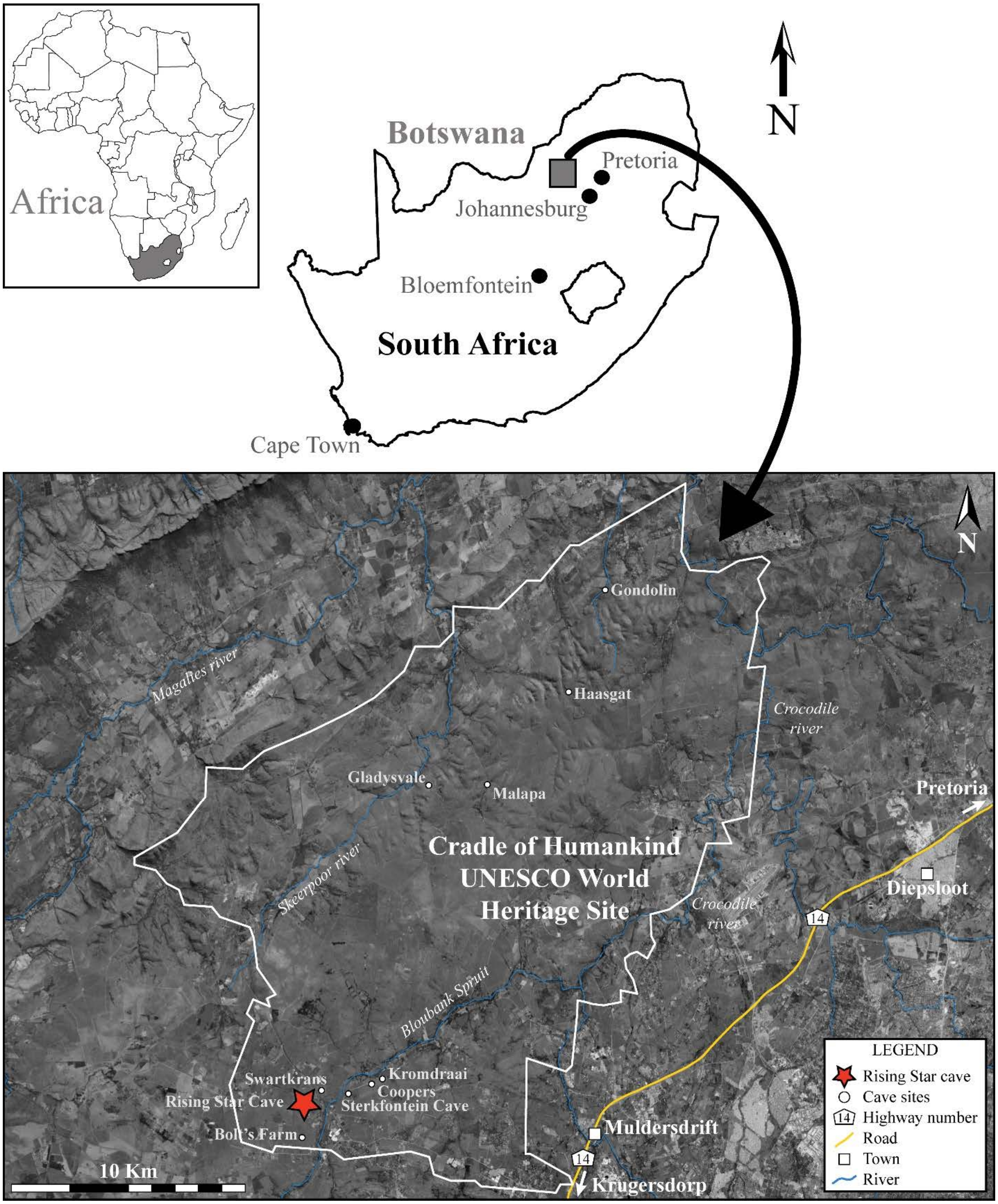

Figure 1. Distribution of major fossil bearing caves, including Rising Star Cave in the Cradle of Humankind, South Africa.

our understanding of human evolution. Moreover, the young age of the 236-335 ka old *Homo naledi* fossils (Dirks et al., 2017) also hint towards the co-existence of different hominin species in Africa in similar geographic areas, including early members of our own species, *Homo sapiens* (Dirks et al., 2017).

Hominins and other important fossil vertebrate faunas from the Cradle of Humankind (CoH) typically occur in cave sediment deposits and some of the most important fossil-yielding cave sites include Sterkfontein, Malapa, Gladysvale, Swartkrans, Coopers, Kromdraai and Rising Star caves (Fig. 1). Fossils either occur as monotaxic (i.e., a single species) or as complex multitaxic vertebrate faunal assemblages and they are typically preserved in well-lithified, clastic cave sediments generally referred to as cave breccias (Keyser, 2000; Berger et al., 2003; Clarke, 2007; Dirks et al., 2010; Bruxelles et al., 2014; Val et al., 2015; Van Zyl et al., 2016), that are clast supported dolomite, chert and quartzite fragments in a lithified sandy matrix (e.g., Martini et al., 2003; Dirks et al., 2010; Bruxelles et al., 2014 and references therein). Cave fossils preserved in unconsolidated cave sediments are far less common throughout the CoH, and, unlike the fairly simple composition of the cave breccia deposits, these sediments consist of a complex mixture of heterogenous allochthonous and autochthonous detrital sediments. This condition is rare but is the case for the *Homo naledi* fossils in Rising Star Cave (Dirks et al., 2015).

1.3. Geological and geomorphological setting

1.3.1 Geology and geomorphology of the Cradle of Humankind UNESCO World Heritage Site, South Africa

The Cradle of Humankind UNESCO World Heritage Site (CoH) is situated in the central part of the Kaapvaal Craton immediately west of a circular Archean basement inlier referred to as the Johannesburg Dome. The Johannesburg Dome is cored by Mesoarchaean (>3.1 Ga) granitic to ultramafic basement gneiss (Anhaeusser, 2006; Robb et al., 2006) and is overlain by Archaean clastic sediments of the gold-bearing Witwatersrand Basin (3.0-2.8 Ga) and volcanics of the Ventersdorp Supergroup (~2.71 Ga). This is in turn surrounded along the east, north, and west by outward dipping Neoarchaean to Paleoproterozic-aged (3.0-2.1 Ga) platform sequences of carbonate, volcanic and siliciclastic lithologies of the Transvaal Supergroup (Eriksson et al., 2006). Many of the Transvaal Supergroup lithologies crop out in the Cradle of Humankind (Figs. 2 and

3), but most notable are the Neoarchean-aged (2.55-2.45 Ga) stromatolite-rich dolomites of the Malmani Subgroup in the central part of the area (Eriksson and Truswell, 1974; Eriksson et al., 2006), which are unconformably overlain by the Lower Pretoria Group chert-breccias of the Rooihoogte Formation and mixed volcanic and shale successions of the Timeball Hill Formation in the northwest (Fig. 2). In the Cradle of Humankind, the Rooihoogte Formation was deposited on top of the gently west-dipping dolomites, cherts and siliciclastics of the Malmani Subgroup. Syn-sedimentary block faulting of this succession during the Palaeoproterozoic resulted in orthogonal and polygonal fracture networks of normal faults that likely accelerated karstification of the landscape onto which the sandy chert breccias of the Rooihoogte Formation were deposited, which locally extend up to 100 m below the paleosurface (Dirks and Berger, 2013). These vertically protruding fractures are wedge-shaped (see Dirks et al., 2013 Fig. 7), and are infilled with heterogenous sediments. The Cradle of Humankind area hosts hundreds of cave systems and it is along these fractures where caves preferentially formed within the Malmani Subgroup dolomites under phreatic and vadose conditions sometime during the last 4 million years (Pliocene). This resulted in the formation of extensive, yet poorly connected, network cave systems. The sedimentary sequences were intruded at ~ 2.06 Ga by the Bushveld Igneous complex to the north, as well as diorite and syenite sills and dykes of undefined Proterozoic age. Horizontally bedded Permian-Triassic sediments of the Karoo Supergroup unconformably overlie the Transvaal Supergroup lithologies. Prior to flexure and extensive erosion, most of the Johannesburg Dome and the Cradle of Humankind would have been covered by these Karoo-aged sediments, but in the present landscape small, eroded remnants of Karoo-aged sediments remain only locally in the CoH where they are preserved in pockets of paleo-karst and along old erosion surfaces across the southern part of the CoH (Dirks and Berger, 2013).

The Malmani Subgroup in the CoH comprises a basal lag conglomerate (the Black Reef Formation) succeeded by a thick succession of dolomite, locally up to 1200 m, and is sub-divided into five formations on the basis of stromatolite morphology, chert content and the presence of shale and chert-breccia horizons (Eriksson and Truswell, 1974). These formations include, from older to younger, the Oaktree, Monte Christo, Lyttelton, Eccles, and Frisco formations (Eriksson and Truswell, 1974). The entire Malmani Subgroup is interpreted as a carbonate platform succession, deposited during long-term transgression in Neoarchean to early Paleoproterozoic (~2.55 Ga) times (Eriksson and Reczko, 1995). The onset of this transgression has been interpreted

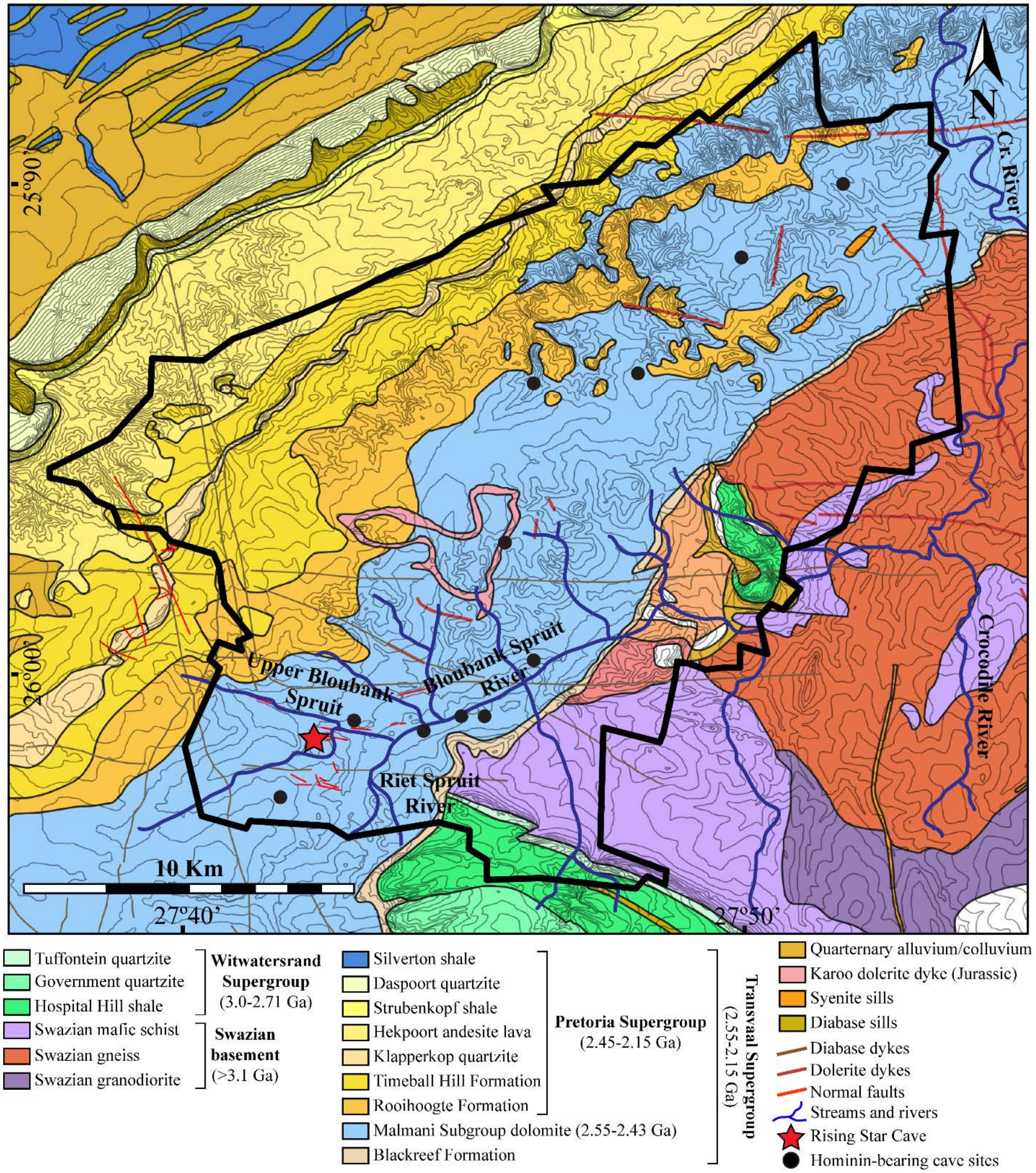

Figure 2. Geological map of the Cradle of Humankind (CoH) and regional area. Rising Star Cave, and other hominin-bearing cave sites throughout the CoH, occur exclusively in the dolomite successions of the Malmani Subgroup.

as the result of thermal subsidence of the Ventersdorp fault systems (Eriksson and Reczko, 1995), developing a shallow epeiric sea in which stromatolite-rich carbonates precipitated. Carbonate production during the Archean was mainly chemically induced, with biogenic roles being far less prevalent, resulting in carbonate successions devoid of calcareous shells and skeletons. Instead, stromatolite-forming cyanobacterial colonies and sea water composition played a crucial role in the production of carbonate deposits of the Malmani Subgroup (Eriksson and Altermann, 1998). Throughout the Malmani Subgroup carbonate strata, irregular karstification and paleosurfaces are present, subsequently overlain by thin shale horizons which are indicative of prolonged periods of subaerial exposure (Eriksson and Altermann, 1998). The karstic paleosurfaces of the uppermost Frisco and Eccles formations are unconformably overlain by the Rooihoogte Formation, which varies regionally in thickness (Dirks et al., 2013; 2015). The Rooihoogte Formation is composed of reworked clast supported chert breccias in a sandstone matrix, likely deposited by paleochannels (Dirks et al., 2013).

Four of the five formations of the Malmani Subgroup crop out in the CoH and most of them host caves (Figs. 2 & 3). At the base are the chert-poor dolomites of the Oaktree Formation (~150 m) with interbedded shale and tuff dated at 2550 ± 3 Ma (Walraven and Martini, 1995) and 2583 ± 5 Ma (Martin et al., 1998). The overlying chert-rich Monte Christo Formation (600-700 m) that hosts Rising Star Cave is generally stromatolite-rich and commonly interbedded with generally thin (<50 cm) shale horizons. It is overlain by the chert-free Lyttelton Formation (150-200m thick), and chert-rich Eccles Formation (< 600 m thick). The Eccles Formation is overlain by chert breccias of the Rooihoogte Formation, which formed above an irregular karstic paleo-topography (Dirks and Berger, 2013).

Across the southern African landscape, preserved remnants of erosion surfaces of different ages provide evidence of multiple uplift events during post-Cretaceous times (Partridge and Maud, 1987; Burke, 1996; Burke and Gunnell, 2008). The most extensive erosion surface preserved on the African continent is the Late Jurassic-Early Cretaceous African Erosion Surface ("African Surface" in Partridge and Maud, 1987) and remnants have been recorded throughout southern and western Africa. Uplift events, identified as domal flexures, warped the African surface, resulting in rejuvenation and subsequent planation with every uplift event. Subsequent headward erosion and incision by fluvial systems resulted in shedding of the sediments in the created accommodation space within the landscape (Dirks and Berger, 2013). Two major post-African erosion surfaces have been described in the area around the Cradle of Humankind; the Miocene Post African I, and Pliocene Post African II erosion surfaces (Partridge and Maud, 1987). Uplift and warping of the

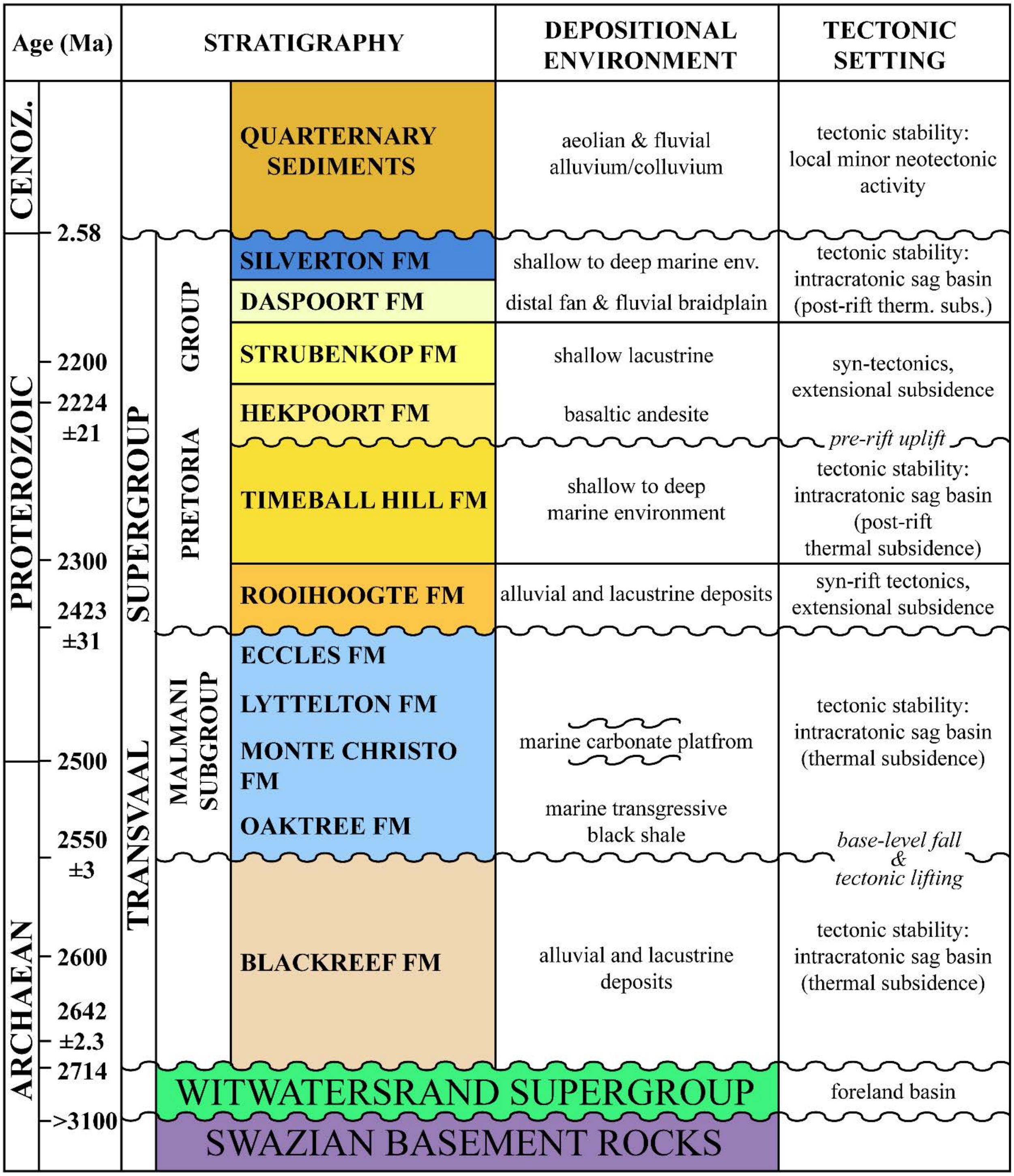

Age (Ma)		STRATIGRAPHY			DEPOSITIONAL ENVIRONMENT	TECTONIC SETTING
CENOZ.				QUARTERNARY SEDIMENTS	aeolian & fluvial alluvium/colluvium	tectonic stability: local minor neotectonic activity
PROTEROZOIC	2.58	TRANSVAAL SUPERGROUP	PRETORIA GROUP	SILVERTON FM	shallow to deep marine env.	tectonic stability: intracratonic sag basin (post-rift therm. subs.)
				DASPOORT FM	distal fan & fluvial braidplain	
	2200			STRUBENKOP FM	shallow lacustrine	syn-tectonics, extensional subsidence
	2224 ±21			HEKPOORT FM	basaltic andesite	*pre-rift uplift*
				TIMEBALL HILL FM	shallow to deep marine environment	tectonic stability: intracratonic sag basin (post-rift thermal subsidence)
	2300 2423 ±31			ROOIHOOGTE FM	alluvial and lacustrine deposits	syn-rift tectonics, extensional subsidence
			MALMANI SUBGROUP	ECCLES FM	marine carbonate platfrom	tectonic stability: intracratonic sag basin (thermal subsidence)
				LYTTELTON FM		
	2500			MONTE CHRISTO FM		
ARCHAEAN				OAKTREE FM	marine transgressive black shale	*base-level fall & tectonic lifting*
	2550 ±3 2600 2642 ±2.3			BLACKREEF FM	alluvial and lacustrine deposits	tectonic stability: intracratonic sag basin (thermal subsidence)
	2714	WITWATERSRAND SUPERGROUP				foreland basin
	>3100	SWAZIAN BASEMENT ROCKS				

Figure 3. Stratigraphic overview, including depositional and tectonic settings in the Cradle of Humankind region, modified from Eriksson et al. (2001). Color-coded formations correspond with the lithologies of the geological maps in figures 2 and 4.

erosion surface in southern Africa appear to have occurred as early as the Oligocene (Burke, 1996; Burke and Gunnell, 2008), followed by warping events during the Miocene and Pliocene (Partridge and Maud, 1987; Partridge, 2010).

The headwaters of the Crocodile River, represented locally by the Skeerpoort River to the north, and the Bloubank River to the south, incise the Post-African erosion surfaces in the Cradle of Humankind, and all hominin-bearing cave localities, including the Rising Star Cave, are situated along tributaries of these rivers (Dirks and Berger, 2013). This suggests that prior to opening of the caves through head-ward erosion and fluvial incision of the erosion surfaces, cave formation was potentially initiated by vadose and phreatic water that saturated dolomitic strata with no apparent surface openings (Dirks and Berger, 2013). Headward erosion and lateral fluvial incision of Post-African erosion surfaces exposed, and subsequently drained, the cave systems in the Cradle of Humankind and phreatic base level waters modified the cave systems further (Dirks and Berger, 2013; Herries et al., 2019).

The landscape across the Cradle of Humankind is old, and erosion of the southern African landscape was slow. Estimated ^{10}Be cosmogenic erosion rates indicate that the Plio-Pleistocene surface of the Cradle of Humankind eroded as little as 3.00-4.15 m/Ma (Dirks et al., 2016), independently of the underlying lithology. Such slow erosion rates suggest that the African landscape had changed little over the last 3-4 million years and that physical, rather than chemical, weathering is the dominant erosional driver (Dirks et al., 2016). Furthermore, cave deposits and fossils appear to not predate early Pliocene-Miocene times, suggesting that while the African surface in the Cradle of Humankind is old, the caves have opened up relatively recently, around ca. 4 million years ago (Dirks et al., 2016). Many of the caves contain clastic sediments, but only a small proportion of these caves are fossiliferous. The distribution of the fossiliferous caves occur in a distinctly clustered pattern throughout the region that appears not coincidental (Dirks et al., 2010; Dirks and Berger, 2013). The reasons for such a clustered distribution are unclear and have been discussed by Dirks and Berger (2013) and references therein. Dirks and Berger (2013) propose that caves that were positioned near local water sources and probably attracted fauna, including hominins, with the potential of the latter engaging in long-term occupation of cave sites.

1.3.2. Upper Bloubank Spruit catchment

The Rising Star Cave occurs in a small catchment area, referred to in this study as the Upper Bloubank Spruit catchment. The catchment area covers ~47 km^2 and it is situated in the southwest corner of the CoH (Figs. 1, 2 & 4). The highest point within the catchment area is ~1670 m and occurs along a prominent ridge of Klapperkop Formation Quartzite that forms the Catchment divide to the northwest. The lowest point in the catchment directly below Rising Star Cave occurs at 1459 m. The catchment forms a small drainage basin with a dendritic network of first- to third-order, ephemeral streams that drain eastward towards the confluence with the Bloubank Spruit and the Riet Spruit. Most of the channels eroded underlying lithologies resulting in shallow, wide gullies. However, the main channel to the north of the catchment follows a straight, northwest trajectory along some prominent scarps suggesting a fault-controlled drainage pattern confirmed by mapping (Fig. 4).

Most of the Upper Bloubank Spruit catchment is underlain by lithologies of the Malmani Subgroup dolomites, chiefly consisting of Monte Christo Formation and the overlying chert-poor Lyttelton and chert-bearing Eccles formation lithologies. The north-western margin of the catchment contains terrestrial siliciclastic strata of the Proterozoic (~2.3 Ga) Lower Pretoria Group, which unconformably overlie the dolomites with chert breccia and conglomerate deposits of the Rooihoogte Formation, followed by shale-rich sandstones of the Timeball Hill Formation and interbedded, coarse-grained quartzite of the Klapperkop Member (Fig. 4). These units were intruded by several generations of east- and north-northwest to north-northeast trending dolerite dykes, which are poorly exposed in the field, but are visible in geophysics. No Karoo-aged erosional remnants have been mapped in the catchment area, but detrital zircon populations obtained from the alluvial terraces and cave sediments (Chapter 4) indicate that remnants of Karoo material could exist in the catchment area. Some of the river valleys in the catchment area, and especially the valley floor north of Rising Star Cave is underlain by a blanket of alluvial sediment that consists of a mixture of clays and micas with sand to cobble-sized particles of quartz, quartzite, chert and dolomite, and abundant secondary iron and manganese oxyhydroxides (see detailed descriptions below).

In the vicinity of Rising Star Cave several northwest- to west-northwest trending normal faults were identified (Fig. 4). Some of these faults are infilled with chert and caves have formed along them (e.g., Dirks et al., 2015), these probably relate to the formation of the breccia of the

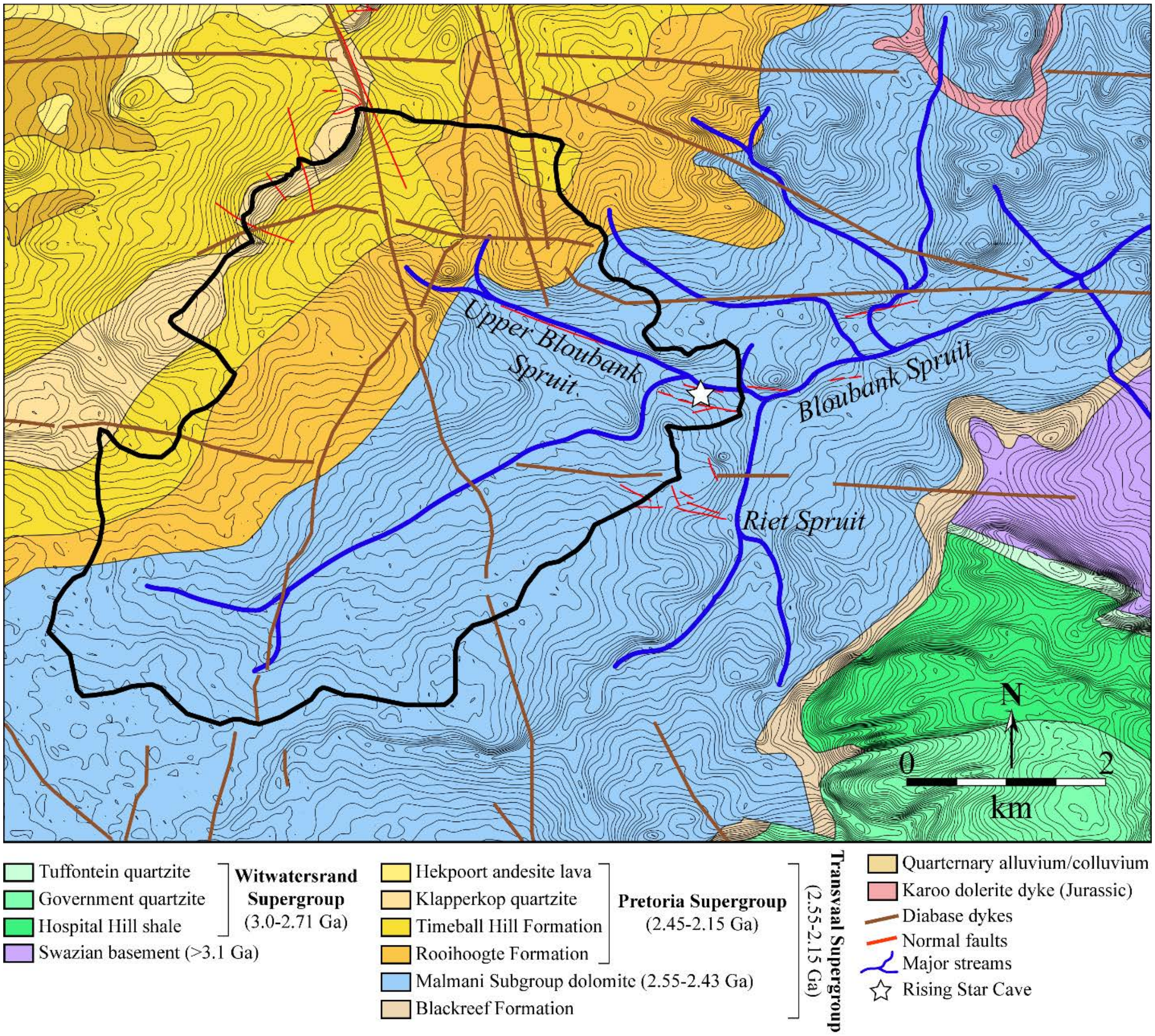

Figure 4. Upper Bloubank Spruit catchment divide (outlined in black) illustrating the local geology, surface geomorphology and major waterways that surround the Rising Star Cave landscape.

Rooihoogte Formation as described in Dirks and Berger (2013). A prominent west-northwest trending scarp, approximately 100 m north of Rising Star Cave, marks a sudden drop in the position of the bedrock surface. This scarp is straight and decorated with chert veins suggesting the presence of a fault surface. Directly north of this scarp, the bedrock is covered by a blanket of alluvial sediment. A water bore hole drilled into this sediment (~30 m north of the scarp) contains 22 m of alluvial sediment before reaching bedrock. The scarp has, therefore, been interpreted as a neo-tectonically active fault with a normal displacement component in recent (Pleistocene?) times of at least 22 m. The current course of the riverbed of the Upper Bloubank Spruit near Rising Star parallels this fault. A similar linear scarp demarcates the northern boundary of the Upper Bloubank Spruit valley, in line with the scarp below Swartkrans Cave to the east and has been interpreted to represent a second north-northwest trending fault (Fig. 2A in Chapter 2). Thus, the valley of the Upper Bloubank Spruit and the direction of river flow is largely controlled by several parallel fault surfaces that appear to have been neo-tectonically (i.e., during the Pliocene) active as a result of large-scale uplift of the region (Partridge, 2010; Dirks and Berger, 2013). This tectonic activity caused localised vertical displacements in the land surface, i.e., the formation of local scarps in the landscape, and causing gradual shifts in the position of the Upper Bloubank Spruit. The latter had profound impacts on the quantity and influx frequency of fluvial sediment deposits in Rising Star Cave (Chapter 2).

1.3.3. Geology of Rising Star Cave

Rising Star Cave is located in the southwest of the Cradle of Humankind UNESCO World Heritage Site, South Africa (7121914 S, 571325 E, Zone 35 J, UTM; WGS 84) in the Bloubank River valley, close to the banks of the Upper Bloubank Spruit, ~800 m, due west of the confluence with the Riet Spruit, approximately 35 km northwest of Johannesburg and ~2.2 and 1.1 km west to southwest of Sterkfontein Caves and Swartkrans, respectively (Figs. 1 & 2. and Chapter 2). The cave is positioned between 1450-1480 m above sea level but sits relatively close to the valley floor and is surrounded along the northeastern margin by a series of down-stepping, abandoned fluvial and strath terraces, possibly linked to earlier stages in the stream pattern of the Upper Bloubank Spruit (Chapter 2). A series of WNW-ESE trending, normal faults occur north and south of the cave (Dirks et al., 2015). A small (ephemeral) tributary streambed, the Upper Bloubank Spruit (Fig. 2), is positioned just north of the fault scarp, and circa 100 meters north from the cave entrance, with a general west-to-east flow direction during times of recharge, feeding into the larger Bloubank Spruit to the east. Currently, the stream bed is dry and borehole measurements indicate that the current water table is ~ 22 m below surface.

Rising Star Cave is classified as a network maze cave that consists of an extensive series of narrow interconnected chambers and passageways that formed in a ~25 m thick, 17 degrees west dipping section of chert-poor, stromatolite-rich dolomite within the Monte Christo Formation (Eriksson et al., 2006; Dirks et al., 2015, 2017) (Fig. 5 cave cross section). The cave is stratigraphically bound by two mylonitic shear zones and the roof of the cave is capped by a ~1-metre-thick intact chert marker horizon (Dirks et al., 2015; Kruger et al., 2016), which indicates that there are no direct connections to surface via this chert boundary. The west dipping strata defines primarily structural and lithologically controlled pathways for water movement, cave genesis, and the direction in which the cave has been, and is, progressing. Although the cave geometry is mostly structurally controlled and follows various joint and fracture patterns within the lower Monte Christo Formation, chemical dissolution along open conduits resulted in a series of dissolution chambers and roof collapse features (Dirks et al., 2015). Figure 5 shows a stratigraphic section of the dolomite interval that hosts the cave, with the stratigraphic position of the different chambers indicated. Most of the cave formed in a relatively chert-free, 18 m thick, section of dolomite above a major sheared shale horizon (i.e., between ~6-24 m in Fig. 5). The cave-hosting rock unit typically contains little siliciclastic detritus (Chapter 4), but local chert-rich and sandier intervals exist within the overall stratigraphy of the lower Monte Christo Formation. Irregular chert bands within this section of dolomite make up ~1.2 m of the stratigraphy, constituting less than 7% of the rock volume. Two micaceous shale horizons towards the base of the section represent <1% of the total rock volume affected by cave formation processes (Fig. 3).

The Rising Star Cave system consists of a series of interconnecting chambers and passageways (Fig. 5A). A small subset of the Rising Star Cave was investigated for this thesis: the Dinaledi Subsystem and Lesedi Chamber, which host the *Homo naledi* fossils, as well as the interconnecting chambers and passageways that connect to surface and lead to the aforementioned chambers, including the Postbox Chamber, Upper and Middle Postbox, Superman Chamber, Superman Crawl, and Dragon's Back Chamber (Fig. 5B). The Dinaledi Subsystem is further subdivided into the Chaos Chamber, Hill Antechamber, and the Dinaledi Chamber (Fig. 5B). Both the Dinaledi and Lesedi chambers host holotype *H. naledi* fossils, including a near complete male skull form the latter chamber (Fig. 6; Berger et al., 2015; Dirks et al., 2015; Hawks et al., 2017), but the vast majority of fossil material is concentrated in the Dinaledi Chamber, which lies ~ 80 m away from the present entrance into the cave system. The Dinaledi Chamber can only be accessed via the Dragon’s Back Chamber, which in turn can be accessed via a direct route that passes through the Postbox Chamber; or along a more complex maze of fractures via the Superman Chamber (Fig. 2B; Dirks et al., 2015).

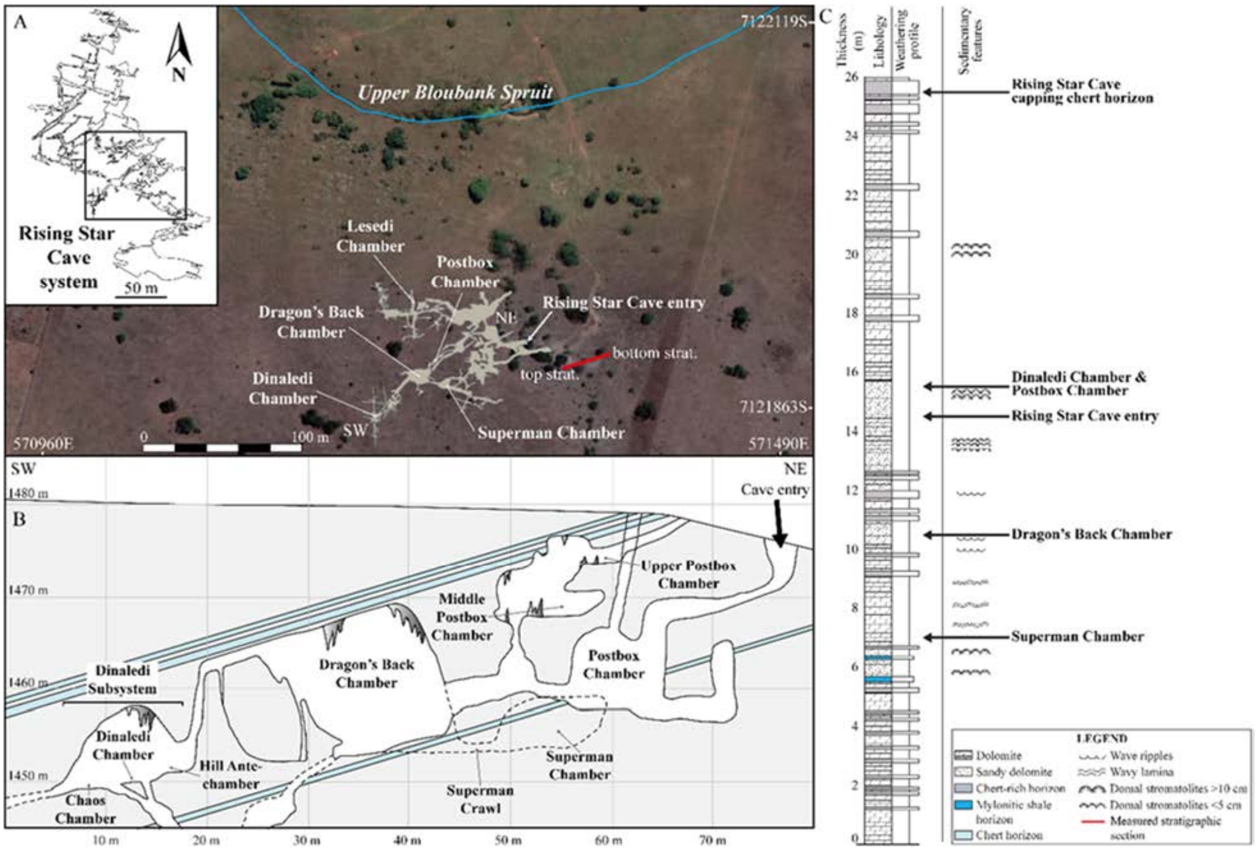

Figure 5. Stratigraphic position of Rising Star Cave within the lower Monte Christo Formation. A. Overview maps of the Rising Star Cave system and Rising Star Cave (inset); B. NE-SW cross section profile of primary investigated Rising Star Cave chambers (the Lesedi Chamber is out of scope of the cross section); C. partial stratigraphic section of the lower Monte Christo Formation illustrating the stratigraphic position of the different cave chambers within the dolomite.

1.3.4. Rising Star Cave sediments

1.3.4.1. Clastic sediments— Clastic sediments primarily consist of poorly consolidated, orange-red sediments that are widely distributed throughout the Postbox, Dragon's Back, Superman and Dinaledi Chambers and include laminated mud, silt, sand and conglomerate (e.g., Dirks et al., 2017). These deposits are primarily rich in micro-mammal, and locally macro-mammal fossils. In the Dinaledi Chamber these sediments are furthermore associated with the *H. naledi* fossils (Dirks et al., 2015; Wiersma et al., 2020). Away from these chambers, in the remainder of the accessible parts of the cave system, little additional sediment accumulated.

The fossiliferous orange-red clastic sediments in the Dinaledi, Dragon's Back, Postbox and Superman chambers, are part of a single depositional system that can be compared to a

Figure 6. *Homo naledi* material collected from Rising Star Cave. A. Composite skeleton and the holotype of *Homo naledi* including associated fossil material comprising multiple skeletons from the Dinaledi Chamber. Length of the skeleton is approximately 1.5 m (image from Berger et al., 2015; fig.1). B. Various, *in situ, H. naledi* long bones, including an ulna on the left (image courtesy of Eric M. Roberts). C. Partial, *in situ*, *H. naledi* femur (image courtesy of Eric M. Roberts). D.

Composite skeleton of additional *Homo naledi* material (specimen LES1, 'Neo') recovered from the Lesedi Chamber. The femur possibly belongs to a different individual from the same chamber (image from Hawks et al., 2017; fig. 4). E. Skull and mandibles from LES1 (image from Hawks et al., 2017; fig. 5).

subterranean debris cone, which partly filled the network of chambers and connecting passageways. The coarsest-grained sediments on this debris cone accumulated in the Postbox Chamber, and the average grain size of sediments decreases when moving into the Dragon’s Back and Superman Chambers. The most distal part of the cone is represented by sediment in the Dinaledi Chamber, which is dominated by mud deposits with little sand and significantly less quartz (Dirks et al., 2015; Wiersma et al., 2020).

The apex of the debris cone is characterized by coarse, poorly sorted conglomerate that entered the cave via a vertical shaft in the roof of the Postbox Chamber. This shaft opened to surface, about 4 m above the current entry point into the cave and is now filled with loosely packed breccia and no longer accessible. From its apex, sediment spilled down cave passages into the Dragon's Back and Superman chambers, where erosion remnants along cave walls indicate that up to 3 m of sediment accumulated. No clastic sediment coarser than sand washed directly from the Dragon’s Back Chamber into the Dinaledi Chamber due to the presence of a 5 m high sill that consists of *in situ* dolomite, which blocked high energy water flow (Dirks et al., 2015, 2017; Wiersma et al., 2020). However, fine-grained orange-red mud and silt, deposited in suspension, did pass through fractures in the walls, and accumulated in the Dinaledi chamber (Wiersma et al., 2020).

Erosional remnants of orange-red sandstone and mudstone indicate that significant volumes of clastic sediment once filled the chambers along the entry route into the Dinaledi Chambers, but most of this sediment was removed via floor drains that exist in most chambers (e.g., Dirks et al., 2015, 2017). Sediment accumulation and erosion alternated with periods of flowstone formation in the cave (e.g., Dirks et al., 2017), and it is common to find accumulations of orange-red sediment covered by a drape of flowstone. Where this happens the sediments below the flowstone are indurated with carbonate cement, and these sediments are semi-lithified. Some flowstones are extensive and can be traced as semi-continuous sheets across most of the chambers. These flowstones have been used to subdivide the sediments into five stratigraphic units that are variably preserved in the different chambers. Locally, these units occur as laterally extensive deposits and as hanging remnants along the cave wall or underneath flowstones. Each of the sedimentary units are architecturally complex and preserve similar facies across individual chambers, but they are not necessarily time equivalent, making inter-chamber stratigraphic correlations difficult, unless bounding flowstones can be traced from one chamber to the next. Nevertheless, a relative age can be determined for each of the units (and their bounding flowstones), which has provided the framework for this study (Chapter 3).

From old to young, the five lithostratigraphic units include: 1) lithified mud clast breccia (LMCB) deposits; 2) semi-lithified layered orange-pink sand (LOS); 3) unlithified laminated orange-red mud (LORM facies in Wiersma et al., 2020); 4) unlithified mud clast breccia (UMCB facies in Wiersma et al., 2020); and 5) unlithified orange-red cave floor sediment (Dirks et al., 2015, 2017). In addition, a coarse chert-dolomite breccia deposit with rare fragments of Klapperkop quartzite, form a further unit near the apex of the debris cone in the Postbox Chamber. This coarse breccia is interlayered with LOS-like deposits and is possibly overlain by LORM sediment.

All five lithostratigraphic units are fossiliferous to some extent, with the UMCB in the Dinaledi Chamber hosting the *H. naledi* fossils (Dirks et al., 2015, 2017). Fossils in the lithified mud clast breccia (LMCB) and LOS sediments consist of isolated elements assigned to large vertebrates (e.g., Bovidae, Felidae and *Papio*) and include vertebrae, limb elements, and few teeth and cranial bones. In the LORM facies, locally dense concentrations of fossils occur within sandier lenses dominated by disarticulated cranial and post-cranial elements of micro-mammals (Rodentia and Soricidae).

The LMCB deposits are the oldest deposits recognized along the access route into the Dinaledi Chamber and are preserved as hanging remnants underneath the oldest generation of flowstones that can be traced as near-continuous sheets from the Dinaledi Chamber via the Dragon's Back Chamber to the Superman, and Postbox chambers (Dirks et al., 2015, 2017). The capping flowstones could not be accurately dated with U-Th and are assumed to be older than 600 ka (Dirks et al., 2017). These LMCB sediments can be found in other parts of the cave as well, and they do not form part of the debris cone described above, but constitute a separate sedimentary system that predated the opening of the roof in the Postbox Chamber and entry of *H. naledi* (Dirks et al., 2017). LMCB sediment consists of clast-supported mud clasts embedded in a dark brown fine-grained matrix of silt and clay. The mud clasts are typically angular, mm-to-cm-sized, and orange-brown in color with local staining of secondary Mn-Fe oxides and oxyhydroxides.

The LOS unit forms extensive deposits in the Dragon's Back Chamber where it occurs as erosion remnants on top of LMCB deposits. It formed prior to the deposition of a prominent flowstone horizon that can be traced across the Dragon's Back chamber and from there into the Superman and Postbox chambers. The capping flowstone was dated to ~500 ka using Al-Be cosmogenic dating techniques (Makhubela et al., 2019), and the LOS sediments form the oldest unit linked to the debris cone, predating the entry of *H. naledi*. LOS sediments consist of orange-pink heterolithic, quartz-rich sandstone composed of medium to coarse-grained, sub-rounded and rounded grains. Locally, fluvial architectures such as cut-and-fill, cross-bedding, and normally graded beds are preserved.

Unlithified LORM sediments are the most widely distributed unit along the debris cone, and have been recorded from the Dragon's Back, Postbox, Superman and the Dinaledi chambers. They were dated in the Dinaledi Chamber from two separate deposits with ages of ~350 ka and ~235 ka (Dirks et al. 2017), while Makhubela et al. (2019) report ages of ~220 ka and ~175 ka for LORM sediments in the Postbox and Dragon's Back chambers respectively. These depositional ages overlap with the age of the *H. naledi* fossils (335-236 ka; Dirks et al., 2017). LORM sediments overlie LMCB and LOS deposits and occur as isolated erosion remnants along the cave floor, as remnants on top of flowstone, as cave wall fracture fill, and as localized patchy remnants along the cave walls (Dirks et al., 2015, 2017; Wiersma et al., 2020). The deposits consist primarily of illite-rich laminated mud that is locally interbedded with fossiliferous sand lenses dominated by very fine to fine-grained, quartz.

The youngest unit in the cave consists of UMCB sediments, which formed highly localized deposits distributed along the cave floors of the Dinaledi, Postbox, and Superman chambers. In the Dinaledi Chamber, UMCB sediments cover ~350 ka LORM sediments and they are covered by flow stones as old as ~105 ka (Dirks et al., 2015, 2017), but their formation locally continues today (Wiersma et al., 2020). The facies formed largely *in situ* from adjacent LORM deposits via sedimentary auto-brecciation (Wiersma et al., 2020), and hence the UMCB deposits always occur together with deposits of LORM. Compositionally and architecturally, the UMCB sediments are similar to LORM sediments; with millimetre-to-centimetre-sized, orange-brown and Mn-Fe-oxide stained, angular mud clasts 'suspended' in a very fine-grained dark brown-grey silt and clay matrix.

In addition to the five units for which erosion remnants are preserved within the cave, the cave floor is covered by floor sediments that are largely composed of loose sand and mud mixed with erosion products of all sediment types as well as fragments of dolomite wall rock and flowstone (e.g., Dirks et al., 2015; Wiersma et al., 2020). Viewed together, the LORM and UMCB sediments formed at the time *H. naledi* interacted with the cave between 335-236 ka (Dirks et al. 2017), and these sediments were targeted for study in chapters 3, 4, and 5. The LORM sediments are distributed widely as part of the debris cone deposits with major sediment input through the roof of the Postbox Chamber and small contributions from the Upper Postbox Chamber. The UMCB deposits resulted from localized reworking of LORM sediments at isolated localities within the cave (Wiersma et al., 2020).

1.3.4.2. Chemical sediments— Chemical sediments, i.e., speleothems in Rising Star Cave, consist chiefly of flowstone deposits and drip points that are widely distributed throughout the cave, with extensive vertical and horizontal flowstone deposits being common. Drip points are common throughout the entire cave, leaching calcite-enriched vadose waters into the cave, and are indicative of direct connections to surface (Dirks et al., 2015; Robbins et al., 2021). Here, only the flowstones are being discussed because they provide the most relevant depositional and erosional context with the clastic sediments, which are described in detail in Chapter 3. Seven stratigraphically distinct flowstone groups are preserved throughout Rising Star Cave and provide relative age constraints obtained from U-series techniques (Robbins et al., 2021) for the clastic sediments in the cave. Three major flowstone groups (collectively referred to from old to young as the 'Green', 'Blue', and 'Red' flowstones in Robbins et al., 2021) are most widely distributed throughout the observed cave chambers and provide the most relevant age constraints for the clastic sediments in the cave. Minor flowstone groups with local, chamber specific, distributions are referred to from old to young as 'Purple', 'Pink', 'Yellow', and 'Grey' flowstones (Robbins et al., 2021).

The oldest, 600 ± 230 ka, 'Green' flowstones are ~25-30 cm thick (Robbins et al. 2021) and is the most extensively distributed series of observed flowstones in the cave, forming a continuous false roof that can be traced throughout the Postbox, Dragon's Back and Superman chambers. The flowstone overlies primarily LMCB deposits and locally intercalates as thin sheets between several

LMCB deposits where it forms demarcating boundaries between clastic sediments, providing temporal constraints for alternating periods of erosion and deposition (Robbins et al., 2021).

The second oldest, ~600 ka, prominent flowstone horizon, termed the "Blue" flowstone (Robbins et al., 2021) forms a semi-continuous undulating sheet that is up to 20 cm thick and covers various accumulations of LMCB deposits. This flowstone deposit is present in the Dragon's Back Chamber and continues into the Superman Chamber occupying a near parallel position, 0.2-2.0 m above the 'Green' flowstones.

The youngest major flowstone horizon, referred to as the 'Red' flowstone yields ages between 500-400 ka (Robbins et al., 2021). This flowstone deposit occurs in the Dragon's Back and Superman chambers and potentially in the Postbox Chamber. In the Dragon's Back Chamber, the flowstone horizon forms a ~15 cm thick false roof in the NW corner of the chamber and overlies primarily erosion remnants of fossiliferous LOS deposits. In the south-central part of the chamber, the 'Red' flowstone formed on top of erosion remnants of 'Green' and 'Blue' flowstone deposits. The 'Red' flowstone occurs as thin hardground erosion remnants in the Superman Chamber, where it is preserved as thin false roofs in crevasses and niches, as well as overlying LOS sediments. In the eastern part of the Superman Chamber, the 'Red' flowstone deposit overlies the west-dipping 'Green' flowstone (Robbins et al., 2021).

Two minor, 'Purple' (~225-190 ka) and 'Pink' (~160 ka), flowstone deposits are exclusively observed in the Dragon's Back Chamber (Robbins et al., 2021). The oldest, 'Purple' flowstones occur in multiple locations within the chamber, most prominently as a 1-5 cm thick drape overlying a small debris cone at the base of the faulted Dragon's Back block in the SW part of the chamber. Other occurrences of the 'Purple' flowstone include a thin, up to 2 cm thick calcite layer on top of the 'Red' flowstone in the eastern part of the chamber, and above the entrance of Superman Crawl. The 'Pink' flowstone occurs as a thin (<1 cm thick) mud-rich drape in the NW corner of Dragon's Back Chamber, covering erosion remnants of LOS and channel infill MOS sediments (Robbins et al. 2021).

In Postbox Chamber, directly below the sediment entry shaft, a single flowstone sheet, <1 m wide and up to 5 cm thick, is referred to as the 'Yellow' flowstone and yields an age of ~300 ka (Robbins et al. 2021). This flowstone overlies a ~600 ±153 ka (Makhubela, 2019) polymictic sediment debris cone and is overlain by clast supported breccia deposits.

The youngest (~110-90, 70, 50, 30 and 10 ka), 'Grey' flowstones consist of clear white calcite and form drapes, curtains, and (drip point) pool rims atop erosion remnants of all other flowstone and sediment deposits in the Dragon's Back and Superman chambers (Robbins et al. 2021).

1.3.4.3. Previous age dating in the Dinaledi Chamber— Cave sediments, flowstones and fossils from Rising Star Cave were targeted for age dating to constrain the age of the *Homo naledi* fossils in the Dinaledi Chamber and Hill Antechamber within the Dinaledi Subsystem (Dirks et al., 2017). Seventeen U-Th disequilibrium ages obtained from three broad groups of flowstones in the Dinaledi subsystem yielded ages ranging from 502 +181/-53 ka to 9.05 ± 0.06 ka (Dirks et al., 2017). The youngest group of flowstones (equivalent to the 'Grey' flowstones in Robbins et al. 2021, and Flowstone group 3 in Dirks et al., 2017) overlies older clastic sediments and range from 104 ka to 9 ka. The second group yielded ages of 290 ± 6 ka and 242 ± 5 ka (Flowstone group 1 of Dirks et al., 2017) and consists of partially resorbed flowstones that were used to constrain the minimum age of *H. naledi* fossils (Dirks et al., 2017; Robbins et al. 2021). The third group consists of multiple layers of old flowstones that make up a hanging remnant which overlies erosion remnants of LMCB sediments and have been interpreted as the equivalent to the 'Green' or 'Blue' flowstones in the Dragon's Back Chamber (Dirks et al., 2017). The upper flowstone layers produced ages of 502-478 ka and the lower part yielded an age >780 ka based on a reverse paleomagnetic polarity (Dirks et al., 2017).

Clastic LORM sediment deposits from the Dinaledi Chamber have also been dated. These sediments are intercalated with flowstone deposits and occur as erosion remnants along the floor of the Dinaledi Chamber (Dirks et al., 2017). Optical Stimulated Luminescence (OSL) ages of these LORM sediments include 353 ± 61 ka for an older phase of LORM sediments (Unit 1a of Dirks et al., 2017) and 241 ± 37 ka and 231 ± 41 ka for a younger phase of microfossil-bearing LORM sediments (Unit 1b of Dirks et al., 2017). The older sediments are covered by UMCB deposits containing *H. naledi* fossils.

The *H. naledi* fossils themselves were dated by combining U-series and Electron Spin Resonance (ESR) techniques and yielded a best age estimate for 2 sets of fossil teeth of 253 +82/–70 ka. In combination with age constraints derived from the flowstones that cover the fossils, this resulted in an age estimate for the fossils of 335-236 ka (Dirks et al., 2017). In addition, U-Th dating of the teeth produced a cluster of ages around 195 ka, 90-115 ka, 80 ka, 70 ka, and 50 ka (Dirks et al., 2017). These ages were interpreted to date U-uptake events in teeth embedded in the sediments, i.e. probably reflecting periods of time that the cave was wet (Robbins et al. 2021).

Chapter Two

Geology and geomorphological setting of the hominin-bearing (*Homo naledi*) Rising Star Cave, Cradle of Humankind, South Africa

Abstract

Investigation of the geomorphic evolution of the Rising Star Cave landscape has led to suggest that the cave opened to surface around 600 ka, initiating coarse sediments to enter the cave via the Postbox Chamber. Sedimentation events become increasingly rare from ~400 ka onwards, and they would have largely stopped by the time *H. naledi* entered the cave.

The landscape surrounding Rising Star Cave consists of three geomorphic domains, two of which are characterised by a series of down-stepping, degraded strath and fluvial terraces interspersed with erosional scarps of exposed chert-bearing dolomite that form subtle, but clear steps in the landscape. This cave system formed in Palaeoproterozoic-aged rocks of the Malmani Subgroup (Transvaal Supergroup). Mapped, WNW trending faults in the host rock near the cave system indicate a possible relationship between fault movement and terrace formation. The third geomorphic domain is located north of the mapped fault and includes the ephemeral Upper Bloubank Spruit riverbed which is positioned in between a pair of alluvial terraces and is underlain by at least 22 m of alluvial material. The current streambed is positioned at 1460 m, ~10 m below the main cave entrance, and ~12 m below a paleo-entrance that existed in the roof of the Postbox Chamber and the Upper Postbox Chamber, both acting as entry points for most of the clastic sediments found in the cave.

The area surrounding Rising Star Cave underwent active geomorphological changes resulting in distinct geomorphologic domains and associated sediment type signatures. The general mineralogy of the various surface sediments blanketing the Rising Star Cave area is largely similar, i.e., the major mineral constituents are quartz, illite, and muscovite, for which the

relative abundance varies little from one geomorphic domain to the next. The underlying lithological units of the lower Monte Christo Formation and especially the shale and chert horizons, seem to be the primary contributors of these minerals. Each of the strath terraces preserves large (up to 20 cm) rounded cobbles of quartzite derived from the Klapperkop Member of the overlying and younger Palaeoproterozoic-aged Timeball Hill Formation (Pretoria Group). In contrast, the soil mineral concentrations including the Mn-Fe-oxyhydroxides and siderite, vary strongly across the various geomorphic domains, reflecting the importance of secondary depositional and soil forming processes, and especially the time over which such processes interacted with the surface sediments. The current morphology of the Rising Star Cave system and the geomorphology of the surrounding land surface of the Upper Bloubank Spruit catchment are the combined result of structural, lithological and chemically controlled Earth surface processes. The main controls on the geomorphology of the cave and the surrounding landscape are: 1. the dolomite lithology and orientation of the primary layering, layer-parallel shears and fracture patterns within the lower Monte Christo Formation dolomite, which determined the morphology of the cave; 2. the faults along the valley floor, which influenced the flow direction of the Upper Bloubank Spruit and deposition of the quaternary deposits north of the fault; and 3. the confluence of the Upper Bloubank Spruit with the Riet Spruit.

2.1. Introduction

Starting approximately 4 million years ago during the Pliocene, uplift and subsequent incision and denudation of the African Erosion Surface on the southern African landscape, resulted in the formation and exposure of hundreds of network maze cave systems (Partridge and Maud, 1987; Dirks & Berger 2013). These caves had formed along layer-parallel shear zones and sets of upright faults and joints, within the 2.55-2.45 Ga chert-rich dolomitic successions of the Malmani Subgroup, in the NE section of the South African Plateau (Martini, 2006; Eriksson et al., 2006; Dirks and Berger, 2013; Dirks et al., 2016). Many of these cave systems are located within the Cradle of Humankind (CoH) UNESCO World Heritage Site in South Africa (Dirks and Berger, 2013), where several of the caves form highly significant palaeoanthropological and geological sites, preserving important Pliocene and Pleistocene-aged fossil hominin remains, including *Homo naledi*, *Australopithecus sediba*, *Au. africanus, Au. robustus, Paranthropus robustus* (Brain, 1993; Tobias, 2000; Berger et al., 2010; Dirks et al., 2010; Berger et al., 2015; Hawks et al., 2017), and other African vertebrate faunas of similar age (e.g., Gommery et al., 2008, 2012; De Ruiter, 2003; Val et al., 2015; Van Zyl et al., 2016 and references therein).

The southern African landscape, including the CoH area, is old and shaped through Mesozoic peneplanation, forming the so-called "African Erosion Surface". This was followed by at least two periods of uplift and rejuvenation during Miocene and Pliocene times (Partridge and Maud, 1987). Extensive incision and denudation of the African Erosion Surface in the CoH region during the last 4 Ma transformed the area into a heterogenous and dissected landscape, characterised by plateau areas underlain by remnants of the African Erosion Surface, and deeply incised valleys. Valley incision exposed the underlying Malmani Subgroup dolomite lithologies and some of the caves hosted within them (Dirks and Berger, 2013; Herries et al., 2019). These caves are preferentially distributed along sheared lithological boundaries within the dolomites (Dirks et al., 2010) in combination with NNE- and ESE-trending, cross-cutting joint sets that became permeable to groundwater and therefore susceptible to cave formation as a result of NW-SE directed extension during uplift (Dirks and Berger, 2013). The formation and opening of the cave systems in the CoH is, thus, a geologically relatively young phenomenon (Dirks and Berger, 2013; Dirks et al., 2016).

Most of the fossiliferous caves in the CoH are situated between 1420-1500 m above sea level. Many caves, especially those along valley slopes occur as deeply eroded and (partly) unroofed remnants, exposing the remains of (fossiliferous) cave breccia and alluvial sediments that once filled the caves (e.g., Berger and Tobias, 1994; Pickering et al., 2007; Dirks et al., 2010; Herries and Shaw, 2011; Braga et al., 2013; Herries and Adams, 2013; Bruxelles et al., 2014; Herries et al., 2014 and references therein). Other caves that are less affected by surficial erosion are left intact or are only partially unroofed and contain naturally eroded openings that consist chiefly of vertical or sloping shafts that connect to surface (e.g., Rising Star Cave, Gladysvale Cave, Sterkfontein Cave). Caves with entries along the valley slopes have been laterally drained through river incision and have become hydrologically abandoned and are no longer being deepened by phreatic water (e.g., Herries et al., 2019).

Although Bailey et al. (2011) argue for a dynamic, fault-controlled landscape in the CoH, slow basin-average erosion rates on the order of 3.0 ± 0.28 m/Ma to 4.15 ± 0.37 m/Ma (Dirks et al., 2010; Dirks et al., 2015; Makubela et al., 2019) suggest that the modern physical landscape in the CoH has changed relatively little over the past few million years, and that the current landscape is a close reflection of the recent past (Dirks and Berger, 2013). Some unroofed cave systems are spatially associated with nearby stream systems, which locally accelerated erosion of the rock surfaces. Thus, erosion along the creek bed below Gladysvale cave locally reached a rate of 53 ± 9 m/Ma (Dirks et al., 2010), whilst the dolomite scarp exposing the entrance into Rising Star Cave and representing the side of an old river channel experienced a denudation rate of 9.5 ± 0.7m/ Ma (Makhubela et al., 2019).

The evolution of Rising Star Cave in relation to the local landscape and geomorphology was investigated by Makhubela et al. (2019), who determined denudation rates and soil residence times for land surfaces above and below Rising Star Cave with the use of cosmogenic ^{10}Be and ^{26}Al isotopes. They found that ^{10}Be denudation rates obtained from pebbles and sand in soil averaged ~3.3 ± 0.3 m/Ma, which is 2-3 times slower than the measured bedrock denudation rate of 9.5 ± 0.7 m/Ma. They also found that the ^{26}Al/^{10}Be ratio of 5.12 ± 0.27 for soil samples is significantly lower than the surface production ratio of 6.75. Their results indicate that the soils above the cave experienced prolonged surface residence times of up to 1.5 Ma whilst they were affected by vertical mixing (bioturbation). Their results also indicate that basin-averaged denudation rates using ^{10}Be alone may underestimate the true denudation rate, whilst recognizing that the erosional scarp along which Rising Star Cave is exposed, was probably cut by past fluvial action.

Whilst the work by Makhubela et al. (2019) placed constraints on the landscape evolution and soil behaviour around Rising Star Cave, their work was not placed within a tightly constrained geomorphological context. The aim of this chapter is to provide a detailed description of the geomorphological setting of Rising Star Cave in relation to the surface geology by utilizing stratigraphic data of the cave-forming lithologies, geomorphic landscape features around the cave, and quantitative and qualitative characterisation of the surface sediments in relation to the different landscape features. In so doing, and by making use of the age constraints provided by Makhubela et al. (2019), Dirks et al. (2017), and Robbins et al. (2021) this research illustrates how the landscape around Rising Star Cave may have changed over time. Importantly the past hydrodynamic regimes of the Upper Bloubank Spruit, which currently flows ~10 m below the cave, is explored as well as its past interactions with the cave system. This is particularly important when assessing if the river may have been able to deposit alluvial sediment into the cave, and how this interaction between the river and the cave changed over time. The interpretations made in this study regarding the geomorphology and past locations of the Upper Bloubank Spruit as well as the timing of fluvial migration are limited to qualitative observations made in the field. This also applies for the presence of the observed fault scarps, which have been interpreted as neo-tectonically active during the Pliocene based on available literature. Further quantitative studies regarding more accurate timing of faulting is necessary to better interpret the timing and characterization of the fault scarps.

2.2. Materials and Methods

2.2.1. Rising Star catchment mapping

Catchment geology was obtained from the 1:1,000,000 scale map of the Johannesburg dome provided by the Council for Geoscience, South Africa. Within the catchment, a small area of ~1 km^2 surrounding Rising Star Cave was mapped for geomorphic landscape features including faults, colluvial surfaces, alluvial, strath- (bedrock) and cut-and-fill terraces, and fluvial features of the Upper Bloubank Spruit. These data were combined with a detailed topographic survey with 0.5 m height intervals, obtained by drone mapping across the Rising Star Cave and its immediate surroundings. Mapping was performed in QGIS 3.4 (Madeira) and Google Earth Pro using field observations combined with open source geospatial and satellite data.

2.2.2. Stratigraphic measurements

An ~140 m thick stratigraphic section of chert-bearing stromatolite-rich dolomite of the lower Monte Christo Formation was measured and described along a ~450 m east-west-running transect, 40 m north of the cave entrance. This stratigraphic interval was described and measured with two main goals in mind: 1) to record lithological patterns and associated sedimentary features throughout the stratigraphic interval, measuring the distribution, density and frequency of dolomitic vs non-dolomitic (chert, shale, and sand) horizons to determine if any particular lithological units controlled cave formation; 2) to determine to what extent the mineral composition of the strata may have contributed to the composition of soil and sediment accumulating on the surface. Stratigraphic measurements were performed using standard geological mapping techniques, graphing paper, a measuring reel, Jacobs staff and Brunton International Transit compass. A Garmin E-trex H GPS unit was used to record the location of sedimentary features. All recordings were made in UTM, WGS84 (zone 35J). Sedimentary features, including lithologies, bedding, cross-stratification, and stromatolites were recorded and photographed using a Nikon 35 mm digital camera. Basic trigonometry was applied to correct for true thickness of the strata measured, using the following equation:

$$Sin\ \theta = \frac{Opposite}{Hypothenuse}$$

"*Theta*" is the stratigraphic dip angle from horizontal (17 degrees), "*Opposite*" is the true thickness of the strata (138 m) and "*Hypothenuse*" is the horizontal distance measured (~450 m).

2.2.3. Rock and sediment sampling methods

Seven rock samples (D1-7) were collected along a 26 m stratigraphic section within the chert-poor lithologies of the lower Monte Christo Formation that hosts the Rising Star Cave (Table 1). Samples include four non-sandy dolomite units (D1, D2, D5, D7); a single sandy dolomite (D4); a shale band (D3); and a shale-rich mylonite sample (D6). These samples were

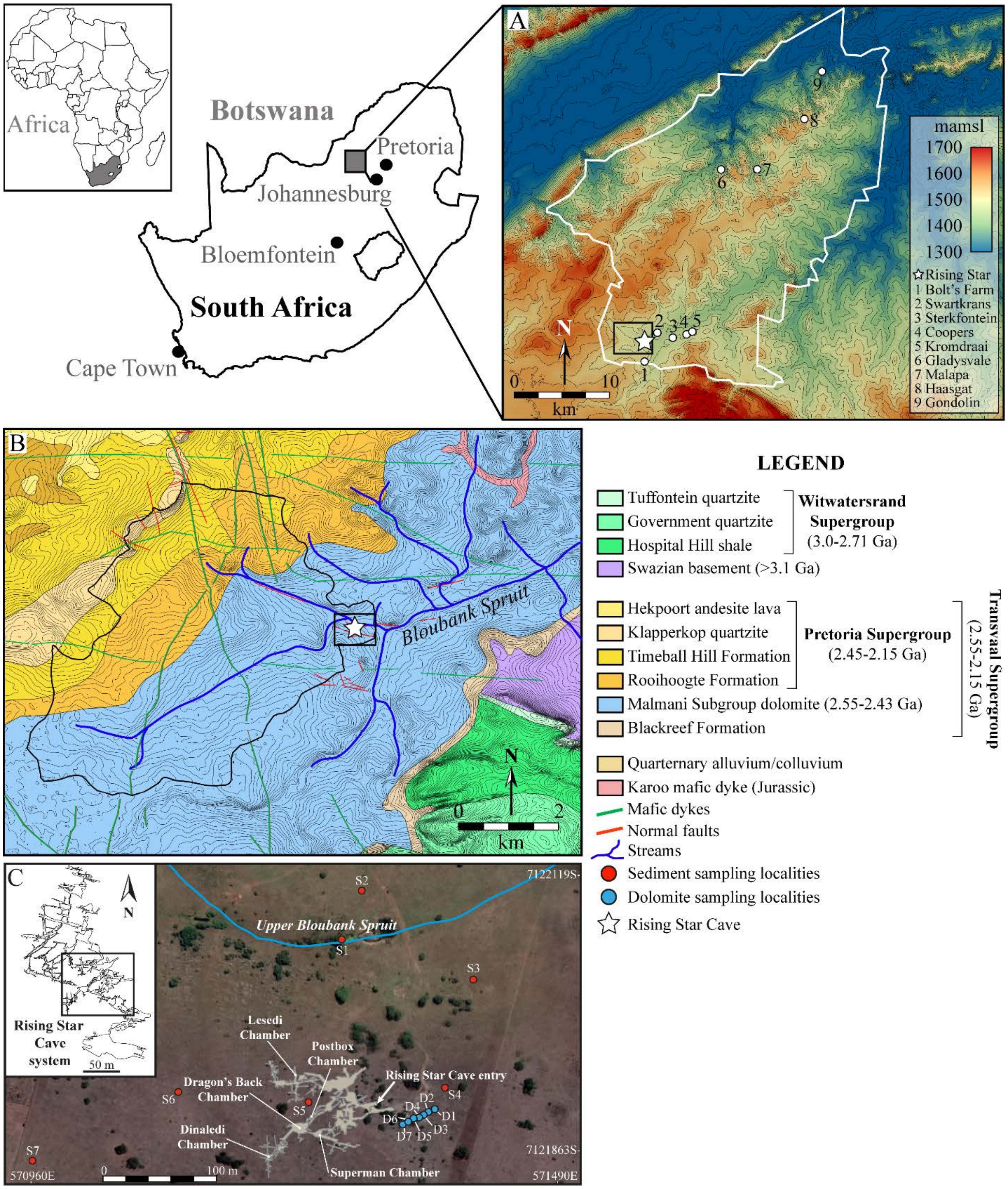

Figure 1. Maps and location of study area. (A), Major hominin-bearing cave localities in the Cradle of Humankind, South Africa; (B), Inset from (A) illustrates the Upper Bloubank Spruit catchment area outlined in black and includes topography, geology and major streams; (C), Close up of the Rising Star Cave site and sample localities.

utilized for thin section petrography and bulk geochemistry x-ray diffraction (XRD) (Table 1, Fig. 1C).

Seven unconsolidated surface sediment samples (S1-S7) were collected from localities near the cave (Table 1, Fig. 1C). To ensure *in situ*, i.e., non-disturbed, soil collection, auger sampling was done at depths of ~15-50 cm. Sample S1 was obtained from the Upper Bloubank Spruit riverbed. Sample S2 was taken from a thick alluvial terrace immediately north of the riverbed. Samples S3 and S4 were collected from two successive strath terraces immediately below the cave entrance. Sediment sample S5 was collected from surface soil directly above the cave, and samples S6 and S7 were collected up-slope, west of the cave. The surface samples were collected for grain size analysis and sediment type classification, XRD, and compositional and textural analysis via mineral liberation analysis (MLA).

Table 1. Samples and analytical methods used in this study.

			Analysis performed		
Sample number	Field number	Lithology	XRD	Thin section petrography	MLA
S1	190517JW1	surface sediment	X		X
S2	190517JW2	surface sediment	X		X
S3	190517JW3	surface sediment	X		X
S4	190517JW4	surface sediment	X		X
S5	190517JW5	surface sediment	X		X
S6	190517JW6	surface sediment	X		X
S7	190517JW7	surface sediment	X		X
D1	160517JW1	non-sandy dolomite	X	X	
D2	160517JW2	non-sandy dolomite		X	
D3	170517JW1	muscovite/illite shale	X	X	
D4	160517JW6	sandy dolomite		X	
D5	160517JW7	non-sandy dolomite		X	
D6	260517JW7	shale-rich mylonite	X	X	
D7	160517JW11	non-sandy dolomite		X	

2.2.4. Analytical methods

Grain-size analyses were performed on the unconsolidated sediments (S1-7) using the ASTM D421 (2007) and ASTM D422 (2007) standardized methods. The initial dry weight for each sample was 200 grams. Size fractions of ≥500 µm were dry-sieved, (4,000-2,800-2,000-1,000-500 µm sieves), whereas the <500 µm size fractions was analysed with the hydrometer method using a calibrated H-152 model hydrometer. To test for sediment types, the cumulative frequency percentages derived from the grain size analysis were implemented into the statistical software package GSSTAT version 2.04 (Poppe et al., 2004) to test each sample for the percent gravel, sand, silt and clay. The analysis was performed using the Inclusive Graphics calculation method (Folk, 1974) with no extrapolation parameters applied, and cumulative frequency percentages selected for file input and output. The resulting GSSTAT data was implemented into the sediment classification software package SEDCLASS version 1.0 (Poppe et al., 2003) to determine the sediment type for each of the unconsolidated sediment samples based on the Folk (1954, 1974) classifications. The sediment types were visualized in SEDPLOT version 1.0 (Poppe et al., 2008) on the Folk (1954, 1974) sediment classification diagram.

Rock samples (D1-7) prepared for thin section petrography were cleaned with water to remove residual dirt and cut into 2x3x5 cm blocks using an electrical rock saw. Conventional covered thin sectionswere prepared by Ingham Petrographics Lab, Ingham, Australia.

Bulk geochemical analyses were carried out using standard X-ray diffraction methods and were performed at the Geo XRD & XRF lab at North West University, South Africa.

Mineral Liberation Analyses (MLA) were carried out to investigate the modal mineralogy of unlithified surface sediments, focusing on the sand size fraction. Mineralogical comparisons were made between the main detrital constituents (e.g. quartz, micas, clays, carbonates and bone fragments), and alteration minerals (e.g. mainly Fe-Mn oxyhydroxides) that formed as a result of diagenetic and soil forming processes (Wiersma et al., 2020). Subsamples of the sediments were sieved, and the 0.5-1 mm size fraction was retained for grain mounts. Each grain mount contained on average ~350 individual grains. A silicone mould with a 2.5 cm inner diameter was placed on the glass plate with double-sided tape, on which approximately 5 gram of the 0.5-1 mm size fraction was mounted. Excess grains were removed from the mount and ~ 6 cc of two-compound resin was poured into the mould to produce a puck. The pucks were polished to expose the mineral grains for analysis. Prior to analysis, the polished pucks were carbon-coated, and samples were analysed using a FEI Quanta 400 scanning electron microscope (SEM) equipped with energy dispersive X-ray (EDX) spectrometers and mineral liberation analyzer software v.3.1.4.683 that automates microscope operation and data acquisition (Sylvester, 2012). The MLA measurements are based on backscatter electron (BSE) image analysis. Shape analyses were carried out for each sample to determine mean roundness and sphericity of the grains, using the 64-bit Fiji software package (Schindelin et al., 2012). Mineral liberation analysis and data processing were performed at the MLA/SEM lab at Memorial University, Newfoundland, Canada.

2.3. Geological and Geomorphological Setting

The following description of the geological setting partly repeats the 'Geological and Geomorphological Setting' section in Chapter 1. However, the repeated material has been included here so as not to disturb the flow of the chapter, which will be submitted as a paper.

2.3.1. Upper Bloubank Spruit catchment

The catchment area of the Upper Bloubank Spruit above Rising Star Cave covers ~47 km^2 and it is situated in the southwest corner of the CoH (Fig. 1B). The highest point within the catchment area is ~1670 metres above sea level and occurs along a prominent quartzitic ridge of Klapperkop Member that forms the Catchment divide to the NW. The lowest point in the catchment directly below Rising Star Cave occurs at 1459 m. The catchment forms a ~47 km^2 drainage basin with a dendritic network of first- to third-order, ephemeral streams that drain generally eastward towards the confluence with the Riet Spruit. Most of the channels eroded underlying lithologies resulting in shallow, wide gullies. However, the main channel to the north of the catchment follows a straight NW trajectory along some prominent scarps and a mapped fault (Fig. 2).

Much of the south-eastern Upper Bloubank Spruit catchment area is underlain by chert-bearing dolomites of the Archean-Proterozoic-aged (2.55-2.45 Ga) Malmani Subgroup, whereas the north-western area is underlain by siliciclastic strata of the younger Proterozoic-aged (~2.3 Ga) Lower Pretoria Group. Carbonate strata comprise chert-bearing stromatolitic dolomites of the Monte Christo Formation, overlain by strata of chert-poor Lyttelton and chert-bearing Eccles formations. The dolomite units are unconformably overlain by chert breccia and conglomerate deposits of the Rooihoogte Formation followed by shaly sandstones of the Timeball Hill Formation interbedded with coarse-grained quartzite of the Klapperkop Member, which forms the northwest boundary of the catchment (Fig. 1B). Both the Malmani Subgroup and Lower Pretoria Group units are intruded by several generations of E- and NNW to NNE trending dolerite dykes, which are poorly exposed in the field, but are visible in geophysics. No Karoo-aged erosion remnants have been mapped in the catchment area, but detrital zircon populations obtained from the surface and cave sediments (see Chapter 4) indicate that remnants of Karroo material could exist in the catchment area. Some of the river valleys in the catchment area, and especially the valley floor north of Rising Star Cave is underlain by a blanket of alluvial sediment that consists of a mixture of clays and micas with sand to cobble-sized particles of quartz, chert and dolomite, and abundant secondary iron and manganese oxyhydroxides.

2.3.2. The area around Rising Star Cave

Rising Star Cave is a maze network cave (Palmer, 1991, 2011) and consists of several kilometres of interconnecting chambers and passageways that formed along mainly NE- and NW-, and to a lesser degree N- and S-trending fractures within a ~15 m thick, chert poor, stromatolitic dolomite succession in the lower Monte Christo Formation with an average dip and dip azimuth of 17/246 (see Fig. 1B in Dirks et al., 2015; fig. 1A in Dirks et al., 2017). The roof of the cave is bound by a 1 m thick intact chert marker horizon (Dirks et al., 2015; Kruger et al., 2016). The west dipping strata define the preferred pathway for water movement, cave genesis, and the cave dissolution direction, evident by deepening of the cave in a westward direction. Although the cave geometry is mostly structurally and lithologically controlled and follows various joint and fracture sets within the lower Monte Christo Formation, chemical dissolution along open conduits has resulted in a series of dissolution chambers and roof collapse features (Dirks et al., 2015).

The Rising Star Cave is positioned close to the banks of the Upper Bloubank Spruit (7121914 S, 571325 E, Zone 35 J, UTM; WGS 84), ~800 m, west of the confluence with the Riet Spruit (Fig. 1B). Below this confluence the merged river to the east is referred to as the Bloubank Spruit. In the vicinity of Rising Star Cave several NW- to WNW- trending normal faults were identified (Figs. 1B, 2). Some of these faults are infilled with chert and caves have formed along them (e.g., Dirks et al., 2015), and they probably relate to the formation of the breccia of the Rooihoogte Formation as described in Dirks and Berger (2013). These small, neo-tectonic faults are likely the result of extensional activity during large-scale uplift of the region during the Pliocene (e.g., Partridge, 2010; Dirks and Berger, 2013). The most prominent scarp occurs directly north of Rising Star Cave and demarcates the boundary between the southern dolomite footwall (in which Rising Star Cave formed) and the northern hanging wall, the latter which is now covered with a thick blanket of alluvium. This particular scarp trends WNW and is relatively straight and marks a noticeable drop in the position of the bedrock surface (Fig. 2). This scarp is decorated with chert veins suggesting the presence of a fault surface (Dirks et al., 2015). Directly north of this scarp, the bedrock is covered by a blanket of alluvial sediment. A water bore hole drilled into this sediment (~30 m north of the scarp) contains 22 m of alluvial sediment before reaching bedrock. The scarp has, therefore, been interpreted as a neo-tectonically active fault with a normal displacement component in recent (Pleistocene ?) times of at least 22 m. The current course of the riverbed of the Upper Bloubank Spruit near Rising Star Cave parallels this fault (Fig. 2A). A similar linear scarp demarcates the northern boundary of the Upper Bloubank Spruit valley, in line with the scarp below Swartkrans Cave to the east and has been interpreted to represent a second NNW trending fault (Fig. 2A). Thus, the valley of the Upper Bloubank Spruit and the direction of river flow is determined by several parallel fault surfaces that appear to be neo-tectonically active, causing localised vertical displacements in the land surface. It is likely that the faults and fault motions are responsible for the gradual shift in the course of the Bloubank Spruit and the formation of the various scarps as discussed in more detail below.

2.4. Results

2.4.1. The geomorphology (and sedimentology) of the landscape around Rising Star Cave

The landscape surrounding Rising Star Cave is characterised by a series of down-stepping, strath and fluvial terraces interspersed with erosional scarps of exposed chert-bearing dolomite that form subtle, but clear steps in the landscape (Fig. 2). The scarps are 5-10 m high and lenticular in outline, and cut through the gently dipping primary sedimentary layering, i.e. they are not controlled by variations in lithology such as the erosion resistant chert-rich horizons. When viewed from the north, four scarps can be seen separated by locally degraded strath terraces (Fig. 2). The uppermost scarp (Scarp 1) occurs ~500 m SW of Rising Star Cave with a base at ~1490 m. The second scarp (Scarp 2) occurs between 1470-1480 m and exposes the entranceways into the Rising Star Cave system. Makhubela et al. (2019) reported an erosion rate of 9.5 ± 0.7 m/ Ma for chert bands exposed along this scarp. A third erosional scarp (Scarp 3) occurs 150 m SE of the cave between ~1464-1458 m, and a fourth scarp (Scarp 4) occurs ~500 m SE of the cave between ~1460-1445 m and forms the current valley side of the Upper Bloubank Spruit directly above the confluence with the Riet Spruit.

A prominent erosional strath terrace has been preserved at ~1464m below Rising Star Cave and Scarp 3. The edge of this terrace follows a fault mapped north of the cave system (Fig. 2), which indicates a possible relationship between fault movement and terrace formation. A second strath terrace, now partly degraded, occurs at ~1472 m directly below Scarp 2 and the entrance into Rising Star Cave. A possible 3rd strath terrace now strongly degraded occurs at ~1484 m above Scarp 3 and above the cave system. Each of these strath terraces preserves remnants of alluvial deposits that include large (up to 20 cm) rounded cobbles of quartzite derived from the Klapperkop Member. Along the entry track to Rising Star Cave, a fourth, alluvial terrace is preserved at 1460 m. This terrace is paired, i.e. it occurs on either side of the current Upper Bloubank Spruit riverbed and is underlain by alluvial material that reaches a thickness of at least 22 m as seen in a groundwater borehole (Figs. 1, 2). Below Rising Star, the current ephemeral streambed cuts into this paired alluvial terrace by 1-2 m. The streambed is positioned ~10 m below the main cave entrance, and ~12 m below a paleo-entrance that existed in the roof of the Postbox Chamber (see Fig. 1; Chapter 1) and the Upper Postbox Chamber, both acting as entry points for most of the clastic sediments found in the cave (see chapters 3 & 4). The position of the erosional scarps and terrace edges have been mapped in Figure 2.

2.4.2. Stratigraphy of the lower Monte Christo Formation

The 140 m thick measured section of lower Monte Christo Formation consists of alternating chert-rich, sand-rich and sand-poor dolomite units, interbedded with a few thin (<40 cm) muscovite-illite-rich shale horizons of which some are sheared (Fig. 3A). Rising Star Cave formed in a relatively chert-poor section in the lower third of the stratigraphy (Fig. 3).

The carbonate lithofacies can be subdivided into clean, non-sandy, non-stromatolitic dolomite, and sandy, stromatolitic dolomite. In outcrop, the clean dolomite weathers dull light-grey, but freshly broken it is uniformly dark grey, and exposed surfaces typically exhibit smooth textures with distinct shallow scalloped, concave-up weathering patterns (Fig 4). The dolomite is generally fine-grained, and when pure it consists almost exclusively of well-developed, intergrown euhedral dolomite crystals (Fig. 5) with no other detrital input (Fig. 6). Most of the dolomite is massive, but horizontally laminated, and ripple and wavy laminated beds occur,

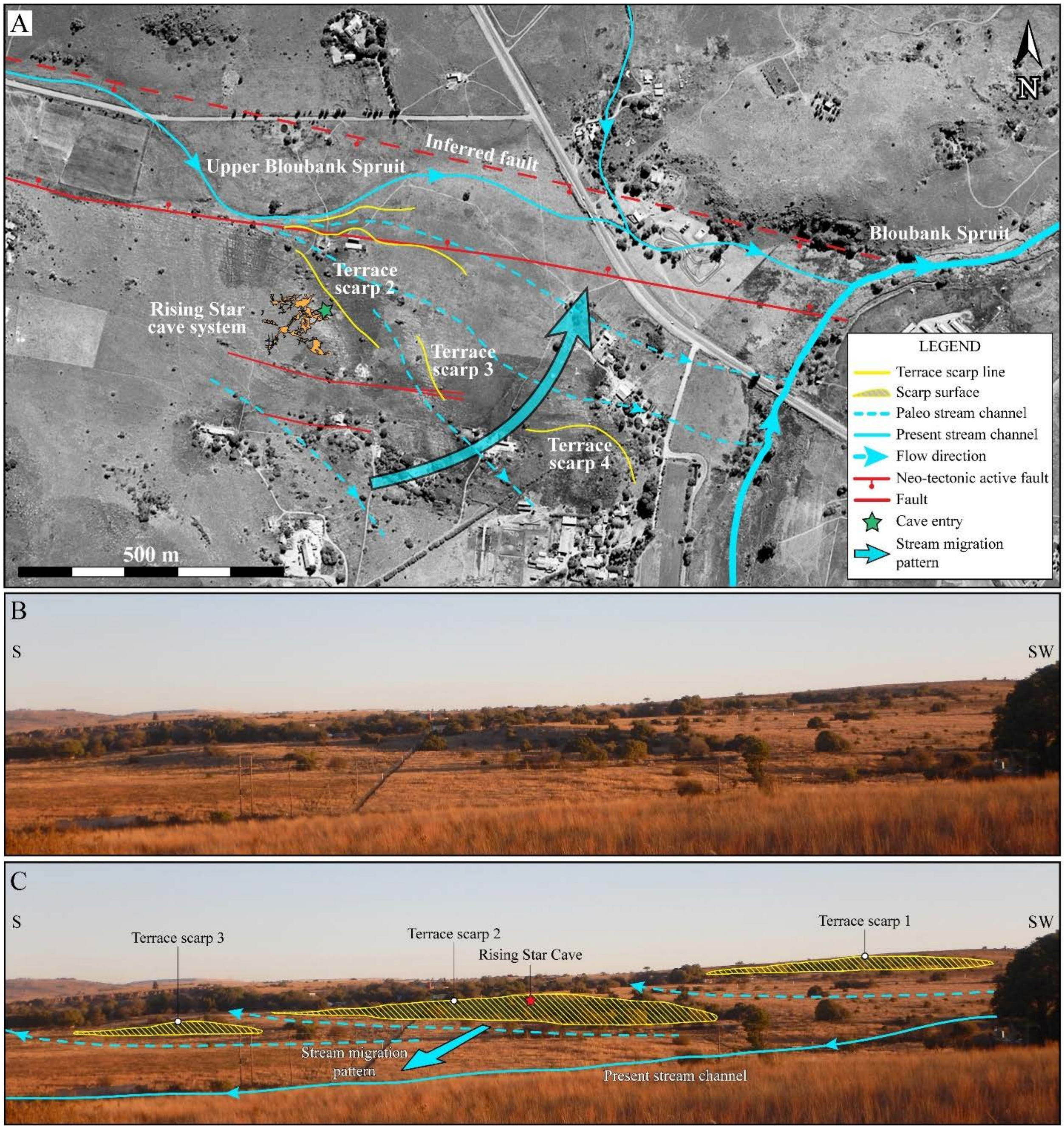

Figure 2. Geomorphology of Rising Star Cave area. (A), Overview of major geomorphic features surrounding Rising Star Cave including major fault scarps and strath and fluvial terraces; (B), Terrace scarps (in the shade) preserved in the landscape surrounding Rising Star Cave; (C), Diagrammatic illustration of terrace scarps and the position of Rising Star Cave within terrace scarp 2 and Upper Bloubank Spruit migration pattern and flow direction.

suggesting that the dolomite originally formed as a micrite or grainstone in a shallow water environment. The bed thickness is variable and ranges from several centimeters to several meters, and stacking patterns appear random, lacking any evidence of thin or thick clustered sets of strata or distinct thickening or thinning upward sequences. Chert horizons are common throughout the dolomite sections.

More than 50 % of the dolomite in the measured section is sandy and contains very fine to medium-grained sand-sized quartz in various quantities. The sandy dolomite weathers light yellowish brown and is slightly more erosion resistant compared to its non-sandy equivalent. Weathered surfaces are shallowly concave scalloped and have a gritty surface texture. The sandy dolomite beds alternate with clean dolomite and chert horizons, resulting in numerous first order, small-scale coarsening upward successions (Fig. 3A). Higher order coarsening or fining upward stratigraphic trends could not be established. The sand component consists almost entirely of non-detrital, amorphous and angular, micro-to-cryptocrystalline secondary, i.e., diagenetic, quartz and chert and trace amounts of accessory rutile (Fig. 5I, J). The quartz grains occur as small, millimetre-sized clustered pockets within the dolomite, whereas chert occupies millimetre-scale, thin fractures within the dolomite. The sandier dolomite typically preserves more sedimentary structures including shallow wave ripples and millimetre-sized ooids (Fig. 7). The wave ripples have a wavelength of ~5 cm and shallow, ~1 cm tall bedforms. Wave ripples and ooids are typically accompanied by the presence of domal stromatolites. Although all observed stromatolite beds occur in the sandier dolomites, there is a distinct correlation between the size of individual stromatolite domes and sedimentary structures. For example, stromatolites with domal diameters between 0.1-1 m occur preferentially with wavy or ripple-laminated beds and ooids, whereas smaller domed and planar stromatolite mats occur within the finely laminated or massive dolomite facies. Stromatolites, wave ripples and ooids are most common in the lower half of the stratigraphy and consistently occur in the upper half or uppermost part of coarsening upward cycles (Fig. 3A). Stromatolite abundance and size steadily decreases in the upper half of the stratigraphy.

Chert layers are abundant, and their stratigraphic distribution is fairly consistent throughout, although the lower third of the stratigraphy is relatively chert-poor and this particular section hosts the Rising Star Cave (Fig. 3B). The chert horizons are more erosion resistant than the under- and overlying dolomites, resulting in differentially weathered karst topography with protruding bands of chert that stand up to several cm above the adjacent dolomite outcrops (Fig. 4). However, in some areas, i.e., on the surface above the cave, unconsolidated sediments and colluvial soil blanket much of these features. Weathered chert outcrops are usually orange brown

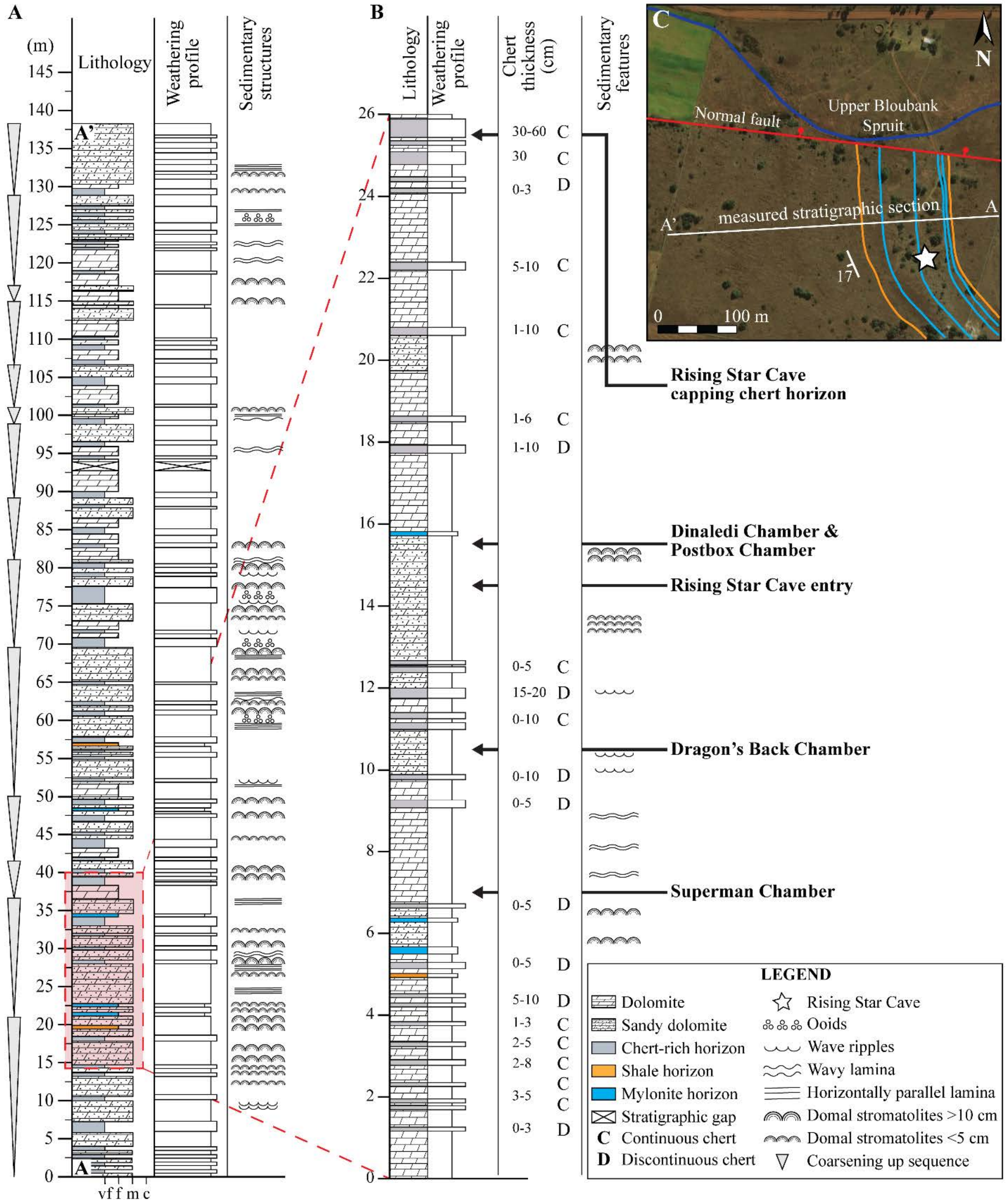

Figure 3. Stratigraphy of the lower Monte Christo Formation in the Rising Star Cave site. (A) Measure section of the stratigraphy. (B) Expanded, chert-poor section of the lower Monte Christo Formation in which the cave formed, including stratigraphic positions of Rising Star Cave chambers (see 'Geology of Rising Star Cave' and Fig. 3 in Chapter 1 for details). (C) Surface map

indicating the location of the measured section, including the mylonite and shale horizons that occur stratigraphically below and above the cave chambers.

to dark grey and freshly broken surfaces are lighter grey. The chert consists of microcrystalline quartz and commonly contains oolitic horizons, wave ripple lamina (Fig. 7), and small domal stromatolites indicating that some of the chert is diagenetic in nature (Fig. 7). Chert horizon thickness ranges from 0.01 – 2 m and their morphology throughout the stratigraphy is either horizontal or highly undulatory and the lateral extent of individual beds are continuous or discontinuous (Fig. 4B).

Interbedded with the dolomite are several shale horizons that occur within the lower half of the stratigraphy, and each is no more than 10-20 cm thick. The shales are locally mylonitic (i.e. strongly sheared) and are commonly overlain by stromatolite-rich facies, possibly preserving transitional regression-transgression facies. Each shale horizon consists primarily of muscovite/illite, with lesser quartz and trace amounts of rutile and vermiculite (Fig. 6). Freshly broken shale is platy and friable and has a metallic lustre (Fig. 4E). The lowest shale horizon occurs at 20 m within the stratigraphy (Fig. 3A) and is not sheared. Four more sheared shale horizons with mylonitic textures occur at 22, 23, 34 and 46 m (Fig. 3A), with the three lowermost horizons coinciding with the stratigraphic level in which the cave developed. Each mylonite horizon is approximately 15-20 cm thick and consists of thinly undulated lamina, of fine-grained muscovite and minor quantities of dolomite (Fig. 6). Dirks and Berger (2013) noted that similar shale horizons commonly control cave formation in the CoH, and it is likely that this is the case also for Rising Star Cave.

Rising Star Cave formed in a 26 m thick stratigraphic section of dolomite which is relatively chert-poor and stromatolite-rich (Fig. 3B; Chapter 1) and is situated in the lower 14-40 m interval of the measured section. The lower 6.5 m of this particular section consist primarily of clean dolomite, interbedded with continuous, mm-cm thick chert horizons, overlain by a single shale band and two mylonite mica schist horizons, as the dolomite becomes increasingly sandier, and stromatolite-rich up section. Most of the cave formed in the ~7-16 m interval, within sandy and stromatolite-rich dolomite (Fig 3B). The transition from non-sandy to sandy dolomite is characterised by two 5-10 cm thin, discontinuous chert horizons. Up section (from 7 to 16 m in Fig. 3B), the dolomite becomes increasingly sandier and stromatolite domes increase in size and abundance. From 16-26 m the dolomite again becomes sand-poor with the exception of a single, 1 m thick sandy stromatolitic section. This dolomite interval is interbedded with mostly continuous chert horizons, ranging from 1-10 cm in thickness, and it is capped by a ~1.0 m thick chert marker horizon which forms the roof to many of the larger chambers in Rising Star Cave (Fig. 3B; Dirks et al., 2015).

2.4.3. Type and composition of surface sediments in different geomorphic domains

The surface sediments can be sub-divided into five discrete sediment types that include, from coarse to fine: muddy gravel, muddy sandy gravel, gravelly muddy sand, muddy sand, and sandy mud (Fig. 8). In general, these sediment types are broadly similar in texture and mineral composition, being extremely poorly sorted and consisting primarily of angular quartz, muscovite, and kaolinite with secondary Fe-Mn oxyhydroxide phases and soil forming carbonates like siderite (Figs. 8A & 9). The surface sediments are notably devoid of calcium carbonates (i.e., dolomite and calcite), despite the underlying geology being mainly composed of dolomitic lithologies. The texture and mineralogy of the five sediment types vary systematically across the geomorphic domains that surround the cave; i.e. the gravel content and the proportion of Mn-oxyhydroxides in the surface sediments decreases as a function of elevation in the landscape (Figs. 8B, C & 9C). These changes will be described in more detail below for each of the geomorphic domains.

2.4.3.1. Degraded terrace above the cave— The surface above Rising Star Cave represents a degraded strath terrace that is now largely covered by colluvium and soil. The surface is generally flat and gently slopes 3-5° to the north (Fig. 2). Chert-bearing dolomite beds and shale horizons are widely outcropping along the surface, and the soil cover is highly irregular in thickness and evens out underlying karst features (Makhubela et al., 2019).

Sediment samples S5-7 obtained from the degraded terrace are classified as muddy gravel (S7) and muddy sandy gravel (S5-6; Fig. 8), consisting chiefly of extremely poorly sorted gravel and sand dominated colluvial sediment (Tables 2 & 3). They contain ~30-40 % sub-angular to sub-rounded quartz and chert gravels, ~30 % sand, 10 % silt and ~25 % clay, and are typically coarser grained compared to sediment on the lower elevated terrace and in the stream bed (Fig.

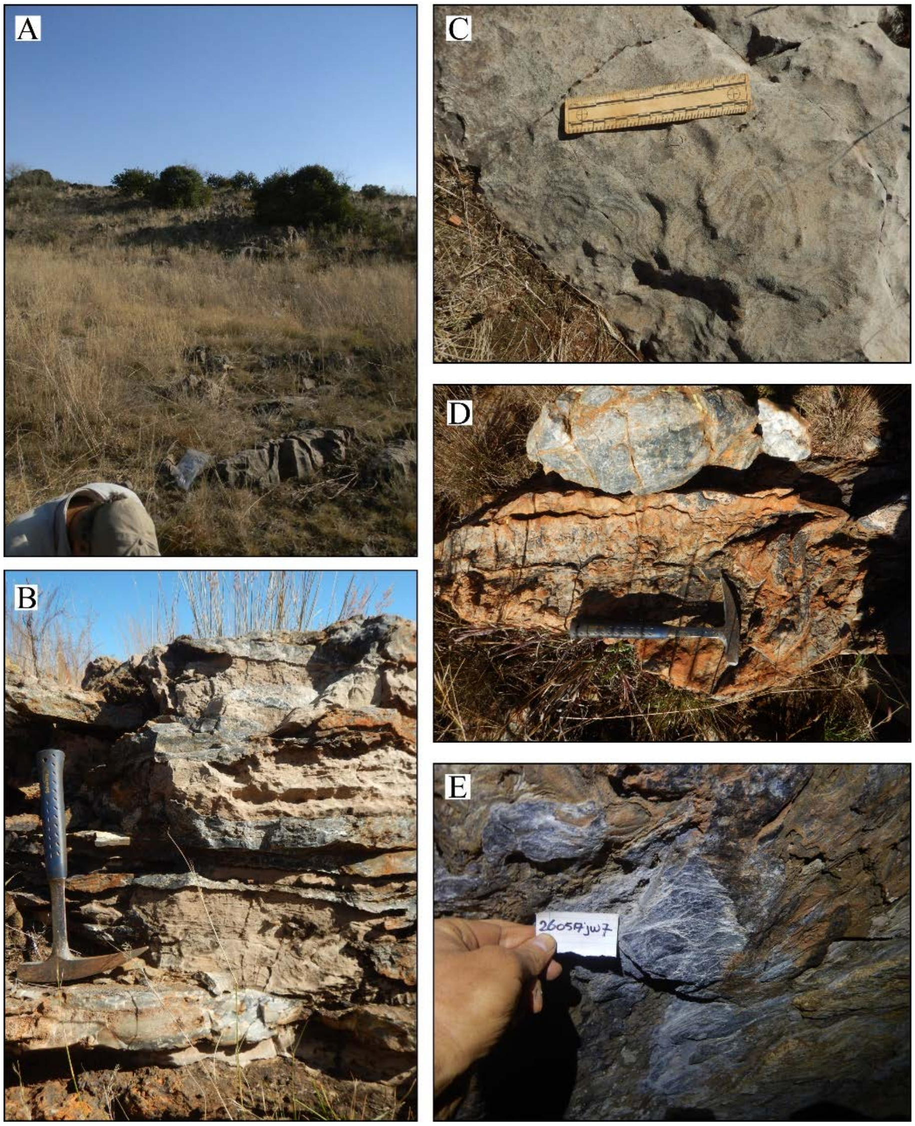

Figure 4. Surface outcrops of lower Monte Christ Formation lithologies. (A) Surface topography of locally outcropping dolomite surrounded by soil deposits. Terrace Scarp 2 is visible in the foreground. (B) Sandy dolomite with interbedded oolithic chert horizons. (C) Stromatolite domes in sandy dolomite. Rising Star Cave formed in similar lithologies of the Monte Christo Formation. (D) Differentially weathered discontinuous chert outcrops protrude from the surrounding dolomite (E) Mylonitic shale horizon in the Postbox Chamber.

8B, C). Well-rounded quartzite gravels and cobbles up to 20 cm in size from the Klapperkop member are relatively rare. The sediment is primarily composed of sub-rounded to angular secondary (diagenetic) quartz and chert mixed with millimetre-to-clay-sized illite, muscovite, and kaolinite clay. Soil minerals (oxides and carbonates) in the form of Fe-Mn oxyhydroxide aggregates and siderite are relatively abundant (Fig. 9). The overall oxyhydroxide concentration

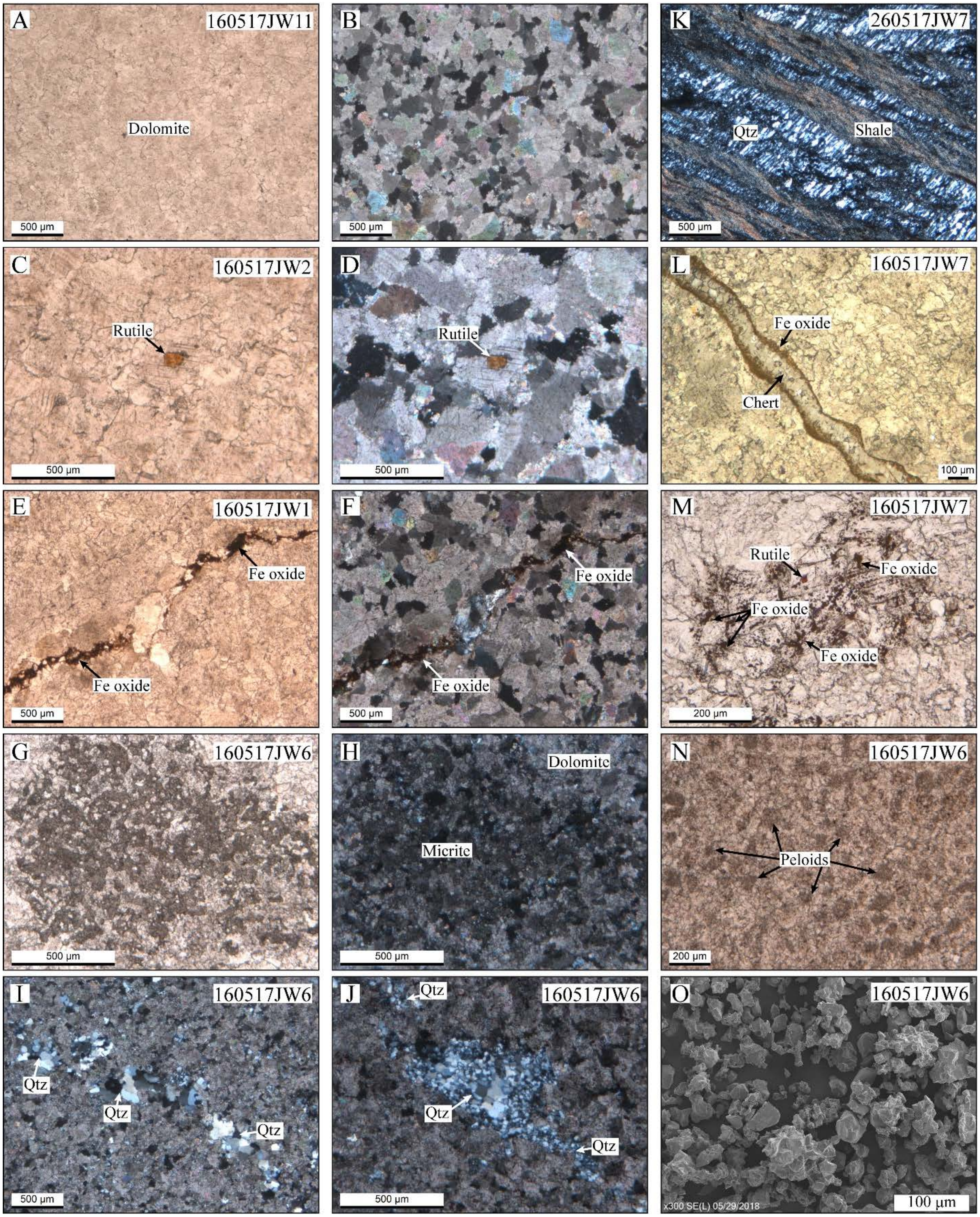

Figure 5. Thin section petrographic images of the chert-poor section within the lower Monte Christo Formation, in which Rising Star Cave formed. Equigranular dolomite crystals in (A) ppl and (B) xpl; amorphous rutile in fine-grained dolomite in (C) ppl and (D) xpl; iron oxides stylolite

in equigranular dolomite in ppl and (F) xpl; cryptocrystalline micrite-filled (carbon?) void in (G) ppl and (H) xpl; (I) diagenetically infilled clusters of amorphous, microcrystalline quartz in fine-grained dolomite. This quartz is a common component in the surface sediments; (J) close up of diagenetic quartz cluster illustrates its amorphous and diagenetic characteristics occupying small irregular voids in the dolomite; (K) mylonitic shear zone in clay-rich shale and quartz; (L) chert-filled fracture with iron oxide margins; (M) rutile and hematite inclusions in coarse dolomite; (N) cryptocrystalline micrite (carbon?) peloids in sandy dolomite; (O) scanning electron microscopy (SEM) image of diagenetic quartz from sandy dolomite. Images I, J, K, in xpl, and L, M, N, in ppl.

in the muddy gravel sediment directly above the cave (sample S5) is reduced by ~40% compared to the muddy sandy gravel sediments that were collected up-slope from the cave (samples S6 and S7; Fig. 9). As a result, the oxide and carbonate mineral signature in sample S5 is more similar to the signatures observed in the sediments from the lower strath terraces (Fig. 9B). Clays are much less abundant within the colluvial sediments on the degraded terrace compared to the lower areas.

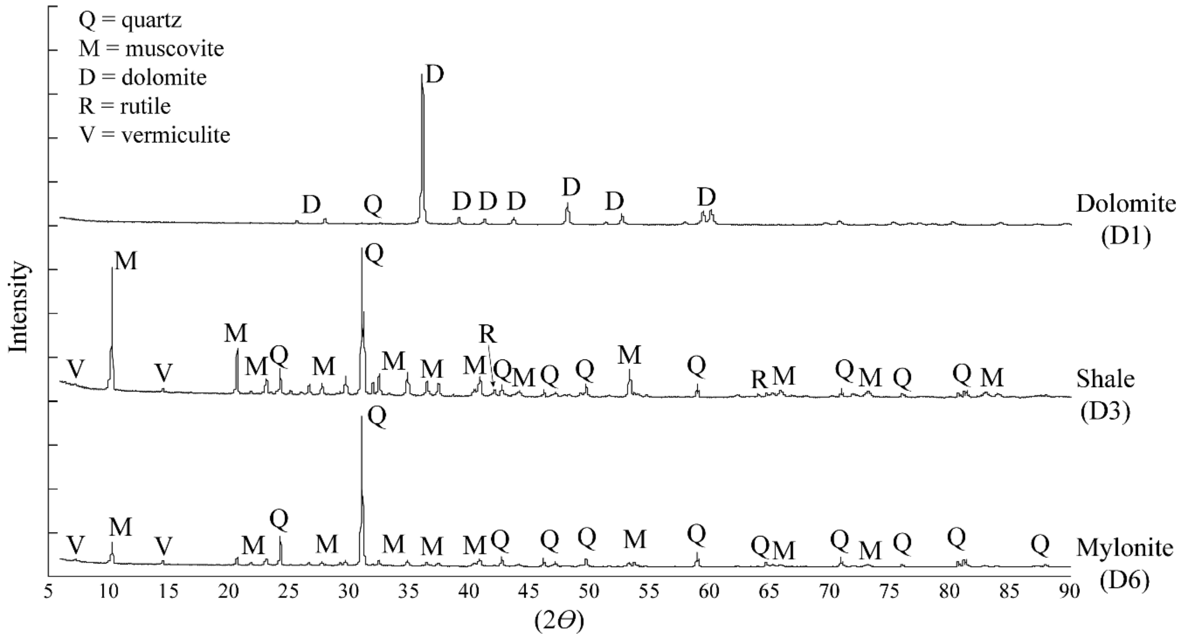

Figure 6. Common XRD mineral phases present in the three dominant lithologies that make up the lower Monte Christo Formation.

2.4.3.2 Partially degraded strath terraces—The two partially degraded strath terraces below scarps 2 and 3 (Fig. 2) have flat surface topographies and shallow sediment/soil profiles, indicating relatively short-lived floodplains that were abandoned after channel migration and shallow downcutting. The unconsolidated sediments on both strath terraces can be classified as poorly sorted gravelly muddy sand (Tables 2, 3; Fig. 8). The sediment on the terraces is sand-rich (~50%) with moderate amounts of sub-angular to sub-rounded gravel (~10-15 %) and 35-40 % mud (Fig. 8B, C). The modal mineralogy consists of angular to sub-rounded quartz and chert sand with minor amounts of sand-sized Fe-Mn oxyhydroxide nodules, millimetre-to-clay-sized illite and muscovite grains, kaolinite clay and few accessory heavy minerals (mainly rutile). Siderite, a mineral indicative of prolonged soil residence times, is relatively rare (Fig. 9). The overall concentration of Mn-Fe oxyhydroxides is relatively high, while limonite and hematite concentrations are low (Fig. 9). Klapperkop member quartzite gravel and cobbles are present but occur infrequently within the surface sediments of the strath terraces.

2.4.3.3 The stream bed of the Upper Bloubank Spruit and alluvial terrace— Currently, the Upper Bloubank Spruit forms an ephemeral streambed that, together with the paired fluvial terraces north of the fault scarp, represent the youngest geomorphic domains near Rising Star Cave (Fig. 1). The streambed contains no natural levees, but instead grades gently into the adjacent alluvial terrace, which slopes gently upwards to the north, perpendicular to the flow direction of the channel.

Sediment in the stream bed can be classified as poorly sorted muddy sand (Tables 2, 3; Fig. 8). It contains ~70 % sand with <5 % gravel and relatively little silt and clay (~25 % combined; Fig. 8B, C). The mineralogy of the streambed sediments consist primarily of sub-rounded to angular grains of quartz, chert, and Fe-Mn oxyhydroxide nodules, interspersed with mm-to-clay-sized illite and muscovite grains and kaolinite clay with elevated levels of limonite/goethite and minor siderite.

The sediment on the alluvial terraces can be classified as poorly sorted, sandy mud with ~40% sand, ~40% clay, ~15-20 % silt and <5 % gravel (Tables 2, 3 & Fig. 8). The mineralogy is similar to that of the streambed, consisting primarily of quartz, muscovite/illite, Fe-Mn oxyhydroxides and minor siderite (Figs. 8A & 9). Overall, compared to sediment in the stream bed, the sediments on the alluvial terrace are less quartz rich, but they contain more oxides and siderite, with nearly 5 times the amount of Mn-oxyhydroxide, and twice the amount of hematite and siderite. Limonite concentrations remain similar (Fig. 9B).

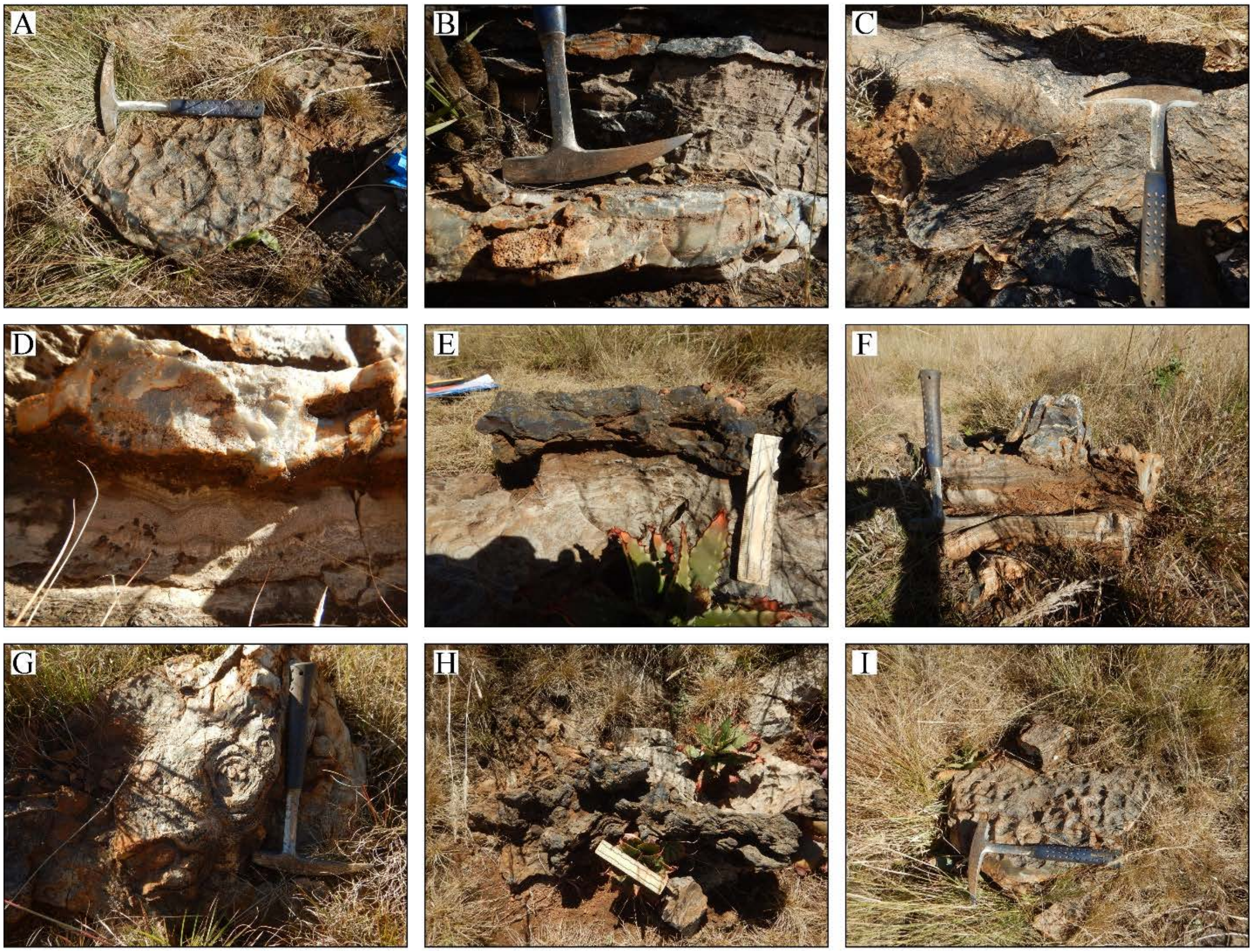

Figure 7. Sedimentary features in the lower Monte Christo Formation. (A) Wave ripples in chert. (B) Oolithic chert. (C) Tepee structures. Hammer head points toward the stratigraphic top. (D) Soft sediment deformation of laminated dolomite underlying an undulated, erosion resistant chert horizon. (E) Small, shallow-domed stromatolites. (F) Broadly domed, large stromatolites. (G) Small stromatolites in chert viewed from above, illustrating concentric microbial "growth rings". (H) and (I) Small stromatolites in chert.

Table 2. Surface sediment types and grain size statistics for Rising Star Cave landscape.

Samples#	**Sediment type**	**Mean**	**Standard deviation (2σ)**	**Sorting**	**Skewedness**
S1	*Muddy sand*	3.5	3.79	very poor	strongly fine
S2	*Sandy mud*	5.31	4.12	extremely poor	near symmetrical
S3	*Gravelly muddy sand*	4.69	4.49	extremely poor	fine
S4	*Gravelly muddy sand*	3.9	4.81	extremely poor	fine
S5	*Muddy sandy gravel*	3.02	5.21	extremely poor	strongly fine
S6	*Mudy sandy gravel*	2.32	4.99	extremely poor	strongly fine
S7	*Muddy gravel*	3.57	5.00	extremely poor	fine

Table 3. Surface sediment types and grain size fractions from various geomorphic features surrounding Rising Star Cave. Sediment type classifications after Folk (1954, 1974).

Sample#	**Geomorph.**	**Sediment type**	**Gravel %**	**Sand %**	**Silt %**	**Clay %**
S1	UBS streambed	*Muddy sand*	4.13	70.03	8.11	17.74
S2	Alluvial terrace	*Sandy mud*	4.7	39.29	15.94	40.07
S3	Strath terrace	*Gravelly muddy sand*	10.15	48.84	12.82	28.19
S4	Strath terrace	*Gravelly muddy sand*	17.77	48.1	13.62	20.51
S5	Degr. terrace	*Muddy sandy gravel*	36.67	31.9	12.07	19.37
S6	Degr. terrace	*Muddy sandy gravel*	42.12	29.11	10.28	18.49
S7	Degr. terrace	*Muddy gravel*	32.2	26.82	13.56	27.42

2.5. Discussion

The current morphology of the Rising Star Cave system and the geomorphology of the surrounding land surface of the Upper Bloubank Spruit catchment surrounding the cave are the combined result of structural, lithological and chemically controlled earth surface processes. Mapping of the cave and the distribution of the alluvial and strath terraces, and erosional scarps surrounding the cave (Figs. 1, 2) indicate that the main controls on the geomorphology of the cave and the surrounding landscape are: 1. the dolomite lithology and orientation of the primary layering, layer-parallel shears and fracture patterns within the dolomite, which determined the morphology of the cave; 2. the faults along the valley floor, which influenced the flow direction of the Upper Bloubank Spruit and deposition of the quaternary deposits north of the fault; and 3. the confluence of the Upper Bloubank Spruit with the Riet Spruit. Each of these controls will be discussed in more detail below.

2.5.1. The dolomites that host Rising Star Cave

The measured strata of the predominantly cherty dolomite units of the lower Monte Christo Formation that host Rising Star Cave (Fig. 3) are interpreted to have formed in a shallow water epeiric carbonate platform or rimmed shelf environment (comprising both inter, supra, and sub-tidal deposits (Button, 1973; Eriksson and Truswell, 1974; Eriksson, 1977; Eriksson and Warren, 1983; Beukes, 1987; Eriksson et al., 2006).

The distribution of cave systems in the CoH is largely controlled by joints and faults within the Malmani Subgroup dolomites, as well as layer-parallel shear zones characterised by shale horizons and secondary chert beds (Kavalieris and Martini, 1976; Dirks and Berger, 2013). A similar pattern has been observed for Rising Star Cave where cave formation occurs primarily in a 20-25 m thick, chert-poor, sandier section of the west dipping dolomite that is bound above and below by mylonitic shear horizons (Fig. 3). Chert and breccia filled fractures are also common. In the case of Rising Star Cave, the main fractures of this type trend ENE and WNW, and they control the dominant trends in the cave system. The floor of the cave system more-or-less occurs along the same stratigraphic level, which closely parallels two prominent sheared shale horizons (Fig. 3) that are exposed near the base of some of the chambers. These observations support the hypothesis that Rising Star Cave formed in a similar manner as described by Dirks and Berger (2013); i.e., cave formation started along subterranean channel ways near the intersection of layer-parallel shear zones and old fracture planes, which were reactivated more recently. This reactivation most likely occurred during uplift of the southern African Plateau, to allow groundwater to penetrate the fractures and dissolve the dolomite (Martini, 2006; Dirks and Berger, 2013). As cavities formed along the shear zones and propagated upwards along the vertical fracture planes, the one-meter-thick erosion resistant chert that occurs higher in the stratigraphic sequence inhibits the upward migration of the cave system, thus forming an erosion and chemically resistant roof to most of the cave chambers (Dirks et al., 2015). As a result, the bulk of Rising Star Cave is restricted to the dolomitic interval between the micaceous shear zones towards the base of the system and the thick chert layer towards the top; i.e., between 20-40 m in the measured stratigraphic section (Fig. 3).

2.5.2. Characteristics of surface sediments in different geomorphic domains

Our data indicate that each of the different geomorphic domains surrounding Rising Star Cave (i.e., the various terraces and the river channel) are underlain by clastic sediment types and soils that, in spite of large overlaps in composition, are distinct from one domain to the next (Figs. 8, 9). These systematic differences, which are important in helping define the provenance of the clastic sediment load that became trapped in the cave (see Chapter 4), were probably the combined effect of primary depositional processes including the relative position of the terrace to the riverbed, in combination with secondary altering processes such as soil formation, and chemical denudation of underlying dolomite, which are directly related to the age of the deposits.

The general mineralogy of the various surface sediment types blanketing the Rising Star Cave area is largely similar (Fig. 9); i.e., the major mineral constituents are quartz, illite, and muscovite, for which the relative abundance varies little from one geomorphic domain to the next. The underlying lithological units of the lower Monte Christo Formation and especially the shale and chert horizons, seem to be the primary contributors of these minerals. In contrast, the soil mineral concentrations including the Mn-Fe-oxyhydroxides and siderite, vary strongly across the various geomorphic domains (Figs. 8 & 9), reflecting the importance of secondary depositional and soil forming processes, and especially the time over which such processes interacted with the surface sediments.

Calcite and dolomite are largely absent in the sediments, reflecting slightly acidic conditions within the surface soils and sediments (Hawker and Thompson, 1988). The dolomites of the Malmani Subgroup are generally enriched in Mn (Eriksson et al., 2006), and, therefore, *in situ* enrichment of Mn-oxyhydroxides in the overlying soils likely resulted from weathering and dissolution of underlying dolomite that was slowly exhumed over time (e.g. Makhubela et al., 2019). This chemical exhumation of dolomite involved the near-complete removal of Mg and Ca, and the relative enrichment of residual Mn and associated Fe in the soils (Hawker and Thompson, 1988; Dowding and Fey, 2007). Under the prevailing slightly acidic, oxidized and hydrated conditions in the surface sediment cover, mineral reactions enhanced by microbial activity would have resulted in the formation of insoluble Mn^{3+}- and Mn^{4+}-rich phases like pyrolusite, birnissite and todorokite, and to a lesser degree Fe-rich phases like hematite, goethite and limonite (Taylor and Schwertman, 1974a, 1974b; Ghiorse, 1984; Tebo et al., 2005; Nogueira et al., 2007; Tebo et al., 2010; Santelli et al., 2011). Makhubela et al., (2019) have shown that the soils above Rising Star Cave record long surface residence times on the order of 100’s ky, indicating that the soils and cover sediments on the old terrace surfaces are old and stable. Therefore, we can assume that the older geomorphic surface on which sediment had collected, i.e., the older colluvial and alluvial sediment cover, the higher the concentration of Mn-Fe oxyhydroxides will be. This process will of course depend on a great number of other variables, but in general our data shows a clear trend of increasing Mn-oxyhydoxide concentrations when going from the youngest geomorphic domain in the river channel (sample S1) to the oldest domains above the cave (samples S6 and S7; Fig. 8). This trend is not clear for Fe- oxyhydoxide concentrations, suggesting that many of the Fe-minerals formed through processes other than soil formation, and that the Fe may have been derived externally (e.g. through surface water flow) rather than via exhumation and dissolution of underlying dolomite.

Apart from the mineralogy of the oxyhydroxide phases, the different geomorphic domains also display a systematic variation in grainsize distribution (Fig. 8). For instance, the terraces are more enriched in silt and clay the younger they are, whilst the streambed contains the least clay. In contrast, the older degraded terrace above Rising Star Cave contains far more cobbles and gravel than the strath terraces and especially the alluvial terrace and the stream bed. Some cobbles on all terraces consist of rounded to sub-rounded pebbles of quartzite from the Klapperkop Member that must have been transported by fluvial activity, which attests to the primary fluvial origin of part of the sediment cover on the terraces. However, the vast majority of the coarse clasts are composed of angular chert fragments, which systematically increase in frequency and size with elevation of the terrace above the current stream bed (Fig. 8B). Again, these differences must be understood as an interplay between primary depositional processes and secondary modifications to the sediment budget, grain size and grain shape distributions, which changed as a function of time.

With time, the gradual chemical denudation of the dolomite underlying the terraces exposed the more resistant, insoluble chert horizons, which would have been mechanically broken up, to become incorporated in the sediments on surface. The older the underlying surface, and the longer this process of secondary, *in situ*, gravel formation happened, the higher the proportion of angular chert clasts in the sediment/soil cover. This process was described and dated by Makhubela et al (2019) for the degraded terrace above Rising Star Cave. They found that whilst the dolomites were eroding at a rate of 7 m/Ma, the soil overlying the surface was relatively stable reflecting younger erosion rates and calculated residence times of 1.1 Ma. They also found that over time the cover sediments and soils were regularly overturned and mixed. In other words, chert clasts weathered from the underlying dolomite, accumulated in the overlying soil over time and became mixed with primary sediments that were deposited as a result of earlier alluvial processes. Thus, the relative abundance of chert clasts on the terraces is not a reflection of a primary, high energy alluvial process, but can be taken as a rough estimate for the age of the terrace, all other things being equal.

The situation is different for the clay and silt component in the sediments. Generally, the muddy gravel and muddy sandy gravel sediments above the cave contain relatively little clay, whilst the clay component increases on the terraces below the cave (Fig. 8). If we assume that following primary deposition via alluvial processes, the original grain size distribution of sediment deposits on all terraces would have been similar, the current systematic variation in clay content with elevation, again suggests that secondary processes modified the overall sediment composition. The cave sediments, which are situated directly below the degraded upper terrace, are rich in silt and clay (e.g., Dirks et al., 2015, 2017; Makhubela et al., 2017; Wiersma et al. 2019). These sediments were mostly externally derived (Wiersma et al. 2019) and can be seen to wash in from the soils above via thin fractures and narrow karst features. It, therefore, follows that the geomorphic domains underlain by extensive karst including caves, will be preferentially depleted in the finer-grained sediment fraction. Our observations suggest that the fine-grained fraction was preferentially winnowed from the surface sediments to be transported into underlying karst. This process may be enhanced, by additional winnowing of the clay fractions during periodic surface runoff. Thus, sediment on older, and more elevated terraces underlain by karst may be depleted in clay.

Our observations indicate that there is a demonstrable link between the elevation of the various terraces relative to the stream bed, the corresponding age of that terrace, and the nature of the sediment cover in terms of grainsize distribution, and concentration of soil forming minerals, especially Mn-oxyhydroxides. It shows that the area surrounding Rising Star Cave underwent active geomorphological changes resulting in distinct geomorphologic domains and associated sediment signatures. It also reflects a dynamic landscape evolution on a relatively small geographic scale and provides a mechanism to identify the source of the clastic sediments that were deposited in the cave over time, together with their macro-fossil load.

The degraded terrace above the cave is interpreted as being the oldest geomorphic feature investigated in the study area, based on the degraded nature of the surface and its relatively elevated content of Fe-Mn-oxyhydroxides, siderite and chert gravel. Over time lowering of the base level of the Upper Bloubank Spruit resulted in the development of two, now partially degraded strath terraces below the cave (Fig. 2). The soil profiles on these terraces are shallow and appear less developed, containing overall less Fe-Mn oxyhydroxides, siderite and chert gravel (Fig. 9). This suggests that these terraces formed more recently, but under similar conditions to the more deeply degraded terrace above the cave, and soils on the strath terraces had less time to develop. The youngest geomorphic domains, the alluvial terrace and the current streambed, are still active depositional environments today. The relatively high clay and silt content on the alluvial terrace, reflects suspension deposits after periods of flooding of the Upper Bloubank Spruit, and possibly provides an indication of the types of sediment that may have been originally deposited on the other terraces before secondary processes modified their composition. The low concentration of Mn-oxyhydroxides in both the alluvial terrace and the streambed is due to the fact that they are still active depositional environments, in which primary, physical depositional processes occur at a much higher rate than the secondary chemical soil forming processes.

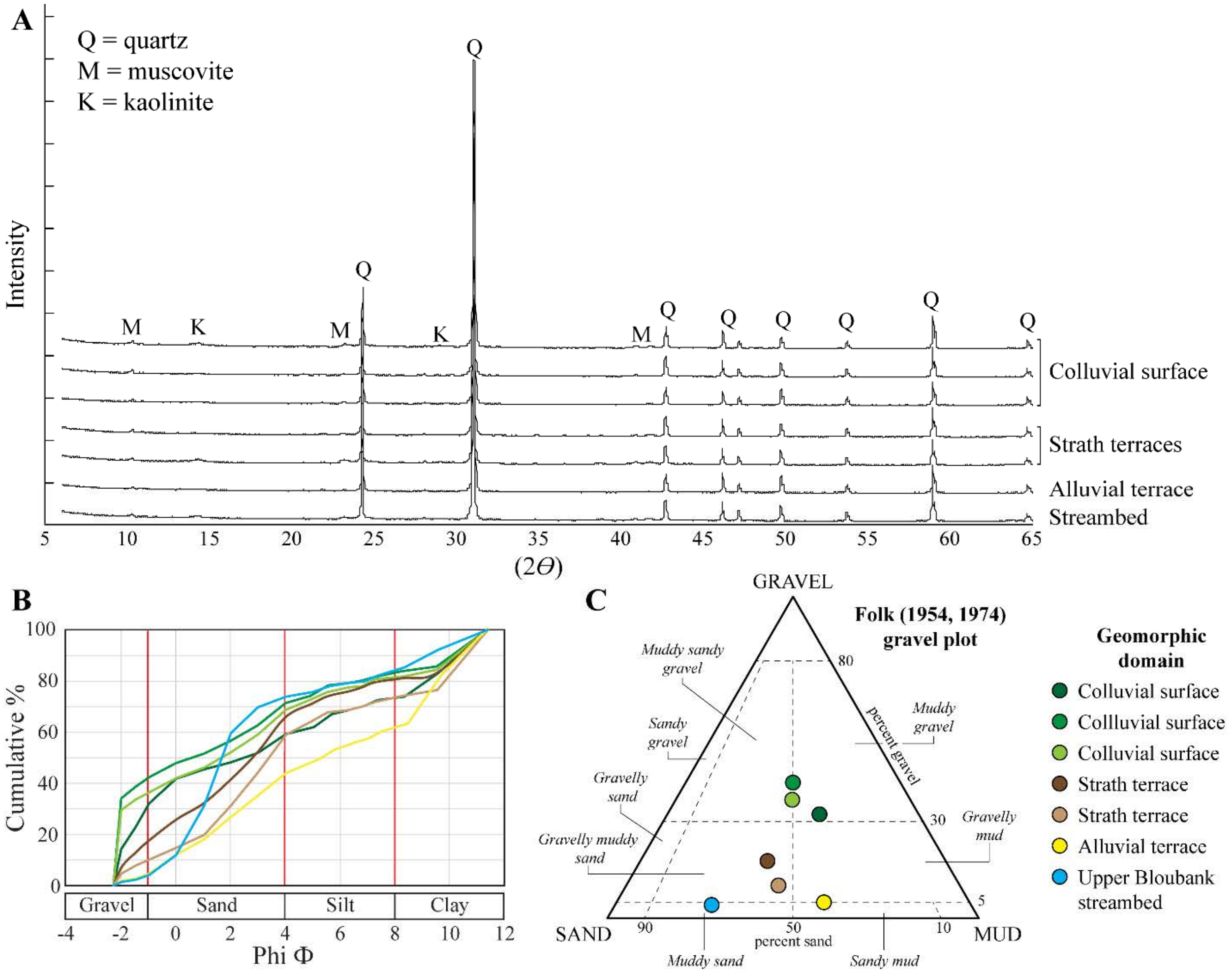

Figure 8. Geochemistry and particle size distribution of surface sediments from the Rising Star Cave site. (A) XRD results from the surface sediments show significant similarity in major geochemical composition. (B) Particle size distribution shows size variations that correlate to unique geomorphic settings in the study area. (C) Ternary plot of the different sediment types and associated geomorphic domains. The mud fraction consists of silt and clay.

2.5.3. When did Rising Star Cave become accessible?

It is clear that Rising Star Cave presents a unique and dynamic geological and geomorphic setting compared to some of the other hominin, or fossiliferous, cave systems in the CoH landscape. Whereas most caves (e.g., Malapa, Kromdraai, Swartkrans) in the COH were filled with chaotic cave breccia with little mud, which formed along valley slopes and plateau areas away from alluvial channels, Rising Star Cave developed close to the valley floor, with abundant unconsolidated sediment fill including fine-grained material that is most likely derived through interaction with the nearby Upper Bloubank Spruit.

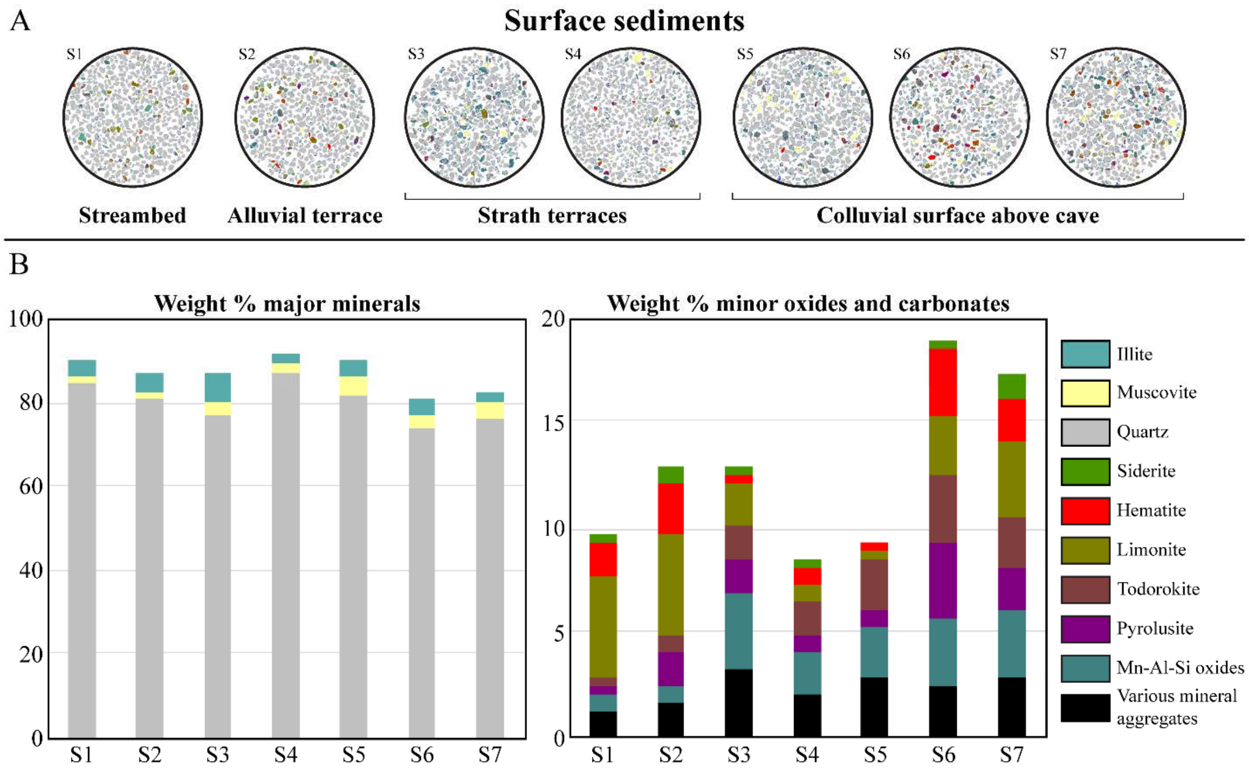

Figure 9. Modal mineralogy of the Rising Star Cave surface sediments. (A) Overview of the different grain mounts from the different geomorphic localities and their qualitative composition. (B) Quantitative composition of the major and minor mineral phases.

Dirks et al. (2015, 2017), Wiersma et al., (2019) and Chapters 3-5 in this thesis focus on the clastic sedimentology in Rising Star Cave and provide detailed descriptions of the clastic sediments that partly filled the cave, including the fossil-bearing, *Homo naledi* deposits. These clastic sediments fall into three categories: 1. clastic sediment derived from the host rocks internal to the cave, i.e. autochtonous sediment; 2. fine-grained sediment that percolated into the cave from the surface via narrow fractures; and 3. fine to coarse-grained sediments that entered the cave through large openings that allowed the entry of cobble sized, allochtonous blocks as well as macro-fossils (Dirks et al., 2015, 2017; Makhubela et al., 2019; Wiersma et al., 2020). All of the fossil-bearing sediments in the cave have a proportion of these three sediment components (see details in Chapter 3), but the externally derived clastic sediments dominate (e.g., Dirks et al., 2015; Chapter 3). These sediments are distributed across a complex debris cone, with its apex in the Postbox Chamber. The sediments entered the cave via narrow vertical shafts connecting to surface (the current entry into the cave is a lateral, blasted opening). These entryways are still visible inside the cave, although they are now chocked with sediment and occur on the landscape as shallow depressions. Coarse, polymict, breccia-conglomerate deposits in the Postbox Chamber (Dirks et al., 2015, 2017; Chapter 3) that contain rare cobbles of Klapperkop quartzite provide the most compelling evidence for this past connectivity to the surface. The question is whether these clastic sediments were transported into the cave as a result of gradual creep of materials from the degraded terrace above the cave opening, or via large flooding events of the Upper Bloubank River. Most likely, sediments entered the cave through a combination of both processes. The more important question is when the cave was open to allow the coarse clastic sediments to enter, and how did this relate to the entry of *H. naledi*?

Age dating of the cave sediments, flowstones and fossils from Rising Star Cave has focussed on the Dinaledi Chamber with the aim of constraining the age of the *H. naledi* fossils (Dirks et al., 2017; Makhubela, 2019; Robbins et al. 2021). Dirks et al., (2017) reported an estimated age for the *H. naledi* fossils of 335-236 ka, further refined to 335-242 ka by Robbins et al. (2021). The fossils were embedded in unconsolidated mud clast breccia (Wiersma et al, 2019), which probably formed after the bulk of the clastic sediments had been deposited in the cave (Dirks et al., 2017; Wiersma et al., 2020; Chapters 3 and 4). Older fine-grained clastic sediments in the Dinaledi Chamber that can possibly be correlated with finer-grained deposits elsewhere in the cave were dated with OSL at 353 ± 61 ka (Dirks et al., 2017). The only age data for sediment in Rising Star Cave outside the Dinaledi Chamber were reported by Makhubela et al. (2019). They used ^{26}Al/^{10}Be ratios to calculate cosmogenic burial ages for coarse-grained clastic sediments in the cave and include an estimate of ~600 ka for the coarse polymict breccia below the sediment entry shaft in the Postbox Chamber, and an estimate of ~520 ka for equivalent sediments in the Dragon's Back Chamber. These ages were interpreted to reflect the age of sediment input from outside the cave (Makhubela, 2019), but they are heavily dependent on assumptions for model parameters including the initial ^{26}Al/^{10}Be ratio (Makhubela et al., 2019), and therefore should be treated with some caution. The ~520 ka age estimate was derived from the stratigraphic top of the oldest unit of clastic sediment in the Dragon’s Back Chamber and it is overlain by a flowstone dated at ~430 ka (Robbins et al., 2021). Sediments deposited on top of this flowstone are generally finer grained (Robbins et al., 2021; Chapter 3). Thus, the currently available age constraints suggest that from 600 ka forward at least, the cave received input of coarse-clastic detrital material from outside the cave, with significant quantities of finer material entering the cave from 400 ka onward (Robbins et al., 2021). Deposition of laminated, fine-grained sediment deposits in the cave stopped by ~150 ka (Robbins et al., 2021). These numbers place important constraints on the rate at which the landscape around the cave evolved. If the coarse sediments in the cave were the result of flooding events linked to the nearby river, then such events appear to have initiated at ~600 ka and become increasingly rare from ~400 ka onwards, and they would have largely stopped by the time *H. naledi* entered the cave.

2.5.4. The evolving landscape around Rising Star Cave

The position of the erosional scarps and strath terraces in the landscape around the Rising Star Cave (Fig. 2) show a stepped distribution with the scarps progressively moving from W to E as the intervening terraces step downwards from 1485 m to 1472 m to 1464 m and finally to the current river level. This shift would have coincided with an eastward shift of the confluence of the Upper Bloubank Spruit with the Riet Spruit. If so, the Upper Bloubank River used to run above Rising Star Cave, then stepped downwards and shifted to a position immediately below the cave to carve the erosional scarp (Scarp 2) that now presents the entrance into the cave system. Over time, the river would have shifted further to the NE in at least two more steps (Fig. 2), as the fluvial system locally transitioned from a bedrock dominated system to an alluvial dominated fluvial system. As the river steps downward, and the terraces become abandoned, secondary soil forming processes on the now inactive terraces became increasingly important thereby modifying the nature of the sediment cover as discussed. At 600 ky ago, probably during flood events, the river would have spilled into the cave at frequent intervals to deposit coarse clastic material. The entry point into the cave was an opening in the roof of the Postbox Chamber now positioned at ~1477 m, which provides an indication for the level to which high-energy flood waters would have risen at the time. By 400 ky ago such occurrences had become less frequent and the sediment flux into the cave became increasingly finer grained and largely stopped around 200-150 ky ago.

The driving mechanism for this migration of the streambed is likely to be faulting. Bailey et al. (2011) argued that much of the Bloubank Spruit valley is tectonically active today and that the valley is connected to the Steelpoort Fault further to the NE. They argued that the landscape of the CoH was repeatedly rejuvenated due to active neo-tectonic activity, resulting in a dissected landscape conducive to hominin occupation. We found evidence for this around Rising Star Cave. At a local scale the edge of the 1464 m strath terrace closely parallels the WNW trending fault north of the cave (Fig. 2A). This same fault appears to have controlled deposition of at least 22 m of alluvial sediments north of the fault as well as controlled the current course of the Upper Bloubank Spruit, which flows directly along the fault scarp. On a more regional scale, the course of the Upper Bloubank Spruit was controlled at least in part by two WNW trending faults on either side of the valley floor. Repeated reactivation of these faults in recent times could have dropped base levels resulting in the accumulation of Quaternary-aged sediments along the valley floor and would have controlled the course of the river as well as the progressive migration of the riverbed in the NE direction around Rising Star Cave.

Thus, prior to the cave opening to allow coarse-clastic sediment to enter the cave, the Upper Bloubank Spruit was positioned higher in the landscape, above, and possibly SW of the cave. Channel widths for the paleo stream are uncertain, but the fact that it did not deeply incise into the underlying dolomites suggests that the channel would erode more broadly and horizontally while contemporaneously migrating in a N-to-NE direction, rather than eroding vertically into the underlying dolomitic bedrock. Some degree of vertical erosion did occur, however, to form the erosional scarps that are currently still visible in the landscape (Fig. 2). As the base level dropped, possibly in response to normal faulting along the valley floor, the river channel would have shifted to the NE partly incising into the dolomite and forming Scarp 2 (Fig. 2) whilst the strath terrace above the cave would start to degrade and become subject to chemical denudation and soil formation. At some point in this process the cave is likely to have opened to allow coarse-clastic detrital sediments from outside to spill into the cave. Although continuing to migrate, the Upper Bloubank Spruit channel must have been positioned close to the cave once opened, and recurring (seasonal, or possibly, monsoonal) flooding events combined with intermittent surface runoff would have deposited substantial quantities of clastic sediment from the surface directly into the cave, forming a polymict debris cone in the Postbox Chamber. Over time the river gradually incised a further two scarps in the landscape as it continued to migrate in a NE direction.

Continuous downward and lateral migration of the river channel would have resulted in a gradual decrease of flood-derived sediments reaching the cave. Instead, surface runoff and passive creep of surface sediment along fractures that connect to cave chambers would become the dominant sediment transport method (Makhubela et al., 2019). Based on available dating this transition from fluvial dominated sedimentation to sedimentation through surface runoff would have occurred sometime between 400 ka and 150 ka.

Whether the opening of the cave was a function of river incision, gradual surface erosion or a combination of both is unclear. It is possible that the north-eastward migrating stream eroded enough surface material above the cave to open it to surface. This could have happened in combination with simultaneous dissolution and widening of vertical dolomite fractures under vadose and phreatic conditions. Once abandoned by the stream, surface and vadose conditions could have facilitated further widening of the opening into the cave. The opening of the Postbox Chamber would have allowed animals, including hominins like *H. naledi* to enter.

2.6. Conclusions

This study demonstrates that the landscape around Rising Star Cave underwent significant landscape variations on a local scale, in the past 600 ky. The immediate surroundings of Rising Star Cave present a dynamic landscape in which the interplay between local structural features (normal faults), the carbonate lithologies and fluvial earth surface processes created a changing landscape that affected the nature and distribution pattern of the clastic sediment fill in Rising Star Cave. The position of erosional scarps and intervening strath terraces in combination with the current position of the streambed suggest that the channel experienced NE ward migration as the confluence of the Upper Bloubank Spruit and Riet Spruit shifted east. This migration was probably facilitated by active faulting, which caused the base level along the valley floor to drop repeatedly since the Pliocene. The main controlling fault causing fluvial migration occurs directly N of the Rising Star Cave system. As the Upper Bloubank Spruit migrated NE-ward, the fluvial system transitioned from a bedrock channel with noncyclic strath terraces positioned S of the fault to an alluvial channel with an associated alluvial cut and fill terrace system positioned on Quaternary cover N of the fault.

After the cave first opened, river sediments would have entered the cave. Continuous downward and lateral migration of the river channel resulted in less frequent flood-derived sedimentation events reaching the cave and instead, surface runoff would become the dominant sediment transport method. Based on available dating this transition from fluvial dominated sedimentation to sedimentation through surface runoff would have occurred sometime between 400 ka and 150 ka, coinciding the entry of *H. naledi* into the cave.

As the river channel migrated and the strath terraces became abandoned, alluvial sediments deposited on these terraces were modified by secondary processes. This involved: 1) the deposition of Mn-Fe-oxyhydroxide phases and siderite in response to microbial-mediated soil forming processes; 2) the accumulation of chert gravel as a result of chemical denudation of the underlying dolomite; and 3) the winnowing of fine-grained clay that was transported into underlying karst. The degree to which secondary processed modified the surface sediments was strongly time dependent resulting in a systematic change in the composition and texture of the sediments when moving from the topographically highest and, therefore, oldest terraces to the current stream bed. These changes in the character of surface sediments can be used to constrain the provenance of cave sediment.

Chapter Three

Sedimentology of fossil-rich clastic sediments in Rising Star Cave, South Africa

Abstract

This study investigates the depositional history and lithostratigraphy of clastic sediments deposited in the Rising Star Cave. Clastic cave sediments are grouped into nine primary sediment types based on their relative proportions of gravel, sand, silt, and clay. These sediment types, coupled with bedding patterns, geochemical patterns and architecture form the basis for identification of nine distinct facies within the cave system, which include from course to fine: 1) clast supported polymictic breccia (CPB); 2) normal to inversely graded, matrix supported gravel facies (GMG); 3) clast supported normal graded gravel facies (CNG); 4) cross-stratified, very fine to very coarse sand facies (CsS); 5) scoured, normal graded, fine to very coarse sand facies (SnS); 6) laminated orange sand facies (LOS); 7) massive, fine to coarse sand and silt facies (MSs); 8) mud clast breccia facies (MCB); and 9) laminated orange red mud facies (LORM). These facies are repeatedly observed in different stratigraphic units throughout the cave. The mineralogy across the different facies is similar and consists mainly of quartz, chert, dolomite illite, muscovite, and insoluble iron and manganese oxyhydroxides. The oxyhydroxides occur in all facies, but are most abundant in undisturbed clay rich LORM and unlithified MCB facies located in relatively isolated and quiescent areas of the Dinaledi Subsystem and the Postbox Chamber. In these areas, it is interpreted that microbial activity and associated chemolithoautotrophic oxidation of insoluble $Fe^{2+} \rightarrow Fe^{3+}$ and $Mn^{2+} \rightarrow Mn^{4+}$ result in locally increasing levels of Fe-Mn oxyhydroxides.

Lithified MCB facies make up the oldest (>600 ka) clastic deposits in the cave, representing a series of widespread erosional remnants throughout the cave, extending beyond the investigated chambers. Their depositional history

and source remain unknown to date. The other unlithified facies in the cave are more abundant and their deposition initiated sometime between 600-400 ka, primarily entering the cave from a single westward fining, polymictic debris cone positioned below a vertical shaft in the Postbox Chamber. The debris cone facies are primarily allochthonous, derived from the surrounding surface that periodically entered the cave through a combination of river flooding, surface runoff, and to some extent, aeolian processes. From 400 ka onward, the quantity of allochthonous sediments entering the cave decreased and then ceased around 150 ka as the Upper Bloubank Spruit migrated in a NE direction, away from, and below the Postbox Chamber cave entrance. This resulted in an overall stratigraphic fining up of the facies in the cave. In addition to periodic sedimentation, seasonality, climatic changes and fluctuating phreatic ground water tables resulted in periodic erosion and redeposition of existing clastic cave sediment deposits further and deeper into the cave. During a period of low sedimentation, sometime around 335-240 ka, *Homo naledi* potentially entered and died or their remains were deliberately placed within the deep, distal reaches of the cave (Dinaledi and Lesedi chambers) where they were preserved.

3.1. Introduction

Typically, caves in the Cradle of Humankind (CoH) preserve a suite of clastic cave sediment deposits comprising well-lithified cave breccias, and younger, heterogenous sediments that are a mixture of quartz, dolomite, chert and ferromanganese nodules, bones, and kaolinite and illite clays (Pickering et al., 2007; Pickering and Kramers, 2010; Herries and Shaw, 2011; Herries and Adams, 2013; Bruxelles et al., 2014; Herries et al., 2014; Braga et al., 2017; Dirks et al., 2015, 2017; Herries et al., 2019; Wiersma et al., 2020). Most of the CoH hominin fossils (as well as other vertebrate fossil faunas) found in the caves are associated with the lithified cave breccias (Keyser, 2000; Berger et al., 2003; Clarke, 2007; Dirks et al., 2010; Bruxelles et al., 2014; Val et al., 2015; Van Zyl et al., 2016). In some instances, such as at Rising Star Cave, fossils (e.g., *Homo naledi*) are preserved in relatively young (~400-200 ka) unconsolidated muddy sediments (Dirks et al., 2015, 2017; Wiersma et al., 2020). The consolidated breccias with fossils that characterize most cave sediments are commonly interpreted as water-laid debris cone deposits that entered the caves through vertical shafts. The fossiliferous cave sites have been interpreted as death traps, scavenging sites, and places of shelter and include caves that experienced prolonged periods of occupation (Vrba, 1995; deMenocal, 2004, 2011; Dirks and Berger, 2013), resulting in the accumulation of diverse fossil fauna assemblages.

The Cradle of Humankind UNESCO World Heritage Site (CoH hereafter), South Africa (Fig. 1), has long been regarded as one of the most important fossil hominin regions in Africa (e.g., Dart, 1925; Broom, 1936; Broom and Schepers, 1946; Tobias, 1985; Brain, 1993), and it has recently enjoyed the discovery of a new, Pleistocene-aged, hominin species, *Homo naledi* (Berger et al., 2015; Dirks et al., 2017; Hawks et al., 2017). The fossils of this new species were discovered deep inside a cave, known as Rising Star Cave, which represent the largest concentration of fossil hominin bones from a single locality in Africa (Berger et al., 2015). Most of the fossils are concentrated approximately 30 m below the surface in the Dinaledi Chamber and are preserved in unlithified and autobrecciated mud clast breccia (Dirks et al., 2015; Wiersma et al., 2020). Subsequent fossil exploration and geological work in the cave system has focused primarily on dating the fossils and contextualising the sedimentology of the fossil-bearing deposits in the Dinaledi Chamber. Dirks et al. (2017) constrained the age of the *Homo naledi* fossils between 335-236 Ma and this age range was further refined by Robbins et al. (2021) to 335-241 ka. A second hominin-bearing chamber, the Lesedi Chamber, produced additional, as yet undated, *Homo naledi* fossils, but they were deposited within a different depositional context, although associated with similarly unconsolidated sediments (Hawks et al., 2017).

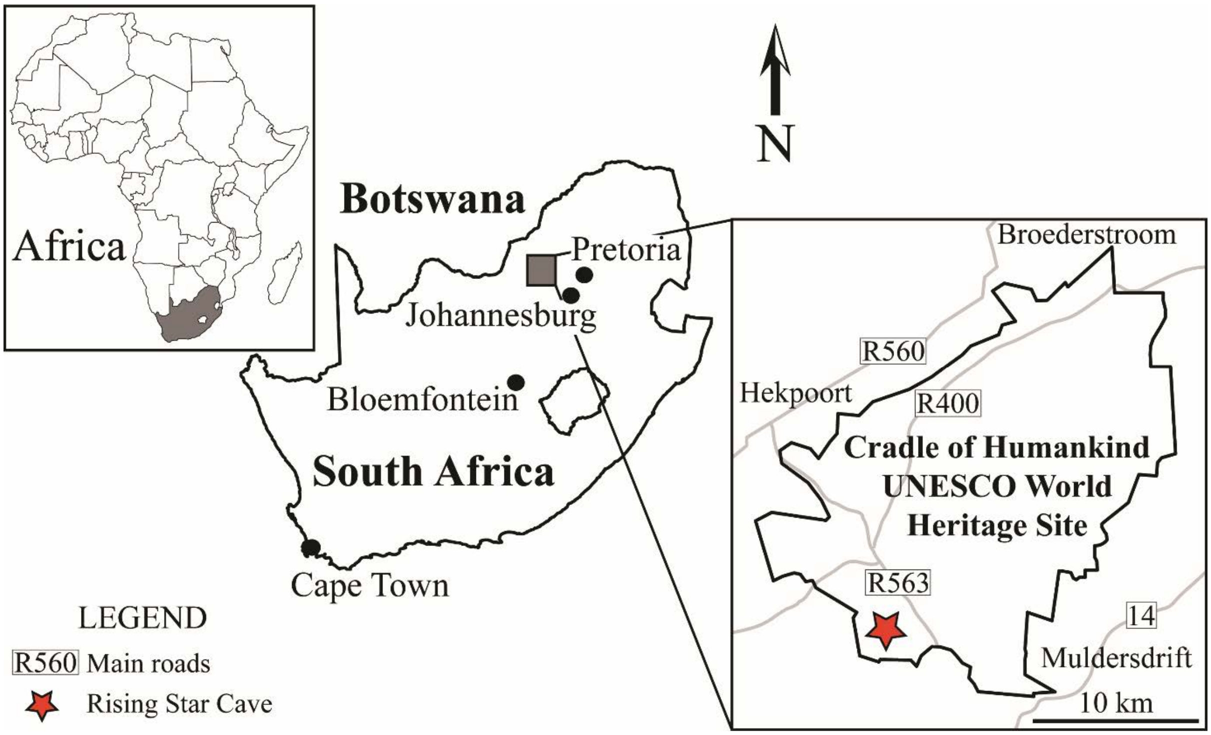

Figure 1. Locality of the Cradle of Humankind and Rising Star Cave.

The unconsolidated cave sediments in which the fossils are embedded, and unusual depositional context associated with the fossil accumulations in Rising Star Cave are different to what has been described from other hominin-bearing caves in the CoH (e.g., Berger et al., 2003; Clarke, 2007; Dirks et al., 2010). Firstly, the cave sediments in Rising Star Cave consist primarily of fine-grained, unlithified to poorly lithified clastic sediments and mud clast breccias, whereas lithified cave breccias are rare (Dirks et al., 2015). Secondly, the hominin fossils contained in the fine-grained sediment in the Dinaledi Chamber occur in dense concentrations of partly articulated remains and do not appear to have been deposited by water action (Dirks et al., 2015; Wiersma et al., 2020), which led to a hypothesis that *Homo naledi* entered the cave on purpose, possibly representing deliberate disposal of the dead (Dirks et al., 2015; Berger et al., 2017).

Many of these unconsolidated sediments in the cave that are associated with fossils consist of distinctive laminated orange-red muds (LORM facies) and hominin-bearing, autobrecciated mud clast breccias (UMCB facies) described by Wiersma et al. (2020). In addition to these two facies, clastic sediments also contain normal graded sandy intervals, local polymict breccia-conglomerates, cut-and-fill sandstone and lithified mud clast breccia deposits (Dirks et al., 2015; Dirks et al., 2017; Wiersma et al., 2020; Robbins et al., 2021). Although several of the sedimentary facies in the Rising Star Cave have been described in detail for the Dinaledi Chamber (Dirks et al., 2015; Dirks et al., 2017; Wiersma et al., 2020), a wider assessment of the different sediment facies, their distribution along the access route into the Dinaledi Chamber, and their association with other facies types has not been undertaken, but is necessary to understand the sedimentary history for the cave in relation to the deposition of the hominin fossils. Holistic sedimentary investigations of cave fill deposits like those in the Rising Start Cave have the potential to also reveal information about cave formation, paleoclimate and landscape evolution (e.g., Chapter 2; Pickering et al., 2007; De Ruiter et al., 2009; Sutton et al., 2009; Dirks et al., 2010; Pickering and Kramers, 2010; Pickering et al., 2010; Herries and Shaw, 2011; Dirks and Berger, 2013; Bruxelles et al., 2014; Val et al., 2015; Dirks et al., 2015; Dirks et al., 2017; Pickering et al. 2018).

This study investigates the main chambers along the access route into the Dinaledi Chamber with the purpose to expand on the detailed sedimentology already conducted in the Dinaledi Chamber and other chambers (e.g., Wiersma et al., 2020; Robbins et al., 2021). The main goal is to provide a more holistic investigation of the clastic facies and stratigraphic relationships of the unconsolidated sediment deposits along the main access routes into the Dinaledi Chamber, and explain the unique setting of the hominin fossils in the cave. This study combines grain size analysis, X-ray diffraction (XRD) and X-ray fluorescence (XRF) geochemistry and sediment mineralogy using mineral liberation analysis (MLA) to characterise the detrital sediment types in the cave. This information was then used to describe and interpret the full range of clastic facies that exist within the cave system. The goal of doing this is to develop a sedimentary infill model and better understand the depositional processes and events associated with this world-class hominin fossil locality.

3.2. Geological Setting and Previous Work

The following description of the geological setting partly repeats the 'Geological and Geomorphological Setting' section in Chapter 1. However, the repeated material has been included here so as not to disturb the flow of the chapter, which will be submitted as a paper.

Cave systems in the CoH and surrounding regions developed some four million years ago during the Plio-Pleistocene (Dirks and Berger, 2013), when they mainly formed within the dolomitic units of the Archean to Palaeoproterozoic aged Malmani Subgroup (Eriksson et al., 2001; Eriksson et al., 2006). Prior to cave formation, these carbonate lithologies were cross-cut by Paleoproterozoic-aged fracture systems induced by NW–SE directed extensional far-field stresses. Although these fractures were initially infilled with breccia deposits containing lithologies assigned to the Rooihoogte Formation of the lower Pretoria Group, they also formed the principal sites for facilitating cave formation during the Plio-Pleistocene. Most of the hominin-bearing caves in the CoH landscape are currently situated between 1330-1540 m above sea level due to Pliocene uplift (Dirks and Berger, 2013). But it is suggested that cave formation was initiated on the African Erosion Surface, prior to the onset of Plio-Pleistocene uplift. Once Pliocene uplift and incision occurred, caves stopped deepening and transitioned into passive sediment traps (Dirks and Berger, 2013).

Rising Star Cave is located in the southwest of the Cradle of Humankind UNESCO World Heritage Site, South Africa and is positioned at 26°01'011 96″S; 27°42'45 97″E near the valley floor in the Bloubank River valley, approximately 35 km northwest of Johannesburg (Fig. 1). The cave occurs in close proximity to other well-known hominin cave sites, some 2.2 km west-southwest of Sterkfontein Caves and 1.2 km west-southwest of Swartkrans. Rising Star Cave is classified as a deep network maze cave (Palmer, 1991, 2011; Dirks et al., 2015), consisting of several kilometres of interconnecting chambers and passageways that formed within a ~25 m-thick, west dipping stratigraphic succession of chert-poor, stromatolite-rich dolomites of the lower Monte Christo Formation (Eriksson et al., 2006; Dirks et al., 2015, 2017). The upper contact of the cave is marked by a ~1-metre-thick chert marker horizon (Dirks et al., 2015; Kruger et al., 2016). The west dipping strata define the preferred pathway for water movement, cave genesis, and cave progression. Although the cave geometry is mostly structurally controlled and follows various joint and fracture patterns within the lower Monte Christo Formation, chemical dissolution along open conduits resulted in widening of cave chambers and localised roof collapse features (Dirks et al., 2015).

On surface, Rising Star Cave is overlain and surrounded by a series of down-stepping, abandoned strath terraces that are degraded to various degrees. Several ESE-trending, neo-tectonic normal faults decorated with chert veins are situated north and south of the cave (Dirks et al., 2015). The best visible fault occurs north of the cave and a distinct fault scarp demarcates the boundary between the southern dolomite footwall, into which Rising Star Cave had formed, and the northern hanging wall which is covered by a >20 m thick layer of alluvium (Chapter 2). Neotectonic activity likely initiated the formation of the terraces in conjunction with a NE migration of the Upper Bloubank Spruit stream, which is currently positioned on the alluvial surface (Chapter 2). The Upper Bloubank Spruit is a (ephemeral) tributary stream bed, which is positioned just north of the fault scarp, circa 100 meters north from the cave entrance (see Fig. 1C in Chapter 2). This small stream periodically feeds into the larger Bloubank Spruit to the east, but the tributary is currently dry and borehole measurements indicate that the water table lies at ~ 22 m below surface. During the Pleistocene, before erosion exposed the Rising Star cave system, the Upper Bloubank Spruit was positioned further to the south and flowed higher in the landscape, above the cave. Dating of flowstone horizons in the cave suggests that between ca. 600-400 ka, flood-borne surface sediments would periodically spill into the Postbox Chamber via a vertical shaft that connected the chamber to surface (Chapter 2, 4; Robbins et al., 2021). Today, this cave opening is closed as it is blocked by a mixture of surface and cave sediments that form a clast supported polymictic breccia. From the surface this closed entrance is recognized as a small depression on the landscape (Dirks et al., 2015; Robbins et al., 2021).

This study (chapter) investigates the sediment fill in the four cave chambers that occur along the main entry routes into the Dinaledi Chamber; the chamber where most of the *Homo naledi* fossils were found (Fig. 2). These chambers include the Dinaledi Subsystem, the adjacent Dragon's Back Chamber, Superman Crawl passage and Superman Chamber, and the higher positioned Postbox Chamber and to some extent, the Lesedi Chamber which is located further to the northwest (Fig. 2). Two additional sub-chambers were explored during fieldwork in 2017 that contain clastic sediments and are introduced here as the 'Middle' and 'Upper' Postbox chambers (Fig. 2B). These small sub-chambers can be accessed through a narrow vertical passage via the eastern part of Dragon's Back Chamber and are roughly positioned above the Postbox Chamber. The 'Upper' Postbox Chamber partially connects to surface via a narrow and shallow west-dipping fracture, which contains surface sediments and live roots from the surface. The Dinaledi Subsystem lies ~80 m away from the present entrance into the cave and is positioned furthest and deepest from the entrance compared to the other chambers. The subsystem is comprised of several smaller chambers, including the Chaos Chamber, Hill Antechamber, and the Dinaledi Chamber

(Fig. 2; Berger et al., 2018). The vast majority of the *Homo naledi* fossils are preserved along the floor of the Dinaledi Chamber where they occur in the upper 20 cm of unlithified and autobrecciated mud clast breccia deposits (Dirks et al., 2015; Wiersma et al., 2020). The Dinaledi Chamber can only be accessed via the Dragon’s Back Chamber, which in turn can be accessed via a direct route that passes through the Postbox Chamber; or along a more complex maze of fractures via the Superman Chamber (Fig. 2; Dirks et al., 2015). In addition to the fossils in the Dinaledi Chamber, the Lesedi Chamber also hosts several *Homo naledi* fossils, including a near complete male skull (Dirks et al., 2015; Hawks et al., 2017).

Clastic sediments are common and widespread in the chambers along the access route into the Dinaledi Chamber, occurring primarily as erosion remnants along walls, underneath flowstones, and as floor sediments in all investigated chambers (Dinaledi Subsystem, Dragon's Back, Superman, Middle and Upper Postbox, and Postbox chambers). The preserved remnants of these unlithified cave sediment accumulations represent a westward dipping clast supported polymictic breccia debris cone (Robbins et al., 2021), with its apex situated in the Postbox Chamber and sediment distributing further into the adjacent Dragon's Back and Superman chambers. These sediments are primarily allochthonous in origin, i.e., transported into the cave directly from the surrounding surface, and occasionally mixed with small amounts of autochthonous sediment (Chapter 3; Dirks et al., 2015; Wiersma et al., 2020). Although the unlithified sediments in Rising Star Cave have been interpreted as a single subterranean debris cone by Dirks et al. (2015, 2017) and Robbins et al. (2021), their work focused mainly on the sediments in the Dinaledi Chamber as well as providing chronological context for the sediments based on flowstone units, respectively, thus lacking a more detailed depositional model regarding the clastic sediments in the cave.

In previous studies, the unlithified cave sediment units have been broadly categorized as laminated muds that locally contain micro-mammal fossils, lithified and unlithified mud clast breccias, and various sandy and gravelly deposits (Dirks et al., 2015, 2017; Wiersma et al., 2020; Robbins et al., 2021). Dirks et al. (2015, 2017) defined unit names in the Dinaledi Chamber and Wiersma et al. (2020) defined facies nomenclature, referred to by Makhubela et al. (2017) and expanded on Robbins et al. (2021). In this chapter, a more holistic analysis of the sedimentology throughout the cave has led to the diagnosis and description of nine repeating facies that can be recognized throughout the cave system. Table 1 provides an overview of the names assigned to each of the discrete clastic facies, including previously designated facies and additional facies described for the first time in this chapter.

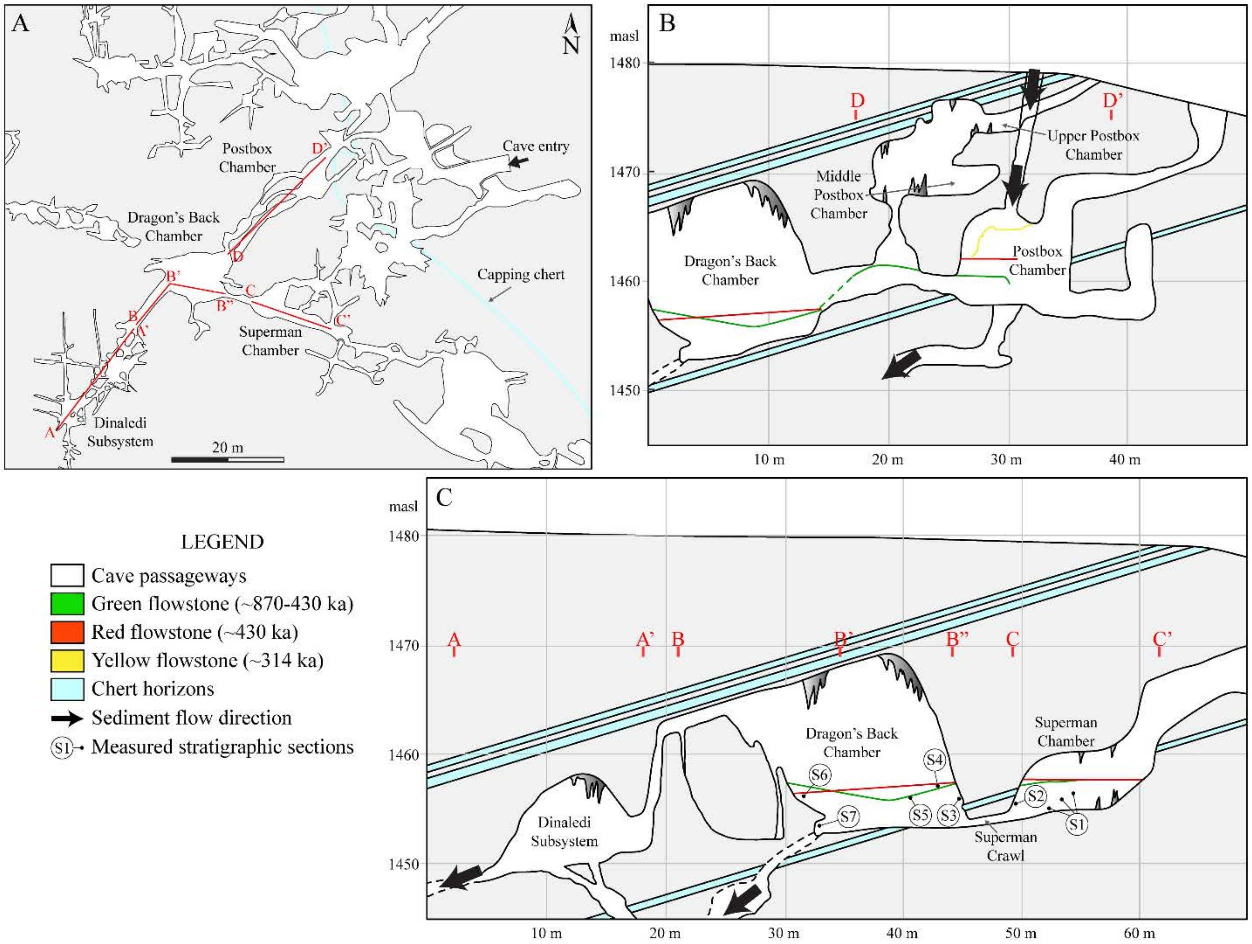

Figure 2. Map overview of Rising Star Cave and cross section areas for the investigated chambers. (A) Total overview of the different chambers in Rising Star Cave. (B) Cross section view of the Dragon's Back, Postbox and Upper and Middle Postbox chambers. (C) Cross section view of the Dinaledi Subsystem, Dragon's Back and Superman chambers, including the localities for measured stratigraphic sections. Note that the Upper and Middle Postbox chambers have not yet been mapped in plan view. Flowstone nomenclature is after Robbins et al., 2021.

Throughout the investigated chambers, grain-size becomes progressively finer the further and deeper into the cave, and transition from breccia and gravelly sand and muds in the Postbox Chamber to sand and muds in the Dragon's Back and Superman chambers to laminated mud and autobrecciated mud in the Dinaledi Subsystem. Throughout the cave, small quantities of autochthonous material mixed with this sediment and include silt-sized secondary quartz, chert, sericite mica, and insoluble Fe and Mn-oxyhydroxides that weathered out from the dolomite host rock during cave formation (Chapter 4). Autochthonous sediment deposits appear highly localized in the cave and are often chamber specific, ranging in concentrations as low as ~1% in the Dinaledi Subsystem and locally up to ~5% in the Superman and Dragon's Back chambers and a cave-wide average of ~3% (Chapter 4). Host rock dolomite walls and exposed sheared mylonitic shale horizons in the chambers are the main contributors to the autochthonous sediment budget in the cave (Chapter 4). Some of the insoluble Fe-Mn-oxyhydroxides in the cave also occur as ~2.1-2.0 Ga-aged, millimetre-sized peloidal nodules derived from surface (Makhubela et al., 2017), and minor quantities of manganese are also derived directly from the dolomite host rock itself (Eriksson et al., 2006). Additionally, these oxyhydroxides are commonly subjected to non-sedimentary cave processes, i.e., diagenetic and chemoautotrophic alterations of metallic ions, primarily oxidizing iron and manganese (Engel, 2012; Wiersma et al., 2020) and secondary growth of sparry calcite and aragonite (Dirks et al., 2015), locally increasing the autochthonous component in the sediment budget. Geochemical analyses of the clastic sediments typically reveal little to no calcite concentrations, which has been interpreted to reflect mildly acidic conditions in the cave (Dirks et al., 2015; Wiersma et al., 2020), which locally dissolve the carbonate grains from the sediment.

Speleothems in Rising Star Cave consist chiefly of flowstone deposits formed beneath numerous drip points that are widely distributed throughout the cave, with extensive vertical and horizontal flowstone deposits being most common. Drip points are common throughout the entire cave also, leaching calcite-enriched vadose waters into the cave, indicating the presence of direct connections to surface (Dirks et al., 2015; Robbins et al., 2021). A total of seven stratigraphically distinct flowstone groups have been described for the central part of Rising Star Cave where the clastic sediments have accumulated (Robbins et al., 2021; Chapter 1). These flowstones provide relative age constraints obtained from U-series techniques (Robbins et al., 2021) for the clastic sediments in the cave. Three major flowstone groups, which were colour coded for easy reference in Robbins et al. (2021), and referred to as 'Green', 'Blue', and 'Red' flowstone horizons can be correlated across several cave chambers. Other flowstone groups enjoy a more localized, chamber specific, distribution and have been referred to from old to young as 'Purple', 'Pink', 'Yellow', and 'Grey' flowstones (Robbins et al., 2021).

Table 1. Clastic facies names for Rising Star Cave

Facies names used in this chapter	**Facies abbreviation**	**Facies names used in previous studies**
Clast supported polymictic breccia	(CPB)	CPB (Robbins et al., 2021)
Matric supported gravel	(GMG)	
Normal graded gravel	(CNG)	
Cross stratified sand	(CsS)	LORM (Wiersma et al., 2020) Facies 1b (Dirks et al., 2015)
Massive sand and silt	(MSs)	
Layered orange sand	(LOS)	LOS (Robbins et al., 2021)
Massive orange sand	(MOS)	MOS (Robbins et al., 2021)
Scoured sand	(SnS)	
Laminated orange red mud	(LORM)	LORM (Wiersma et al., 2020; Robbins et al., 2021)
Mud clast breccia	(MCB)	
Unlithified mud clast breccia sub-facies	(UMCB)	UMCB (Wiersma et al., 2020; Robbins et al., 2021) Unit 3a: fossil-poor (Dirks et al., 2017); Unit 3b: *Homo naledi*-bearing (Dirks et al., 2017) Facies 2 (Dirks et al., 2015)
Lithified mud clast breccia sub-facies	(LMCB)	LCMB (Robbins et al., 2021) Unit 1a: fossil-poor (Dirks et al., 2017); Unit 1b: micromammal fossil rich (Dirks et al., 2017) Facies 1a (Dirks et al., 2015) Facies 1b (Dirks et al., 2015)

The 'Green' flowstone group includes multiple flowstone horizons that were defined in all chambers as overlying lithified mud clast breccia deposits (LMCB facies in Robbins et al., 2021). The flowstone has been broadly dated at >600 ka with an estimated age range of 600-1100 ka (Dirks et a., 2017; Robbins et al., 2021). Remnants of a prominent ‘Green’ flowstone horizon can be traced throughout the Postbox, Dragon's Back and Superman chambers, and possibly correlates with similar deposits in the Dinaledi Subsystem (Robbins et al. (2021). The second oldest, "Blue" flowstone group (Robbins et al., 2021) also overlies LMCB deposits and forms a semi-continuous undulating sheet and occurs stratigraphically above the ‘Green’ flowstones in the Dragon's Back and Superman Chambers. It has been dated at >600 ka with an estimated age range of 900-600 ka (Robbins et al., 2021). The 'Red' flowstone group overlies the semi-consolidated, sandy clastic sediments that are a major focus of this study and forms a prominent near-horizontal horizon in the Dragon's Back Chamber with further small occurrences in the Post Box and Superman

Chambers. Age estimates for this flowstone group are 500-400 ka (Makhubela, 2019; Robbins et al., 2021).

Two younger flowstone groups represented by more localized deposits, termed 'Purple' (~225-190 ka) and 'Pink' (~160 ka), occur mainly in the Dragon's Back Chamber (Robbins et al., 2021). This flowstone group includes two distinct depositional events around 225 ka and 200 ka and occupies multiple locations within the Dragon’s Back Chamber where it overlies remnants of partly eroded sandy clastic sediments including a small debris cone at the base of the Dragon's Back block in the SW portion of the chamber. The 'Pink' flowstone occurs as a thin (<1 cm thick) drape in the NW corner of Dragon's Back Chamber, covering erosion remnants of layered orange sands (LOS) and channel infill containing massive orange sands (MOS facies in Robbins et al. 2021).

In the Postbox Chamber, directly below the sediment entry shaft, a single <1 m wide flowstone sheet referred to as the 'Yellow' flowstone yields an age of ~300 ka (Robbins et al. 2021). Using Al-Be cosmogenic dating techniques, Makhubela (2019) provide a best estimate of ~450 ka for clast supported, breccia deposits underlying the “Yellow” flowstone. The 'Grey' flowstone group represents the youngest suite of flowstone deposits in the cave. They consist of clear white calcite and form drapes, curtains, and (drip point) pool rims atop erosion remnants of all other flowstone and sediment deposits in all chambers. They comprise a number of depositional episodes dated at ~110-90, 70, 50, 30 and 10 ka (Robbins et al. 2021).

While the LMCB that occurs in association with the ‘Green’ and ‘Blue’ flowstone units will be described and discussed, this study will focus on the sedimentary evolution of the semi- to un-consolidated clastic sediments that accumulated above the ‘Green’ and ‘Blue’ and below the ‘Red’ flowstone unit, as well as the clastic sediments that occur interlayered with the ‘Purple’, ‘Pink’ and ‘Yellow’ flowstones, i.e. the clastic sediments that were deposited and partly reworked between ~600 ka and 150 ka along the subterranean debris cone (Robbins et al., 2021).

3.3. Methods

3.3.1. Description of cave stratigraphy

Over two field seasons in 2016-2017, extensive geological investigations were conducted throughout the Rising Star Cave system. Field work was carried out with the assistance of a team of cavers as part of the Rising Star Project. All work was conducted with permission of the South African Heritage Resource Agency, Department of Arts and Culture (Permit ID: 952). Lithostratigraphic sections were measured at the centimetre-scale and described, focusing on the sedimentology and stratigraphic architectures of individual sections that are preserved in the cave to establish a facies framework. In addition to descriptive work, sedimentary facies and significant characteristics, e.g., grading, fossil content, and bedding structures were photographed, using a Nikon, 35 mm digital camera. Previously described facies, including LORM and UMCB facies from the Dinaledi Subsystem, e.g., Dinaledi Chamber and Hill Antechamber (Dirks et al. 2015, 2017; Wiersma et al., 2020) are integrated and summarized in this work.

A total of seven stratigraphic sections were measured and described. Two stratigraphic sections from different locations in the Superman Chamber (Fig. 2C), which include: section 1) laminated mud and sand remnants directly above the Superman Crawl entry; section 2) laminated mud remnants in a vertical fracture along the south wall and sand dominated and laminated mud remnants atop flowstone along the northern wall. Five stratigraphic sections were measured from the Dragon's Back Chamber (Fig. 2C) and include the following locations: section 3) laminated mud and sand positioned directly above the Superman Crawl entry; section 4) a sandy remnant underneath a flowstone, 2 m west of section 1 above the Superman Crawl entry; section 5) lithified mud clast breccia and channelized sandstone in the central part of the chamber; section 6) coarsening upward sand to gravel deposits in the northwest corner of the chamber; section 7) gravel and sand deposits in a small alcove underneath the Dragon's Back block. Sediment remnants observed in the Postbox Chamber and the Upper and Middle Postbox chambers were described and have been assigned to facies where possible. Only small quantities of sediment are preserved in the Upper and Middle Postbox chambers, occurring primarily in solution pockets of the cave wall and as floor sediments.

3.3.2. Grain size distribution and sediment types

Thirty-three unlithified clastic cave sediment samples were collected and tested for grain size variability throughout the different cave chambers. Samples were collected from different facies in the Dinaledi Subsystem, Dragon's Back, Superman, and Postbox chambers. For each grain size analysis, ASTM D421 (2007) and D422 (2007) standardized methods were followed, using ~75-200 grams per sample. Size fractions ≥500 µm were dry-sieved, using 4,000-2,800-2,000-

1,000-500 µm sieves, whereas the <500 µm size fractions were carried out applying the hydrometer method with a calibrated H-152 model hydrometer. Hydrometer and temperature readings were taken at 2, 5, 15, 30, 60, 250 and 1440 minutes, totaling 24 hours. The resulting grain size distributions were plotted as cumulative frequency graphs in Microsoft Excel.

The obtained grain size data was statistically tested for percent gravel, sand, silt and clay, median and mean grain size, standard deviation, sorting, and skewness, using the software package GSSTAT version 2.04 (Poppe et al., 2004) to test for grain size distribution of each sample. The analyses were performed using the Inclusive Graphics calculation method of Folk (1974) with no extrapolation parameters applied, and cumulative frequency percentages selected for file input and output.

The software package SEDCLASS version 1.0 (Poppe et al., 2003) was then used to quantify different sediment types, and categorize them based on percentages of gravel, sand, silt and clay, derived from the GSSTAT statistical analysis. The results were visualized in SEDPLOT version 1.0 (Poppe et al., 2008) on the Shepard (1954), Schlee (1973), and Folk (1954, 1974) sediment classification diagrams. The grain size distributions for each sediment type were visualised on cumulative frequency precent graphs and plotted on a ternary diagram to further visualize variations in sediment types.

3.3.3. Geochemistry

3.3.3.1. Mineral liberation analysis (MLA)—Mineral liberation analysis was carried out on sediment samples from the all the investigated chambers to identify the weighted percent modal mineralogy of the unlithified cave sediments. Samples were individually sieved, and the 0.5-1 mm size fraction was chosen for grain mounts so that individual grains could be identified and analysed. The clay size fraction was removed from the samples and excluded from the grain mounts to avoid formation of aggregates that could lead to erroneous interpretation of mineral characteristics. Instead, the clay mineralogy for each sample was determined with XRD and XRF analysis. Each sample was polished and carbon coated and consists of ~300-350 individual grains that are 0.5-1 mm in size.

The samples were analysed in the scanning electron microscope (SEM) lab at Memorial University, Newfoundland, Canada, using a FEI Quanta 400 SEM equipped with energy dispersive X-ray (EDX) spectrometers and mineral liberation analyser software v.3.1.4.683 (Sylvester, 2012).

The mineral liberation measurements are based on backscatter electron (BSE) image analysis. Shape analyses were carried out for each sample to determine mean roundness and sphericity of the grains, using the 64-bit Fiji software package (Schindelin et al., 2012).

3.3.3.2. X-ray diffraction and X-ray fluorescence—Cave and surface sediment samples were analysed for bulk and clay mineralogy and geochemistry using X-ray diffraction (XRD) and X-ray fluorescence (XRF). Prior to the analysis, clay was separated from the samples and all samples were then oven-dried at 40°C for 48 hours to remove excess moisture. The bulk geochemical analyses (XRD & XRF) were carried out at North West University, South Africa, and clay geochemistry was analysed via XRD at James Cook University in Australia using a Bruker D2 Phaser with an SSD-160 detector (Bruker, Billerica, MA, USA) using preferred orientations only, omitting the glycolated and thermally heated methods. X-ray fluorescence was carried out in a Bruker S2 PUMA EDXRF spectrometer, equipped with a SSD HighSense LE detector and 50W X-ray tube (Bruker, Billerica, MA, USA). Glass beads composed of 1.0 gram of sample mixed with 8.0 gram of flux (catch weight) were fused into glass discs.

3.3.4. Facies analysis

A suite of nine facies were identified in this investigation which includes the documentation of five newly defined facies and several previously established facies by Wiersma et al. (2020) and Robbins et al. (2021), see Table 1. Each of these facies, new and old, is based on a combination of unique grain-size (sediment type) and bedding patterns. Newly defined facies in this study, are given names consistent with the facies nomenclature in Miall (2006). In this study, the LORM facies as described by Wiersma et al. (2020) is further refined, focusing only on the laminated clay and silt rich component (facies 1a in Dirks et al., 2015). The interbedded sand lenses referred to as facies 1b in Dirks et al. (2015) are distinct enough to warrant a separate facies (Table 2). Some of the facies, i.e., the CPB and GMG facies, could not be sampled for analysis due to the deposits being unstable and/or the risk of collapse of overhanging rocks being too great.

3.4. Results

3.4.1. Grain-size (sediment types)

The starting point for establishing the primary clastic facies in the Rising Star cave is detailed grain-size analysis, which resulted in the documentation of eight distinct grain size classes or sediment types (Figs. 3 and 4). The cave sediments are dominant in sand, silt and clay and contain on average <10% gravel (Fig. 5). They are very to extremely poorly sorted with standard deviations for sorting ranging from 2.3-5.02. The data is positively and negatively skewed, ranging from -0.51 (= strongly coarse skewed) to 0.53 (= strongly fine skewed), see Poppe et al. (2004). The eight cave sediment types are described in more detail below.

3.4.1.1. Muddy sandy gravel—A single sample collected from the floor sediments of Superman Crawl at a depth of ~25 cm below the floor level has been classified as muddy sandy gravel (Table 2). It is the coarsest of the unlithified clastic cave sediments and is extremely poorly sorted (1σ st.dev. = 4.61). The grain size distribution shows a strong bimodal distribution but is biased towards the coarser size fractions (Fig. 4A). This sediment type contains the largest proportion of gravel (~40%) and sand (35%) (Table 2; Fig. 5) and relatively little silt (<10%) and clay (~16%).

The dominant XRD phases include quartz, muscovite, and kaolinite (Fig. 6A). X-ray fluorescence shows elevated levels of Al_2O_3 (3.86%) and Fe_2O_3 (5.01%) compared to MnO (0.97%), CaO (1.36%) and other oxides (<1%) other than quartz (Fig. 5B), corresponding to the presence of kaolinite, muscovite and illite clays in the sediment, as well as high levels of iron oxides and oxyhydroxides that were identified through mineral liberation analysis (Fig. 4B). Most of the sediment comprises quartz (72.25%) followed by kaolinite (11.02%), muscovite (9.43%), and minor contributions of illite (3.55%). Iron and manganese oxides and (oxy)hydroxides constitute 5.65% of the sediment composition, including hematite and magnetite (2.14%) and limonite and goethite (1.21%), followed by low concentrations of pyrolusite (0.88%) and todorokite (1.43%). The altered mineral epidote is present but occurs at low concentrations of <2%. Calcite constitutes 3.19% of the total sediment composition whilst other carbonate minerals concentrations are well below 1%. Low concentrations of calcium phosphate (0.01%) and apatite (1.03%) coincide with the lack of fossil material present in the sediment.

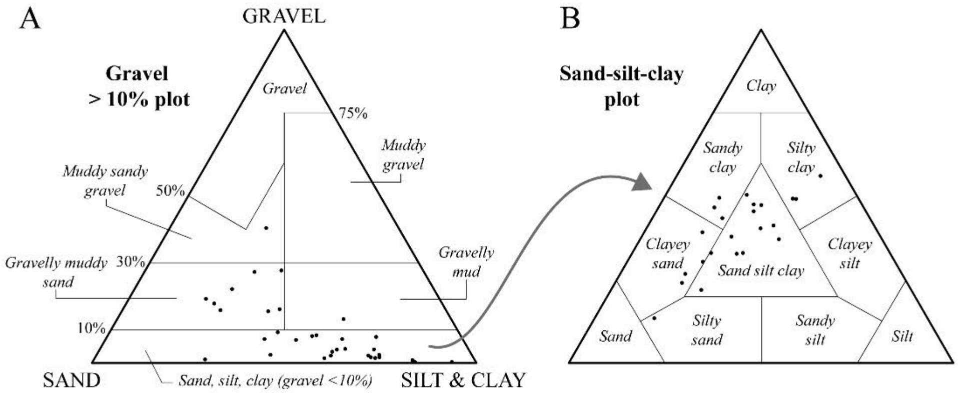

Figure 3. Sediment types for clastic sediments in Rising Star Cave. (A) Distribution of clastic sediment samples (black dots) within the Gravel-Sand-Silt/Clay sediment type ternary diagram, modified after Shepard (1944) and Schlee (1973) and Folk (1953, 1974). (B) Distribution of sediment samples that contain less than 10% gravel in the Sand-Silt-Clay ternary diagram after Shepard (1954) and Schlee (1973).

3.4.1.2. Gravelly muddy sand—Eight samples collected from floor sediments and erosion remnants along the walls from the Dragon's Back, Postbox, Upper and Middle Postbox, and Superman chambers were classified as gravelly muddy sand (Table 2). This sediment type is extremely poorly sorted (1σ st.dev = 4.85) and shows a bimodal grain size distribution with peaks emphasizing the sand and clay fractions (Fig. 4A). The sediment type is primarily composed of sand (50%), followed by gravel (20%), clay (18%), and 12% silt (Table 2). Moderate amounts of micromammal fossils are present in the sediment in the form of isolated teeth, jaw fragments and long bones.

The main XRD phases include quartz, kaolinite, muscovite, and calcite (Fig 5A). X-ray fluorescence shows elevated levels of Al_2O_3 (5.34%), Fe_2O_3 (6.42%), CaO (1.99%) and P_2O_5 (2.63%) compared to the other oxides (<1%) The elevated oxide concentrations correspond to the presence of kaolinite, muscovite and illite clays as well as the presence of iron and manganese oxides and oxyhydroxides and organic phosphates from fossil content. Mineral liberation analysis confirms elevated levels of calcite, other carbonates, and epidote (Fig. 4B). Most of the sediment consists of quartz (66.67%). Iron and manganese oxides and (oxy)hydroxides constitute 4.94%, the bulk consisting of magnetite and hematite (0.64%), goethite and limonite (1.4%). Manganese oxyhydroxides include pyrolusite (1.47%) and todorokite (1.44%). Calcite makes up 3.34% of the sediment budget, but other carbonate minerals are rare, with <1% dolomite, rhodochrosite and siderite. Elevated values of apatite (2.39%) derived from fossil material occur, but calcium phosphate values remain low at 0.23% (Fig. 4B).

3.4.1.3. Gravelly mud—A single sample was collected ~5 cm below the *Homo naledi*-bearing unlithified mud clast breccia floor sediments in the Dinaledi Chamber. The sediment is classified as gravelly mud (Table 2) and is extremely poorly sorted (1σ st.dev. = 4.46), showing a modest bimodal grain size distribution with a strong bias toward the clay fraction (Fig. 4A). The sediment type is primarily clay-dominant (~44%), also containing moderate amounts of sand (~28%), gravel (~13%) and silt (~15%). The sediment is devoid of fossil material.

The main XRD phases include quartz, muscovite, kaolinite and goethite (Fig. 6A). X-ray fluorescence shows significant concentrations of Al_2O_3 (14.08%), Fe_2O_3 (13.96%) and MnO (4.66%) compared to most other oxides (Fig. 6B), and correlate to the particularly high concentrations of illite, muscovite, and iron-manganese oxides and oxyhydroxides detected in mineral liberation analysis (Fig. 4B). The modal mineralogy detected low quantities of quartz (21.47%), but records elevated mica concentrations (48.84%), identified as muscovite and illite (Fig. 4B). Iron and manganese oxides and oxyhydroxides consist of limonite and goethite (1.99%), todorokite (1.82%), and elevated values of pyrolusite (5.8%) and Mn-Al-Si oxides (4.78%). Hematite and magnetite concentrations are low (0.04%). Carbonates are nearly absent from the sediment with only trace values of dolomite (0.01%) and rhodochrosite (0.02%) detected. No calcium phosphate was detected, and apatite values are very low (0.01%).

3.4.1.4. Silty sand—A single sample was collected from an erosion remnant of unlithified sediment in the Superman Chamber and is classified as silty sand (Table 2). The grain size distribution is bimodal with peaks occurring in the sand and clay fraction, resulting in very poorly sorted sediment (1σ st dev= 2.62). Silty sand is a sand dominated (70%) sediment and contains the highest concentration of sand compared to other cave sediment types. The sediment is very gravel poor, constituting 1.05% of the grain size fraction and contains moderate amounts of silt (15%) and clay (16%). This sediment type is rich in micromammal fossils, consisting of isolated teeth, partial skulls and long bones.

The XRD detected mainly quartz and possibly muscovite (Fig. 6A). X-ray fluorescence shows elevated concentrations of Al_2O_3 (6.8%), Fe_2O_3 (4.15%) and P_2O_5 (3.46%) compared to most other oxides (Fig. 6B). Elevated levels of P_2O_5 coincides with the presence of fossil content in the sediment. Quartz (68.4%) is the most abundant mineral (Fig. 4B), followed by illite (9.23%) and muscovite (8.12%). The sediment records low values of iron and manganese oxides and oxyhydroxides, with limonite and goethite concentrations (1.52) being the most prominent, compared to the low values of hematite and magnetite (0.35), pyrolusite (1.17%) and todorokite (0.89%). Mn-Al-Si- oxide values of 1.96% are also low. Low values of calcite (0.96%) are also detected but records the highest carbonate value compared to dolomite (0.22%) and siderite (0.02%). Only moderate amounts of apatite (1.81%) was detected, but no calcium phosphate.

3.4.1.5. Clayey sand—Four samples were collected from unlithified floor and along wall sediments in the Dinaledi, Dragon's Back and Superman chambers (Table 2). The grain size distribution of the sediment is extremely poorly sorted (1σ st. dev. = 4.45) and bimodally distributed, being primarily sand (45%) and clay (30%) dominated with moderate amounts of gravel (7.5%) and silt (18%) (Fig. 4A). The sediment type is rich in micromammal fossils.

The main XRD phases include quartz and muscovite, but also show a clear presence of calcite (Fig. 6A). X-ray fluorescence shows elevated concentrations of Al_2O_3 (8.97%), Fe_2O_3 (8.13%) and CaO (4.58%) and moderate amounts of MnO (1.96%) and P_2O_5 (1.89%) (Fig. 6B). Quartz (48.46%) is the most abundant mineral, followed by illite (19.79%) and muscovite (4.67%). Clayey sand records the highest concentration of apatite (5.53%) compared to other sediment types (Fig. 4B), which coincides with the presence of abundant fossil content. Although clearly present in XRD, carbonate values are low, with calcite being the main constituent recording a value of 1.17%. The overall concentration of iron and manganese oxides and oxyhydroxides is >10%, with pyrolusite (4.53%) recording the highest values, followed by todorokite (2.35%) and goethite and limonite (1.7%) and manganese-aluminum-silica oxide aggregates (3.2%). Magnetite and hematite values are low (0.13%).

3.4.1.6. Sandy clay—Three samples were collected from unlithified floor and cave wall sediments from the Dinaledi and Hill Antechamber, and Superman chambers (Table 2). The sediments are overall fine-grained, and the grain size distribution is extremely poorly sorted (1σ st. dev. = 4.33) and coarsely skewed, producing a major peak in the clay fraction and minor peaks in the gravel-sand fractions. The sandy clay sediments are clay dominant (46.51%), followed by sand (33.35%), silt (15.8%), and minor amounts of gravel (4.34%) (Fig. 4A). The sediment is relatively fossil poor.

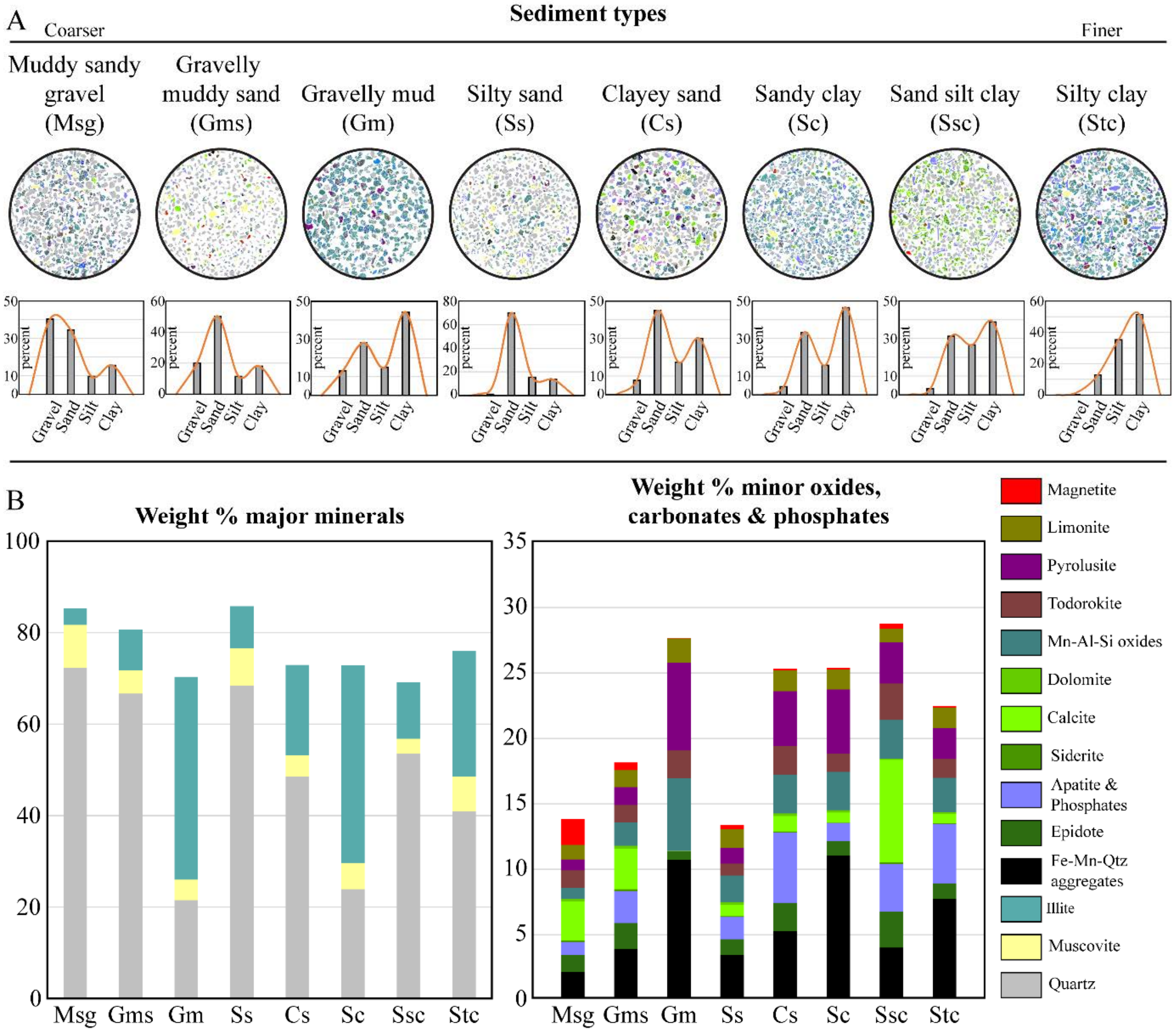

Figure 4. Rising Star Cave sediment types. (A) Modal mineralogy of the different sediment types including first order grain size distributions. (B) Major and minor mineral composition for the individual sediment types.

The main XRD phases include quartz, muscovite, and some goethite (Fig. 5A). X-ray fluorescence shows elevated concentrations of Al_2O_3 (13.81%), Fe_2O_3 (13.31%) and MnO (4.1%) (Fig. 6B). Illite (53.5%) is the most abundant mineral, followed by low concentrations of quartz (23.87%) and muscovite (3.28%) (Fig. 4B). The overall concentration of iron and manganese oxides and oxyhydroxides is >10% (Fig. 4B). Pyrolusite (5.28%) records the highest values, followed by goethite and limonite (1.64%) and todorokite (1.51%). Magnetite and hematite values are low (0.14%).

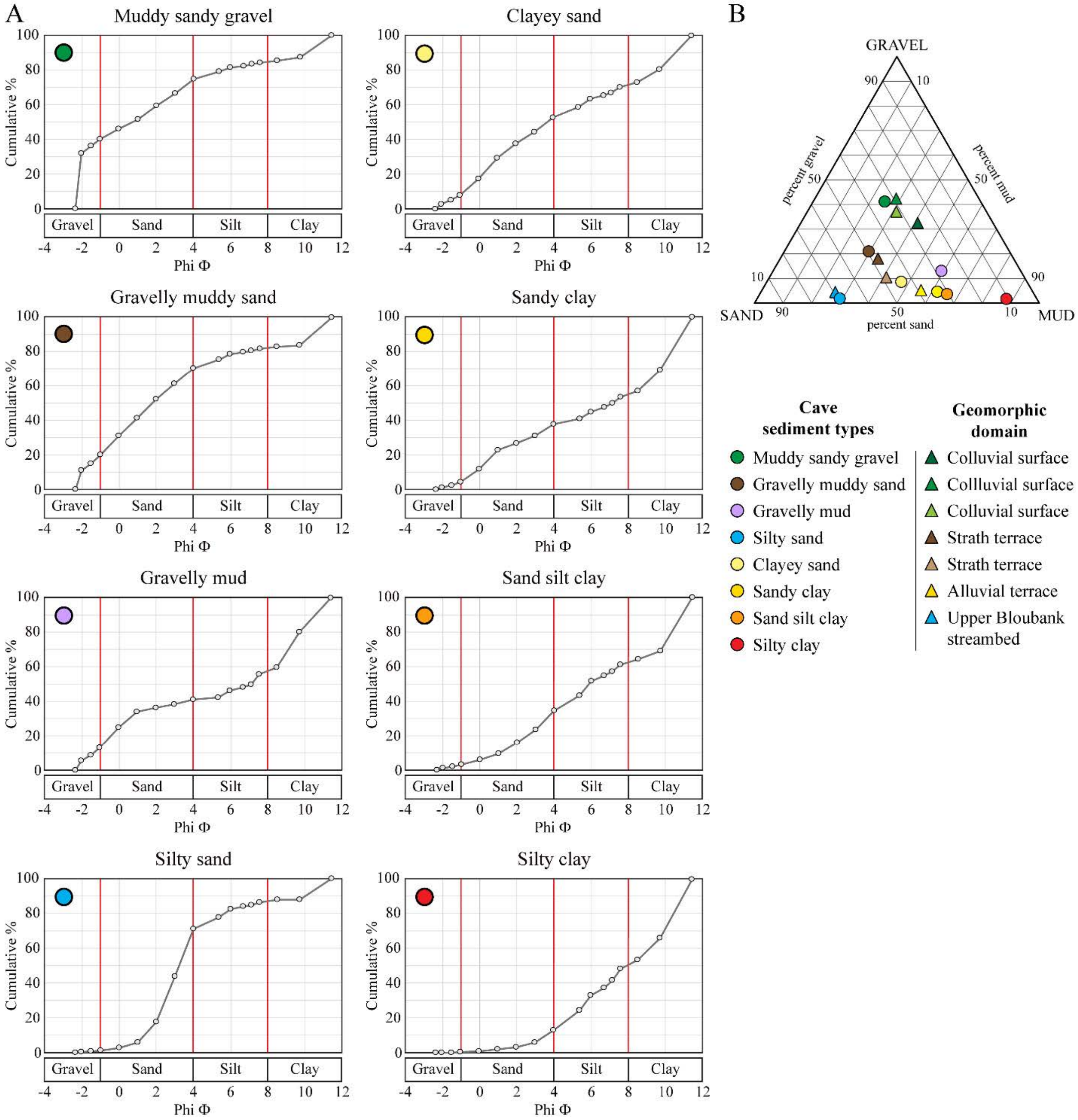

Figure 5. Cumulative frequency graphs for the different sediment types within Rising Star Cave (A) and sediment types and associated geomorphic domains plotted on a Gravel-Sand-Mud ternary diagram (B) to illustrate the overall finer-grained character of clastic sediments in Rising Star Cave. The color coding for each sediment type corresponds to the colored dots on the ternary

diagram. Data for the geomorphic domains in the ternary plot has been taken from Chapter 2 and is integrated with the new data in this chapter.

3.4.1.7. Sand silt clay—Twelve sediment samples were identified as sand silt clay sediment types (Table 2). They occur commonly throughout the cave and were collected from unlithified floor and cave wall sediments in the Dinaledi Chamber, Dragon's Back, Postbox, Upper and Middle Postbox, and Superman chambers (Table 2). The sediments are very poorly sorted (1σ st. dev. = 3.87) and the grain size distribution is bimodally distributed, showing a strong peak in the clay fraction as well as a moderate peak in the sand-silt fractions (Fig. 4A). Clay is the dominant size fraction, constituting 38.89% of the sediment composition, whereas gravel content is low, making up 3.22% of the total size fraction. Sand and silt fractions occur in concentrations of 31.22% and 26.67%, respectively. Sand-silt-clay sediments are generally rich in micromammal fossils.

The main XRD phase consists primarily of quartz with low counts of muscovite and kaolinite detected (Fig. 6A). X-ray fluorescence shows elevated concentrations of Al_2O_3 (10.5%), Fe_2O_3 (4.86%) and CaO (3.19%) and moderate amounts of MnO (1.21%). MgO (1.61%) and P_2O_5 (2.44%) (Fig. 6B). Quartz (53.5%) is the most abundant major mineral, followed by illite (12.36%) and muscovite (3.28%). Although not clearly present in XRD, mineral liberation analysis detected high calcite values of 8.47% (Fig. 4B). Iron and manganese oxides and oxyhydroxides consist of magnetite and hematite (0.43%), goethite and limonite (1.12%), pyrolusite (3.39%), and todorokite (3%). No calcium phosphates were detected but apatite values are 3.9%, coinciding with the presence of fossil content in the sediment.

3.4.1.8. Silty clay—Three samples were classified as silty clay and collected from unlithified floor and wall sediments in the Hill Antechamber and Superman Chamber (Table 2). Silty clay sediments are the most clay-rich and finest grained, consisting nearly entirely of clay (51.46%) and silt (35.34%), constituting ~90% of the total grain size fraction (Fig. 4A). Silty clay sediments contains moderate amounts of sand (12.86%) and the gravel size fraction is negligible (0.35%). The grain size is bimodally distributed, showing distinct peaks in the clay and silt fractions (Fig. 4A), but are very poorly sorted (1σ st. dev. = 2.83). The sediment is locally fossil-rich, including micromammal and *Homo naledi* fossils.

Table 2. Cave sediment types, grain size statistics, and associated facies in Rising Star Cave. Abbreviations: DB Ch = Dragon's Back Chamber; Din Ch = Dinaledi Chamber; HA Ch = Hill Antechamber; Pb Ch = Postbox Chamber; MPb Ch = Middle Postbox Chamber; UPb Ch = Upper Postbox Chamber; SM Ch = Superman Chamber; SMC = Superman Crawl.

Samples (n=33)	**Sample locality**	**Sediment type**	**Facies**	**Mean grain size (φ)**	**Sorting standard deviation (1σ)**	**Sorting**	**Skewedness**
100517JW6	SMC	*Muddy sandy gravel*	CNG	1.9	4.61	extremely poor	strongly fine
100517JW5	DB Ch	*Gravelly muddy sand*	CsS	4.17	4.84	extremely poor	fine
240517JW6	SM Ch		CNG	3.15	5.05	extremely poor	strongly fine
240517JW7	SM Ch		CsS	2.41	4.24	extremely poor	strongly fine
240517JW10	SM Ch		CsS/MSs	3.27	4.46	extremely poor	strongly fine
240517JW11	SM Ch		CsS	1.76	3.53	very poor	fine
240517JW12	SM Ch		CsS	1.66	3.49	very poor	strongly fine
260517JW3	UPb Ch		CsS/MSs	4.03	4.78	extremely poor	fine
260517JW4	MPb Ch		CNG	3.37	5.1	extremely poor	fine
UW-101 1783G	Din Ch	*Gravelly mud*	UMCB	5.5	4.67	extremely poor	strongly coarse
240517JW8	SM Ch	*Silty sand*	LOS	3.91	2.62	very poor	strongly fine
100517JW3	DB Ch	*Clayey sand*	SnS	4.94	4.24	extremely poor	fine
130716JW4	DB Ch		SnS	4.23	4.42	extremely poor	strongly fine
240517JW5	SM Ch		SnS	4.52	4.44	extremely poor	fine
UW-101 1783L	Din Ch		UMCB	4.84	4.32	extremely poor	near symmetrical
100517 101-6	HA Ch	*Sandy clay*	LORM	5.93	4.33	extremely poor	strongly coarse
240517JW9	SM Ch		LORM	6.72	3.83	very poor	strongly coarse
UW-101 1783H	Din Ch		UMCB	5.59	4.29	extremely poor	strongly coarse
110517JW1	DB Ch	*Sand silt clay*	SnS	5.7	3.91	very poor	fine
110517JW2	DB Ch		LORM	6.66	3.37	very poor	near symmetrical
240517JW1	SM Ch		LORM	6.19	3.97	very poor	near symmetrical
240517JW2	SM Ch		SnS	5.62	3.73	very poor	fine
240517JW3	SM Ch		LORM	6.38	3.37	very poor	near symmetrical
260517JW1	UPb Ch		SnS	5.05	4.44	extremely poor	near symmetrical
260517JW2	UPb Ch		LOS	5.19	3.56	very poor	strongly fine
260517JW8	Pb Ch		LORM	6.7	3.59	very poor	near symmetrical
260517JW9	Pb Ch		LORM	6.55	3.74	very poor	near symmetrical
260517JW10	Pb Ch		SnS	5.94	3.94	very poor	near symmetrical
UW-101 1783A	Din Ch		UMCB	6.75	3.39	very poor	strongly coarse
UW-101 1783C	Din Ch		UMCB	6.61	3.94	very poor	strongly coarse
100517 101-7	HA Ch	*Silty clay*	LORM	7.49	3.1	very poor	coarse
240517JW4	SM Ch		LORM	7.52	2.94	very poor	coarse
240517JW19	SM Ch		LORM	8.17	2.3	very poor	strongly coarse

Four major phases were detected from XRD, including quartz, kaolinite, and muscovite, and goethite (Fig. 6A). X-ray fluorescence records high concentrations of Al_2O_3 (23.91%) and Fe_2O_3 (10.38%) compared to other oxides besides SiO_2 (Fig. 6B). Quartz is the most abundant major mineral (40.91%), followed by illite (27.43%) and muscovite (7.6%) (Fig. 4B). Mineral liberation analysis detected low values of carbonates, mainly consisting of calcite (0.76%). Iron and manganese oxide and oxyhydroxide concentrations consist of hematite and magnetite (0.10%), limonite and goethite (1.71%), pyrolusite (2.54%) and todorokite (1.55%). Apatite concentrations are 4.87%, but calcium phosphate concentrations occur in trace amounts of 0.01%.

3.4.2. Rising Star Cave facies

Facies descriptions and interpretations presented below expand upon the purely textural (grain-size) descriptions and classifications presented in the last section and are utilized to better understand the genesis and depositional processes in the cave. Facies take into account both the combination of textural (grain-size) and compositional nature of sediments, but also their bedding, grading, sedimentary and biogenic structures. Nine repeated sedimentary facies are recognized in the different chambers in Rising Star Cave (Fig. 7; Table 3). Most of these consist of multiple sediment types (Fig. 8), and some facies occur both as unlithified and lithified deposits. The Rising Star Cave facies include:

3.4.2.1. CPB facies (Clast supported polymictic breccia)—The CPB facies occurs exclusively in the Postbox Chamber (Figs. 9 and 10) and was described by Robbins et al. (2021) and will only be briefly summarized in this chapter. The facies consists of a mixture of poorly consolidated angular and rounded clasts that range from cobble to boulder (>1.5 m) in size. Notably, the angular blocks consist mainly of host rock dolomite and chert, whereas a single rounded cobble consist of quartzite from the Klapperkop Member in the overlying Pretoria Group lithologies (see provenance Chapter 4). Clasts are locally suspended in a sandy, but clay- and silt-rich, matrix that locally contains macro and micromammal fossils, consisting of vertebrae, partial skulls, long bones and teeth. However, no hominin fossils occur in these sediments. Locally, small rootlets occur within the upper portion of the facies, indicating a close position to surface. In some cases, modern living rootlets are observed in this facies. The CPB facies are highly localized within the Postbox Chamber and partially overlain by 'Yellow' flowstone deposits (Robbins et al., 2021).

Interpretation of CPB facies—The CPB facies in the Postbox Chamber represents the apex of a subterranean debris cone. The combination of angular and rounded clasts indicate that

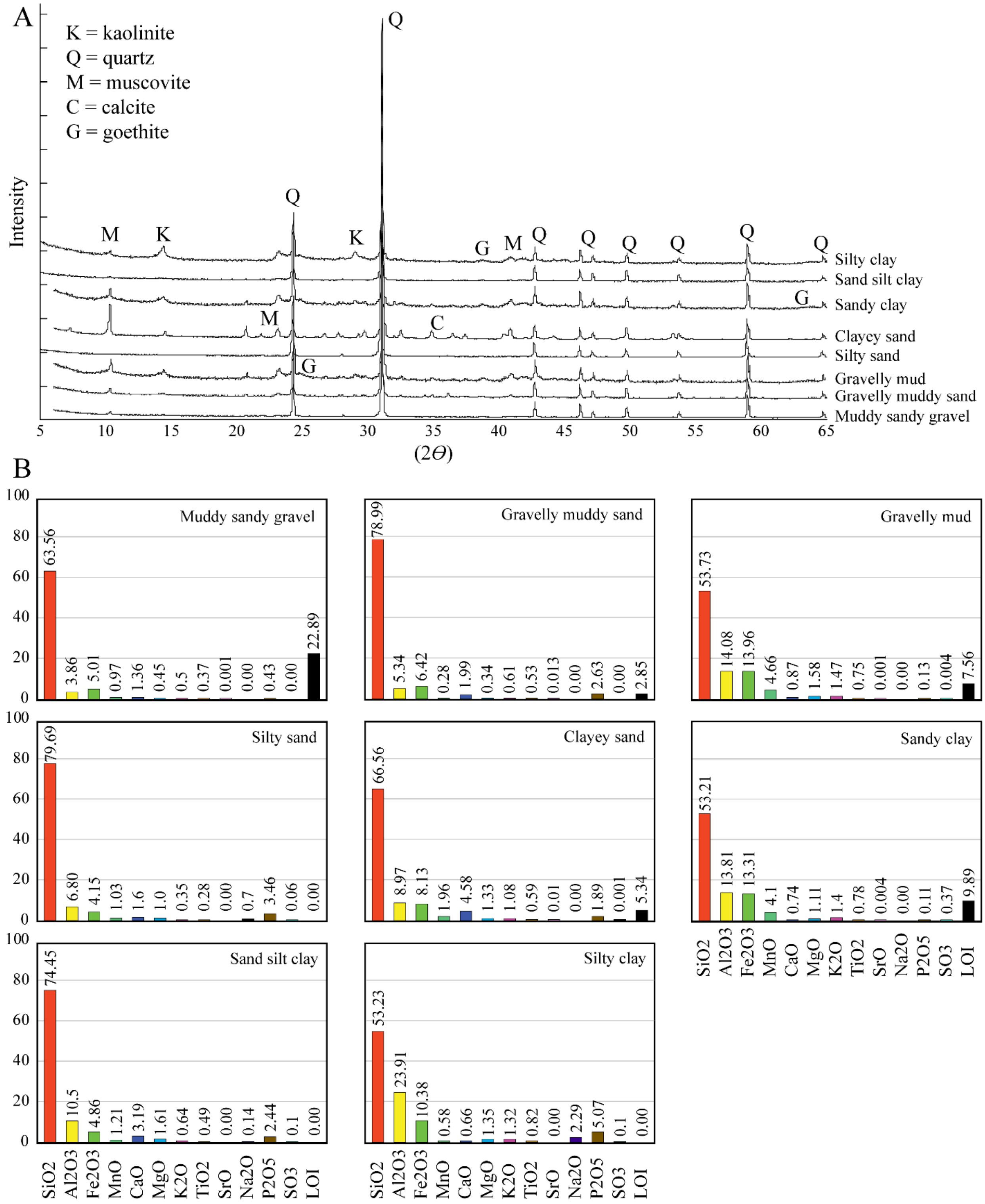

Figure 6. XRD (A) and XRF (B) results for the eight sediment types in Rising Star Cave.

Table 3. Rising Star Cave facies.

Facies	**Composition**	**Characteristics**	**Depositional interpretation**
CPB	Angular and rounded cobbles and boulders of dolomite, chert and quartzite in sandy and muddy matrix	Poorly sorted polymictic breccia Locally fossiliferous	High energy water-laid deposits
GMG	Sub-rounded dolomite, chert and quartzite gravel and pebbles in in sandy matrix	Poorly sorted breccio-conglomerate Micro- and micromammal fossils Normal and inverse grading Well cemented	High energy, low strength surficial or fluvial sheet flooding
CNG	Sub-rounded to angular quartz, dolomite, chert, and clay	Moderately well sorted Clast supported Normal grading Fossil poor Well cemented	High energy, low strength surficial or fluvial sheet flooding
LOS	Angular to sub-rounded quartz and dolomite gravel and sand and clay pebbles	Moderately sorted Cut-and-fill channels Trough crossbedding Locally fossiliferous	High energy, sheeted, debris flow deposits
SnS	Sub-rounded to angular dolomite, chert, and quartz sand Fe/Mn oxide nodules	Clast supported Normal grading Planar laminated Scoured bases Moderately well to poorly Sorted Weakly cemented Locally fossiliferous Rich in charcoal	High energy, shallow sheet flow deposits
CsS	Angular to sub-rounded quartz and chert sand and silt Fe/Mn oxide granules	Massive beds Planar and ripple cross lamination Highly fossiliferous	Low energy sheet flow deposits
MSs	Angular to sub-rounded quartz, chert, illite and muscovite sand and silt Fe/Mn oxide nodules	Poorly consolidated Planar lamination Moderately well sorted Fossil poor Normal graded	High flow, lower flow regime shallow deposits
LORM	Quartz sand, silt and clay Fe/Mn	Planar laminated Capping sequence Locally low concentrations of micromammal fossils Locally bioturbated Desiccation fractures along exposed, dry surfaces Poorly consolidated	Low energy, suspension settled deposits
MCB	Quartz sand, silt and clay	Mud clasts Lithified (LCMB sub-facies) Unlithified (UMCB sub-facies) *Homo naledi* fossils (UMCB only)	Sedimentary auto-brecciation

much of the high energy water-laid sediment represents a combination of local host rock blocks and surface derived fluvial cobbles. The sand matrix is fluvially derived and was washed into the Post Box Chamber and accumulated between the larger clasts, locally containing fossils and normal graded and layered architectures.

3.4.2.2. GMG facies (normal to inversely graded, matrix supported gravel)—

GMG facies sediments occur locally in the Dragon's Back (Figs. 9 and 11) and Superman (Figs. 9 and 12) chambers where they are preserved as erosion remnants underneath the 'Red' flowstone deposit (Fig. 7A; Robbins et al., 2021). It was not possible to adequately sample this facies. However, based on field observations and descriptions, GMG facies deposits consist of muddy gravel and muddy sandy gravels (Fig. 8). The GMG facies is a well-lithified, matrix supported sediment consisting of poorly sorted, brown-reddish to grey, heterolithic clasts of very coarse sand to polymict breccio-conglomeratic gravel and pebbles. The clasts and sandy matrix are cemented by calcite. Clast shapes are variable and range from well-rounded to angular, and clast sizes vary from coarse sand to coarse gravel. Gravel clasts range in size from 1-6 cm and are composed of quartz, quartzite, dolomite, chert and calcite (i.e., flowstone) fragments. Larger clasts, 20-30 cm in size and composed of angular mud clasts and dolomite, are rare. Clay-rich mud clasts are commonly Fe/Mn oxide stained and are semi-consolidated. They are relatively soft and can easily be broken up. Silt and clay fractions consist of muscovite/illite and kaolinite, and commonly form small, angular mud clasts. Iron and manganese oxyhydroxides are common and occur as small, millimetre-sized nodules. The facies is typically massive, with 3-4 cm thick beds with broadly scoured bases and thin horizons of crudely stratified, clast supported, inversely graded beds with locally scoured bases. Rare, ~5 mm-thin lenses of clasts are suspended in a well-sorted, fine-grained quartz and illite/muscovite matrix, in which quartz grains are sub-rounded to angular. Small, weathered bone flakes are visible within the matrix. Both micromammal and large (>5 cm) mammal fossils are common (Fig. 7A), and include long bones, ribs, teeth, vertebrae, and cranial material. Many of the bones are brittle and flaky and stained with Fe and Mn oxides, resulting in highly discoloured, yellowish white to grey black bones. Some of the bones are longitudinally cracked along the shaft and have their proximal-distal ends eroded away, exposing the internal trabecular bone.

Interpretation of GMG facies—The deposition of the GMG facies is interpreted as the result of short-lived, low strength surficial or fluvial sheet flooding events that entered the cave under high energy flow conditions occurring as a small subterranean debris flow. During the sedimentation event, the entire sediment mass is entrained and moves as suspended load, but ultimately deposits as poorly sorted, structureless beds, similar to the diamicton facies in Bosch and White (2004). Given the limited distribution of the GMG facies sediments throughout the cave, these deposits settled out quickly during the sedimentation event.

3.4.2.3. CNG facies (Clast supported normally graded gravel facies)—The CNG facies is observed in the Dragon's Back (Figs. 9 and 11) and Superman (Figs. 9 and 12) chambers where it occurs as individual beds that range from 1-4 cm in thickness (Fig. 7B). The facies is composed of muddy sandy gravel and gravelly muddy sand (Fig. 8) and consists of moderately well-sorted, clast supported, normal graded, tan-grey colored, very coarse sand to fine gravel deposits. Basal scour is common and gravelly beds grade normally into fine < 1 mm-sized clasts and is overlain by LORM deposits. Clasts range from 0.5 mm to 1.5 cm in size and consist of sub-rounded to angular quartz, dolomite, chert, tan/pinkish ovoid clay pebbles, calcite, and Mn/Fe oxide nodules. The facies is typically non-fossiliferous, and the overall color of the deposits is drab brownish at the base and becomes progressively tan-greyish towards the finer-grained top. Much of the facies is clast supported with interstitial muddy sandy matrix filling the pore spaces. The matrix consists of 1millimetre-sized sub-rounded to angular quartz sand, silt and kaolinite/muscovite/illite mud. The clasts and matrix are well cemented with calcite.

Interpretation of CNG facies—The deposition of the CNG facies in the Rising Star Cave is interpreted as the result of short-lived, low strength surficial or fluvial sheet flooding events that entered the cave under high energy flow conditions. Transport of the water saturated coarse bedload scour into finer grained underlying beds and form the base of succeeding sandier deposits, resulting in normally graded beds under reducing flow conditions, similar to the diamicton/channel facies in Bosch and White (2004). Given the limited distribution of the individual CNG beds, these deposits settled out quickly during sedimentation events.

3.4.2.4. LOS facies (Layered orange sand)—The LOS facies was described in Robbins et al. (2021) and consists of lithified, tan-pink and reddish-brown colored quartz sand that has been observed in two localities in the Dragon's Back Chamber (Figs. 9 and 11; Robbins et al., 2021). These deposits are semi-lithified and preserve as rounded, hanging erosion remnants along the west wall of the chamber, and as secondary cut-and-fill sand deposits in erosional pockets within LMCB facies (Fig. 7C). The LOS facies lacks clear bedding and is generally structureless and massive and composed of silty sand and sand-silt-clay (Fig. 8), consisting of moderately sorted, fine to medium-grained silty sandstone with very coarse sand to coarse gravel components. Very coarse, angular quartz, dolomite and mud clasts dominate the large grain sizes in the facies, 0.2-3.0 cm in size and evenly distributed throughout the section. Some small, 1-2 mm-sized charcoal fragments are also present throughout the deposit. Sedimentary structures include cut and fill channels and trough crossbedding within the section. Channels grade normally from a clast supported, very coarse-grained sand and fine gravel base into coarse angular quartz and dolomite sand. The channels and lenses also contain significant amounts of dolomite and orange-red mud clasts and the deposit is locally weakly cemented with calcite. Micromammal fossils are common and can be locally concentrated. Fossil elements consist of long bones, mandibles and teeth, including a rare, single baboon tooth from this facies.

Interpretation of LOS facies—The coarse sands of the LOS facies are interpreted as high energy, sheeted, debris flow deposits, carrying a mix of sand, gravel and fossils (e.g., Pickering et al., 2007; Bruxelles et al., 2014; Robbins et al., 2021). These deposits form local intraformational cut-and-fill structures.

3.4.2.5. SnS facies (Scoured, normal graded, fine to very coarse sand facies)—

The SnS facies has a small-scale spatial distribution in the cave that is limited to the Dragon's Back (Figs. 9 and 11) and Superman (Figs. 9 and 12) chambers and occurs repeatedly throughout several stratigraphic sections. The facies is particularly extensive in stratigraphic sections in the NW corner of the Dragon's Back Chamber where it occurs as thin beds underlying LORM sediments (Fig. 7D). The SnS facies is commonly composed of clayey sand and sand-silt-clay sediment types (Fig. 8), consisting of clast supported, normal graded, planar laminated beds that are ~3-4 cm in thickens and have broadly scoured bases. The coarser-grained base is commonly purplish-red in color and transitions into reddish brown towards the finer, upper portion of the bed. The sediment is overall moderately well-to-poorly sorted. Individual beds are generally cemented together with calcite. The basal half of each bed consists of 0.25-5 mm-sized clast supported, medium to very

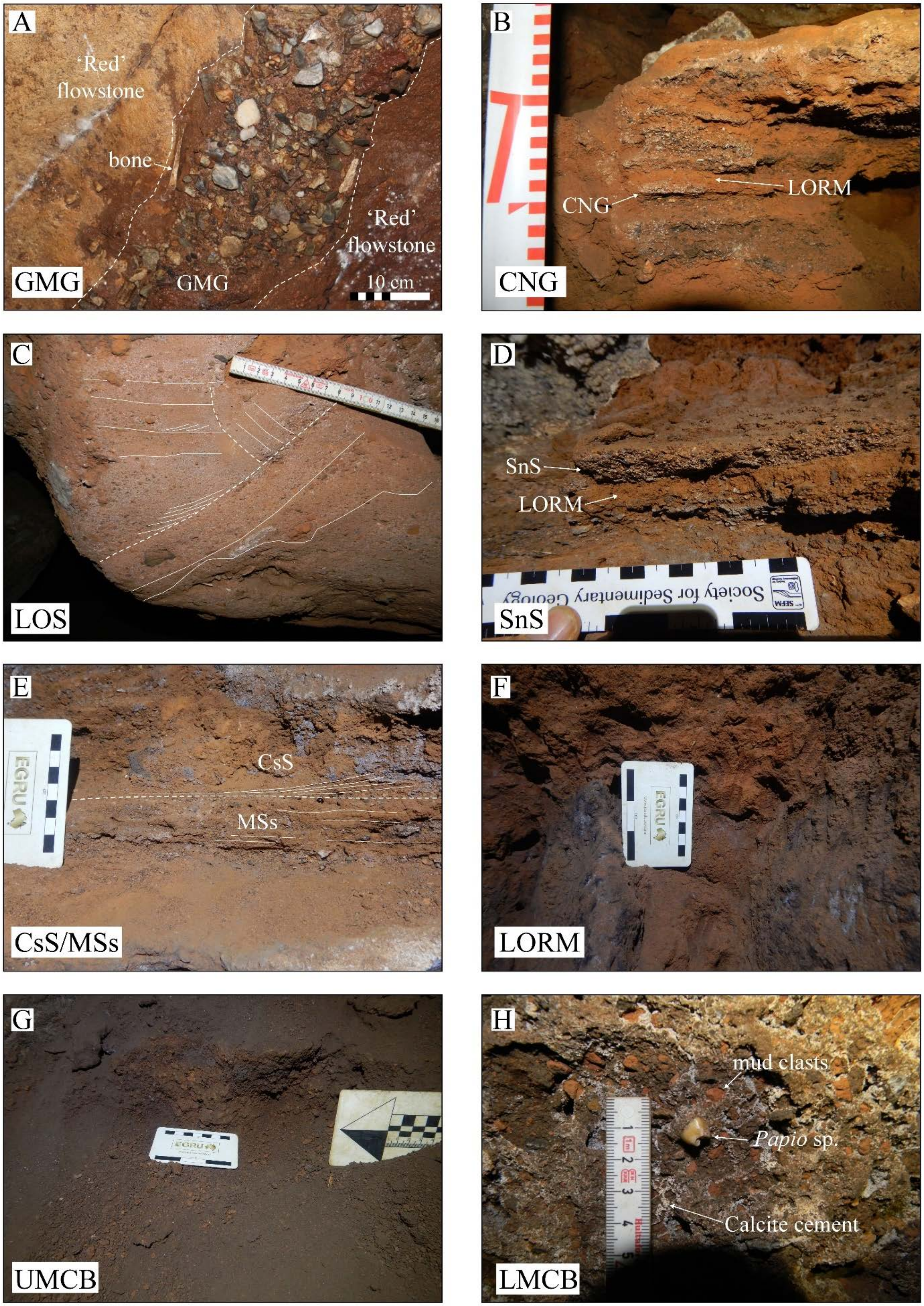
A
'Red' flowstone
bone
'Red' flowstone
GMG
GMG
10 cm
B
LORM
CNG
CNG
C
LOS
D
SnS
LORM
Society for Sedimentary Geology
SEPM
SnS
E
CsS
MSs
EGRU
CsS/MSs
F
EGRU
LORM
G
EGRU
UMCB
H
mud clasts
Papio sp.
Calcite cement
LMCB

Figure 7. The clastic sediment facies in Rising Star Cave. (A) GMG facies (normal to inversely graded, matrix supported gravel) in the NW corner of the Dragon's Back Chamber. (B) CNG facies (clast supported normal graded gravel) from the Dragon's Back Chamber. (C) LOS facies (laminated orange sand) in the Dragon's Back Chamber. (D) SnS facies (scoured, normal graded, fine to very coarse sand) in the Dragon's Back Chamber. (E) MSs facies (massive, fine to coarse sand and silt) and CsS facies (cross-stratified, very fine to very coarse sand) in the Superman Chamber. (F) LORM facies (laminated orange red mud) from the lower parts of the Postbox Chamber. The sediment shows vast amounts of porcupine chew marks. (G) UMCB facies (unlithified mud clast breccia facies) in the Superman Chamber, just below the entry point. (H) LCMB facies (lithified mud clast breccia) in the western part of Dragon's Back Chamber, in an alcove below the Dragon's Back block.

coarse sand to fine gravel, the latter being limited to the scoured bed forms that grade into very coarse sand. Grains are sub-rounded to angular, and composed of globular and angular chert, calcite and dolomite fragments, angular clear and white-to-yellowish quartz and locally interstitial black angular Mn/Fe oxide-coated grains, and minor quantities of mm-sized charcoal fragments. Mn/Fe oxide and charcoal fragments make up between 1-5 percent of the clast content. The beds fine upward into reddish-brown, very fine to fine quartz sand, silt and (wavy) laminated orange red mud (LORM) deposits. Locally, traces of small (<1 mm) Mn/Fe oxide and charcoal fragments occur within the facies.

Fossil content varies strongly between deposits of SnS. Where fossils are present, they are primarily preserved within the coarser sediments, locally forming small, but dense concentrations. Long bones are clearly positioned parallel to bedding and show unidirectional flow directions. Fossil material consists of micromammal (rodent and lagomorph) material, preserved in various conditions, ranging from complete elements to severely broken and fragmented bones. Elements include long bones, ribs, skulls, mandibles and teeth, but few axial elements (i.e., vertebrae) were observed. Some of the largest elements include rodent mandibles, measuring ~ 2-3 cm in size. Bones are typically yellow white in color, but some beds contain bones that show grey to black manganese oxide staining.

Interpretation of SnS facies— The sediments of the SnS facies are interpreted as frequently recurring, high energy sheet flow deposits.

3.4.2.6. CsS facies (Cross-stratified, very fine to very coarse sand facies)—The CsS facies is composed of gravelly muddy sand and gravelly mud (Figs. 7E and 8) and is widely distributed across the Dragon's Back (Figs. 9 and 11), Superman (Figs. 9 and 12), and Dinaledi (see Fig. 3 in Dirks et al., 2015) chambers, and shows a notable decrease in bed thickness between the different chambers away from the debris cone apex. The bed thickness ranges from ~5 cm in the Superman and Dragon's Back chambers to millimetre-thick lenses in the Dinaledi Chamber. The beds lack scoured bases and are massive, consisting of angular to sub-rounded, very fine to coarse-grained, quartz and chert sand, silt and Fe/Mn oxide grains, rich in randomly oriented and distributed fossils. Sedimentary structures include thin, planar and ripple cross laminated beds.

Interpretation of CsS facies—The CsS facies is interpreted as having formed through low energy pulses of allochthonous sheet flow sediment being washed into the cave under moderate flow conditions within the lower flow regime, resulting in the deposition of sandy ripple cross laminated facies (sensu Miall, 2010).

3.4.2.7. MSs facies (Massive, fine to coarse sand and silt facies)—The MSs facies is restricted to the Dragon's Back (Figs. 9 and 11) and Superman (Figs. 9 and 12) chambers but is stratigraphically and spatially widely distributed. The facies is composed of gravelly muddy sand and gravelly mud (Fig. 8) and consists of unconsolidated massive red brown, very fine to medium-grained sub-rounded to angular quartz sand and silt beds (Fig. 7E). Bed thickness ranges from 1-5 cm, and beds are commonly planar. Very fine-grained to mm-sized illite and muscovite micas are locally common. Few fine-grained Fe/Mn oxide nodules and mm-sized, thin laths of charcoal are present throughout the facies. The facies is typically moderately well sorted, but larger clasts constitute between 1-5% of the total sediment volume, and occur evenly distributed throughout the facies, consisting of coarse to very coarse, angular quartz, dolomite, chert and mud clasts. Fossil content is low and consists of micromammal (rodent) teeth and long bones.

Interpretation of MSs facies—The MSs facies is interpreted as a normal graded, sand and silt deposit that developed under relatively high flow velocities, based on the presence of planar bedding that characterizes the facies.

3.4.2.8. LORM facies (Laminated orange red mud facies)—The LORM facies sediments occur widely distributed across the debris cone and accumulated in the Dinaledi Chamber, Hill Antechamber (see Fig. 2 in Dirks et al., 2017), Postbox (Figs. 9 and 10), Dragon's Back (Figs. 9 and 11), and Superman (Figs. 9 and 12) chambers. LORM facies sediments typically consist of silty clay and sand-silt-clay sediment types (Fig. 8). LORM facies deposits are typically composed of red-brown, 5-15 cm thick clay-rich mud beds that are horizontally laminated. The sediment locally contains very fine to fine-grained quartz sand. Laminae can be internally deformed and undulatory, commonly adopting irregular topographies that mimic the underlying substrate. LORM facies sediments commonly occur as a capping sequence, forming a deposit on top of coarser, fine to coarse-grained sand beds (Fig 7B and D), but are also commonly preserved as erosion remnants along the cave wall (Fig. 7F). The fossil content is typically low in LORM deposits, but low concentrations of fossil material are observed locally, consisting of randomly oriented micromammal teeth, ribs and long bones that lack preferred current direction. Bioturbation, although rarely occurring and only observed in the Dinaledi Chamber, consists of small, 2-5 mm wide, vertical insect burrows that are infilled by fine-grained sand and silt (see Fig. 4B in Dirks et al., 2015). Desiccation fractures commonly develop along exposed horizontal surfaces and slumped outcrop margins.

Interpretation of LORM facies (*sensu* Wiersma et al., 2020)—Most of the deposition and formation of LORM facies sediments in Rising Star Cave occurred under low-energy hydrological conditions as post-flooding suspension settling (= slackwater facies, *sensu* Bosch and White, 2007). Desiccation fractures in LORM sediment is present on subaerially exposed surfaces under dryer cave conditions, either when phreatic or flood water tables drop below LORM facies deposits. Internally deformed, i.e., undulated, laminae result from soft sediment deformation through slumping and compaction of partially wet sediment, particularly in areas where LORM sediments were deposited on irregular topographies on underlying substrates, e.g., flowstone deposits.

3.4.2.9. MCB facies (Mud clast breccia facies)—The mud clast breccia facies can be subdivided into two sub-facies based on their degree of lithification and include an unlithified mud clast breccia (UMCB; Wiersma et al., 2020) and lithified mud clast breccia sub-facies (LMCB; Robbins et al., 2021). The LMCB sub-facies is one of the oldest clastic sediment deposits thus far known in Rising Star Cave but their exact age is currently uncertain. LMCB deposits occur

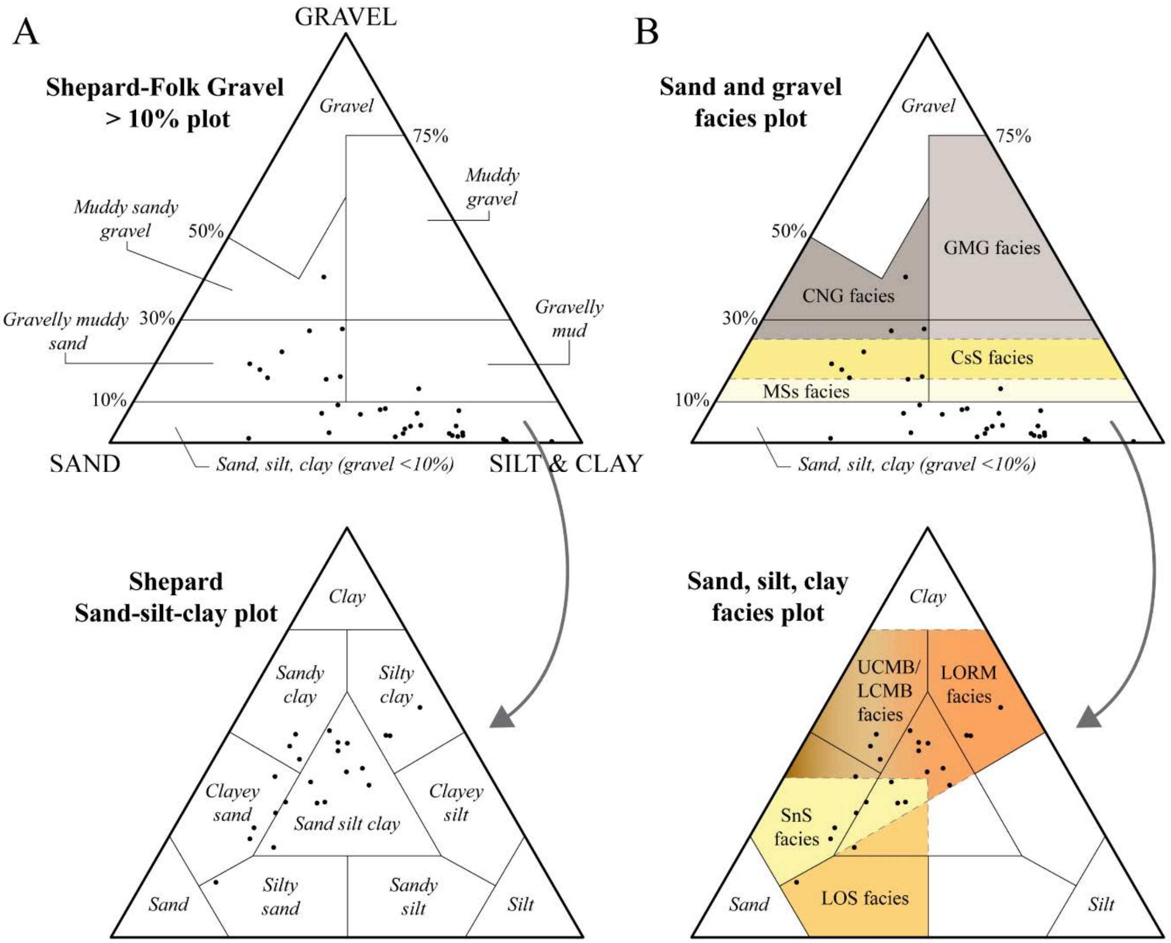

Figure 8. Sediment types and associated facies for clastic sediments in Rising Star Cave. (A) The data points on the sediment type plot illustrate that most of the sediments in the cave are relatively sandy and fine grained. The gravel plot is modified after Shepard (1973) and Folk (1953, 1974). (B) The different facies show that many of the facies in Rising Star Cave consist of multiple sediment types.

as smoothly weathered erosion remnants underneath the 'Green', and 'Blue' flowstone units (Robbins et al., 2021) in the Dinaledi (see Fig. 2B in Dirks et al., 2017), Postbox (Fig. 10), Dragon's Back (Fig. 11), and Superman (Fig. 12) chambers as well as along the roof of the Superman Crawl (Fig. 12), however, it is also observed in many other chambers in the cave that are not included in this study. The UMCB facies, however, is much more locally distributed and is primarily observed as floor sediments in the Dinaledi Subsystem and to some extent in the Superman and Postbox chambers (Dirks et al., 2015, 2017; Wiersma et al., 2020) (Fig. N). The MCB facies occurs in various degrees of lithification, with the LMCB sub-facies being mostly semi- to well lithified in

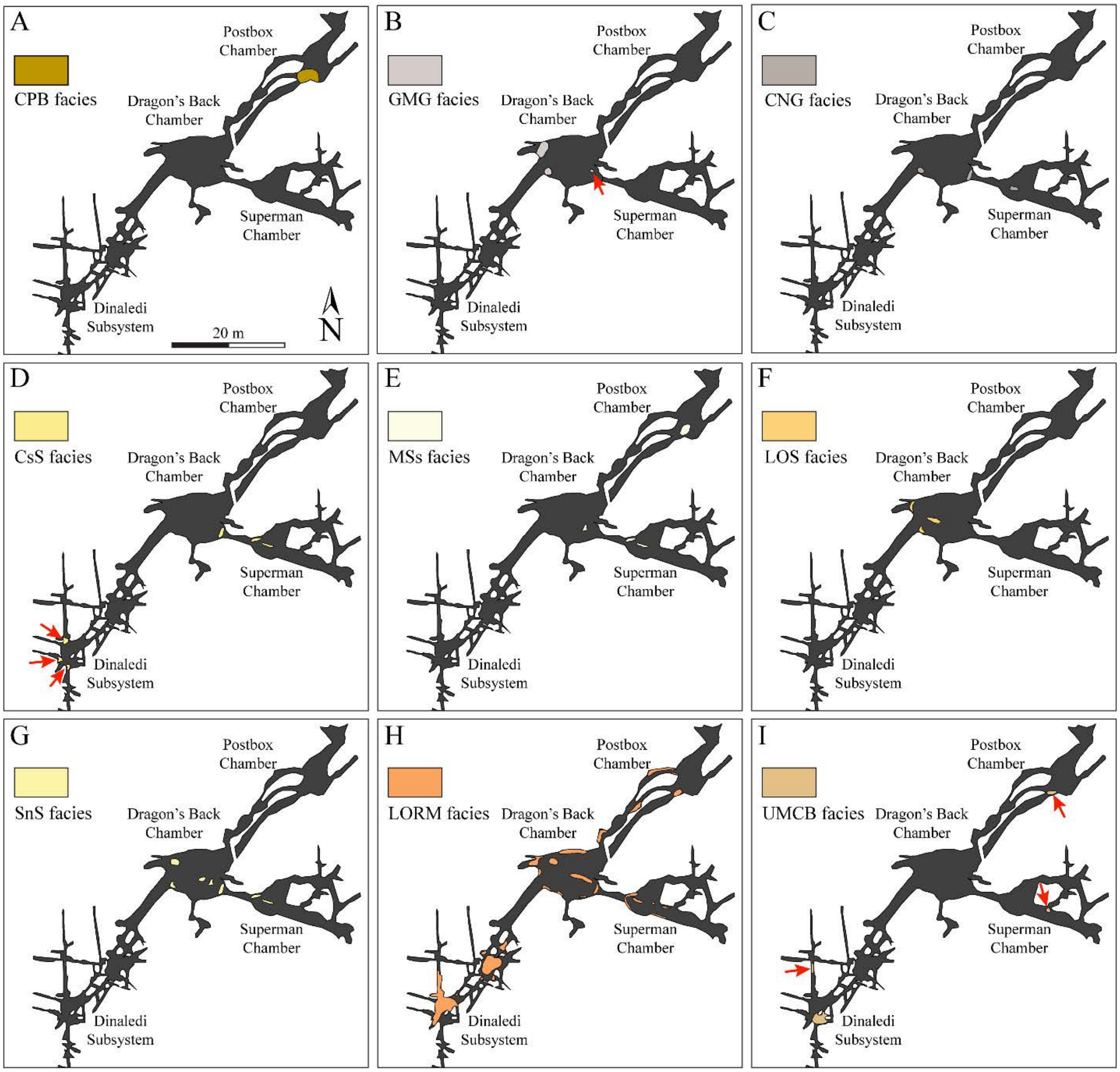

Figure 9. Distribution of the different unlithified facies that contributed to the polymictic debris cone in Rising Star Cave. Cave chambers have been shaded and red arrows are added to better highlight the distribution of some of the more obscure and small outcrops of certain facies. Distribution of: (A) CPB facies in the Postbox Chamber; (B) GMG facies in the Dragon's Back Chamber; (C) CNG facies in the Superman and Dragon's Back chambers; (D) CsS facies in the Superman and Dragon's Back chambers and the Dinaledi Subsystem; (E) MSs facies in the Postbox, Superman, and Dragon's Back chambers; (F) LOS facies in Dragon's Back Chamber; (G) SnS facies in Superman and Dragon's Back chambers; (H) LORM facies in Postbox, Superman and Dragon's Back chambers and the Dinaledi Subsystem; (I) UMCB facies Postbox and Superman Chambers and the Dinaledi Subsystem.

calcite cement, enveloping individual mud clasts and forming extensive, mm-sized, networks of calcite within the matrix. The UMCB facies occurs primarily as unlithified deposits with locally minor degrees of lithification in calcite.

In general, both sub-facies share a similar make up and having a coarse character due the presence of mud clasts Fig. 7G-H. The facies is very fine-grained, consisting primarily of clay and silt with minor contributions of quartz and dolomitic sand, classified as clayey sand and sandy clay sediment types (Fig. 8). Much of the facies consists of dense concentrations of largely unlithified, orange red to dark brown, angular mud clasts in a carbonate-poor, brown-to-grey quartz silt and clay matrix. Rare, small pockets of dark grey, sand-sized dolomite and chert matrix also occur. Individual mud clasts are angular in appearance and composed of silt and kaolinite clay and are commonly internally laminated accompanied by mm-sized desiccation fractures. Mud clasts range from 0.2 to ~10 cm in size, but on average, clast sizes are less than 3 cm in length. They are formed from autobrecciated LORM facies sediments (Tables 2 and 3; Wiersma et al., 2020). Mud clasts are soft to semi-hard and break easily and conchoidally. Sub-aerially exposed mud clast surfaces are typically weathered and commonly coated in brown-black Fe/Mn oxide. Although the mud clast breccia is predominantly matrix supported, the upper profile of the facies transitions towards a more clast supported character where the upper few centimeters display a weak inversely graded profile; mud clasts in the uppermost portion are larger than the mud clasts situated immediately below, sometimes resulting in stacked, inversely graded beds. Grading is less obvious in the typically matrix supported lower profile of the facies in which the average mud clast size is also smaller.

Interpretation of MCB facies (*sensu* Wiersma et al., 2020)—The formation of the mud clast breccia facies in Rising Star Cave is a direct result of *in situ* sedimentary autobrecciation of LORM facies host sediments (Wiersma et al., 2020) through prolonged erosion, desiccation and diagenesis, brecciating LORM sediments into angular mud clast deposits.

3.4.3. Rising Star Cave Stratigraphy and Sedimentology

The sediments observed in the investigated chambers in Rising Star Cave show a distinct fining trend in grain size away from the debris cone in the Postbox Chamber towards the more distal Dinaledi Subsystem (Fig. 13). However, the Middle and Upper Postbox chambers are not part of the debris cone deposits; they are positioned well above the Postbox Chamber and instead form a separate entry point for sediments to enter the cave. Sedimentary facies and grain size distributions in Dragon's Back and Superman Chamber are similar and consist mainly of sand and LORM dominated sediments compared to the gravel-rich sediments in Postbox Chamber. The Dinaledi Subsystem contains primarily muddy LORM, LMCB and UMCB. The following sections describes the facies distribution for the investigated chambers.

3.4.3.1. Postbox Chamber—The oldest sediments in Postbox Chamber consist of the lithified mud clast breccia (LMCB) facies, which is extensively preserved at the entry into the chamber, preserving as deeply weathered erosion remnants underneath 'Green' flowstone deposits (Fig. 10). Younger sediments include LORM and SnS facies deposits that occur widespread throughout the lower parts of the chamber and can be locally very fossiliferous. LORM sediments contain elevated levels of Fe and Mn oxyhydroxides (Fig. 14). Fossils consist only of micromammals. UMCB facies deposits occur in the chamber but are localized and occur on a small scale in the upper parts of the chamber. The CPB facies sediments that form the apex of the subterranean debris cone spills into the chamber via a vertical fracture that connects to surface and consists of sand, dolomite and chert breccia blocks in a muddy sand and silt matrix. Vertebrate fossils are common, but hominin fossils have not been recorded from this facies to date. The sediments are in part overlain by the 'Yellow' flowstone (Robbins et al., 2021). Although fine-grained clastic sediment remnants are abundant in the Postbox Chamber, they are structureless and preserve no distinct stratigraphic units.

3.4.3.2. Middle and Upper Postbox chambers—The Upper Postbox chamber connects to surface and sediment shedding into the chamber are coarse to very fine sand SnS, LOS and MSs facies sediments (Fig. 10). The little sediment preserved in Middle Postbox chamber is mostly situated along the floor and some erosion remnants preserve along the walls and consists of very fine grained CNG facies gravels and sand (Fig. 10). No LORM and MCB deposits are preserved in these chambers because they are too shallow to build up these types of facies. The unconsolidated sediments in both the Middle and Upper Postbox chambers record higher siderite concentrations compared to the other chambers, and more similar to those found on the colluvial surface above the cave (see Chapter 2). They slope upwards and contain live roots, suggesting they are closely connected to surface.

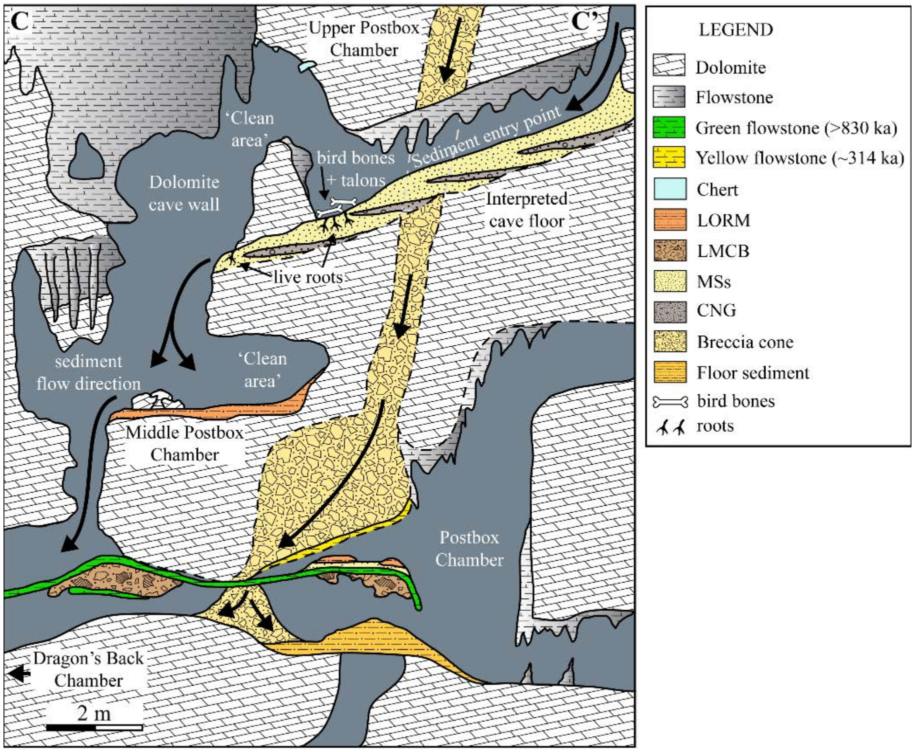

Figure 10. Cartoon cross section of the Postbox Chamber and Middle and Upper Postbox chambers, showing sediment and facies distribution.

3.4.3.3. Superman Chamber—The oldest sediments in the chamber consist of LMCB that are preserved underneath 'Green' and 'Blue' flowstone deposits. Few remnants of unlithified sediments in the Superman Chamber are exposed as small patches along the cave wall, in fractures, and atop flowstone deposits. The overall grain size distribution is somewhat similar to that in the Dragon's Back Chamber (Fig. 12). Stratigraphic successions consist of alternating MSs and CsS facies that fine upward into SnS facies that are overlain by LORM facies, indicating recurrent sedimentation events. Locally, sediments consist of complex cm-thick, alternating CNG-CsS facies deposits, lacking any LORM deposits in between. All the sediments are overlain by undated flowstones that can potentially be correlated to the 'Red' flowstone units. Although the sediment outcrops occur in close proximity to one another throughout the chamber, lateral continuity and local correlations are difficult to establish due to the discontinuous nature of exposure of the deposits and covering by the 'Grey' flowstone. The floor sediments consist partially of LORM facies deposits which are locally undergoing autobrecciation underneath the northern entry of the Superman Chamber.

3.4.3.4. Dragon's Back Chamber—Most of the sedimentary facies described in this study are preserved in Dragon's Back Chamber, and some of the oldest, and most widely distributed facies in this chamber are the lithified mud clast breccia facies (LMCB). The facies is locally >1.5 m thick, where it is primarily preserved underneath the 'Green' and ‘Blue’ flowstone (Fig 11). The LMCB facies occurs widespread throughout the chamber and is locally >1.5 m thick. Less common are the LOS facies deposits which are only preserved in the western half of the chamber, underneath older LMCB facies deposits (Fig. 11).

The younger sediment deposits are mostly unlithified and produce stratigraphic trends that consist of successions of alternating sand and fine gravel deposits that are sharply overlain by suspension settled LORM deposits. The basal most, and possibly the oldest of unlithified sediments are preserved in a small alcove, below the dropped Dragon's Back block (Fig. 11) and consist of CMG facies, alternated with sandy LOS intervals. Sediments preserved in more elevated locations in the chamber become temporally finer grained, with most of the CNG facies being replaced by SnS facies. Here, the SnS facies are individually overlain by LORM deposits, indicating repeated sediment input of high energy sedimentation and subsequent suspension settled LORM deposits.

3.4.3.5. Dinaledi Subsystem—The sedimentology of the Dinaledi Subsystem (i.e., Dinaledi Chamber and Hill Antechamber) have been extensively discussed in previous work (Dirks et al., 2015, 2017; Wiersma et al., 2020) and will only be briefly discussed. Clastic sediment in the Dinaledi Subsystem is very fine-grained and preserved two dominant facies; sand poor, kaolinite clay-rich, laminated orange red mud (LORM) and LORM-derived, autobrecciated, unlithified mud clast breccia (UMCB) deposits (Wiersma et al., 2020), the latter hosting the holotype *Homo naledi* fossils (Dirks et al., 2015, 2017). Both LORM and UMCB deposits in the Dinaledi Subsystem, particularly the Dinaledi Chamber and Hill Antechamber, contain elevated levels of Fe and Mn oxyhydroxides (Fig. 14; Dirks et al., 2015; Wiersma et al., 2020). Locally intercalated, thin quartz sand lenses occur within the LORM as well as locally abundant assemblages of micromammal fossils. The sandier lithologies consist of medium to very fine angular to sub-rounded quartz and nodular Fe/Mn sand and minor, silt-sized, chert and dolomite. Remnants of older, lithified mud clast breccia (LMCB) are preserved primarily underneath flowstone deposits, positioned near the entry of the chamber.

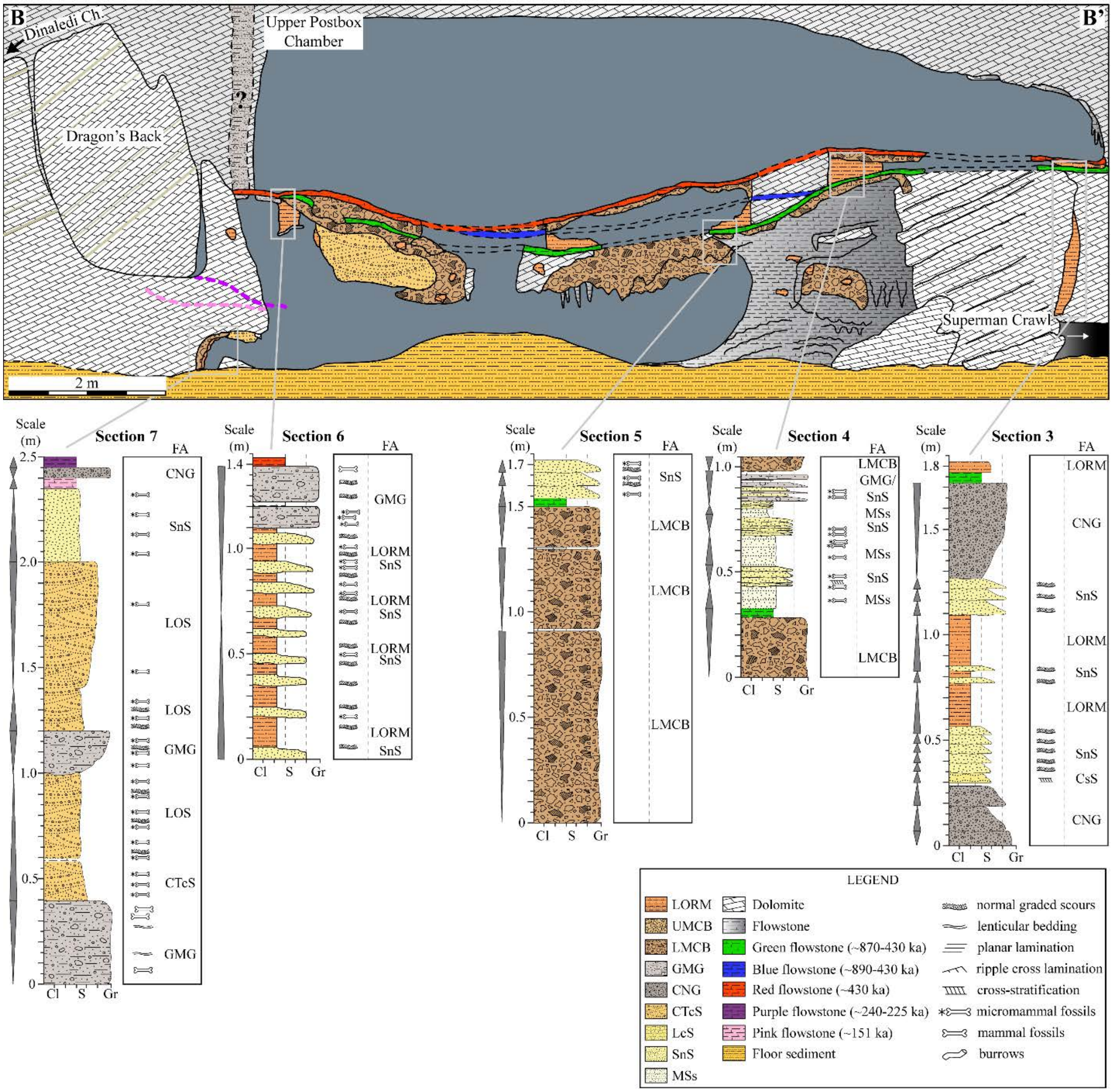

Figure 11. Cartoon cross section of Dragon's Back Chamber showing the relative age and depositional relationships between the sediments, facies and flowstone deposits in the chamber.

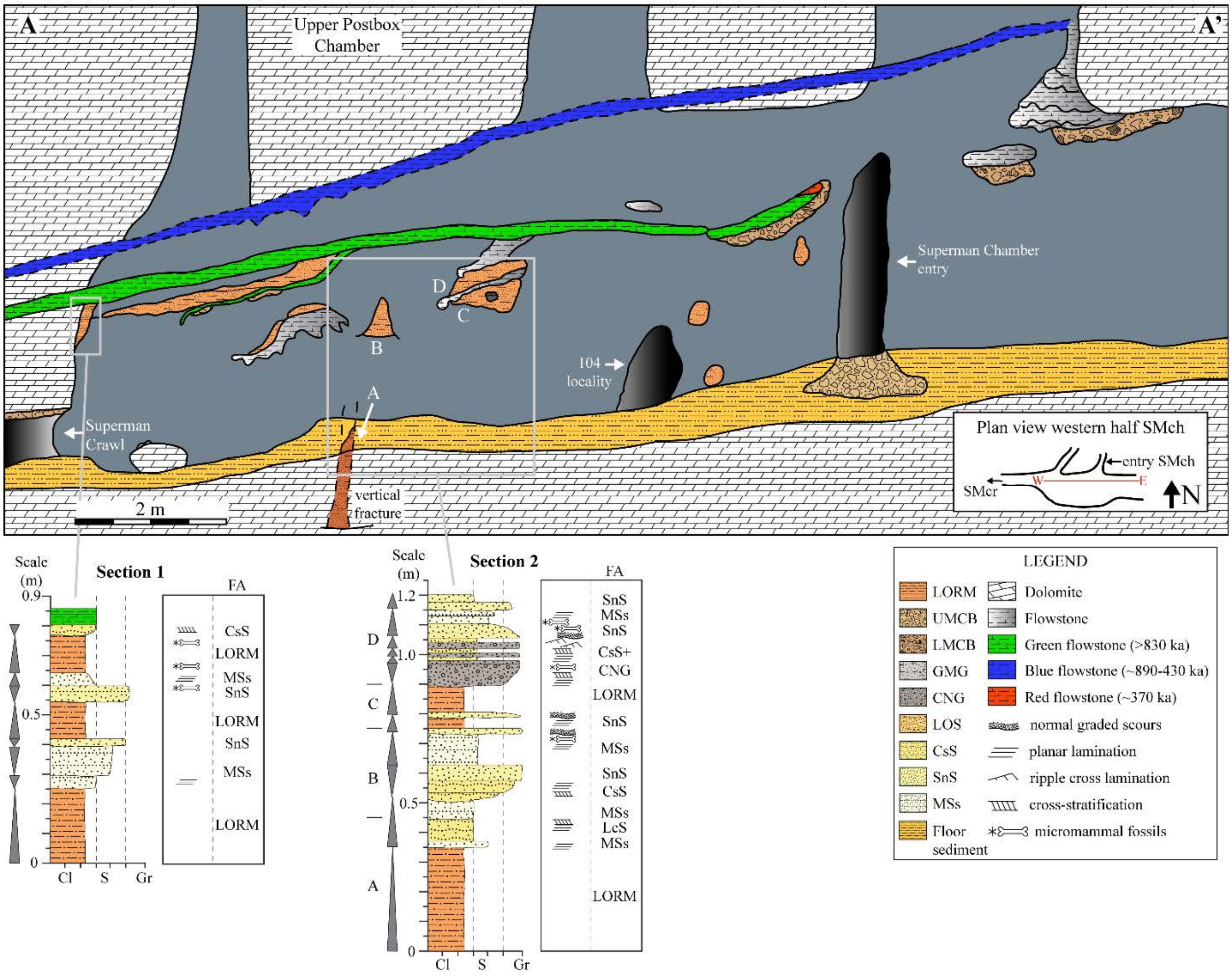

Figure 12. Cartoon cross section of the Superman Chamber showing the relative age and depositional relationships and distribution of sediments, facies and flowstone deposits.

3.5. Discussion

3.5.1. Grain-size and facies patterns in Rising Star Cave

From a grain-size perspective on a cave-wide scale, the clastic sediments in Rising Star Cave preserve a characteristic downward and distally fining trend (Fig. 13) which agrees with the typical geometry and internal architecture of an outward (westerly) fanning debris cone, somewhat similar to alluvial fan deposits on surface (Miall, 2006). The coarsest debris cone sediments (CPB facies) are preserved in the Postbox Chamber and the finest clay rich LORM and UMCB sediments dominate in the Dinaledi Subsystem (Fig. 13). The cave sediment facies generally show a similar distal and downward fining trend; whereas at the bed level, individual units typically show an overall fining upward trend indicative of pulsed sedimentation events with waning flow conditions. For example, in the Superman Chamber, underneath the 'Red' flowstones consists predominantly of fining upward successions of CsS and MSs facies in the eastern part of the chamber, whereas towards the Superman Crawl entry in the western part of the chamber, finer-grained SnS facies and capping LORM sediments are more dominant (Figs. 8 and 11). This trend continues onward into the Dragon's Back Chamber. In the eastern part of this chamber, clastic red sediments preserved above the entry to the Superman Crawl contain CNG facies deposits, but the majority consists of alternating sandy CsS and SnS facies type sediments capped by LORM facies (Fig. 12). In the center and towards the western parts of the chamber, sediments become sandier and include predominantly alternating successions of normal graded, fine-grained sandy MSs and SnS facies (Fig. 12). Continuing further towards the NW corner of the chamber, there are alternating successions of fine-grained sandy SnS facies capped with thick deposits of LORM facies. In the Dragon's Back Chamber, the coarse GMG facies was deposited on top of the LORM and SnS units that represents a distinct stratigraphic unit with a different cave entry point to most other sediments in the cave—likely introduced into the cave along a fracture which infilled with clasts and bones as a result of soil creep and surface runoff occurring directly above the cave, prior to being overlain by the 'Red' flowstone. Al/Be dating of chert clasts from the GMG facies indicate a depositional age around 540 ka (Makhubela et al., 2019).

The furthest and deepest chambers in the cave are located in the Dinaledi Subsystem. Apart from a few very thin (<1 cm), locally intercalated CsS lenses in the Dinaledi Chamber and Hill Antechamber (Dirks et al., 2015; Wiersma et al., 2020), the bulk of the deposits in these chambers consists of *Homo naledi*-bearing UMCB and LORM type facies sediments, preserving the largest concentrations of distally, suspension settled clay-rich sediments in the cave.

3.5.2. Generalized lithostratigraphic and depositional trends in Rising Star Cave

The sedimentology and facies in the cave system preserve evidence of a complex depositional and stratigraphic history, influenced in part by punctuated neotectonic events and the northeastward migration of the Upper Bloubank Spruit (Chapter 2) combined with long-term climatic shifts, i.e., glacial-interglacial stadia (see Fig. 6 in Robbins et al., 2021), resulting in fluctuating phreatic water tables and punctuated depositional events. The oldest known clastic

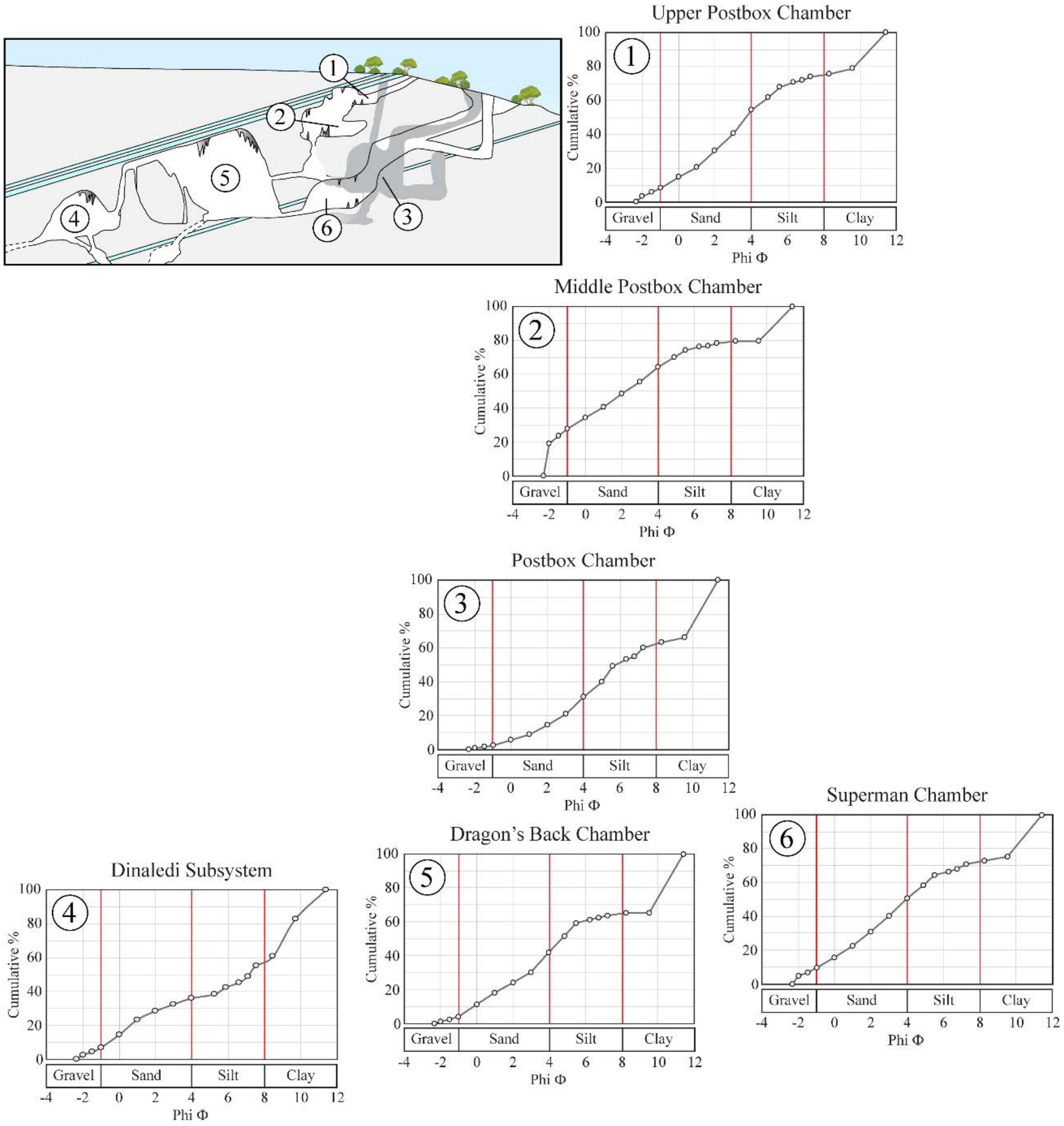

Figure 13. Grain size distribution for clastic sediments in Rising Star Cave show a characteristic downward and westward sloping decrease in grain size, preserving the architectural remnants of a subterranean debris cone. The coarsest sediments and facies (CPB) are found in Postbox Chamber (shaded in gray), whereas the finest facies (LORM and UMCB) dominate in the Dinaledi Subsystem.

deposits in the cave are a series of erosion remnants of LMCB underneath the >600 ky old 'Green' and 'Blue' flowstones (Dirks et al., 2015, 2017; Robbins et al., 2021), predating the opening of the Postbox Chamber to surface (Makhubela, 2019; Robbins et al., 2021), and the ingress of the remaining unconsolidated clastic debris cone sediments into the cave. These flowstone age constraints suggest that oldest LMCB sediments did not enter the cave via the Postbox Chamber pathway but were introduced via alternative entry points (e.g., fractures) that are now filled with flowstone or unknown. LMCB deposits are among the most wide-spread deposits observed in the cave, occurring in many other chambers and passageways other than the investigated chambers. The similarity in composition and architecture of old LCMB deposits to its unlithified (UMCB) equivalent, strongly suggests that LMCB facies formed in similar ways as the UMCB facies, i.e., through sedimentary autobrecciation of pre-existing LORM-type sediments. The UMCB deposits were subsequently calcified to form the LMCB sub-facies during periods of elevated phreatic water tables. The presence of LMCB deposits further points towards cyclical inundation and drying of the cave before the cave opened up to surface in the Postbox Chamber to allow coarse clastic sediments in the cave of the type now present along the access route to the Dinaledi Chamber.

The unconsolidated clastic sediments and associated facies in the four main chambers along the access route into the Dinaledi Chamber represent a westward sloping subterranean debris cone with its apex located in the Postbox Chamber (Fig. 2). The most distal deposits associated with this debris apron point source are located in the Dinaledi Subsystem. Much of these sediments were deposited during the Pleistocene, sometime between ~500-225 ka (Robbins et al., 2021), which entered the cave via the Postbox Chamber along a vertical shaft that connected to surface. Sediments in and around the apex consist mainly of CPB facies intercalated with lenses of fossiliferous SnS facies, overlain by a ~300 ka 'Yellow' flowstone deposit (Robbins et al., 2021). As sediments continued to enter the cave from this point source, the were transported further and deeper into the cave, in a general westerly direction. The unconsolidated sediments that deposited into the Dragon's Back and Superman chambers became increasingly sandier and muddier and are locally richer in micromammal fossils.

The most recent deposits of clastic sediments consist primarily of clay rich LORM and UCMB sediments that overlie <225 ka 'Purple' flowstone deposits. These young successions of richly fossiliferous LORM deposits form the most continuous fine-grained successions in the cave. Based on various U-Th, OSL, and Al-Be age determinations from various cave chambers (Makhubela, 2019; Robbins et al., 2021), it appears that the youngest externally sourced LORM sediments were introduced into the cave ~240-190 ka. External delivery of sediment appeared to have ceased largely around 180 ka, suggesting that during this time the Postbox Chamber was closed off from surface (Robbins et al., 2021). However, a near constant process of weathering and erosion associated with fluctuating water tables and climate, has led to near continuous deposition, reworking and redeposition of LORM and UCMB facies in different portions of the cave system. In some areas, like the Dinaledi Chamber, the stratigraphy of these deposits is well studied and relatively well constrained in relation to the timing of fossil deposition (Dirks et al., 2017). However, even in the parts of the Dinaledi Chamber, there are clear examples of down-dip erosion and redeposition of LORM and UCMB facies (and hominin bones) into new deposits, some of which overlie well-dated flowstones younger than 30 ka on the floor at the base of the chamber. Similar patterns are observed in many other chambers, including the Lesedi Chamber, and along many narrow fractures between chambers. Hence, it is beyond the scope of this study to attempt to correlate all the different deposits throughout the cave system.

3.5.3. Chamber-specific elevated oxide concentrations in Rising Star Cave

Iron and manganese oxyhydroxides are the most common metallic oxides found in various concentrations in the sediments in Rising Star Cave. They occur as mm-sized nodules in the coarser clastic sediments, but they also occur as grain coatings within clay-rich sediments such as the LORM facies. Elevated concentrations are particularly noted in LORM and UMCB deposits that are located deeper in the cave, such as the Dinaledi Chamber and the lower parts of the Postbox Chamber (Fig. 14). When comparing the iron and manganese oxide concentrations with aluminum oxide concentrations, the different facies and bulk sediments per chamber show a strong correlation between clay content and Mn and Fe enrichment, particularly in the LORM and UMCB facies of Dinaledi Subsystem and lower portion of Postbox Chamber (Fig. 14). These facies occur abundantly in the aforementioned two chambers and represent deeper and relatively undisturbed areas of the cave. This suggests that the diagenetic alteration and enrichment of these metallic ions is not a function of sediment type or grain size, but rather a function of highly localized and *in situ* microbial and geochemically controlled processes (Wiersma et al., 2020). These low-energy, quiescent conditions likely aided in the facilitation of iron and manganese oxidation by chemoautotrophic processes (Engel, 2012). Also, the LORM and UMCB sediments contain little to no nodular Fe-Mn oxyhydroxides, further indicating that the enrichment is most likely highly localized and microbially induced, whereas with the coarser sediments, the incorporation of Fe-Mn oxyhydroxides is likely physical, i.e., depositional, similar to, and derived from the sediments found on surface (see Chapter 2). The cave host rock also contains minor concentrations of interstitial Mn within the dolomite (Eriksson et al., 2006) but contributions of Mn incorporating in the clastic cave sediments from the dissolution of dolomite is minimal on a cave-wide scale, compared to Mn concentrations derived from surface sediments and *in situ* microbial activity.

3.5.4. Sediment pathways into Rising Star Cave

The current route used to enter Rising Star Cave was artificially created through past mining activity and was not a plausible entry point for cave sediments from the surface nor for *Homo naledi* to have accessed the cave. Hence, the dolomite walls and much of the floor of the modern access route into the cave is devoid of allochthonous clastic sediment deposits until one reaches the northern entrance of the Superman Chamber. The Upper Postbox Chamber and main Postbox Chamber are the two chambers that maintain a natural connection to surface (Figs. 2 and 10) and appear to be the only plausible entry points for Pleistocene-aged surface sediments to have entered the cave. However, the Upper Postbox chamber does not form part of the debris cone system that characterizes the main Postbox Chamber. Instead, the Upper Postbox (and Middle Postbox) chamber contains relatively little sediment, and deposits are largely confined to shallow sloping sandy and gravelly CNG and MSs facies floor sediments and few erosion remnants of LORM-like facies preserved along the lower portions of the cave walls (Fig. 10). The modal mineralogy of these sediments contains elevated soil mineral signatures, notably siderite, compared to the other chambers below, which are largely devoid of siderite. Elevated siderite signatures are also present in the colluvial sediments on surface directly above the cave (Chapter 2). This suggests that nearby colluvial sediments likely spilled directly into the Upper (and Middle) Postbox chamber. Given the limited quantity and distribution of sediments in these chambers, it appears that very little of these sediments have spilled into the underlying main Postbox Chamber, suggesting only small quantities of sediment entered the Upper Postbox chamber at any given time. This is further demonstrated by the absence of clastic sediments on the cave walls and ceilings along the western parts of the Upper and Middle Postbox chambers (Fig. 10). Also, the sediment deposits are typically structureless and massive and contain very little to no fossil content, which suggests that sediments have been introduced to these chambers under a separate depositional system that is unrelated to the mostly high energy depositional mode that formed the debris cone deposits found in the Postbox Chamber. The overall low quantity of sediments, its sandy and very fine gravelly nature, and lack of fluvial structures in these sediments suggests that they possibly entered the cave after the Upper Bloubank Spruit had migrated away from the cave and are likely transported into the cave during periods of rainfall or seasonal surface runoff and aeolian processes. This potentially means that the Upper Postbox Chamber opened up to surface much more recently, compared to the main Postbox Chamber.

The dominant, long-lived source of most of the sediments into the cave was a fracture system above the main Postbox Chamber, which formed the distinctive debris cone at the base of it due to periodic flooding of the Upper Bloubank Spruit when it was positioned above the cave. Seasonal, or possibly, monsoonal flooding events introduced large quantities of sediment and other debris into the cave resulting in cave-wide distribution of sediment that might occasionally have led to confined, pipe-full flow conditions. Most of the sedimentary architectures of the unconsolidated sediments that are preserved in Dinaledi Subsystem, Dragon's Back and Superman Chamber show evidence of unidirectional current transport of sediment into the cave (i.e., unidirectional cross beds, ripple laminated beds, laminated beds, and suspension-settled deposits.

The second mode of deposition is transitional, consisting of a combination of fluvial avulsion and surface sheet flood of colluvial runoff into the cave as the Upper Bloubank Spruit migrated away from the cave in a northeastern direction as indicated by the alluvial terraces in the modern landscape surrounding the cave (Chapter 2). During this stage, recurring flooding events resulted in decreased quantities of less coarse sediments washing into the cave and the now colluvial surface above the cave would likely have been less frequently inundated by floodplain deposits. Fluvial flood deposits are partially replaced by surface sheet floods, washing colluvial sediments into the cave with a more soil-rich mineral profile, primarily enriched in Fe and Mn oxides and minor amounts of siderite (Fig. 4, and see Figs. 8 and 9 in Chapter 2).

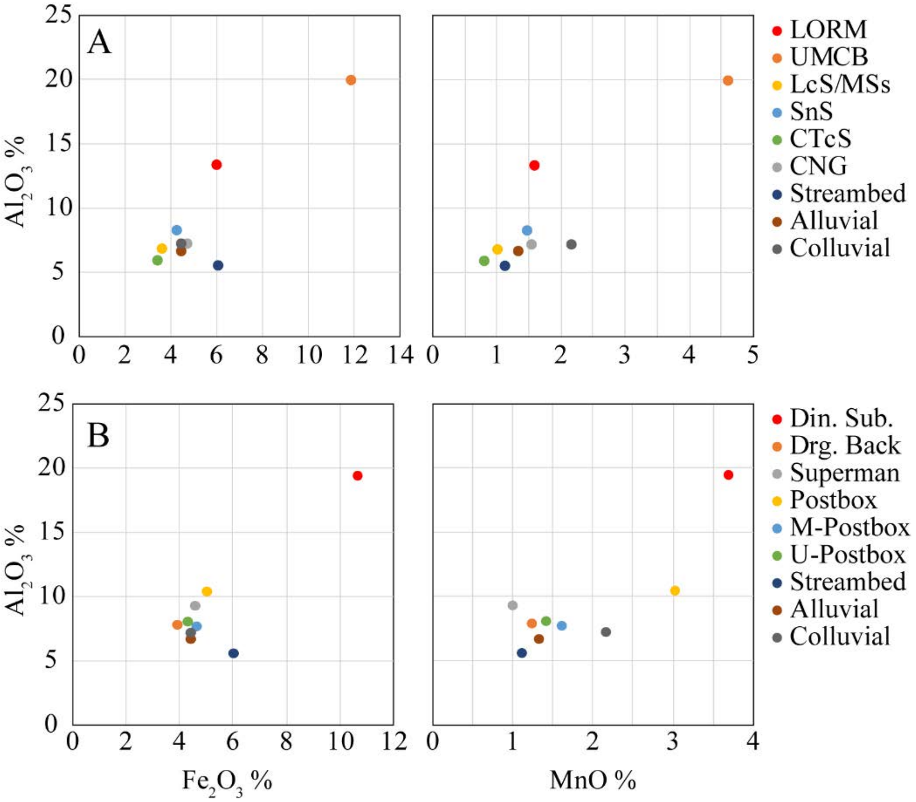

Figure 14. Metallic mineral concentrations in different facies and chambers in Rising Star Cave. (A) Aluminum-iron and aluminum-manganese concentrations in the different Rising Star Cave sediment facies show there is a correlation between elevated levels of Al, Fe and Mn and the fine grained LORM and UCMB facies. (B) Highest concentrations of Fe and Mn occur primarily in the deeper parts of the cave, such as the Dinaledi Subsystem and lower portions of the Postbox Chamber. This suggests that facilitation of microbially induced Fe and Mn oxidation preferentially occurs in the more quiescent parts of the cave.

3.6. Conclusions

Rising Star Cave hosts a suite of nine distinct clastic facies that are repeatedly observed throughout the cave system, which represent a suite of distinct depositional processes that are primarily influenced by the spatial relationship of deposits with the sediment entrance points. A distinctive down dip decrease in grain-size and facies types is documented through the cave system, suggesting a single primary entry point for most sediments into the cave system resulting in a large debris cone apron centered in the Postbox Chamber. The nature of the preserved unlithified sediments in the cave are the result of a complex depositional history that reflects two primary, and somewhat (para)contemporaneous, recurring modes of sediment delivery into the cave above the Postbox Chamber: river flooding and colluvial surface runoff.

Sediment delivered into the cave was then dispersed deeper into the cave through a serious of complex depositional processes, dominated by shallow current flows along the cave floor, along with slow sedimentation of fine-grained facies into the deepest and farthest reaches of the cave system. Repeated processes of wetting and drying in the cave has led to a complex stratigraphy associated with deposition and redeposition of different facies. Although full lithostratigraphic correlations of the sediments in the cave are difficult to establish due to constant reworking, erosion, deposition, and localized diagenetic and geochemical processes of pre-existing sediments in the cave, the facies elucidate the broad depositional history, microbial, and geochemical processes of clastic sediments in Rising Star Cave.

Chapter Four

Constraining the local provenance of clastic sediments associated with *Homo naledi* in Rising Star Cave, South Africa

Abstract

Knowledge of the composition and provenance of sediment that envelops the *H. naledi* remains in the Dinaledi Chamber of Rising Star Cave helps to constrain conditions under which the fossils were deposited. The composition of "Laminated Orange Mud" (LORM) and overlying "Unlithified Mud Clast Breccia" (UMCB) deposited in the cave between 150-350 ka, together with nearby surface sediments were analysed using U-Pb detrital zircon geochronology, and mineral liberation analysis. This was combined with dolomite dissolution to estimate the relative contribution of different source materials. Neither of these techniques have been used before to characterise cave sediments in the Cradle of Humankind, and this study, therefore, provides a test for the usefulness of these techniques in a cave environment. Dissolution of dolomite samples from the lower Monte Christo Formation that hosts the cave yields on average ~3 % clastic sediment consisting mostly of secondary quartz with no clay and no detrital zircon. Combined with <7 % of clastic material derived from interbedded chert and shale horizons, the total autochthonous component for the sediment budget inside the Rising Star Cave is <10%. The LORM and UMCB sediments were deposited after two generations of older sediments had been removed from the chambers through internal erosional processes. This, therefore, means the vast majority of the fine-grained sediments was derived from outside the cave, and distributed in the cave across a subterranean debris cone. U-Pb detrital zircon geochronology shows that zircon populations in all cave and surface sediments are near identical and reflect every major tectonic event that affected the Kaapvaal Craton up to the formation of the Permian-Jurassic Karoo basin. The homogenised nature of the zircon

populations reflects a process of repeated recycling of detrital material eroded from older rocks into younger basins, with sediments of the Karoo basin being the likely immediate source for zircons in the cave. The lack of a differentiated zircon signature disqualifies detrital zircon geochronology as a useful technique to fingerprint the precise provenance of cave sediments. The lack of Cretaceous and Cenozoic-aged zircon populations from the Kalahari Basin suggests that aeolian sediments from this basin contributed little to the local sediment budget. Mineral Liberation Analysis (MLA) demonstrates that the sand-sized fraction in the LORM and UCMB sediments is broadly similar to sediment in the nearby river and overlying soils. The clay component of the cave sediments increases with depth into the cave. While surface sediments were affected by secondary deposition of mainly Fe oxyhydroxides, cave sediments experienced more enrichment in Mn-oxyhydroxides and especially pyrolusite, probably reflecting the Mn-rich nature of the drip waters and biogenic soil-forming processes in the cave. The UCMB sediments that occur in direct association with the *H. naledi* fossils display an anomalous sediment signature when compared to UCMB sediments that underlie the fossils. Similar to detrital zircons, the resolution of the MLA technique is too limited to provide indications of the precise provenance (i.e. alluvial vs soil) of the cave sediments.

4.1. Introduction

Numerous cave systems are known in the predominantly dolomitic Transvaal Supergroup across NE South Africa (Martini, 2006; Dirks and Berger 2013), with the highest concentration of caves occurring west of Johannesburg, in the general area where the Cradle of Humankind (CoH), UNESCO, World Heritage site is situated (Fig. 1A). The formation and exposure of theses cave systems has been linked to uplift and denudation of the high-elevation plateau of southern Africa since the Plio-Pleistocene (e.g., Partridge, 1973; Kavalieris and Martini, 1976; Partridge and Maud, 1987; Martini, 2006; Partridge, 2010; Dirks et al., 2010; Dirks and Berger, 2013). Uplift resulted in extension of the upper crust, which probably facilitated cave formation as fracture systems in dolomite opened to allow dissolution in the vadose zone (Dirks and Berger, 2013). As the rising plateau of the African Erosion Surface was incised, caves were drained by lateral incision of eroding streams and further sculpted through collapse and cave propagation along fractures and joints (Partridge and Maud, 1987; Martini, 2006; Dirks and Berger, 2013). Following incision and exposure, the cave systems became accessible to a wide variety of hominids, and sediment started to collect within them (e.g., Dirks and Berger, 2013).

Sediment accumulation in cave systems is most common in caves exposed between Pretoria and Krugersdorp (i.e. around the CoH), in the upper reaches of the Crocodile River catchment (e.g., Martini, 2006; Dirks and Berger, 2013). West of this area and towards areas where the African Erosion Surface is largely intact and not incised by rivers, little cave fill has been reported from any of the accessible caves (Martini 2006; Partridge, 2010). This pattern indicates that the history of sediment fill and access of hominids to caves is related to the uplift history and evolution of the landscape (e.g., Partridge and Maud, 2000; Moore et al., 2009; Bailey et al., 2011; Dirks et al., 2013). Therefore, one way to reconstruct the hominin paleo-environment, is by reconstructing the infill history of the sediments within which hominid fossil bones were deposited.

Caves in the CoH are generally characterized by complex networks of passages along joint systems and layer-parallel shear zones (e.g., Kavalieris and Martini, 1976; Martini 2006; Dirks and Berger 2013). They form network maze caves that can be 100’s meters across individually, but that are poorly interconnected resulting in slow flow of groundwater, with no through flow of streams (Witthüser and Holland, 2007; Holland and Witthüser, 2008; Hobbs and de Meillon, 2017). Over time, some of the mazes expanded into large chambers such as Sterkfontein Cave

(Martini et al., 2003), but these too remained isolated from other nearby systems. As a result of their geometry caves that developed openings to surface acted as sediment traps, and also trapped animals (e.g., Dirks et al., 2010; Bruxelles et al., 2014).

Geological studies of fossil-bearing cave breccias in the CoH indicate that most deposits formed in broadly similar settings involving clastic sediments that entered the cave via shafts or roof openings to be distributed on debris cones that spread across chambers and adjacent passageways (Partridge and Watt, 1991; Brain, 1993; Pickering et al, 2007; Pickering and Kramers, 2010; Dirks et al., 2010; Bruxelles et al., 2014). Gravel- to boulder-sized breakdown from ceilings and walls mixed with allochthonous and autochthonous sand- to clay-sized debris and was distributed across the talus cones as debris flows and sheet wash (e.g., Dirks et al., 2010; Bruxelles et al., 2014). Considering that the geomorphological position of most caves with large debris cone deposits such as Sterkfontein Cave (Pickering and Kramers, 2010) or Gladysvale Cave (Pickering et al., 2007) occur along valley slopes it can be assumed that the source of the cave sediments was the surrounding soils, which entered the caves as sheet wash during heavy rain events (e.g., Dirks et al., 2010; Makhubela et al., 2017, 2019).

Over time the clastic sediments were cemented by drip waters to become lithified polymict breccia. Few sediment deposits with hominid fossils have been described from caves in the CoH where such lithification of sediments did not occur. Rising Star Cave is the most notable example where lithification did not occur extensively (Dirks et al., 2015, 2017; Wiersma et al., 2020), because many of the sediments are relatively young (<0.6 My; Dirks et al., 2017). Compared to the lithified cave breccias, the young unconsolidated deposits in Rising Star Cave are much easier to investigate for sedimentary processes and depositional dynamics; firstly because the internal cave morphology did not change dramatically since the sediments were laid down, as demonstrated by the slow erosion of the land surface above the cave (<5 m/Ma; Makhubela et al., 2019); and secondly because the unconsolidated nature of the sediments in the cave greatly facilitates comparative provenance studies with nearby soils and alluvial sediments from surface.

Establishing the sediment dynamics for Rising Star Cave is of particular significance, because the fossils of *H. naledi* were found in a unique context in the Dinaledi Camber, deep inside the dark zone, where the bones were embedded in fine-grained sediment with no other fossil macro-fauna (Dirks et al., 2015, 2017; Wiersma et al., 2020). This context led Dirks et al. (2015) to suggest that the fossils may have entered the cave on purpose. Although it has been argued that the fossils were transported into their current position by flowing water (e.g., Val, 2016), the fine-grained, clay-rich mineralogy and autobrecciation process of the sediments deposited with the fossils, are not consistent with this (Dirks et al., 2015; Wiersma et al., 2020).

While it has been established that the sediments in the Dinaledi Chamber are generally finer grained, their relationship with sediment in the rest of the cave has not been studied, and it is not clear to what degree the sediments were transported from outside, or, alternatively, were derived from internal cave processes. In determining the source of the sediments in the cave it is also important to establish to what degree the sediments were derived from reworked soils above the cave as opposed to alluvial or aeolian fill, because the nature (and age) of the source sediments greatly influences how Al-Be ages for the sediments internal to the cave must be interpreted (Makhubela et al., 2019).

This study will focus on establishing the provenance and sediment budget for the unconsolidated sediment units in Rising Star Cave that were deposited during the time *H. naledi* may have interacted with the cave, i.e. sometime between 150-350 ka. We have applied three different techniques to constrain the provenance and estimate the sediment budget including: dolomite dissolution; detrital zircon geochronology; and Mineral Liberation Analysis (MLA), all of which are standard techniques in sedimentology, but none of which have been applied to cave sediments in the CoH. Part of the aim of this paper is, therefore, to test the usefulness of these techniques for characterising cave sediments in the CoH. Dolomite dissolution together with careful stratigraphic logging will provide estimates for the amount and composition of insoluble material in the dolomites, which likely ended up in the caves. Detrital zircon geochronology is a useful tool to characterise provenance in a wide variety of sedimentary settings (e.g., Fassett and Steiner, 1997; Roberts et al., 2013; Beveridge et al., 2020), but it is not commonly used to characterise the origin of cave sediment, and we have tested its applicability for provenance characterisation in the CoH. MLA will be applied to compare the composition of the sand fraction in soils, alluvial sediments and cave sediments to further constrain the provenance of the latter. Previous studies in Rising Star Cave have shown that many of the sand grains in the cave sediments and nearby soils are complex aggregates held together by Fe-Mn oxyhydroxides, and their composition was observed to vary in different parts of the cave (e.g., Dirks et al., 2015; Makhubela et al., 2019). The coarser grain fraction, therefore, appears to “fingerprint” the sediment type, and was targeted in this study for MLA analyses.

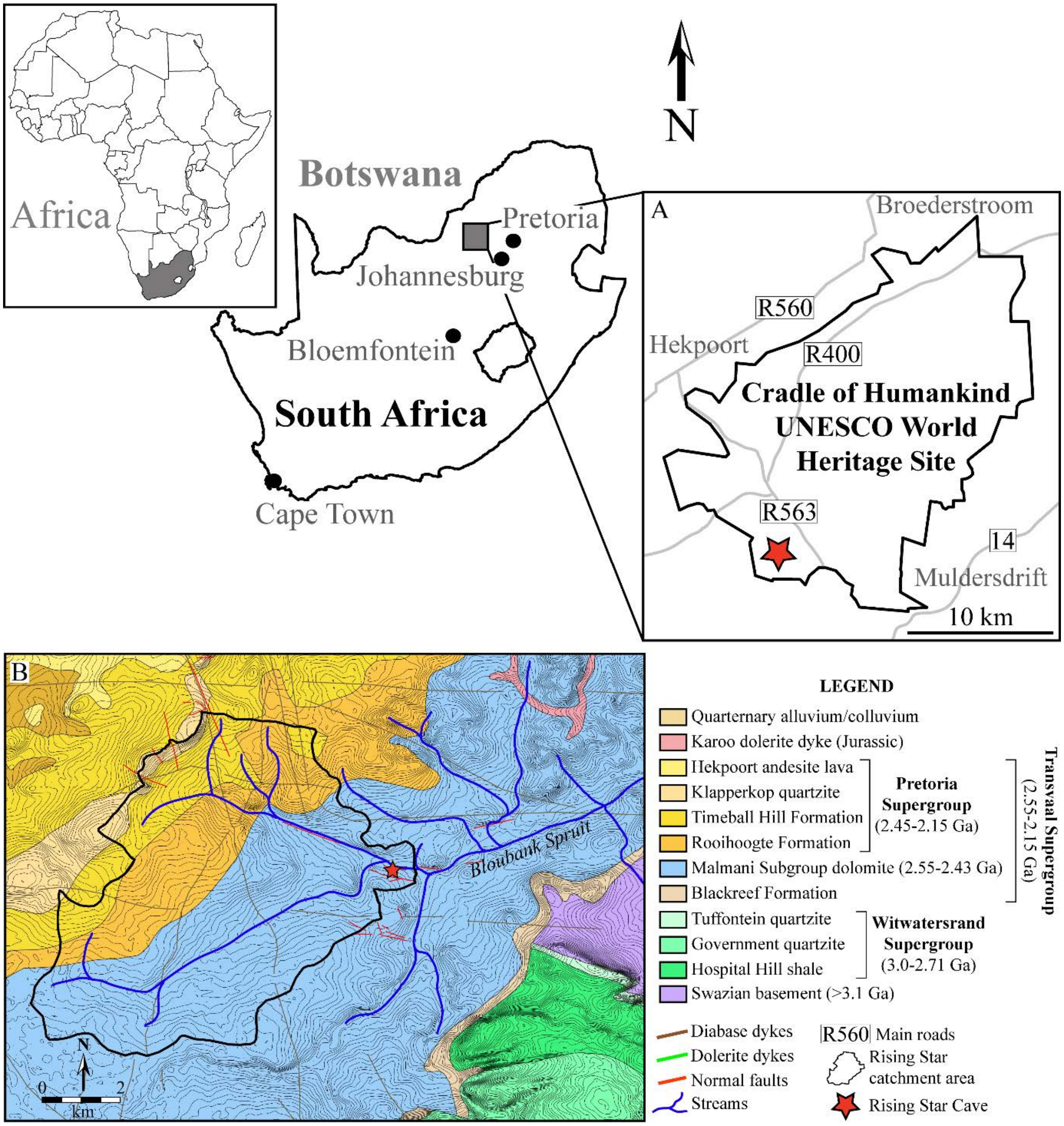

Figure 1. Rising Star Cave and regional geology. (A) Location of the Rising Star Cave, indicated by the red star in the inset, in the Cradle of Humankind, South Africa (modified from Wiersma et al., 2020). (B) Geological map of the Rising Star Cave catchment area. The lithological outcrops within the boundaries of the catchment consist of various ages that possibly shed into the catchment area. Most of the geological units correlate well with the detrital zircon age data in this study.

4.2. Geological Setting

The CoH World Heritage area is situated in the central part of the Kaapvaal Craton immediately west of a circular Archean basement inlier referred to as the Johannesburg Dome. The Johannesburg Dome is cored by Mesoarchaean (>3.1 Ga) basement gneiss (Anhaeusser, 2006; Robb et al., 2006) overlain by Archaen clastic sediments of the gold-bearing Witwatersrand Basin (3.0-2.8 Ga) and volcanics of the Ventersdorp Supergroup (~2.71 Ga). To its east, north and west, the dome is surrounded by outward dipping successions of sedimentary and volcanic rocks of Neoarchaean to Paleoproterozoic (2.5-2.1 Ga) age. These include stromatolite-rich dolomite of the late-Archaean to early Paleoproterozoc Malmani Subgroup (2.55-2.45 Ga; Eriksson et al., 2006), which host the cave deposits in the CoH, overlain by deeper water siliciclastics and volcanics of the Pretoria Group (2.4-2.2 Ga; Eriksson et al., 1995). These sedimentary successions were intruded by the Bushveld Igneous complex (2.06 Ga) to the north, and they were unconformably overlain by horizontally-bedded Permian-Triassic deposits of the Karoo Supergroup, remnants of which locally extend into the CoH (Dirks and Berger, 2013).

4.2.1. Geology of the Cradle of Humankind

The Cradle of Humankind UNESCO World Heritage Site (CoH) is situated towards the southwest edge of the Johannesburg Dome. It covers granitic to ultramafic basement gneiss with overlying Ventersdorp volcanics and Witwatersrand metasediments (e.g., quartzite) and volcanics along its eastern boundary. The southern margin of the CoH is underlain by dolomite of the Malmani Subgroup that hosts the fossiliferous caves. Metasedimentary rocks of the Pretoria Group are preserved along the northwest margin of the CoH. These units are intruded by dolerite and syenite dykes of undefined Proterozoic age and overlain by rare eroded remnants of Permian-aged deposits of the Karoo Supergroup which are preserved in pockets of paleo-karst and along old erosion surfaces across the southern part of the CoH (Dirks and Berger, 2013).

The Malmani Subgroup in the CoH comprises a basal lag conglomerate (the Black Reef Formation) overlain by dolomite, which was sub-divided into five formations on the basis of stromatolite morphology, chert content and the presence of shale and chert-breccia horizons (Eriksson and Truswell, 1974). Four of the five formations crop out in the CoH. At the base are the chert-poor dolomites of the Oaktree Formation (~150m) with interbedded shale and tuff dated at 2550 ± 3 Ma (Walraven and Martini, 1995) and 2583 ± 5 Ma (Martin et al., 1998). The overlying chert-rich Monte Christo Formation (600-700m) is stromatolite-rich and commonly interbedded with generally thin (<50 cm) shale horizons. It is overlain by the chert-free Lyttelton Formation (150-200m thick), and chert-rich Eccles Formation (< 600m thick). This is topped by chert breccia of the Rooihoogte Formation, which formed above an irregular karstic paleo-topography (Dirks and Berger, 2013).

The catchment area of the Bloubank Spruit upstream from Rising Star Cave is underlain by all four formations in the Malmani Subgroup, but also includes the Rooihoogte Formation, shales of the Timeball Hill Formation and coarse ortho-quartzites of the Timeball Hill Formation Klapperkop Member of the Pretoria Group (Fig. 1B). The latter forms a high ridge that marks the drainage divide at the head of the Bloubank Spruit (Fig. 1B). Cosmogenic Al-Be dating indicates that erosion rates in the CoH were generally low (<5 m/ Ma), and soils are old and experienced significant reworking over long periods of time (Dirks et al., 2010, 2016; Makhubela et al., 2019). These observations indicate that for the past half a million years, the physical landscape of the Bloubank Spruit catchment area did not change much. This is the period of time when the unconsolidated sediments and *H. naledi* fossils accumulated in Rising Star Cave (Dirks et al., 2017).

4.2.2. Geology of Rising Star Cave

Rising Star Cave is positioned between 1450-1480 m above sea level and located close to the valley floor of the Bloubank Spruit (Fig. 2), near the confluence with the Riet Spruit, ~2 km west of Sterkfontein Cave. Directly east of the cave entrance, two unpaired strath terraces and a single paired fluvial terrace are preserved along the banks of the Bloubank Spruit, which currently forms an ephemeral streambed positioned ~100 m north of the cave. The strath terraces contain a thin (less than 0.5 m) unconsolidated alluvial cover overlying the dolomite bedrock, whereas the fluvial terraces consist of unconsolidated alluvium deposited in the hanging wall of a normal fault (Dirks et al., 2015; Makhubela et al., 2019). The terraces broadly parallel the riverbed and represent earlier stages of stream flow along the Bloubank Spruit.

Rising Star Cave is hosted in chert-poor, stromatolite-rich dolomite of the Monte Christo Formation (Fig. 3). Figure 3 shows a stratigraphic section of the dolomite interval that hosts the cave, with the stratigraphic position of the different chambers indicated. Most of the cave formed

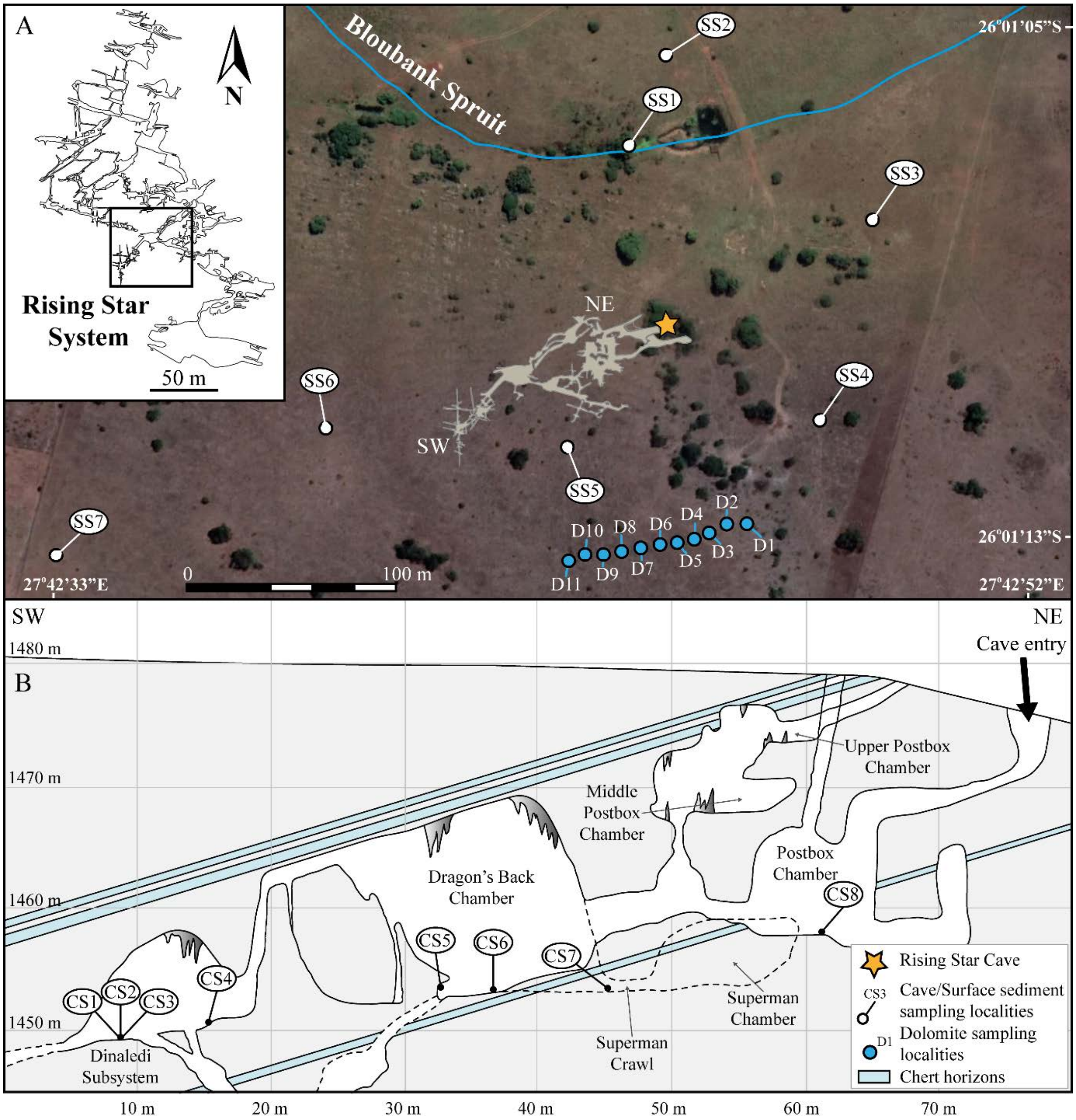

Figure 2. Sample locality map. A) surface sample localities for the collection of detrital zircon samples (white circles) and the dolomite samples used for dissolution (blue samples); B) Detrital zircon sample localities inside the Rising Star Cave.

in a relatively chert-free, 18 m thick section of dolomite above a major sheared shale horizon (i.e. between ~6-24 m in Fig. 3). Irregular chert bands within this section of dolomite make up ~1.2 m of the stratigraphy, constituting less than 7% of the rock volume. Two micaceous shale horizons towards the base of the section represent <1% of the total rock volume affected by cave formation processes (Fig. 3).

The Rising Star Cave is a network maze cave system consisting of a series of narrow interconnected chambers and passages that formed along shallowly W-dipping dolomite strata (Dirks et al., 2015; Figs 1 and 2). The *H. naledi* fossils were found in the Dinaledi and Lesedi Chambers (Dirks et al., 2015; Hawks et al., 2017), with the majority of fossil material concentrated in the Dinaledi Chamber, which lies ~ 80 m away from the present entrance into the cave system. The Dinaledi Chamber can only be accessed via the Dragon's Back Chamber, which in turn can be accessed via a direct route that passes through the Postbox Chamber; or along a more complex maze of fractures via the Superman Chamber (Fig. 2B; Dirks et al., 2015).

Poorly consolidated, orange-red clastic sediments are widely distributed throughout the Postbox, Dragon's Back, Superman and Dinaledi Chambers, and include laminated mud, silt, sand and conglomerate (e.g., Dirks et al., 2017). These deposits are fossiliferous, and in the Dinaledi Chamber they occur in association with the *H. naledi* fossils (Dirks et al., 2015; Wiersma et al., 2020). Away from these chambers, in the remainder of the accessible parts of the cave system, little additional sediment accumulated.

The fossiliferous orange-red clastic sediments in the Dinaledi, Dragon's Back, Postbox and Superman chambers, are part of a single depositional system that can be compared to a subterranean debris cone, which partly filled the network of chambers and connecting passageways. The coarsest-grained sediments on this debris cone accumulated in the Postbox Chamber, and the average grain size of sediments decreases when moving into the Dragon's Back and Superman Chambers. The most distal part of the cone is represented by sediment in the Dinaledi Chamber, which is dominated by mud deposits with little sand and significantly less quartz (Dirks et al., 2015; Wiersma et al., 2020).

The apex of the debris cone is characterised by coarse, poorly sorted conglomerate that entered the cave via a vertical shaft in the roof of the Postbox Chamber. This shaft opened to surface, about 4 m above the current entry point into the cave and is now filled with loosely packed breccia and no longer accessible. From its apex, sediment spilled down cave passages into the Dragons's Back and Superman chambers, where erosion remnants along cave walls indicate that up to 3 m of sediment accumulated. No clastic sediment coarser than sand washed directly from the Dragon's Back Chamber into the Dinaledi Chamber due to the presence of a 5 m high sill that consists of *in situ* dolomite, which blocked high energy water flow (Dirks et al., 2015, 2017; Wiersma et al., 2020). However, fine-grained orange-red mud and silt, deposited from suspension, did pass through fractures in the walls, and accumulated in the Dinaledi chamber (Wiersma et al., 2020).

Erosional remnants of orange-red sandstone and mudstone indicate that significant volumes of clastic sediment once filled the chambers along the entry route into the Dinaledi Chambers, but most of this sediment was removed via floor drains that exist in most chambers (e.g., Dirks et al., 2015, 2017). Sediment accumulation and erosion alternated with periods of flowstone formation in the cave (e.g., Dirks et al., 2017), and it is common to find accumulations of orange-red sediment covered by a drape of flowstone. Where this happens the sediments below the flowstone are indurated with carbonate cement, and these sediments are semi-lithified. Some flowstones are extensive and can be traced as semi-continuous sheets across most of the chambers. These flowstones have been used to subdivide the sediments into five stratigraphic units that are variably preserved in the different chambers. Locally, these units occur as laterally extensive deposits and as hanging remnants along the cave wall or underneath flowstones. Each of the sedimentary units are architecturally complex and preserve similar facies across individual chambers, but they are not necessarily time equivalent, making inter-chamber stratigraphic correlations difficult, unless bounding flowstones can be traced from one chamber to the next. Nevertheless, a relative age can be determined for each of the units (and their bounding flowstones), which has provided the framework for this study.

From old to young, the five lithostratigraphic units include: 1) lithified mud clast breccia (LMCB) deposits; 2) semi-lithified layered orange-pink sand (LOS); 3) unlithified laminated orange-red mud (LORM facies in Wiersma et al., 2020); 4) unlithified mud clast breccia (UMCB facies in Wiersma et al., 2020); and 5) unlithified orange-red cave floor sediment (Dirks et al., 2015, 2017). In addition, a coarse chert-dolomite breccia deposit with rare fragments of Klapperkop quartzite, form a further unit near the apex of the debris cone in the Postbox Chamber. This coarse breccia is interlayered with LOS-like deposits and is possibly overlain by LORM sediment. The breccia has not been further investigated in this study.

All five lithostratigraphic units are fossiliferous to some extent, with the UMCB in the Dinaledi Chamber hosting the *H. naledi* fossils (Dirks et al., 2015, 2017). Fossils in the LMCB and LOS sediments include isolated elements such as vertebrae, limb elements, and a few teeth and cranial bones assigned to large vertebrates (e.g., Bovidae, Felidae, *Papio*). In the LORM facies, locally dense concentrations of fossils occur within sandier lenses dominated by disarticulated cranial and post-cranial elements of micro-mammals (Rodentia and Soricidae).

The LMCB deposits are the oldest deposits recognised along the access route into the Dinaledi Chamber and are preserved as hanging remnants underneath the oldest generation of flowstones that can be traced as near-continuous sheets from the Dinaledi Chamber via the Dragon's Back Chamber to the Superman, and Postbox chambers (Dirks et al., 2015, 2017). The capping flowstones could not be accurately dated with U-Th and are, therefore, older than 600 ka (Dirks et al., 2017). These LMCB sediments can be found in other parts of the cave as well, and they do not form part of the debris cone described above, but constitute a separate sedimentary system that predated the opening of the roof in the Postbox Chamber and entry of *H. naledi* (Dirks et al., 2017). LMCB sediment consists of clast-supported mud clasts embedded in a dark brown fine-grained matrix of silt and clay. The mud clasts are typically angular, millimetre-to-centimetre-sized, and orange-brown in colour with local staining of secondary Mn-Fe oxides and oxyhydroxides.

The LOS unit forms extensive deposits in the Dragon’s Back Chamber where it occurs as erosion remnants on top of LMCB deposits. It formed prior to the deposition of a prominent flowstone horizon that can be traced across the Dragon’s Back chamber and from there into the Superman and Postbox chambers. The capping flowstone was dated to ~500 ka using Al-Be cosmogenic dating techniques (Makhubela et al., 2019), and the LOS sediments form the oldest unit linked to the debris cone, predating the entry of *H. naledi*. LOS sediments consist of orange-pink heterolithic, quartz-rich sandstone composed of medium to coarse-grained, sub-rounded and rounded grains. Locally, fluvial architectures such as cut-and-fill, cross-bedding, and normally graded beds are preserved.

Unlithified LORM sediments are perhaps the most widely distributed unit along the debris cone, and have been recorded from the Dragon's Back, Postbox, Superman and the Dinaledi chambers. They were dated in the Dinaledi Chamber from two separate deposits with ages of ~350 ka and ~235 ka (Dirks et al. 2017), while Makhubela et al. (2019) report ages of ~220 ka and ~175 ka for LORM sediments in the Postbox and Dragon’s Back chambers respectively. These depositional ages overlap with the age of the *H naledi* fossils (335-236 ka; Dirks et al., 2017). LORM sediments overlie LMCB and LOS deposits and occur as isolated erosion remnants along the cave floor, as remnants on top of flowstone, as cave wall fracture fill, and as localized patchy

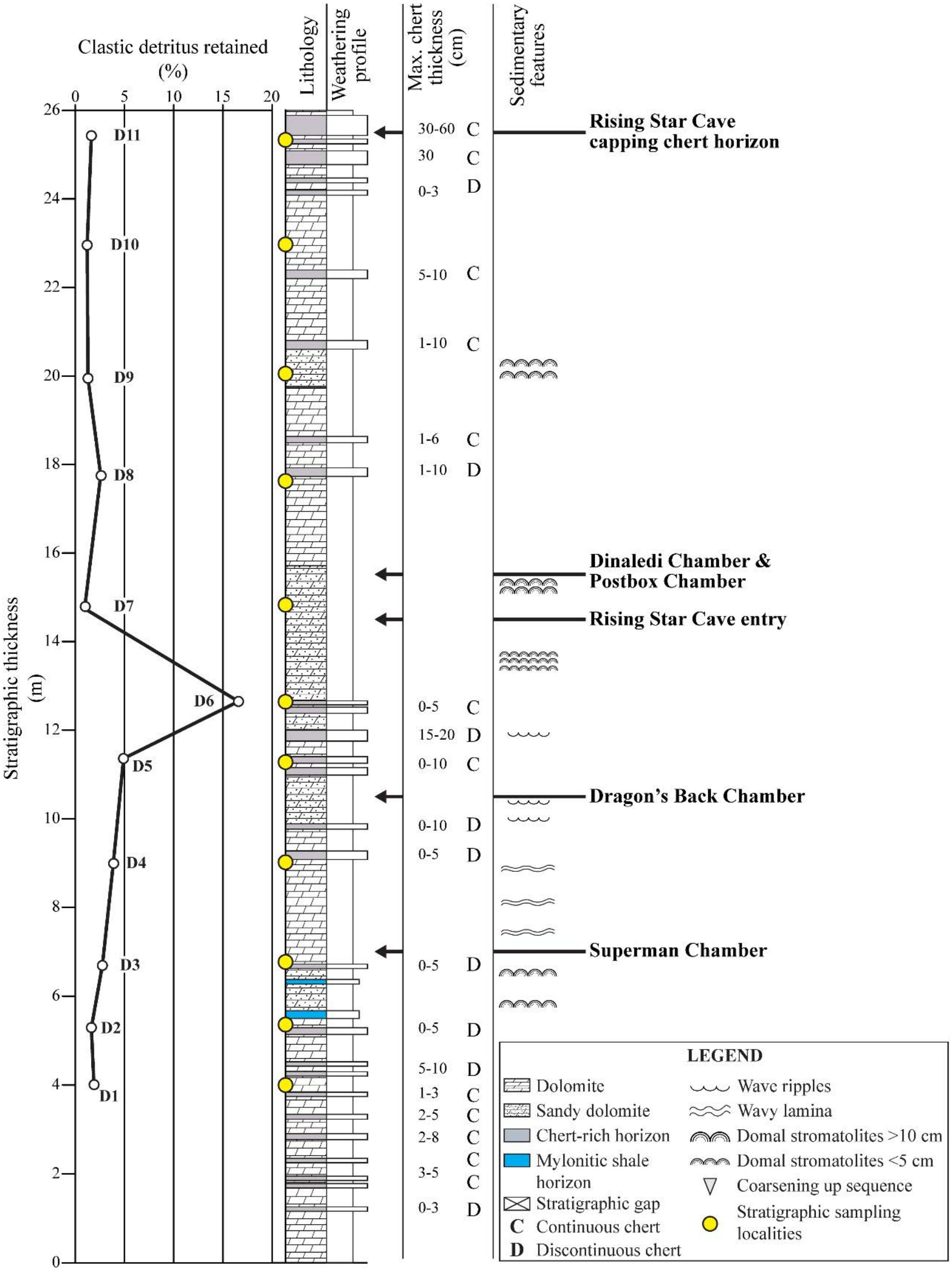

Figure 3. Lower Monte Christo Formation stratigraphy. Measured stratigraphic section of the lower Monte Christo Formation and dolomite sampling localities in relation to the position of the various chambers of the Rising Star Cave.

remnants along the cave walls (Dirks et al., 2015, 2017; Wiersma et al., 2020). The deposits consist primarily of illite-rich laminated mud that is locally interbedded with fossiliferous sand lenses dominated by very fine to fine-grained, quartz.

The youngest unit in the cave consists of UMCB sediments, which formed highly localized deposits distributed along the cave floors of the Dinaledi, Postbox, and Superman chambers. In the Dinaledi Chamber, UMCB sediments cover ~350 ka LORM sediments and they were covered by flow stones as old as ~105 ka (Dirks et al., 2015, 2017), but their formation locally continues today (Wiersma et al., 2020). The facies formed largely *in situ* from adjacent LORM deposits via sedimentary auto-brecciation (Wiersma et al., 2020), and hence the UMCB deposits always occur together with deposits of LORM. Compositionally and architecturally, the UMCB sediments are similar to LORM sediments; with millimetre-to-centimentre-sized, orange-brown and Mn-Fe-oxide stained, angular mud clasts 'suspended' in a very fine-grained dark brown-grey silt and clay matrix.

In addition to the five units for which erosion remnants are preserved within the cave, the cave floor is covered by floor sediments that are largely composed of loose sand and mud mixed with erosion products of all sediment types as well as fragments of wall rock and flowstone (e.g., Dirks et al., 2015; Wiersma et al., 2020). Viewed together, the LORM and UMCB sediments formed at the time *H. naledi* interacted with the cave between 335-236 ka (Dirks et al. 2017), and these sediments were targeted in this study. The LORM sediments are distributed widely as part of the debris cone deposits with sediment input through the roof of the PostBox Chamber. The UMCB deposits resulted from localised reworking of LORM sediments at isolated localities within the cave (Wiersma et al., 2020).

4.3. Materials and Methods

Sample preparation, mineral separation, CL-imaging, and detrital zircon U-Pb geochronology analyses were carried out at the Advanced Analytical Centre at James Cook University. Mineral Liberation Analysis (MLA) was carried out at the SEM-MLA facility at Memorial University of Newfoundland, St Johns, Canada.

4.3.1. Sample materials

In total, twenty-six samples were collected for this study, which are summarized in Table 1. These samples consist of rock fragments of dolomite that hosts the cave (n=11), and LORM and UMCB sediments (n=6). In addition, floor sediments (n=2) and sediments from outside the cave (n = 7) were collected for comparison with the LORM and UMCB sediments. To avoid the usage of lengthy sample field numbers, names have been abbreviated throughout this paper. The dolomite samples will be referred to as D1-D11, cave sediment samples as CS1-CS8, and surface sediment samples as SS1-SS7 (Table 1).

Eleven dolomite samples (D1-D11; Table 1) were collected along a ~26 m thick stratigraphic section of the lower Monte Christo Formation that hosts the chambers along the route into the Dinaledi Chamber (Fig. 3). Samples were collected at regular intervals of 1-2 m for heavy mineral extraction and dissolution experiments to determine the wt % of insoluble material within the dolomite (Fig. 3). Most samples were similar in appearance and consisted of dark-grey massive dolomite with variably developed stromatolitic laminations that varied from thin parallel laminations to small-scale (<10 cm) domal geometries. One sample (D6) was distinct in that the dolomite has a granular sandy texture and yellow colour. This yellow dolomite occurs as a distinct, ~1.5 m wide marker horizon in the centre of the section, and it can be traced throughout the cave system.

Fifteen unlithified samples of cave and surface sediments (CS1-CS8, SS1-SS7, Fig. 2 and Table 1) were collected for both LA-ICP-MS and MLA analyses to compare the composition of the cave sediments with their possible source materials on surface. Cave sediment samples include LORM and UMCB sediments collected from the Dinaledi Chamber (n=4), Dragon’s Back Chamber (n=3) and Postbox Chamber (n=1). In the Dinaledi Chamber, samples CS1-3 were collected from *H. naledi*-bearing UMCB sediments in the excavation pit described in Dirks et al. (2015) at depth of 10, 20, and 55 cm (Table 1). Sample CS4 was collected from LORM sediment underlying the UMCB deposits. In the Dragon's Back Chamber, a sample (CS5) of LORM sediment was collected from the northwest corner of the chamber, while samples CS6 and CS7 were taken from cave floor sediment; CS6 from the centre of the chamber at 15 cm depth, and CS7 from the floor below the Superman Crawl at 15 cm depth. In the Postbox Chamber one sample (CS8) was taken from LORM sediment in the lower part of the chamber.

Seven surface sediment samples (SS1-SS7; Table 1) were collected from localities near the cave (Fig. 2). To ensure *in situ*, i.e. non-disturbed, soil collection, auger sampling was done at depths of ~0.2-1 m (Table 2). Sample SS1 was obtained from the Bloubank Spruit riverbed. Sample SS2 was taken from a thick alluvial terrace immediately north of the riverbed. Samples SS3 was taken from the same alluvial terrace to the south of the riverbed and sample SS4 was collected from a strath terrace immediately below the cave entrance. Sediment sample SS5 was collected from surface soil directly above the cave, and samples SS6 and SS7 were collected up-slope, west of the cave (Fig. 2).

Table 1. Samples used for the multiple analyses performed in this study.

Sample number	**Field number**	**Facies/rock type**	**Sampling locality**	**Analysis**
D1	160517JW1	Dolomite rock	Monte Christo Fm	Dissolution, SEM
D2	160517JW2	Dolomite rock	Monte Christo Fm	Dissolution, SEM
D3	160517JW3	Dolomite rock	Monte Christo Fm	Dissolution, SEM
D4	160517JW4	Dolomite rock	Monte Christo Fm	Dissolution, SEM
D5	160517JW5	Dolomite rock	Monte Christo Fm	Dissolution, SEM
D6	160517JW6	Dolomite rock	Monte Christo Fm	Dissolution, SEM
D7	160517JW7	Dolomite rock	Monte Christo Fm	Dissolution, SEM
D8	160517JW8	Dolomite rock	Monte Christo Fm	Dissolution, SEM
D9	160517JW9	Dolomite rock	Monte Christo Fm	Dissolution, SEM
D10	160517JW10	Dolomite rock	Monte Christo Fm	Dissolution, SEM
D11	160517JW11	Dolomite rock	Monte Christo Fm	Dissolution, SEM
CS1	UW101-1783A	UMCB sediment	Dinaledi Chamber	LA-ICP-MS, MLA
CS2	UW101-1783C	UMCB sediment	Dinaledi Chamber	LA-ICP-MS, MLA
CS3	UW101-1783L	UMCB sediment	Dinaledi Chamber	LA-ICP-MS, MLA
CS4	OSL-4	LORM sediment	Dinaledi Chamber	LA-ICP-MS
CS5	260517JW8	LORM sediment	Dragon's Back Ch.	LA-ICP-MS, MLA
CS6	100517JW3	Cave floor sediment	Dragon's Back Ch.	LA-ICP-MS, MLA
CS7	100517JW5	Cave floor sediment	Dragon's Back Ch.	LA-ICP-MS, MLA
CS8	100517JW6	LORM sediment	Postbox Chamber	LA-ICP-MS, MLA
SS1	190517JW1	Fluvial sediment	Streambed	LA-ICP-MS, MLA
SS2	190517JW2	Alluvial sediment	Alluvial terrace	LA-ICP-MS, MLA
SS3	190517JW3	Alluvial sediment	Alluvial terrace	LA-ICP-MS, MLA
SS4	190517JW4	Alluvial sediment	Strath terrace	LA-ICP-MS, MLA
SS5	190517JW5	Colluvial sediment	Surface-above cave	LA-ICP-MS, MLA
SS6	190517JW6	Colluvial sediment	Surface-above cave	LA-ICP-MS, MLA
SS7	190517JW7	Colluvial sediment	Surface-above cave	LA-ICP-MS, MLA

4.3.2. Dolomite dissolution

Each of the eleven dolomite rock samples was dissolved in hydrochloric (HCl) acid to determine the quantity of insoluble clastic detritus present within the rock. Prior to dissolution, initial sample weights were recorded. The samples were subsequently crushed into 500µm fragments using a Retsch DM-200 disc mill, and post-crushing weights were recorded. The crushed samples were placed into 800 ml glass beakers and dissolved in 250 ml, 10 mol/L, 32% HCl for a period of 24 hours to ensure all the dolomite was dissolved. The retained insoluble residue was collected and rinsed with distilled water and oven-dried for 24 hours at 100°C to remove excess moisture. It was then weighed, and the percentage clastic detritus was calculated for each sample using the formula:

$$C_{cd} = A_{ipc}/B_{dis}*100$$

Were C_{cd} is the amount of clastic detritus in the sample in percentage, A_{ipc} is the weight of the sample after crushing, and B_{dis} is the weight of the insoluble clastic detritus after dissolution in HCL.

Table 2. Surface samples collected for detrital zircon U-Pb geochronology and mineral liberation analysis.

Sample number	**Geomorphological features**	**Sampling locality UTM**	**Surface elevation above sea level**	**Sampling depth below surface**
SS1	Bloubank Spruit dry streambed	0571269/7122086	1461 m	0.75 m
SS2	Alluvial terrace	0571290/7122136	1464 m	1.0 m
SS3	Alluvial terrace	0571407/7122044	1468 m	0.5 m
SS4	Strath terrace	0571371/7121935	1470 m	0.2 m
SS5	Colluvial surface above cave	0571239/7121922	1477 m	0.3 m
SS6	Colluvial surface west of cave	0571104/7121931	1478 m	0.3 m
SS7	Colluvial surface southwest of cave	0570961/7121869	1486 m	0.4 m

4.3.3. Detrital zircon sample preparation

All samples were investigated for detrital zircon. The cave and surface sediment samples were clay-rich and clay removal was necessary prior to heavy mineral separation to avoid contaminating the heavy liquid. The clay fraction was removed by placing each sample in 800 mL beakers and submerging the sediment using tap water. Twenty-five mL of 40 g/L solution of sodium hexametaphosphate was added as a dispersing agent to prevent flocculation of clay. Sediments were agitated to bring clay in suspension and clay was decanted after a 5-minute settling period. This process was repeated ~20-50 times per sample, depending on clay content. In addition, the sediments were treated for 10-minutes in an ultrasonic bath to ensure disintegration of clay aggregates to facilitate the removal of clay. The number of ultrasonic treatments varied per sample. After clay removal, the sediments were oven-dried for 24 hours at 70°C to remove excess moisture.

Following clay removal, magnetic minerals were separated with a hand magnet and a Frantz magnetic separator. Heavy liquid, lithium polytungstate (LST), with a density of 2.85 was used to separate the heavy mineral separation from the non-magnetic fraction. Concentrates were washed, oven-dried for 24 hours at 70°C, and zircons were hand-picked and mounted in 25 mm epoxy resin pucks. The pucks were polished to expose the zircons for cathodoluminescence (CL) imaging, using a Jeol JSM5410LV scanning electron microscope, equipped with a CL detector. The CL images were used to map zircons for LA-ICP-MS U-Pb analysis. Additionally, CL images of concordant zircon grains were used for shape analysis and classification into euhedral, subhedral, rounded, or broken morphologies.

For the rock samples of dolomite (D1-D11), detrital minerals were separated from the clastic residue left after dissolution. The residues contained no clay and few magnetic minerals, and heavy mineral concentrates were obtained with the use of heavy liquid as described above. Heavy mineral concentrates were inspected under a binocular microscope, and subsamples of the clastic detritus were imaged, using a Hitachi SU5000 field emission gun scanning electron microscope (FEG-SEM) equipped with a secondary electron and backscatter electron detector, using 4.0 kV accelerator voltage.

4.3.4. LA-ICP-MS U-Pb dating

Data acquisition was carried out using a Photon Machines Analyte G2 193 nm ArF Excimer laser ablation system connected to a Thermo iCAP-RQ ICP-MS. The ablation cell was connected to the iCAP-RQ via Tygon tubing. Ablation was conducted in a HelEx II Active 2-Volume Cell using high-purity helium as the carrier gas, which was subsequently mixed with argon and nitrogen gases prior to introduction into the ICP-MS.

The ICP-MS was regularly optimized using auto tune on a solution basis. It was tuned further for maximum sensitivity in laser ablation mode using glass NIST 610 under robust plasma conditions (U/Th = ~1) while maintaining oxide production rates (ThO/Th) to below 0.5%. RSD of ^{238}U, ^{232}Th, and ^{206}Pb signals during line scan of NIST 610 is typically better than 2%. This method is described in Tucker et al. (2013) and Spandler et al. (2016).

Conventional spot analyses were used for data acquisition of samples. Laser fluence was set to ~3 J/cm^2 at the sample surface with a laser repetition rate and a beam diameter of 5 Hz and 30 µm, respectively. Each individual analysis contains 30s background and 40s sample integration. Analytes included ^{29}Si (10 ms), ^{49}Ti (20 ms), ^{91}Zr (10 ms), ^{200}Hg (10 ms), ^{204}(Pb + Hg) (10ms), ^{206}Pb (30 ms), ^{207}Pb (70 ms), ^{208}Pb (10 ms), ^{232}Th (10 ms), and ^{238}U (20 ms). Integration time of a single sweep was set at ~0.2 s, so each sweep corresponds with a single laser shot. Samples were intercalated with standards GJ1, FC1, Plesovice, 91500, and NIST610. GJ1 was used for the fractionation correction and instrumental drift calibration while FC1, Plesovice, 91500 and NIST 610 were used for quality control.

Iolite v3.63 was used for data reduction as described in Paton et al. (2011). Isoplot 4.15 was used to produce concordia and weighted mean average plots. For analyses used in this study, a 15% concordance filter was used, i.e. analyses with a concordance between 85-115% have been treated as concordant. Discordant grains were excluded from all interpretations. Detrital zircon grains >1.0 Ga were interpreted using ^{207}Pb/^{206}Pb ages, whereas ^{206}Pb/^{238}U ages were used for grains <1.0 Ga. To test for zircon provenance similarities between the 15 sediment samples, a Kolmogorov-Smirnov (K-S) statistical test was used, with P-value errors in the CDF.

4.3.5. Mineral Liberation Analysis

Mineral Liberation Analyses (MLA) were carried out on samples CS1-8 and SS1-7 to investigate the modal mineralogy of unlithified cave and surface sediments. Mineralogical comparisons were made between the main detrital constituents (e.g., quartz, micas, clays, carbonates and bone fragments), and alteration minerals (e.g., mainly Fe-Mn oxyhydroxides) that formed as a result of diagenetic and soil forming processes (Wiersma et al., 2020). Subsamples of cave and surface sediment were sieved, and the 0.5-1 mm size fraction was retained for grain mounts. Each grain mount contained on average ~350 individual grains. A silicone mould with a 2.5 cm inner diameter was placed on the glass plate with double-sided tape, on which approximately 5 gram of the 0.5-1 mm size fraction was mounted. Excess grains were removed from the mount and ~ 6 cc of two-compound resin was poured into the mould to produce a puck. The pucks were polished to expose the mineral grains for analysis.

Prior to analysis, the polished pucks were carbon-coated, and samples were analysed using a FEI Quanta 400 scanning electron microscope (SEM) equipped with energy dispersive X-ray

(EDX) spectrometers and mineral liberation analyzer software v.3.1.4.683 that automates microscope operation and data acquisition (Sylvester, 2012). The MLA measurements are based on backscatter electron (BSE) image analysis. Shape analyses were carried out for each sample to determine mean roundness and sphericity of the grains, using the 64-bit Fiji software package (Schindelin et al., 2012).

4.4. Results

4.4.1. Clastic components in dolomite

Detailed logging of the stratigraphic section of dolomite that hosts the Rising Star Cave chambers showed that ~7% of the rock volume in which the caves formed consisted of chert horizons (Fig. 3). This is a maximum estimate based on the average thicknesses of chert layers measured along the stratigraphic section. However, it was noted that many of the chert intercalations are highly irregular in width, and some occur as trails of discontinuous pods. This suggests that the true chert content of the dolomite section is probably considerably less than 7%. Only two 10-15 cm thick sericite-quartz-rich shale horizons were found in the cave, mostly near the floor of the Postbox chamber. Considering that these layers do not intersect the Dragon's Back or Dinaledi Chambers, they make up considerably less than 1% of the rock volume in the cave.

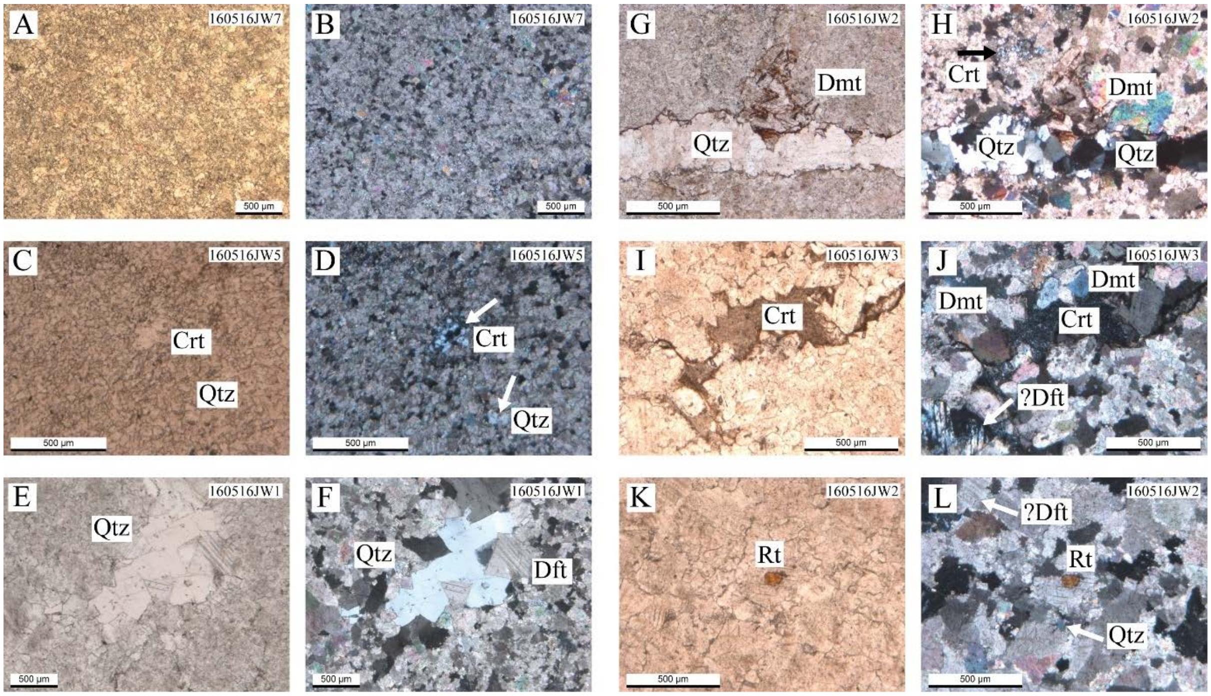

Figure 4. Thin section petrography photographs of dolomite samples collected from the surface surrounding the Rising Star Cave. Fine-grained dolomite, magnified 2.5X in A) PPL; and B) XPL. Diagenetic infill of voids with granular chert and quartz cement enclaves in fine-grained dolomite, magnified 5X in C) PPL; and D) XPL. Millimeter-sized quartz cement infill in fine-to-medium-grained dolomite with local deformation twins. Magnification 2.5X in E) PPL; and F) XPL. Diagenetic horizontal quartz vein and chert cement enclave (black arrow) in fine-medium-grained dolomite. Minor amounts of coarser-grained dolomite crystals are also visible. Magnification 5X in G) PPL; and H) XPL. Diagenetic infill of void with chert cement in fine-medium-grained dolomite with possibly local deformation twins. Magnification 5X in I) PPL; and J) XPL. Granular quartz and rutile in medium-grained dolomite. Some of the dolomite grains possibly contain deformation twinning. Magnification 5X in K) PPL; and L) XPL. Abbreviations: Crt: chert; Dft: deformation twinning; Dmt: dolomite; Qtz: quartz; Rt: rutile.

Clastic insoluble detritus was recovered from all dolomite samples with concentrations ranging from 0.56-15.61 % (Table 3) across the stratigraphy (Fig. 3), averaging 3.07 %. When corrected for the relative volume of material involved, this estimate for the average content of insoluble material drops to ~2.7%. The highest concentrations of detritus occur in the lower half of the measured stratigraphy (4-13 m), in which the Superman and Dragon's Back chambers occur. Here the clastic concentrations range from 1.17-15.61 %, averaging 4.7 %. The upper stratigraphic section (13-26 m) hosts the Dinaledi and Postbox chambers and here clastic concentrations range from 0.56-2.14 %, averaging 1.12 % (Fig. 3). Most of the retained insoluble material consists of micro- and cryptocrystalline quartz, mm-thin, sheet-like chert and rare grains of long-prismatic rutile (Fig. 4) as well as organic material. The quartz is highly angular and irregular shaped (Fig. 5). Petrographic thin sections show that the fine-grained chert and quartz commonly occur as small clusters, occupying void spaces throughout the dolomite (Fig. 4A-B) that formed during diagenesis or metamorphism as secondary fill in voids and along fractures. Detrital quartz grains with characteristically rounded shapes and frosted surfaces were not observed. None of the dissolved dolomite samples contained zircon grains.

Samples D1-5 show an upward trend in the clastic components within the dolomite, steadily increasing from 1.42 to 4.32 %. This is followed by a sharp increase in clastic detritus to 15.6 % in sample D6 (Fig. 3), after which a sharp decline occurs in sample D7 (0.56 %), with low concentrations in clastic detritus continuing onwards up to sample D11. Samples D7, D9, and D10 are particularly quartz-poor, retaining less than 1 % insoluble detritus, and were collected from stromatolite-poor dolomite. Samples D1-5, D8, and D11with insoluble detritus ranging between

1-5 % contain considerable quartz. Samples D6 retained the most clastic detritus (>15 %) and is also quartz rich. Samples D2, D3, D7, and D9 were collected from stromatolite-rich sections and are more quartz-rich compared to stromatolite-poor horizons.

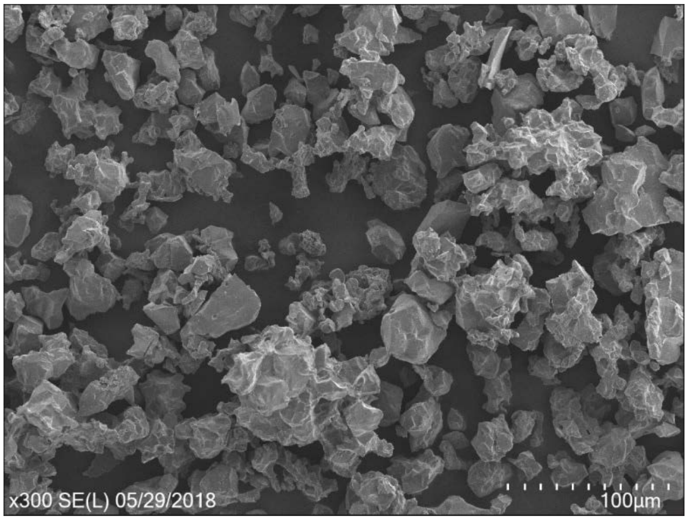

Figure 5. Quartz fragments from Monte Christo Formation dolomite. SEM image illustrating quartz morphology from dissolved dolomite in the Monte Christo Formation.

Table 3. Surface dolomite samples used for dissolution in HCl and clastic insoluble retention.

Sample number	**Post-milling weight (gr)**	**Insoluble detritus weight (gr)**	**% insoluble detritus**	**SiO_2-poor dolomite (0.5-1.0 %)**	**SiO2-fair dolomite (1.0-5.0 %)**	**SiO2-rich dolomite (>10 %)**
D1	38.00	0.5389	1.42		**X**	
D2	53.00	0.6214	1.17		**X**	
D3	133.00	3.0795	2.32		**X**	
D4	104.00	3.5086	3.37		**X**	
D5	91.00	3.9271	4.32		**X**	
D6	101.00	15.7682	15.61			**X**
D7	121.00	0.6797	0.56	**X**		
D8	150.00	3.2077	2.14		**X**	
D9	115.00	0.9846	0.86	**X**		
D10	69.00	0.5731	0.83	**X**		
D11	128.00	1.5394	1.20		**X**	

4.4.2. Detrital zircon age populations and grain morphology

All the radio-isotopic data are summarized in Supplemental File 1. The 15 analysed samples yielded a total of 1017 detrital zircons of which 886 grains produced concordant ages, ranging from Palaeoarchaean to Jurassic in age (Fig. 6A). Eighty-one percent of the zircons analysed (n=709) produced ages younger than the 2.55-2.45 Ga Malmani Subgroup dolomites and 19 % of the zircons (n=168) are older than Malmani Subgroup. Few grains were obtained that overlap in age with the late Archaean age for the lower parts of the Malmani dolomite estimated at 2550 Ma (Walraven and Martini, 1995), which include two rounded grains and one subhedral grain from samples CS7, SS5, SS1, producing ages of 2581±20, 2563 ±19 and 2534 ± 19 Ma, respectively.

The concordant detrital zircon grains (n=886) produced ten discrete age populations (Fig. 6A), which coincide with major orogenic or basin formation events on and surrounding the Kalahari craton (Johnson et al, 2006a and references therein). From oldest to youngest these are: (1) a Paleoarchaean to Mesoarchaean population (3213.9 to 3106 Ma) marking the age of rocks in the Johannesburg dome (e.g., Poujol et al., 2003); (2) a Mesoarchaean to Neoarchaean population (3106 to 2708 Ma) that overlaps with the age of the Dominion and Witwatersrand Groups (Johnson et al., 2006a); (3) a Neoarchaean population (2708 to 2688 Ma) that coincides with the age of the Ventersdorp volcanics; (4) a Neoarchaean to Paleoproterozoic population (2688 to 2061 Ma) overlapping in age with late Archaean granite-greenstones and overlying platform sediments of the Malmani Subgroup and Pretoria Group (Poujol et al., 2003; Eriksson et al., 2006); (5) a Paleoproterozoic population (2100 to 2002 Ma) that coincides with the age of emplacement of the Bushveld complex (Olsson et al., 2010); (6) a Paleoproterozoic population (2002 to 1885 Ma) that correspond with baddeleyite ages for dolerites intruding the Waterberg Group (Hanson et al., 2004) and possibly the Moshaneng dolerite which intrudes the Mannyeyalong Formation in Botswana (Carney et al., 1994); (7) a Mesoproterozoic population (1204 to 1101 Ma) reflecting activity in the Namaqua-Natal belt along the southern margin of the craton; (8) a Mesoproterozoic to Neoproterozoic population (1099 to 850.2 Ma) and (9) a Neoproterozoic to Cambrian population (854.4 to 500.8 Ma) both reflecting activity in the Mozambique belt to the east of the craton; and (10) an Permian to Lower Jurassic population (298.7 to 182.6 Ma) of Karoo age (Fildani et al., 2009; Viglietti et al., 2017).

4.4.3. Age populations in cave sediments

The detrital zircon age populations in UMCB (CS1-3) and LORM (CS4) sediments in the Dinaledi Chamber are similar (Fig. 6B). Collectively, the three UMCB **samples C1-C3** yielded a small number of zircons (n=46) that produced five main zircon populations (Fig. 6B), including:

(1) 3065 to 2984 Ma (n=4); (2) 2459 to 2202 Ma (n=5); (3) 2064 to 1989 Ma (n=15); (4) 1098 to 987 Ma (n=5); and (5) 761 to 511.9 Ma (n=12); plus some Triassic grains. The LORM **sample CS4** produced 49 concordant dates, ranging from Archean to Triassic in age (Fig. 6B) with six age populations: (1) 3130 to 3056 Ma (n=5); (2) 2865 to 2774 Ma (n=6); (3) 2107 to 2034 Ma (n=14); (4) 1174 to 900 Ma (n=7); (5) 733 to 440 Ma (n=10); and (6) 270.24 to 246.6 Ma (n=4).

The three samples collected from the Dragon's Back Chamber produced similar age populations (Fig. 6B). **Sample CS5** of LORM sediments yielded few zircons (n=20) with an age distribution that ranged from Palaeoarchean to late Middle Triassic (Fig. 6B) and produced four main populations at: (1) 2077 to 2048 Ma (n=6); (2) 910.9 to 852 Ma (n=3); (3) 533.3 to 530.3 Ma (n=3); and (4) 282 to 241.3 Ma (n=3). **Sample CS6** of floor sediment yielded 135 zircons with ages ranging from Paleoarchean to late Early Jurassic (Fig. 6B), with seven main populations at: (1) 3222 to 2890 Ma (n=19); (2) 2788 to 2688 Ma (n=8); (3) 2269 to 1970 Ma (n=28); (4) 1791 to 1664 Ma (n=4); (5) 1209 to 892 Ma (n=27); (6) 645 to 454 Ma (n=26); and (7) 336.4 to 182.6 Ma (n=16). **Sample CS7** also of floor sediments yielded 106 concordant zircons with ages ranging from Paleoarchean to late Middle Triassic (Fig. 6B), and six main age populations at: (1) 3203 to 2757 Ma (n=28); (2) 2399 to 2363 Ma (n=4); (3) 2293 to 1938 Ma (n=21); (4) 1153 to 884 Ma (n=17); (5) 873 to 506 Ma (n=20); and (6) 311.4 to 243 Ma (n=7).

The LORM sediment **sample CS8** from the Postbox Chamber, yielded only 12 concordant zircon grains that range in age from Mesoarchean to Devonian (Fig. 6B) with two major populations at: (1) 2233 to 2002 Ma (n=5) and (2) 1118 to 816.8 Ma (n=3).

4.4.4. Age populations from surface sediments

The seven surface sediment samples produced zircon age distributions that are similar to the cave sediment samples (Fig 6B). **Sample SS1** from the Bloubank Spruit riverbed, produced 41 concordant zircon grains that range in age from Paleoarchean to Early Triassic (Fig. 6B), with six main age populations, which at: (1) 3213.9 to 3060.2 Ma (n=5), (2) 2860 to 2755 Ma (n=4), (3) 2534 to 2377 Ma (n=3), (4) 2106 to 2051 Ma (n=7), (5) 1308 to 1021 Ma (n=9), and (6) 831.9 to 417.1 Ma (n=11).

Sample SS2 obtained from the alluvial terrace near the river yielded 50 concordant zircons with ages ranging from Mesoarchean to late Middle Triassic (Fig. 6B), and populations at: (1) 3026 to 2754 Ma (n=10), (2) 2401 to 2021 Ma (n=16), (3) 1368 to 1298 Ma (n=3), (4) 1125 to 979

Ma (n=4), (5) 813 to 803 Ma (n=3), (6) 665 to 460 Ma (n=10), and (7) 301 to 238 Ma (n=4). **Sample SS3** collected from a terrace northeast of the cave yielded 101 concordant zircon grains with ages ranging from Paleoarchean to Early Triassic (Fig. 6B). They define eight statistically distinct age populations at: (1) 3206.1 to 2983 Ma (n=7); (2) 2864 to 2662 Ma (n=6); (3) 2467 to 2234 Ma (n=7); (4) 2100 to 1664 Ma (n=15); (5) 1272 to 992.1 Ma (n=20); (6) 932.6 to 750.6 Ma (n=10); (7) 671.3 to 425.2 Ma (n=26); and (8) 339.2 to 248 Ma (n=8). **Sample SS4** obtained from a terrace near the cave entrance yielded 90 zircons that produced concordant ages ranging from Paleoarchean to Middle Triassic (Fig. 6B), with five primary populations at: (1) 3223 ± 15 to 2708±25 Ma (n=14); (2) 2260 to 1861 Ma (n=26); (3) 1307 to 890.4 Ma (n=17); (4) 733 to 439.4 Ma (n=27); and (5) 272.3 to 238 Ma (n=4).

Sample SS5 was collected from above the cave, and yielded 89 concordant detrital zircon grains, ranging from Mesoarchean to Early Permian in age (Fig. 6B). Six statistically significant age populations were identified at: (1) 3186 to 2563 Ma (n=21); (2) 2419 to 2382 Ma (n=3); (3) 2263 to 1865 Ma (n=21); (4) 1247 to 1023 Ma (n=9); (5) 992 to 766.2 Ma (n=8); and (6) 727 to 513.5 Ma (n=23). **Sample SS6**, collected upslope from the cave, yielded 94 zircon grains with concordant ages ranging from Paleoarchean to Middle Triassic (Fig. 6B). Five statistically significant age populations were identified at: (1) 3222 to 2626 Ma (n=18); (2) 2154 to 2023 Ma (n=19); (3) 1284 to 1023 Ma (n=17); (4) 850.2 to 464.2 Ma (n=26); and (5) 312.1 to 244 Ma (n=11). **Sample SS7** was collected further upslope from SS6 and yielded 53 concordant zircon grains with ages ranging from Paleoarchean to Middle Permian (Fig. 6B), and five statistically significant populations at: (1) 3203 to 2915 Ma (n=5); (2) 2396 to 2376 Ma (n=3); (3) 2115 to 1737 Ma (n=17); (4) 1101 to 854.4 Ma (n=10); and (5) 739 to 453.5 Ma (n=16).

The grain shape analysis on the concordant zircon grains (n=886) did not establish a clear correlation between the degree of rounding and the age of the grains (Fig. 7). The majority (>50 %) of the grains are rounded (n=451) and occur evenly across the entire age spectrum. Subhedral (n=262) and broken (n=130) grains are also distributed across a broad age range. Euhedral grains are least abundant (n=43) and mostly record Palaeoproterozoic (2263 to 1859 Ma) (n=28), Mesoarchaean (3183 to 2932 Ma) (n=5) and Permian (298.7 to 268 Ma) (n=5) ages.

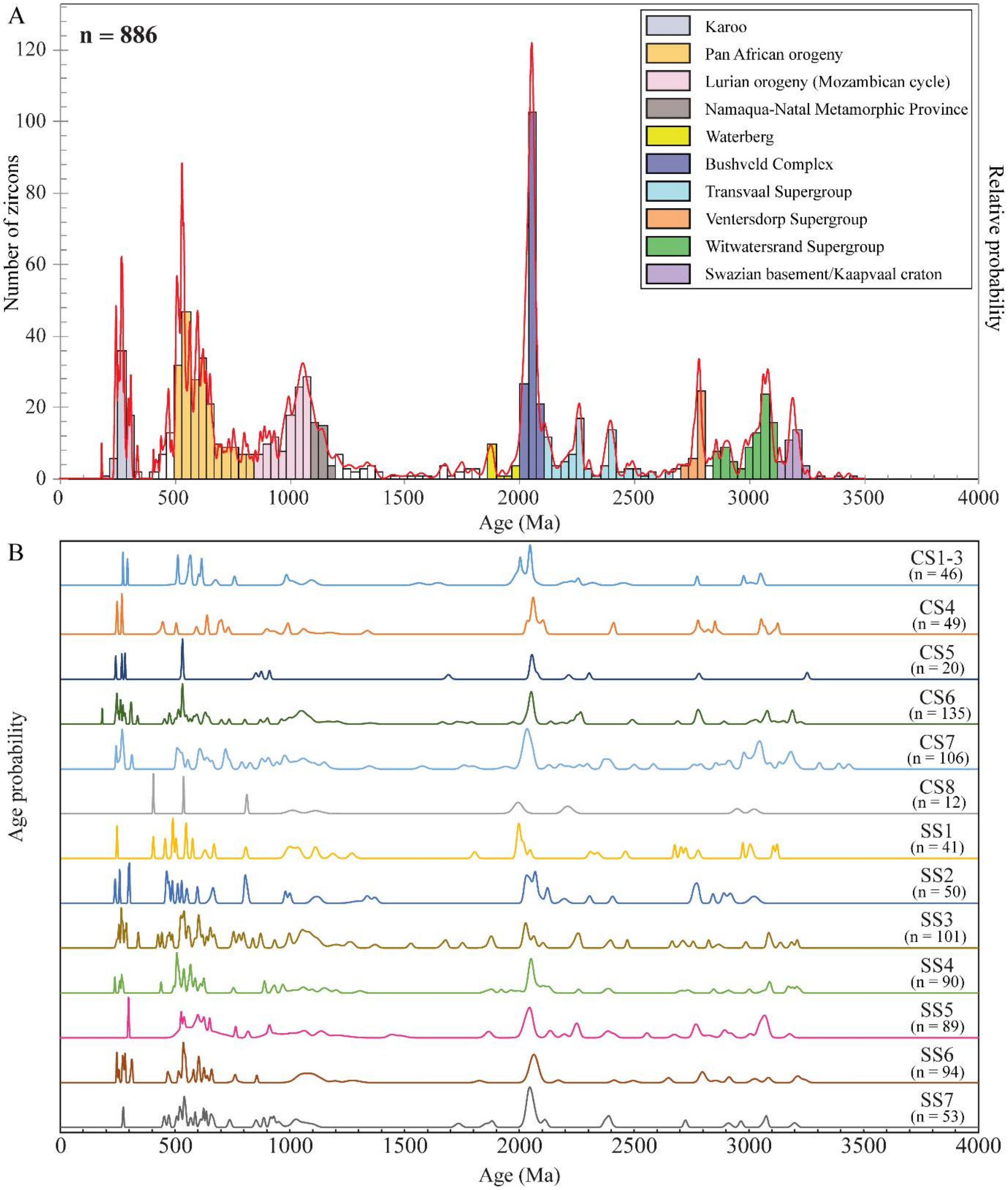

Figure 6. Rising Star Cave detrital zircon distribution. (A) Probability density frequency graph of the combined total concordant detrital zircon grain suite (n=886) for the Rising Star Cave and surface samples. (B) Age correlations for individual samples are illustrated below the probability density frequency plot and show a strong correlation in zircon age populations between the individual samples as well as with the combined samples. Both plots agree with a predominant allochthonous source for the majority (95 %) of clastic detrital sediments inside the cave.

4.4.5. Mineral liberation analysis

All the mineralogical data linked to MLA are summarized in Supplemental File 2. The percentages mentioned in this section refer to weight percent, unless stated otherwise. Except for the LORM and deeper UCMB sediments in the Dinaledi chamber, quartz is the dominant phase in all samples (Fig. 8), and quartz concentrations are consistently higher and less variable in the surface sediments. Here, quartz ranges from ~74-87 % with an average of 80 % with 9.78 (2σ) compared to the average of 51 % with 45.20 (2σ) for the cave sediments (Fig. 8). In the cave, quartz concentrations are highest for the floor sediments in the Dragon's Back Chamber (CS6-7), which are most similar to the sediments outside the cave. Quartz concentrations are lowest in the Dinaledi Chamber (CS2-4), and clay-sized micas including, muscovite and illite are significantly more abundant. Samples CS2-4 contain up to 60 % illite, compared to an average of ~4 % in cave samples from outside the Dinaledi Chamber. In general, micas are more abundant in the cave sediments with weight percentages averaging 5.19 % muscovite and 20.3 % illite, compared to average concentrations of 2.80 % muscovite and 4.12 % illite in the surface samples (Fig. 8). Sediments from the Dinaledi (CS1-4) and Dragon's Back (CS5, CS7) chambers contain low amounts of carbonate rock, ranging from 0.02-0.2 % dolomite and 0.01-3.42 % calcite (Fig. 8). Dolomite fragments are also rare in surface sediments and were only recorded in sample SS-5 at a concentration of 0.01 %. Occurrences of the mafic metamorphic mineral epidote are generally rare. The highest concentration of epidote is 5.5 % and was recorded from the LORM facies sediments (CS-5) in the Dragon's Back Chamber. Other concentrations of epidote range from 0.01-1.42 % in cave and surface sediments.

Fossil material is identified as calcium phosphates and is only found in cave sediments. Apatite occurs in all cave sediment samples (Fig. 8), but concentrations are generally low, averaging 1.84 %. The highest concentrations are found in the LORM sediments from the Dragon's Back Chamber (samples CS5, 9.44 %) and Postbox Chamber (sample CS8, 3.24 %). Only half of the cave sediments (CS4-7) record calcium phosphate and concentrations range from 0.01-1.88 %. Apatite and calcium phosphates were not recorded from any of the surface sediment samples.

Secondary, soil-forming minerals including Fe-Mn-oxyhydroxides are dominated by pyrolusite, todorokite, hematite, goethite and limonite in both the cave (average concentration of 3.48 %) and surface sediments (average concentration of 2.31 %; Fig. 8.), with highest concentrations occurring in UMCB sediments (CS2-3) in the Dinaledi Chamber, where pyrolusite is particularly common. Dirks et al. (2015) also described birnessite in the Dinaledi Chamber, but this phase was not recognised with MLA. Composite aggregates of Fe-Mn oxides and oxyhydroxides are common in all but sample CS6, making the exact identification of each phase difficult. Low concentrations of siderite were recorded and ranged from 0.01-0.85 %.

Mineral phase aggregates are present in all samples and were difficult to assess. In some samples they are abundant, e.g., in sample CS4 aggregates make up >15 % of the total sample. The aggregates are generally rounded and form small clusters, commonly forming around angular quartz grains (Fig. 9A). They are compositionally and texturally complex with individual mineral phases identified as single pixels, thereby challenging the resolution of the MLA technique and resulting in a mosaic of interwoven mineral phases (Fig. 9A), including μm-sized quartz, micas and clay fragments in a matrix of Mn-Fe-oxihydroxides (Fig. 9B-G).

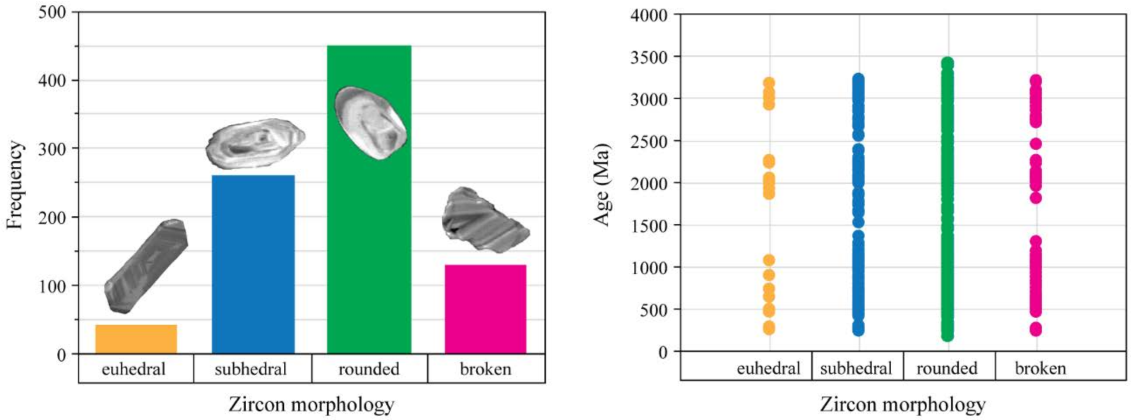

Figure 7. Rising Star detrital zircon grain morphology. Grain morphology derived from all 15 detrital zircon samples from the Rising Star Cave. Left graph shows the occurrence of the various zircon grain shapes, which is dominated by subhedral and rounded grain morphologies. The right graph correlates grain morphologies with age, showing no distinct trend in grain morphology with age. The euhedral zircon grains with ages around 3.0 Ga, 2.0 Ga, and 1.0-0.5 Ga are likely to be derived from local source terranes. Euhedral zircons with a 2.0 Ga are very likely derived from the local Bushveld Complex source terrain.

4.5. Discussion

Age dating and mapping in Rising Star Cave (e.g., Dirks et al., 2015, 2017) has made it clear that *Homo naledi* made its way into the Dinaledi Chamber at a time that mostly fine-grained sediments described by Wiersma et al. (2019) as LORM and UCMB were accumulating. These sediments could have been derived from four principle sources involving different processes including the nearby river during periods of flood; the overlying soils as a result of slope creep and sheet flows during rain events (e.g., Dirks et al., 2010); wind-blown dust during dry periods; or the cave itself as a result of dolomite dissolution. In this study we have attempted to establish the relative contribution of these four sources in the LORM and UMCB sediments, by analysing detrital zircon populations and the fine sand fraction in the sediments in combination with volume estimates for insoluble materials in dolomite. A full characterisation of the cave sediments across the entire grain size range in all chambers is outside the scope of this study and will be presented elsewhere.

When discussing the sediment budget in Rising Star Cave it is important that the boundary conditions of the cave as a depositional environment are understood (White and Culver, 2012). Unlike many well-known, (fossil bearing) cave systems in North America (e.g., Mammoth Cave, Kentucky; Norman Cave, West Virginia; Blue Spring Cave, Indiana), or SE Asia (e.g., Duoi U'Oi cave, Vietnam; Ford and Williams, 2007; Bacon et al., 2008; Palmer, 2012; White and Culver, 2012 and references therein), which contain subterranean streams that influence the sediment budget, the caves in the CoH are maze cave systems with limited lateral groundwater permeability, which lack all evidence of streams having been active in the transport of sediment through the cave. All sediments in these caves either percolated through fractures and joints in the roof of cave chambers, or they accumulated on subterranean debris cones (e.g., Martini, 2006; Pickering et al., 2007, 2010, Dirks et al., 2010; Bruxelles et al., 2014). The same holds true for the LORM and UCMB sediments that were targeted in this study.

4.5.1. The extent of allochthonous vs autochthonous sediment in Rising Star Cave

The distribution of the orange-red conglomerates, sands and muds along a subterranean debris cone with its entry point through a hole in the roof of the PostBox chamber, illustrates that the bulk of these sediments were derived from outside the cave. This includes the LORM and UCMB sediments that developed relatively late in the history of sedimentation along the debris cone (Dirks et al., 2017; Wiersma et al., 2020). Relative to other hominin-bearing caves in the CoH, Rising Star Cave holds much more fine-grained unconsolidated sediment. MLA results (Figs 8 and 9) confirm that the sediments along the access route into the cave increase in clay content when one traverses deeper into the cave. This increase in clay content is even visible in sand-sized particles in which clay is clumped together and bound by secondary interstitial Mn-Fe-oxyhydroxide species (Fig. 9; Dirks et al., 2015; Makubela et al., 2017; Wiersma et al. 2019), including todorokite, pyrolusite, goethite and birnessite. These secondary Mn-Fe minerals also increase in abundance deeper in the cave (Fig. 8), which probably reflects the high primary Mn content in the Malmani dolomites (e.g., Hawker and Thompson, 1988; Eriksson et al., 2006; Dowding and Fey, 2007). The increased clay content in sediments deeper inside the cave could be interpreted to indicate that external sediments introduced down the debris cone, mixed with mud derived from the dissolution of dolomite that may have existed as background deposits (e.g., Dirks et al., 2015). The dissolution experiment of dolomite has shown that this is highly unlikely.

The rocks of the lower Monte Christo Formation that host Rising Star Cave contain <7% intercalated chert, <1% schist, and an average of ~3% of non-soluble material (Fig. 3, Table 3) that includes no clay and almost no heavy minerals (and no zircons were detected in the studied samples). The insoluble component in the dolomite is almost entirely made up of angular, silt-sized quartz grains and grain clusters that formed from diagenetic/hydrothermal processes, mostly by infill of pore spaces in stromatolite-rich horizons. Therefore, the dolomite could have contributed no more than ~10% of the total cave volume to the sediment load in the cave, and this sediment would have consisted largely of angular quartz, with some fairly coarse-grained illite-muscovite from the few schist horizons with almost no detrital minerals and few zircons. This is not consistent with the composition and morphology of the LORM sediments described here (Fig. 8).

When considering the possible amount of autochthonous material in the LORM sediments, it is important to first account for the deposition and erosion of sediments that existed before. The LMCB sediments are the oldest deposits recognised in the cave and would have contained the largest proportion of autochthonous cave material, but they were largely removed before the roof opened in the Postbox Chamber and LOS sediments were introduced. In a similar manner, the LOS sediments that formed during an earlier stage of deposition on the debris cone, were largely removed from the chambers by erosional process internal to the cave (Dirks et al., 2017). These sediments too may have contained some autochthonous material, but that proportion would have been less than for LMCB sediments, and probably small in absolute terms. When the LORM sediments were deposited on the debris cone to cover erosion remnants of older LMCB and LOS sediments, little, if any, of the original autochthonous sediment would have remained in the chambers. Besides, the geometry of the cave at the time of deposition of the LORM sediments would have been similar to what it is today (Makhubela et al., 2019), with little additional dissolution of dolomite, and, therefore, limited additional input of autochthonous material. Thus, the overwhelming bulk of material in the LORM sediments must have been externally derived, allochthones material.

This inference is consistent with textural and compositional data for the LORM sediments. Firstly, all LORM samples contain abundant detrital zircon, which cannot have come from the surrounding dolomite. Secondly, the rounded to sub-angular shape morphology of detrital quartz grains in the LORM sediments indicate that these grains did not come from the dolomite or the interlayered chert horizons. Thirdly, MLA shows that the sand grain fraction in LORM sediments and external sediments is similar. The UMCB sediments, which formed from the reworking of LORM deposits (Wiersma et. al. 2019), must therefore also be almost entirely composed of allochthones material.

The higher clay content of LORM sediment detected by MLA in the semi-isolated Dinaledi Chamber, when compared to LORM sediment from the Dragon’s Back and Postbox chambers, cannot be explained by the progressive mixing with autochthonous clays that had collected over time deeper in the cave as suggested in Dirks et al. (2015). Instead the increase in clay in the Dinaledi Chamber was the result of progressive winnowing of coarser-grained material as sediment enters deeper parts of the cave (e.g., Wiersma et al., 2020). Sediment-laden flood waters may have spilled into the cave through the roof of the Postbox Chamber and flowed largely unimpeded via cave passages into the Dragon’s Back Chamber. But here these waters would have pooled, and they could only flow into the Dinaledi Chamber and beyond, through narrow fractures that filtered coarse sediment and stopped strong water flow. Thus, only suspension load could enter the Dinaledi Chamber resulting in the clay-rich nature of the LORM sediments there (Dirks et al., 2015; Wiersma et al., 2020). In addition, fine sand and clay would have seeped through roof fractures from the surface to deposit additional fine clastic material in all chambers (e.g., Dirks et al., 2015), and the relative effects of this would have been greater in the more distal Dinaledi Chamber. This study confirms that the dolomite of the lower Monte Christo Formation was a minimal contributor to clastic sediment and detrital zircon grains in the fine-grained LORM and UMCB sediments that surround the *H. naledi* fossils, and most of the clay seeped into the cave from the surface.

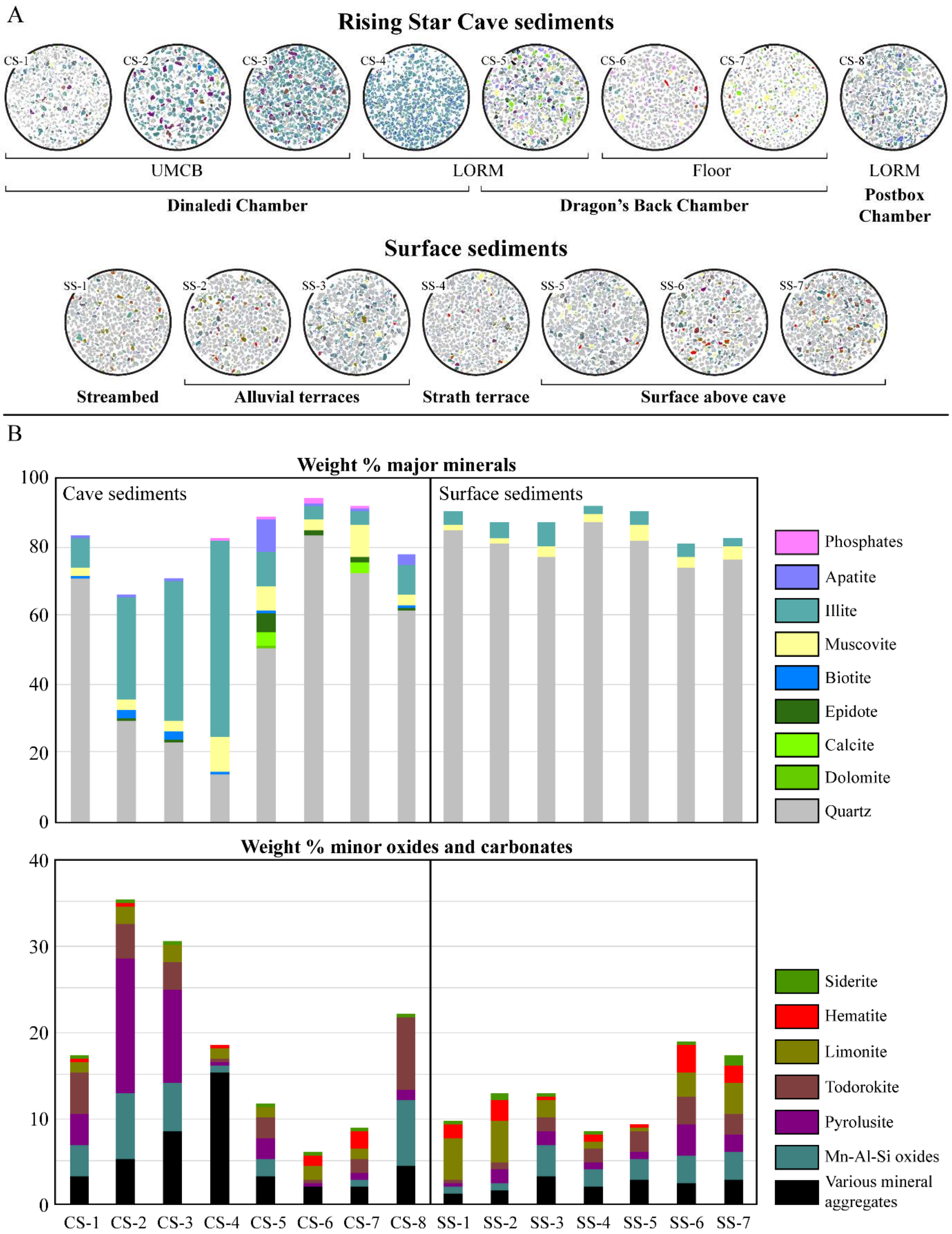

Figure 8. Mineralogy of Rising Star sediments. A) Modal mineralogy pucks of the Rising Star Cave and surface sediments showing the variety in mineralogical composition in each of the

samples. The different facies include the following: UMCB = unlithified mud clast breccia facies; LORM = laminated orange-red mud facies. B) Weighted percentage mineral distribution for the cave and surface sediments.

4.5.2. Detrital zircon geochronology and provenance of the cave sediments

The zircon populations found in all surface and cave sediment samples are near- identical, with variations only resulting from the fact that some sample sizes were too small to yield the full range of statistically valid populations (Fig. 6B). There are no noticeable differences in zircon populations from LORM samples collected in different cave chambers, and populations obtained in surface samples from soils and alluvial sediments are identical (Fig. 6B); i.e., we were not able to use detrital zircons to determine the relative contribution of soil vs alluvial sediment input into the cave. This result is disappointing, but it does not mean that the detrital zircon population does not provide other interesting insights.

All zircon samples contain concordant grains reflecting every major tectonic phase in the history of the Kaapvaal Craton and its surrounding mobile belts and cover sequences (Johnson et al., 2006a). This includes populations of Neoarchean and Paleoproterozoic-aged zircons of the Limpopo Belt (e.g., Kröner et al., 1999) to the northeast of the Transvaal Basin, and Neo- and Mesoproterozoic zircons of Namaqua-Natal, and Mozambique Belt age (Cornell et al., 2006) that must have come from areas that are currently not exposed anywhere near the Johannesburg Dome. The youngest zircon grains are Permian to Jurassic in age that must have been sourced from the Cape Fold Belt. Most likely, these grains were recycled from older Kalahari Group sediments and incorporated into Karoo-aged sediment deposits.. The wide range of detrital zircon ages cannot have originated from the rocks exposed within the catchment area of the Bloubank Spruit, which is largely underlain by dolomite of the Malmani Subgroup known to yield few zircons (Poujol et al., 2003; Eriksson et al., 2006), with only a small part of the catchment to the southwest underlain by the lower Pretoria Group (Fig. 2). Karoo aged rocks were not mapped in the catchment.

The homogenous nature of the detrital zircon population in all sediment types reflects a process of repeated reworking of sedimentary sequences that were deposited on top of the Kaapvaal Craton (Andersen et al., 2016). The last of these sedimentary sequences was the Permo-Triassic Karoo foreland basin, which at one stage covered all of the CoH (e.g., Johnson et al., 2006b; Partridge, 2010; Dirks and Berger, 2013). Erosion remnants of Karoo material have been described from near Malapa Cave, north of Rising Star Cave (Dirks and Berger, 2013), and continuous outcrops of Dwyka and Ecca formation shales and sandstones start only ~20 km south of the cave. Given that Karoo-aged zircon populations are well represented in all tested samples, it is likely that the source of the detrital zircons in the cave sediments links back to reworked zircon populations contained in Karoo sequences that were only recently removed from the CoH landscape. Heavy mineral sand accumulations with enrichment in ilmenite and zircon are known to exist in the central Ecca Formation of the lower Karoo Supergroup around Johannesburg (e.g., Behr, 1986), and these accumulations could have been partly reworked along the African Erosion Surface, and from there into the soils and sediments around Rising Star Cave.

The homogenisation of zircon populations in cover sediments on top of the Kaapvaal craton is known from other parts of South Africa as well (e.g., Andersen et al., 2016; Viglietti et al., 2017) and indicates that the process of reworking older sediments into younger basins is common, and that the soils that currently cover the CoH and the Bloubank River catchment are derived from reworked older sediments (e.g., Makhubela et al., 2017, 2019). This is consistent with the generally rounded shape of the majority of the detrital zircon grains found in the samples (Fig. 7). This also confirms observations made by Makhubela et al., (2017), who dated Mn-nodules from the Dinaledi Chamber and found that the nodules were ~2 Ga old, meaning that the Mn-nodules did not form inside the cave, but were derived, similar to the zircons, from reworked older sediment.

It is not just the zircon populations that exist in the sediments that are informative, but also the zircon populations that are not there. For instance, no Cretaceous to Cenozoic-aged zircon signatures were detected in any of the samples. This could place some constraints on the provenance regarding the sediment sources and modes of transport into the Upper Bloubank Spruit catchment. For example, Cretaceous-Cenozoic-aged zircon grains have been reported from Kalahari Group sediments (Gärtner et al., 2014), but their persistent absence in the studied cave and surface sediment samples suggest that these sediments did not reach the Rising Star Cave area and possibly the Cradle of Humankind. This might be affected by the drainage patterns of some of southern Africa's major rivers (e.g., Zambezi and Okavango), which drain sediments, including Kalahari Group sediments, in a southeastern direction, which was adopted sometime during Upper Cretaceous times (Gärtner et al., 2014). Although a long shot, this could be interpreted to mean that the contribution of distal aeolian detritus from the northern desert areas is insignificant in the sediments in the Upper Bloubank Spruit catchment area.

4.5.3. MLA as a tool to characterize sediment types

The MLA results from the cave and surface sediments reveal two main trends: 1) the basic mineralogy of the cave and surface sediments is similar, consisting mainly of quartz, muscovite, illite, and soil-forming minerals, albeit in varying concentrations; 2) the cave sediments are relatively enriched in clay-sized minerals and secondary Mn-oxyhydroxides (especially pyrolusite, MnO_2), while surface sediments are relatively enriched in Fe-oxyhydroxides (goethite, limonite and haematite). In addition, the mineralogy of the cave sediments is slightly more diverse compared to the surface sediments (Fig. 8), containing carbonates (dolomite, calcite) and organic minerals (apatite, phosphate – i.e., bone). Considering the fossil-rich nature of sediments in the Rising Star Cave, the amount of organic material recorded in the cave sediments is low, but fossil content was actively removed from UMCB sediments in the Dinaledi Chamber during excavations, skewing its actual concentrations. Of the cave sediments, the floor sediments in the Dragon's Back Chamber most closely resemble the surface material, which probably reflects their relatively young age, and direct link to sediment input from outside the cave in modern times.

Regarding the surface sediments, MLA results are similar, but they show increased concentrations in Fe-Mn-oxyhydroxides in samples above the cave that are furthest away from the river channel. The surface sediments above the Rising Star Cave consist of homogenized and vertically mixed authigenic soils that are old, with calculated average surface residency times of ~ 1.1 million years, occurring on the landscape in a relatively steady state (Makhubela et al., 2019). Their long residence time on surface and interaction with various biogenically (bacterially) facilitated soil-forming processes probably resulted in increased concentrations of secondary Fe-Mn-oxyhydroxides.

In the cave, concentrations of secondary Fe-oxyhydroxites are low, but Mn-oxide in the form of pyrolusite and various other complex Mn-hydroxide phases are common especially in the loosely packed (i.e. highly permeable) deposits of UMCB sediment in the Dinaledi Chamber. These sediments contain abundant mineral clusters bound in a matrix of secondary Mn-oxyhydroxides, illustrating that manganese deposition is more common deeper in the cave. We assumed that Mn is derived from dissolution of the Malmani Subgroup dolomites, which is strongly enriched in Mn (e.g., Hawker and Thompson, 1988; Eriksson et al., 2006; Dowding and Fey, 2007), and there are several places in the cave where crusts of Mn-oxyhydroxides are deposited below drip points. Thus, the increase in Mn and corresponding decrease in Fe deeper in the cave may be partly explained by the reduced input of Fe-oxyhydroxide particles from surface, and an increased interaction between ground water and the rock column above deeper chambers leading to higher concentrations of Mn in drip waters. The precipitation of the secondary Mn minerals was probably facilitated by microorganisms in the loosely packed and fossil-rich sediments as a result of microbial chemoautotrophic processes (Caumartin, 1963; Sarbu et al., 1996; Engel, 2007; Engel, 2012; Simon, 2012; Wiersma et al., 2020). Makhubela et al. (2017) assumed that this process, therefore, meant that secondary Mn-nodules in the Dinaledi Chamber would provide a minimum age for the cave sediments. However, they found that, at least for some of the well-formed Mn nodules, this did not apply, and these grains were old, and therefore detrital. Nevertheless, the MLA results and the grain textures strongly suggest that much of the Mn-oxyhydroxide deposition in the cave did indeed take place after deposition of the LORM and UMCB sediments.

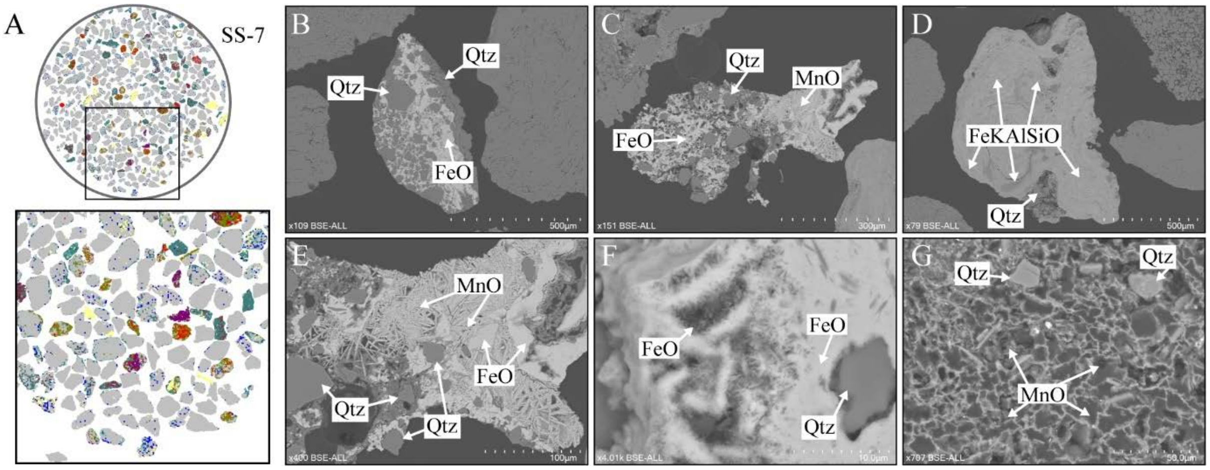

Figure 9. Mineral aggregates in Rising Star sediments. A) Modal mineralogy of surface sample SS7 and enlarged section below illustrating mineral aggregates on, and consisting of, individual grains. B) Individual grain in which angular quartz grains are encased by iron oxides; C) aggregate grain containing angular quartz grains surrounded by manganese and iron oxides; D) individual grain predominantly consisting of FeKAlSiO; E) close-up of C, showing detailed euhedral manganese oxide mineral structures; F) Euhedral and amorphous iron oxide mineral growth surrounding a single angular quartz grain; G) angular quartz grains in amorphous manganese oxide matrix.

The MLA results for the three UMCB samples from the Dinaledi Chamber (CS1-3) show a further interesting aspect about the cave fill in the Dinaledi Chamber around the time the *H.*

naledi remains were deposited. All three samples were taken from the original excavation pit from which the bulk of the *H. naledi* material described in Berger et al (2015) was collected. The fossils occurred down to a depth of ~15-20 cm (Dirks et al. 2015), and, therefore, sample CS1 occurred in association with the fossils and CS2 occurred at the lower boundary of the fossil-bearing horizon, whilst CS3 was collected from well below the *H. naledi* fossils. The compositions of CS2 and CS3 are very similar, whereas CS1 near the floor surface is significantly more quartz rich with less clay and pyrolusite. CS1 represents the sediment most closely associated with the *H. naledi* fossils, and its anomalous composition relative to the underlying UCMB sediments suggests that the top layer of UCMB material in the Dinaledi Chamber may have been disturbed and contaminated with additional quartz (as well as the fossil material), while being less permeable to Mn-bearing fluids. This is an interesting observation, although the exact meaning of it is not clear.

What the characterisation of sand-sized particles with MLA has not allowed us to do, is estimate to what degree the cave sediments were derived from either the alluvial sediments in the creek or from soil above the cave. MLA does not provide a definitive fingerprint for the mineralogy of the different sediment sources on surface, and similar to the detrital zircon geochronology, the use of MLA for provenance work in the CoH has limitations. Nevertheless, MLA-based modal mineralogy estimates are informative, and complement the U-Pb detrital zircon geochronology data in constraining the sediment budget in the cave, including the degree to which dissolved dolomite contributed to the sediment load through the precipitation of secondary Mn-rich mineral phases.

4.6. Conclusions

This study was conducted to determine the source of the fine-grained LORM and UCMB sediments that formed in the cave during the period of time when *H. Naledi* interacted with the cave. Detailed mapping of the distribution pattern of the sediments along a subterranean debris cone, in combination with studies of the amount of insoluble material in the dolomite host rocks, MLA analysis of sand-sized particles and detrital zircon geochronology in cave sediments and surface sediments demonstrate that only a small proportion (<1%) of the LORM and UCMB sediments are autochthonous (i.e., associated with dissolution and erosion of the Malmani Dolomite cave walls). The majority of the cave sediments are derived from soils and alluvial deposits outside the cave. The increase in clay content in the LORM sediments, deeper in the cave did not result from mixing of quartz-rich surface sediments with autochthonous clays, but instead reflect a gradual fining of the sediment load as it penetrates deeper into the cave. The dolomites contain no clays, and few detrital minerals including zircon, and they are not the main source of the clay rich sediments. The high Mn-content of the dolomites in combination with microbial activity is, however, probably responsible for the precipitation of secondary Mn-oxyhydroxides in permeable UMCB deposits in deeper parts of the cave.

The cave and surface sediments have identical detrital zircon populations that provide U-Pb age estimates for virtually every major tectonic event that affected the Kaapvaal Craton since the early Archaean. Most importantly, this includes Permian to Jurassic populations derived from the Cape Fold Belt that were recycled and ultimately became incorporated in Karoo sediments. The Karoo sediments probably provided the source for most zircons in the cave and on the surface surrounding Rising Star Cave. Although Karoo outcrops have not been mapped in the Bloubank Spruit catchment, remnants of Karoo have been mapped in the CoH, and the last remains of lower Karoo sediment cover was probably only removed in relatively recent times, since Plio-Pleistocene uplift of the African land surface. Reworking of older sediments into new basins has been a common process in the Kaapvaal Craton and has led to homogenised zircon populations across the land surface, thereby limiting the use of detrital zircon geochronology as a way of determining detailed provenance for the sediment deposits in caves of the CoH. The absence of Kalahari-aged detrital zircons may suggest that the input of aeolian sediment from desert areas to the northwest was limited, or removed by uplift prior to opening of the caves.

Virtually all of the sediments that were deposited with *H. Naledi* in Rising Star Cave, were externally derived from local sources that could include the nearby tributary river during periods of flood, and the soils above the cave through a process of soil creep and surface runoff. The contribution to the sediments from the host dolomite is restricted to some quartz and chert, secondary Mn-Fe-oxyhydroxide minerals, but no clays. The MLA and zircon geochronology techniques are useful in providing a broad characterisation of the sediment types in the cave and on the surface, but their use for detailed provenance studies to determine the exact source of the cave sediments is limited.

Chapter Five

Formation of mud clast breccias and the process of sedimentary autobrecciation in the hominin-bearing (*Homo naledi*) Rising Star Cave system, South Africa

Published in *Sedimentology*

Abstract

Unconsolidated mud clast breccia facies in the hominin-bearing (*Homo naledi*) Rising Star Cave, Cradle of Humankind, South Africa, are interpreted to have formed through a process termed sedimentary autobrecciation in this study. This process, by which most of the angular mud clast breccia deposits are thought to have formed autochthonously to para-autochthonously via a combination of erosion, desiccation, diagenesis and microbial alteration of laminated mud deposits, is thought to have taken place under relatively dry (i.e., non-flooded) conditions inside the cave. Subsequently, gravitational slumping and collapse was the dominant mechanism that produced the mud clast breccia deposits, which commonly accumulate into debris aprons. The mud clast breccia is typically associated with (micro)mammal fossils and is a common facies throughout the cave system, occurring in lithified and unlithified form. This facies has not been described from other cave localities in the Cradle of Humankind. Additionally, sedimentary autobrecciation took place during the deposition of some of the fossils within the Rising Star Cave, including the abundant *Homo naledi* skeletal remains found in the Dinaledi Subsystem. Reworking of the mud clasts breccia deposits occurs in some chambers as they slump towards floor drains, resulting in the repositioning of fossils embedded in the breccias as evidenced by cross cutting manganese staining lines on some *Homo naledi* fossil remains. The formation of the unlithified mud clast breccia deposits is a slow process, with first order formation rates estimated to be ~8 x 10-4 mm/year. The slow formation of the unlithified mud clast breccia facies sediments and lack of laminated mud facies within these deposits, indicates that conditions in the Dinaledi chamber were probably stable and dry for at least the

last ~ 300 ka, meaning that this study excludes *Homo naledi* being actively transported by fluvial mechanisms during the time their remains entered the cave.

5.1. Introduction

Cave systems are openings in the subsurface that act as natural traps with the potential to accumulate large quantities of allochthonous and autochthonous sediment, as well as organic, and chemical debris (Ford and Williams, 2007; Springer, 2012). Historically, chemical cave sediments (speleothems) have been investigated widely, because they record robust palaeoclimatic signatures, but the clastic component of cave sediments has not had the same level of scrutiny. However, scientific attention to clastic cave sediments has increased recently (e.g. Springer and Kite, 1997; Bosch and White, 2007; White, 2007; Farrant and Smart, 2011; Martini, 2011). Allochthonous clastic sediments enter passages and chambers via several transport mechanisms, e.g., rivers, storm waters, fluctuating groundwater tables, ice, gravity, wind, earthquakes and biological activity (Ford and Williams, 2007; Springer, 2012). The sediments that end up as cave deposits are diverse and vary greatly in composition and grain-size; clasts can range between metre-sized boulders, cobbles and gravel, to sand, silt and clay-sized particles. The distribution and dispersal of sediments in caves ultimately depends on the geometry (morphology, length) and location of the cave system, transport medium (e.g., gravity-driven, water, wind), and sediment source, type and quantity. The resulting deposits often comingle with pre-existing deposits, producing highly complex sedimentary and stratigraphic architectures ranging from diamictons and coarse-grained colluvium to sand, silt and clay deposits, produced by mass-wasting, slumping, flooding and aeolian activity (e.g. Bosch and White, 2007; Springer, 2012; O'Connor et al., 2017).

Five cave lithofacies classes were identified and defined by Bosch and White (2007) and White (2007) based on stream power transport mechanisms, sorting, and particle size of clastic components, grouping clastic cave deposits within specific lithofacies (fig. 3 in Bosch and White, 2007). One of those facies is the slackwater facies (Gillieson, 1996), defined as clay and silt transported as suspended load that disperse throughout cave localities where hydraulic energies are reduced or cease and ponding of water occurs (Bosch and White 2007; White, 2007). In these quiescent areas, suspended clay and silt settle out and accumulate as very fine-grained laminated strata (Bosch and White, 2007; White 2007), commonly forming the capping succession to previously deposited, coarser grained clastic sediments in the cave (referred to as channel facies in Bosch and White, 2007; White, 2007). Although slackwater facies occur in many cave types, they are more common in maze and network caves (Bosch and White, 2007), which contain closed chambers, fractures and blind passages that lack full conduit throughflow, allowing suspended sediment to settle and accumulate over time.

Slackwater facies, in particular their clay content, form an important component in the clastic deposits in caves worldwide (e.g. Butzer, 1981; Valen et al., 1996; Pickering, 2006; Wadley and Jacobs, 2006; Knapp et al., 2007; Bacon et al., 2008), because they have the potential to preserve strong palaeoclimatic and palaeomagnetic signatures, revealing climate, provenance and weathering conditions during and after the deposition of silts and clays (e.g. Ellwood et al., 1996; Ellwood et al., 2004; Pickering et al., 2007; Kadlec et al., 2008; Sasowski, 2012). However, reworking and diagenesis of these muddy deposits have received far less attention and few studies describe these processes in detail (e.g. Bull, 1981; Albrecht and Benson, 2001). In the Cradle of Humankind (CoH), South Africa, clay-rich cave sediments have been observed in only but a few hominin-bearing caves, i.e., Coopers and Gladysvale (Pickering et al., 2007), Sterkfontein Caves (Tobias et al., 1993; Martini et al., 2003; Clarke, 2007; Pickering and Kramers, 2010; Bruxelles et al., 2014), but have been investigated primarily from a lithostratigraphic point of view and sediment reworking processes, which could lead to the formation of mud clast breccia deposits in these caves, are rarely discussed.

Fine-grained, laminated mud and mud clast breccia deposits have also been described from the Rising Star Cave in the CoH, South Africa (Fig. 1), specifically within the Dinaledi Subsystem (Dirks et al., 2015, 2017; Berger et al., 2018), where the unlithified mud clast breccia deposits host the holotype and paratype fossils of the new hominin species *Homo naledi* (Berger et al., 2015) as part of the largest assemblage of fossil hominin remains from a single location in Africa (Berger et al., 2015; Kivell et al., 2015; Val, 2016; Berger et al., 2017; Hawks et al., 2017; Egeland et al., 2018). The fine-grained laminated sediments are widely distributed throughout the Rising Star Cave (Figs 2 and 3) and are architecturally similar to the slackwater facies (Bosch and White, 2007). The abundant unlithified mud clast breccia deposits are widely distributed inside the cave, primarily as cave floor deposits. The formation of these mud clast breccia deposits, and by association, preservation of the dense accumulation of fossils, appear intimately related, but the processes resulting in such deposits remain poorly understood. This study describes the laminated mud and unconsolidated mud clast breccia deposits in Rising Star Cave and attempts to provide an explanation for the processes by which the clay-rich laminated (slackwater) sediments and the formation of ubiquitous mud clasts and subsequent mud clast breccia deposits could have formed.

Understanding the process of mud clast breccia formation in the Rising Star Cave is of palaeoanthropological and taphonomical relevance, because these deposits partially envelop the *Homo naledi* fossils, and were probably forming during the time *H. naledi* remains entered the cave.

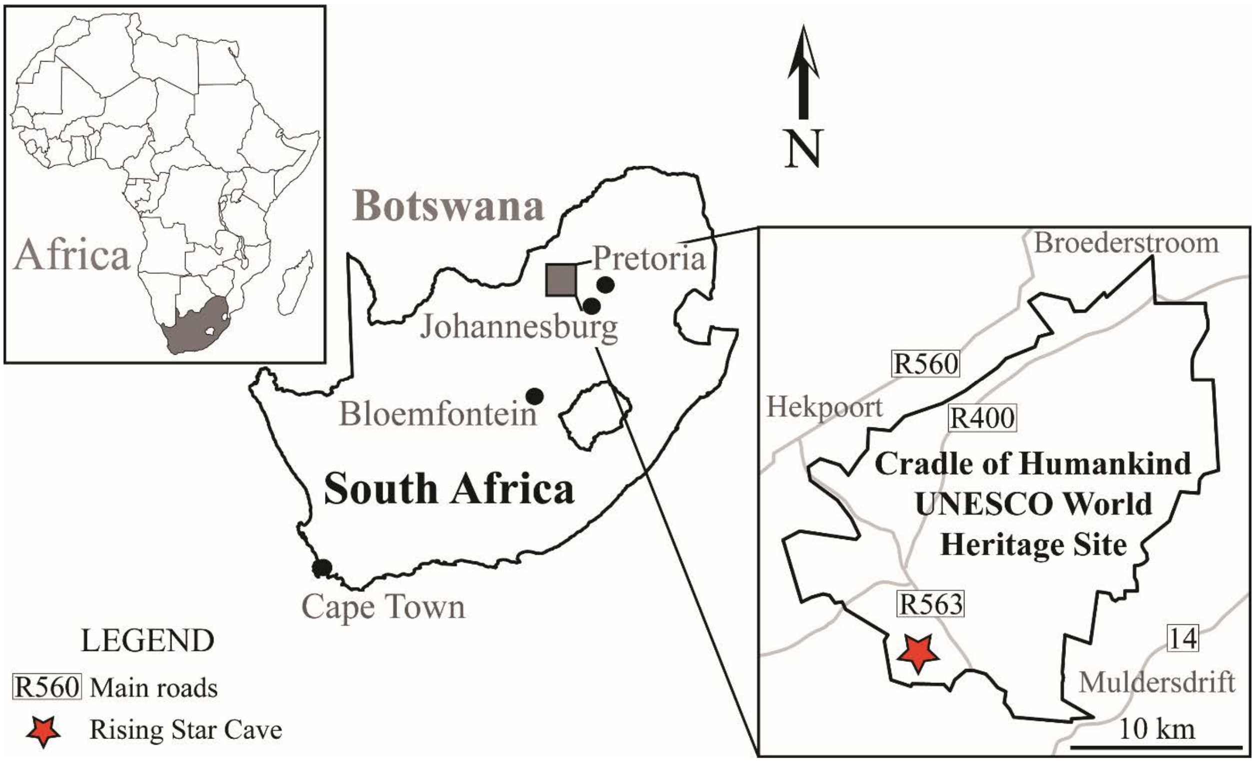

Figure 1. Location of the Rising Star Cave, indicated by the red star in the insert, in the Cradle of Humankind, South Africa.

5.2. Rising Star Cave Setting

5.2.1. Geology and geomorphology

The Rising Star Cave is positioned ~1450 to 1480 m above sea-level in the Bloubank River valley (26° 01' 11.96" S, 27° 42' 45.97" E), in the CoH UNESCO World Heritage Site in South Africa, and is located approximately 2 km west of Sterkfontein Caves and 35 km northwest of Johannesburg (Fig. 1). The cave is situated close to the valley floor in the Plio-Pleistocene landscape of the CoH. Directly east-southeast of the cave entrance, several abandoned river terraces are preserved, possibly linked to earlier stages in the stream pattern of the Bloubank Spruit.

Caves in the CoH, including the Rising Star Cave, formed in late Archaean-aged (~2.5 Ga) stromatolitic dolomite platform sequences that make up the Malmani Subgroup (Eriksson and Altermann, 1998; Eriksson et al., 2006). The Rising Star Cave is a network maze cave system consisting of a series of interconnected chambers and passages that formed in a 20 to 30-m-thick chert-poor section of stromatolite-rich, dolomite strata of the lower Monte Christo Formation (Dirks et al., 2015). The cave system is stratigraphically bound by two mylonitic shear zones and the roof of the Rising Star Cave is capped by a ~1-m-thick intact chert horizon (Fig. 2), which acts as a physical barrier that prevents immediate connections to the surface across this boundary (Dirks et al., 2015; Kruger et al., 2016). The strata dip ~17 degrees to the west and define the preferred pathway for water movement, cave genesis and cave progression. Although the cave geometry is mostly structurally controlled and follows various joint and fracture patterns within the lower Monte Christo Formation, chemical dissolution along open conduits resulted in a series of dissolution chambers and roof collapse features (Dirks et al., 2015).

5.2.2. Cave sediments

The surrounding landscape is largely underlain by Pretoria Group and Malmani Subgroup strata, together with patchy remnants of younger, Karoo-aged (~250 Ma) sediments (Dirks and Berger, 2013). A broad range of allochthonous and autochthonous clastic and chemical sedimentary deposits are preserved throughout the Rising Star Cave. The cave chambers that host these sediments include the Dinaledi Subsystem, Dragon's Back Chamber, Superman Crawl and the chambers that lead to Postbox and Superman Crawl. The latter two chambers have not been formally named, but for the sake of simplicity, they will be referred to as Postbox Chamber and Superman Chamber, respectively (see Fig. 2). The sediments preserved in the cave consist broadly of fossiliferous cross-bedded sands, fine-grained laminated orange-red muds, mud clast breccias, and speleothems (Dirks et al., 2015). The mud clast breccias occur in lithified and unlithified forms that are compositionally similar. The former occur throughout the cave as hanging erosion remnants underneath flowstone sheets and various cave chamber ceilings (Dragon's Back Chamber, Superman Crawl and Superman Chamber), whereas the latter occur on the cave floor of the Dinaledi Subsystem, i.e., the Dinaledi Chamber and Hill Antechamber, Postbox Chamber and Superman Chamber (Fig. 3A to D). The different facies and varying degrees of lithification point

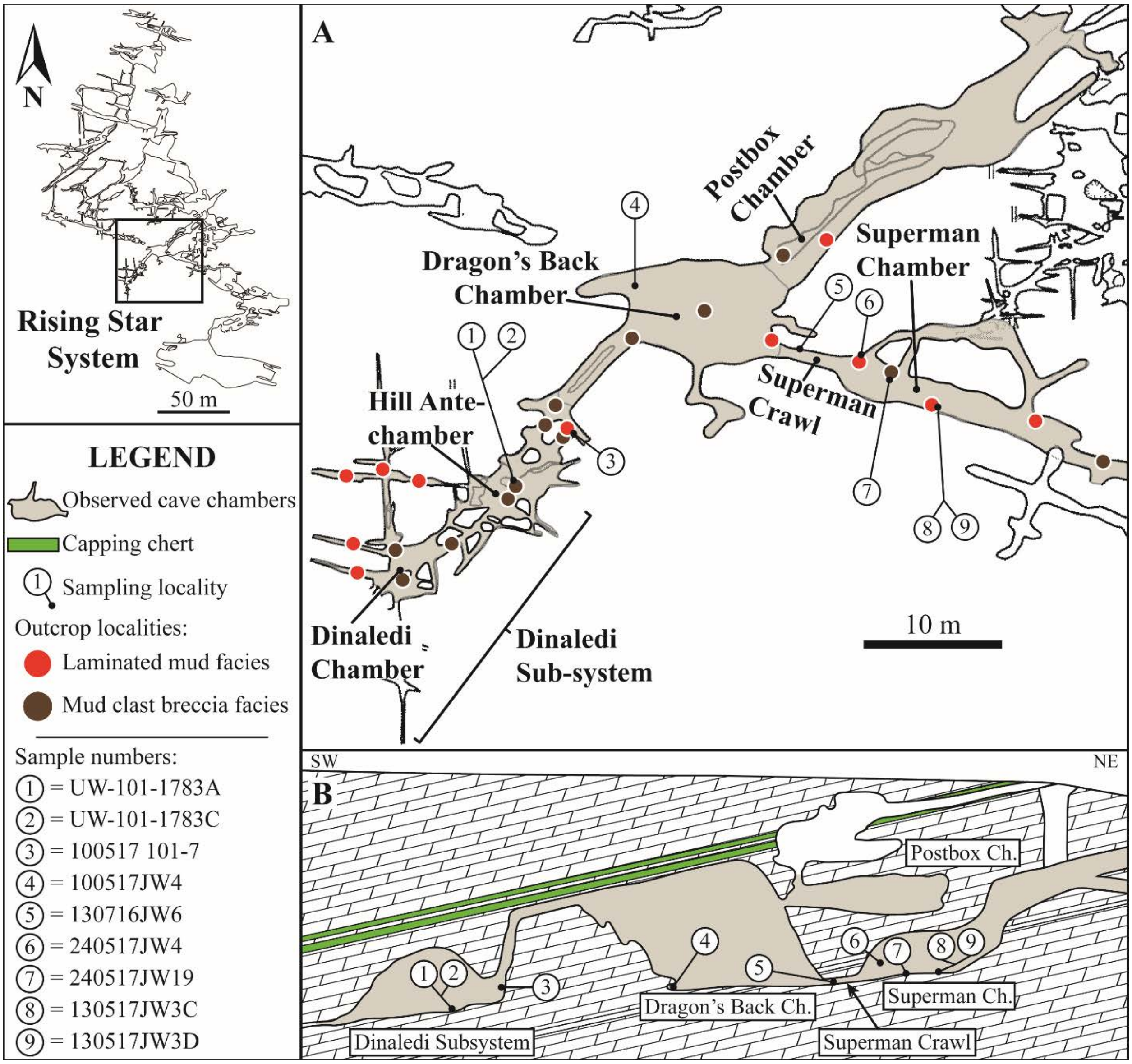

Figure 2. Distribution of laminated orange-red mud facies and mud clast breccia facies throughout the Rising Star cave system. (A) Map view of the different facies and sample localities, and (B) cross section view of the Rising Star Cave showing sample localities. Cross section not to scale. Ch. = chamber.

towards recurring cycles of deposition, erosion, re-mobilization in suspension and diagenesis, resulting in the preservation of distinct facies architectures and compositions throughout the cave system. Proximal chambers, i.e., Dragon's Back Chamber, Postbox Chamber and Superman Chamber generally contain a larger quantity of coarser sand facies compared to the more distal chambers in the Dinaledi Subsystem (Dirks et al., 2015, 2017). The laminated orange-red mud and mud clast breccia facies are widespread throughout the cave system (Fig. 2). These unlithified, fine-grained sediments consist primarily of clay-rich muds and are preserved in a suite of settings within the Dinaledi Subsystem (units 1 and 3 in Dirks et al., 2017), Dragon's Back Chamber, Postbox Chamber and Superman Chamber.

5.3. Methodology

5.3.1. Field methods

The stratigraphic distribution of clay-rich deposits and mud clast breccias throughout the Rising Star Cave was determined through cave mapping, detailed lithostratigraphic description and facies correlations where possible. This study describes the laminated orange-red mud facies and sampled unlithified mud clasts and lithified mud clast breccia sediments from the Postbox, Superman, Dragon’s Back and the Dinaledi chambers (Fig. 2). Samples of different facies in the Dinaledi, Dragon’s Back and Superman chambers were photographed to document macroscopic properties with a mounted Canon Eos 750D digital SLR camera with 24-megapixel resolution, using an 18-135 mm lens (Canon, Tokyo, Japan). The properties that have been described include clast morphology and size variability, laminations, desiccation cracks, iron (Fe) and manganese (Mn) oxide and oxyhydroxide staining, and the presence of secondary growth of calcite and aragonite minerals in clay clast fractures. To test for the presence of aragonite in the cave, Feigl's solution (Feigl, 1937), a mixture of Ag, $MnSO_4$ and distilled water, was directly applied to carbonates. When applied to aragonite, the carbonate turns black in <30 minutes, whereas in calcite the reaction takes at least 10 times longer.

5.3.2. Petrographic methods

Petrographic analysis of clay samples was conducted through scanning electron microscopy (SEM) imaging, focusing on textural, fabric, configuration and mechanical growth properties. Five clay clast samples (Table 1) for SEM imaging were manually prepared. Approximately 5.0 gram of each sample was suspended in a 100 ml sized vial containing 80 ml distilled water with 10 % strength sodium hexametaphosphate (Calgon) to prevent flocculation. Samples were shaken for 30 seconds and allowed a settling time of 5 minutes before extracting the remaining suspended particles with a syringe. The extracted liquid was transferred into a glass funnel lined with clingwrap and left at room temperature for 24 hours, allowing the suspended particles to settle. After the 24-hour settling period, the samples were oven-dried for 96 hours at 40°C, to remove excess moisture. The resulting clay samples were crushed into <0.5 mm size fractions and mounted on a 12 mm SEM specimen pin stub with double-sided tape. An ultra-thin platinum coating was applied to the sample to create a constant conductive layer during SEM analysis as well as enhancing the topographic examination. SEM analysis was carried out in the Advanced Analytical Centre at James Cook University, Australia, using a Hitachi SU5000 field emission gun scanning electron microscope (FEG-SEM) equipped with a secondary electron and backscatter electron detector, using 4.0 kV accelerator voltage (Hitachi, Tokyo, Japan).

5.3.3. Geochemical methods

Four mud samples from the Dinaledi Subsystem and the Superman Chamber (Fig. 2) were analyzed for bulk mineralogy and geochemistry (Table 2); two mud clast samples (130517JW3C, 130517JW3D) from laminated orange-red mud facies, and two samples (240517JW19, UW101-1783A) from the mud clast breccia facies. Prior to the analysis, mud clasts were broken into mm-sized fractions and oven dried at 40°C for 48 hours to remove excess moisture. All geochemical analyses [X-ray diffraction (XRD) and X-ray fluorescence (XRF)] were carried out in the Advanced Analytical Centre at James Cook University in Australia. X-ray diffraction was carried out using approximately 1.0 to 2.0 gram of sample packed into a mount that was analyzed in a Bruker D2 Phaser with an SSD-160 detector (Bruker, Billerica, MA, USA) using preferred orientations only, omitting the glycolated and thermally heated methods. X-ray fluorescence was carried out in a Bruker S2 PUMA EDXRF spectrometer, equipped with a SSD HighSense LE detector and 50W X-ray tube (Bruker, Billerica, MA, USA). Glass beads composed of 1.0 gram of sample mixed with 8.0 gram of flux (catch weight) were fused into glass discs, using 12-22 flux prior to the analysis. All geochemical results are summarized in Table 2.

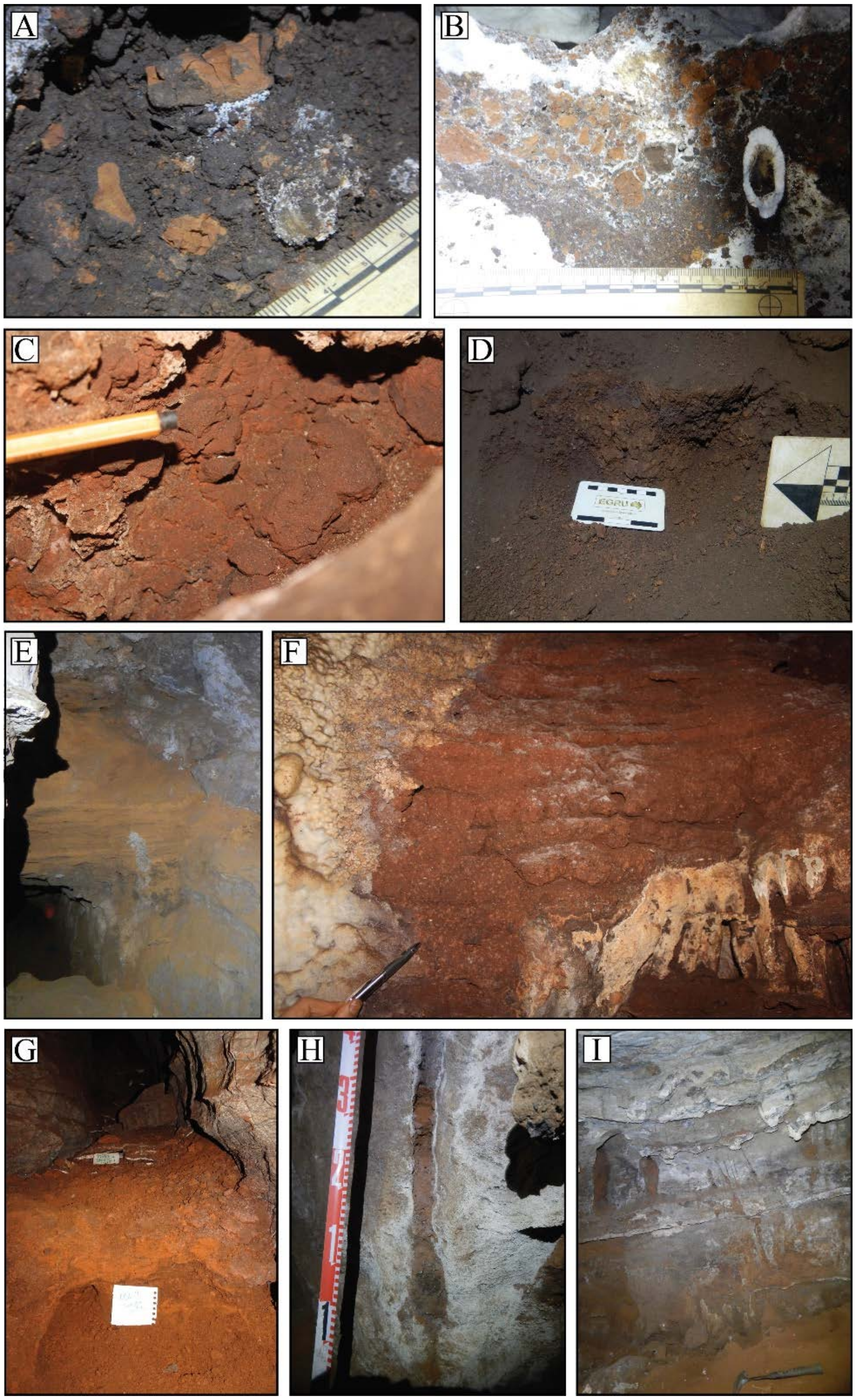

Figure 3. Overview of laminated orange-red mud (LORM) facies and unlithified mud clast breccia (UMCB) facies in the Rising Star Cave. UMCB facies: (A) in the *Homo naledi*-bearing sub-unit 3b (Dirks et al., 2017) along the floor of the Dinaledi Chamber. (B) Occurrence of UMCB between two separate flowstone deposits in the Dinaledi Chamber. In this case, the mud clast breccia has been cemented together by calcite cement, enveloping individual clasts. (C) Close-up of autobrecciation process forming angular mud clasts. Note the highly oxidized and dark grey

manganese staining on the surface of the mud clasts (D) Active autobrecciation of LORM facies on the cave floor of the Superman Chamber. Note the talus slope and downward sloping apron of angular mud clasts. LORM facies: (E) above the Superman Crawl in the Dragon's Back Chamber; (F) as cave floor sediments (sub-unit 1a in Dirks et al., 2017) in the Dinaledi Chamber; (G) as undulated sediments along flowstone ledge in the Dragon's Back Chamber; (H) in vertical fractures in the Superman Chamber; (I) in vertical fractures and floor sediments in the Superman Chamber.

5.3.4. Grain size analysis

Grain-size analyses were performed on two laminated orange-red mud (100517 101-7, 240517JW4) and two unlithified mud clast breccia samples (UW101-1783A, 240517JW19) from the Dinaledi Chamber and the Superman Chamber (Fig. 2; Table 1). ASTM D421 (2007) and D422 (2007) standardized methods were followed for the analysis. The initial dry weight for each sample was 200 grams. Size fractions ≥500 μm were dry-sieved, (4,000-2,800-2,000-1,000-500 μm sieves), whereas the <500 μm size fractions were carried out applying the hydrometer method with a calibrated H-152 model hydrometer.

Table 1. Overview of the laminated mud and mud clast samples that were collected from various localities within the Rising Star Cave. The samples were subjected to bulk geochemical (XRD/XRF), scanning electron microscopy (SEM), and grain size analyses (GSA).

Sample	Cave Locality	Analyses		
UW-101-1783C	Dinaledi Chamber	SEM		
130716JW6	Superman Crawl	SEM		
100517JW4	Dragon's Back Chamber	SEM		
130517JW3C	Superman Chamber	SEM	XRD/XRF	
130517JW3D	Superman Chamber		XRD/XRF	
240517JW19	Superman Chamber	SEM	XRD/XRF	GSA
240517JW4	Superman Chamber			GSA
UW-101-1783A	Dinaledi Chamber		XRD/XRF	GSA
100517 101-7	Dinaledi Chamber			GSA

5.4. Results

Descriptions are provided below for two mud facies preserved within the Rising Star Cave; the laminated orange-red mud and the unlithified mud clast breccia deposits, referred to hereafter as the LORM and UMCB facies, respectively. The lithological descriptions provide a framework for understanding the processes that might lead to the formation of the UMCB facies in the cave, particularly in the Dinaledi Chamber, where it is most abundant. Facies descriptions occur in sequential order, i.e., starting with the LORM host sediments. Although this paper focuses on the UMCB deposits, occasionally reference is made to older, lithified mud clast breccias to discuss diagenetic features not observed in UMCB.

Table 2. Major element weight percentages obtained from XRF analysis on mud clast and mud clast breccia samples from the Rising Star Cave. LOI = Loss on ignition at 1000^{o}C.

Major elements	Sample numbers LORM		Sample numbers UMCB		Detection limit (%)	
weight percent	130517JW3C	130517JW3D	240517JW19	UW101-1783A	upper	lower
SiO_2	63.05	71.4	64.61	50.91	78	35
TiO_2	0.87	0.58	0.9	0.76	3.80	0.04
Al_2O_3	16.17	10.26	15.69	13.42	45	7
Fe_2O_3	5.72	6.59	6.93	13.47	26	0.5
MnO	0.39	0.33	0.9	4.82	0.4	0.02
MgO	1.43	1.46	1.46	1.64	14	0.1
CaO	1.58	0.57	0.26	0.99	16	0.1
Na_2O	0.33	0.49	0.39	0	4.5	0.01
K2O	1.74	0.98	1.48	1.47	9	0.1
P_2O_5	0.1	0.1	0.1	0.21	1	0.02
SO_3	0.1	0.04	0.04	0.04	0.15	0.02
SrO	0.01	0	0	0.01	0.17	0.01
LOI	9.55	7.67	8.63	10.98		
Total	101	100.4	101.4	99.06		

5.4.1. Distribution of the LORM facies in the Rising Star Cave

The LORM facies is widely recognized throughout the Rising Star Cave and is recorded from the Dinaledi Subsystem, Dragon's Back, Postbox and Superman chambers (Fig. 2). It was first described in the Dinaledi Chamber as units 1a and 2 by Dirks et al. (2015). It was observed that two types of deposits of LORM facies sediment are currently present inside the cave, namely: (i) deposits preserved as erosion remnants on the cave floor and walls, in dolomite fractures, alcoves, and on top of flowstone and chert ledges (Fig. 3); and (ii) accumulation of water-saturated muds in dolomite fractures and on flowstone and chert ledges that are actively forming. The latter is a localized process, but it has been observed throughout the cave system.

Bulk XRD and XRF data reveal that the LORM facies consists primarily of SiO_2 (63.05 to 71.4 wt %), Al_2O_3 (10.26 to 16.17 wt %), Fe_2O_3 (5.72 to 6.59 wt %), and minor amounts of K_2O (0.98 to 1.74 wt %), MgO (1.43 to 1.46 wt %), MnO (0.33 to 0.39 wt %), and CaO (0.57 to 1.58 wt %) (Fig. 4A and B and Table 2). Most abundant minerals include quartz (SiO_2) (36.7 to 54.5

%), kaolinite $(Al_2SiO_5)(OH)_4$ (17.99 to 26.75 %), muscovite $KAl_3(Si_3)(O_{10})(OH)_2$ (8.26 to 14.68 %), and hematite (Fe_2O_3) (5.72 to 6.59 %). Minor amounts of pyrolusite (MnO_2) (0.4 to 0.48 %) and dolomite ($MgCa(CO_3)_2$) (1.29 to 1.79 %) were also identified (Table 2). Calculated mineral concentrations are summarized in Table 3. SEM imaging confirms the presence of kaolinite and muscovite (possibly illite) within the LORM facies (Fig. 5A to C), with kaolinite forming the dominant clay fraction. Kaolinite mineral textures display clear booklets of hexagonal and pseudo-hexagonal symmetries on the micrometre and nanometre scale (Fig. 5B and D). Both types of LORM facies deposits share a similar lithological composition, but their distribution patterns vary. The sedimentary characteristics of both types of LORM facies deposits are described and discussed in detail in the following sections below.

Table 3. Calculated minimum percentage of minerals present in mud clast samples from the Rising Star Cave.

	LORM sample numbers		UMCB sample numbers	
Identified minerals	130517JW3C	130517JW3D	240517JW19	UW101-1783A
Kaolinite ($Al_2Si_2O_5(OH)_4$)	26.75	17.99	27.61	21.87
Muscovite ($KAl_3Si_3O_{10}(OH,F)_2$)	14.68	8.26	12.54	12.44
Quartz (SiO_2)	36.7	54.5	38.72	35.09
Hematite (Fe_2O_3)	5.72	6.59	6.93	13.47
Pyrolusite (MnO_2)	0.48	0.4	1.1	5.91
Dolomite ($CaMg(CO_3)_2$)	1.79	1.29	0.85	0
Other minerals and LOI	13.88	10.97	12.25	10.28

5.4.2. Description of the LORM facies in erosion remnants

The majority of LORM facies sediment deposits within the Rising Star Cave occur as erosion remnants that are preserved in a suite of locations throughout the cave (Fig. 3E to I). These eroded remnants create topographies that locally display desiccation features along exposed margins (Fig. 6A to E). Erosion remnants of LORM facies sediments that protrude from the surrounding cave floor layers are particularly preserved in the proximity of floor drains as observed in the Dinaledi and Dragon's Back chambers (Dirks et al., 2015). The exact thickness of accumulations of this facies throughout the cave is uncertain but remains are at least 0.5 m thick in places within the Dinaledi Subsystem, Superman Chamber and the Postbox Chamber (Dirks et al., 2017). Throughout the Rising Star Cave, erosion remnants of LORM facies sediments share a similar general stratigraphic and sedimentary architecture.

LORM sediments typically form successive series of 5 to 15 cm thick beds of horizontally laminated mud that are rich in clay (42 to 48 %) and silt (30 to 40 %) and mixed with fine-grained to very fine-grained quartz sand (~6 to 13 %) (Figs 7A and 8). Well-developed fine laminations are readily preserved in most of the LORM facies (Fig. 3E to G). Locally, 0.5 to 5 cm thick interstitial lenses of fine to medium-grained, ripple-laminated and cross-bedded sands are interbedded with the LORM facies (Fig. 3G). These sandy lenses are largely composed of quartz with minor fractions of fine-to-coarse-grained iron and manganese nodules, subangular chert and dolomite grains. These lenses can be fossil-rich, consisting of randomly oriented small rodent skulls, mandibles, isolated teeth, long bones and pelvic elements. Additionally, LORM facies sediments form as ~2 cm thick, fossil-poor, capping beds, situated concordantly above 10 to 15 cm thick co-sets of normally graded, fine to coarse-grained, current ripple-laminated sands rich in micromammal fossils (Fig. 3G).

Aside from the locally fossiliferous sandy lenses, the fossil content in LORM facies sediments is generally low and consists of non-oriented micromammal teeth, ribs and long bones, lacking signs of current direction. The remnants of LORM facies sediments occurring on the cave floor in the Dinaledi Chamber are locally bioturbated, evidenced by vertical 2 to 5 mm wide insect burrows that are infilled by fine-grained sand and silt (Fig. 4B in Dirks et al., 2015).

Internally deformed laminated beds in LORM facies sediment deposits are observed on more elevated repositories, commonly involving ledges with irregular surface topographies, as seen in the Dragon's Back Chamber. Here, laminated beds undulate and follow the underlying substrate topography and the sediment slumps towards the margins of the ledges (Figs 3G and 6E), away from the cave wall. Desiccation fractures commonly develop along the horizontal surfaces and outcrop margins of these slumped zones, particularly where LORM sediments exceed 5 cm in thickness (Fig. 3D). Here, wedge-like segments of LORM tend to slump-off onto debris cones. Well-exposed erosion surfaces are commonly weathered and stained with dark brown-to-black Fe and Mn oxides and oxyhydroxides.

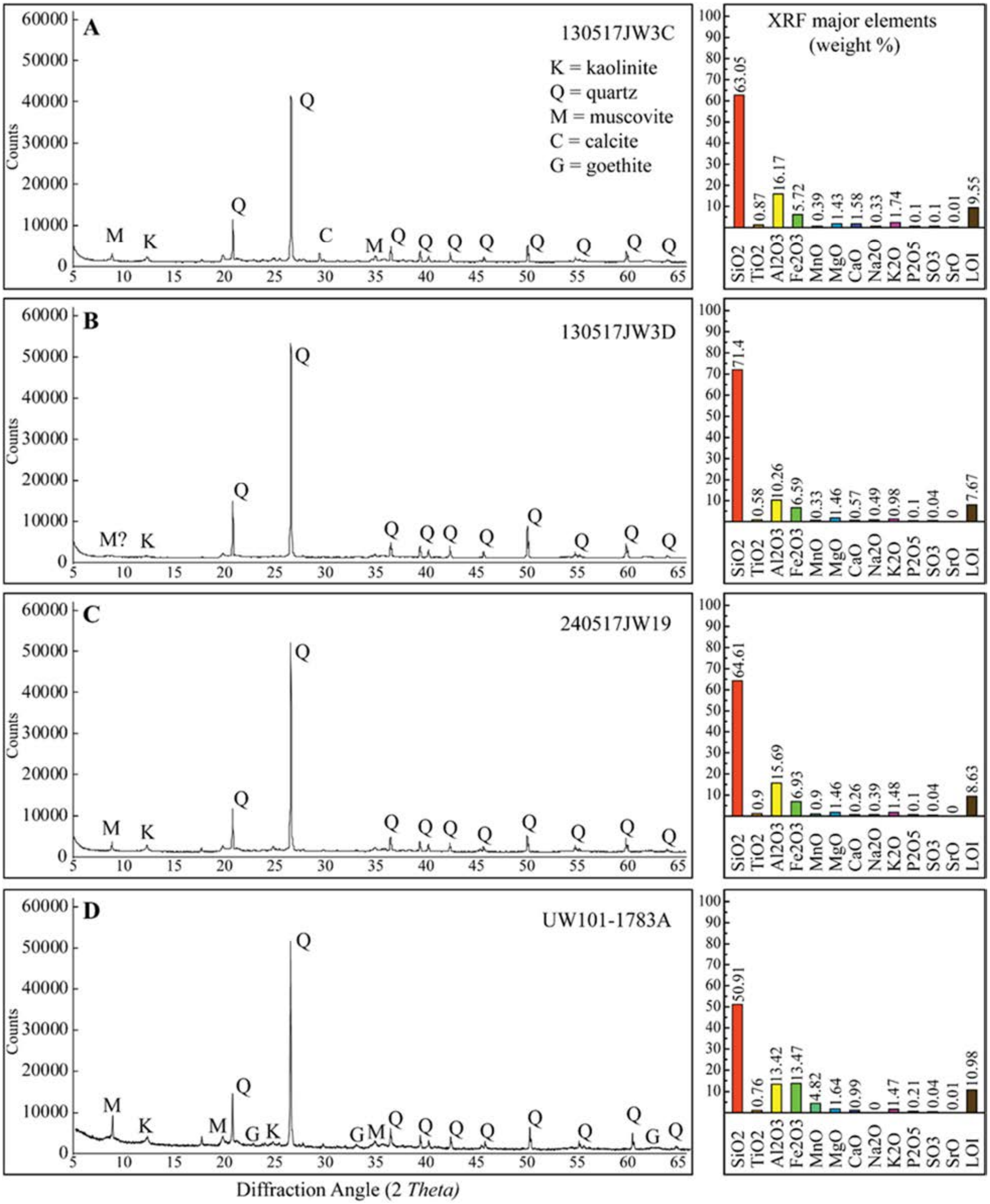

Figure 4. XRD and XRF results for LORM samples (A) 130517JW3C; (B) 130517JW3D and UMCB samples (C) 240517JW19; (D) UW101-1783A.

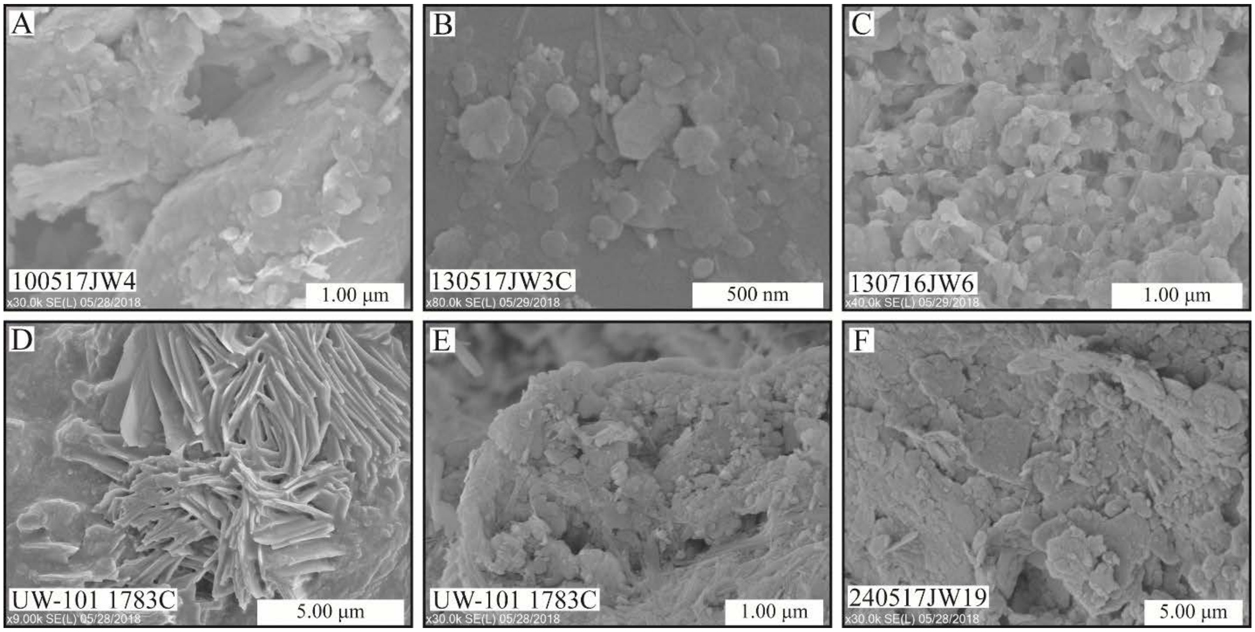

Figure 5. SEM images of various clay samples and associated facies from the Rising Star Cave. LORM facies. (A) Kaolinite clay platelets situated on much larger muscovite clay booklets from the Dragon’s Back Chamber. (B) Mixture of kaolinite and muscovite clay platelets from the Dragon’s Back Chamber. (C) Kaolinite clay platelets from the Dragon’s Back Chamber. UMCB facies. (D) Kaolinite clay booklets in a clay sample taken at 25to 30 cm depth from the *Homo naledi*-bearing mud clast breccia floor deposits in the Dinaledi Chamber. (E) Kaolinite clay platelets in a clay sample taken at 25 to 30 cm depth from the *Homo naledi*-bearing mud clast breccia floor deposits in the Dinaledi Chamber. (F) Stacked muscovite booklets with minor quantities of kaolinite platelets from the Superman Chamber.

5.4.3. Interpretation of the LORM facies as erosion remnants

The formation of the LORM facies in the Rising Star Cave resulted from two modes of deposition; suspension settling (= slackwater facies, *sensu* Bosch and White, 2007) and deposition via vadose drip water. Both LORM facies are compositionally and architecturally similar to sub-unit 1a (Dirks et al., 2017), described from the Dinaledi Subsystem but interpreted as slackwater facies only (Dirks et al., 2015). Based on the fine-grained lithology in combination with the finely laminated architectures preserved within the LORM erosion remnants, the current study interprets these sediments as representing formerly extensive deposits that filled the cave chambers and side passages, and formed via suspension settling in post-flooding, quiescent or ponded waters. Subsequent lowering of the water table in the cave and post-depositional erosion removed the bulk of the LORM sediments via floor drains (e.g., in the Dragon's Back Chamber, Dinaledi Chamber, and potentially Superman Chamber) that connect to deeper chambers in the cave (Dirks et al., 2015), leaving widespread erosion remnants behind that have been preserved in many locations throughout the cave chambers. The exposed erosion remnants are subject to desiccation, slumping, and collapse after the water table fell and the cave started to dry up. Undulating internal laminations along the margins of the ledge deposits likely resulted from slumping and compaction of partially wet sediment when the cave was drying up.

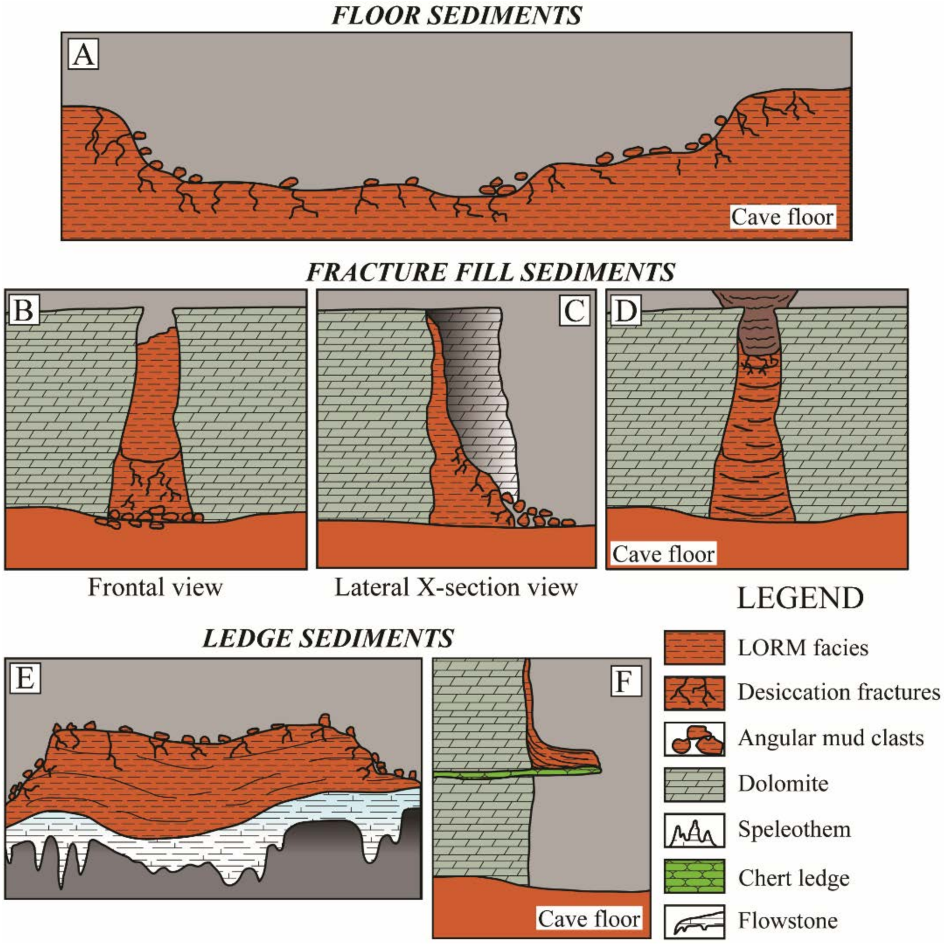

Figure 6. Cartoon overview of the various outcrops that preserve laminated orange-red mud (LORM) facies including desiccation locations and formation of mud clasts. (A) Erosion remnants of the LORM facies in the Dinaledi Chamber, primarily located along the cave floor. These sediments deposited via suspension settling and representing the slackwater facies. (B) Frontal view of erosion remnants of LORM facies sediment preserved as fracture fill and (C) in cross-section view, illustrating slumping deposits. Desiccation occurs primarily at the lower half of the outcrop, resulting in formation and accumulation of angular mud clasts at the terminus of the slope.

(D) Occurrence of LORM facies depositing as active deposits, accumulating water-saturated sediment in fractures forming distinct meniscate laminae. (E) LORM facies deposited along prominent flowstone and/or chert ledges. Sediments enter the chamber and drape onto ledges via fractures or along the cave wall. Note how internal laminations follow the topography of the ledge. Lateral and proximal margins of the outcrop display intense desiccation and fracturing, leading up to formation of angular mud clasts. (F) Active LORM facies sediment deposition on small ledges. Note the foreset-type laminae forming in the sediment where the cave wall meets the ledge.

5.4.4. Description of the LORM facies as active deposits

The LORM facies is also actively being deposited on small ledges and within dolomite fractures that possibly connect to the surface, however, these phenomena only occur locally and constitute a minor portion of the total LORM facies preserved in the cave. LORM deposits on ledges are typically 1 to 1.5 cm thick, and consist of water-saturated, fine-grained silt and clay-rich mud. These deposits are non-fossiliferous and do not contain interbedded sandy lenses. In cross-section, small, foreset-like laminations are commonly observed where walls intersect with the ledges. (Fig. 6F). Desiccation features have not been observed within these LORM deposits. Active deposition of LORM facies sediments also occur in certain vertical dolomite fractures that occur at any height along the cave wall and are commonly connected to the chamber ceiling. LORM facies sediments preserved in these fractures consist of laminated silt and clay-rich mud with few millimetre-thin interbedded lenses of fine to medium-grained quartz sand, and the facies is typically fossil-poor. The internal lamina in the LORM form concave up, meniscate lenses (Fig. 6D).

5.4.5. Interpretation of the LORM facies as active deposits

This study’s interpretation is that the fine-grained silt and clay-rich LORM are locally filtered through the vadose zone and are aqueously transported along cave walls via, and within, fractures that are possibly connected to the surface, either directly or indirectly (e.g., interconnected with other fractures). Water-saturated sediments accumulate as thin and very finely laminated micro-mud deposits on small chert ledges. It is deduced that this is a slow, infrequent depositional process, that primarily takes place in the form of autogenic recharge when meteoric surface waters filter through the soil into the cave via preferred fracture pathways. LORM sediments that accumulate in the fractures are typically sandier compared to the ledge deposits, which is possibly due to local filtering biases of the sediment passing through the fractures (fracture size, direct-indirect connectivity to the surface, etc.). Within these fractures, LORM sediments develop characteristic concave-up, meniscate laminations throughout the stratigraphy (Fig. 6D). These meniscate features might be a result of hydrostatic properties of the clay, collecting along the interior fracture walls during deposition, or post-depositional compaction.

5.4.6. Distribution of the UMCB facies in the Rising Star Cave

The UMCB facies was first described in the Dinaledi Subsystem as Unit 3 (Dirks et al. 2015). Later, Dirks et al. (2017) subdivided the UMCB facies (Unit 3) into two separate sub-units, sub-units 3a and 3b, based on the presence or absence of *Homo naledi* fossils, respectively. The vast majority of *H. naledi* bones were deposited in the upper 20 cm of the bone-bearing UMCB floor deposits (Fig. 3A) in the Dinaledi Chamber (fig. 8 in Dirks et al., 2017).

The UMCB facies occurs most extensively in the Dinaledi Subsystem, but also exists in other chambers of the Rising Star Cave, including the Postbox Chamber and Superman Chamber (Fig. 2), where *in situ* formation of UMCB deposits can be observed immediately adjacent to slumping and eroding LORM deposits. Unconsolidated, i.e., recently formed (414 to 236 Ka; Dirks et al., 2017), UMCB deposits were not observed in the Dragon's Back Chamber or Superman Crawl. Instead, these chambers preserve erosion remnants of well-lithified (Fig. 9A to D), i.e., older, mud clast breccia deposits, commonly capped by flowstone sheets (Fig. 3B). In the Hill Antechamber of the Dinaledi Subsystem (Fig. 2), deposits of the UMCB facies occur near the entry chute towards the top of the chamber, beneath remnants of older, lithified mudstone breccia deposits (Dirks et al., 2015). The majority of UMCB deposits occur along the floor of the Dinaledi Chamber where they are preserved as unconsolidated sediments that sit directly adjacent to thick outcrops of eroded and desiccated LORM deposits. Around the main *Homo naledi* excavation site, deposits of UMCB facies sediments are at least 70 cm thick (Dirks et al., 2017). Ground penetrating radar analysis of the Dinaledi Chamber suggests that the UMCB deposits may locally reach thicknesses of 1.5 m (Naidoo, 2016).

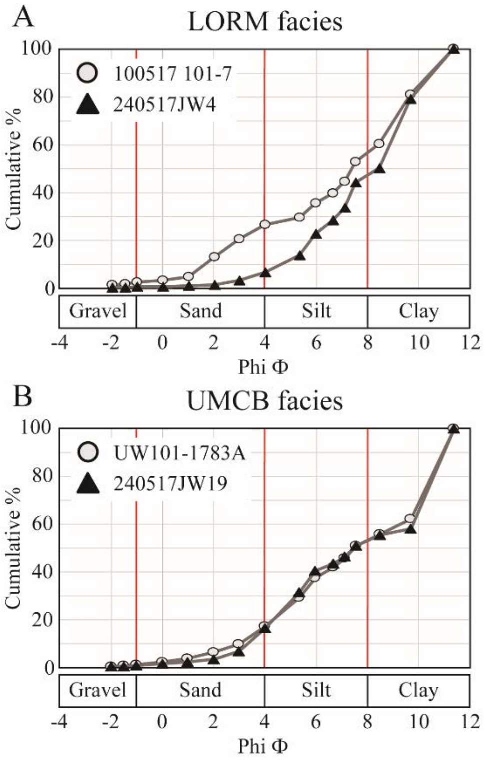

Figure 7. Grain-size analysis results for the (A) LORM facies and (B) UMCB facies from Rising Star Cave.

5.4.7. Description of UMCB facies

The UMCB facies is primarily clast supported and consists of largely unlithified, orange-red to dark brown, angular mud clasts surrounded by brown-grey silt and clay matrix (Fig. 3A to B and D). The UMCB deposits are carbonate-poor (Table 2), but the matrix may locally contain small pockets of highly concentrated dark grey, sand-sized dolomite and chert fragments. Although this type of matrix is rarely observed, it locally accumulates where UMCB rests against the dolomite cave wall (Fig. 3A). The matrix is moist and more water-saturated compared to the relatively drier mud clasts.

Angular mud clasts within the UMCB facies are defined as 0.2 to 10 cm large, semi-dry and angular aggregates composed of silt and clay. On average, the mud clasts are <3 cm in size (Fig. 9). Exposed mud clast surfaces are commonly weathered and coated in brown-black staining, forming a weathering rind composed of Mn oxyhydroxides, clay and silt-sized quartz grains that surround many of the clasts. Typically, the UMCB facies displays weak inverse grading with respect to mud clast size in the upper few centimetres of the deposit (Fig. 9E) and in places stacked,

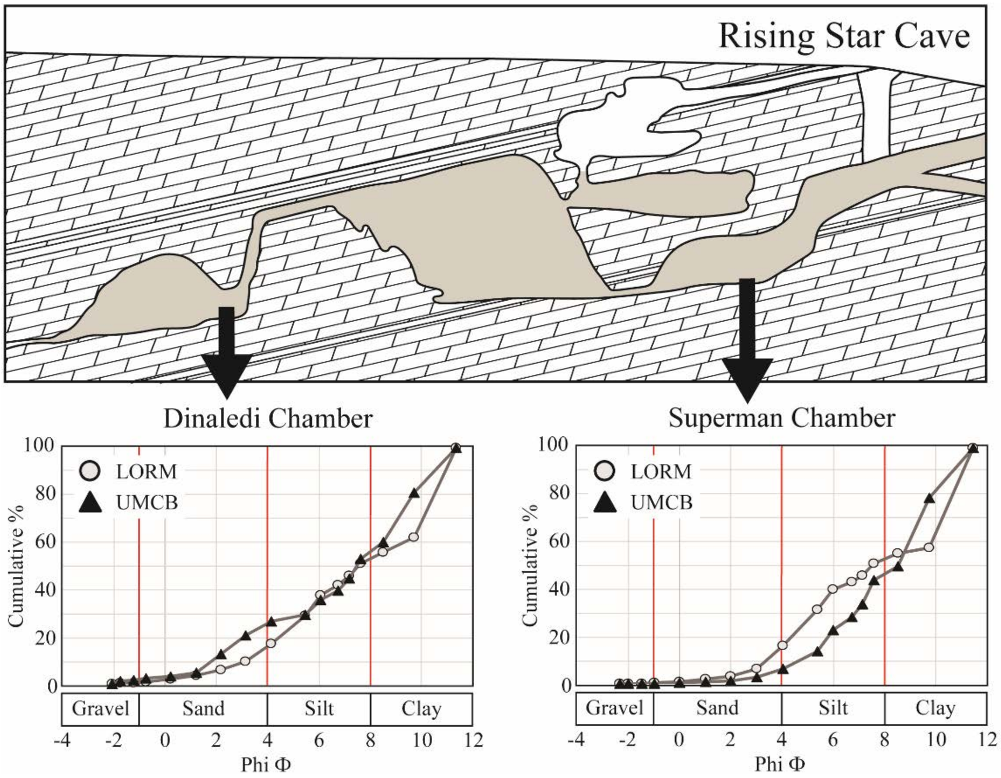

Figure 8. Grain-size distributions of LORM and UMCB facies from the Dinaledi Chamber compared to the Superman Chamber. Grain size distributions in the LORM facies are significantly similar between both chambers, suggesting a single sediment source and mode of deposition for the LORM facies. The LORM facies are the protolith sediments for the UMCB facies, which also contain similar grain size distributions.

inversely graded beds occur. Grading is less obvious in the typically matrix supported lower profile of the UMCB facies but becomes progressively clast supported in the uppermost section.

The UMCB facies is compositionally similar to the LORM facies (Tables 2 and 3) and primarily consists of silt (36 to 38 %) and clay (~46 %) with low concentrations of fine-very fine sand (6 to 13 %) (Figs 7B and 8). Mud clasts are rich in kaolinite (~18 to 28 %) and muscovite (~8 to 15 %) (Fig. 5D to F; Table 3). The mud clasts are generally soft to semi-hard and break conchoidally. Fine-scaled, internal laminae are common within individual mud clasts, together with mm-sized fractures (Fig. 9F and G). These fractures break non-conchoidally, parallel to the laminated surfaces or cross-cut the laminations at 90° to 110° angles and are locally filled with sparry calcite-aragonite or Fe-Mn oxides and oxyhydroxides, forming mm-wide veinlets (Fig. 9F to H). Fractures are most commonly present in the drier parts of the UMCB outcrops, particularly occurring along the margins and slopes of the deposit. Thin calcite coatings partially or completely cover the external surface of some clasts, forming a mm-thin interface between the clasts and the surrounding matrix (Fig. 9B to D).

The geochemical results for the UMCB facies (Fig. 4; Table 2) show high percentages of SiO_2 (50.91 to 64.61 wt %) and Al_2O_3 (13.42 to 15.69 wt %). Values of K_2O (1.47 to 1.48 wt %), MgO (1.46 to 1.64 wt %) and CaO (0.26 to 0.99 wt %) are similar to the LORM facies (Fig. 4C and D; Table 2). Elevated values of Fe_2O_3 (6.93 to 13.47 wt %), MnO (0.9 to 4.82 wt %) and P_2O_2 (0.08 to 0.21 wt %) were detected in the sample from the Dinaledi Chamber (Fig. 4D). Most abundant minerals include quartz (SiO_2) (35.09 to 38.72 %), kaolinite $(Al_2SiO_5)(OH)_4$ (21.87 to 27.61 %), muscovite $KAl_3(Si_3)(O_{10})(OH)_2$ (12.44 to 12.54 %), and hematite (Fe_2O_3) (6.93 to 13.47 %). Minor amounts of pyrolusite (MnO_2) (1.1 to 5.91 %) and minor dolomite ($MgCa(CO_3)_2$) (0 to 0.85 %) were also identified (Table 3).

5.4.8. Interpretation of UMCB facies

The formation of the UMCB facies in the Rising Star Cave is interpreted as a product of erosion and diagenetic processes occurring within the LORM facies host sediments. Erosion, combined with lowering (semi-phreatic) water tables in the cave, periodically resulted in removal of LORM facies sediments via floor drains in the Dragon's Back Chamber, Dinaledi Chamber and Superman Chamber (Fig. 2), transporting them deeper into the cave. As a result, erosion remnants of LORM facies sediments are left behind in various locations inside the cave chambers (e.g., the cave floor, ledges, fractures, etc.), and surface topographies develop within LORM erosion remnants, primarily along the cave floor and along ledges. Desiccation fractures, and subsequently diagenesis, was observed to preferentially occur along these topographically exposed and eroded LORM surfaces. Prolonged erosion, in combination with desiccation, and diagenetic alteration of these topographic surfaces possibly caused marginal LORM sediments to slump and collapse, which then further brecciate into angular mud clast piles. These mud clasts slowly accumulate over time along the cave floor as *in situ* deposits from adjacent LORM deposits or as gravitational slump deposits derived from LORM deposits preserved along flowstone and/or chert ledges, accumulating along the cave floor to form locally extensive (i.e., Dinaledi Chamber) UMCB facies.

The presence of Fe-rich and Mn-rich mud matrix in the UMCB can be explained through weathering of the external mud clast surfaces, during which distinct weathering rinds, composed of Fe and Mn oxide-rich silt and clay, develop around the clasts. The weathering rinds easily slough off the clasts and disintegrate into fine-grained, unconsolidated, and autochthonous mud to form the matrix within the UMCB facies. It is interpreted that the inverse grading of the UMCB facies resulted from this diagenetic process; mud clasts in the lower profile are smaller because they represent older, *in situ* deposits that are deeply weathered and progressively more disintegrated compared to the more recently deposited, larger mud clasts in the upper profile of the UMCB facies (Fig. 9E). The elevated values of P_2O_2 (Fig. 4D) obtained from the UMCB facies in the Dinaledi Chamber could coincide with the high concentration of decomposing bones that are present in the chamber.

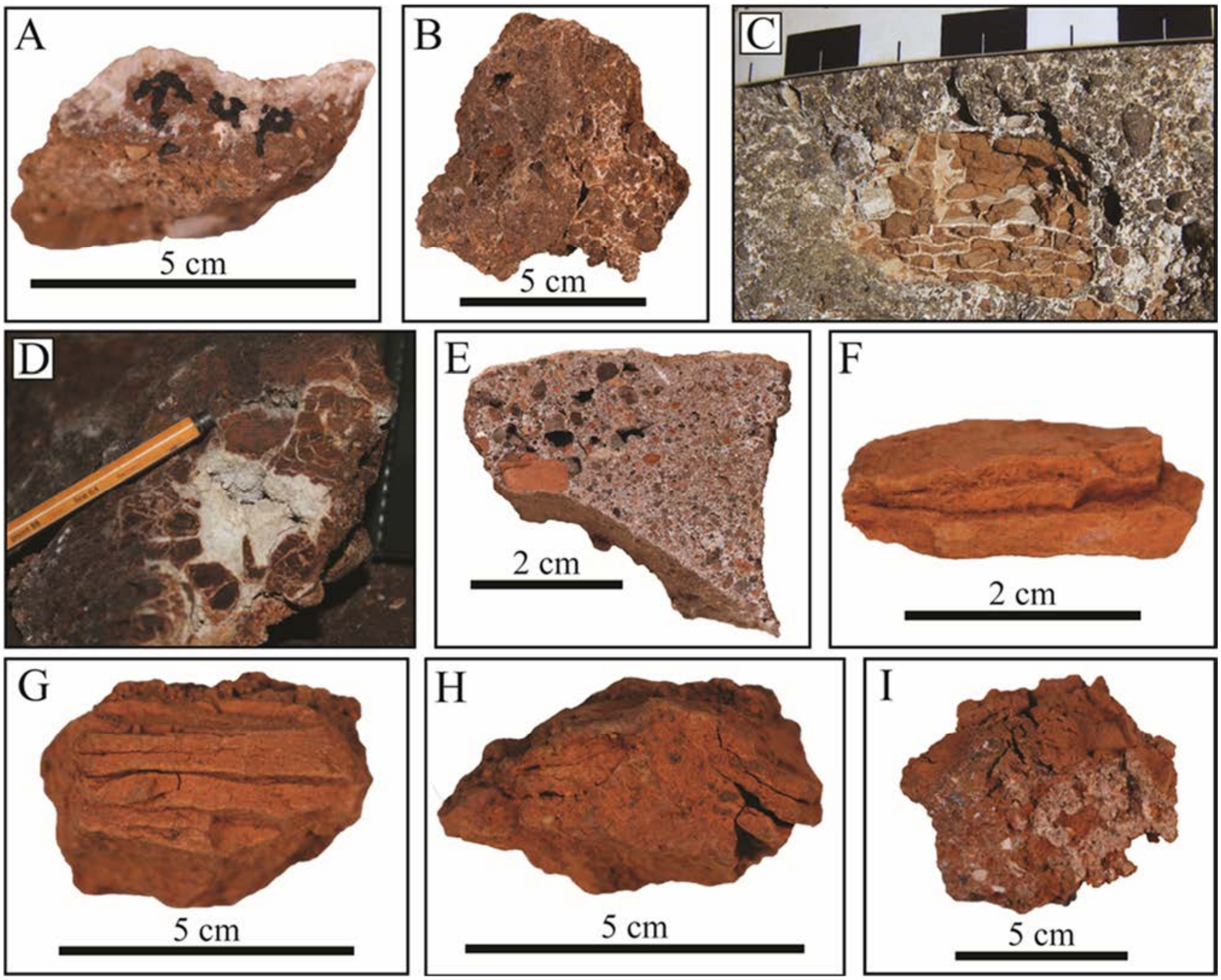

Figure 9. UMCB facies mud clasts. (A) Thin hardground overlying and indurating mud clast breccia. (B) Honeycomb network of sparry calcite infiltrating the right half of mud clast breccia. (C and D) Diagenetic growth of sparry calcite occupying interstitial spaces along bedding planes and desiccation cracks of medium-sized mud clasts from mud clast breccia facies in the Dragon's Back Chamber and Dinaledi Chamber, respectively. (E) Size distribution and coarsening upward sedimentary architecture of subrounded to angular clay clasts of mud clast breccia facies in the Dragon's Back Chamber, similar to Unit 2 from the Dinaledi Chamber in Dirks et al. (2015). (F) Close up of individual mud clasts in which fracturing occurs clearly along horizontal lamina. (G) Propagation of desiccation cracks parallel and perpendicular to horizontal lamina. (H) Oblique propagation of desiccation cracks in individual mud clast, furthering fragmentation of the clast. (I) Active desiccation and crack propagation along the clay-rich surface (top) of mud clast breccia in the Dragon's Back Chamber.

5.5. Discussion

5.5.1. Potential driving mechanisms for sedimentary autobrecciation

The term sedimentary autobrecciation is proposed to describe the process of unlithified mud clast breccia (UMCB) formation, derived from the LORM host sediments in the Rising Star Cave (Fig. 10); the term autobrecciation is normally used to describe certain volcanic brecciation processes (e.g. Mellors et al., 1988; Sato et al., 1992; Alidibirov and Panov, 1998; Calder et al., 2002). Within the Rising Star Cave, sedimentary autobrecciation takes place through a combination of multiple (contemporaneous) processes, i.e., flooding, erosion and drainage, desiccation and slumping, diagenesis, chemosynthetic oxidation, and potentially bioturbation, which are discussed in more detail below. Observations indicate that most of the angular mud clasts found in the Rising Star Cave formed autochthonously to para-autochthonously from the unconsolidated LORM facies and accumulated in large volumes to form deposits of UMCB facies under dry (i.e., non-flooded) cave conditions. In addition to the geochemical and mineralogical similarities between both facies (Fig. 4; Tables 2 and 3), the sedimentary make-up and grain size distribution of the LORM and UMCB facies appear relatively consistent and uniform within different chambers in the cave (Fig. 8). LORM and UMCB facies observed in the Superman Chamber and Dinaledi Chamber show equally similar grain size properties (Fig. 7). These observations suggest that both facies share a common sediment source and are, thus intimately related, meaning that LORM facies are likely the protolith sediments for the UMCB facies. Similar observations were made by Laureano et al. (2016) from the non-fossiliferous Lapa Doce cave in Brazil.

Currently, the cave is dry, meaning there is no standing or phreatic water present in the chambers and the average temperature inside the cave is ~18°C with a relative humidity of 97 to 99 %. It is thought that autobrecciation begins with lowering of the (phreatic) water table inside the cave, subaerially exposing and eroding the LORM facies sediments, developing vertically exposed surfaces that stand out as topographic highs within the remaining LORM erosion remnants. The original accumulations of LORM facies sediment were removed from the chambers (i.e., Dinaledi, Dragon's Back and Superman chambers) via observed floor drains that are situated along the cave chamber floors and transport the sediments deeper into the cave. Prolonged drying of the cave system caused desiccation and strain within the kaolinite-rich LORM sediments, particularly along the outer surfaces that are exposed along the cave floor, along walls and on ledges, etc. (Fig. 3A and D). The extent to which desiccation can take place within the LORM facies is partly influenced by clay content and contraction behaviour of clay species in the sediment, as well as secondary diagenetic infill of developing desiccation cracks, continuous sediment removal through floor drains and subsequent rejuvenation of topography and bioturbation (Farrand, 2001; Ford and Williams, 2007).

The tensile and shrinking properties of clay rely heavily on the types of clay and clay concentrations present in the sediment and determine the amount of desiccation taking place in the sediments as they dry out (Albrecht and Benson, 2001; Aksu et al., 2015; Morley et al., 2017). Kaolinite and muscovite (illite) constitute nearly 100 % of the clay-size fractions in both the LORM and UMCB facies (Fig. 4; Table 3), and they contribute between 42 to 50 % of the total sediment volume (Fig. 7). Although a non-swelling clay, kaolinite can shrink when dehydrated, creating volume changes of up to 15 % (Aksu et al., 2015), that can result in vertically propagating desiccation fractures (e.g. Morley et al., 2017). For the measured concentrations of kaolinite in the LORM sediments, this is sufficient to produce the observed desiccation fractures in the cave along exposed outer surfaces of erosion remnants (Fig. 11). Prolonged desiccation and extensional stresses along the outcrop slopes could cause continuous vertical fracture propagation that ultimately results in slumping and gravitational collapse of sediment along the margins of the LORM facies to produce nearly *in situ* breccia (UMCB) deposits (Fig. 10) that spread outward into debris aprons.

The drying and desiccation of water-saturated LORM facies sediments alone does not fully explain the process of sedimentary autobrecciation in the Rising Star Cave. Desiccation fractures and interstitial laminations in LORM (and UMCB) facies provide occupation sites for diagenesis and chemosynthetic (microbial) oxidation to occur, thereby furthering the process. In the case of diagenesis, interstitial growth of calcite and aragonite in clastic sediment is rare in the Rising Star Cave and has been observed in the UMCB facies, but not in the *in situ* (desiccated) LORM protolith facies. Calcite-aragonite infillings occur primarily in fractured and laminated mud clasts (Fig. 9D to F), suggesting that the mud clasts must have been exposed to some level of desiccation prior to carbonate precipitation. Calcite production and growth likely occurred locally in spots where drip waters saturated with Ca^{2+} + HCO_3^- ions, precipitate $CaCO_3$ inside the fractures and/or along the fresh surface of some mud clasts, cementing them together. As shown by the general absence of calcite fragments in the UMCB sediments (Table 2), dissolution of calcite in mud clasts could take place once active drips stop, thereby removing calcite from the fractures due to the overall mildly acidic conditions in the UMCB sediment, and furthering autobrecciation via internal collapse of the mud clasts.

Microbial activity in oxidizing cave environments are commonly known to produce Fe and Mn oxides and oxyhydroxides (Caumartin, 1963; Engel, 2012). Iron-oxide and manganese-oxide crusts and concretions are abundant in the LORM and UMCB facies throughout the Rising Star Cave (Dirks et al., 2015, 2017), confirming an oxidizing cave environment, and the lack of carbonate in most of the LORM floor sediments indicates mildly acidic conditions. Manganese oxyhydroxides such as birnessite were detected in the LORM and UMCB facies of the Dinaledi Chamber (Dirks et al., 2015). Birnessite has a clay-like structure and displays swelling behaviour similar to montmorillonite (Appelo and Postma, 1999; Liu et al., 2000) with the potential to expand significantly in aqueous conditions that are enriched in Ca^{2+} and Mg^{2+} cations (Appelo and Postma, 1999). Dolomite is the host rock in which the Rising Star Cave formed, and provides a direct source of Ca^{2+} and Mg^{2+} which could have been microbially utilized during the production of birnessite, and therefore actively contributing to furthering the propagation of pre-existing fractures or laminations—promoting and/or accelerating desiccation within LORM and UMCB facies (Fig. 3C).

Insect remains as well as small (millimetre to centimetre) vertical burrows are preserved within the Rising Star Cave, but the latter are rare, and have only been observed in the LORM facies of the Dinaledi Chamber (Dirks et al., 2015). The presence of bioturbation features in the LORM sediments, as well as the observation that bone material has been affected by beetles and snails (Dirks et al., 2015) indicates that some invertebrates were present and could have contributed to the autobrecciation process, but to what extent is uncertain.

Another model to be considered as contributing to autobrecciation is the possibility of freeze-thaw cycles and the growth of ice crystals within the desiccated fractures and laminations (White, 2012). Frost wedging has the potential to contribute to, and likely accelerate, the mechanical break up of LORM and UMCB facies sediments, however for this phenomenon to take place, significant temperature fluctuations and sub-zero cave temperatures would be required. Currently, the temperature inside Rising Star Cave is ~18 °C. and this remains constant reflecting the Modern Mean Annual Temperature ($\mathrm{MAT}_{\mathrm{modern}}$) in the area (e.g. Talma and Vogel, 1992; Holt et al., 2016). The minimum mean annual surface temperature in southern Africa during the Last Glacial Maximum has been quantified as $\mathrm{MAT}_{\mathrm{modern}}$ minus 6 °C using noble gas data obtained from groundwater (Stute and Schlosser, 2000). This indicates that the temperatures inside Rising Star Cave in the last million years or so are unlikely to have dropped much below 12 °C, and sub-zero conditions would never have been experienced, not even during glacial maxima. Thus, for the Rising Star Cave, frost-wedging effects can be excluded as a possible sedimentary autobrecciation mechanism.

Extensive radioisotopic and palaeomagnetic analyses performed on the *H. naledi* fossils and encasing UMCB sediments and flowstones in the Dinaledi Subsystem produced an age estimate for the fossils of 335 to 236 ka (Dirks et al., 2017). The fossils are covered by up to 20 cm of UCMB deposits (sub-unit 3b in Dirks et al., 2017), below which no further hominid fossils can be found (Dirks et al., 2015). The age estimates for the fossils combined with the depths from which they have been obtained provide a first-order estimate of ~8×10^{-4} mm/year for the formation rate of UMCB facies along the cave floor, i.e. the formation and deposition of UMCB facies sediments is a slow process. Optical Stimulated Luminescence (OSL) dating of LORM facies sediments (sub-unit 1a) from the Dinaledi Chamber yielded an age of 353±61 ka (Dirks et al., 2017). Using this age data conservatively, combined with the slow, continuous accumulation of UMCB facies sediments and lack of onlapping or overlying, younger, LORM facies within the fossiliferous deposits, indicates that conditions in the Dinaledi chamber were probably stable and dry for at least the last ~ 300 ka.

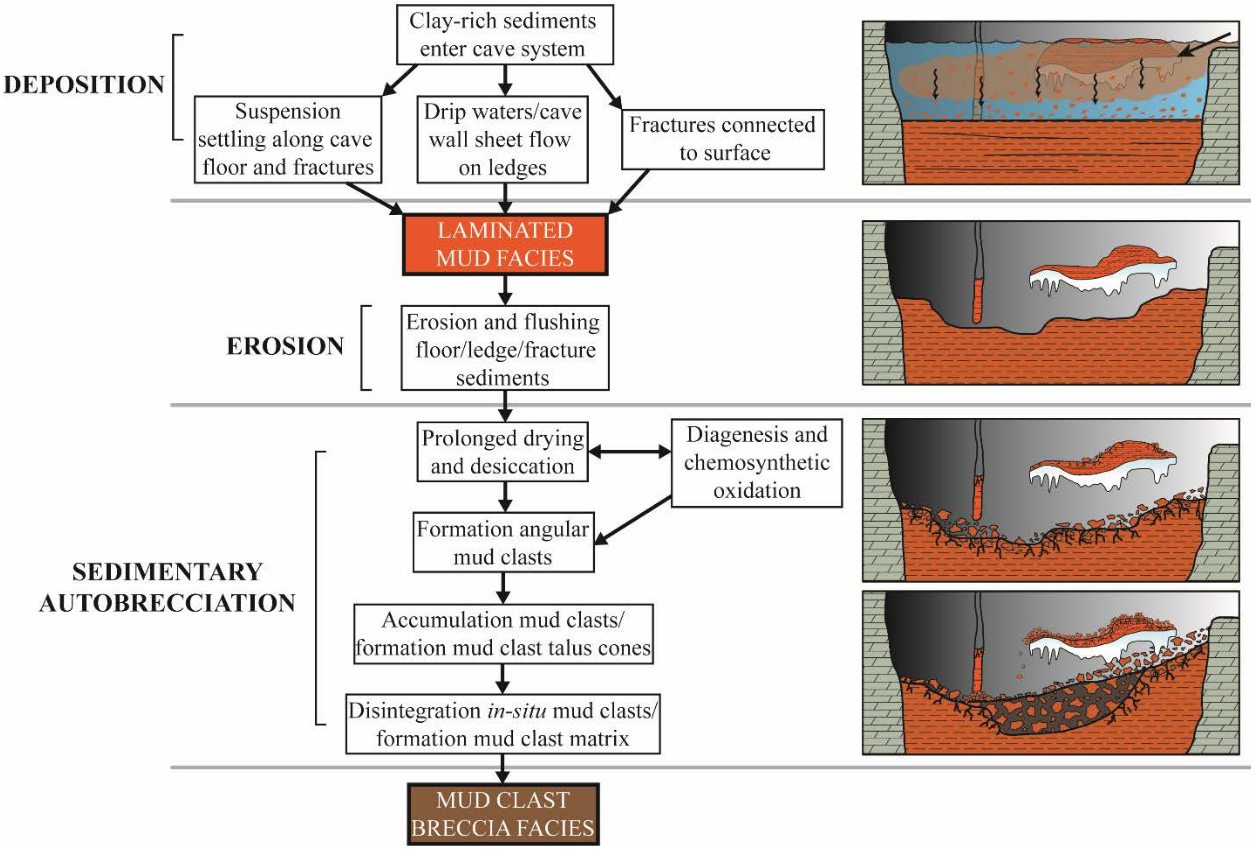

Figure 10. Illustrated flow diagram and cartoons depicting various depositional scenarios resulting in the process of sedimentary autobrecciation in the Rising Star Cave. The sequence of events starts with deposition of clay-rich sediments and the formation of the laminated orange-red mud (LORM) facies which ultimately lead to the formation of the mud clast breccia facies.

5.5.2. Comparison with other hominin-bearing caves in the CoH

Apart from Rising Star Cave (Dirks et al., 2015, 2017) and Gladysvale Cave (Pickering et al., 2007), nearly all fossil-bearing caves in the Cradle of Humankind (CoH) contain hominin and other macro-fossil remains preserved in hard-rock breccia deposits, consisting of angular, boulder to gravel-sized quartz, dolomite, chert and vein quartz clasts embedded in a fine-grained sandy matrix [e.g., Sterkfontein (Clarke, 1998, 2007; Bruxelles et al., 2014) Drimolen (Keyser et al., 2000), Gondolin (Watson, 1993a,b; Adams et al., 2007), Malapa (Berger et al., 2010; Dirks and Berger, 2013), Kromdraai (Braga et al., 2017) and Coopers (Berger et al., 2003)]. The difference in cave breccia composition and types between these caves appears to be a function of geology, geomorphology and their topographic position within the CoH landscape; network maze caves situated closer to, or within the river valleys (e.g., Rising Star Cave, Gladysvale) are more subject to flooding and collect far muddier sediment, and thus, have the potential to form mud clast breccias, whereas caves positioned higher in the landscape are far less likely to do so (Dirks and Berger, 2013). In the latter situation, cave breccias may form via mass wasting, unroofing or chamber collapse inside the cave, resulting in diamicton facies-type cave breccias. The different position of caves on the landscape could explain why LORM and UMCB facies-type sediments are not observed in any of the other hominin-bearing caves in the CoH.; they simply do not form in caves that are less prone to mass flooding, and therefore collect little or no LORM facies-type sediments.

5.5.3. Documentation of LORM-like and UMCB-like facies in caves worldwide

LORM-like (i.e., slackwater facies) deposits are commonly observed in (fossiliferous) caves around the world [e.g., Selminum Tem Cave in Papua New Guinea (Gillieson, 1986), Agen Allwedd cave in South Wales, England (Bull, 1981), Bather's Cave, Virginia, USA, (Knapp, et al., 2007) and Liang Bua, Indonesia (Sutikna et al., 2016; Morley, et al., 2017)], but UMCB-like facies appear to have been reported on only from non-fossiliferous caves [e.g., Botovskaya Cave in Siberia (Filippov, 2000; Kadlec et al., 2008) and Lapa Doce cave in northeast Brazil (Laureano et al., 2016)]. Archaeologically and palaeoanthropologically important cave systems, primarily from Africa, Europe, and southeast Asia, host thick successions of LORM facies-type deposits. For example, prominent hominin-bearing sites in southeast Asia show evidence of slackwater type sediment deposition, and include the Liang Bua cave in Indonesia, known for its *Homo floresiensis* fossils (Brown et al., 2004; Morwood et al., 2004). These fossil remains are recorded from silty clay deposits that are covered by laminated slope wash sediments (Sutikna et al., 2016; Morley et al., 2017), and include brecciated clasts consisting of andesite, limestone, and tuffaceous extraclasts but mud clasts and mud clast breccias are not reported. Similar stratigraphic architectures are recorded from the fossiliferous Laang Spean Cave, Cambodia (Forestier et al., 2015), preserving non-hominin vertebrate and invertebrate faunal remains in unlithified, desiccation cracked, silty-clay sediments that are comingled with large limestone breccia blocks. Although these sediments are clay-rich, no mud clast breccia deposits are recorded. The Tam Pa Ling cave in Laos preserves early modern human fossil remains in silty clay, but also does not contain mud clast breccia (Demeter et al., 2012, 2015). It is noteworthy that no UMCB facies-type sediment deposits such as found in the Rising Star Cave have been reported from other important fossil-bearing cave sites. Thus, the common presence of slackwater facies-type (LORM) sediments in cave systems does not guarantee the formation of mud clast breccia (i.e., UMCB) facies. This suggests that sedimentary autobrecciation processes in caves occur under very specific conditions present in the Rising Star Cave and other caves throughout the world. As discussed above, these conditions would include: (i) the presence of maze caves in river valleys where deposits of LORM facies sediments can form in caves; (ii) a drop of the water table and subsequent erosion and drying out of LORM-like deposits to form UMCB deposits; and (iii) relatively stable dry conditions that allow the accumulation of significant deposits of UMCB facies sediment.

5.5.4. Autobrecciation and implications for the burial and taphonomical history of *Homo naledi*

The slow formation rate of 8×10^{-4} mm/year of the UMCB facies sediments in the Dinaledi Chamber occurred in dry cave conditions for at least ~300 ka. The estimated depositional age of 236 ka for *H. naledi* (Dirks et al., 2017) indicates that the fossils were deposited on UMCB sediments that represented the Dinaledi Chamber cave floor at that time, and that the fossils entered the cave under dry (non-flooded) conditions. Thus, fluvial mechanisms can be confidently excluded as a mode of transporting the *H. naledi* material into the cave. It is therefore highly unlikely that the fossils were washed into the cave, which agrees with the observations made by Dirks et al. (2015).

The mud clast breccia deposits are dynamic in the sense that they probably slowly slump towards floor drains within the Dinaledi Chamber, thereby moving the fossils with them downslope. Some of the fossils within UMCB facies have slumped into a floor drain in the Dinaledi Chamber as described by Dirks et al., (2015). Additionally, the presence of multiple cross-cutting manganese staining lines across some of the bones indicate that periodic movement and repositioning of the bones occurs within the slumping UMCB facies. The sedimentary

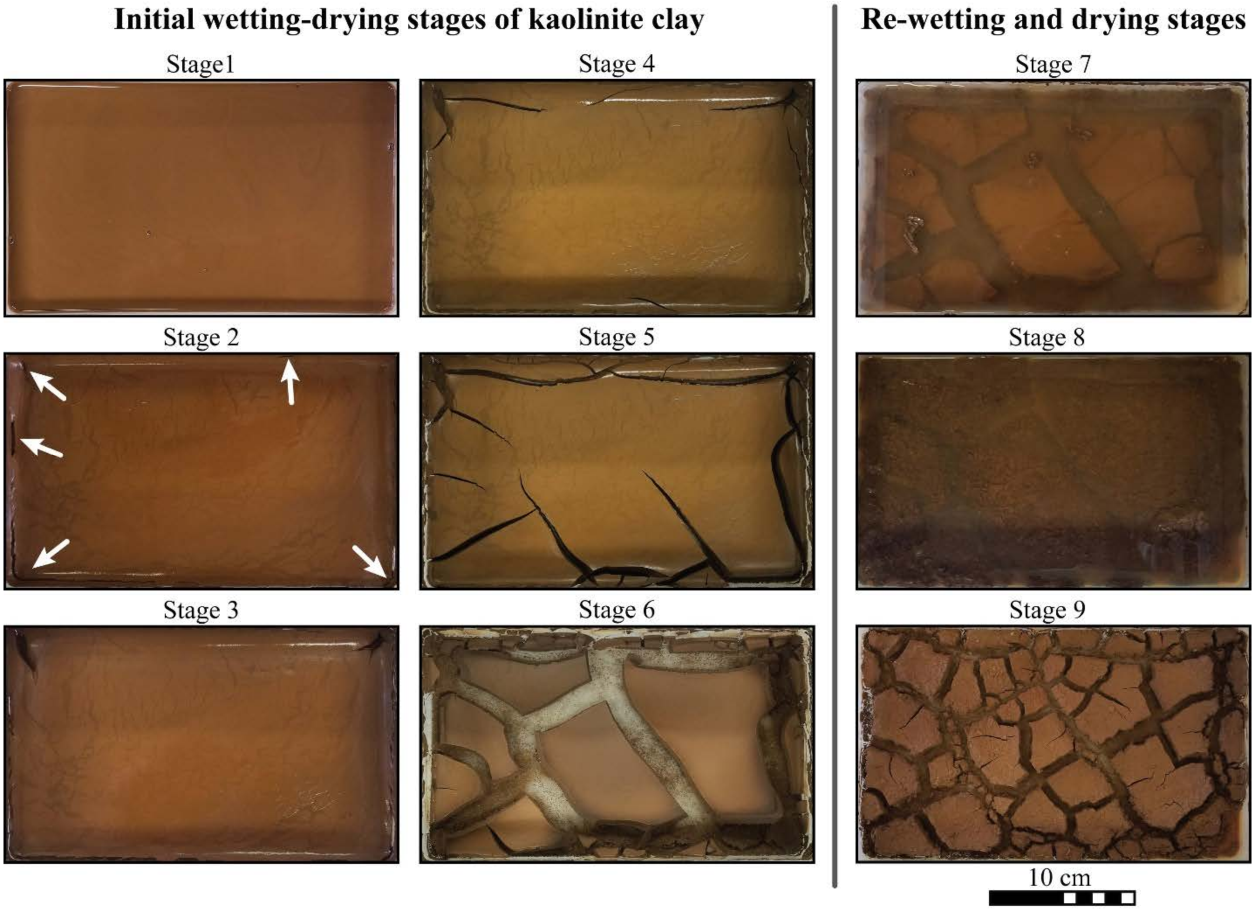

Figure 11. Experimental simulation of wetting and drying of clay-rich LORM sediment from the Dinaledi Chamber of the Rising Star Cave, demonstrating the desiccation potential of kaolinite clay, and possibly the formation of mud clasts in the cave. The experiment was performed under normal atmospheric conditions and the sediment was kept in an oven at a constant temperature of 40°C. Stage 1) clay-rich sediment suspended in water; Stage 2) initial desiccation fracture propagation sites (white arrows) occur after surface water has evaporated and clay-rich sediment begins to dry; Stage 3) intensification and continued propagation of desiccation fractures with further drying of sediment; Stage 4) additional desiccation fractures form; Stage 5) ongoing addition of new desiccation fractures begin to show the outlines of major 'mud clasts'; Stage 6) desiccation of the LORM sediment is complete after all the water from the sediment has evaporated. Complete desiccation of kaolinite clay results in significant shrinkage of the sediment to form fully isolated individual, 'mud clasts'; Stage 7) secondary submersion of the desiccated LORM sediment in water; Stage 8) disintegration of the large individual 'mud clasts' and formation of small additional desiccation fractures and mud flakes on the surface of the 'mud clasts', however, the delineated boundaries between individual segments remain visible; Stage 9) complete desiccation of the LORM sediment, resulting in secondary, angular, fragmentation of the initially large 'mud clasts' from Stage 6. The main outlines of the formerly large 'mud clasts' remain visible.

autobrecciation process and slumping also have the potential to explain the active erosion of *Homo naledi* fossils out of the slope margins of UMCB facies sediment near the entrance of the Hill Antechamber, reworking and redepositing them across the cave floor. The *Homo naledi* fossils, some of which are articulated, i.e., a single hand and foot (Berger et al., 2015; Dirks et al., 2015), are partly covered by accumulating UMCB deposits, and additionally overlie deeper deposits of UMCB. The articulated remains are preserved within a predominantly disarticulated bone assemblage. This could imply that reworking of UMCB sediment, and the fossil bones, can be a locally discriminant process, excluding some of the fossil content, possibly those that are deposited further away from the floor drains, and thus less affected by slumping and movement of the UMCB sediments.

5.6. Conclusions

This study proposes a process termed sedimentary autobrecciation, which is being described from the Rising Star Cave in the Cradle of Humankind, South Africa. The process describes the autochthonous to para-autochthonous physical and diagenetic break-up of kaolinite-rich laminated orange-red mud facies into mud clasts and subsequently the formation of the unlithified mud clast breccia facies throughout the Rising Star Cave in the Cradle of Humankind, South Africa. Sedimentary autobrecciation is initiated by erosion and subsequent drying (desiccation) of previously water-saturated laminated orange-red mud (LORM) facies and promoted by the diagenetic formation of interstitial calcite-aragonite and microbially induced Mn-Fe oxides in desiccated fractures and laminae. Slumping and collapse of desiccated sediment fragments break into angular mud clasts that accumulate into gravity-induced, unconsolidated debris cones, aprons and layers along the cave floor and on top of ledges along the cave walls, forming the unlithified mud clast breccia (UMCB) facies in the Rising Star Cave. Once deposited, mud clast deposits continue to autobrecciate *in situ*, thereby reducing clasts in size and ultimately disintegrating them into mud matrix. This results in a distinctive inverse grading profile in the upper few centimetres of the deposits in which older, smaller, mud clasts are overlain by more recently deposited larger clasts. The process of sedimentary autobrecciation differs from the process that leads to traditional brecciation in caves in the following way: it is a local, gravity-driven, and *in situ* process that requires minimal hydrological transport mechanisms compared to traditional breccia deposits that are highly heterolithic deposits formed via fluvial and mass wasting transport mechanisms. The formation of UMCB facies is a slow process, with breccia formation rates of approximately 8 x 10^{-4} mm/year. The absence of LORM facies (slackwater facies) in between UMCB deposits in the Dinaledi Chamber suggests that this facies formed under dry (non-flooded) cave conditions, that started at least ~300 ka ago.

The UMCB deposits and associated *Homo naledi* fossils from the Dinaledi Chamber form a unique and previously undocumented depositional setting in hominin-bearing cave studies. The sedimentary autobrecciation process improves upon current understanding regarding the pre-depositional and post-depositional taphonomy of the *H. naledi* fossils in the Dinaledi Chamber. Hence, local reworking and slumping of the unconsolidated mud clast breccia facies towards floor drains in the Dinaledi Chamber undoubtedly affected the depositional history and position of some *Homo naledi* fossils once they entered the chamber. However, in other parts of the chamber, the presence of articulated elements (i.e., hands and feet) suggests that some material is still *in situ* and has not been reworked, indicating that the UMCB sediments and the associated *Homo naledi* material are not water-laid deposits.

Chapter Six

Thesis summary and future work

The discovery of *Homo naledi* undoubtedly represents one of the most impactful hominin discoveries in recent years from Africa. The Dinaledi Chamber fossil discovery site in Rising Star Cave represents the single largest accumulation of hominin bones ever found in Africa, and this site is even more significant because of its young age (335-240 ka), buried within unconsolidated muddy sediments at shallow depths in a deep, difficult to access chamber that exhibits a unique depositional setting not previously observed in other hominin-bearing cave localities in the Cradle of Humankind. This unique setting is significant in that it provides insights into the more recent, i.e., less than one million years ago, aspects of the geological history of the Cradle of Humankind during the early Pleistocene.

This thesis project was initiated to investigate the clastic sedimentology and geomorphology of the Rising Star Cave system and the surrounding landscape. Over the course of four years, the author worked alongside the palaeoanthropologists excavating in the cave system, as well as other researchers working on many other aspects of the *Homo naledi* puzzle. The results of this thesis project on the clastic sedimentology of Rising Star Cave, include those sediments that entombed the *Homo naledi* fossils, are critical to deciphering the genesis of the cave sedimentology, the deposition of the fossils and the geomorphic evolution of the landscape surrounding the Rising Star Cave system. The thesis was designed as five stand-alone chapters or manuscripts, but when combined, help to reconstruct the clastic sedimentology of the cave and inform on its geological history.

Chapter 2, which focuses on the geomorphology of the Rising Star landscape, demonstrates that in the past >600 ka, punctuated neo-tectonic (normal) faulting and repeated base level drop of the valley floor along the WNW trending fault scarps likely facilitated the northeast migration of the Upper Bloubank Spruit fluvial system. Three distinct geomorphic domains developed on the Plio-Pleistocene landscape surrounding Rising Star Cave as a result of fluvial migration, and each domain preserves unique sediment types and mineral concentrations that reflect the various stages of landscape evolution. The immediate surroundings of Rising Star Cave present a dynamic landscape in which the interplay between local structural features (normal faults), the carbonate lithologies and fluvial processes created a changing landscape that affected the nature and distribution pattern of the clastic sediment fill in Rising Star Cave. The main controlling fault causing fluvial migration occurs directly North of the Rising Star Cave system. As the Upper Bloubank Spruit migrated NE-ward, the fluvial system transitioned from a bedrock channel with noncyclic strath terraces positioned S of the fault to an alluvial channel with an associated alluvial cut and fill terrace system positioned on Quaternary cover N of the fault.

During the opening of the cave around ~600 ka, clastic sediments comprised primarily of river sediments entered the cave via the vertical shaft in the Postbox Chamber. During this time, the Upper Bloubank Spruit was positioned further south on the landscape near the cave opening. Ongoing downward and lateral migration of the river channel resulted in less frequent fluvial flood-derived sedimentation events reaching the cave and instead, surface runoff became the dominant sediment transport method. Based on available dating this transition from fluvial dominated sedimentation to sedimentation through surface runoff would have occurred sometime between 400 ka and 150 ka, coinciding the entry of *H. naledi* into the cave.

As the river channel migrated and the strath terraces became abandoned, alluvial sediments deposited on these terraces were modified by secondary processes. This involved: 1) the deposition of Mn-Fe-oxyhydroxide phases and siderite in response to microbial-mediated soil forming processes; 2) the accumulation of chert gravel as a result of chemical denudation of the underlying dolomite; and 3) the winnowing of fine-grained clay that was transported deeper into the cave. The degree to which secondary processed modified the surface sediments was strongly time dependent resulting in a systematic change in the composition and texture of the sediments when moving from the topographically highest and, therefore, oldest terraces to the current stream bed. These changes in the character of surface sediments can be used to constrain the provenance of cave sediment. These data provide a temporal framework which applies to the sedimentary history of the cave, both clastic and chemically. Sedimentation events into the cave began once fracture systems connected to larger chambers, i.e., Postbox Chamber and Upper Postbox Chamber, and were also exposed to surface so that sediment laden floodwaters from the channel and surface runoff periodically flow into the cave.

Chapter 3 focuses on the clastic sedimentology and general stratigraphic patterns in the Rising Star Cave. Nine repeated clastic facies are recognized and detailed descriptions and interpretations of each are presented. This chapter demonstrates that most clastic sediment in the cave system is delivered via a vertical shaft in the Postbox Chamber, beneath which a polymictic debris cone developed. Throughout the investigated chambers, a distinct vertical and lateral fining distribution of sediment particles, most notably between the Dinaledi, Dragon's Back and Superman chambers is observed. In Dinaledi Chamber, the mineralogy of the sediment consists primarily of very fine-grained and clay-rich laminated orange-red mud (LORM) facies, dominated by kaolinite and illite clays, elevated manganese concentrations, and minor quantities of fine to medium-grained, subangular to angular quartz sand. The fine-grained nature and thinly laminated architecture of these sediments indicate a suspension-settled deposit in quiescent water conditions. These deposits and the unusually high clay-rich sediments are explained through the accumulation of new clay minerals with each additional sedimentation event, slow and minor, but continuous, clay deposits through vertical fractures in the dolomite, as well as the reworking of older clay minerals from associated chambers, i.e., Dragon's Back Chamber. Additionally, local chemoautotrophic processes taking place in the Dinaledi Chamber have partially led to an enrichment of common manganese and iron oxides such as pyrolusite, haematite and magnetite, and more rare species such as todorokite. In comparison, the Dragon's Back Chamber and Superman Chamber are much sandier with gravel facies, and preserve evidence of current flow, including cross lamination, ripples, scoured beds and normal grading. The Postbox Chamber contains the coarsest sediment and appears to be the proximal source of sediment distribution in Rising Star Cave. The chamber contains a clear vertical shaft that is now chocked by sediment debris but clearly connected to surface. The sediment consists of a poorly sorted polymict debris cone which spreads out laterally and spills winnowed sediments into the Dragon's Back Chamber. A minor secondary sediment entry point exists in the Upper Postbox Chamber. This entry point shed sediments into the cave more diagonally and is also directly connected to surface but has a lower distribution potential and contains a strong soil mineral signature. Sediment influx in Rising Star Cave is thus differential, both in source and quantity/frequency. Sediments from Postbox Chamber deposited sometime between 600-150 ka and are mainly flood-derived and have a cave-wide distribution, whereas lesser sediment quantities enter via the Upper Postbox Chamber by less frequent surface runoff events, soil creep and aeolian activity. Exactly when the Upper Postbox Chamber opened up to surface is currently unknown but given the gravelly and generally coarse nature of the clastic sediments and presence of elevated soil mineral signatures in the Upper Postbox Chamber suggests that the chamber opened up to surface well after the Postbox Chamber and when the Upper Bloubank Spruit was no longer positioned above the cave.

The clastic sediments preserved on surrounding landscape surface show strong similarities with the clastic sediments found in Rising Star Cave, both in mineral composition as well as the detrital zircon age populations they contain. Although there are clear differences in mineral concentrations between the sediments in the cave and those on surface, we have demonstrated that majority of the clastic sediments preserved in the cave are derived from the surrounding surface and have been washed into the cave as flood-derived sediments (and later redistributed by internal sedimentary processes). Autochthonous sediments derived from dissolution of the dolomite cave walls only contributes between 5-10 % of the total clastic sediment budget in the cave and consist chiefly of secondary diagenetic quartz and chert. Chapters 3 and 5 are concerned with the sedimentology of the cave and the results obtained therein demonstrate that once sediments are deposited into the cave they are subjected to a new suite of ongoing, cave-related processes, physically and chemically, resulting in different sediment types and facies architectures that distinguishes them from those on surface. These internal processes modify the mineral species ratios and chemical concentrations, differentiating them from the surface sediments, yet retaining distinct signatures that traces them to surface, e.g., mineral species composition and detrital zircon populations (Chapter 4). Processes taking place in the cave include erosion and reworking of older sedimentary units and redistribution and redeposition into new deposits, via fracture systems interconnecting chambers further and deeper into the cave. Sediment composition and modification is also microbially controlled within the cave. Specifically, biochemical processes referred to as chemoautotrophy, in which microbially induced oxidation of metallic cations occurs in certain facies.

The results from Chapter 5 describe a new cave sediment process that was observed within the Dinaledi Chamber. The process, termed sedimentary autobrecciation, occurs through desiccation and subsequent disintegration of the laminated orange red mud (LORM) facies. During this process the sediment brecciates, and the resulting mud clasts accumulate and form themselves a new facies, the unlithified mud clast breccia (UMCB) facies. Currently, this process occurs primarily in the Dinaledi Chamber, but UMCB facies have also been observed in the Lesedi, Postbox, and Superman chambers, as well as along some passageways between these chambers. In contrast, the older and lithified mud clast breccia (LMCB) facies has a much more extensive distribution throughout the cave and demonstrates that sedimentary autobrecciation occurred on a much larger scale than is currently the case. Understanding this process was a critical element of the project because the *Homo naledi* fossils are preserved within this unusual facies. The formation of the unlithified mud clast breccia deposits is a slow process, with first order formation rates estimated to be ~8 x 10^{-4} mm/year. The slow formation of the unlithified mud clast breccia facies sediments and the absence of younger laminated mud (LORM) facies succeeding these deposits, indicates that conditions in the Dinaledi chamber were probably stable and dry for most of their depositional history, and strongly argues against *Homo naledi* being transported by fluvial mechanisms before or after their remains entered the cave.

The many aspects of this study help to better understanding the interplay between local geomorphology and landscape dynamics, and their quantitative and qualitative impact on the sediment deposits in Rising Star Cave and the taphonomical implications for *Homo naledi.* Some of the methods applied in this work are not typically applied in cave settings, like the application of U-Pb detrital zircon sediment provenance to test for the cave sediment origin, and mineral liberation analysis to test for compositional differences between cave and surface sediments. Although detailed information regarding the sediment provenance and their source rocks did not prove possible, the combination of this approach with mineral liberation analysis and dolomite dissolution experiments proved this approach to be a useful application in determining sediment budget, mineral composition and sediment source. This study confirmed that the origin of most of the cave sediments are local with respect to surface sediments, but that they did not primarily derive from weathering of the dolomite host. Indeed, the results of this work indicate that much of the sediment currently present on the landscape and filling the caves is probably recycled many times over the course of tens of millions of years, with the most recent sediment source likely being the Karoo Supergroup, which is only know from a few erosional remnants on the landscape in the Cradle of Humankind today. The data suggests that Karoo sediments likely covered much of the Rising Star Cave landscape and other portions of the Cradle of Humankind. These now eroded Karoo sediments formed largely the source of the sediment on surface and in the cave. These results might appear straightforward, perhaps even expected, but the methods applied here demonstrate that these hypotheses can be tested. This approach has not been applied in previous studies on caves and cave sediments elsewhere in the Cradle of Humankind, but this study has demonstrated that the methods are significant and provide important new insights regarding cave geology, and it is recommended that these techniques are applied on other caves also. This work can be further expanded by testing the regional source and sink provenance of the zircon populations obtained from the cave and surface sediments to reconstruct an even broader and more detailed story regarding the source and recycling history of the sediments. This approach is considered outside the scope of this study, but deserves further investigation in future studies.

There is still much work to be done, and some of the work provided in this thesis will undoubtedly be revised and refined along its way. But my hope is that this work has positively contributed to the science of cave geology, providing several novel and useful tool kits, and elucidating on a few new fundamental aspects of the science that hopefully will be considered and implemented in the work of future generations of cave geologists to come.

Thesis References

Adams, J.W., Herries, A.I.R., Kuykendall, K.L. and Conroy, G.C. (2007) Taphonomy of a South African cave: geological and hydrological influences on the GD 1 fossil assemblage at Gondolin, A Plio-Pleistocene paleocave system in the Northwest Province, South Africa. *Quaternary Science*, 26, 2526-2543.

Aksu, I., Bazilevskaya, E. and Karpyn, Z.T. (2015) Swelling of clay minerals in unconsolidated media and its impact on permeability. *GeoResJ*, 7, 1-13.

Albrecht, B.A. and Benson, C.H. (2001) Effect of desiccation on compacted natural clays. *Journal of Geotechnical and Geoenvironmental Engineering*, 127, 67-75.

Alidibirov, M. and Panov, V. (1998) Magma fragmentation dynamics: experiments with analogue porous low-strength material. *Bulletin of Volcanology,* 59, 481-489.

Appelo, C.A.J. and Postma, D. (1999) Variable dispersivity in a column experiment containing MnO_2 and FeOOH-coated sand. *Journal of Contaminant Hydrology*, 40, 95-106.

ASTM D421-85 (2007) Standard Practice for Dry Preparation of Soil Samples for Particle-Size Analysis and Determination of Soil Constants (Withdrawn 2016), ASTM International, West Conshohocken, PA, 2007, www.astm.org

ASTM D422-63 (2007) Standard Test Method for Particle-Size Analysis of Soils (Withdrawn 2016), ASTM International, West Conshohocken, PA, 2007, www.astm.org

Bacon, A.M., Demeter, F., Duringer, P., Helm, C., Bano, M., The Long, V., Thi Kim Thuy, N., Antoine, P.O., Thi Mai, B., Thi Mai Huong, N., Dodo, Y., Chabaux, F. and Rihs, S. (2008) The Late Pleistocene Duoi U'Oi cave in northern Vietnam: palaeontology, sedimentology, taphonomy and palaeoenvironments. *Quaternary Science Reviews*, 27, 1627-1654.

Berger, L.R. and Tobias, P.V. (1994) New discoveries at the early hominid site of Gladysvale, South Africa. *South African Journal of Science*, 90, 223-226.

Berger, L.R., De Ruiter, D.J., Churchill, S.E., Schmid, P., Carlson, K.J., Dirks, P.H.G.M. and Kibii, J.M. (2010) *Australopithecus sediba*: a new species of *Homo*-like australopith from South Africa. *Science*, 328, 195-204.

Berger, L.R., De Ruiter, D.J., Steininger, C.M. and Hancox, J. (2003) Preliminary results of excavations at the newly investigated Coopers D deposit, Gauteng, South Africa. *South African Journal of Science*, 99, 276-278.

Berger, L.R., De Ruiter, D.J., Steininger, C.M. and Hancox, J. (2003) Preliminary results of excavations at the newly investigated Coopers D deposit, Gauteng, South Africa. *South African Journal of Science*, 99, 276-278.

Berger, L.R., Elliott, M.C., Peixotto, B., Morris, H., Feuerriegel, E.M., Tucker, S.J., Kruger, A., Hunter, R., Van Rooyen, D., Ramalepa, M., Tsikoane, M., Roberts, E., Spandler, C., Dirks, P. and Hawks, J. (2018) A new naming scheme for the Dinaledi Chamber System and associated antechambers and passages of the Rising Star cave system, South Africa. *American Association of Physical Anthropologists Program and Abstracts* 2018, 124.

Berger, L.R., Hawks, J., De Ruiter, D.J., Churchill, S.E., Schmid, P., Delezene, L.K., Kivell, T.L., Garvin, H.M., Williams, S.A., DeSilva, J.M., Skinner, M.M., Musiba, C.M., Cameron, N., Holliday, T.W., Harcourt-Smith, W., Ackermann, R.R., Bastir, M., Bogin, B., Bolter, D., Brophy, J., Cofran, Z.D., Congdon, K.A., Deane, A.S., Dembo, M., Drapeau, M., Elliott., M.C., Feuerriegel, E.M., Garcia-Martinez, D., Green, D.J., Gurtov, A., Irish, J.D., Kruger, A., Laird, M.F., Marchi, D., Meyer, M.R., Nalla, S., Negash, E.W., Orr, C.M., Radovcic, D., Schroeder, L., Scott, J.E., Throckmorton, Z., Tocheri, M.W., Van Sickle, C., Walker, C.S., Wei, P. and Zipfel, B. (2015) *Homo naledi*, a new species of the genus *Homo* from the Dinaledi Chamber, South Africa. *eLife* 4:e09560. doi: 10.7554/eLife.09560

Berger, L.R., Hawks, J., Dirks, P.H.G.M., Elliott, M. and Roberts, E.M. (2017) *Homo naledi* and Pleistocene hominin evolution in subequatorial Africa. *eLife* 6:e24234. doi: 10.7554/eLife.24234

Berger, L.R., Keyser, A.W. and Tobias, P.V. (1993) Gladysvale: First early hominid site discovered in South Africa since 1948. *American Journal of Physical Anthropology*, 92, 107-111.

Beukes, N.J. (1987) Facies relations, depositional environments and diagenesis in a major early Proterozoic stromatolitic carbonate platform to basinal sequence, Campbellrand Subgroup, Transvaal Supergroup, southern Africa. *Sedimentary Geology*, 54, 1-46.

Bosch, R.F. and White, W.B. (2007) Lithofacies and transport of clastic sediments in karstic aquifers. In: Studies of Cave Sediments Physical and Chemical Records of Paleoclimate (Eds I.D. Sasowski and J.E. Mylroie) revised edn., pp. 1-22. Kluwer Academic/Plenum Publishers, New York.

Braga, J., Thackeray, J.F., Bruxelles, L., Dumoncel, J. and Fourvel, J. (2017) Stretching the time span of hominin evolution at Kromdraai (Gauteng, South Africa): recent discoveries. *Human Palaeontology and Prehistory*, 16, 58-70.

Braga, J., Thackeray, J.F., Dumoncel, J., Descouens, D., Bruxelles, L., Loubes, J., Kahn, J., Stamponi, M., Bam, L., Hoffman, J., De Beer, F. and Spoor, F. (2013) A new partial temporal bone of a juvenile hominin from the site of Kromdraai B (South Africa). *Journal of Human Evolution*, 65, 447-456.

Brain, C.K. (1981) The hunters or the hunted? Introduction to African cave taphonomy. The University of Chicago Press, Chicago, pp. 376.

Brain, C.K. (1993) Swartkrans: A Cave's Chronicle of Early Man. Transvaal Museum, Pretoria.

Brain, C.K. (1995) The Influence of Climatic Changes on the Completeness of the Early Hominin Record in Southern African Caves, with Particular Reference to Swartkrans. In: Palaeoclimate and Evolution, with Emphasis on Human Origins (Ed. E.S. Vrba), pp. 385-424. Yale University Press, New Haven.

Broom, R. (1936) A new fossil anthropoid skull from South Africa. *Nature*, 138, 486-488.

Broom, R., and Schepers, G.W.H. (1946) The South African Fossil Ape-Men, the australopithecinae. Pretoria: Transvaal Museum Memoir No. 2.

Brown, P., Sutikna, T., Morwood, M.J., Soejono, R.P., Jatmiko, Wayhu Saptomo, E. and Rokus Due Awe. (2004) A new small-bodied hominin from the Late Pleistocene of Flores, Indonesia. *Nature*, 431, 1055-1061.

Bruxelles, L., Clarke, R.J., Maire, R., Ortega, R. and Stratford, D. (2014) Stratigraphic analysis of the Sterkfontein StW 573 *Australopithecus* skeleton and implications for its age. *Journal of Human Evolution*, 70, 36-48.

Bull, P.A. (1981) Some fine-grained sedimentation phenomena in caves. *Earth Surface Processes and Landforms*, 6, 11-22.

Button, A. (1973) The stratigraphic history of the Malmani Dolomite in the eastern and north-eastern Transvaal. *Transactions of the Geological Society of South Africa*, 76, 229-247.

Butzer, K.W. (1976) Lithostratigraphy of the Swartkrans Formation. *South African Journal of Science*, 72, 136-141.

Butzer, K.W. (1981) Cave Sediments, Upper Pleistocene Stratigraphy and Mousterian Facies in Cantabrian Spain. *Journal of Archaeological Science,* 8, 133-183.

Calder, E.S., Luckett, R., Sparks, R.S.J. and Voight, B. (2002) Mechanisms of lava dome instability and generation of rockfalls and pyroclastic flows at Soufriere Hills Volcano, Montserrat. Geological Society of London Memoirs, 21, 173-190.

Carney, J.N., Aldiss, D.T. and Lock, N.P. (1994) The Geology of Botswana, Geological Survey Department Bulletin Series, Volume 37, pp. 113.

Catuneanu, O. and Eriksson, P.G. (2002) Sequence stratigraphy of the Precambrian Rooihoogte-Timeball Hill rift succession, Transvaal Basin, South Africa. *Sedimentary Geology*, 147, 71-88.

Catuneanu, O. Wopfner, H., Eriksson, P.G., Cairncross, B., Rubidge, B.S., Smith, R.M.H. and Hancox, P.J. (2005) The Karoo basins of south-central Africa. *Journal of African Earth Sciences*, 43, 211-253.

Caumartin, V. (1963) Review of the microbiology of underground environments. *National Speleological Society Bulletin*, 25, 1-14.

Clarke, R.J. (1998). First ever discovery of a well-preserved skull and associated skeleton of Australopithecus. *South African Journal of Science*, 94, 460-463.

Clarke, R.J. (2007) A deeper understanding f the stratigraphy of Sterkfontein fossil hominid site. *Transactions of the Royal Society of South Africa*, 61:2, 111-120. doi: 10.1080/00359190609519960

Clarke, R.J. (2008) Latest information on Sterkfontein's *Australopithecus* skeleton and a new look at *Australopithecus*. *South African Journal of Science*, 104, 443-449.

Clarke, R.J. and Tobias, P.V. (1995) Sterkfontein Member 2: foot bones of the oldest South African hominid. *Science* 269, 521-524.

Collias, E.E., Rona, M.R., McManus, D.A. and Creager, J.S. (1963) Machine processing of geological data. University of Washington Technical Report Number 87, 119pp

Cornell, D.H. and Schütte, S.S. (1995) A volcanic-exhalative origin for the world’s largest (Kalahari) Manganese field. *Mineralium Deposita*, 30, 146–151.

Dart, R.A. (1925) *Australopithecus Africanus*, the Man-Ape of South Africa, *Nature*, 115, 195-199.

De Ruiter, D.J. (2003) Revised faunal list for Members 1–3 of Swartkrans, South Africa. Annals of the Transvaal Museum, 40, 29–41.

De Ruiter, D.J., Pickering, R., Steininger, C.M., Kramers, J.D., Hancox, P.J., Churchill, S.E., Berger, L.R. and Backwell, L. (2009) *Journal of Human Evolution*, 56, 497-513.

Deer, W.A., Howie, R.A. and Zussman, J. An introduction to the rock-forming minerals, 2nd ed, Longman Scientific & Technical, UK. 549 pp.

deMenocal, P.B. (2004) African climate change and faunal evolution during the Pliocene–Pleistocene. *Earth and Planetary Science Letters*, 220, 3–24.

deMenocal, P.B. (2011) Climate and human evolution. *Science*, 331, 540–541.

Demeter, F., Shackleford, L., Bacon, A.M., Duringer, Ph., Westaway, K., Sayavongkhamdy, T., Braga, J., Phonephanh, S., Khamdalavong, P., Ponche, J.-L., Wang, H., Lundstrom, C., Patole-Edoumba, E. and Karpoff, A.-M. (2012) Anatomically modern human in Southeast Asia (Laos) by 46 ka. *Proceedings of the National Academy of Science*, 109, 14375-14380. doi: 10.1073/pnas.1208104109

Demeter, F., Shackleford, L., Westaway, K., Duringer, P., Bacon, A.M., Ponche, J., Wu, X., Sayavongkhamdy, T., Zhao, J.X., Barnes, L., Boyon, M., Sichanthongtip, P., Sénégas, F., Karpoff, A.M., Patole-Edoumba, E., Coppens, Y. and Braga, J. Early modern humans and morphological variation in Southeast Asia: Fossil evidence from Tam Pa Ling, Laos. *PloS One*. doi:10.1371/journal.pone.0121193

Dirks, P.H.G.M. and Berger, L.R. (2013). Hominin-bearing caves and landscape dynamics in the Cradle of Humankind, South Africa. *Journal of African Earth Sciences*, 78, 109-131.

Dirks, P.H.G.M., Berger, L.R., Roberts, E.M., Kramers, J.D., Hawks, J., Randolph-Quinney, P.S., Elliott, M., Musiba, C.M., Churchill, S.E., de Ruiter, D.J., Schmid, P., Backwell, L.R., Belyanin, G.A., Boshof, P., Eaves, K.L., Feuerriegel, E.M., Gurtov, A., Harrison, J du G., Hunter, R., Kruger, A., Morris, H., Makhubela, T.V., Peixotto, B. and Tucker, S. (2015) Geological and taphonomic evidence for deliberate body disposal by the primitive hominin species *Homo naledi* from the Dinaledi Chamber, South Africa. *eLife* 4:e09561. http://dx.doi.org/10.7554/eLife.09561

Dirks, P.H.G.M., Kibii, J.M., Kuhn, B.F., Steininger, C., Churchill, S.E., Kramers, J.D., Pickering, R., Farber, D.L., Mériaux, A., Herries, A.I.R., King, G.C.P. and Berger, L.R. (2010) Geological setting and age of *Australopithecus sediba* from southern Africa. *Science*, 328, 205-208. DOI: 10.1126/science.1184950

Dirks, P.H.G.M., Placzek, C.J., Fink, D., Dosseto, A and Roberts, E. (2016) Using 10Be cosmogenic isotopes to estimate erosion rates and landscape changes during Plio-Pleistocene in the Cradle of Humankind, South Africa. *Journal of Human Evolution*, 96, 19-34.

Dirks, P.H.G.M., Roberts, E.M., Hilbert-Wolf, H., Kramers, J.D., Hawks, J., Dossetto, A., Duval, M., Elliott, M., Evans, M., Grün, R., Hellstrom, J., Herries, A.I.R., Joannes-Boyau, R., Makhubela, T.V., Placzek, C.J., Robbins, J., Spandler, C., Wiersma, J., Woodhead, J. and Berger, L.R. 2017. The age of *Homo naledi* and associated sediments in the Rising Star cave, South Africa. *eLife* 6:e24231. http://dx.doi.org/10.7554/elife.24231

Dowding, C.E. and Fey, M.V. (2007) Morphological, chemical and mineralogical properties of some manganese-rich oxisols derived from dolomite in Mpumalanga province, South Africa. *Geoderma*, 141, 23-33.

Egeland, C.P., Domínguez-Rodrigo, M., Pickering, T.R., Menter, C.G. and Heaton, J.L. (2018) Hominin skeletal part abundances and claims of deliberate body disposal of corpses in the Middle Pleistocene. *Proceedings of the National Academy of Sciences*, doi/10.1073/pnas.1718678115.

Ellwood, B.B., Petruso, K.M., Harrold, F.B. and Korkuti, M. (1996) Paleoclimate characterization and intra-site correlation using magnetic susceptibility measurements: an example from Konispol Cave, Albania. *Journal of Field Archaeology*, 23, 263-271.

Els, B.G., Van den Berg, W.A. and Mayer, J.J. (1995) The Black Reef Quartzite Formation in the western Transvaal: sedimentological and economic aspects, and significant for basin evolution. *Mineralium Deposita*, 30, 112-123.

Engel, A.S. (2012) Chemoautotrophy. In: Encyclopedia of Caves (Eds W.B. White and D.C. Culver), 2nd edn, pp. 125–134. Academic Press, Oxford.

Eriksson K.A. (1977) Tidal flat and subtidal sedimentation in the 2250 m.y. Malmani Dolomite, Transvaal, South Africa. *Sedimentary Geology*, 18, 223-244.

Eriksson K.A. and Warren, J.K. (1983) A paleohydrologic model for early Proterozoic dolomitization and silicification. *Precambrian Research*, 21, 299-321.

Eriksson P.G., Altermann W. and Hartzer F.J. (2006) The Transvaal Supergroup and its precursors. In: The Geology of South Africa (Eds M.R. Johnson, C.R. Anhaeusser and R.J. Thomas), pp. 237-260. Geological Society of South Africa Press, Pretoria.

Eriksson, K.A. and Truswell, J.F. (1974) Tidal flat associations from a Lower Proterozoic carbonate sequence in South Africa. *Sedimentology*, 21, 293-309.

Eriksson, P.G. and Altermann, W. (1998) An overview of the geology of the Transvaal Supergroup dolomites (South Africa). *Environmental Geology*, 36, 179-188.

Eriksson, P.G. and Reczko, B.F.F. (1995) The sedimentary and tectonic setting of the Transvaal Supergroup floor rocks to the Bushveld complex. *Journal of African Earth Sciences*, 21, 487-504.

Eriksson, P.G., Altermann, W. and Hartzer, F.J. (2006) The Transvaal Supergroup and its precursors. In: M.R. Johnson, C.R. Anhaeusser and R.J. Thomas, eds. The Geology of South Africa. The Geological Society of South Africa, Pretoria, 237-260.

Eriksson, P.G., Altermann, W., Catuneanu, O., Van der Merwe, R. and Bumby, A.J. (2001) Major influences on the evolution of the 2.67-2.1 Ga Transvaal basin, Kaapvaal craton. *Sedimentary Geology*, 141-142, 205-231.

Eriksson, P.G., Reczko, B.F.F. (1995) The sedimentary and tectonic setting of the Transvaal Supergroup floor rocks to the Bushveld Complex. *Journal of African Earth Sciences*, 21, 487-504.

Eriksson, P.G., Reczko, B.F.F., Merkle, R.K.W., Schreiber, U.M., Engelbrecht, J.P., Res, M. and Snyman, C.P. (1994) Early Proterozoic black shales of the Timeball Hill Formation, South Africa: volcanogenic and palaeoenvironmental influences. *Journal of African Earth Sciences*, 18, 325-337.

Farrand, W.R. (2001) Sediments and stratigraphy in rock shelters and caves: a personal perspective on principles and pragmatics. *Geoarchaeology*, 16, 537-557.

Farrant, A.R., and Smart, P.L. (2011) Role of sediment in Speleogenesis; sedimentation and paragenesis. *Geomorphology*, 134, 79-93.

Feigl, F. (1937) Qualitative analysis by spot tests. Nordemann Publishing Company, New York, 400 pp.

Filippov, A.G. (2000) Speleogenesis of Botovskaya Cave, Eastern Siberia, Russia. In: Speleogenesis: Evolution of Karst Aquifers (Eds A.B. Klimchouk, D.C. Ford, A.N. Palmer and W. Dreybrodt), pp 282-286. National Speleological Society, Huntsville.

Folk, R.L. (1954). The distinction between grain size and mineral composition in sedimentary rock nomenclature. *Journal of Geology*, 62 (4), 344–359.

Folk, R.L. (1974) Petrology of Sedimentary Rocks. Hemphill Publishing Co., Austin, TX, 182 pp.

Ford, D.C. and Williams, P. (2007) Karst Hydrogeology and Geomorphology. Wiley, Chichester, 562 pp.

Forestier, H., Sophady, H., Puaud, S., Celiberti, V., Frère, S., Zeitoun, V., Mourer-Chauviré, Mourer, R., Than, H. and Billault, L. (2015) The Hoabinhian from Laang Spean Cave in its stratigraphic, chronological, typo-technological and environmental context (Cambodia, Battambang province). *Journal of Archaeological Science: Reports*, 3, 194-206.

Ghiorse, W.C. (1984) Biology of iron- and manganese-depositing bacteria. *Annual Review Microbiology*, 38, 515-550.

Gillieson, D. (1986) Cave sedimentation in the New Guinea Highlands. *Earth Surface Processes and Landforms*, 11, 533-543.

Gillieson, D. (1996) Caves: Processes, Development and Management, Blackwell Science, Oxford, 324 pp.

Gommery, D., Badenhorst, S., Sénégas, F., Potze, S. and Kgasi, L. (2012) Minnaar’s Cave: a Plio-Pleistocene site in the Cradle of Humankind, South Africa: its history, location, and fauna. *Annals of the Ditsong National Museum of Natural History*, 2, 19–31.

Gommery, D., Thackeray, J.F., Sénégas, F. Potze, S. and Kgasi, L. (2008) The earliest primate (*Parapapio* sp.) from the Cradle of Humankind World Heritage site (Waypoint 160, Bolt's Farm, South Africa). *South African Journal of Science*, 104:9–10, 405–408.

Hanson, R.E., Gose, W.A., Crowley, J.L., Ramezani, J., Bowring, S.A., Bullen, D.D., Hall, R.P., Pancake, J.K. and Mukwakwami, J. (2004) Paleoproterozoic intraplate magmatism and basin development on the Kaapvaal Craton: Age, paleomagnetism and geochemistry of ~1.93 to ~1.87 Ga post-Waterberg dolerites. *South African Journal of Geology*, 107, 233-254.

Hawker, L.C., and Thompson, J.G. (1988) Weathering sequence and alteration products in the genesis of the Graskop manganese residua, Republic of South Africa. *Clays and Clay Minerals*, 36-5, 448-454.

Hawks, J., Elliott, M., Schmid, P., Churchill, S.E., De Ruiter, D.J., Roberts, E.M., Hilbert-Wolf, H., Garvin, H.M., Williams, S.A., Delezene, L.K., Feuerriegel, E.M., Randolph-Quinney, P., Kivell, T.L., Laird, M.F., Tawane, G., DeSilva, J.M., Bailey, S.E., Brophy, J.K., Meyer, M.R., Skinner, M.M., Tocheri, M.W., VanSickle, C., Walker, C.S., Campbell, T.L., Kuhn, B., Kruger, A., Tucker, S., Gurtov, A., Hlophe, N., Hunter, R., Morris, H., Peixotto, B., Ramalepa, M., Van Rooien, D., Tsikoane, M., Boshoff, P., Dirks, P.H.G.M. and Berger, L.R. (2017) New fossil remains of Homo naledi from the Lesedi Chamber, South Africa. *eLife* 6:e24232. DOI: 10.7554/eLife.24232

Herries, A.I.R. and Adams, J.W. (2013) Clarifying the context, dating and age range of the Gondolin hominins and *Paranthropus* in South Africa. *Journal of Human Evolution*, 65, 676-681.

Herries, A.I.R. and Shaw, J. (2011) Palaeomagnetic analysis of the Sterkfontein palaeocave deposits: Implications for the age of the hominin fossils and stone tool industries. *Journal of Human Evolution*, 60, 523-539.

Herries, A.I.R., Kappen, P., Kegley, A.D.T., Patterson, D., Howard, D.L., De Jonge, M.D., Potze, S. and Adams, J.W. (2014) Palaeomagnetic and synchrotron analysis of >1.95 Ma fossil-bearing palaeokarst at Haasgat, South Africa. *South African Journal of Science*, 110, 1-12. http://dx.doi.org/10.1590/sajs.2014/20130102

Herries, A.I.R., Reed, K.E., Kuykendall, K.L. and Latham, A.G. (2006) Speleology and magnetostratigraphic chronology of the Buffalo cave fossil site, Makapansgat, South Africa. *Quaternary Research*, 66, 233-245.

Herries. A.I.R., Adams, J.W., Joannes-Boyau, R., Armstrong, B., Baker, S., Blackwood, A.F., Boschian, G., Caruana, M.V., Penzo-Kajewski, P., Murszewski, A. and Rovinski, D.S. (2019) Integrating palaeocaves into landscapes: An analysis of cave levels and karstification history across the Gauteng Malmani dolomite, South Africa. *Quaternary Science Reviews*, 220, 31-334.

Hughes, A. R. and Tobias, P.V. (1977) A fossil skull probably of the genus Homo from Sterkfontein, Transvaal. *Nature*, 265, 310-312.

Johnson, M.R., Anhaeusser, C.R. and Thomas, R.J. (2006) The Geology of South Africa. Geological Society of South Africa and Council for Geoscience Publication, Pretoria, 691 pp.

Johnson, M.R., van Vuuren, C.J., Visser, J.N.J., Cole, D.I., de Wickens, H., Christie, A.D.M. and Roberts, D.L. (1997) The Foreland Karoo Basin, South Africa. In: African Basins (Ed R.C. Selley), pp. 269–317. Sedimentary Basins of the World 3.

Johnson, M.R., van Vuuren, C.J., Visser, J.N.J., Cole, D.I., Wickens, H.de V., Christie, A.D.M., Roberts, D.L. and Brandl, G. (2006). Sedimentary rocks of the Karoo Supergroup. In: The Geology of South Africa. (Eds. M.R. Johnson, C.R. Anhaeusser and R.J. Thomas), pp. 462–499. The Geological Society of South Africa, Pretoria.

Kadlec, J., Chadima, M., Lisa, L., Hercman, H., Osintev, A. and Oberhänsli, H. (2008) Clastic cave deposits in Botovskaya Cave (Eastern Siberia, Russian Federation). *Journal of Cave and Karst Studies*, 70, 142-155.

Kavalieris, I. and Martini, J. (1976) Structural controls on some western Transvaal caves. *South African Journal of Science*, 72, 308-309.

Keyser, A.W. (2000) The Drimolen skull: the most complete australopithecine cranium and mandible to date. *South African Journal of Science*, 96, 189-197.

Keyser, A.W., Menter, C.G., Moggi-Cecchi, J., Pickering, T.R. and Berger, L.R. (2000) Drimolen: a new hominid-bearing site in Gauteng, South Africa. *South African Journal of Science*, 96, 193-197.

Kivell, T.L., Deane, A.S., Tocheri, M.W., Orr, C.M., Schmid, P., Hawks, J., Berger, L.R. and Churchill, S.E. (2015) The hand of *Homo naledi*. *Nature Communications*, 6, 1-9. doi: 10.1038/ncomms9431

Knapp, E.P., Terry, D.O., Harbor, D.J. and Thren, R.C. (2007) Reading Virginia's Paleoclimate from the Geochemistry and Sedimentology of Clastic Cave Sediments. In: Studies of Cave Sediments Physical and Chemical Records of Paleoclimate (Eds I.D. Sasowsky and J. Mylroie) revised edn, pp. 95-106. Springer, Dordrecht.

Kröner, A. and Hofmann, A. (2019) The Archaean Geology of the Kaapvaal Craton, Southern Africa. Springer International Publishing, Switzerland, 302 pp.

Kröner, A., Jaeckel, P., Brandl, G., Nemchin, A.A. and Pidgeon, R.T. (1999) Single zircon ages for graitoid gneisses in the Central Zone of the Limpopo Belt, Southern Africa and geodynamic significance. *Precambrian Research*, 93:4, 299-337.

Kruger, A., Randolph-Quinney, P. and Elliott, M. (2016) Multimodal spatial mapping and visualization of Dinaledi Chamber and Rising Star Cave. *South African Journal of Science*, 112, 1-11. http://dx.doi.org/10.17159/sajs.2016/20160032

Krumbein, W.C. and Pettijohn, F.J. (1938) Manual of Sedimentary Petrography. Appleton-Century-Crofts, New York, 549 pp.

Latham, A.G., Herries, A.I.R. and Kuykendall, K. (2003) The formation and sedimentary infilling of the Limework Cave, Makapansgat, South Africa. *Palaeontologia Africana*, 39, 69-82.

Laureano, F.V., Karmann, I., Granger, D.E., Auler, A.S., Almeida, R.P., Cruz, F.W., Strícks, N.M. and Novello, V.F. (2016) Two million years of river and cave aggradation in NE Brazil: Implications for speleogenesis and landscape evolution. *Geomorphology*, 273, 63-77. http://dx.doi.org/10.1016/j.geomorph.2016.08.009.

Liu, Z., Ooi, K., Kanoh, H., Tang, W. and Tomida, T. (2000) Swelling and Delamination Behaviors of Birnesite-Type Manganese Oxide by Intercalation of Tetraalkylammonium Ions. *Langmuir*, 16, 4154-4164.

Makhubela, T.V, Kramers, J.D., Belyanin, G.A., Dirks P.H.G.M. and Roberts E.M. (2017) Proterozoic 40Ar/39Ar ages from cave deposits of the Malapa, Sterkfontein and Dinaledi fossil sites, Cradle of Humankind, South Africa. *South African Journal of Geology*, 120, 21-44. DOI: 10.25131/gssajg.120.1.21

Makhubela, T.V., 2019. Multiple isotope studies relating to cave development and landscape evolution in the Cradle of Humankind, South Africa. Ph.D. Dissertation, University of Johannesburg.

Makhubela, T.V., Kramers, J.D., Scherler, D., Wittmann, H., Dirks, P.H.G.M. and Winkler, S.R., (2019) Effects of long soil surface residence times on apparent cosmogenic nuclide denudation rates and burial ages in the Cradle of Humankind, South Africa. *Earth Surface Processes and Landforms,* doi:10.1002/esp.4723

Martin, D.McB., Clendenin, C.W., Krapez, B. and McNaughton, N.J. (1998) Tectonic and geochronological constraints on late Archaean and Palaeoproterozoic stratigraphic correlation within and between the Kaapvaal and Pilbara Cratons. *Journal of the Geological Society of London*, 155, 311-322.

Martini, I. (2011) Cave clastic sediments and implications for speleogenesis: New insights from the Mugnano Cave (Montagnola Senese, Northern Apennines, Italy). *Geomorphology*, 134, 452-460.

Martini, J.E.J. (2006) Karsts and caves. In: The Geology of South Africa (Eds M.R. Johnson, C.R. Anhaeusser and R.J. Thomas). pp. 661–668. Geological Society of South Africa and Council for Geoscience Publication, Pretoria.

Martini, J.E.J., Wipplinger, P.E., Moen, H.F.G. and Keyser, A. (2003) Contribution to the speleology of Sterkfontein Cave, Gauteng Provence, South Africa. *International Journal of Speleology*, 32, 43-69.

Mellors, R.A., Waitt, R.B. and Swanson, D.A. (1988) Generation of pyroclastic flows and surges by hot-rock avalanches from the dome of Mount St. Helens Volcano, USA. *Bulletin of Volcanology*, 50, 14-25.

Miall, A. (2006) Methods of Architectural-Element Analysis. In: The Geology of Fluvial Deposits. Sedimentary Facies, Basin Analysis and Petroleum Geology (Ed A. Miall), pp. 75-98. Springer-Verlag, Berlin Heidelberg New York.

Miall, A. (2010) Alluvial Deposits. In: Facies Models 4 (Eds N.P. James and R.W. Dalrymple), pp. 105-138. Geological Association of Canada, Newfoundland.

Morley, M.W., Goldberg, P., Sutikna, T., Tocheri, M.W., Prinsloo, L.C., Jatmiko, Wayhu Saptomo, E., Wasisto, S. and Roberts, R.G. (2017) Initial micromorphological results from Liang Bua, Flores (Indonesia): Site formation processes and hominin activities at the type locality of *Homo floresiensis*. *Journal of Archaeological Science*, 77, 125-142.

Morwood, M.J., Soejono, R.P., Roberts, R.G., Sutikna, T., Turney, C.S.M., Westaway, K.E., Rink, W.J., Zhao, J.X., Van Den Bergh, G.D., Rokus Due Awe, Hobbs, D.R., Moore, M.W., Bird, M.I. and Fifield, L.K. (2004) Archaeology and age of a new hominin from Flores in eastern Indonesia. *Nature*, 431, 1087-1091.

Naidoo M. (2016) Geophysics of the Rising Star Cave System. Honors thesis: University of the Witwatersrand, Johannesburg, South Africa. 34 pp.

Nogueira, M.A., Nehl, U., Hampp, R., Poralla, K. and Cardoso, E.J.B.N. (2007) Mycorrhiza and soil bacteria influence extractable iron and manganese in soil and uptake by soybean. *Plant Soil*, 298, 273-284. DOI 10.1007/s11104-007-9379-1

Oberholzer, J.D. and Eriksson P.G. (2000) Subaerial volcanism in the Palaeoproterozoic Hekpoort Formation (Transvaal Supergroup), Kaapvaal craton. *Precambrian Research,* 101, 193-210.

O'Connor, S., Barham, A., Aplin, K. and Maloney, T. (2017) Cave stratigraphies and cave breccias: Implications for sediment accumulation and removal models and interpreting the record of human occupation. *Journal of Archaeological Science*, 77, 143-159.

Palmer, A.N. (1991) Origin and morphology of limestone caves. *Geological Society of America Bulletin*, 103, 1-21.

Palmer, A.N. (2011) Distinction between epigenic and hypogenic maze caves. *Geomorphology*, 134, 9-22.

Palmer, A.N. (2012). Cave Geology, pp. 454. Cave Books, Dayton, Ohio.

Partridge, T.C. (1973) Geomorphological dating of Cave Openings at Makapansgat, Sterkfontein, Swartkrans and Taung. *Nature,* 246, 75–79. doi: 10.1038/246075a0

Partridge, T.C. (1979) Re-appraisal of the lithostratigraphy of the Makapansgat Limeworks hominid site. *Nature*, 279, 484-488.

Partridge, T.C. (2000) Hominid-bearing cave and tufa deposits. In: The Cenozoic in Southern Africa (Eds T.C. Partridge and R.R. Maud), pp. 100-125. Oxford Monographs on Geology and Geophysics No. 40. Oxford University Press, Oxford.

Partridge, T.C. (2010) Tectonics and geomorphology of Africa during the Phanerozoic. In: Cenozoic Mammals of Africa (Eds L. Werdelin and W.J. Sanders), pp. 3-17. California Scholarship Online doi: http://dx.doi.org/10.1525/California/9780520257214.003.0001.

Partridge, T.C. and Maud, R.R. (1987) Geomorphic evolution of southern Africa since the Mesozoic. *South African Journal of Geology*, 90, 165-184.

Partridge, T.C., Granger, D.E., Caffee, M.W. and Clarke, R.J. (2003) Lower Pliocene hominid remains from Sterkfontein. *Science,* 300, 607-612.

Paton, C., Hellstrom, J., Paul, B., Woodhead, J. and Hergt, J. (2011) Iolite: Freeware for the visualization and processing of mass spectrometric data. *JAAS*, doi: 10.1039/c1ja10172b

Pickering, R. (2006) Regional geology, setting and sedimentology of the Sibudu Cave. *Southern African Humanities*, 18, 123-129.

Pickering, R. and Kramers, J.D. (2010) Re-appraisal of the stratigraphy and determination of new U-Pb dates for the Sterkfontein hominin site, South Africa. *Journal of Human Evolution,* 59, 70-86. doi:10.1016/j.jhevol.2010.03.014

Pickering, R., Hancox, P.J., Lee-Thorp, JA., Grün, R., Mortimer, G.E., McCulloch, M. and Berger, L.R. (2007) Stratigraphy, U-Th chronology, and paleoenvironments at Gladysvle Cave: insights into the climate control of South African hominin-bearing cave deposits. *Journal of Human Evolution*, 53, 602-619.

Pickering, R., Herries, A.I.R., Woodhead, J.D., Hellstrom, J.C., Green, H.E., Paul, B., Ritzman, T., Strait, D.S., Schoville, B.J. and Hancox, P.J. (2018) U-Pb-dated flowstones restrict South African early hominin record to dry climate phases. *Nature Letter,* doi.org/10.1038/s41586-018-0711-0

Pickering, R., Kramers, J.D., Hancox, P.J., De Ruiter, D.J. and Woodhead, J.D. (2011) Contemporary flowstone development links early hominin bearing cave deposits in South Africa. *Earth and Planetary Science Letter*, 306, 23–32. doi: 10.1016/j.epsl.2011.03.019

Pickering, R., Kramers, J.D., Partridge, T., Kodolanyi, J. and Pettke, T. (2010) U-Pb dating of calcite-aragonite layers in peleothems from hominin sites in South Africa by MC-ICP-MS. *Quaternary Geochronology*, 5, 544-558.

Poppe, L.J. and Eliason, A.E. (2008) A Visual Basic program to plot sediment grain-size data on ternary diagrams. *Computers and Geosciences*, 34, 561-565.

Poppe, L.J., Eliason, A.H. and Hastings, M.E. (2003) A Visual Basic program to classify sediments based on gravel-sand-silt-clay ratios. *Computers and Geosciences*, 29:6, 805-809.

Poppe, L.J., Eliason, A.H. and Hastings, M.E. (2004) A Visual Basic program to generate sediment grain-size statistics and to extrapolate particle distributions. *Computers and Geosciences*, 30:7, 791-795.

QGIS.org (2020). QGIS Geographic Information System. Open Source Geospatial Foundation Project. http://qgis.org.

Rincón-Tomás, B., Khonsari, B., Mühlen, D., Wickbold, C., Schäfer, N., Hause-Reitner, D., Hoppert, M. and Reitner, J. (2016) Manganse carbonates as possible relics in Archaen settings. *International Journal of Astrobiology*, 15-3, 219-229.

Robbins, J.L., Dirks, P.H.G.M., Roberts, E.M., Kramers, J.D., Makhubela, T.V., Hilbert-Wolf, H.L., Elliott, M., Wiersma, J., Placzek, C., Evans, M. and Berger, L. (2021) Providing context to the *Homo naledi* fossils: Constraints on the age of sediment deposits in the Rising Star Cave, South Africa. *Chemical Geology*, 567, 1-23. https://doi.org/10.1016/j.chemgeo.2021.120108

Santelli, C.M., Webb, S.M., Dohnalkova, A.C. and Hansel, C.M. (2011) Diversity o fMn oxides produced by Mn(II)-oxidizing fungi. Geochimica et Cosmochimica Acta, 75, 2762-2776.

Sasowski, I.D. (2012) Paleomagnetic records in cave sediments. In: Encyclopedia of Caves (Eds W.B. White and D.C. Culver) 2nd edn, pp. 583-590. Academic Press, Amsterdam.

Sasowski, I.D., Mylroie, J. (2007) Studies of Cave Sediments Physical and Chemical Records of Paleoclimate, revised edition, pp. 329. Springer, The Netherlands.

Sato, H., Fujii, T. and Nakada, S. (1992) Crumbling dacite dome lava and generation of pyroclastic flows at Unzen Volcano. *Nature*, 360, 664-666.

Schindelin, J., Arganda-Carreras, I., Frise, E., Kaynig, V., Longair, M., Pietzsch, T., Preibisch, S., Rueden, C., Saalfeld, S., Schmid, B., Tinevez, J., White, D.J., Hartenstein, V., Eliceire, K., Tomancak, P. and Cardona, A. (2012) Fiji: an open-source platform for biological image analysis. *Nature Methods*, 9(7), 676-682. doi:10.1038/nmeth.2019

Schlee, J.S. (1973) Atlantic continental shelf and slope of the United States—sediment texture of the northeastern part. US Geological Survey Professional Paper 529-L, 64 pp.

Shepard, F.P. (1954) Nomenclature based on sand–silt–clay ratios. *Journal of Sedimentary Petrology*, 24 (3), 151–158.

Springer, G.S. (2012) Clastic sediments in caves. In: Encyclopedia of Caves (Eds W.B. White and D.C. Culver) 2nd edn, pp. 134-140. Academic Press, Amsterdam.

Springer, G.S. and Kite, J.S. (1997) River-derived slackwater sediments in caves along Cheat River, West Virginia. *Geomorphology,* 18, 91-100.

Stute, M. and Schlosser, P. (2000) Atmospheric Noble Gases. In: Environmental tracers in subsurface hydrology. (Eds P. Cook and A. Herczeg) pp. 349-377. Kluwer Academic Publishers, Massachusetts.

Sutikna, T., Tocheri, M.W., Morwood, M.J., Wahyu Saptomo, E., Jatmiko, Rokus Due Awe, Sri Wasisto, Westaway, K.E., Aubert, M., Li, B., Zhao, J.X. Storey, M., Alloway, B.V., Morley, M.W., Meijer, H.J.M., Van Den Bergh, G.D., Grün, R., Dosseto, A., Brumm, A., Jungers, W.L. and Roberts, R.G. (2016) Revised stratigraphy and chronology for *Homo floresiensis* at Liang Bua in Indonesia. *Nature*, 532, 366-369.

Sutton, M.B., Pickering, T.R., Pickering, R., Brain, C.K., Clarke, R.J., Heaton, J.L. and Kuman, K. (2009) Newly discovered fossil- and artifact-bering deposits, uranium-series ages, and Plio-Pleistocene hominids at Swartkrans Cave, South Africa. *Journal of Human Evolution*, 57, 688-696.

Sylvester, P.J. (2012) Use of the Mineral Liberation Analyzer (MLA) for mineralogical studies of sediments and sedimentary rocks. Mineralogical Association of Canada Short Course 42, St. John's NL, Canada, 1-16.

Talma, A.S. and Vogel, J.C. (1992) Late Quaternary paleotemperatures derived from a speleothem from Cango Caves, Cape Province, South Africa. *Quaternary Research,* 37, 203-213.

Taylor, R.M. and Schwertman, U. (1974a) Maghemite in soils and its origin: I. Properties and observations on soil maghemites. *Clay Minerals*, 10:4, 289-298.

Taylor, R.M. and Schwertman, U. (1974b) Maghemite in soils and its origin: II. Maghemite synthesis at ambient temperatures and pH 7. *Clay Minerals*, 10:4, 299-310.

Tebo B.M., Geszvain K. and Lee, S.W. (2010) The Molecular Geomicrobiology of Bacterial Manganese(II) Oxidation. In: Geomicrobiology: Molecular and Environmental Perspective (Eds. L. Barton, M. Mandl and A. Loy), pp. 285-308. Springer, Dordrecht. https://doi-org.elibrary.jcu.edu.au/10.1007/978-90-481-9204-5_13

Tebo, B.M., Johnson, H.A., McCarthy, J.K. and Templeton, A.S. (2005) Geomicrobiology of manganese(II) oxidation. *TRENDS in Microbiology*, 13:9, 421-428.

Thackeray, J.F., De Ruiter, D.J., Berger, L.R. and Van der Merwe, N.J. (2001) Hominid fossils from Kromdraai: a revised list of specimens discovere since 1938. *Annals of the Transvaal Museum*, 38, 43-56.

Tobias, P.V. (1985) Hominid Evolution. Past, Present and Future. Alan R. Liss, New York.

Tobias, P.V. (2000) The fossil hominids. In: The Cenozoic of Southern Africa (Eds. T.C. Partridge and R.R. Maud), pp. 252–276. Oxford University Press, Oxford.

Tobias, P.V., Clarke, R.J. and White, H. (1993) 27th Annual Report of the Palaeo-Anthropology Research Unit, University of the Witwatersrand.

Val, A. (2016) Deliberate body disposal by hominins in the Dinaledi Chamber, Cradle of Humankind, South Africa. *Journal of Human Evolution*, 96, 149-153.

Val, A., Dirks, P.H.G.M., Backwell, L.R., d'Errico, F. and Berger, L. (2015) Taphonomic analysis of the faunal assemblage associated with the hominins (*Australopithecus sediba*) from the Early Pleistocene cave deposits of Malapa, South Africa. *PLoS ONE*, 10(6): e0126904. doi:10.1371/journal.pone.0126904

Valen, V., Mangerud, J., Larsen, E. and Hufthammer, A.K. (1996) Sedimentology and stratigraphy in the Hamnsundhelleren, western Norway. *Journal of Quaternary Science*, 11, 185-201.

Van Zyl, W., Badenhorst, S. and Brink, J. S. (2016) Pleistocene Bovidae from X Cave on Bolt’s Farm in the Cradle of Humankind in South Africa. *Annals of the Ditsong National Museum of Natural History*, 6, 39–73

Vrba, E.S., 1995. The fossil record of African antelopes (Mammalia, Bovidae) in relation to human evolution and paleoclimate. In: Paleoclimate and Evolution with Emphasis on Human Origins (E. Vrba, G. Denton, L. Burckle and T Partridge, Eds.), pp. 262–288. New Haven. Yale University Press.

Wadley, L. and Jacobs, Z. (2006) Sibudu cave: background to the excavations, stratigraphy and dating. *Southern African Humanities*, 18, 1-26.

Watson, V. (1993a) Composition of the Swartkrans bone accumulations, in terms of skeletal parts and animals represented. In: *Swartkrans:* A Cave’s Chronicle of Early Man (Ed. C. Brain), pp. 35-74. Transvaal Museum, Pretoria.

Watson, V. (1993b) Glimpses from Gondolin: a faunal analysis of a fossils site near Broederstroom, Transvaal, South Africa. *Palaeontologica Africana*, 30, 35-42.

White, E.L. (2012) Breakdown. In: *Encyclopedia of Caves* (Eds W.B. White and D.C. Culver) 2nd edn, pp. 68-74. Academic Press, Oxford.

White, W.B. (2007) Cave sediments and paleoclimate. *Journal of Cave and Karst Studies*, 69, 76-93.

Wiersma, J.P., Hilbert-Wolf, H.L., Placzek, C.J., Dirks, P.H. and Roberts, E.M. (2017) Investigating ^{234}U/^{238}U activity ratios and U uptake in vertebrate microfossil teeth from the Rising Star Cave (Cradle of Humankind, South Africa) to reconstruct phreatic water table fluctuations associated with Pleistocene climate change in southern Africa. *Society of Vertebrate Paleontology 77th Annual Meeting, Program and Abstracts*, 37, 213.

Wiersma, J.P., Roberts, E.M. and Dirks, P.H.G.M. (2020). Formation of mud clast breccias and the process of sedimentary autobrecciation in the hominin-bearing (*Homo naledi*) Rising Star Cave system, South Africa. *Sedimentology*, DOI: 10.1111/sed.12666.

Wilkinson, M.J. (1985) Lower-lying and possibly older fossiliferous deposits at Sterkfontein. In: Tobias P. V (Ed). Hominid Evolution: Past, Present and Future. p. 165–170.

Appendix 1

Supplementary data for Chapters 2 & 3

Table A1.1. Cumulative frequency probability data derived from GS-STAT (Poppe et al., 2004) for Rising Star surface and cave sediment samples (n=40).

SAMPLEID	LATITUDE	LONGITUDE	PHI_11	PHI_10	PHI_9	PHI_8	PHI_7	PHI_6.7	PHI_6	PHI_5	PHI_4	PHI_3	PHI_2	PHI_1	PHI_0	PHIM1	PHIM1.5	PHIM2	PHIM3	PHIM4	PHIM5
Surface sediments																					
190517JW1			100	92.32	85.30	82.26	79.96	79.31	78.19	75.62	74.16	69.88	59.88	31.35	11.88	4.13	2.20	1.09	0	0	0
190517JW2			100	82.18	63.38	59.93	57.32	55.65	53.15	49.41	43.99	34.95	27.01	18.06	11.87	4.70	2.96	1.76	0	0	0
190517JW3			100	76.39	73.89	71.81	69.73	68.76	67.79	63.85	58.99	44.09	31.24	19.95	14.81	10.15	7.77	4.55	0	0	0
190517JW4			100	83.01	81.09	79.49	77.51	75.97	74.10	71.15	65.86	52.52	41.61	32.24	25.90	17.77	13.14	7.57	0	0	0
190517JW5			100	84.29	81.47	80.63	78.13	77.30	75.72	72.91	68.57	59.02	51.98	46.03	42.06	36.67	33.55	29.82	0	0	0
190517JW6			100	85.69	83.94	81.51	80.24	79.09	78.27	74.31	71.23	62.69	56.80	51.66	47.86	42.12	38.68	33.97	0	0	0
190517JW7			100	83.37	73.93	72.58	70.23	68.74	67.24	62.01	59.02	51.68	48.39	45.34	41.50	32.20	22.80	13.89	0	0	0
Cave sediments																					
UW101_1783A			100	80.94	60.03	52.61	44.34	39.32	35.27	29.26	26.26	20.24	12.55	4.37	3.12	2.21	1.53	1.13	0	0	0
UW101_1783C			100	78.00	55.55	49.62	41.77	36.70	33.93	29.40	28.50	24.53	19.53	12.82	8.92	3.84	2.05	0.91	0	0	0
UW101_1783G			100	80.19	59.51	55.89	49.85	48.03	46.25	42.16	40.96	38.49	36.14	33.90	24.62	12.99	8.66	5.52	0	0	0
UW101_1783H			100	86.39	62.00	56.44	50.50	47.25	43.63	40.93	38.24	35.51	32.71	27.95	16.36	7.02	3.95	2.18	0	0	0
UW101_1783L			100	88.43	66.03	60.89	57.30	55.23	52.72	50.24	45.77	43.29	41.07	37.40	18.63	8.20	5.16	2.86	0	0	0
100517JW3			100	80.99	72.77	69.71	65.22	63.06	60.89	55.48	50.01	38.23	28.43	18.80	12.08	6.61	4.95	3.00	0	0	0
100517JW5			100	80.37	77.18	74.28	73.55	70.96	70.44	65.77	59.03	47.38	39.58	31.30	24.69	16.03	12.62	9.14	0	0	0
100517JW6			100	87.29	85.51	84.42	83.36	82.12	81.64	79.06	74.77	66.50	59.45	51.60	46.32	40.28	36.41	31.91	0	0	0
100517_101_6			100	68.18	55.92	53.44	49.99	48.62	46.04	42.62	38.74	34.79	32.13	30.58	12.40	1.99	0.61	0.21	0	0	0
100517_101_7			100	61.92	55.54	50.68	45.62	41.66	37.20	28.79	16.99	9.30	5.90	3.42	1.83	0.63	0.30	0.09	0	0	0
110517JW1			100	63.51	63.51	62.16	61.15	60.98	58.03	49.19	38.87	25.02	18.06	12.88	8.23	3.11	1.80	0.51	0	0	0
110517JW2			100	53.90	53.90	52.44	51.74	49.85	48.50	40.38	28.21	14.64	9.12	5.58	3.31	1.53	1.09	0.69	0	0	0
130517JW4			100	78.11	78.11	76.08	74.07	73.12	71.28	65.43	58.61	50.41	44.97	35.65	21.96	7.00	3.76	1.68	0	0	0
260517JW1			100	75.05	69.16	67.12	64.41	62.39	60.31	53.17	46.59	34.70	27.63	20.97	14.82	7.85	5.03	2.52	0	0	0
260517JW2			100	79.88	79.88	78.07	77.70	76.29	72.48	64.78	54.62	34.65	19.36	5.74	3.56	2.23	1.96	0.87	0	0	0
260517JW3			100	81.06	77.84	76.03	74.01	72.78	70.89	66.62	61.69	51.92	43.81	34.77	26.12	15.29	10.26	7.23	0	0	0
260517JW4			100	79.56	79.56	78.31	76.75	76.23	74.18	70.05	64.41	55.41	48.33	40.69	34.52	27.52	23.35	18.97	0	0	0
260517JW8			100	66.95	62.97	58.90	52.94	51.29	45.57	35.84	26.11	16.89	12.11	8.42	4.68	1.62	0.64	0.18	0	0	0
260517JW9			100	58.02	56.15	54.45	51.81	50.39	47.09	38.56	29.08	20.01	14.17	7.80	4.53	2.16	1.36	0.80	0	0	0
260517JW10			100	72.95	71.24	67.01	60.24	58.45	54.73	45.77	38.16	25.91	17.66	10.64	7.33	3.75	2.34	1.01	0	0	0
240517JW1			100	60.80	60.80	59.78	56.65	55.09	53.35	42.41	29.92	18.48	13.80	9.98	8.67	7.66	7.13	6.86	0	0	0
240517JW2			100	71.49	71.49	67.38	65.35	62.18	60.51	51.02	39.95	29.10	19.07	8.88	4.13	1.21	0.24	0.00	0	0	0
240517JW3			100	65.81	65.81	63.77	59.00	56.85	51.43	39.21	26.99	16.68	10.25	5.64	3.29	1.44	0.45	0.11	0	0	0
240517JW4			100	57.73	55.16	50.86	46.02	43.16	40.16	31.16	16.16	6.19	3.14	1.79	0.92	0.26	0.11	0.06	0	0	0
240517JW5			100	74.77	74.77	73.24	71.18	69.23	69.23	62.71	56.24	44.79	35.42	25.06	16.33	8.90	6.03	3.90	0	0	0
240517JW6			100	83.53	83.53	82.45	81.88	81.02	80.70	77.00	71.32	62.49	54.42	43.98	35.61	27.05	22.36	17.75	0	0	0
240517JW7			100	85.71	85.71	85.71	83.03	81.76	80.01	78.09	74.42	66.96	56.71	45.76	33.74	21.95	16.88	11.66	0	0	0
240517JW8			100	87.73	87.73	86.42	84.79	84.04	82.52	77.67	70.94	43.72	17.53	5.65	2.65	1.05	0.71	0.41	0	0	0
240517JW9			100	53.39	53.39	50.57	49.34	47.21	45.20	39.11	36.09	22.86	15.17	10.22	6.57	4.00	2.64	1.30	0	0	0
240517JW10			100	84.07	84.07	83.32	83.07	82.45	81.07	79.73	74.35	65.80	54.14	35.50	22.33	15.62	12.48	9.79	0	0	0
240517JW11			100	87.61	87.61	87.19	86.62	86.14	85.63	83.65	79.81	70.53	58.71	43.93	30.74	19.16	12.84	7.85	0	0	0
240517JW12			100	88.33	88.33	87.63	86.09	86.01	85.22	82.45	76.93	70.28	62.64	54.43	40.10	17.79	7.80	3.22	0	0	0
240517JW19			100	78.78	49.95	44.08	33.51	28.10	22.64	13.61	6.46	2.78	1.19	0.59	0.33	0.16	0.00	0.00	0	0	0

Table A1.2. Cumulative frequency probability data derived from GS-STAT (Poppe et al., 2004) for Rising Star surface and cave sediment types.

SAMPLEID	LATITUDE	LONGITUDE	PHI_11	PHI_10	PHI_9	PHI_8	PHI_7	PHI_6	PHI_5	PHI_4	PHI_3	PHI_2	PHI_1	PHI_0	PHIM1	PHIM2	PHIM3	PHIM4	PHIM5
Surface sediment types																			
Muddy_sand			100	92.32	85.3	82.26	79.96	78.19	75.62	74.16	69.88	59.88	31.35	11.88	4.13	1.09	0	0	0
Sandy_mud			100	83.37	73.93	72.58	70.23	67.24	62.01	59.02	51.68	48.39	45.34	41.5	32.2	13.89	0	0	0
Gravelly_muddy_sand			100	83.235	72.425	70.28	67.725	64.435	61.16	56.28	46.985	39.495	32.045	26.965	20.685	15.79	0	0	0
Muddy_sandy_gravel			100	79.7	77.49	75.65	73.62	70.945	67.5	62.425	48.305	36.425	26.095	20.355	13.96	6.06	0	0	0
Muddy_gravel			100	85.69	83.94	81.51	80.24	78.27	74.31	71.23	62.69	56.8	51.66	47.86	42.12	33.97	0	0	0
Cave sediment types																			
Muddy_sandy_gravel			100	87.29	85.51	84.42	83.36	81.64	79.06	74.77	66.5	59.45	51.6	46.32	40.28	31.91	0	0	0
Gravelly_muddy_sand			100	82.31	81.67	80.42	79.03	76.87	73.15	67.68	58.6	49.87	39.11	28.61	17.63	9.12	0	0	0
Gravelly_mud			100	78.64	65.04	61.64	57.32	52.86	47.4	41.91	34.78	29.96	24.83	15.86	8.39	3.82	0	0	0
Silty_sand			100	87.73	87.73	86.42	84.79	82.52	77.67	70.94	43.72	17.53	5.65	2.65	1.05	0.41	0	0	0
Clayey_sand			100	80.58	72.92	69.98	66.94	63.53	58.47	52.66	44.18	37.47	29.23	17.25	7.68	2.86	0	0	0
Sandy_clay			100	69.32	57.1	53.49	49.94	44.96	40.89	37.69	31.05	26.67	22.92	11.78	4.34	1.23	0	0	0
Sand_silt_clay			100	68.94	64.21	61.11	57.26	51.77	43.25	34.44	23.4	16.11	9.48	6.22	3.22	1.3	0	0	0
Silty_clay			100	66.14	53.55	48.54	41.72	33.33	24.52	13.2	6.09	3.41	1.93	1.03	0.35	0.05	0	0	0

Table A1.3. Grain size data derived from SedClass (Poppe et al., 2003) for Rising Star surface and cave sediments (n=40).

SampleID	Latitude	Longitude	%Gravel	%Sand	%Silt	%Clay
Surface sediments						
190517JW1			4.133	70.025	8.106	17.736
190517JW2			4.696	39.297	15.940	40.067
190517JW3			10.151	48.838	12.822	28.189
190517JW4			17.767	48.097	13.622	20.514
190517JW5			36.670	31.897	12.066	19.367
190517JW6			42.119	29.112	10.277	18.491
190517JW7			32.199	26.822	13.563	27.416
Cave sediments						
UW101_1783A			2.208	24.053	26.353	47.386
UW101_1783C			3.837	24.658	21.129	50.376
UW101_1783G			12.987	27.974	14.927	44.113
UW101_1783H			7.019	31.216	18.208	43.557
UW101_1783L			8.197	37.576	15.113	39.114
100517JW3			6.613	43.398	19.695	30.293
100517JW5			16.027	43.002	15.249	25.722
100517JW6			40.275	34.490	9.653	15.582
100517_101_6			1.989	36.752	14.702	46.556
100517_101_7			0.627	16.359	33.691	49.324
110517JW1			3.108	35.766	23.285	37.841
110517JW2			1.533	26.679	24.224	47.564
130517JW4			7.003	51.602	17.470	23.925
260517JW1			7.846	38.744	20.528	32.882
260517JW2			2.226	52.394	23.446	21.934
260517JW3			15.285	46.402	14.346	23.967
260517JW4			27.522	36.891	13.900	21.687
260517JW8			1.617	24.490	32.793	41.100
260517JW9			2.165	26.917	25.372	45.546
260517JW10			3.754	34.403	28.852	32.991
240517JW1			7.660	22.257	29.859	40.224
240517JW2			1.208	38.742	27.432	32.618
240517JW3			1.439	25.551	36.783	36.227
240517JW4			0.260	15.897	34.701	49.142
240517JW5			8.903	47.339	16.995	26.763
240517JW6			27.048	44.274	11.128	17.550
240517JW7			21.952	52.470	11.283	14.294
240517JW8			1.055	69.888	15.482	13.576
240517JW9			4.004	32.087	14.483	49.427
240517JW10			15.625	58.723	8.971	16.682
240517JW11			19.161	60.646	7.379	12.814
240517JW12			17.790	59.143	10.696	12.372
240517JW19			0.155	6.308	37.614	55.923

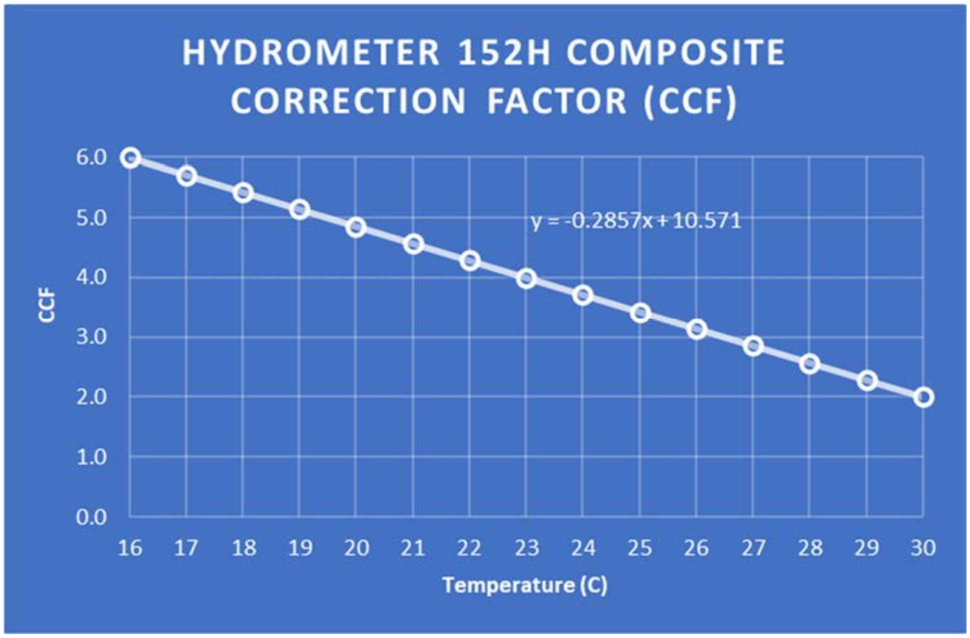

Figure A1.1. Composite Correction Factor calibration for the 152H hydrometer model that was used to perform the grain size analysis. Calibration was performed using a125 ml solution of sodium hexametaphosphate (40 gram/L) in 875 ml of distilled water.

Table A1.4. Hydrometer readings for <0.5 mm grain size fractions for Rising Star surface and cave sediment samples (n=40).

SURFACE SEDIMENTS

Sample number	Total oven-dry fine-grained mass	Air dry sample mass used for analysis (gr)	C-hygro Hygroscopic moisture correction factor = M-oven dry (g) /M-air dry (g)	W Oven-dry mass of soil=C-hygro*M-air dry sample for hydrometer (g)	T Reading taken (min)	Hydrometer reading actual	Temp (C)	C (composite correction factor)	R (Corrected hydrometer reading)	P (percentage soils remaining in suspension) P=((R*a)/W)*100	K value	L (depth of hydrometer in cm)	D (diameter soil particles in mm) D=K*sqrt(L/T)	Percent per grain size fraction	Percentage and particle size at 2.65 g/cm3 specific gravity		
															K value	Particle Diameter (mm)	Percentage
190517JW1	96.35	94.68	0.989	93.64	2	28	26	3.2	25	25%	0.012	12.2	0.02966	2.05	0.01272	0.03142	2.14
				93.64	5	26	26	3.2	23	23%	0.012	12.5	0.01899	3.59	0.01272	0.02011	3.74
				93.64	15	22.5	26	3.2	19	20%	0.012	13.2	0.01127	1.57	0.01272	0.01193	1.63
				93.64	30	21	26	3.3	18	18%	0.012	13.3	0.00800	0.91	0.01272	0.00847	0.95
				93.64	60	20	26	3.1	17	17%	0.012	13.5	0.00570	3.22	0.01272	0.00603	3.36
				93.64	250	17	26	3.3	14	14%	0.012	14	0.00284	4.25	0.01272	0.00301	4.42
				93.64	1440	13	25	3.4	10	10%	0.012	14.7	0.00123	9.81	0.01286	0.00130	10.22
190517JW2	115.86	100	0.984	98.40	2	49	26	3.1	46	45%	0.012	8.8	0.02519	6.34	0.01272	0.02668	6.61
				98.40	5	42.5	26	3.1	39	38%	0.012	9.9	0.01690	4.39	0.01272	0.01790	4.57
				98.40	15	38	26	3.1	35	34%	0.012	10.6	0.01010	2.93	0.01272	0.01069	3.05
				98.40	30	35	26	3.1	32	31%	0.012	11.1	0.00731	1.95	0.01272	0.00774	2.03
				98.40	60	33	26	3.1	30	29%	0.012	11.4	0.00524	3.07	0.01272	0.00554	3.19
				98.40	250	30	26	3.3	27	26%	0.012	11.9	0.00262	4.04	0.01272	0.00278	4.21
				98.40	1440	26	25	3.4	23	22%	0.012	12.5	0.00113	22.02	0.01286	0.00120	22.94
190517JW3	83.99	83.41	0.988	82.41	2	21	26	3.1	18	23%	0.012	13.3	0.03097	6.37	0.01272	0.03280	6.07
				82.41	5	16	26	3.1	13	16%	0.012	14.2	0.02024	5.17	0.01272	0.02144	4.92
				82.41	15	12	26	3.1	9	11%	0.012	14.8	0.01193	1.27	0.01272	0.01263	0.00
				82.41	30	11	26	3.1	8	10%	0.012	14.8	0.00844	1.27	0.01272	0.00893	2.43
				82.41	60	10	26	3.1	7	9%	0.012	15.2	0.00604	2.73	0.01272	0.00640	2.60
				82.41	250	8	26	3.3	5	6%	0.012	15.5	0.00299	2.73	0.01272	0.00317	2.60
				82.41	1440	6	25	3.4	3	3%	0.012	15.8	0.00127	3.28	0.01286	0.00135	3.12
190517JW4	92.26	91.45	0.99	90.54	2	26	26	3.1	23	24%	0.012	12.5	0.03003	7.48	0.01272	0.03180	7.79
				90.54	5	19	26	3.1	16	17%	0.012	13.7	0.01988	4.18	0.01272	0.02106	4.36
				90.54	15	15	26	3.1	12	13%	0.012	14.3	0.01173	2.65	0.01272	0.01242	2.76
				90.54	30	12.5	26	3.1	9	10%	0.012	14.8	0.00844	2.18	0.01272	0.00893	2.27
				90.54	60	10.5	26	3.1	7	8%	0.012	15.2	0.00604	2.80	0.01272	0.00640	2.92
				90.54	250	8	26	3.3	5	5%	0.012	15.5	0.00299	2.27	0.01272	0.00317	2.37
				90.54	1440	6	25	3.4	3	3%	0.012	15.8	0.00127	2.73	0.01286	0.00135	2.84
190517JW5	69.76	69.2	0.988	68.37	2	23	26	3.1	20	28%	0.012	13	0.03062	7.72	0.01272	0.03243	8.04
				68.37	5	17.5	26	3.1	14	20%	0.012	14	0.02010	4.99	0.01272	0.02128	5.20
				68.37	15	14	26	3.1	11	15%	0.012	14.5	0.01181	2.81	0.01272	0.01251	2.93
				68.37	30	12	26	3.1	9	12%	0.012	14.8	0.00844	1.48	0.01272	0.00893	1.55
				68.37	60	11	26	3.2	8	11%	0.012	15	0.00601	4.45	0.01272	0.00636	4.64
				68.37	250	8	25	3.4	5	6%	0.012	15.5	0.00303	1.48	0.01286	0.00320	1.55
				68.37	1440	7	25	3.4	4	5%	0.012	15.6	0.00126	5.01	0.01286	0.00134	5.22
190517JW6	64.96	63.33	0.991	62.76	2	22	26	3.2	19	29%	0.012	13.2	0.03085	6.12	0.01272	0.03268	6.37
				62.76	5	18	26	3.2	15	23%	0.012	13.8	0.01995	7.87	0.01272	0.02113	8.19
				62.76	15	13	25	3.4	10	15%	0.012	14.7	0.01203	1.62	0.01286	0.01273	1.68
				62.76	30	12	25	3.4	9	13%	0.012	14.8	0.00853	2.29	0.01286	0.00903	2.39
				62.76	60	10.5	25	3.4	7	11%	0.012	15.2	0.00612	2.51	0.01286	0.00647	2.62
				62.76	250	9	25	3.6	5	8%	0.012	15.5	0.00303	4.83	0.01286	0.00320	5.03
				62.76	1440	5.5	26	3.2	2	3%	0.012	16	0.00127	3.47	0.01272	0.00134	3.62

Table A1.4. Hydrometer readings and <0.5 mm grain size fractions for Rising Star surface and cave sediment samples (Continued).

Sample number	Total oven-dry fine-grained mass	Air dry sample mass used for analysis (gr)	C-hygro Hygroscopic moisture correction factor = M-oven dry (g) /M-air dry (g)	W Oven-dry mass of soil=C-hygro*M-air dry sample for hydrometer (g)	T Reading taken (min)	Hydrometer reading actual	Temp (C)	C (composite correction factor)	R (Corrected hydrometer reading)	P (percentage soils remaining in suspension) P=((R*a)/W)*100	K value	L (depth of hydrometer in cm)	D (diameter soil particles in mm) D=K*sqrt(L/T)	Percent per grain size fraction	Percentage and particle size at 2.65 g/cm3 specific gravity		
															K value	Particle Diameter (mm)	Percentage
SURFACE SEDIMENTS																	
190517JW7	78.07	74.76	0.978	73.12	2	36	25	3.4	33	43%	0.012	10.9	0.02836	5.25	0.01286	0.03002	5.47
				73.12	5	32	25	3.4	29	38%	0.012	11.5	0.01843	9.19	0.01286	0.01950	9.57
				73.12	15	25	25	3.4	22	28%	0.012	12.7	0.01118	2.63	0.01286	0.01183	2.74
				73.12	30	23	25	3.4	20	26%	0.012	13	0.00800	2.63	0.01286	0.00847	2.74
				73.12	60	21	25	3.4	18	23%	0.012	13.3	0.00572	4.13	0.01286	0.00605	4.30
				73.12	250	18	25	3.6	14	19%	0.012	14	0.00288	2.36	0.01286	0.00304	2.46
				73.12	1440	16	25	3.4	13	17%	0.012	14.2	0.00121	16.58	0.01286	0.00128	17.27
CAVE SEDIMENTS																	
UW101-1783A	188.43	100	0.958	95.80	2	58	26	3.2	55	55%	0.012	7.3	0.02295	3.01	0.01272	0.02430	3.13
				95.80	5	55	26	3.2	52	52%	0.012	7.8	0.01500	6.04	0.01272	0.01589	6.29
				95.80	15	49	26	3.3	46	46%	0.012	8.8	0.00920	4.07	0.01272	0.00974	4.24
				95.80	30	45	25	3.3	42	42%	0.012	9.4	0.00680	5.04	0.01286	0.00720	5.25
				95.80	60	40	25	3.3	37	37%	0.012	10.2	0.00501	8.30	0.01286	0.00530	8.65
				95.80	250	32	24	3.6	28	28%	0.012	11.5	0.00264	7.44	0.01301	0.00279	7.75
				95.80	1440	24	26	3.1	21	21%	0.012	12.9	0.00114	20.99	0.01272	0.00120	21.86
UW101-1783C	164.95	100	0.962	96.20	2	58	25	3.4	55	55%	0.012	7.3	0.02321	1.00	0.01286	0.02457	1.04
				96.20	5	57	25	3.4	54	54%	0.012	7.4	0.01478	4.99	0.01286	0.01564	5.20
				96.20	15	52	25	3.4	49	49%	0.012	8.3	0.00904	3.05	0.01286	0.00957	3.18
				96.20	30	49	25	3.4	46	45%	0.012	8.8	0.00658	5.57	0.01286	0.00697	5.81
				96.20	60	43.5	25	3.5	40	40%	0.012	9.7	0.00489	8.65	0.01286	0.00517	9.01
				96.20	250	35	24	3.7	31	31%	0.012	11.2	0.00260	6.53	0.01301	0.00275	6.80
				96.20	1440	28	26	3.2	25	25%	0.012	12.2	0.00111	24.72	0.01272	0.00117	25.75
UW101-1783G	130.56	59.29	0.955	56.62	2	37	25	3.4	34	57%	0.012	10.7	0.02810	1.74	0.01286	0.02975	1.82
				56.62	5	36	25	3.4	33	55%	0.012	10.9	0.01794	5.93	0.01286	0.01899	6.18
				56.62	15	32.5	25	3.4	29	49%	0.012	11.4	0.01059	2.59	0.01286	0.01121	2.70
				56.62	30	31	25	3.5	28	47%	0.012	11.7	0.00759	2.64	0.01286	0.00803	2.75
				56.62	60	29.5	25	3.5	26	44%	0.012	12	0.00543	8.77	0.01286	0.00575	9.13
				56.62	250	24.5	24	3.7	21	35%	0.012	12.9	0.00279	5.26	0.01301	0.00296	5.47
				56.62	1440	21	26	3.3	18	30%	0.012	13.3	0.00115	30.03	0.01272	0.00122	31.29
UW101-1783H	144.31	83.41	0.961	80.16	2	57	25	3.4	54	64%	0.012	7.4	0.02337	3.59	0.01286	0.02474	3.74
				80.16	5	54	25	3.4	51	61%	0.012	7.9	0.01527	3.59	0.01286	0.01616	3.74
				80.16	15	51	25	3.4	48	57%	0.012	8.4	0.00909	4.82	0.01286	0.00962	5.03
				80.16	30	47	25	3.5	44	52%	0.012	9.1	0.00669	4.33	0.01286	0.00708	4.51
				80.16	60	43.5	25	3.6	40	48%	0.012	9.7	0.00489	7.92	0.01286	0.00517	8.25
				80.16	250	37	24	3.7	33	40%	0.012	10.9	0.00257	7.41	0.01301	0.00272	7.72
				80.16	1440	30.5	25	3.4	27	32%	0.012	11.9	0.00110	32.49	0.01286	0.00117	33.84
UW101-1783L	120.9	65.78	0.959	63.08	2	46.5	25	3.5	43	65%	0.012	9.2	0.02606	6.85	0.01286	0.02758	7.13
				63.08	5	42	25	3.5	38	59%	0.012	9.9	0.01710	3.80	0.01286	0.01810	3.96
				63.08	15	39.5	25	3.5	36	55%	0.012	10.4	0.01012	3.85	0.01286	0.01071	4.01
				63.08	30	37	25	3.5	33	51%	0.012	10.7	0.00726	3.17	0.01286	0.00768	3.31
				63.08	60	35	24	3.6	31	48%	0.012	11.2	0.00531	5.50	0.01301	0.00562	5.73
				63.08	250	31.5	24	3.7	28	42%	0.012	11.7	0.00266	7.89	0.01301	0.00281	8.22
				63.08	1440	26	25	3.4	23	34%	0.012	12.5	0.00113	34.35	0.01286	0.00120	35.78

Table A1.4. Hydrometer readings and <0.5 mm grain size fractions for Rising Star surface and cave sediment samples (Continued).

CAVE SEDIMENTS															Percentage and particle size at 2.65 g/cm3 specific gravity		
Sample number	**Total oven-dry fine-grained mass**	**Air dry sample mass used for analysis (gr)**	**C-hygro** Hygroscopic moisture correction factor = M-oven dry (g) /M-air dry (g)	**W** Oven-dry mass of soil=C-hygro*M-air dry sample for hydrometer (g)	**T Reading taken (min)**	**Hydrometer reading actual**	**Temp (C)**	**C** (composite correction factor)	**R** (Corrected hydrometer reading)	**P** (percentage soils remaining in suspension) **P=((R*a)/W)*100**	**K value**	**L** (depth of hydrometer in cm)	**D** (diameter soil particles in mm) **D=K*sqrt(L/T)**	**Percent per grain size fraction**	**K value**	**Particle Diameter (mm)**	**Percentage**
100517JW3	78.21	76.8	0.977	75.03	2	32	25	3.4	29	37%	0.012	11.5	0.02913	6.47	0.01286	0.03084	6.74
				75.03	5	27	25	3.4	24	30%	0.012	12.4	0.01913	6.40	0.01286	0.02025	6.66
				75.03	15	22	25	3.4	19	24%	0.012	13.2	0.01140	2.56	0.01286	0.01206	2.67
				75.03	30	20	25	3.4	17	21%	0.012	13.5	0.00815	2.56	0.01286	0.00863	2.67
				75.03	60	18	25	3.4	15	19%	0.012	13.8	0.00583	5.30	0.01286	0.00617	5.52
				75.03	250	14	25	3.6	10	13%	0.012	14.7	0.00295	3.62	0.01286	0.00312	3.77
				75.03	1440	11	25	3.4	8	10%	0.012	15	0.00124	9.72	0.01286	0.00131	10.13
100517JW5	69.23	67.03	0.988	66.23	2	24	25	3.4	21	30%	0.012	12.9	0.03086	9.42	0.01286	0.03266	9.81
				66.23	5	17.5	25	3.4	14	20%	0.012	14	0.02033	6.52	0.01286	0.02152	6.79
				66.23	15	13	25	3.4	10	14%	0.012	14.7	0.01203	0.72	0.01286	0.01273	0.75
				66.23	30	12.5	25	3.4	9	13%	0.012	14.8	0.00853	3.62	0.01286	0.00903	3.77
				66.23	60	10	25	3.4	7	10%	0.012	15.2	0.00612	1.01	0.01286	0.00647	1.06
				66.23	250	9.5	24	3.6	6	9%	0.012	15.3	0.00304	4.06	0.01301	0.00322	4.23
				66.23	1440	6.5	25	3.4	3	4%	0.012	15.8	0.00127	4.45	0.01286	0.00135	4.64
100517JW6	60.15	57.57	0.978	56.30	2	18	25	3.4	15	25%	0.012	13.8	0.03192	8.53	0.01286	0.03378	8.88
				56.30	5	13	25	3.4	10	16%	0.012	14.7	0.02083	5.12	0.01286	0.02205	5.33
				56.30	15	10	25	3.4	7	11%	0.012	15.2	0.01223	0.95	0.01286	0.01295	0.99
				56.30	30	9.5	25	3.5	6	10%	0.012	15.3	0.00868	2.46	0.01286	0.00918	2.56
				56.30	60	8	25	3.4	5	8%	0.012	15.5	0.00618	2.09	0.01286	0.00654	2.18
				56.30	250	7	24	3.7	3	6%	0.012	15.8	0.00309	2.17	0.01301	0.00327	2.26
				56.30	1440	5.5	25	3.4	2	4%	0.012	16	0.00128	3.53	0.01286	0.00136	3.68
100517 101 6	130.51	55.18	0.973	53.69	2	26	26	3.2	23	41%	0.012	12.5	0.03003	5.36	0.01272	0.03180	5.59
				53.69	5	23	26	3.2	20	35%	0.012	13	0.01937	4.73	0.01272	0.02051	4.92
				53.69	15	20.5	25	3.4	17	31%	0.012	13.5	0.01153	3.58	0.01286	0.01220	3.73
				53.69	30	18.5	25	3.4	15	27%	0.012	13.8	0.00824	1.89	0.01286	0.00872	1.97
				53.69	60	17.5	25	3.4	14	25%	0.012	14	0.00587	4.78	0.01286	0.00621	4.98
				53.69	250	15	24	3.6	11	20%	0.012	14.5	0.00296	3.42	0.01301	0.00313	3.57
				53.69	1440	13	25	3.5	9	17%	0.012	14.8	0.00123	16.96	0.01286	0.00130	17.67
100517 101 7	197.19	100	0.982	98.20	2	49	25	3.3	46	45%	0.012	8.8	0.02549	11.73	0.01286	0.02698	12.22
				98.20	5	37	25	3.3	34	33%	0.012	10.7	0.01777	8.37	0.01286	0.01881	8.71
				98.20	15	28.5	25	3.4	25	25%	0.012	12.2	0.01096	4.43	0.01286	0.01160	4.61
				98.20	30	24	25	3.4	21	20%	0.012	12.9	0.00797	3.94	0.01286	0.00843	4.10
				98.20	60	20	25	3.4	17	16%	0.012	13.5	0.00576	5.03	0.01286	0.00610	5.24
				98.20	250	15	25	3.6	11	11%	0.012	14.5	0.00293	4.83	0.01286	0.00310	5.03
				98.20	1440	10	25	3.5	6	6%	0.012	15.3	0.00125	6.34	0.01286	0.00133	6.60
110517JW1	37.28	30.1	0.982	29.56	2	10.5	26	3.1	7	24%	0.012	15.2	0.03311	11.37	0.01272	0.03507	11.84
				29.56	5	7	26	3.1	4	13%	0.012	15.6	0.02121	9.74	0.01272	0.02247	10.15
				29.56	15	4	26	3.1	1	3%	0.012	16.1	0.01244	3.25	0.01272	0.01318	3.38
				29.56	30	3	26	3.1	0	-0.463790%	0.012	16.3	0.00885	0.19	0.01272	0.00938	0.19
				29.56	60	3	26	3.2	0	-0.649371%	0.012	16.3	0.00626	1.11	0.01272	0.00663	1.16
				29.56	250	3	25	3.5	-1	-1.762857%	0.012	16.4	0.00311	1.48	0.01286	0.00329	1.55
				29.56	1440	2	27	3.0	-1	-3.247667%	0.012	16.4	0.00127	-3.25	0.01258	0.00134	-3.38

Table A1.4. Hydrometer readings and <0.5 mm grain size fractions for Rising Star surface and cave sediment samples (Continued).

CAVE SEDIMENTS

															Percentage and particle size at 2.65 g/cm3 specific gravity		
Sample number	**Total oven-dry fine-grained mass**	**Air dry sample mass used for analysis (gr)**	**C-hygro** Hygroscopic moisture correction factor = M-oven dry (g) /M-air dry (g)	**W** Oven-dry mass of soil=C-hygro*M-air dry sample for hydrometer (g)	**T Reading taken (min)**	**Hydrometer reading actual**	**Temp (C)**	**C** (composite correction factor)	**R** (Corrected hydrometer reading)	**P** (percentage soils remaining in suspension) P=((R*a)/W)*100	**K value**	**L** (depth of hydrometer in cm)	**D** (diameter soil particles in mm) D=K*sqrt(L/T)	**Percent per grain size fraction**	**K value**	**Particle Diameter (mm)**	**Percentage**
110517JW2	42.51	35.59	0.981	34.91	2	11.5	26	3.1	8	25%	0.012	15	0.03289	13.53	0.01272	0.03484	12.89
				34.91	5	7	26	3.1	4	12%	0.012	15.6	0.02121	9.02	0.01272	0.02247	8.59
				34.91	15	4	26	3.1	1	3%	0.012	16.1	0.01244	1.50	0.01272	0.01318	1.43
				34.91	30	3.5	26	3.1	0	1%	0.012	16.1	0.00880	2.11	0.01272	0.00932	2.00
				34.91	60	3	25	3.3	0	-1%	0.012	16.3	0.00633	0.77	0.01286	0.00670	0.74
				34.91	250	3	24	3.6	-1	-2%	0.012	16.4	0.00315	1.63	0.01301	0.00333	1.55
				34.91	1440	2	26	3.1	-1	-3%	0.012	16.4	0.00128	-3.44	0.01272	0.00136	-3.27
130716JW4	34.55	33.53	0.984	32.99	2	12.5	26	3.1	9	27%	0.012	14.8	0.03267	10.18	0.01272	0.03460	10.61
				32.99	5	9	26	3.1	6	17%	0.012	15.3	0.02101	8.73	0.01272	0.02225	9.09
				32.99	15	6	26	3.1	3	8%	0.012	15.8	0.01233	2.74	0.01272	0.01305	2.86
				32.99	30	5.2	26	3.3	2	6%	0.012	16	0.00877	1.41	0.01272	0.00929	1.47
				32.99	60	4.8	25	3.4	1	4%	0.012	16.1	0.00629	2.99	0.01286	0.00666	3.12
				32.99	250	4	24	3.6	0	1%	0.012	16.3	0.00314	3.03	0.01301	0.00332	3.16
				32.99	1440	2.5	26	3.1	-1	-2%	0.012	16.4	0.00128	-1.87	0.01272	0.00136	-1.95
260517JW1	81.19	79.45	0.983	78.10	2	31.5	25	3.4	28	35%	0.012	11.7	0.02939	7.99	0.01286	0.03110	8.32
				78.10	5	25	25	3.4	22	27%	0.012	12.7	0.01936	8.67	0.01286	0.02050	9.04
				78.10	15	18	25	3.4	15	18%	0.012	13.8	0.01165	2.53	0.01286	0.01233	2.63
				78.10	30	16	25	3.5	13	15%	0.012	14.2	0.00836	2.46	0.01286	0.00885	2.56
				78.10	60	14	25	3.5	11	13%	0.012	14.5	0.00597	3.28	0.01286	0.00632	3.42
				78.10	250	11.5	24	3.7	8	10%	0.012	15	0.00301	2.48	0.01301	0.00319	2.58
				78.10	1440	9	26	3.2	6	7%	0.012	15.3	0.00124	7.16	0.01272	0.00131	7.46
260517JW2	43.19	37.82	0.981	37.10	2	12	25	3.4	9	22%	0.012	14.8	0.03305	10.35	0.01286	0.03498	10.78
				37.10	5	8	25	3.4	5	12%	0.012	15.5	0.02139	7.84	0.01286	0.02264	8.16
				37.10	15	5	25	3.5	2	4%	0.012	16	0.01255	3.88	0.01286	0.01328	4.04
				37.10	30	3.5	25	3.5	0	0%	0.012	16.3	0.00896	1.44	0.01286	0.00948	1.50
				37.10	60	3	25	3.5	-1	-1%	0.012	16.4	0.00635	0.37	0.01286	0.00672	0.39
				37.10	250	3	24	3.7	-1	-2%	0.012	16.4	0.00315	1.85	0.01301	0.00333	1.93
				37.10	1440	2	25	3.4	-1	-4%	0.012	16.4	0.00130	-3.55	0.01286	0.00137	-3.70
260517JW3	82.88	80.59	0.985	79.38	2	27	25	3.4	24	29%	0.012	12.4	0.03025	7.26	0.01286	0.03202	7.56
				79.38	5	21	25	3.4	18	21%	0.012	13.3	0.01982	6.29	0.01286	0.02097	6.55
				79.38	15	15.8	25	3.4	12	15%	0.012	14.3	0.01186	2.78	0.01286	0.01256	2.90
				79.38	30	13.5	25	3.4	10	12%	0.012	14.7	0.00851	1.81	0.01286	0.00900	1.89
				79.38	60	12	25	3.4	9	10%	0.012	14.8	0.00603	2.97	0.01286	0.00639	3.10
				79.38	250	9.6	25	3.5	6	7%	0.012	15.3	0.00301	2.66	0.01286	0.00318	2.77
				79.38	1440	7	26	3.1	4	5%	0.012	15.6	0.00125	4.73	0.01272	0.00132	4.93
260517JW4	63.38	58.85	0.983	57.85	2	17.5	25	3.4	14	23%	0.012	14	0.03215	9.13	0.01286	0.03402	9.51
				57.85	5	12	25	3.4	9	14%	0.012	14.8	0.02090	6.69	0.01286	0.02213	6.96
				57.85	15	8	25	3.4	5	8%	0.012	15.5	0.01235	3.32	0.01286	0.01307	3.46
				57.85	30	6	25	3.4	3	4%	0.012	15.8	0.00882	0.83	0.01286	0.00933	0.86
				57.85	60	5.5	25	3.4	2	3%	0.012	16	0.00627	2.54	0.01286	0.00664	2.64
				57.85	250	4	25	3.5	1	1%	0.012	16.1	0.00308	2.02	0.01286	0.00326	2.10
				57.85	1440	2.5	26	3.2	-1	-1%	0.012	16.4	0.00128	-1.11	0.01272	0.00136	-1.16

Table A1.4. Hydrometer readings and <0.5 mm grain size fractions for Rising Star surface and cave sediment samples (Continued).

CAVE SEDIMENTS

															Percentage and particle size at 2.65 g/cm3 specific gravity		
Sample number	Total oven-dry fine-grained mass	Air dry sample mass used for analysis (gr)	C-hygro Hygroscopic moisture correction factor = M-oven dry (g) /M-air dry (g)	W Oven-dry mass of soil=C-hygro*M-air dry sample for hydrometer (g)	T Reading taken (min)	Hydrometer reading actual	Temp (C)	C (composite correction factor)	R (Corrected hydrometer reading)	P (percentage soils remaining in suspension) P=((R*a)/W)*100	K value	L (depth of hydrometer in cm)	D (diameter soil particles in mm) D=K*sqrt(L/T)	Percent per grain size fraction	K value	Particle Diameter (mm)	Percentage
260517JW8	82.12	76.82	0.980	75.28	2	37	25	3.4	34	43%	0.012	10.7	0.02810	10.20	0.01286	0.02975	10.63
				75.28	5	29	25	3.4	26	33%	0.012	12	0.01882	10.20	0.01286	0.01992	10.63
				75.28	15	21	25	3.4	18	22%	0.012	13.3	0.01144	5.99	0.01286	0.01211	6.24
				75.28	30	16.3	25	3.4	13	16%	0.012	14.2	0.00836	1.73	0.01286	0.00885	1.80
				75.28	60	15	25	3.5	12	15%	0.012	14.3	0.00593	6.25	0.01286	0.00628	6.51
				75.28	250	10.1	25	3.5	7	8%	0.012	15.2	0.00300	4.26	0.01286	0.00317	4.44
				75.28	1440	6.5	26	3.2	3	4%	0.012	15.8	0.00126	4.17	0.01272	0.00133	4.35
260517JW9	169.08	100	0.976	97.60	2	34	25	3.4	31	30%	0.012	11.2	0.02875	9.86	0.01286	0.03043	10.28
				97.60	5	24	25	3.4	21	20%	0.012	12.9	0.01952	8.88	0.01286	0.02066	9.25
				97.60	15	15	25	3.4	12	11%	0.012	14.3	0.01186	3.44	0.01286	0.01256	3.59
				97.60	30	11.5	25	3.4	8	8%	0.012	15	0.00859	1.48	0.01286	0.00909	1.54
				97.60	60	10	25	3.4	7	6%	0.012	15.2	0.00612	2.75	0.01286	0.00647	2.87
				97.60	250	7.2	25	3.4	4	4%	0.012	15.6	0.00304	1.77	0.01286	0.00321	1.84
				97.60	1440	5.2	26	3.2	2	2%	0.012	16	0.00127	1.94	0.01272	0.00134	2.02
260517JW10	55.7	53.91	0.980	52.83	2	24	25	3.4	21	37%	0.012	12.9	0.03086	8.18	0.01286	0.03266	8.52
				52.83	5	19.5	25	3.4	16	29%	0.012	13.7	0.02011	9.63	0.01286	0.02129	10.03
				52.83	15	14.2	25	3.4	11	20%	0.012	14.5	0.01195	4.00	0.01286	0.01264	4.16
				52.83	30	12	25	3.4	9	16%	0.012	14.8	0.00853	1.92	0.01286	0.00903	2.00
				52.83	60	11	25	3.5	8	14%	0.012	15	0.00608	7.27	0.01286	0.00643	7.57
				52.83	250	7	25	3.5	4	6%	0.012	15.6	0.00304	4.54	0.01286	0.00321	4.73
				52.83	1440	4.3	26	3.3	1	2%	0.012	16.1	0.00127	1.84	0.01272	0.00134	1.92
240517JW1	39.13	29.52	0.976	28.81	2	13	25	3.4	10	35%	0.012	14.7	0.03294	14.58	0.01286	0.03486	13.88
				28.81	5	9	25	3.4	6	20%	0.012	15.3	0.02125	12.76	0.01286	0.02250	12.15
				28.81	15	5.5	25	3.4	2	8%	0.012	16	0.01255	2.03	0.01286	0.01328	1.93
				28.81	30	5	25	3.5	2	6%	0.012	16	0.00887	1.82	0.01286	0.00939	1.74
				28.81	60	4.5	25	3.5	1	4%	0.012	16	0.00627	3.64	0.01286	0.00664	3.47
				28.81	250	3.5	25	3.5	0	0%	0.012	16.3	0.00310	1.20	0.01286	0.00328	1.14
				28.81	1440	3	25	3.3	0	-1%	0.012	16.3	0.00129	-1.15	0.01286	0.00137	-1.09
240517JW2	33.95	29.63	0.972	28.80	2	12	25	3.4	9	29%	0.012	14.8	0.03305	11.67	0.01286	0.03498	12.15
				28.80	5	8.5	25	3.4	5	17%	0.012	15.5	0.02139	10.00	0.01286	0.02264	10.42
				28.80	15	5.5	25	3.4	2	7%	0.012	16	0.01255	1.76	0.01286	0.01328	1.84
				28.80	30	5	25	3.5	2	5%	0.012	16	0.00887	3.33	0.01286	0.00939	3.47
				28.80	60	4	25	3.5	1	2%	0.012	16.1	0.00629	2.14	0.01286	0.00666	2.23
				28.80	250	3.5	24	3.6	0	0%	0.012	16.3	0.00314	4.33	0.01301	0.00332	4.51
				28.80	1440	2	25	3.4	-1	-5%	0.012	16.4	0.00130	-4.67	0.01286	0.00137	-4.86
240517JW3	24.92	23.73	0.976	23.16	2	12	25	3.4	9	36%	0.012	14.8	0.03305	12.43	0.01286	0.03498	12.95
				23.16	5	9	25	3.4	6	23%	0.012	15.3	0.02125	12.43	0.01286	0.02250	12.95
				23.16	15	6	25	3.4	3	11%	0.012	15.8	0.01247	5.51	0.01286	0.01320	5.74
				23.16	30	4.7	25	3.5	1	5%	0.012	16.1	0.00890	2.19	0.01286	0.00942	2.28
				23.16	60	4.2	25	3.5	1	3%	0.012	16.1	0.00629	4.86	0.01286	0.00666	5.06
				23.16	250	3.2	24	3.7	0	-2%	0.012	16.3	0.00314	2.07	0.01301	0.00332	2.16
				23.16	1440	2.5	25	3.5	-1	-4%	0.012	16.4	0.00130	-3.97	0.01286	0.00137	-4.13

Table A1.4. Hydrometer readings and <0.5 mm grain size fractions for Rising Star surface and cave sediment samples (Continued).

CAVE SEDIMENTS

															Percentage and particle size at 2.65 g/cm3 specific gravity		
Sample number	**Total oven-dry fine-grained mass**	**Air dry sample mass used for analysis (gr)**	**C-hygro** Hygroscopic moisture correction factor = M-oven dry (g) /M-air dry (g)	**W** Oven-dry mass of soil=C-hygro*M-air dry sample for hydrometer (g)	**T Reading taken (min)**	**Hydrometer reading actual**	**Temp (C)**	**C** (composite correction factor)	**R** (Corrected hydrometer reading)	**P** (percentage soils remaining in suspension) **P=((R*a)/W)*100**	**K value**	**L** (depth of hydrometer in cm)	**D** (diameter soil particles in mm) **D=K*sqrt(L/T)**	**Percent per grain size fraction**	**K value**	**Particle Diameter (mm)**	**Percentage**
240517JW4	128.65	100.01	0.982	98.21	2	45	25	3.4	42	41%	0.012	9.4	0.02634	14.66	0.01286	0.02788	15.27
				98.21	5	30	25	3.4	27	26%	0.012	11.9	0.01874	8.80	0.01286	0.01984	9.16
				98.21	15	21	25	3.4	18	17%	0.012	13.3	0.01144	2.93	0.01286	0.01211	3.05
				98.21	30	18	25	3.4	15	14%	0.012	13.8	0.00824	2.79	0.01286	0.00872	2.91
				98.21	60	15.2	25	3.5	12	11%	0.012	14.3	0.00593	4.73	0.01286	0.00628	4.93
				98.21	250	10.5	24	3.6	7	7%	0.012	15.2	0.00303	4.20	0.01301	0.00321	4.38
				98.21	1440	6	25	3.4	3	3%	0.012	15.8	0.00127	2.51	0.01286	0.00135	2.62
240517JW5	43.6	41.31	0.982	40.57	2	13	25	3.5	10	25%	0.012	14.7	0.03294	9.06	0.01286	0.03486	8.63
				40.57	5	9.5	25	3.5	6	16%	0.012	15.3	0.02125	9.13	0.01286	0.02250	8.70
				40.57	15	6	25	3.5	3	7%	0.012	15.8	0.01247	1.29	0.01286	0.01320	1.23
				40.57	30	5.5	25	3.5	2	5%	0.012	15.8	0.00882	1.44	0.01286	0.00933	1.37
				40.57	60	5	25	3.5	1	4%	0.012	16.1	0.00629	2.88	0.01286	0.00666	2.75
				40.57	250	4	24	3.7	0	1%	0.012	16.3	0.00314	2.14	0.01301	0.00332	2.04
				40.57	1440	3	25	3.5	0	-1%	0.012	16.3	0.00129	-1.26	0.01286	0.00137	-1.20
240517JW6	38.98	35.59	0.978	34.81	2	10	25	3.5	6	18%	0.012	15.3	0.03361	9.73	0.01286	0.03557	10.14
				34.81	5	6.5	25	3.6	3	8%	0.012	15.8	0.02160	6.34	0.01286	0.02286	6.61
				34.81	15	4.2	25	3.6	1	2%	0.012	16.1	0.01259	0.55	0.01286	0.01332	0.57
				34.81	30	4	25	3.6	0	1%	0.012	16.3	0.00896	1.46	0.01286	0.00948	1.52
				34.81	60	3.5	24	3.6	0	0%	0.012	16.3	0.00641	0.98	0.01301	0.00678	1.03
				34.81	250	3.2	24	3.7	0	-1%	0.012	16.3	0.00314	1.85	0.01301	0.00332	1.93
				34.81	1440	2.5	24	3.6	-1	-3%	0.012	16.4	0.00131	-3.11	0.01301	0.00139	-3.24
240517JW7	25.45	23.15	0.976	22.59	2	7.5	25	3.5	4	17%	0.012	15.6	0.03393	6.49	0.01286	0.03592	6.77
				22.59	5	6	25	3.5	2	10%	0.012	16	0.02173	3.40	0.01286	0.02300	3.54
				22.59	15	5.2	25	3.5	2	7%	0.012	16	0.01255	3.10	0.01286	0.01328	3.22
				22.59	30	4.5	25	3.6	1	4%	0.012	16.1	0.00890	2.25	0.01286	0.00942	2.34
				22.59	60	4	24	3.6	0	2%	0.012	16.3	0.00641	4.73	0.01301	0.00678	4.93
				22.59	250	3	24	3.7	-1	-3%	0.012	16.4	0.00315	-0.36	0.01301	0.00333	-0.38
				22.59	1440	3	24	3.6	-1	-3%	0.012	16.4	0.00131	-2.67	0.01301	0.00139	-2.78
240517JW8	55.45	45.73	0.990	45.27	2	10	25	3.4	7	14%	0.012	15.2	0.03350	6.85	0.01286	0.03545	7.13
				45.27	5	6.8	25	3.5	3	7%	0.012	15.8	0.02160	4.94	0.01286	0.02286	5.14
				45.27	15	4.5	25	3.5	1	2%	0.012	16.1	0.01259	1.54	0.01286	0.01332	1.61
				45.27	30	3.8	25	3.5	0	1%	0.012	16.3	0.00896	0.76	0.01286	0.00948	0.79
				45.27	60	3.5	25	3.6	0	0%	0.012	16.3	0.00633	1.67	0.01286	0.00670	1.74
				45.27	250	2.8	24	3.7	-1	-2%	0.012	16.4	0.00315	1.33	0.01301	0.00333	1.39
				45.27	1440	2.2	24	3.7	-1	-3%	0.012	16.4	0.00131	-3.15	0.01301	0.00139	-3.28
240517JW9	48.21	45.73	0.976	44.63	2	10.5	25	3.5	7	15%	0.012	15.2	0.03350	3.23	0.01286	0.03545	3.36
				44.63	5	9	25	3.5	6	12%	0.012	15.3	0.02125	6.51	0.01286	0.02250	6.79
				44.63	15	6	25	3.5	3	5%	0.012	15.8	0.01247	2.15	0.01286	0.01320	2.24
				44.63	30	5	25	3.5	2	3%	0.012	16	0.00887	2.27	0.01286	0.00939	2.37
				44.63	60	4	25	3.5	0	1%	0.012	16.3	0.00633	1.32	0.01286	0.00670	1.38
				44.63	250	3.5	24	3.7	0	0%	0.012	16.3	0.00314	3.01	0.01301	0.00332	3.14
				44.63	1440	2.1	24	3.7	-2	-3%	0.012	16.5	0.00132	-3.35	0.01301	0.00139	-3.49

Table A1.4. Hydrometer readings and <0.5 mm grain size fractions for Rising Star surface and cave sediment samples (Continued).

CAVE SEDIMENTS

Sample number	Total oven-dry fine-grained mass	Air dry sample mass used for analysis (gr)	C-hygro Hygroscopic moisture correction factor = M-oven dry (g) /M-air dry (g)	W Oven-dry mass of soil=C-hygro*M-air dry sample for hydrometer (g)	T Reading taken (min)	Hydrometer reading actual	Temp (C)	C (composite correction factor)	R (Corrected hydrometer reading)	P (percentage soils remaining in suspension) P=((R*a)/W)*100	K value	L (depth of hydrometer in cm)	D (diameter soil particles in mm) D=K*sqrt(L/T)	Percent per grain size fraction	Percentage and particle size at 2.65 g/cm3 specific gravity K value	Particle Diameter (mm)	Percentage
240517JW10	49.62	48.55	0.988	47.97	2	10	25	3.5	7	13%	0.012	15.2	0.03350	8.01	0.01286	0.03545	8.34
				47.97	5	6	25	3.5	3	5%	0.012	15.8	0.02160	2.00	0.01286	0.02286	2.08
				47.97	15	5	25	3.5	2	3%	0.012	16	0.01255	2.06	0.01286	0.01328	2.14
				47.97	30	4	25	3.5	0	1%	0.012	16.3	0.00896	0.91	0.01286	0.00948	0.95
				47.97	60	3.6	25	3.6	0	0%	0.012	16.3	0.00633	0.37	0.01286	0.00670	0.39
				47.97	250	3.5	24	3.7	0	0%	0.012	16.3	0.00314	1.12	0.01301	0.00332	1.16
				47.97	1440	3	24	3.7	-1	-1%	0.012	16.4	0.00131	-1.43	0.01301	0.00139	-1.49
240517JW11	59.73	59.12	0.986	58.29	2	11	25	3.5	8	12%	0.012	15	0.03327	6.59	0.01286	0.03522	6.86
				58.29	5	7	25	3.5	4	6%	0.012	15.6	0.02146	3.39	0.01286	0.02272	3.53
				58.29	15	5	25	3.5	1	2%	0.012	16.1	0.01259	0.87	0.01286	0.01332	0.91
				58.29	30	4.5	25	3.6	1	2%	0.012	16.1	0.00890	0.82	0.01286	0.00942	0.86
				58.29	60	4	25	3.6	0	1%	0.012	16.3	0.00633	0.96	0.01286	0.00670	1.00
				58.29	250	3.5	24	3.7	0	0%	0.012	16.3	0.00314	0.73	0.01301	0.00332	0.76
				58.29	1440	3	24	3.6	-1	-1%	0.012	16.4	0.00131	-0.99	0.01301	0.00139	-1.03
240517JW12	32.79	31.18	0.980	30.56	2	10.5	25	3.5	7	22%	0.012	15.2	0.03350	11.62	0.01286	0.03545	12.11
				30.56	5	6.8	25	3.5	3	10%	0.012	15.8	0.02160	5.83	0.01286	0.02286	6.08
				30.56	15	5	25	3.5	1	5%	0.012	16.1	0.01259	1.66	0.01286	0.01332	1.73
				30.56	30	4.5	25	3.6	1	3%	0.012	16.1	0.00890	0.18	0.01286	0.00942	0.19
				30.56	60	4.5	24	3.6	1	3%	0.012	16.1	0.00637	3.23	0.01301	0.00674	3.37
				30.56	250	3.5	24	3.7	0	0%	0.012	16.3	0.00314	1.48	0.01301	0.00332	1.54
				30.56	1440	3	24	3.6	-1	-2%	0.012	16.4	0.00131	-1.97	0.01301	0.00139	-2.06
240517JW19	57.63	57.14	0.974	55.65	2	44	25	3.5	40	70%	0.012	9.7	0.02676	6.90	0.01286	0.02832	7.19
				55.65	5	40	25	3.5	36	63%	0.012	10.4	0.01752	8.72	0.01286	0.01855	9.09
				55.65	15	35	25	3.6	31	54%	0.012	11.2	0.01050	5.27	0.01286	0.01111	5.49
				55.65	30	32	24	3.6	28	49%	0.012	11.7	0.00768	5.22	0.01301	0.00812	5.44
				55.65	60	29	24	3.7	25	44%	0.012	12.2	0.00554	10.20	0.01301	0.00587	10.63
				55.65	250	23	25	3.6	19	34%	0.012	13.2	0.00279	5.67	0.01286	0.00296	5.90
				55.65	1440	19.8	24	3.7	16	28%	0.012	13.7	0.00120	27.85	0.01301	0.00127	29.01

Table A1.5. Sieve and hydrometer data for Rising Star surface and cave sediment samples (n=40).

SURFACE SEDIMENTS

Sample		Sieve Size (mm)	Phi (Ø)	Oven-dried weight total sample (gr)	Subsample weight mechanical sieve and hydrometer (gr)	Oven-dried hygrosc. corr. sample mass used for hydrometer analysis	Fraction weight Sieve	Fraction weight Hydrometer analysis for G	Fraction WT Percent of fine-grained hydrometer sample	Fraction weight total fine-grained mass for F	WT Percent retained of total sample	Cumulative percentage	Percentage passed
190517JW1	**MECHANICAL SIEVING**	5	-2.3	140.35	44		0				0.00	0.00	100
		4	-2.0				1.53				1.09	1.09	98.91
		2.8	-1.5				1.56				1.11	2.20	97.80
		2	-1.0				2.71				1.93	4.13	95.87
		1	0.0				10.87				7.74	11.88	88.12
		0.5	1.0				27.33				19.47	31.35	68.65
	HYDROMETER ANALYSIS <0.5mm	0.25	2.0		96.35	93.64		38.92	41.56	40.05	28.53	59.88	40.12
		0.125	3.0					13.63	14.56	14.02	9.99	69.88	30.12
		0.063	4.0					5.84	6.24	6.01	4.28	74.16	25.84
		0.03142	5.0					2.00	2.14	2.06	1.47	75.62	24.38
		0.02011	5.6					3.50	3.74	3.60	2.57	78.19	21.81
		0.01193	6.4					1.53	1.63	1.57	1.12	79.31	20.69
		0.00847	6.9					0.89	0.95	0.91	0.65	79.96	20.04
		0.00603	7.4					3.14	3.36	3.23	2.30	82.26	17.74
		0.00301	8.4					4.14	4.42	4.26	3.04	85.30	14.70
		0.00130	9.6					9.57	10.22	9.85	7.02	92.32	7.68
		0.00037	11.4					10.48	11.19	10.78	7.68	100.00	0.00
190517JW2	**MECHANICAL SIEVING**	5	-2.3	141.4	25.54		0				0.00	0.00	100
		4	-2.0				2.49				1.76	1.76	98.24
		2.8	-1.5				1.7				1.20	2.96	97.04
		2	-1.0				2.45				1.73	4.70	95.30
		1	0.0				10.15				7.18	11.87	88.13
		0.5	1.0				8.75				6.19	18.06	81.94
	HYDROMETER ANALYSIS <0.5mm	0.25	2.0		115.86	98.4		10.75	10.92	12.66	8.95	27.01	72.99
		0.125	3.0					9.53	9.68	11.22	7.94	34.95	65.05
		0.063	4.0					10.86	11.04	12.79	9.04	43.99	56.01
		0.02668	5.2					6.50	6.61	7.65	5.41	49.41	50.59
		0.01790	5.8					4.50	4.57	5.30	3.75	53.15	46.85
		0.01069	6.5					3.00	3.05	3.53	2.50	55.65	44.35
		0.00774	7.0					2.00	2.03	2.35	1.67	57.32	42.68
		0.00554	7.5					3.14	3.19	3.70	2.62	59.93	40.07
		0.00278	8.5					4.14	4.21	4.88	3.45	63.38	36.62
		0.00120	9.7					22.57	22.94	26.58	18.80	82.18	17.82
		0.00037	11.4					21.40	21.75	25.20	17.82	100.00	0.00

Table A1.5. Sieve and hydrometer data for Rising Star surface and cave sediment samples (Continued).

SURFACE SEDIMENTS

Sample		Sieve Size (mm)	Phi (Ø)	Oven-dried weight total sample (gr)	Subsample weight mechanical sieve and hydrometer (gr)	Oven-dried hygrosc. corr. sample mass used for hydrometer analysis	Fraction weight Sieve	Fraction weight Hydrometer analysis for G	Fraction WT Percent of fine-grained hydrometer sample	Fraction weight total fine-grained mass for F	WT Percent retained of total sample	Cumulative percentage	Percentage passed
190517JW3	**MECHANICAL SIEVING**	5	-2.3	104.92	20.93		0				0.00	0.00	100
		4	-2.0				4.77				4.55	4.55	95.45
		2.8	-1.5				3.38				3.22	7.77	92.23
		2	-1.0				2.5				2.38	10.15	89.85
		1	0.0				4.89				4.66	14.81	85.19
		0.5	1.0				5.39				5.14	19.95	80.05
	HYDROMETER ANALYSIS <0.5mm	0.25	2.0		83.99	82.41		11.62	14.10	11.84	11.29	31.24	68.76
		0.125	3.0					13.23	16.05	13.48	12.85	44.09	55.91
		0.063	4.0					15.34	18.61	15.63	14.90	58.99	41.01
		0.03280	4.9					5.00	6.07	5.10	4.86	63.85	36.15
		0.02144	5.5					4.06	4.92	4.13	3.94	67.79	32.21
		0.01263	6.3					1.00	1.21	1.02	0.97	68.76	31.24
		0.00893	6.8					1.00	1.21	1.02	0.97	69.73	30.27
		0.00640	7.3					2.14	2.60	2.18	2.08	71.81	28.19
		0.00317	8.3					2.14	2.60	2.18	2.08	73.89	26.11
		0.00135	9.5					2.57	3.12	2.62	2.50	76.39	23.61
		0.00037	11.4					24.31	29.49	24.77	23.61	100.00	0.00
190517JW4	**MECHANICAL SIEVING**	5	-2.3	136.15	43.89		0				0.00	0.00	100
		4	-2.0				10.3				7.57	7.57	92.43
		2.8	-1.5				7.59				5.57	13.14	86.86
		2	-1.0				6.3				4.63	17.77	82.23
		1	0.0				11.07				8.13	25.90	74.10
		0.5	1.0				8.63				6.34	32.24	67.76
	HYDROMETER ANALYSIS <0.5mm	0.25	2.0		92.26	90.54		12.53	13.84	12.77	9.38	41.61	58.39
		0.125	3.0					14.57	16.09	14.85	10.90	52.52	47.48
		0.063	4.0					17.83	19.69	18.17	13.34	65.86	34.14
		0.03180	5.0					7.06	7.795	7.19	5.28	71.15	28.85
		0.02106	5.6					3.94	4.355	4.02	2.95	74.10	25.90
		0.01242	6.3					2.50	2.761	2.55	1.87	75.97	24.03
		0.00893	6.8					2.06	2.272	2.10	1.54	77.51	22.49
		0.00640	7.3					2.64	2.919	2.69	1.98	79.49	20.51
		0.00317	8.3					2.14	2.367	2.18	1.60	81.09	18.91
		0.00135	9.5					2.57	2.840	2.62	1.92	83.01	16.99
		0.00037	11.4					22.69	25.07	23.13	16.99	100.00	0.00

Table A1.5. Sieve and hydrometer data for Rising Star surface and cave sediment samples (Continued).

SURFACE SEDIMENTS

Sample		Sieve Size (mm)	Phi (Ø)	Oven-dried weight total sample (gr)	Subsample weight mechanical sieve and hydrometer (gr)	Oven-dried hygrosc. corr. sample mass used for hydrometer analysis	Fraction weight Sieve	Fraction weight Hydrometer analysis for G	Fraction WT Percent of fine-grained hydrometer sample	Fraction weight total fine-grained mass for F	WT Percent retained of total sample	Cumulative percentage	Percentage passed
190517JW5	MECHANICAL SIEVING	5	-2.3	129.26	59.5		0				0.00	0.00	100
		4	-2.0				38.54				29.82	29.82	70.18
		2.8	-1.5				4.83				3.74	33.55	66.45
		2	-1.0				4.03				3.12	36.67	63.33
		1	0.0				6.97				5.39	42.06	57.94
		0.5	1.0				5.13				3.97	46.03	53.97
	HYDROMETER ANALYSIS <0.5mm	0.25	2.0		69.76	68.37		7.54	11.03	7.69	5.95	51.98	48.02
		0.125	3.0					8.92	13.05	9.10	7.04	59.02	40.98
		0.063	4.0					12.09	17.68	12.34	9.54	68.57	31.43
		0.03243	4.9					5.50	8.04	5.61	4.34	72.91	27.09
		0.02128	5.6					3.56	5.20	3.63	2.81	75.72	24.28
		0.01251	6.3					2.00	2.93	2.04	1.58	77.30	22.70
		0.00893	6.8					1.06	1.55	1.08	0.83	78.13	21.87
		0.00636	7.3					3.17	4.64	3.24	2.50	80.63	19.37
		0.00320	8.3					1.06	1.55	1.08	0.83	81.47	18.53
		0.00134	9.5					3.57	5.22	3.64	2.82	84.29	15.71
		0.00037	11.4					19.91	29.11	20.31	15.71	100.00	0.00
190517JW6	MECHANICAL SIEVING	5	-2.3	134.38	69.42		0				0.00	0.00	100
		4	-2.0				45.65				33.97	33.97	66.03
		2.8	-1.5				6.33				4.71	38.68	61.32
		2	-1.0				4.62				3.44	42.12	57.88
		1	0.0				7.71				5.74	47.86	52.14
		0.5	1.0				5.11				3.80	51.66	48.34
	HYDROMETER ANALYSIS <0.5mm	0.25	2.0		64.96	62.76		6.67	10.63	6.90	5.14	56.80	43.20
		0.125	3.0					7.65	12.19	7.92	5.89	62.69	37.31
		0.063	4.0					11.09	17.67	11.48	8.54	71.23	28.77
		0.03268	4.9					4.00	6.37	4.14	3.08	74.31	25.69
		0.02113	5.6					5.14	8.19	5.32	3.96	78.27	21.73
		0.01273	6.3					1.06	1.68	1.09	0.81	79.09	20.91
		0.00903	6.8					1.50	2.39	1.55	1.16	80.24	19.76
		0.00647	7.3					1.64	2.62	1.70	1.27	81.51	18.49
		0.00320	8.3					3.16	5.03	3.27	2.43	83.94	16.06
		0.00134	9.5					2.27	3.62	2.35	1.75	85.69	14.31
		0.00037	11.4					18.58	29.60	19.23	14.31	100.00	0.00

Table A1.5. Sieve and hydrometer data for Rising Star surface and cave sediment samples (Continued).

Sample		Sieve Size (mm)	Phi (Ø)	Oven-dried weight total sample (gr)	Subsample weight mechanical sieve and hydrometer (gr)	Oven-dried hygrosc. corr. sample mass used for hydrometer analysis	Fraction weight Sieve	Fraction weight Hydrometer analysis for G	Fraction WT Percent of fine-grained hydrometer sample	Fraction weight total fine-grained mass for F	WT Percent retained of total sample	Cumulative percentage	Percentage passed
SURFACE SEDIMENTS													
190517JW7	**MECHANICAL SIEVING**	5	-2.3	142.83	64.76		0				0.00	0.00	100
		4	-2.0				19.84				13.89	13.89	86.11
		2.8	-1.5				12.72				8.91	22.80	77.20
		2	-1.0				13.43				9.40	32.20	67.80
		1	0.0				13.29				9.30	41.50	58.50
		0.5	1.0				5.48				3.84	45.34	54.66
	HYDROMETER ANALYSIS <0.5mm	0.25	2.0		78.07	73.12		4.08	5.58	4.36	3.05	48.39	51.61
		0.125	3.0					4.4	6.02	4.70	3.29	51.68	48.32
		0.063	4.0					9.82	13.43	10.49	7.34	59.02	40.98
		0.03002	5.1					4.00	5.47	4.27	2.99	62.01	37.99
		0.01950	5.7					7.00	9.57	7.47	5.23	67.24	32.76
		0.01183	6.4					2.00	2.74	2.14	1.50	68.74	31.26
		0.00847	6.9					2.00	2.74	2.14	1.50	70.23	29.77
		0.00605	7.4					3.14	4.30	3.36	2.35	72.58	27.42
		0.00304	8.4					1.80	2.46	1.92	1.35	73.93	26.07
		0.00128	9.6					12.63	17.27	13.48	9.44	83.37	16.63
		0.00037	11.4					22.24	30.42	23.75	16.63	100.00	0.00
CAVE SEDIMENTS													
UW101 1783A	**MECHANICAL SIEVING**	5	-2.3	197.04	8.61		0				0	0	100
		4	-2.0				2.23				1.13	1.1	98.87
		2.8	-1.5				0.78				0.40	1.5	98.47
		2	-1.0				1.34				0.68	2.2	97.79
		1	0.0				1.8				0.91	3.1	96.88
		0.5	1.0				2.46				1.25	4.4	95.63
	HYDROMETER ANALYSIS <0.5mm	0.25	2.0		188.43	95.80		8.19	8.55	16.1	8.18	12.5	87.45
		0.125	3.0					7.71	8.05	15.2	7.70	20.2	79.76
		0.063	4.0					6.03	6.29	11.9	6.02	26.3	73.74
		0.02430	5.4					3.00	3.13	5.9	2.99	29.3	70.74
		0.01589	6.0					6.03	6.29	11.9	6.02	35.3	64.73
		0.00974	6.7					4.06	4.24	8.0	4.05	39.3	60.68
		0.00720	7.1					5.03	5.25	9.9	5.02	44.3	55.66
		0.00530	7.6					8.29	8.65	16.3	8.27	52.6	47.39
		0.00279	8.5					7.43	7.75	14.6	7.42	60.0	39.97
		0.00120	9.7					20.94	21.86	41.2	20.91	80.9	19.06
		0.00037	11.4					19.10	19.94	37.6	19.06	100.0	0.00

Table A1.5. Sieve and hydrometer data for Rising Star surface and cave sediment samples (Continued).

CAVE SEDIMENTS

Sample		Sieve Size (mm)	Phi (Ø)	Oven-dried weight total sample (gr)	Subsample weight mechanical sieve and hydrometer (gr)	Oven-dried hygrosc. corr. sample mass used for hydrometer analysis	Fraction weight Sieve	Fraction weight Hydrometer analysis for G	Fraction WT Percent of fine-grained hydrometer sample	Fraction weight total fine-grained mass for F	WT Percent retained of total sample	Cumulative percentage	Percentage passed
UW101 1783C	**MECHANICAL SIEVING**	5	-2.3	189.2	24.25		0				0	0.0	100
		4	-2.0				1.72				0.91	0.9	99.09
		2.8	-1.5				2.15				1.14	2.0	97.95
		2	-1.0				3.39				1.79	3.8	96.16
		1	0.0				9.61				5.08	8.9	91.08
		0.5	1.0				7.38				3.90	12.8	87.18
	HYDROMETER ANALYSIS <0.5mm	0.25	2.0		164.95	96.2		7.41	7.70	12.7	6.72	19.5	80.47
		0.125	3.0					5.51	5.73	9.4	4.99	24.5	75.47
		0.063	4.0					4.38	4.55	7.5	3.97	28.5	71.50
		0.02457	5.3					1.00	1.04	1.7	0.91	29.4	70.60
		0.01564	6.0					5.00	5.20	8.6	4.53	33.9	66.07
		0.00957	6.7					3.06	3.18	5.2	2.77	36.7	63.30
		0.00697	7.2					5.59	5.81	9.6	5.06	41.8	58.23
		0.00517	7.6					8.67	9.01	14.9	7.86	49.6	50.38
		0.00275	8.5					6.54	6.80	11.2	5.93	55.6	44.45
		0.00117	9.7					24.77	25.75	42.5	22.45	78.0	22.00
		0.00037	11.4					24.27	25.23	41.6	22.00	100.0	0.00
UW101 1783G	**MECHANICAL SIEVING**	5	-2.3	197.51	66.95		0				0.00	0	100
		4	-2.0				10.91				5.52	5.5	94.48
		2.8	-1.5				6.19				3.13	8.7	91.34
		2	-1.0				8.55				4.33	13.0	87.01
		1	0.0				22.97				11.63	24.6	75.38
		0.5	1.0				18.33				9.28	33.9	66.10
	HYDROMETER ANALYSIS <0.5mm	0.25	2.0		130.56	56.62		1.92	3.39	4.4	2.24	36.1	63.86
		0.125	3.0					2.01	3.55	4.6	2.35	38.5	61.51
		0.063	4.0					2.12	3.74	4.9	2.48	41.0	59.04
		0.02975	5.1					1.03	1.82	2.4	1.20	42.2	57.84
		0.01899	5.7					3.50	6.18	8.1	4.09	46.2	53.75
		0.01121	6.5					1.53	2.70	3.5	1.78	48.0	51.97
		0.00803	7.0					1.56	2.75	3.6	1.82	49.8	50.15
		0.00575	7.4					5.17	9.13	11.9	6.04	55.9	44.11
		0.00296	8.4					3.10	5.47	7.1	3.62	59.5	40.49
		0.00122	9.7					17.71	31.29	40.8	20.68	80.2	19.81
		0.00037	11.4					16.97	29.97	39.1	19.81	100.0	0.00

Table A1.5. Sieve and hydrometer data for Rising Star surface and cave sediment samples (Continued).

CAVE SEDIMENTS

Sample		Sieve Size (mm)	Phi (Ø)	Oven-dried weight total sample (gr)	Subsample weight mechanical sieve and hydrometer (gr)	Oven-dried hygrosc. corr. sample mass used for hydrometer analysis	Fraction weight Sieve	Fraction weight Hydrometer analysis for G	Fraction WT Percent of fine-grained hydrometer sample	Fraction weight total fine-grained mass for F	WT Percent retained of total sample	Cumulative percentage	Percentage passed
UW101 1783H	MECHANICAL SIEVING	5	-2.3	200.3	55.99		0				0.00	0	100
		4	-2.0				4.37				2.18	2.18	97.82
		2.8	-1.5				3.54				1.77	3.95	96.05
		2	-1.0				6.15				3.07	7.02	92.98
		1	0.0				18.71				9.34	16.36	83.64
		0.5	1.0				23.22				11.59	27.95	72.05
	HYDROMETER ANALYSIS <0.5mm	0.25	2.0		144.31	80.16		5.29	6.60	9.5	4.75	32.71	67.29
		0.125	3.0					3.12	3.89	5.6	2.80	35.51	64.49
		0.063	4.0					3.03	3.78	5.5	2.72	38.24	61.76
		0.02474	5.3					3.00	3.74	5.4	2.70	40.93	59.07
		0.01616	6.0					3.00	3.74	5.4	2.70	43.63	56.37
		0.00962	6.7					4.03	5.03	7.3	3.62	47.25	52.75
		0.00708	7.1					3.61	4.51	6.5	3.25	50.50	49.50
		0.00517	7.6					6.61	8.25	11.9	5.95	56.44	43.56
		0.00272	8.5					6.19	7.72	11.1	5.56	62.00	38.00
		0.00117	9.7					27.13	33.84	48.8	24.38	86.39	13.61
		0.00037	11.4					15.15	18.90	27.3	13.61	100.00	0.00
UW101 1783L	MECHANICAL SIEVING	5	-2.3	193.12	72.22		0				0.00	0	100
		4	-2.0				5.53				2.86	2.86	97.14
		2.8	-1.5				4.43				2.29	5.16	94.84
		2	-1.0				5.87				3.04	8.20	91.80
		1	0.0				20.14				10.43	18.63	81.37
		0.5	1.0				36.25				18.77	37.40	62.60
	HYDROMETER ANALYSIS <0.5mm	0.25	2.0		120.9	63.08		3.7	5.87	7.1	3.67	41.07	58.93
		0.125	3.0					2.24	3.55	4.3	2.22	43.29	56.71
		0.063	4.0					2.5	3.96	4.8	2.48	45.77	54.23
		0.02758	5.2					4.50	7.13	8.6	4.47	50.24	49.76
		0.01810	5.8					2.50	3.96	4.8	2.48	52.72	47.28
		0.01071	6.5					2.53	4.01	4.8	2.51	55.23	44.77
		0.00768	7.0					2.09	3.31	4.0	2.07	57.30	42.70
		0.00562	7.5					3.61	5.73	6.9	3.59	60.89	39.11
		0.00281	8.5					5.19	8.22	9.9	5.15	66.03	33.97
		0.00120	9.7					22.57	35.78	43.3	22.40	88.43	11.57
		0.00037	11.4					11.66	18.48	22.3	11.57	100.00	0.00

Table A1.5. Sieve and hydrometer data for Rising Star surface and cave sediment samples (Continued).

CAVE SEDIMENTS

Sample		Sieve Size (mm)	Phi (Ø)	Oven-dried weight total sample (gr)	Subsample weight mechanical sieve and hydrometer (gr)	Oven-dried hygrosc. corr. sample mass used for hydrometer analysis	Fraction weight Sieve	Fraction weight Hydrometer analysis for G	Fraction WT Percent of fine-grained hydrometer sample	Fraction weight total fine-grained mass for F	WT Percent retained of total sample	Cumulative percentage	Percentage passed
100517JW3	**MECHANICAL SIEVING**	5	-2.3	96.32	18.11		0				0.00	0.00	100
		4	-2.0				2.89				3.00	3.00	97.00
		2.8	-1.5				1.88				1.95	4.95	95.05
		2	-1.0				1.6				1.66	6.61	93.39
		1	0.0				5.27				5.47	12.08	87.92
		0.5	1.0				6.47				6.72	18.80	81.20
	HYDROMETER ANALYSIS <0.5mm	0.25	2.0		78.21	75.03		8.9	11.86	9.28	9.63	28.43	71.57
		0.125	3.0					9.05	12.06	9.43	9.79	38.23	61.77
		0.063	4.0					10.89	14.51	11.35	11.78	50.01	49.99
		0.03084	5.0					5.06	6.74	5.27	5.47	55.48	44.52
		0.02025	5.6					5.00	6.66	5.21	5.41	60.89	39.11
		0.01206	6.4					2.00	2.67	2.08	2.16	63.06	36.94
		0.00863	6.9					2.00	2.67	2.08	2.16	65.22	34.78
		0.00617	7.3					4.14	5.52	4.32	4.48	69.71	30.29
		0.00312	8.3					2.83	3.77	2.95	3.06	72.77	27.23
		0.00131	9.6					7.60	10.13	7.92	8.22	80.99	19.01
		0.00037	11.4					17.56	23.41	18.31	19.01	100.00	0.00
100517JW5	**MECHANICAL SIEVING**	5	-2.3	100.77	31.54		0				0.00	0.00	100
		4	-2.0				9.21				9.14	9.14	90.86
		2.8	-1.5				3.51				3.48	12.62	87.38
		2	-1.0				3.43				3.40	16.03	83.97
		1	0.0				8.73				8.66	24.69	75.31
		0.5	1.0				6.66				6.61	31.30	68.70
	HYDROMETER ANALYSIS <0.5mm	0.25	2.0		69.23	66.23		7.98	12.05	8.34	8.28	39.58	60.42
		0.125	3.0					7.52	11.36	7.86	7.80	47.38	52.62
		0.063	4.0					11.23	16.96	11.74	11.65	59.03	40.97
		0.03266	4.9					6.50	9.81	6.79	6.74	65.77	34.23
		0.02152	5.5					4.50	6.79	4.70	4.67	70.44	29.56
		0.01273	6.3					0.50	0.75	0.52	0.52	70.96	29.04
		0.00903	6.8					2.50	3.77	2.61	2.59	73.55	26.45
		0.00647	7.3					0.70	1.06	0.73	0.73	74.28	25.72
		0.00322	8.3					2.80	4.23	2.93	2.90	77.18	22.82
		0.00135	9.5					3.07	4.64	3.21	3.19	80.37	19.63
		0.00037	11.4					18.92	28.58	19.78	19.63	100.00	0.00

Table A1.5. Sieve and hydrometer data for Rising Star surface and cave sediment samples (Continued).

CAVE SEDIMENTS

Sample		Sieve Size (mm)	Phi (Ø)	Oven-dried weight total sample (gr)	Subsample weight mechanical sieve and hydrometer (gr)	Oven-dried hygrosc. corr. sample mass used for hydrometer analysis	Fraction weight Sieve	Fraction weight Hydrometer analysis for G	Fraction WT Percent of fine-grained hydrometer sample	Fraction weight total fine-grained mass for F	WT Percent retained of total sample	Cumulative percentage	Percentage passed
100517JW6	**MECHANICAL SIEVING**	5	-2.3	124.27	64.12		0				0.00	0.00	100
		4	-2.0				39.66				31.91	31.91	68.09
		2.8	-1.5				5.59				4.50	36.41	63.59
		2	-1.0				4.8				3.86	40.28	59.72
		1	0.0				7.51				6.04	46.32	53.68
		0.5	1.0				6.56				5.28	51.60	48.40
	HYDROMETER ANALYSIS <0.5mm	0.25	2.0		60.15	56.30		9.13	16.22	9.75	7.85	59.45	40.55
		0.125	3.0					8.2	14.56	8.76	7.05	66.50	33.50
		0.063	4.0					9.62	17.09	10.28	8.27	74.77	25.23
		0.03378	4.9					5.00	8.88	5.34	4.30	79.06	20.94
		0.02205	5.5					3.00	5.33	3.20	2.58	81.64	18.36
		0.01295	6.3					0.56	0.99	0.60	0.48	82.12	17.88
		0.00918	6.8					1.44	2.56	1.54	1.24	83.36	16.64
		0.00654	7.3					1.23	2.18	1.31	1.06	84.42	15.58
		0.00327	8.3					1.27	2.26	1.36	1.09	85.51	14.49
		0.00136	9.5					2.07	3.68	2.21	1.78	87.29	12.71
		0.00037	11.4					14.78	26.25	15.79	12.71	100.00	0.00
100517 101-6	**MECHANICAL SIEVING**	5	-2.3	188.01	57.5		0				0.00	0.00	100
		4	-2.0				0.39				0.21	0.21	99.79
		2.8	-1.5				0.76				0.40	0.61	99.39
		2	-1.0				2.59				1.38	1.99	98.01
		1	0.0				19.58				10.41	12.40	87.60
		0.5	1.0				34.18				18.18	30.58	69.42
	HYDROMETER ANALYSIS <0.5mm	0.25	2.0		130.51	53.69		1.2	2.24	2.92	1.55	32.13	67.87
		0.125	3.0					2.05	3.82	4.98	2.65	34.79	65.21
		0.063	4.0					3.06	5.70	7.44	3.96	38.74	61.26
		0.03180	5.0					3.00	5.59	7.29	3.88	42.62	57.38
		0.02051	5.6					2.64	4.92	6.42	3.42	46.04	53.96
		0.01220	6.4					2.00	3.73	4.86	2.59	48.62	51.38
		0.00872	6.8					1.06	1.97	2.57	1.37	49.99	50.01
		0.00621	7.3					2.67	4.98	6.49	3.45	53.44	46.56
		0.00313	8.3					1.91	3.57	4.65	2.48	55.92	44.08
		0.00130	9.6					9.49	17.67	23.06	12.26	68.18	31.82
		0.00037	11.4					24.61	45.83	59.82	31.82	100.00	0.00

Table A1.5. Sieve and hydrometer data for Rising Star surface and cave sediment samples (Continued).

CAVE SEDIMENTS

Sample		Sieve Size (mm)	Phi (Ø)	Oven-dried weight total sample (gr)	Subsample weight mechanical sieve and hydrometer (gr)	Oven-dried hygrosc. corr. sample mass used for hydrometer analysis	Fraction weight Sieve	Fraction weight Hydrometer analysis for G	Fraction WT Percent of fine-grained hydrometer sample	Fraction weight total fine-grained mass for F	WT Percent retained of total sample	Cumulative percentage	Percentage passed
100517 101-7	**MECHANICAL SIEVING**	5	-2.3	204.18	6.99		0				0.00	0.00	100
		4	-2.0				0.18				0.09	0.09	99.91
		2.8	-1.5				0.43				0.21	0.30	99.70
		2	-1.0				0.67				0.33	0.63	99.37
		1	0.0				2.46				1.20	1.83	98.17
		0.5	1.0				3.25				1.59	3.42	96.58
	HYDROMETER ANALYSIS <0.5mm	0.25	2.0		197.19	98.20		2.52	2.57	5.06	2.48	5.90	94.10
		0.125	3.0					3.46	3.52	6.95	3.40	9.30	90.70
		0.063	4.0					7.81	7.95	15.68	7.68	16.99	83.01
		0.02698	5.2					12.00	12.22	24.10	11.80	28.79	71.21
		0.01881	5.7					8.56	8.71	17.18	8.42	37.20	62.80
		0.01160	6.4					4.53	4.61	9.09	4.45	41.66	58.34
		0.00843	6.9					4.03	4.10	8.09	3.96	45.62	54.38
		0.00610	7.4					5.14	5.24	10.33	5.06	50.68	49.32
		0.00310	8.3					4.94	5.03	9.93	4.86	55.54	44.46
		0.00133	9.6					6.49	6.60	13.02	6.38	61.92	38.08
		0.00037	11.4					38.72	39.43	77.76	38.08	100.00	0.00
110517JW1	**MECHANICAL SIEVING**	5	-2.3	42.79	5.51		0				0.00	0.00	100
		4	-2.0				0.22				0.51	0.51	99.49
		2.8	-1.5				0.55				1.29	1.80	98.20
		2	-1.0				0.56				1.31	3.11	96.89
		1	0.0				2.19				5.12	8.23	91.77
		0.5	1.0				1.99				4.65	12.88	87.12
	HYDROMETER ANALYSIS <0.5mm	0.25	2.0		37.28	29.56		1.76	5.95	2.22	5.19	18.06	81.94
		0.125	3.0					2.36	7.98	2.98	6.96	25.02	74.98
		0.063	4.0					4.7	15.90	5.93	13.85	38.87	61.13
		0.03507	4.8					3.50	11.84	4.41	10.32	49.19	50.81
		0.02247	5.5					3.00	10.15	3.78	8.84	58.03	41.97
		0.01318	6.2					1.00	3.38	1.26	2.95	60.98	39.02
		0.00938	6.7					0.06	0.19	0.07	0.17	61.15	38.85
		0.00663	7.2					0.34	1.16	0.43	1.01	62.16	37.84
		0.00329	8.2					0.46	1.55	0.58	1.35	63.51	36.49
		0.00134	9.5					0.00	0.00	0.00	0.00	63.51	36.49
		0.00037	11.4					12.38	41.89	15.62	36.49	100.00	0.00

Table A1.5. Sieve and hydrometer data for Rising Star surface and cave sediment samples (Continued).

CAVE SEDIMENTS

Sample		Sieve Size (mm)	Phi (Ø)	Oven-dried weight total sample (gr)	Subsample weight mechanical sieve and hydrometer (gr)	Oven-dried hygrosc. corr. sample mass used for hydrometer analysis	Fraction weight Sieve	Fraction weight Hydrometer analysis for G	Fraction WT Percent of fine-grained hydrometer sample	Fraction weight total fine-grained mass for F	WT Percent retained of total sample	Cumulative percentage	Percentage passed
110517JW2	**MECHANICAL SIEVING**	5	-2.3	45.02	2.51		0				0.00	0.00	100
		4	-2.0				0.31				0.69	0.69	99.31
		2.8	-1.5				0.18				0.40	1.09	98.91
		2	-1.0				0.2				0.44	1.53	98.47
		1	0.0				0.8				1.78	3.31	96.69
		0.5	1.0				1.02				2.27	5.58	94.42
	HYDROMETER ANALYSIS <0.5mm	0.25	2.0		42.51	34.91		1.31	3.75	1.59	3.54	9.12	90.88
		0.125	3.0					2.04	5.84	2.48	5.52	14.64	85.36
		0.063	4.0					5.02	14.38	6.11	13.58	28.21	71.79
		0.03484	4.8					4.50	12.89	5.48	12.17	40.38	59.62
		0.02247	5.5					3.00	8.59	3.65	8.11	48.50	51.50
		0.01318	6.2					0.50	1.43	0.61	1.35	49.85	50.15
		0.00932	6.7					0.70	2.00	0.85	1.89	51.74	48.26
		0.00670	7.2					0.26	0.74	0.31	0.70	52.44	47.56
		0.00333	8.2					0.54	1.55	0.66	1.47	53.90	46.10
		0.00136	9.5					0.00	0.00	0.00	0.00	53.90	46.10
		0.00037	11.4					17.04	48.82	20.75	46.10	100.00	0.00
130517JW4	**MECHANICAL SIEVING**	5	-2.3	53.69	19.14		0				0.00	0.00	100
		4	-2.0				0.9				1.68	1.68	98.32
		2.8	-1.5				1.12				2.09	3.76	96.24
		2	-1.0				1.74				3.24	7.00	93.00
		1	0.0				8.03				14.96	21.96	78.04
		0.5	1.0				7.35				13.69	35.65	64.35
	HYDROMETER ANALYSIS <0.5mm	0.25	2.0		34.55	32.99		4.78	14.49	5.01	9.32	44.97	55.03
		0.125	3.0					2.79	8.46	2.92	5.44	50.41	49.59
		0.063	4.0					4.2	12.73	4.40	8.19	58.61	41.39
		0.03460	4.9					3.50	10.61	3.67	6.83	65.43	34.57
		0.02225	5.5					3.00	9.09	3.14	5.85	71.28	28.72
		0.01305	6.3					0.94	2.86	0.99	1.84	73.12	26.88
		0.00929	6.8					0.49	1.47	0.51	0.95	74.07	25.93
		0.00666	7.2					1.03	3.12	1.08	2.01	76.08	23.92
		0.00332	8.2					1.04	3.16	1.09	2.03	78.11	21.89
		0.00136	9.5					0.00	0.00	0.00	0.00	78.11	21.89
		0.00037	11.4					11.22	34.02	11.75	21.89	100.00	0.00

Table A1.5. Sieve and hydrometer data for Rising Star surface and cave sediment samples (Continued).

CAVE SEDIMENTS													
Sample		Sieve Size (mm)	Phi (Ø)	Oven-dried weight total sample (gr)	Subsample weight mechanical sieve and hydrometer (gr)	Oven-dried hygrosc. corr. sample mass used for hydrometer analysis	Fraction weight Sieve	Fraction weight Hydrometer analysis for G	Fraction WT Percent of fine-grained hydrometer sample	Fraction weight total fine-grained mass for F	WT Percent retained of total sample	Cumulative percentage	Percentage passed
260517JW1	**MECHANICAL SIEVING**	5	-2.3	102.73	21.54		0				0.00	0.00	100
		4	-2.0				2.59				2.52	2.52	97.48
		2.8	-1.5				2.58				2.51	5.03	94.97
		2	-1.0				2.89				2.81	7.85	92.15
		1	0.0				7.16				6.97	14.82	85.18
		0.5	1.0				6.32				6.15	20.97	79.03
	HYDROMETER ANALYSIS <0.5mm	0.25	2.0		81.19	78.10		6.58	8.43	6.84	6.66	27.63	72.37
		0.125	3.0					6.99	8.95	7.27	7.07	34.70	65.30
		0.063	4.0					11.75	15.04	12.21	11.89	46.59	53.41
		0.03110	5.0					6.50	8.32	6.76	6.58	53.17	46.83
		0.02050	5.6					7.06	9.04	7.34	7.14	60.31	39.69
		0.01233	6.3					2.06	2.63	2.14	2.08	62.39	37.61
		0.00885	6.8					2.00	2.56	2.08	2.02	64.41	35.59
		0.00632	7.3					2.67	3.42	2.78	2.70	67.12	32.88
		0.00319	8.3					2.01	2.58	2.09	2.04	69.16	30.84
		0.00131	9.6					5.83	7.46	6.06	5.90	75.05	24.95
		0.00037	11.4					24.65	31.56	25.63	24.95	100.00	0.00
260517JW2	**MECHANICAL SIEVING**	5	-2.3	45.82	2.63		0				0.00	0.00	100
		4	-2.0				0.4				0.87	0.87	99.13
		2.8	-1.5				0.5				1.09	1.96	98.04
		2	-1.0				0.12				0.26	2.23	97.77
		1	0.0				0.61				1.33	3.56	96.44
		0.5	1.0				1				2.18	5.74	94.26
	HYDROMETER ANALYSIS <0.5mm	0.25	2.0		43.19	37.10		5.36	14.45	6.24	13.62	19.36	80.64
		0.125	3.0					6.02	16.23	7.01	15.29	34.65	65.35
		0.063	4.0					7.86	21.18	9.15	19.97	54.62	45.38
		0.03498	4.8					4.00	10.78	4.66	10.16	64.78	35.22
		0.02264	5.5					3.03	8.16	3.53	7.69	72.48	27.52
		0.01328	6.2					1.50	4.04	1.75	3.81	76.29	23.71
		0.00948	6.7					0.56	1.50	0.65	1.42	77.70	22.30
		0.00672	7.2					0.14	0.39	0.17	0.36	78.07	21.93
		0.00333	8.2					0.71	1.93	0.83	1.81	79.88	20.12
		0.00137	9.5					0.00	0.00	0.00	0.00	79.88	20.12
		0.00037	11.4					7.92	21.34	9.22	20.12	100.00	0.00

Table A1.5. Sieve and hydrometer data for Rising Star surface and cave sediment samples (Continued).

CAVE SEDIMENTS

Sample		Sieve Size (mm)	Phi (Ø)	Oven-dried weight total sample (gr)	Subsample weight mechanical sieve and hydrometer (gr)	Oven-dried hygrosc. corr. sample mass used for hydrometer analysis	Fraction weight Sieve	Fraction weight Hydrometer analysis for G	Fraction WT Percent of fine-grained hydrometer sample	Fraction weight total fine-grained mass for F	WT Percent retained of total sample	Cumulative percentage	Percentage passed
260517JW3	**MECHANICAL SIEVING**	5	-2.3	127.05	44.17		0				0.00	0.00	100
		4	-2.0				9.19				7.23	7.23	92.77
		2.8	-1.5				3.84				3.02	10.26	89.74
		2	-1.0				6.39				5.03	15.29	84.71
		1	0.0				13.76				10.83	26.12	73.88
		0.5	1.0				10.99				8.65	34.77	65.23
	HYDROMETER ANALYSIS <0.5mm	0.25	2.0		82.88	79.38		11	13.86	11.48	9.04	43.81	56.19
		0.125	3.0					9.87	12.43	10.30	8.11	51.92	48.08
		0.063	4.0					11.89	14.98	12.41	9.77	61.69	38.31
		0.03202	5.0					6.00	7.56	6.26	4.93	66.62	33.38
		0.02097	5.6					5.20	6.55	5.43	4.27	70.89	29.11
		0.01256	6.3					2.30	2.90	2.40	1.89	72.78	27.22
		0.00900	6.8					1.50	1.89	1.57	1.23	74.01	25.99
		0.00639	7.3					2.46	3.10	2.57	2.02	76.03	23.97
		0.00318	8.3					2.20	2.77	2.30	1.81	77.84	22.16
		0.00132	9.6					3.91	4.93	4.09	3.22	81.06	18.94
		0.00037	11.4					23.05	29.04	24.07	18.94	100.00	0.00
260517JW4	**MECHANICAL SIEVING**	5	-2.3	106.86	43.48		0				0.00	0.00	100
		4	-2.0				20.27				18.97	18.97	81.03
		2.8	-1.5				4.68				4.38	23.35	76.65
		2	-1.0				4.46				4.17	27.52	72.48
		1	0.0				7.48				7.00	34.52	65.48
		0.5	1.0				6.59				6.17	40.69	59.31
	HYDROMETER ANALYSIS <0.5mm	0.25	2.0		63.38	57.85		7.45	12.88	8.16	7.64	48.33	51.67
		0.125	3.0					6.91	11.94	7.57	7.08	55.41	44.59
		0.063	4.0					8.78	15.18	9.62	9.00	64.41	35.59
		0.03402	4.9					5.50	9.51	6.03	5.64	70.05	29.95
		0.02213	5.5					4.03	6.96	4.41	4.13	74.18	25.82
		0.01307	6.3					2.00	3.46	2.19	2.05	76.23	23.77
		0.00933	6.7					0.50	0.86	0.55	0.51	76.75	23.25
		0.00664	7.2					1.53	2.64	1.67	1.57	78.31	21.69
		0.00326	8.3					1.21	2.10	1.33	1.24	79.56	20.44
		0.00136	9.5					0.00	0.00	0.00	0.00	79.56	20.44
		0.00037	11.4					19.94	34.47	21.84	20.44	100.00	0.00

Table A1.5. Sieve and hydrometer data for Rising Star surface and cave sediment samples (Continued).

CAVE SEDIMENTS													
Sample		Sieve Size (mm)	Phi (Ø)	Oven-dried weight total sample (gr)	Subsample weight mechanical sieve and hydrometer (gr)	Oven-dried hygrosc. corr. sample mass used for hydrometer analysis	Fraction weight Sieve	Fraction weight Hydrometer analysis for G	Fraction WT Percent of fine-grained hydrometer sample	Fraction weight total fine-grained mass for F	WT Percent retained of total sample	Cumulative percentage	Percentage passed
260517JW8	**MECHANICAL SIEVING**	5	-2.3	89.67	7.55		0				0.00	0.00	100
		4	-2.0				0.16				0.18	0.18	99.82
		2.8	-1.5				0.41				0.46	0.64	99.36
		2	-1.0				0.88				0.98	1.62	98.38
		1	0.0				2.75				3.07	4.68	95.32
		0.5	1.0				3.35				3.74	8.42	91.58
	HYDROMETER ANALYSIS <0.5mm	0.25	2.0		82.12	75.28		3.03	4.02	3.31	3.69	12.11	87.89
		0.125	3.0					3.93	5.22	4.29	4.78	16.89	83.11
		0.063	4.0					7.58	10.07	8.27	9.22	26.11	73.89
		0.02975	5.1					8.00	10.63	8.73	9.73	35.84	64.16
		0.01992	5.6					8.00	10.63	8.73	9.73	45.57	54.43
		0.01211	6.4					4.70	6.24	5.13	5.72	51.29	48.71
		0.00885	6.8					1.36	1.80	1.48	1.65	52.94	47.06
		0.00628	7.3					4.90	6.51	5.34	5.96	58.90	41.10
		0.00317	8.3					3.34	4.44	3.65	4.07	62.97	37.03
		0.00133	9.6					3.27	4.35	3.57	3.98	66.95	33.05
		0.00037	11.4					27.17	36.09	29.64	33.05	100.00	0.00
260517JW9	**MECHANICAL SIEVING**	5	-2.3	183.38	14.3		0				0.00	0.00	100
		4	-2.0				1.46				0.80	0.80	99.20
		2.8	-1.5				1.04				0.57	1.36	98.64
		2	-1.0				1.47				0.80	2.16	97.84
		1	0.0				4.34				2.37	4.53	95.47
		0.5	1.0				5.99				3.27	7.80	92.20
	HYDROMETER ANALYSIS <0.5mm	0.25	2.0		169.08	97.60		6.75	6.92	11.69	6.38	14.17	85.83
		0.125	3.0					6.18	6.33	10.71	5.84	20.01	79.99
		0.063	4.0					9.6	9.84	16.63	9.07	29.08	70.92
		0.03043	5.0					10.03	10.28	17.37	9.47	38.56	61.44
		0.02066	5.6					9.03	9.25	15.64	8.53	47.09	52.91
		0.01256	6.3					3.50	3.59	6.06	3.31	50.39	49.61
		0.00909	6.8					1.50	1.54	2.60	1.42	51.81	48.19
		0.00647	7.3					2.80	2.87	4.85	2.65	54.45	45.55
		0.00321	8.3					1.80	1.84	3.12	1.70	56.15	43.85
		0.00134	9.5					1.97	2.02	3.42	1.86	58.02	41.98
		0.00037	11.4					44.44	45.53	76.99	41.98	100.00	0.00

Table A1.5. Sieve and hydrometer data for Rising Star surface and cave sediment samples (Continued).

CAVE SEDIMENTS													
Sample		**Sieve Size (mm)**	**Phi (Ø)**	**Oven-dried weight total sample (gr)**	**Subsample weight mechanical sieve and hydrometer (gr)**	**Oven-dried hygrosc. corr. sample mass used for hydrometer analysis**	**Fraction weight Sieve**	**Fraction weight Hydrometer analysis for G**	**Fraction WT Percent of fine-grained hydrometer sample**	**Fraction weight total fine-grained mass for F**	**WT Percent retained of total sample**	**Cumulative percentage**	**Percentage passed**
260517JW10	**MECHANICAL SIEVING**	5	-2.3	62.33	6.63		0				0.00	0.00	100
		4	-2.0				0.63				1.01	1.01	98.99
		2.8	-1.5				0.83				1.33	2.34	97.66
		2	-1.0				0.88				1.41	3.75	96.25
		1	0.0				2.23				3.58	7.33	92.67
		0.5	1.0				2.06				3.30	10.64	89.36
	HYDROMETER ANALYSIS <0.5mm	0.25	2.0		55.7	52.83		4.15	7.86	4.38	7.02	17.66	82.34
		0.125	3.0					4.88	9.24	5.14	8.25	25.91	74.09
		0.063	4.0					7.24	13.70	7.63	12.25	38.16	61.84
		0.03266	4.9					4.50	8.52	4.74	7.61	45.77	54.23
		0.02129	5.6					5.30	10.03	5.59	8.96	54.73	45.27
		0.01264	6.3					2.20	4.16	2.32	3.72	58.45	41.55
		0.00903	6.8					1.06	2.00	1.11	1.79	60.24	39.76
		0.00643	7.3					4.00	7.57	4.22	6.77	67.01	32.99
		0.00321	8.3					2.50	4.73	2.64	4.23	71.24	28.76
		0.00134	9.5					1.01	1.92	1.07	1.72	72.95	27.05
		0.00037	11.4					15.99	30.27	16.86	27.05	100.00	0.00
240517JW1	**MECHANICAL SIEVING**	5	-2.3	43.47	4.34		0				0.00	0.00	100
		4	-2.0				2.98				6.86	6.86	93.14
		2.8	-1.5				0.12				0.28	7.13	92.87
		2	-1.0				0.23				0.53	7.66	92.34
		1	0.0				0.44				1.01	8.67	91.33
		0.5	1.0				0.57				1.31	9.98	90.02
	HYDROMETER ANALYSIS <0.5mm	0.25	2.0		39.13	28.81		1.22	4.23	1.66	3.81	13.80	86.20
		0.125	3.0					1.5	5.21	2.04	4.69	18.48	81.52
		0.063	4.0					3.66	12.70	4.97	11.43	29.92	70.08
		0.03486	4.8					4.00	13.88	5.43	12.50	42.41	57.59
		0.02250	5.5					3.50	12.15	4.75	10.94	53.35	46.65
		0.01328	6.2					0.56	1.93	0.76	1.74	55.09	44.91
		0.00939	6.7					0.50	1.74	0.68	1.56	56.65	43.35
		0.00664	7.2					1.00	3.47	1.36	3.12	59.78	40.22
		0.00328	8.3					0.33	1.14	0.45	1.03	60.80	39.20
		0.00137	9.5					0.00	0.00	0.00	0.00	60.80	39.20
		0.00037	11.4					12.55	43.54	17.04	39.20	100.00	0.00

Table A1.5. Sieve and hydrometer data for Rising Star surface and cave sediment samples (Continued).

CAVE SEDIMENTS

Sample		Sieve Size (mm)	Phi (Ø)	Oven-dried weight total sample (gr)	Subsample weight mechanical sieve and hydrometer (gr)	Oven-dried hygrosc. corr. sample mass used for hydrometer analysis	Fraction weight Sieve	Fraction weight Hydrometer analysis for G	Fraction WT Percent of fine-grained hydrometer sample	Fraction weight total fine-grained mass for F	WT Percent retained of total sample	Cumulative percentage	Percentage passed
240517JW2	**MECHANICAL SIEVING**	5	-2.3	37.26	3.31		0				0.00	0.00	100
		4	-2.0				0				0.00	0.00	100.00
		2.8	-1.5				0.09				0.24	0.24	99.76
		2	-1.0				0.36				0.97	1.21	98.79
		1	0.0				1.09				2.93	4.13	95.87
		0.5	1.0				1.77				4.75	8.88	91.12
	HYDROMETER ANALYSIS <0.5mm	0.25	2.0		33.95	28.80		3.22	11.18	3.80	10.19	19.07	80.93
		0.125	3.0					3.17	11.01	3.74	10.03	29.10	70.90
		0.063	4.0					3.43	11.91	4.04	10.85	39.95	60.05
		0.03498	4.8					3.50	12.15	4.13	11.07	51.02	48.98
		0.02264	5.5					3.00	10.42	3.54	9.49	60.51	39.49
		0.01328	6.2					0.53	1.84	0.62	1.67	62.18	37.82
		0.00939	6.7					1.00	3.47	1.18	3.16	65.35	34.65
		0.00666	7.2					0.64	2.23	0.76	2.03	67.38	32.62
		0.00332	8.2					1.30	4.51	1.53	4.11	71.49	28.51
		0.00137	9.5					0.00	0.00	0.00	0.00	71.49	28.51
		0.00037	11.4					9.01	31.28	10.62	28.51	100.00	0.00
240517JW3	**MECHANICAL SIEVING**	5	-2.3	26.41	1.49		0				0.00	0.00	100
		4	-2.0				0.03				0.11	0.11	99.89
		2.8	-1.5				0.09				0.34	0.45	99.55
		2	-1.0				0.26				0.98	1.44	98.56
		1	0.0				0.49				1.86	3.29	96.71
		0.5	1.0				0.62				2.35	5.64	94.36
	HYDROMETER ANALYSIS <0.5mm	0.25	2.0		24.92	23.16		1.13	4.88	1.22	4.60	10.25	89.75
		0.125	3.0					1.58	6.82	1.70	6.44	16.68	83.32
		0.063	4.0					2.53	10.92	2.72	10.31	26.99	73.01
		0.03498	4.8					3.00	12.95	3.23	12.22	39.21	60.79
		0.02250	5.5					3.00	12.95	3.23	12.22	51.43	48.57
		0.01320	6.2					1.33	5.74	1.43	5.41	56.85	43.15
		0.00942	6.7					0.53	2.28	0.57	2.15	59.00	41.00
		0.00666	7.2					1.17	5.06	1.26	4.77	63.77	36.23
		0.00332	8.2					0.50	2.16	0.54	2.04	65.81	34.19
		0.00137	9.5					0.00	0.00	0.00	0.00	65.81	34.19
		0.00037	11.4					8.39	36.23	9.03	34.19	100.00	0.00

Table A1.5. Sieve and hydrometer data for Rising Star surface and cave sediment samples (Continued).

CAVE SEDIMENTS

Sample		Sieve Size (mm)	Phi (Ø)	Oven-dried weight total sample (gr)	Subsample weight mechanical sieve and hydrometer (gr)	Oven-dried hygrosc. corr. sample mass used for hydrometer analysis	Fraction weight Sieve	Fraction weight Hydrometer analysis for G	Fraction WT Percent of fine-grained hydrometer sample	Fraction weight total fine-grained mass for F	WT Percent retained of total sample	Cumulative percentage	Percentage passed
240517JW4	**MECHANICAL SIEVING**	5	-2.3	130.99	2.34		0				0.00	0.00	100
		4	-2.0				0.08				0.06	0.06	99.94
		2.8	-1.5				0.06				0.05	0.11	99.89
		2	-1.0				0.2				0.15	0.26	99.74
		1	0.0				0.86				0.66	0.92	99.08
		0.5	1.0				1.14				0.87	1.79	98.21
	HYDROMETER ANALYSIS <0.5mm	0.25	2.0		128.65	98.21		1.35	1.37	1.77	1.35	3.14	96.86
		0.125	3.0					3.05	3.11	4.00	3.05	6.19	93.81
		0.063	4.0					9.97	10.15	13.06	9.97	16.16	83.84
		0.02788	5.2					15.00	15.27	19.65	15.00	31.16	68.84
		0.01984	5.7					9.00	9.16	11.79	9.00	40.16	59.84
		0.01211	6.4					3.00	3.05	3.93	3.00	43.16	56.84
		0.00872	6.8					2.86	2.91	3.74	2.86	46.02	53.98
		0.00628	7.3					4.84	4.93	6.34	4.84	50.86	49.14
		0.00321	8.3					4.30	4.38	5.63	4.30	55.16	44.84
		0.00135	9.5					2.57	2.62	3.37	2.57	57.73	42.27
		0.00037	11.4					42.27	43.04	55.37	42.27	100.00	0.00
240517JW5	**MECHANICAL SIEVING**	5	-2.3	58.18	14.58		0				0.00	0.00	100
		4	-2.0				2.27				3.90	3.90	96.10
		2.8	-1.5				1.24				2.13	6.03	93.97
		2	-1.0				1.67				2.87	8.90	91.10
		1	0.0				4.32				7.43	16.33	83.67
		0.5	1.0				5.08				8.73	25.06	74.94
	HYDROMETER ANALYSIS <0.5mm	0.25	2.0		43.6	40.57		5.61	13.83	6.03	10.36	35.42	64.58
		0.125	3.0					5.07	12.50	5.45	9.37	44.79	55.21
		0.063	4.0					6.2	15.28	6.66	11.45	56.24	43.76
		0.03486	4.8					3.50	8.63	3.76	6.47	62.71	37.29
		0.02250	5.5					3.53	8.70	3.79	6.52	69.23	30.77
		0.01320	6.2					0.00	0.00	0.00	0.00	69.23	30.77
		0.00933	6.7					1.06	2.61	1.14	1.95	71.18	28.82
		0.00666	7.2					1.11	2.75	1.20	2.06	73.24	26.76
		0.00332	8.2					0.83	2.04	0.89	1.53	74.77	25.23
		0.00137	9.5					0.00	0.00	0.00	0.00	74.77	25.23
		0.00037	11.4					13.66	33.67	14.68	25.23	100.00	0.00

Table A1.5. Sieve and hydrometer data for Rising Star surface and cave sediment samples (Continued).

CAVE SEDIMENTS

Sample		Sieve Size (mm)	Phi (Ø)	Oven-dried weight total sample (gr)	Subsample weight mechanical sieve and hydrometer (gr)	Oven-dried hygrosc. corr. sample mass used for hydrometer analysis	Fraction weight Sieve	Fraction weight Hydrometer analysis for G	Fraction WT Percent of fine-grained hydrometer sample	Fraction weight total fine-grained mass for F	WT Percent retained of total sample	Cumulative percentage	Percentage passed
240517JW6	**MECHANICAL SIEVING**	5	-2.3	69.58	30.6		0				0.00	0.00	100
		4	-2.0				12.35				17.75	17.75	82.25
		2.8	-1.5				3.21				4.61	22.36	77.64
		2	-1.0				3.26				4.69	27.05	72.95
		1	0.0				5.96				8.57	35.61	64.39
		0.5	1.0				5.82				8.36	43.98	56.02
	HYDROMETER ANALYSIS <0.5mm	0.25	2.0		38.98	34.81		6.49	18.64	7.27	10.45	54.42	45.58
		0.125	3.0					5.01	14.39	5.61	8.06	62.49	37.51
		0.063	4.0					5.49	15.77	6.15	8.84	71.32	28.68
		0.03557	4.8					3.53	10.14	3.95	5.68	77.00	23.00
		0.02286	5.5					2.30	6.61	2.58	3.70	80.70	19.30
		0.01332	6.2					0.20	0.57	0.22	0.32	81.02	18.98
		0.00948	6.7					0.53	1.52	0.59	0.85	81.88	18.12
		0.00678	7.2					0.36	1.03	0.40	0.57	82.45	17.55
		0.00332	8.2					0.67	1.93	0.75	1.08	83.53	16.47
		0.00139	9.5					0.00	0.00	0.00	0.00	83.53	16.47
		0.00037	11.4					10.23	29.40	11.46	16.47	100.00	0.00
240517JW7	**MECHANICAL SIEVING**	5	-2.3	46.92	21.47		0				0.00	0.00	100
		4	-2.0				5.47				11.66	11.66	88.34
		2.8	-1.5				2.45				5.22	16.88	83.12
		2	-1.0				2.38				5.07	21.95	78.05
		1	0.0				5.53				11.79	33.74	66.26
		0.5	1.0				5.64				12.02	45.76	54.24
	HYDROMETER ANALYSIS <0.5mm	0.25	2.0		25.45	22.59		4.56	20.18	5.14	10.95	56.71	43.29
		0.125	3.0					4.27	18.90	4.81	10.25	66.96	33.04
		0.063	4.0					3.11	13.76	3.50	7.47	74.42	25.58
		0.03592	4.8					1.53	6.77	1.72	3.67	78.09	21.91
		0.02300	5.4					0.80	3.54	0.90	1.92	80.01	19.99
		0.01328	6.2					0.73	3.22	0.82	1.75	81.76	18.24
		0.00942	6.7					0.53	2.34	0.60	1.27	83.03	16.97
		0.00678	7.2					1.11	4.93	1.26	2.67	85.71	14.29
		0.00333	8.2					0.00	0.00	0.00	0.00	85.71	14.29
		0.00139	9.5					0.00	0.00	0.00	0.00	85.71	14.29
		0.00037	11.4					5.95	26.35	6.71	14.29	100.00	0.00

Table A1.5. Sieve and hydrometer data for Rising Star surface and cave sediment samples (Continued).

CAVE SEDIMENTS

Sample		Sieve Size (mm)	Phi (Ø)	Oven-dried weight total sample (gr)	Subsample weight mechanical sieve and hydrometer (gr)	Oven-dried hygrosc. corr. sample mass used for hydrometer analysis	Fraction weight Sieve	Fraction weight Hydrometer analysis for G	Fraction WT Percent of fine-grained hydrometer sample	Fraction weight total fine-grained mass for F	WT Percent retained of total sample	Cumulative percentage	Percentage passed
240517JW8	**MECHANICAL SIEVING**	5	-2.3	58.77	3.32		0				0.00	0.00	100
		4	-2.0				0.24				0.41	0.41	99.59
		2.8	-1.5				0.18				0.31	0.71	99.29
		2	-1.0				0.2				0.34	1.05	98.95
		1	0.0				0.94				1.60	2.65	97.35
		0.5	1.0				1.76				2.99	5.65	94.35
	HYDROMETER ANALYSIS <0.5mm	0.25	2.0		55.45	45.27		5.7	12.59	6.98	11.88	17.53	82.47
		0.125	3.0					12.57	27.77	15.40	26.20	43.72	56.28
		0.063	4.0					13.06	28.85	16.00	27.22	70.94	29.06
		0.03545	4.8					3.23	7.13	3.95	6.73	77.67	22.33
		0.02286	5.5					2.33	5.14	2.85	4.85	82.52	17.48
		0.01332	6.2					0.73	1.61	0.89	1.52	84.04	15.96
		0.00948	6.7					0.36	0.79	0.44	0.74	84.79	15.21
		0.00670	7.2					0.79	1.74	0.96	1.64	86.42	13.58
		0.00333	8.2					0.63	1.39	0.77	1.31	87.73	12.27
		0.00139	9.5					0.00	0.00	0.00	0.00	87.73	12.27
		0.00037	11.4					5.89	13.00	7.21	12.27	100.00	0.00
240517JW9	**MECHANICAL SIEVING**	5	-2.3	53.7	5.49		0				0.00	0.00	100
		4	-2.0				0.7				1.30	1.30	98.70
		2.8	-1.5				0.72				1.34	2.64	97.36
		2	-1.0				0.73				1.36	4.00	96.00
		1	0.0				1.38				2.57	6.57	93.43
		0.5	1.0				1.96				3.65	10.22	89.78
	HYDROMETER ANALYSIS <0.5mm	0.25	2.0		48.21	44.63		2.46	5.51	2.66	4.95	15.17	84.83
		0.125	3.0					3.82	8.56	4.13	7.68	22.86	77.14
		0.063	4.0					6.58	14.74	7.11	13.24	36.09	63.91
		0.03545	4.8					1.50	3.36	1.62	3.02	39.11	60.89
		0.02250	5.5					3.03	6.79	3.27	6.09	45.20	54.80
		0.01320	6.2					1.00	2.24	1.08	2.01	47.21	52.79
		0.00939	6.7					1.06	2.37	1.14	2.13	49.34	50.66
		0.00670	7.2					0.61	1.38	0.66	1.24	50.57	49.43
		0.00332	8.2					1.40	3.14	1.51	2.82	53.39	46.61
		0.00139	9.5					0.00	0.00	0.00	0.00	53.39	46.61
		0.00037	11.4					23.17	51.92	25.03	46.61	100.00	0.00

Table A1.5. Sieve and hydrometer data for Rising Star surface and cave sediment samples (Continued).

CAVE SEDIMENTS

Sample		Sieve Size (mm)	Phi (Ø)	Oven-dried weight total sample (gr)	Subsample weight mechanical sieve and hydrometer (gr)	Oven-dried hygrosc. corr. sample mass used for hydrometer analysis	Fraction weight Sieve	Fraction weight Hydrometer analysis for G	Fraction WT Percent of fine-grained hydrometer sample	Fraction weight total fine-grained mass for F	WT Percent retained of total sample	Cumulative percentage	Percentage passed
240517JW10	**MECHANICAL SIEVING**	5	-2.3	76.93	27.31		0				0.00	0.00	100
		4	-2.0				7.53				9.79	9.79	90.21
		2.8	-1.5				2.07				2.69	12.48	87.52
		2	-1.0				2.42				3.15	15.62	84.38
		1	0.0				5.16				6.71	22.33	77.67
		0.5	1.0				10.13				13.17	35.50	64.50
	HYDROMETER ANALYSIS <0.5mm	0.25	2.0		49.62	47.97		13.86	28.89	14.34	18.64	54.14	45.86
		0.125	3.0					8.67	18.07	8.97	11.66	65.80	34.20
		0.063	4.0					6.36	13.26	6.58	8.55	74.35	25.65
		0.03545	4.8					4.00	8.34	4.14	5.38	79.73	20.27
		0.02286	5.5					1.00	2.08	1.03	1.34	81.07	18.93
		0.01328	6.2					1.03	2.14	1.06	1.38	82.45	17.55
		0.00948	6.7					0.46	0.95	0.47	0.61	83.07	16.93
		0.00670	7.2					0.19	0.39	0.19	0.25	83.32	16.68
		0.00332	8.2					0.56	1.16	0.58	0.75	84.07	15.93
		0.00139	9.5					0.00	0.00	0.00	0.00	84.07	15.93
		0.00037	11.4					11.85	24.70	12.26	15.93	100.00	0.00
240517JW11	**MECHANICAL SIEVING**	5	-2.3	106.52	46.79		0				0.00	0.00	100
		4	-2.0				8.36				7.85	7.85	92.15
		2.8	-1.5				5.32				4.99	12.84	87.16
		2	-1.0				6.73				6.32	19.16	80.84
		1	0.0				12.33				11.58	30.74	69.26
		0.5	1.0				14.05				13.19	43.93	56.07
	HYDROMETER ANALYSIS <0.5mm	0.25	2.0		59.73	58.29		15.37	26.37	15.75	14.79	58.71	41.29
		0.125	3.0					12.29	21.08	12.59	11.82	70.53	29.47
		0.063	4.0					9.64	16.54	9.88	9.27	79.81	20.19
		0.03522	4.8					4.00	6.86	4.10	3.85	83.65	16.35
		0.02272	5.5					2.06	3.53	2.11	1.98	85.63	14.37
		0.01332	6.2					0.53	0.91	0.54	0.51	86.14	13.86
		0.00942	6.7					0.50	0.86	0.51	0.48	86.62	13.38
		0.00670	7.2					0.59	1.00	0.60	0.56	87.19	12.81
		0.00332	8.2					0.44	0.76	0.45	0.43	87.61	12.39
		0.00139	9.5					0.00	0.00	0.00	0.00	87.61	12.39
		0.00037	11.4					12.88	22.09	13.20	12.39	100.00	0.00

Table A1.5. Sieve and hydrometer data for Rising Star surface and cave sediment samples (Continued).

CAVE SEDIMENTS

Sample		Sieve Size (mm)	Phi (Ø)	Oven-dried weight total sample (gr)	Subsample weight mechanical sieve and hydrometer (gr)	Oven-dried hygrosc. corr. sample mass used for hydrometer analysis	Fraction weight Sieve	Fraction weight Hydrometer analysis for G	Fraction WT Percent of fine-grained hydrometer sample	Fraction weight total fine-grained mass for F	WT Percent retained of total sample	Cumulative percentage	Percentage passed
240517JW12	**MECHANICAL SIEVING**	5	-2.3	71.95	39.16		0				0.00	0.00	100
		4	-2.0				2.32				3.22	3.22	96.78
		2.8	-1.5				3.29				4.57	7.80	92.20
		2	-1.0				7.19				9.99	17.79	82.21
		1	0.0				16.05				22.31	40.10	59.90
		0.5	1.0				10.31				14.33	54.43	45.57
	HYDROMETER ANALYSIS <0.5mm	0.25	2.0		32.79	30.56		5.51	18.03	5.91	8.22	62.64	37.36
		0.125	3.0					5.12	16.76	5.49	7.64	70.28	29.72
		0.063	4.0					4.46	14.60	4.79	6.65	76.93	23.07
		0.03545	4.8					3.70	12.11	3.97	5.52	82.45	17.55
		0.02286	5.5					1.86	6.08	1.99	2.77	85.22	14.78
		0.01332	6.2					0.53	1.73	0.57	0.79	86.01	13.99
		0.00942	6.7					0.06	0.19	0.06	0.09	86.09	13.91
		0.00674	7.2					1.03	3.37	1.10	1.53	87.63	12.37
		0.00332	8.2					0.47	1.54	0.51	0.70	88.33	11.67
		0.00139	9.5					0.00	0.00	0.00	0.00	88.33	11.67
		0.00037	11.4					7.82	25.60	8.40	11.67	100.00	0.00
240517JW19	**MECHANICAL SIEVING**	5	-2.3	57.97	0.34		0				0.00	0.00	100
		4	-2.0				0				0.00	0.00	100.00
		2.8	-1.5				0				0.00	0.00	100.00
		2	-1.0				0.09				0.16	0.16	99.84
		1	0.0				0.1				0.17	0.33	99.67
		0.5	1.0				0.15				0.26	0.59	99.41
	HYDROMETER ANALYSIS <0.5mm	0.25	2.0		57.63	55.65		0.34	0.61	0.35	0.61	1.19	98.81
		0.125	3.0					0.89	1.60	0.92	1.59	2.78	97.22
		0.063	4.0					2.06	3.70	2.13	3.68	6.46	93.54
		0.02832	5.1					4.00	7.19	4.14	7.15	13.61	86.39
		0.01855	5.8					5.06	9.09	5.24	9.03	22.64	77.36
		0.01111	6.5					3.06	5.49	3.17	5.46	28.10	71.90
		0.00812	6.9					3.03	5.44	3.14	5.41	33.51	66.49
		0.00587	7.4					5.91	10.63	6.12	10.56	44.08	55.92
		0.00296	8.4					3.29	5.90	3.40	5.87	49.95	50.05
		0.00127	9.6					16.14	29.01	16.72	28.84	78.78	21.22
		0.00037	11.4					11.88	21.34	12.30	21.22	100.00	0.00

Appendix 2

Supplementary data for Chapter 4

Sample 190517JW1

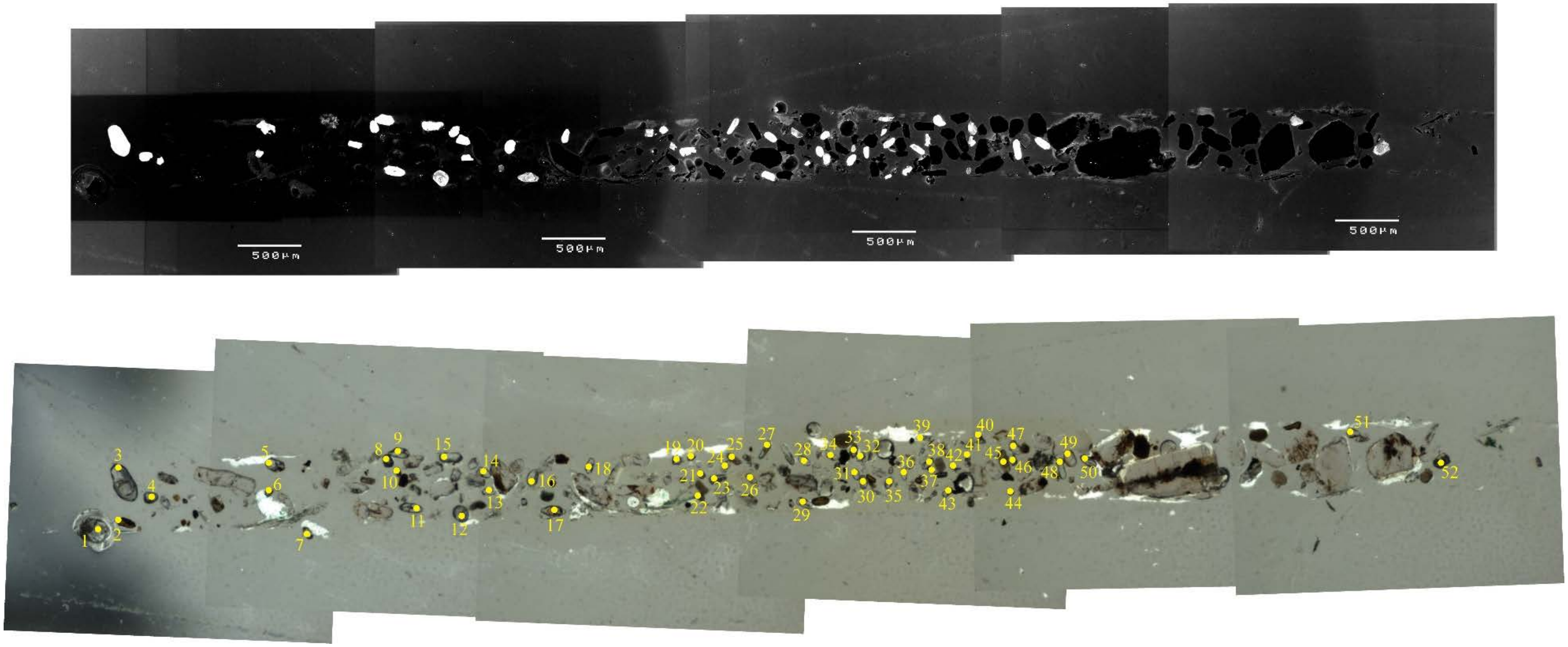

Figure A2.1. Spot locations for U-Pb detrital zircon analysis on Rising Star Cave surface and cave sediment samples (n=15).

Sample 190517JW2

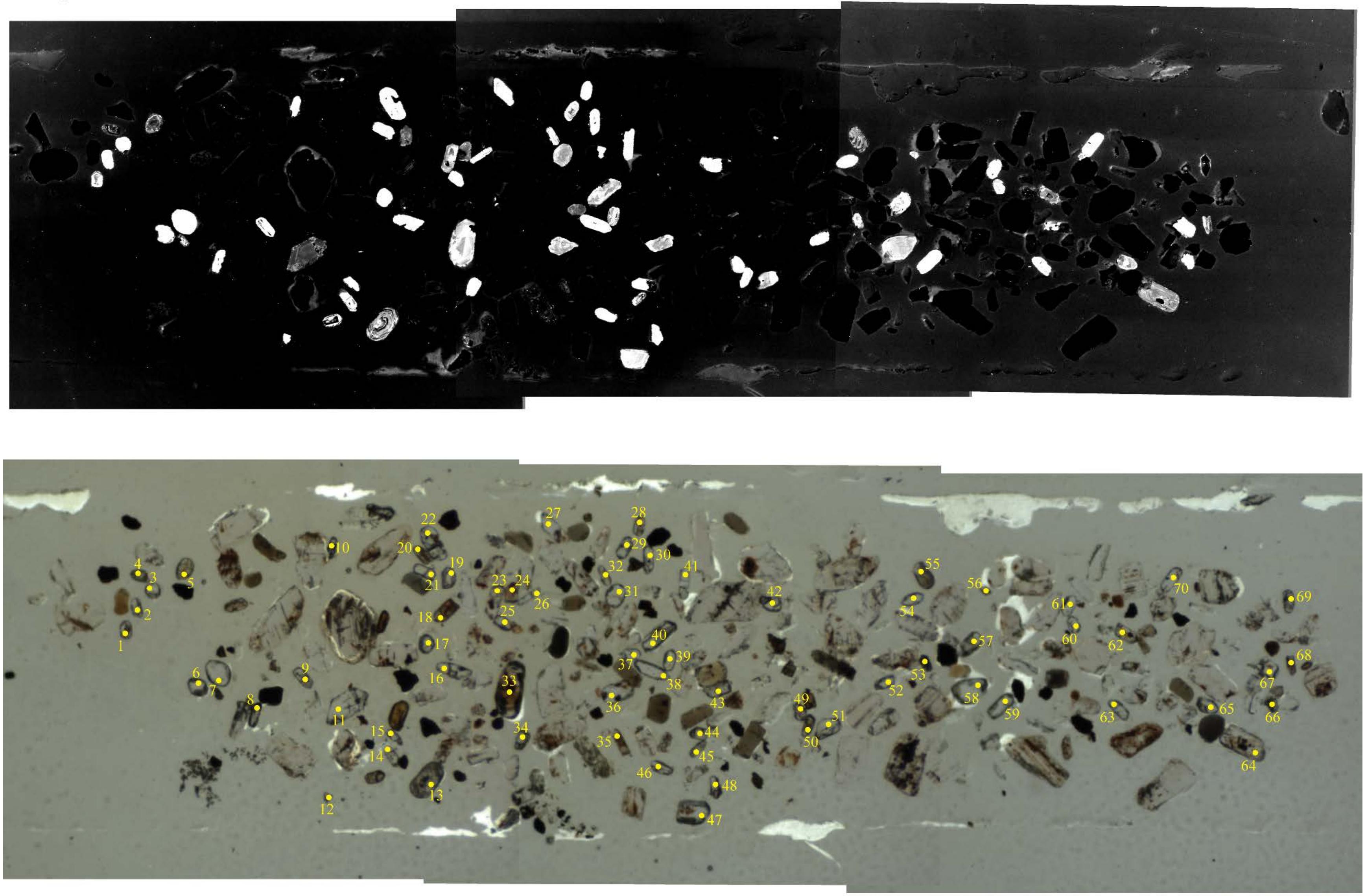

Figure A2.1. Spot locations for U-Pb detrital zircon analysis on Rising Star Cave surface and cave sediment samples (Continued).

Sample 190517JW3

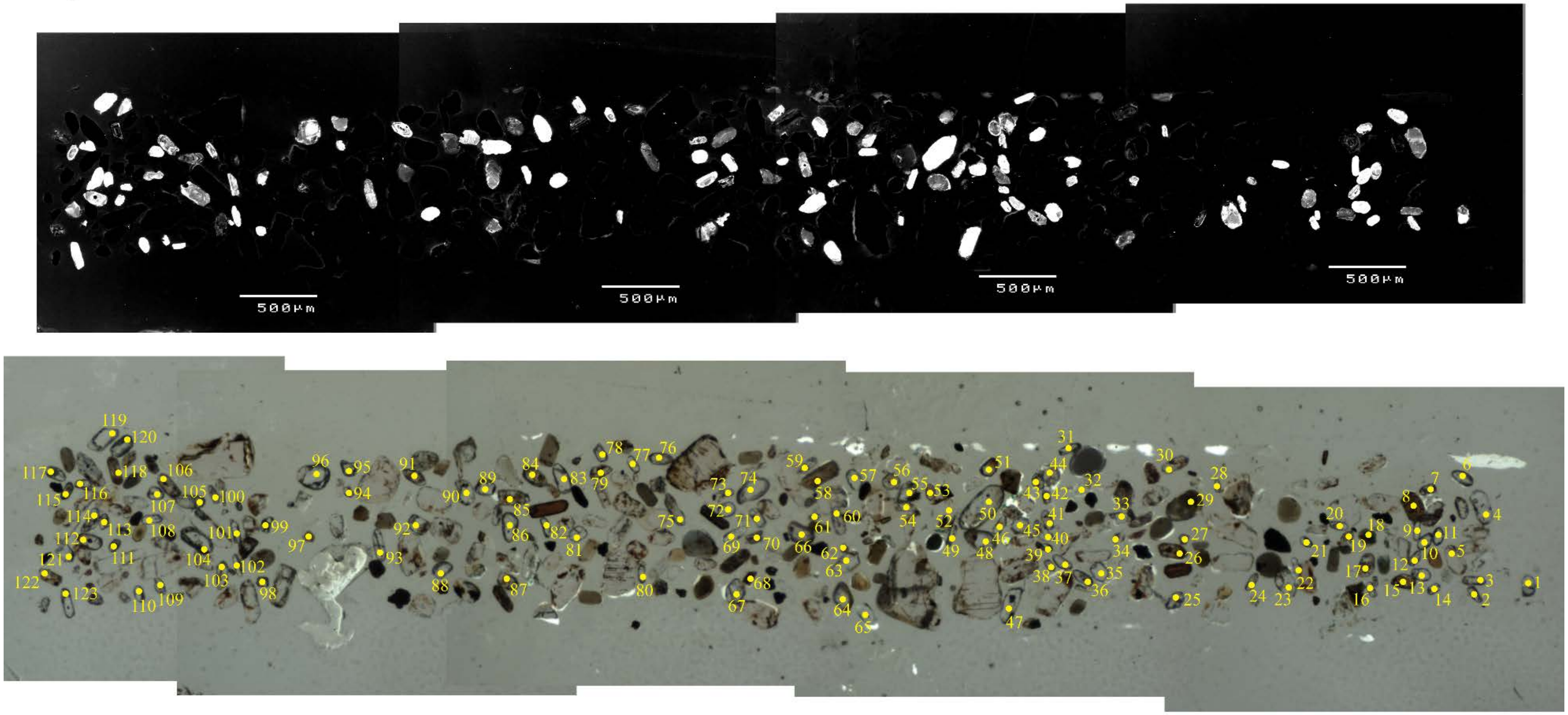

Figure A2.1. Spot locations for U-Pb detrital zircon analysis on Rising Star Cave surface and cave sediment samples (Continued).

Sample 190517JW4

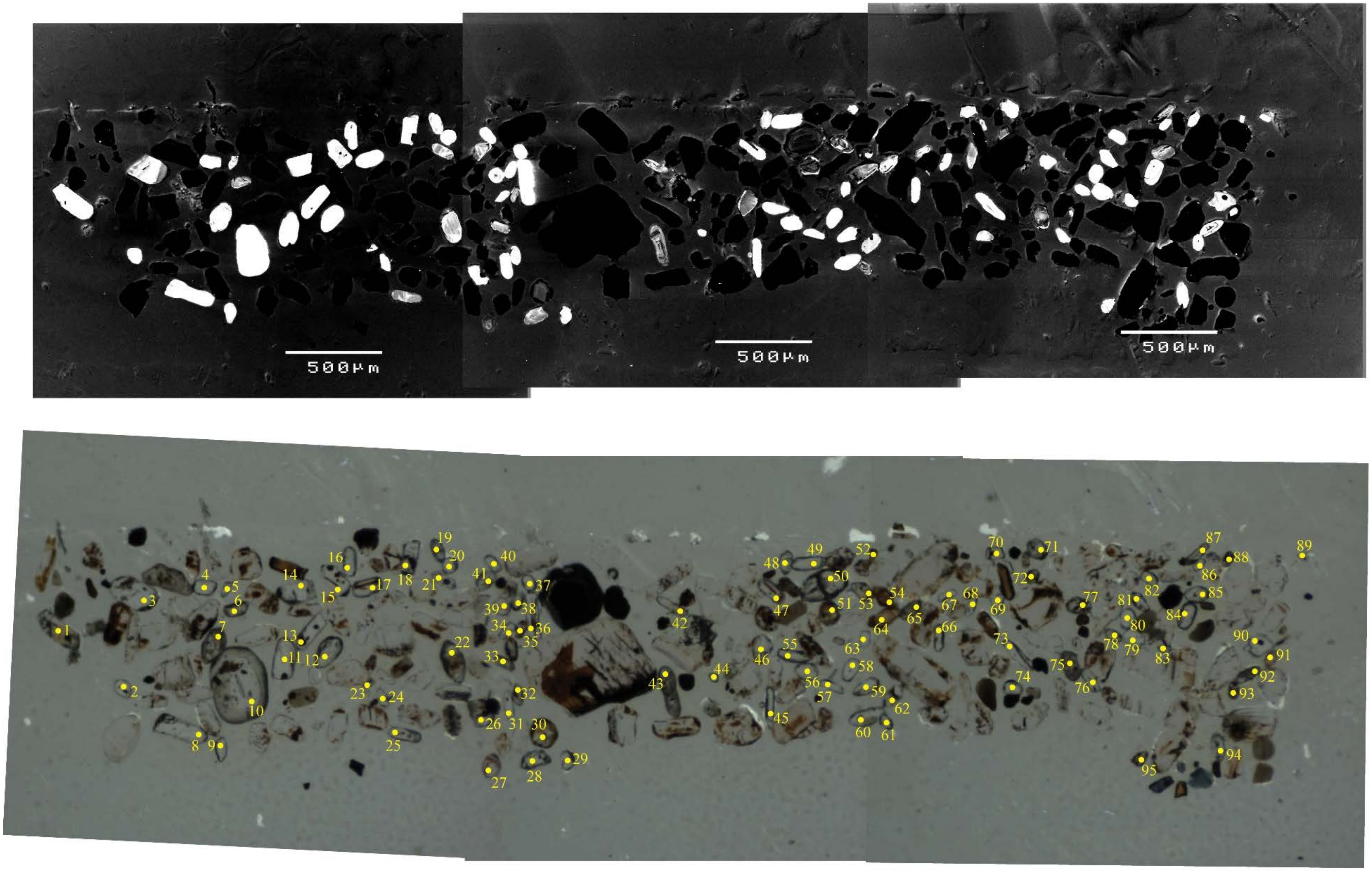

Figure A2.1. Spot locations for U-Pb detrital zircon analysis on Rising Star Cave surface and cave sediment samples (Continued).

Sample 190517JW5

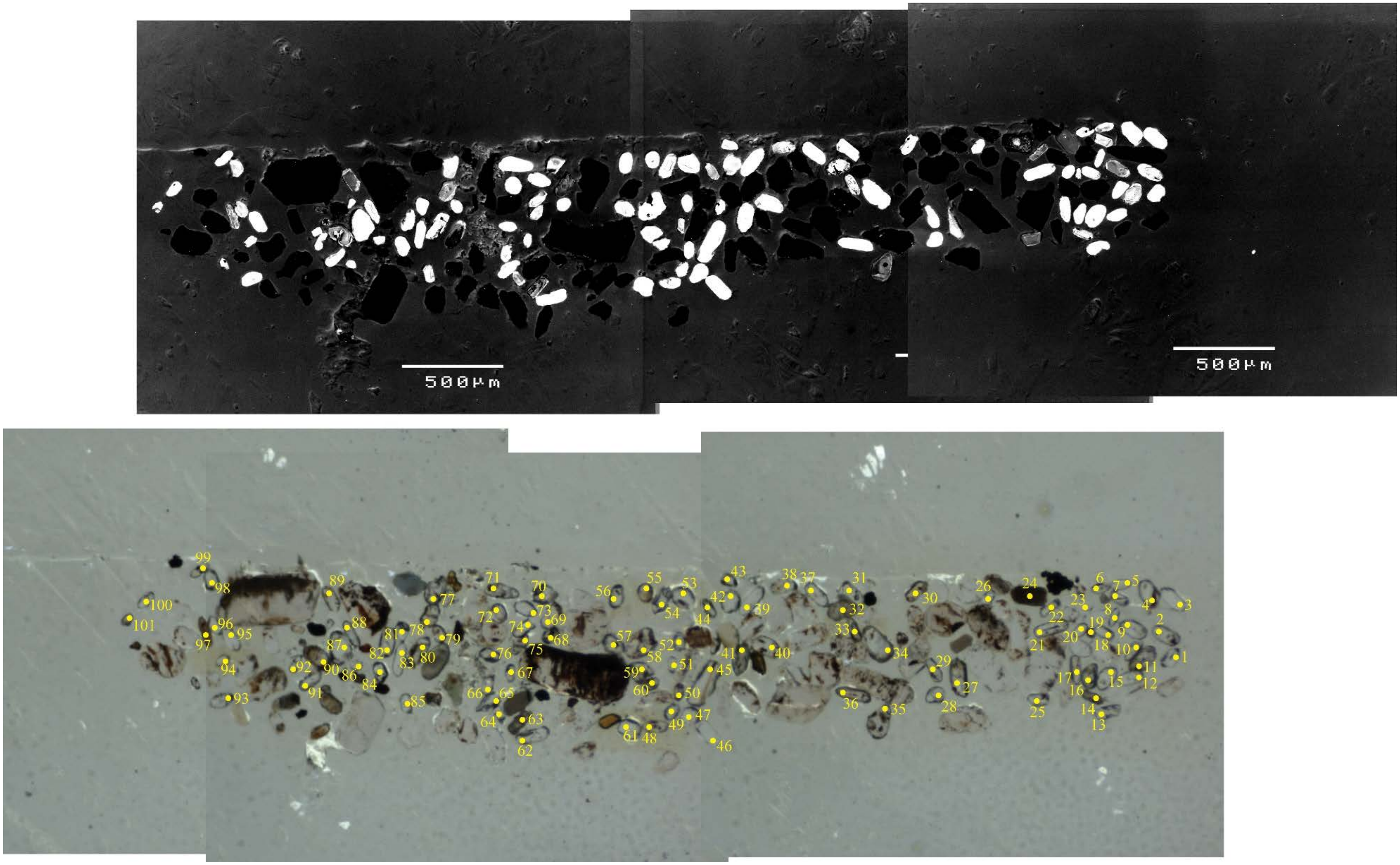

Figure A2.1. Spot locations for U-Pb detrital zircon analysis on Rising Star Cave surface and cave sediment samples (Continued).

Sample 190517JW6

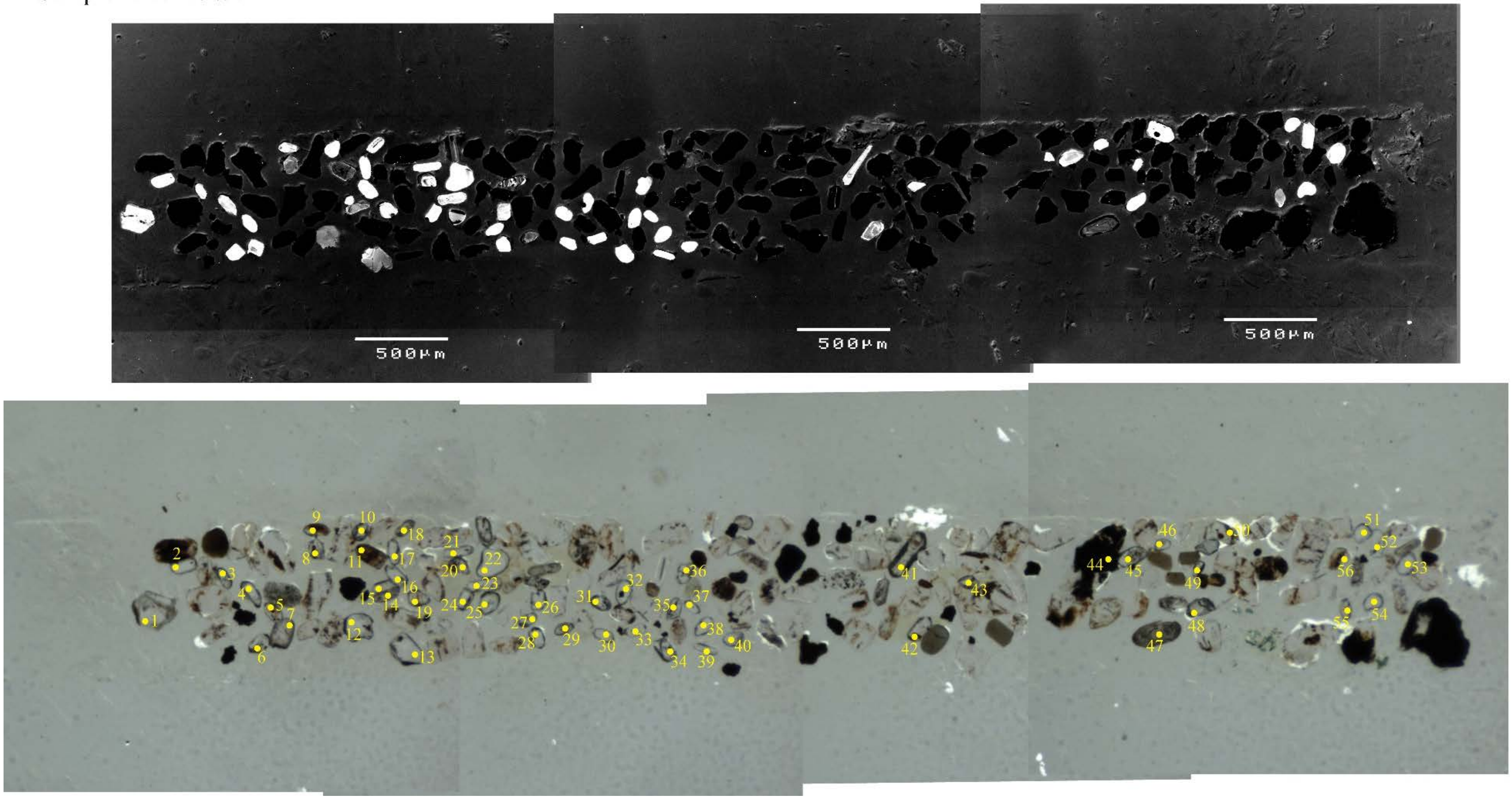

Figure A2.1. Spot locations for U-Pb detrital zircon analysis on Rising Star Cave surface and cave sediment samples (Continued).

Sample 190517JW7

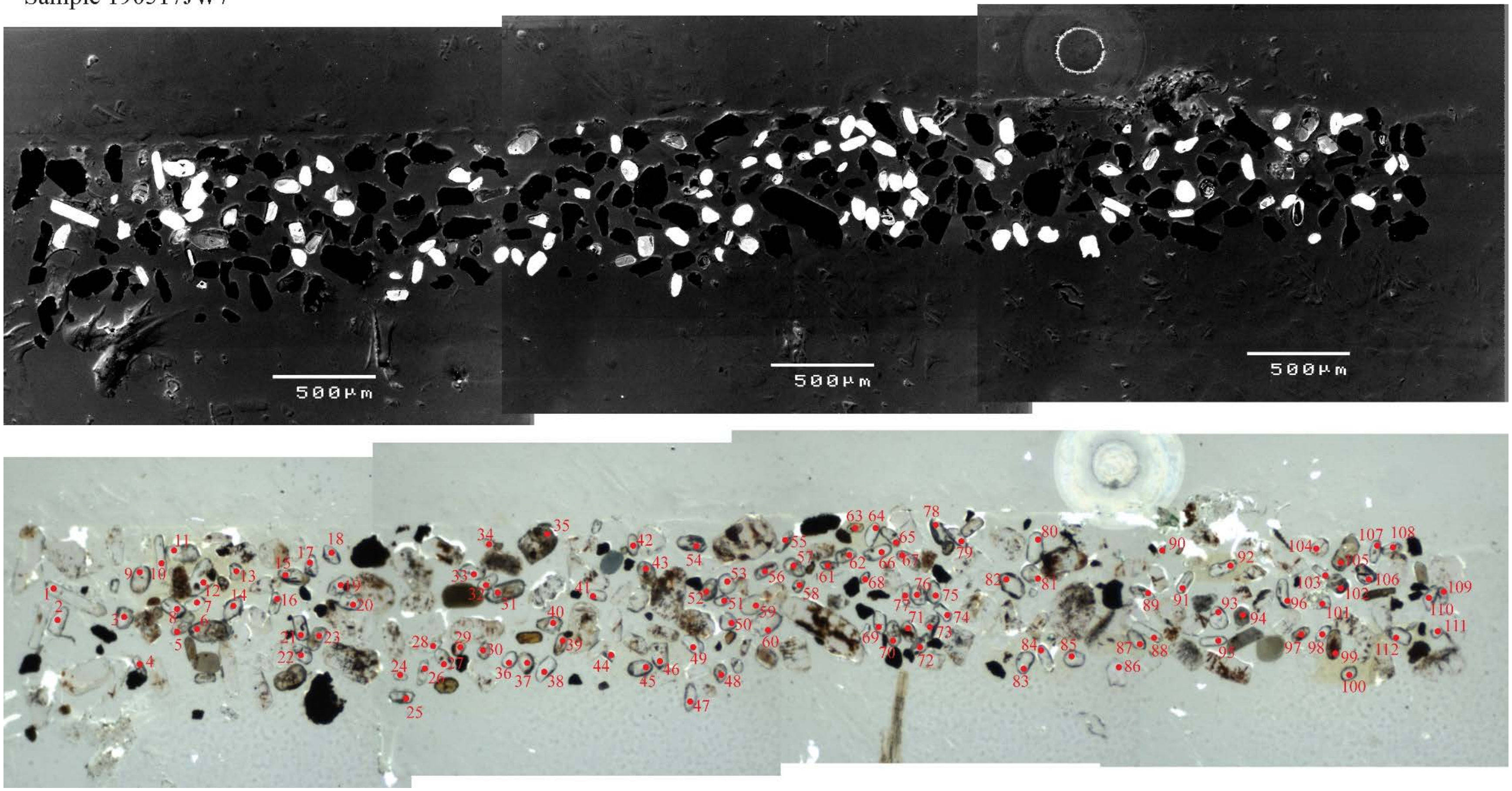

Figure A2.1. Spot locations for U-Pb detrital zircon analysis on Rising Star Cave surface and cave sediment samples (Continued).

Sample 100517JW3

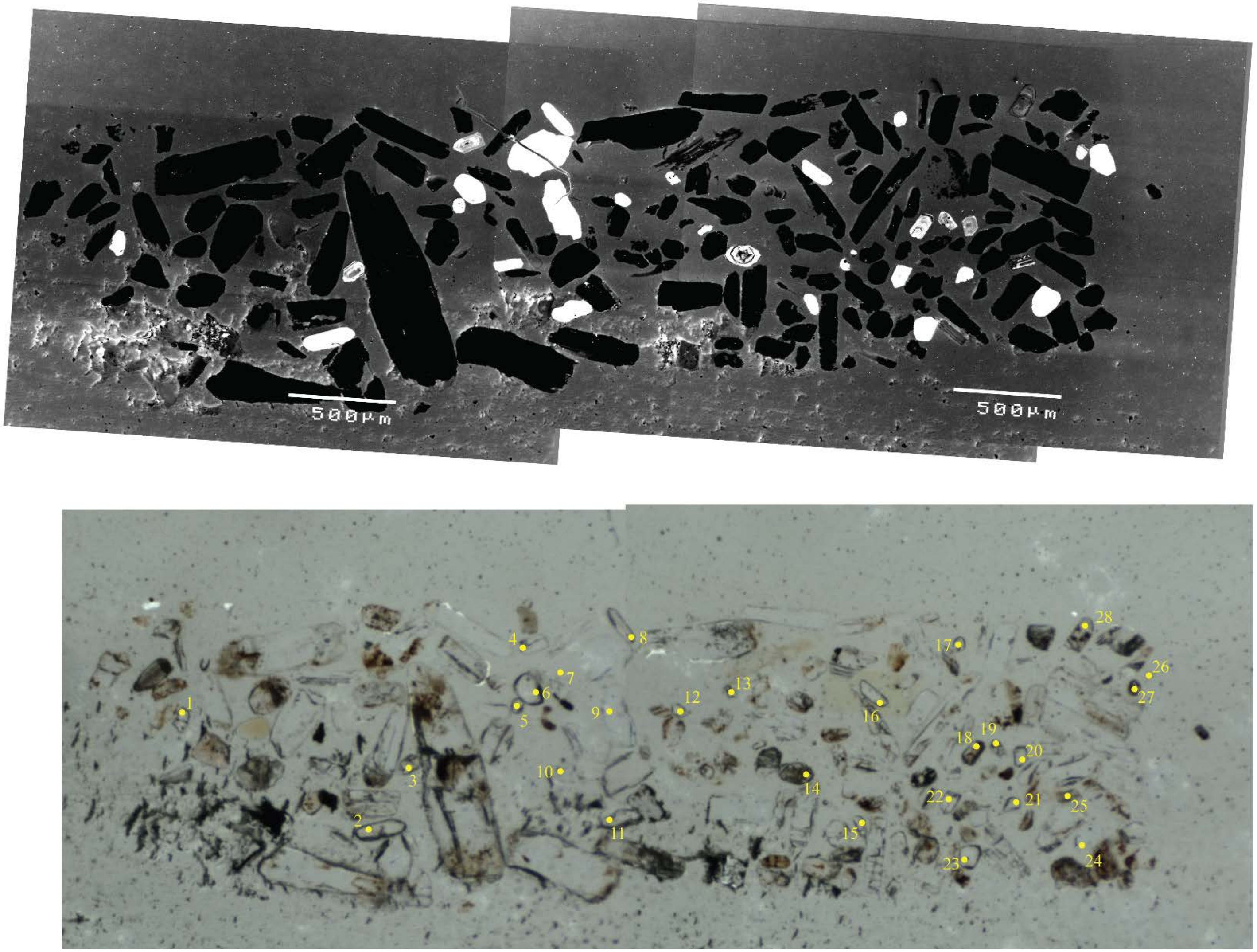

Figure A2.1. Spot locations for U-Pb detrital zircon analysis on Rising Star Cave surface and cave sediment samples (Continued).

Sample 100517JW5

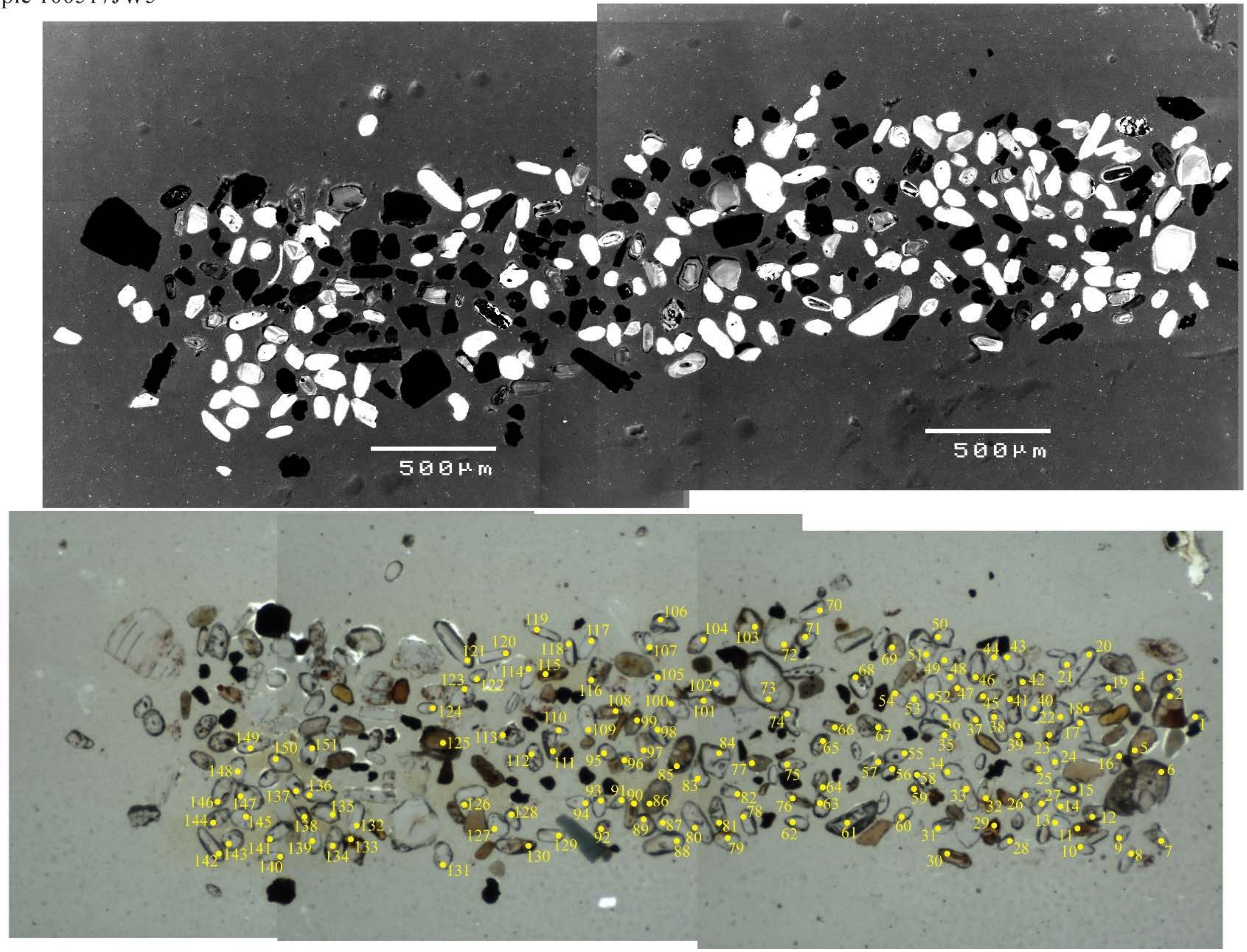

Figure A2.1. Spot locations for U-Pb detrital zircon analysis on Rising Star Cave surface and cave sediment samples (Continued).

Sample 100517JW6

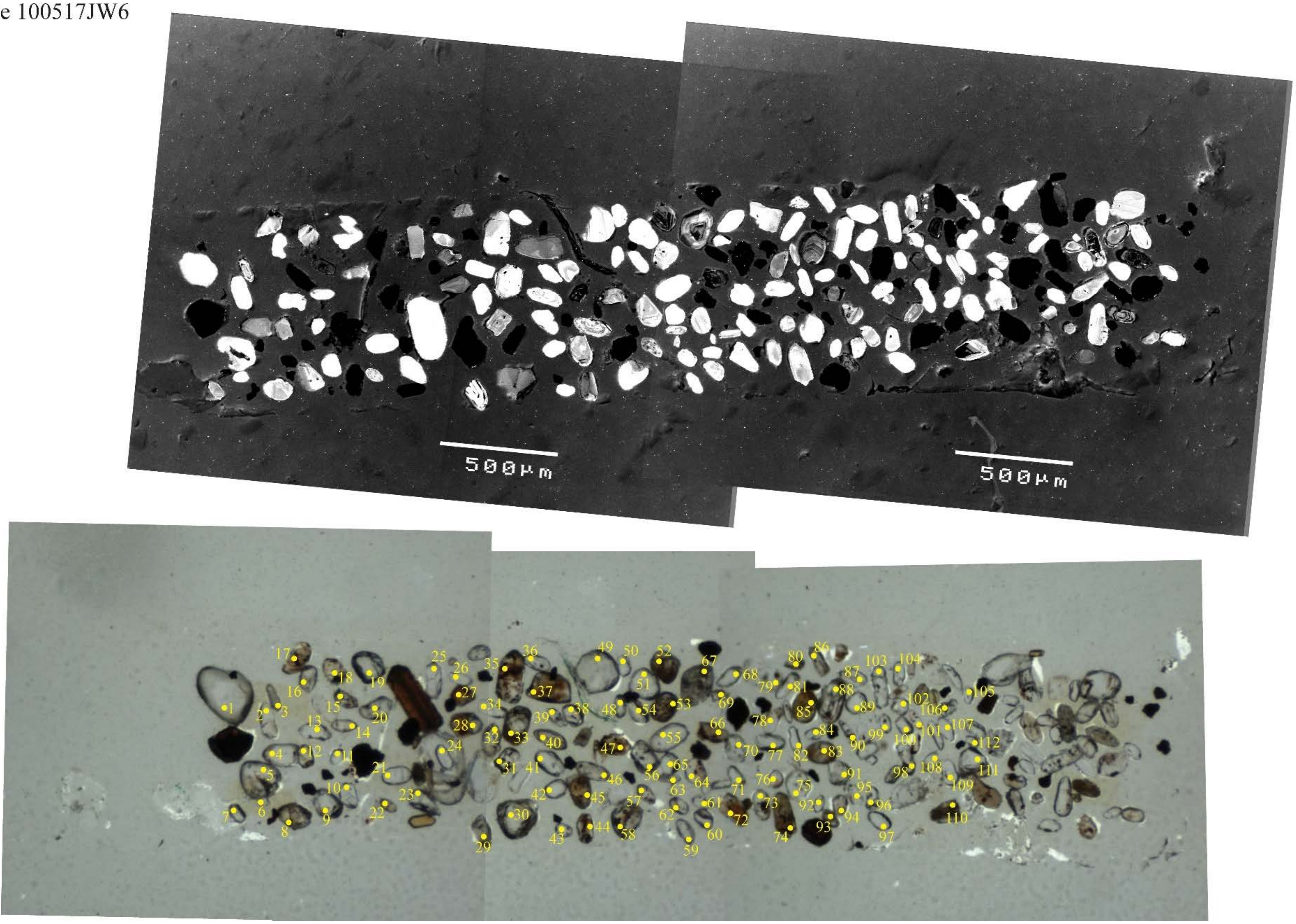

Figure A2.1. Spot locations for U-Pb detrital zircon analysis on Rising Star Cave surface and cave sediment samples (Continued).

Sample 260517JW8

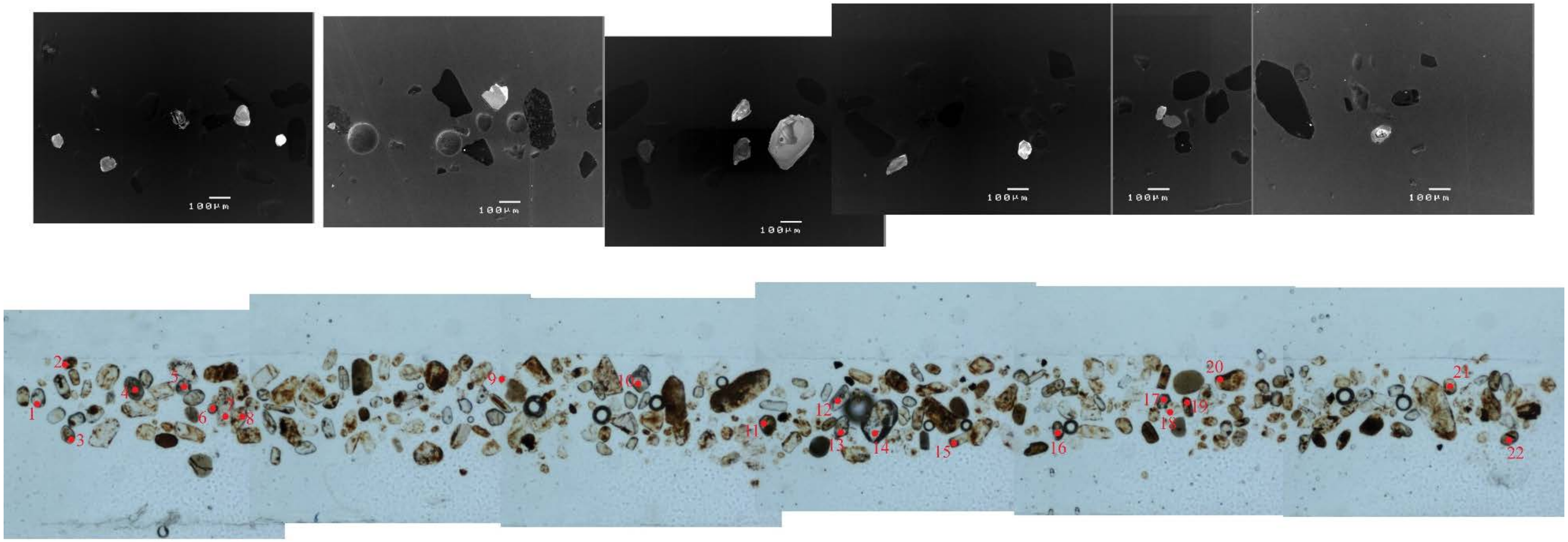

Figure A2.1. Spot locations for U-Pb detrital zircon analysis on Rising Star Cave surface and cave sediment samples (Continued).

Sample OSL-4

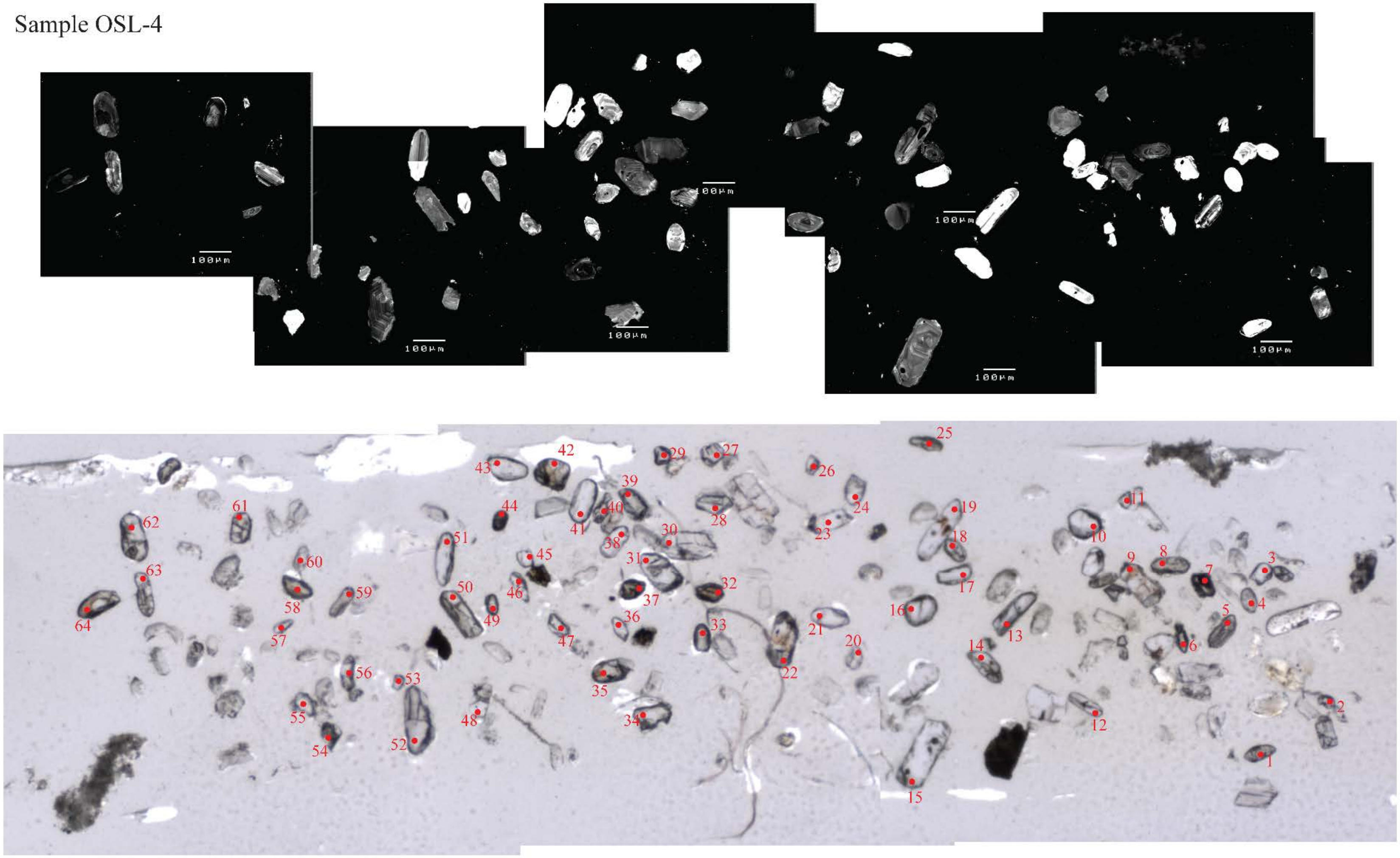

Figure A2.1. Spot locations for U-Pb detrital zircon analysis on Rising Star Cave surface and cave sediment samples (Continued).

Sample UW101-1783A

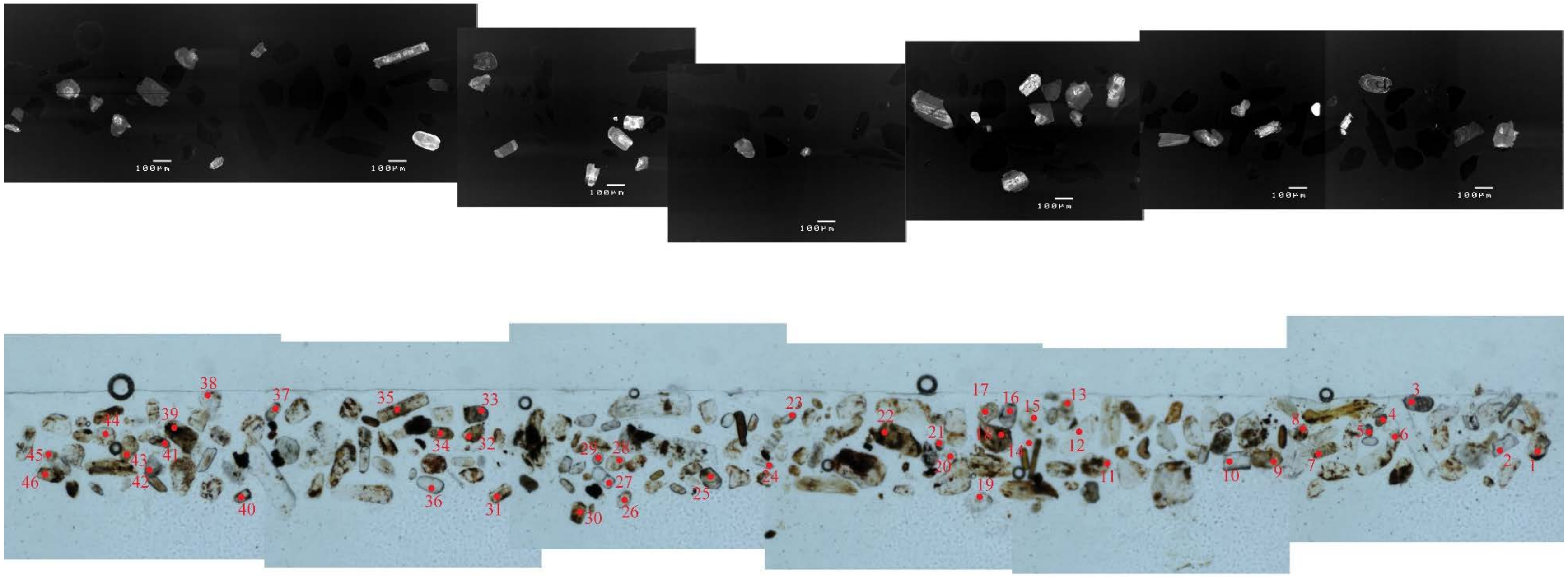

Figure A2.1. Spot locations for U-Pb detrital zircon analysis on Rising Star Cave surface and cave sediment samples (Continued).

Sample UW101-1783C

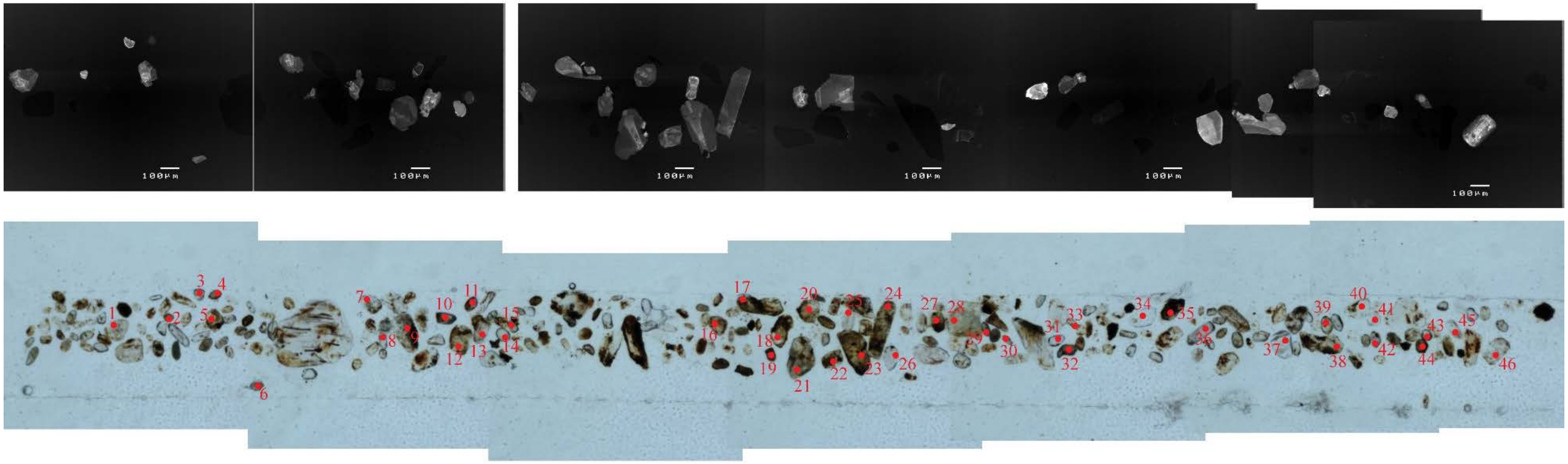

Figure A2.1. Spot locations for U-Pb detrital zircon analysis on Rising Star Cave surface and cave sediment samples (Continued).

Sample UW101-1783L

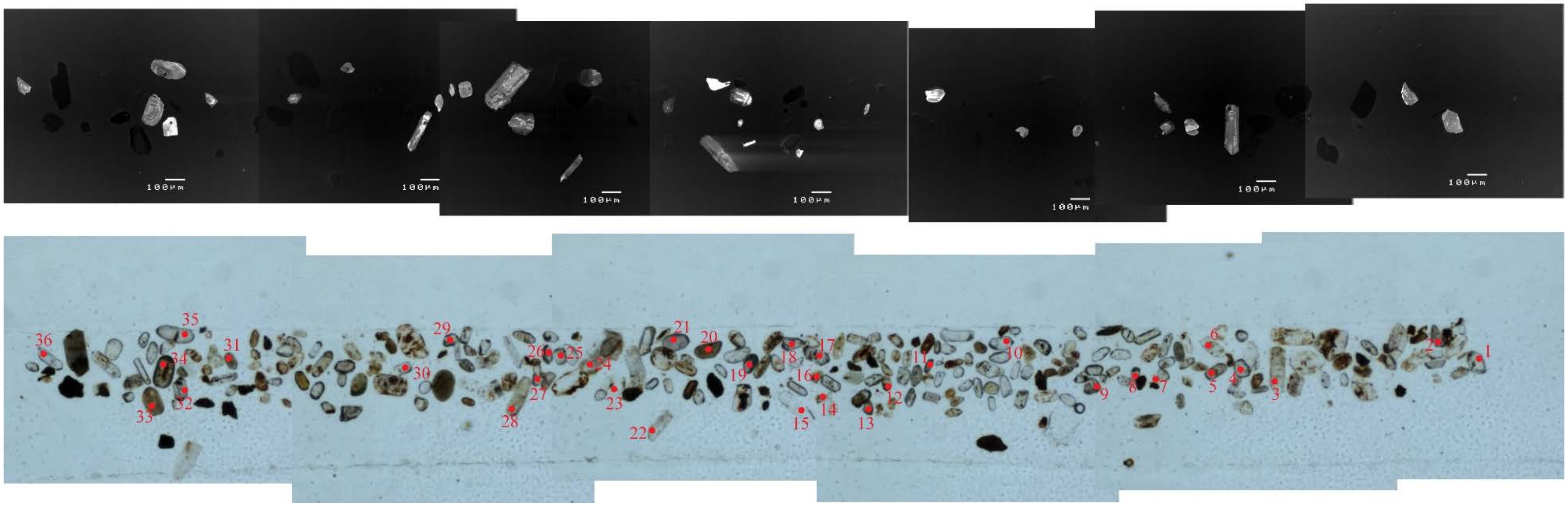

Figure A2.1. Spot locations for U-Pb detrital zircon analysis on Rising Star Cave surface and cave sediment samples (Continued).

Table A2.1. U-Pb isotopic data for Rising Star cave and surface samples (n=15).

Sample #_Spot #	U (in ppm)	Th (in ppm)	Pb (in ppm)	Th/U	Pb207 /U235	± 2σ	Pb206 /U238	± 2σ	Pb207 /Pb206	± 2σ	Pb207 /U235	± Ma	Pb206 /U238	± Ma	Pb207 /Pb206	± Ma	Preferred Age	± Ma	Age System	U-Pb/U-Pb Discordance (%)	U-Pb/Pb-Pb Discordance (%)
UW1011783A_1	0.0338	0.194	4.76	no value	no value	NAN	no value	NAN	no value	NAN	no value	NAN	no value	NAN	no value	NAN	#VALUE!	#VALUE!	#VALUE!	#VALUE!	#VALUE!
UW1011783A_2	227.7	218.1	1209	1.1068	6.444	0.091	0.3675	0.003	0.12665	0.00085	2037.3	12	2017.3	14	2049	12	2049	12	FinalAge207_206	0.981691454	1.547096144
UW1011783A_3	125.22	137.3	1107	0.974	19.32	0.29	0.6056	0.0063	0.2307	0.0017	3058.1	15	3051	25	3055	12	3055	12	FinalAge207_206	0.232170302	0.130932897
UW1011783A_4	168.3	246	1421	0.735	8.11	0.12	0.4086	0.0041	0.1428	0.0012	2242.1	14	2208	19	2262	15	2262	15	FinalAge207_206	1.520895589	2.387267905
UW1011783A_5	16.64	41.21	60.7	0.4232	0.722	0.044	0.0903	0.0021	0.059	0.0037	541	27	557	12	420	130	557	12	FinalAge206_238	-2.957486137	-32.61904762
UW1011783A_6	0.0062	0.195	7.7	no value	no value	NAN	no value	NAN	no value	NAN	no value	NAN	no value	NAN	no value	NAN	#VALUE!	#VALUE!	#VALUE!	#VALUE!	#VALUE!
UW1011783A_7	0.0032	2.61	14.9	no value	no value	NAN	no value	NAN	no value	NAN	no value	NAN	no value	NAN	no value	NAN	#VALUE!	#VALUE!	#VALUE!	#VALUE!	#VALUE!
UW1011783A_8	0.0103	0.07	9.4	no value	no value	NAN	no value	NAN	no value	NAN	no value	NAN	no value	NAN	no value	NAN	#VALUE!	#VALUE!	#VALUE!	#VALUE!	#VALUE!
UW1011783A_9	0.0294	1.79	9.3	no value	no value	NAN	no value	NAN	no value	NAN	no value	NAN	no value	NAN	no value	NAN	#VALUE!	#VALUE!	#VALUE!	#VALUE!	#VALUE!
UW1011783A_10	92	97.4	533	0.979	6.355	0.099	0.3624	0.0034	0.1266	0.0012	2024.5	14	1993	16	2048	18	2048	18	FinalAge207_206	1.555939738	2.685546875
UW1011783A_11	99.9	91.8	758	1.067	17.44	0.25	0.5719	0.0052	0.2206	0.0015	2958	14	2917	22	2984	11	2984	11	FinalAge207_206	1.38607167	2.245308311
UW1011783A_12	713	2365	12740	0.2951	6.003	0.079	0.3505	0.0027	0.1237	0.00056	1976.4	12	1936.8	13	2008.6	8	2008.6	8	FinalAge207_206	2.003642987	3.574629095
UW1011783A_13	0.0501	1.54	7.7	no value	no value	NAN	no value	NAN	no value	NAN	no value	NAN	no value	NAN	no value	NAN	#VALUE!	#VALUE!	#VALUE!	#VALUE!	#VALUE!
UW1011783A_14	0.0029	0.0018	0.9	no value	no value	NAN	no value	NAN	no value	NAN	no value	NAN	no value	NAN	no value	NAN	#VALUE!	#VALUE!	#VALUE!	#VALUE!	#VALUE!
UW1011783A_15	0.0297	1.49	13.8	no value	no value	NAN	no value	NAN	no value	NAN	no value	NAN	no value	NAN	no value	NAN	#VALUE!	#VALUE!	#VALUE!	#VALUE!	#VALUE!
UW1011783A_16	312	302	1567	1.0322	6.151	0.087	0.3522	0.0031	0.12687	0.00078	1996.5	12	1945	15	2053	11	2053	11	FinalAge207_206	2.57951415	5.260594252
UW1011783A_17	0.0144	1.58	14.6	no value	no value	NAN	no value	NAN	no value	NAN	no value	NAN	no value	NAN	no value	NAN	#VALUE!	#VALUE!	#VALUE!	#VALUE!	#VALUE!
UW1011783A_18	0.0277	0.54	4.47	no value	no value	NAN	no value	NAN	no value	NAN	no value	NAN	no value	NAN	no value	NAN	#VALUE!	#VALUE!	#VALUE!	#VALUE!	#VALUE!
UW1011783A_19	0.0047	1.747	8.72	no value	no value	NAN	no value	NAN	no value	NAN	no value	NAN	no value	NAN	no value	NAN	#VALUE!	#VALUE!	#VALUE!	#VALUE!	#VALUE!
UW1011783A_20	0.0014	3.8	0.87	no value	no value	NAN	no value	NAN	no value	NAN	no value	NAN	no value	NAN	no value	NAN	#VALUE!	#VALUE!	#VALUE!	#VALUE!	#VALUE!
UW1011783A_21	123.6	127.3	364.4	0.9076	1.843	0.035	0.1751	0.0019	0.0766	0.0013	1058.8	13	1039.6	10	1098	33	1098	33	FinalAge207_206	1.813373631	5.318761384
UW1011783A_22	0.244	1.7	166	no value	no value	NAN	no value	NAN	no value	NAN	no value	NAN	no value	NAN	no value	NAN	#VALUE!	#VALUE!	#VALUE!	#VALUE!	#VALUE!
UW1011783A_23	0.001	0.0028	1.22	no value	no value	NAN	no value	NAN	no value	NAN	no value	NAN	no value	NAN	no value	NAN	#VALUE!	#VALUE!	#VALUE!	#VALUE!	#VALUE!
UW1011783A_24	0.0021	25	0.72	no value	no value	NAN	no value	NAN	no value	NAN	no value	NAN	no value	NAN	no value	NAN	#VALUE!	#VALUE!	#VALUE!	#VALUE!	#VALUE!
UW1011783A_25	66.81	76.9	652	0.81	19.21	0.3	0.6046	0.0068	0.2323	0.002	3051.5	15	3047	27	3065	14	3065	14	FinalAge207_206	0.147468458	0.587275693
UW1011783A_26	0.0465	1.501	9.5	no value	no value	NAN	no value	NAN	no value	NAN	no value	NAN	no value	NAN	no value	NAN	#VALUE!	#VALUE!	#VALUE!	#VALUE!	#VALUE!
UW1011783A_27	339.7	297.6	490	1.073	0.839	0.017	0.1004	0.001	0.06083	0.00093	617.4	9.1	616.7	6	617	33	616.7	6	FinalAge206_238	0.113378685	0.048622366
UW1011783A_28	-0.000195145	0.952	5.03	no value	no value	NAN	no value	NAN	no value	NAN	no value	NAN	no value	NAN	no value	NAN	#VALUE!	#VALUE!	#VALUE!	#VALUE!	#VALUE!
UW1011783A_29	67.2	82	150	0.848	1.132	0.07	0.1109	0.0031	0.0772	0.0061	769	35	678	18	1050	150	678	18	FinalAge206_238	11.83355007	35.42857143
UW1011783A_30	0.117	1.49	12	no value	no value	NAN	no value	NAN	no value	NAN	no value	NAN	no value	NAN	no value	NAN	#VALUE!	#VALUE!	#VALUE!	#VALUE!	#VALUE!
UW1011783A_31	0.0061	97	3.57	no value	no value	NAN	no value	NAN	no value	NAN	no value	NAN	no value	NAN	no value	NAN	#VALUE!	#VALUE!	#VALUE!	#VALUE!	#VALUE!
UW1011783A_32	0.0591	0.98	6.62	no value	no value	NAN	no value	NAN	no value	NAN	no value	NAN	no value	NAN	no value	NAN	#VALUE!	#VALUE!	#VALUE!	#VALUE!	#VALUE!
UW1011783A_33	137.5	190.8	1245	0.81	17.22	0.31	0.505	0.0067	0.2481	0.0019	2945	18	2634	29	3170	12	0	0	Discordant	10.56027165	16.90851735
UW1011783A_34	276.5	375	2148	0.821	7.73	0.16	0.4019	0.0073	0.141	0.0022	2202	19	2177	33	2235	27	2235	27	FinalAge207_206	1.135331517	2.5950783
UW1011783A_35	0.0018	0.11	2.4	no value	no value	NAN	no value	NAN	no value	NAN	no value	NAN	no value	NAN	no value	NAN	#VALUE!	#VALUE!	#VALUE!	#VALUE!	#VALUE!
UW1011783A_36	149.7	26.11	40.4	6.315	0.743	0.019	0.0912	0.0012	0.0593	0.0013	563.5	11	562.8	7	554	46	562.8	7	FinalAge206_238	0.124223602	-1.588447653
UW1011783A_37	231.4	314.7	1760	0.8039	6.326	0.1	0.3632	0.0044	0.127	0.0011	2020.2	14	1998	21	2055	16	2055	16	FinalAge207_206	1.098901099	2.773722628
UW1011783A_38	0.0243	0.422	3.56	no value	no value	NAN	no value	NAN	no value	NAN	no value	NAN	no value	NAN	no value	NAN	#VALUE!	#VALUE!	#VALUE!	#VALUE!	#VALUE!
UW1011783A_39	0.0473	1.439	12.5	no value	no value	NAN	no value	NAN	no value	NAN	no value	NAN	no value	NAN	no value	NAN	#VALUE!	#VALUE!	#VALUE!	#VALUE!	#VALUE!
UW1011783A_40	-0.000080421	-0.000073049	0.32	no value	no value	NAN	no value	NAN	no value	NAN	no value	NAN	no value	NAN	no value	NAN	#VALUE!	#VALUE!	#VALUE!	#VALUE!	#VALUE!
UW1011783A_41	328	1370	1174	0.2279	3.269	0.083	0.181	0.0042	0.1311	0.0014	1469	20	1071	23	2109	19	0	0	Discordant	27.09326072	49.21763869
UW1011783A_42	0.0642	1	8.3	no value	no value	NAN	no value	NAN	no value	NAN	no value	NAN	no value	NAN	no value	NAN	#VALUE!	#VALUE!	#VALUE!	#VALUE!	#VALUE!
UW1011783A_43	0.0367	0.978	12.7	no value	no value	NAN	no value	NAN	no value	NAN	no value	NAN	no value	NAN	no value	NAN	#VALUE!	#VALUE!	#VALUE!	#VALUE!	#VALUE!
UW1011783A_44	0.0475	0.741	6.08	no value	no value	NAN	no value	NAN	no value	NAN	no value	NAN	no value	NAN	no value	NAN	#VALUE!	#VALUE!	#VALUE!	#VALUE!	#VALUE!
UW1011783A_45	0.0017	18	1.1	no value	no value	NAN	no value	NAN	no value	NAN	no value	NAN	no value	NAN	no value	NAN	#VALUE!	#VALUE!	#VALUE!	#VALUE!	#VALUE!
UW1011783A_46	0.0015	0.055	1.78	no value	no value	NAN	no value	NAN	no value	NAN	no value	NAN	no value	NAN	no value	NAN	#VALUE!	#VALUE!	#VALUE!	#VALUE!	#VALUE!
UW1011783C_1	0.0193	2.06	18.2	no value	no value	NAN	no value	NAN	no value	NAN	no value	NAN	no value	NAN	no value	NAN	#VALUE!	#VALUE!	#VALUE!	#VALUE!	#VALUE!
UW1011783C_2	44.8	49.8	212	0.875	3.172	0.096	0.2339	0.0042	0.0977	0.0023	1443	23	1354	22	1567	44	1567	44	FinalAge207_206	6.167706168	13.59285258
UW1011783C_3	286	250.5	542	1.112	1.251	0.027	0.1253	0.0019	0.0724	0.0011	823	12	761	11	987	31	761	11	FinalAge206_238	7.533414338	22.89766971
UW1011783C_4	820	623	969	1.334	1.049	0.038	0.1008	0.0016	0.0743	0.0019	722	18	618.6	9.2	1024	48	618.6	9.2	FinalAge206_238	14.32132964	39.58984375
UW1011783C_5	0.059	0.727	6.8	no value	no value	NAN	no value	NAN	no value	NAN	no value	NAN	no value	NAN	no value	NAN	#VALUE!	#VALUE!	#VALUE!	#VALUE!	#VALUE!
UW1011783C_6	121.8	250	676	0.4973	1.823	0.044	0.1654	0.0024	0.0794	0.0016	1053	16	987	13	1178	39	987	13	FinalAge206_238	6.267806268	16.2139219
UW1011783C_7	0.0154	1.32	9.8	no value	no value	NAN	no value	NAN	no value	NAN	no value	NAN	no value	NAN	no value	NAN	#VALUE!	#VALUE!	#VALUE!	#VALUE!	#VALUE!

Table A2.1. U-Pb isotopic data for Rising Star cave and surface samples (Continued).

Sample #_Spot #	U (in ppm)	Th (in ppm)	Pb (in ppm)	Th/U	Pb207 /U235	± 2σ	Pb206 /U238	± 2σ	Pb207 /Pb206	± 2σ	Pb207 /U235	± Ma	Pb206 /U238	± Ma	Pb207 /Pb206	± Ma	Preferred Age	± Ma	Age System	U-Pb/U-Pb Discordance (%)	U-Pb/Pb-Pb Discordance (%)
UW1011783C_8	0.0027	0.0037	1.99	no value	no value	NAN	no value	NAN	no value	NAN	no value	NAN	no value	NAN	no value	NAN	#VALUE!	#VALUE!	#VALUE!	#VALUE!	#VALUE!
UW1011783C_9	0.254	7.57	34.7	no value	no value	NAN	no value	NAN	no value	NAN	no value	NAN	no value	NAN	no value	NAN	#VALUE!	#VALUE!	#VALUE!	#VALUE!	#VALUE!
UW1011783C_10	221.9	197.5	1094	1.128	6.484	0.1	0.3706	0.005	0.1268	0.0011	2041.8	14	2031	23	2052	15	2052	15	FinalAge207_206	0.528945048	1.023391813
UW1011783C_11	1.2	0.28	-0.01	4.3	0.61	0.04	0.085	0.011	0.0523	0.0046	484	25	524	68	290	200	524	68	FinalAge206_238	-8.26446281	-80.68965517
UW1011783C_12	0.0252	0.192	3.16	no value	no value	NAN	no value	NAN	no value	NAN	no value	NAN	no value	NAN	no value	NAN	#VALUE!	#VALUE!	#VALUE!	#VALUE!	#VALUE!
UW1011783C_13	-0.000025543	1.017	6.73	no value	no value	NAN	no value	NAN	no value	NAN	no value	NAN	no value	NAN	no value	NAN	#VALUE!	#VALUE!	#VALUE!	#VALUE!	#VALUE!
UW1011783C_14	98.1	109.8	151.8	0.896	0.676	0.023	0.0827	0.0013	0.0594	0.002	523	14	511.9	7.6	521	74	511.9	7.6	FinalAge206_238	2.122370937	1.746641075
UW1011783C_15	280.4	379.6	2948	0.7351	14.4	0.22	0.5328	0.0059	0.1949	0.0013	2774.6	14	2752	25	2781	11	2781	11	FinalAge207_206	0.814531824	1.042790363
UW1011783C_16	0.0094	0.022	4.9	no value	no value	NAN	no value	NAN	no value	NAN	no value	NAN	no value	NAN	no value	NAN	#VALUE!	#VALUE!	#VALUE!	#VALUE!	#VALUE!
UW1011783C_17	0.0429	0.231	1.99	no value	no value	NAN	no value	NAN	no value	NAN	no value	NAN	no value	NAN	no value	NAN	#VALUE!	#VALUE!	#VALUE!	#VALUE!	#VALUE!
UW1011783C_18	0.022	0.0336	1.08	no value	no value	NAN	no value	NAN	no value	NAN	no value	NAN	no value	NAN	no value	NAN	#VALUE!	#VALUE!	#VALUE!	#VALUE!	#VALUE!
UW1011783C_19	0.049	0.28	12.4	no value	no value	NAN	no value	NAN	no value	NAN	no value	NAN	no value	NAN	no value	NAN	#VALUE!	#VALUE!	#VALUE!	#VALUE!	#VALUE!
UW1011783C_20	0.0047	0.0288	40.4	no value	no value	NAN	no value	NAN	no value	NAN	no value	NAN	no value	NAN	no value	NAN	#VALUE!	#VALUE!	#VALUE!	#VALUE!	#VALUE!
UW1011783C_21	0.0486	0.224	2.73	no value	no value	NAN	no value	NAN	no value	NAN	no value	NAN	no value	NAN	no value	NAN	#VALUE!	#VALUE!	#VALUE!	#VALUE!	#VALUE!
UW1011783C_22	0.0238	0.263	2.06	no value	no value	NAN	no value	NAN	no value	NAN	no value	NAN	no value	NAN	no value	NAN	#VALUE!	#VALUE!	#VALUE!	#VALUE!	#VALUE!
UW1011783C_23	0.0216	0.274	1.9	no value	no value	NAN	no value	NAN	no value	NAN	no value	NAN	no value	NAN	no value	NAN	#VALUE!	#VALUE!	#VALUE!	#VALUE!	#VALUE!
UW1011783C_24	0.0229	0.4	4.78	no value	no value	NAN	no value	NAN	no value	NAN	no value	NAN	no value	NAN	no value	NAN	#VALUE!	#VALUE!	#VALUE!	#VALUE!	#VALUE!
UW1011783C_25	0.0037	0.0032	8.4	no value	no value	NAN	no value	NAN	no value	NAN	no value	NAN	no value	NAN	no value	NAN	#VALUE!	#VALUE!	#VALUE!	#VALUE!	#VALUE!
UW1011783C_26	-0.000152857	-0.000186429	1.1	no value	no value	NAN	no value	NAN	no value	NAN	no value	NAN	no value	NAN	no value	NAN	#VALUE!	#VALUE!	#VALUE!	#VALUE!	#VALUE!
UW1011783C_27	0.0374	0.845	6.62	no value	no value	NAN	no value	NAN	no value	NAN	no value	NAN	no value	NAN	no value	NAN	#VALUE!	#VALUE!	#VALUE!	#VALUE!	#VALUE!
UW1011783C_28	0.0233	0.285	2.14	no value	no value	NAN	no value	NAN	no value	NAN	no value	NAN	no value	NAN	no value	NAN	#VALUE!	#VALUE!	#VALUE!	#VALUE!	#VALUE!
UW1011783C_29	349	1720	1380	0.2096	7.4	0.38	0.258	0.013	0.2149	0.0041	2129	46	1465	67	2941	31	0	0	Discordant	31.18835134	50.18701122
UW1011783C_30	-0.000150124	-0.000187503	0.01	no value	no value	NAN	no value	NAN	no value	NAN	no value	NAN	no value	NAN	no value	NAN	#VALUE!	#VALUE!	#VALUE!	#VALUE!	#VALUE!
UW1011783C_31	204.2	164.1	355.2	1.216	1.796	0.051	0.1764	0.0015	0.07307	0.0016	1042	19	1047	8.2	1006	45	1006	45	FinalAge207_206	-0.479846449	-4.07554672
UW1011783C_32	143.2	173.9	841	0.8049	13.59	0.39	0.4484	0.0047	0.2128	0.0041	2716	29	2387	21	2927	30	0	0	Discordant	12.11340206	18.44892381
UW1011783C_33	0.0081	0.14	2.9	no value	no value	NAN	no value	NAN	no value	NAN	no value	NAN	no value	NAN	no value	NAN	#VALUE!	#VALUE!	#VALUE!	#VALUE!	#VALUE!
UW1011783C_34	1.89	28.01	97.4	0.0667	15.6	2	0.332	0.026	0.41	0.042	2830	120	1840	130	3840	170	0	0	Discordant	34.98233216	52.08333333
UW1011783C_35	0.0315	0.49	4.21	no value	no value	NAN	no value	NAN	no value	NAN	no value	NAN	no value	NAN	no value	NAN	#VALUE!	#VALUE!	#VALUE!	#VALUE!	#VALUE!
UW1011783C_36	166.4	126.2	506	1.309	6.575	0.17	0.3753	0.0027	0.1224	0.0024	2054.1	23	2055	13	1989	35	1989	35	FinalAge207_206	-0.043814809	-3.318250377
UW1011783C_37	10.43	172.1	478	0.06061	9.94	0.4	0.2741	0.0057	0.2631	0.0086	2419	36	1562	28	3246	52	0	0	Discordant	35.42786275	51.87923598
UW1011783C_38	0.0666	0.812	3.76	no value	no value	NAN	no value	NAN	no value	NAN	no value	NAN	no value	NAN	no value	NAN	#VALUE!	#VALUE!	#VALUE!	#VALUE!	#VALUE!
UW1011783C_39	149.4	327.2	356.3	0.4561	0.8	0.029	0.0984	0.0016	0.0561	0.0016	594	16	604.8	9.2	431	65	604.8	9.2	FinalAge206_238	-1.818181818	-40.32482599
UW1011783C_40	-0.000134871	0.05	0.89	no value	no value	NAN	no value	NAN	no value	NAN	no value	NAN	no value	NAN	no value	NAN	#VALUE!	#VALUE!	#VALUE!	#VALUE!	#VALUE!
UW1011783C_41	0.00087	0.025	0.5	no value	no value	NAN	no value	NAN	no value	NAN	no value	NAN	no value	NAN	no value	NAN	#VALUE!	#VALUE!	#VALUE!	#VALUE!	#VALUE!
UW1011783C_42	1182	697	2008	1.718	3.447	0.1	0.1531	0.0016	0.15948	0.003	1511	25	918.2	8.9	2450.3	31	0	0	Discordant	39.23229649	62.52703751
UW1011783C_43	68.7	100.4	380	0.684	6.84	0.24	0.3838	0.0041	0.1279	0.003	2082	34	2093	19	2064	41	2064	41	FinalAge207_206	-0.528338136	-1.40503876
UW1011783C_44	296	820	1458	0.3677	5.58	0.18	0.2833	0.0042	0.1412	0.0028	1905	31	1606	21	2239	34	0	0	Discordant	15.69553806	28.2715498
UW1011783C_45	0.0572	3.58	13	no value	no value	NAN	no value	NAN	no value	NAN	no value	NAN	no value	NAN	no value	NAN	#VALUE!	#VALUE!	#VALUE!	#VALUE!	#VALUE!
UW1011783C_46	0.0132	0.566	3.17	no value	no value	NAN	no value	NAN	no value	NAN	no value	NAN	no value	NAN	no value	NAN	#VALUE!	#VALUE!	#VALUE!	#VALUE!	#VALUE!
UW1011783L_1	221	193.9	689.1	1.1597	6.505	0.17	0.3736	0.0028	0.12247	0.0024	2044.9	23	2046	13	1991	36	1991	36	FinalAge207_206	-0.053792361	-2.762430939
UW1011783L_2	231.9	245.2	804	0.968	5.9	0.29	0.3698	0.0041	0.1239	0.0026	1956	48	2028	19	2011	38	2011	38	FinalAge207_206	-3.680981595	-0.845350572
UW1011783L_3	0.008	2.38	10.3	no value	no value	NAN	no value	NAN	no value	NAN	no value	NAN	no value	NAN	no value	NAN	#VALUE!	#VALUE!	#VALUE!	#VALUE!	#VALUE!
UW1011783L_4	219.1	192.8	361	1.169	1.967	0.059	0.1864	0.0016	0.07627	0.0016	1101	22	1101.6	8.7	1096	43	1096	43	FinalAge207_206	-0.054495913	-0.510948905
UW1011783L_5	232	318	701	0.81	3.847	0.13	0.2809	0.0044	0.1016	0.0021	1594	33	1595	22	1650	38	1650	38	FinalAge207_206	-0.062735257	3.333333333
UW1011783L_6	0.0066	15	2.9	no value	no value	NAN	no value	NAN	no value	NAN	no value	NAN	no value	NAN	no value	NAN	#VALUE!	#VALUE!	#VALUE!	#VALUE!	#VALUE!
UW1011783L_7	0.0061	1.6	1.67	no value	no value	NAN	no value	NAN	no value	NAN	no value	NAN	no value	NAN	no value	NAN	#VALUE!	#VALUE!	#VALUE!	#VALUE!	#VALUE!
UW1011783L_8	256.8	324.2	581.6	0.8046	1.824	0.056	0.1774	0.0013	0.0731	0.0016	1050	22	1052.5	7.2	1008	43	1008	43	FinalAge207_206	-0.238095238	-4.41468254
UW1011783L_9	22.94	37.13	202.2	0.6318	19.41	0.56	0.6113	0.0071	0.2256	0.005	3049	36	3073	28	3016	36	3016	36	FinalAge207_206	-0.787143326	-1.889920424
UW1011783L_10	116.5	105.1	404.1	1.126	7.93	0.23	0.4102	0.0048	0.1382	0.0029	2215	31	2215	22	2202	35	2202	35	FinalAge207_206	0	-0.590372389
UW1011783L_11	121.5	53.5	73.1	2.294	0.856	0.029	0.0925	0.0012	0.0676	0.0022	627	17	570	7	818	73	570	7	FinalAge206_238	9.090909091	30.31784841
UW1011783L_12	0.053	0.25	22.8	no value	no value	NAN	no value	NAN	no value	NAN	no value	NAN	no value	NAN	no value	NAN	#VALUE!	#VALUE!	#VALUE!	#VALUE!	#VALUE!
UW1011783L_13	0.038	0.19	8.2	no value	no value	NAN	no value	NAN	no value	NAN	no value	NAN	no value	NAN	no value	NAN	#VALUE!	#VALUE!	#VALUE!	#VALUE!	#VALUE!
UW1011783L_14	0.11	1.88	27	no value	no value	NAN	no value	NAN	no value	NAN	no value	NAN	no value	NAN	no value	NAN	#VALUE!	#VALUE!	#VALUE!	#VALUE!	#VALUE!

Table A2.1. U-Pb isotopic data for Rising Star cave and surface samples (Continued).

Sample #_Spot #	U (in ppm)	Th (in ppm)	Pb (in ppm)	Th/U	Pb207 /U235	± 2σ	Pb206 /U238	± 2σ	Pb207 /Pb206	± 2σ	Pb207 /U235	± Ma	Pb206 /U238	± Ma	Pb207 /Pb206	± Ma	Preferred Age	± Ma	Age System	U-Pb/U-Pb Discordance (%)	U-Pb/Pb-Pb Discordance (%)
UW1011783L_15	24.9	62	316	0.91	14.2	2.1	0.313	0.017	0.278	0.02	2490	110	1737	78	3244	95	0	0	Discordant	30.24096386	46.45499383
UW1011783L_16	2.8	30.3	106.6	0.0927	12.1	1.3	0.362	0.017	0.247	0.024	2546	93	1979	79	3000	150	0	0	Discordant	22.27022781	34.03333333
UW1011783L_17	507	495	246	1.037	0.3096	0.011	0.04339	0.00048	0.0513	0.0014	273.2	8.3	273.8	3	243	61	273.8	3	FinalAge206_238	-0.219619327	-12.67489712
UW1011783L_18	132.5	138.5	540.9	0.9587	6.59	0.19	0.3753	0.0032	0.1251	0.0025	2054	28	2055	15	2026	36	2026	36	FinalAge207_206	-0.048685492	-1.431391905
UW1011783L_19	121.7	130.4	510.6	0.937	6.62	0.19	0.3777	0.0035	0.1239	0.0026	2057	27	2065	17	2010	36	2010	36	FinalAge207_206	-0.388915897	-2.736318408
UW1011783L_20	705	2250	1674	0.3098	2.886	0.1	0.1194	0.0023	0.1729	0.0034	1374	26	726	13	2584	33	0	0	Discordant	47.16157205	71.90402477
UW1011783L_21	158.9	280.2	1200	0.5563	7.075	0.19	0.3892	0.0035	0.1275	0.0026	2120	23	2119	16	2059	35	2059	35	FinalAge207_206	0.047169811	-2.91403594
UW1011783L_22	0.0021	21	1.08	no value	no value	NAN	no value	NAN	no value	NAN	no value	NAN	no value	NAN	no value	NAN	#VALUE!	#VALUE!	#VALUE!	#VALUE!	#VALUE!
UW1011783L_23	0.0184	2.45	9	no value	no value	NAN	no value	NAN	no value	NAN	no value	NAN	no value	NAN	no value	NAN	#VALUE!	#VALUE!	#VALUE!	#VALUE!	#VALUE!
UW1011783L_24	0.0311	0.945	4.43	no value	no value	NAN	no value	NAN	no value	NAN	no value	NAN	no value	NAN	no value	NAN	#VALUE!	#VALUE!	#VALUE!	#VALUE!	#VALUE!
UW1011783L_25	142.7	262.2	153	0.5367	0.336	0.015	0.04659	0.00057	0.0512	0.0019	293.4	11	293.5	3.5	233	80	293.5	3.5	FinalAge206_238	-0.034083163	-25.96566524
UW1011783L_26	173.8	132.9	140.4	1.305	0.664	0.024	0.08305	0.00097	0.06	0.002	514	15	514.2	5.7	565	70	514.2	5.7	FinalAge206_238	-0.038910506	8.991150442
UW1011783L_27	51.24	16.21	25.9	3.143	0.85	0.039	0.0923	0.0014	0.0666	0.0028	618	21	569	8.5	747	91	569	8.5	FinalAge206_238	7.928802589	23.82864793
UW1011783L_28	0.0021	0.44	4.9	no value	no value	NAN	no value	NAN	no value	NAN	no value	NAN	no value	NAN	no value	NAN	#VALUE!	#VALUE!	#VALUE!	#VALUE!	#VALUE!
UW1011783L_29	79.2	152.3	690	0.506	9.31	0.38	0.436	0.01	0.1606	0.0037	2354	43	2328	46	2459	40	2459	40	FinalAge207_206	1.104502974	5.327368849
UW1011783L_30	0.0401	1.011	7.8	no value	no value	NAN	no value	NAN	no value	NAN	no value	NAN	no value	NAN	no value	NAN	#VALUE!	#VALUE!	#VALUE!	#VALUE!	#VALUE!
UW1011783L_31	0.0011	0.17	1.94	no value	no value	NAN	no value	NAN	no value	NAN	no value	NAN	no value	NAN	no value	NAN	#VALUE!	#VALUE!	#VALUE!	#VALUE!	#VALUE!
UW1011783L_32	190.9	209.7	880	0.8939	6.41	0.18	0.3652	0.0044	0.124	0.0026	2029	27	2005	21	2008	37	2008	37	FinalAge207_206	1.182848694	0.14940239
UW1011783L_33	0.0023	0.053	1.01	no value	no value	NAN	no value	NAN	no value	NAN	no value	NAN	no value	NAN	no value	NAN	#VALUE!	#VALUE!	#VALUE!	#VALUE!	#VALUE!
UW1011783L_34	103.2	117.6	649	0.855	15.33	0.76	0.492	0.019	0.2294	0.0048	2803	54	2555	87	3044	34	0	0	Discordant	8.847663218	16.06438896
UW1011783L_35	59.2	51	267.6	1.138	9.39	0.28	0.4483	0.0054	0.1486	0.0032	2370	30	2386	24	2324	37	2324	37	FinalAge207_206	-0.675105485	-2.667814114
UW1011783L_36	196.9	192	825	1.016	6.5	0.19	0.3697	0.0047	0.1243	0.0026	2036	32	2029	23	2013	37	2013	37	FinalAge207_206	0.343811395	-0.794833582
OSL4_1	896	630	301	3.92	0.652	0.018	0.0708	0.0036	0.0697	0.0029	509	11	440	22	878	74	440	22	FinalAge206_238	13.55599214	49.88610478
OSL4_2	181	124.9	1003	1.469	10.29	0.67	0.326	0.02	0.2285	0.0035	2434	61	1808	95	3038	24	0	0	Discordant	25.7189811	40.48716261
OSL4_3	646.4	567	472	1.152	0.3045	0.0064	0.04246	0.00056	0.0519	0.001	269.6	5	268	3.5	266	44	268	3.5	FinalAge206_238	0.59347181	-0.751879699
OSL4_4	0.00107	-8.16114E-05	1.91	no value	no value	NAN	no value	NAN	no value	NAN	no value	NAN	no value	NAN	no value	NAN	#VALUE!	#VALUE!	#VALUE!	#VALUE!	#VALUE!
OSL4_5	387	726	2510	0.535	8.02	0.14	0.3299	0.0053	0.1764	0.0015	2231	16	1837	26	2617	14	0	0	Discordant	17.66024204	29.80512037
OSL4_6	0.0009	0.01	2.66	no value	no value	NAN	no value	NAN	no value	NAN	no value	NAN	no value	NAN	no value	NAN	#VALUE!	#VALUE!	#VALUE!	#VALUE!	#VALUE!
OSL4_7	0.0074	-8.14161E-05	10.8	no value	no value	NAN	no value	NAN	no value	NAN	no value	NAN	no value	NAN	no value	NAN	#VALUE!	#VALUE!	#VALUE!	#VALUE!	#VALUE!
OSL4_8	155.3	245.7	1376	0.612	17.36	0.27	0.526	0.008	0.24	0.003	2954	15	2724	34	3117	20	3117	20	FinalAge207_206	7.78605281	12.60827719
OSL4_9	259.7	230.6	1131	1.093	6.694	0.11	0.3821	0.0059	0.1273	0.0014	2070	14	2085	28	2058	19	2058	19	FinalAge207_206	-0.724637681	-1.311953353
OSL4_10	91.7	133.9	930	0.6668	18.63	0.21	0.5851	0.0071	0.2309	0.0018	3022	11	2969	29	3056	13	3056	13	FinalAge207_206	1.753805427	2.846858639
OSL4_11	151.2	138.4	624	1.066	6.68	0.15	0.376	0.0065	0.1302	0.0022	2069	19	2057	31	2097	30	2097	30	FinalAge207_206	0.579990333	1.907486886
OSL4_12	250.5	147.3	252.6	1.666	0.966	0.022	0.1047	0.0015	0.0672	0.0014	685	11	641.7	8.7	829	42	641.7	8.7	FinalAge206_238	6.321167883	22.59348613
OSL4_13	315.6	1014	588	0.3051	0.284	0.016	0.039	0.00095	0.0527	0.003	253	13	246.6	5.9	280	120	246.6	5.9	FinalAge206_238	2.529644269	11.92857143
OSL4_14	0.0015	-8.52254E-05	4.8	no value	no value	NAN	no value	NAN	no value	NAN	no value	NAN	no value	NAN	no value	NAN	#VALUE!	#VALUE!	#VALUE!	#VALUE!	#VALUE!
OSL4_15	211	191.3	964	1.0901	6.448	0.077	0.3726	0.0047	0.12554	0.00096	2037.9	11	2041	22	2034	14	2034	14	FinalAge207_206	-0.152117376	-0.344149459
OSL4_16	66.95	172.8	1299	0.3844	15.16	0.27	0.5497	0.0081	0.2005	0.0023	2822	17	2822	34	2826	19	2826	19	FinalAge207_206	0	0.141542817
OSL4_17	148.4	85.2	211.5	1.677	1.133	0.023	0.1153	0.0017	0.0717	0.0014	768	11	703.4	9.9	961	40	703.4	9.9	FinalAge206_238	8.411458333	26.80541103
OSL4_18	309	261	1425	1.163	13.95	0.17	0.4967	0.0063	0.2038	0.0011	2744.9	12	2598	27	2855	8.8	2855	8.8	FinalAge207_206	5.351743233	9.001751313
OSL4_19	227.1	295.6	1128	0.741	2.022	0.045	0.1933	0.0033	0.0758	0.0018	1122	15	1139	18	1084	48	1084	48	FinalAge207_206	-1.515151515	-5.073800738
OSL4_20	192	282	605	0.691	1.872	0.055	0.1553	0.005	0.0873	0.0023	1068	19	930	28	1361	54	930	28	FinalAge206_238	12.92134831	31.66789126
OSL4_21	131.2	307.5	605	0.4088	0.91	0.022	0.1041	0.0015	0.0635	0.0015	656	12	638.3	9	705	50	638.3	9	FinalAge206_238	2.698170732	9.460992908
OSL4_22	143.5	142.6	1043	0.966	6.894	0.11	0.3853	0.005	0.1295	0.0013	2096	14	2101	23	2088	18	2088	18	FinalAge207_206	-0.238549618	-0.622605364
OSL4_23	162.1	160.7	1000	0.9695	6.46	0.076	0.3725	0.0043	0.1257	0.001	2039.5	10	2043	21	2038	14	2038	14	FinalAge207_206	-0.171610689	-0.245338567
OSL4_24	102.6	73.8	229	1.37	1.898	0.06	0.1759	0.0042	0.0789	0.0023	1078	21	1044	23	1174	53	1174	53	FinalAge207_206	3.153988868	11.07325383
OSL4_25	-0.000091898	-0.000078402	1.98	no value	no value	NAN	no value	NAN	no value	NAN	no value	NAN	no value	NAN	no value	NAN	#VALUE!	#VALUE!	#VALUE!	#VALUE!	#VALUE!
OSL4_26	280.5	198.6	444	1.373	1.068	0.027	0.1133	0.0016	0.0681	0.0015	737	13	691.8	9.5	865	44	691.8	9.5	FinalAge206_238	6.132971506	20.02312139
OSL4_27	77.9	63.7	111.4	1.55	1.009	0.044	0.1156	0.0033	0.0631	0.0021	704	23	704	19	681	73	704	19	FinalAge206_238	0	-3.377386197
OSL4_28	333.3	379.3	1854	0.9641	6.953	0.08	0.3861	0.0047	0.1309	0.0011	2104.8	10	2104	22	2107	14	2107	14	FinalAge207_206	0.038008362	0.142382534
OSL4_29	193.1	374	1115	0.558	2.755	0.044	0.2316	0.003	0.0864	0.0011	1342	12	1342	15	1339	25	1339	25	FinalAge207_206	0	-0.224047797
OSL4_30	123.1	231.4	1649	0.5785	19.63	0.22	0.6116	0.0077	0.2333	0.0017	3072.5	11	3078	30	3073	12	3073	12	FinalAge207_206	-0.179007323	-0.162707452
OSL4_31	293.5	343	1398	0.968	6.554	0.078	0.3752	0.0047	0.12697	0.00099	2052.1	11	2053	22	2054	14	2054	14	FinalAge207_206	-0.043857512	0.048685492

Table A2.1. U-Pb isotopic data for Rising Star cave and surface samples (Continued).

Sample #_Spot #	U (in ppm)	Th (in ppm)	Pb (in ppm)	Th/U	Pb207 /U235	± 2σ	Pb206 /U238	± 2σ	Pb207 /Pb206	± 2σ	Pb207 /U235	± Ma	Pb206 /U238	± Ma	Pb207 /Pb206	± Ma	Preferred Age	± Ma	Age System	U-Pb/U-Pb Discordance (%)	U-Pb/Pb-Pb Discordance (%)
OSL4_32	607	1057	1617	0.6204	2.166	0.026	0.173	0.0022	0.09088	0.00085	1169.5	8.4	1028.6	12	1440	18	0	0	Discordant	12.04788371	28.56944444
OSL4_33	1097	140	361	11.54	1.563	0.042	0.15	0.0031	0.0752	0.00075	952	16	900	18	1069	20	900	18	FinalAge206_238	5.462184874	15.80916745
OSL4_34	312.9	502	1625	0.659	5.582	0.07	0.3176	0.0042	0.12756	0.00091	1912.1	11	1777	21	2062	13	2062	13	FinalAge207_206	7.065530045	13.82153249
OSL4_35	202.5	233.7	1640	0.916	16.09	0.25	0.5051	0.0076	0.2308	0.0016	2879	15	2634	33	3058	11	3058	11	FinalAge207_206	8.509899271	13.86527142
OSL4_36	694	499	697	1.421	0.72	0.015	0.0817	0.0014	0.0638	0.0011	550	8.9	505.9	8.1	731	37	505.9	8.1	FinalAge206_238	8.018181818	30.79343365
OSL4_37	235.5	347	2091	0.679	11.72	0.21	0.3661	0.0071	0.232	0.0021	2581	17	2010	33	3064	14	0	0	Discordant	22.12320806	34.39947781
OSL4_38	190.4	345	970	0.558	1.824	0.028	0.1667	0.0022	0.0793	0.0011	1053	10	995.1	12	1171	28	995.1	12	FinalAge206_238	5.498575499	15.02134927
OSL4_39	55.1	50.6	431.3	1.093	14.64	0.21	0.5404	0.0077	0.1967	0.0022	2790	13	2784	32	2795	19	2795	19	FinalAge207_206	0.215053763	0.393559928
OSL4_40	346	405	2600	0.861	14.57	0.91	0.543	0.032	0.1941	0.0027	2768	56	2770	130	2774	21	2774	21	FinalAge207_206	-0.072254335	0.144196107
OSL4_41	141.4	74	176.1	2.014	0.867	0.028	0.0965	0.002	0.0648	0.002	631	15	594	12	735	70	594	12	FinalAge206_238	5.863708399	19.18367347
OSL4_42	196	149.9	1030	1.334	9.812	0.12	0.4548	0.0057	0.1563	0.0011	2416.4	11	2419	26	2416	11	2416	11	FinalAge207_206	-0.10759808	-0.124172185
OSL4_43	110.5	199.9	128.5	0.5678	0.279	0.012	0.03925	0.00077	0.0516	0.0021	250.3	9.1	248.2	4.8	248	86	248.2	4.8	FinalAge206_238	0.838993208	-0.080645161
OSL4_44	233.1	196.8	752	1.217	2.362	0.036	0.1924	0.0026	0.089	0.0012	1229.7	11	1134	14	1398	26	0	0	Discordant	7.782385948	18.88412017
OSL4_45	553	660	1750	1.62	1.73	0.022	0.1679	0.002	0.07487	0.00078	1019.9	8.4	1000.2	11	1060	21	1060	21	FinalAge207_206	1.931561918	5.641509434
OSL4_46	305.1	337.8	2559	0.9129	14.52	0.16	0.5393	0.0068	0.1948	0.0012	2783.6	11	2782	29	2781.5	9.9	2781.5	9.9	FinalAge207_206	0.057479523	-0.017975912
OSL4_47	112	108.4	606	0.988	6.729	0.091	0.3793	0.0048	0.1288	0.0013	2075	12	2072	22	2077	18	2077	18	FinalAge207_206	0.144578313	0.240731825
OSL4_48	201.4	177.4	976	1.08	6.43	0.087	0.3647	0.005	0.1281	0.0011	2035.2	12	2004	24	2069	15	2069	15	FinalAge207_206	1.533018868	3.141614306
OSL4_49	0.0052	-0.000090514	7.4	no value	no value	NAN	no value	NAN	no value	NAN	no value	NAN	no value	NAN	no value	NAN	#VALUE!	#VALUE!	#VALUE!	#VALUE!	#VALUE!
OSL4_50	261.7	236.1	1186	1.054	6.581	0.096	0.3763	0.0059	0.1272	0.0014	2058	12	2058	28	2057	19	2057	19	FinalAge207_206	0	-0.048614487
OSL4_51	201.2	248	173	0.799	0.3055	0.0098	0.04281	0.00072	0.0521	0.0018	271.4	8	270.2	4.4	271	75	270.2	4.4	FinalAge206_238	0.442151805	0.295202952
OSL4_52	171.7	150.5	816	1.103	6.669	0.084	0.3785	0.0048	0.12771	0.00099	2067.4	11	2069	22	2066	14	2066	14	FinalAge207_206	-0.077391893	-0.145208132
OSL4_53	60.9	76.4	615	0.775	14.36	0.29	0.5089	0.0083	0.2054	0.0027	2773	19	2650	36	2865	22	2865	22	FinalAge207_206	4.435629282	7.504363002
OSL4_54	144.4	130.5	761	1.072	6.867	0.096	0.3811	0.0055	0.1308	0.0015	2093	12	2081	26	2105	20	2105	20	FinalAge207_206	0.573339704	1.140142518
OSL4_55	244.5	283.2	1549	0.8402	6.623	0.079	0.3766	0.0046	0.12757	0.00095	2061.3	10	2060	22	2062	13	2062	13	FinalAge207_206	0.063066997	0.09699321
OSL4_56	435.4	660.1	3162	0.6499	8.47	0.15	0.2548	0.0052	0.2411	0.002	2280	16	1462	26	3125	13	0	0	Discordant	35.87719298	53.216
OSL4_57	312	203	460	2.39	0.654	0.026	0.0719	0.0016	0.0658	0.0023	509	16	447.5	9.9	779	80	447.5	9.9	FinalAge206_238	12.08251473	42.55455712
OSL4_58	961	1411	2560	0.864	0.655	0.013	0.0687	0.0012	0.06907	0.00097	510.8	7.9	428.1	7.2	891	29	0	0	Discordant	16.19028974	51.95286195
OSL4_59	705	373	3540	2.82	13.44	0.3	0.4068	0.0086	0.2395	0.0024	2705	22	2197	39	3113	17	0	0	Discordant	18.78003697	29.42499197
OSL4_60	0.029	0.0081	62	no value	no value	NAN	no value	NAN	no value	NAN	no value	NAN	no value	NAN	no value	NAN	#VALUE!	#VALUE!	#VALUE!	#VALUE!	#VALUE!
OSL4_61	1718	604	5390	4.54	1.794	0.039	0.1653	0.0028	0.07844	0.0008	1041	14	986	16	1153	20	986	16	FinalAge206_238	5.283381364	14.4839549
OSL4_62	293.4	1045	16900	0.394	8.58	0.12	0.4003	0.0067	0.1557	0.0013	2293	13	2169	31	2407	14	2407	14	FinalAge207_206	5.407762756	9.887827171
OSL4_63	438	1066	15600	0.569	17.27	0.25	0.5151	0.007	0.2417	0.0015	2948	14	2677	30	3130	10	3130	10	FinalAge207_206	9.192672999	14.47284345
OSL4_64	2310	1279	3263	2.273	1.207	0.024	0.1205	0.0022	0.07252	0.00055	802	11	733	13	997	15	733	13	FinalAge206_238	8.603491272	26.47943831
260517JW8_1	260.2	310.4	647	0.839	1.821	0.055	0.1759	0.0014	0.07345	0.0016	1047	23	1044.2	7.8	1017	45	1017	45	FinalAge207_206	0.267430755	-2.67453294
260517JW8_2	0.0144	0.24	10.4	no value	no value	NAN	no value	NAN	no value	NAN	no value	NAN	no value	NAN	no value	NAN	#VALUE!	#VALUE!	#VALUE!	#VALUE!	#VALUE!
260517JW8_3	696	399.8	417.2	1.734	0.704	0.022	0.08737	0.00064	0.05764	0.0012	539.9	14	539.9	3.8	512	47	539.9	3.8	FinalAge206_238	0	-5.44921875
260517JW8_4	560	950	1600	0.678	3.44	0.24	0.1995	0.0071	0.1301	0.0027	1507	52	1170	38	2095	37	0	0	Discordant	22.36230922	44.15274463
260517JW8_5	247.8	192.5	150	1.2902	0.498	0.018	0.06529	0.00062	0.0543	0.0014	408.4	13	407.6	3.7	364	59	407.6	3.7	FinalAge206_238	0.195886386	-11.97802198
260517JW8_6	77.1	69.8	154.6	1.133	1.956	0.067	0.1787	0.0018	0.0776	0.0021	1094	24	1059.5	9.8	1118	53	1118	53	FinalAge207_206	3.153564899	5.23255814
260517JW8_7	-0.00007257	-0.000216184	0.1	no value	no value	NAN	no value	NAN	no value	NAN	no value	NAN	no value	NAN	no value	NAN	#VALUE!	#VALUE!	#VALUE!	#VALUE!	#VALUE!
260517JW8_8	-0.000071828	-0.000216452	0.23	no value	no value	NAN	no value	NAN	no value	NAN	no value	NAN	no value	NAN	no value	NAN	#VALUE!	#VALUE!	#VALUE!	#VALUE!	#VALUE!
260517JW8_9	0.232	5.32	24.8	no value	no value	NAN	no value	NAN	no value	NAN	no value	NAN	no value	NAN	no value	NAN	#VALUE!	#VALUE!	#VALUE!	#VALUE!	#VALUE!
260517JW8_10	168.6	158.8	974	1.0659	18.21	0.51	0.5901	0.0039	0.2179	0.0041	2988	38	2991	16	2963.6	31	2963.6	31	FinalAge207_206	-0.100401606	-0.924551221
260517JW8_11	196.7	150.5	709	1.319	8.643	0.22	0.4292	0.0028	0.139	0.0027	2300	23	2302	13	2212	34	2212	34	FinalAge207_206	-0.086956522	-4.068716094
260517JW8_12	144.4	145.5	1400	1.023	7.99	0.35	0.4181	0.004	0.1408	0.0029	2237	36	2251	18	2233	36	2233	36	FinalAge207_206	-0.625838176	-0.806090461
260517JW8_13	238	286.3	1110	0.8329	6.308	0.17	0.3592	0.0024	0.12369	0.0024	2017	24	1977.9	11	2007	35	2007	35	FinalAge207_206	1.938522558	1.449925262
260517JW8_14	17.08	197.2	808	0.08665	6.41	0.23	0.3673	0.0048	0.1248	0.0037	2026	32	2015	23	2004	54	2004	54	FinalAge207_206	0.542941757	-0.548902196
260517JW8_15	52.27	89.9	452	0.5838	17.89	0.49	0.5617	0.0078	0.2282	0.0047	2981	28	2871	32	3038	34	3038	34	FinalAge207_206	3.6900369	5.497037525
260517JW8_16	160.7	168.3	289.8	0.9601	1.359	0.045	0.1351	0.0014	0.0718	0.0017	872	18	816.8	7.9	970	47	816.8	7.9	FinalAge206_238	6.330275229	15.79381443
260517JW8_17	160	185	693	0.839	6.195	0.17	0.356	0.003	0.1233	0.0025	2003	25	1964	14	2002	37	2002	37	FinalAge207_206	1.947079381	1.898101898
260517JW8_18	0.0019	0.8	0.8	no value	no value	NAN	no value	NAN	no value	NAN	no value	NAN	no value	NAN	no value	NAN	#VALUE!	#VALUE!	#VALUE!	#VALUE!	#VALUE!
260517JW8_19	0.00034	-0.000221533	16.1	no value	no value	NAN	no value	NAN	no value	NAN	no value	NAN	no value	NAN	no value	NAN	#VALUE!	#VALUE!	#VALUE!	#VALUE!	#VALUE!
260517JW8_20	-0.000058512	-0.000221799	0.56	no value	no value	NAN	no value	NAN	no value	NAN	no value	NAN	no value	NAN	no value	NAN	#VALUE!	#VALUE!	#VALUE!	#VALUE!	#VALUE!

Table A2.1. U-Pb isotopic data for Rising Star cave and surface samples (Continued).

Sample #_Spot #	U (in ppm)	Th (in ppm)	Pb (in ppm)	Th/U	Pb207 /U235	± 2σ	Pb206 /U238	± 2σ	Pb207 /Pb206	± 2σ	Pb207 /U235	± Ma	Pb206 /U238	± Ma	Pb207 /Pb206	± Ma	Preferred Age	± Ma	Age System	U-Pb/U-Pb Discordance (%)	U-Pb/Pb-Pb Discordance (%)
260517JW8_21	0.0169	0.099	15	no value	no value	NAN	no value	NAN	no value	NAN	no value	NAN	no value	NAN	no value	NAN	#VALUE!	#VALUE!	#VALUE!	#VALUE!	#VALUE!
260517JW8_22	155.3	285	1053	0.5405	7.02	0.44	0.3578	0.0096	0.1671	0.0033	1964	110	1964	45	2525	33	0	0	Discordant	0	22.21782178
190517JW1_1	0.00095	-0.000068925	114	no value	no value	NAN	no value	NAN	no value	NAN	no value	NAN	no value	NAN	no value	NAN	#VALUE!	#VALUE!	#VALUE!	#VALUE!	#VALUE!
190517JW1_2	0.0958	0.283	20.9	no value	no value	NAN	no value	NAN	no value	NAN	no value	NAN	no value	NAN	no value	NAN	#VALUE!	#VALUE!	#VALUE!	#VALUE!	#VALUE!
190517JW1_3	123.3	66.2	221.5	1.856	1.279	0.028	0.1378	0.0021	0.0672	0.0015	835	13	831.9	12	832	46	831.9	12	FinalAge206_238	0.371257485	0.012019231
190517JW1_4	200.6	177.3	406.8	1.1325	1.018	0.02	0.1129	0.0017	0.0654	0.0011	711.6	9.8	689.3	9.6	776	34	689.3	9.6	FinalAge206_238	3.133783024	11.17268041
190517JW1_5	212.1	358	1404	0.635	6.209	0.088	0.3548	0.0052	0.1271	0.0013	2004	12	1957	25	2055	17	2055	17	FinalAge207_206	2.345309381	4.768856448
190517JW1_6	224.6	146.2	491	1.617	2.348	0.039	0.2003	0.0027	0.085	0.0011	1225	12	1178	15	1308	26	1308	26	FinalAge207_206	3.836734694	9.93883792
190517JW1_7	0.001	-7.62755E-05	51.3	no value	no value	NAN	no value	NAN	no value	NAN	no value	NAN	no value	NAN	no value	NAN	#VALUE!	#VALUE!	#VALUE!	#VALUE!	#VALUE!
190517JW1_8	185	261.4	825	0.7188	1.771	0.032	0.1733	0.0026	0.0743	0.0012	1033	12	1030	14	1041	33	1041	33	FinalAge207_206	0.290416263	1.056676273
190517JW1_9	133	149.9	213.1	0.9028	0.642	0.018	0.0757	0.0011	0.0617	0.0017	502	11	470.3	6.9	627	60	470.3	6.9	FinalAge206_238	6.314741036	24.99202552
190517JW1_10	-0.000152305	-0.000074202	-0.06	no value	no value	NAN	no value	NAN	no value	NAN	no value	NAN	no value	NAN	no value	NAN	#VALUE!	#VALUE!	#VALUE!	#VALUE!	#VALUE!
190517JW1_11	197	126	332	1.642	2.082	0.037	0.1855	0.0028	0.0814	0.0012	1141	12	1096	15	1222	28	1222	28	FinalAge207_206	3.943908852	10.31096563
190517JW1_12	558	286	204.5	1.999	0.722	0.012	0.08147	0.0012	0.06438	0.00083	551.3	6.9	504.8	7.1	745	28	504.8	7.1	FinalAge206_238	8.434609106	32.24161074
190517JW1_13	254.7	255.5	294.8	0.98	0.664	0.013	0.08388	0.0011	0.05733	0.00098	516.2	7.7	519.2	6.7	488	38	519.2	6.7	FinalAge206_238	-0.581170089	-6.393442623
190517JW1_14	312	395	984	0.794	1.919	0.026	0.1781	0.0024	0.07787	0.00079	1087.8	8.8	1056.6	13	1141	21	1141	21	FinalAge207_206	2.868174297	7.397020158
190517JW1_15	70.7	72.5	411.7	0.951	9.45	0.14	0.4477	0.0067	0.1533	0.0019	2380	14	2384	30	2377	21	2377	21	FinalAge207_206	-0.168067227	-0.294488851
190517JW1_16	233.6	219.9	287.7	1.0396	0.744	0.014	0.0914	0.0012	0.059	0.0011	563.6	8.1	563.7	7.2	552	39	563.7	7.2	FinalAge206_238	-0.01774308	-2.119565217
190517JW1_17	203.1	314.3	1559	0.6348	20	0.25	0.5243	0.0069	0.2765	0.0017	3089.9	12	2716	29	3343	10	0	0	Discordant	12.10071523	18.75560873
190517JW1_18	307	158.5	432	2.05	1.778	0.024	0.1714	0.0022	0.07534	0.00091	1036.5	8.6	1019.9	12	1071	24	1071	24	FinalAge207_206	1.601543657	4.77124183
190517JW1_19	141.7	136.1	727	1.027	6.553	0.085	0.3754	0.0049	0.1268	0.0012	2053.1	12	2054	23	2051	17	2051	17	FinalAge207_206	-0.04383615	-0.146270112
190517JW1_20	183.3	744	465	0.256	1.099	0.03	0.106	0.0027	0.075	0.0017	751	14	649	16	1062	44	649	16	FinalAge206_238	13.58189081	38.88888889
190517JW1_21	126.6	125.2	999	0.9901	14.45	0.17	0.5359	0.0068	0.1951	0.0014	2778.6	11	2765	28	2783	12	2783	12	FinalAge207_206	0.489455121	0.646784046
190517JW1_22	172.3	248.9	1425	0.6766	6.661	0.086	0.3683	0.0048	0.1308	0.0012	2066.5	11	2021	22	2106	16	2106	16	FinalAge207_206	2.201790467	4.036087369
190517JW1_23	164.1	252	426.9	0.823	4.65	0.15	0.2685	0.0088	0.1254	0.0013	1747	27	1529	45	2030	18	0	0	Discordant	12.47853463	24.67980296
190517JW1_24	214.9	231	955	0.915	6.16	0.079	0.3487	0.0046	0.1285	0.001	1997.4	11	1928	22	2077	14	2077	14	FinalAge207_206	3.474516872	7.173808377
190517JW1_25	683	938	4440	0.729	7.84	0.63	0.228	0.016	0.2516	0.0042	2190	72	1322	85	3186	26	0	0	Discordant	39.6347032	58.50596359
190517JW1_26	208.4	402	956	0.514	5.904	0.093	0.3379	0.0058	0.1271	0.0012	1961	14	1876	28	2055	16	2055	16	FinalAge207_206	4.334523202	8.710462287
190517JW1_27	440	1640	2440	1.69	0.851	0.015	0.09643	0.0012	0.06405	0.00099	624.2	8.2	593.4	6.9	737	32	593.4	6.9	FinalAge206_238	4.934315924	19.4843962
190517JW1_28	252.5	251.4	1540	0.9762	12.22	0.15	0.4628	0.0061	0.1917	0.0012	2620.3	11	2451	27	2755	10	2755	10	FinalAge207_206	6.461092241	11.03448276
190517JW1_29	78.72	74.08	190.7	1.043	1.744	0.037	0.1713	0.0027	0.0738	0.0014	1024	13	1019	15	1029	39	1029	39	FinalAge207_206	0.48828125	0.971817298
190517JW1_30	297	509.5	2281	0.571	5.292	0.097	0.3379	0.0051	0.1139	0.0013	1866	16	1876	25	1858	21	1858	21	FinalAge207_206	-0.535905681	-0.968783638
190517JW1_31	185.5	46.4	434	4.19	15.64	0.34	0.5523	0.011	0.2043	0.0021	2853	21	2834	45	2860	17	2860	17	FinalAge207_206	0.66596565	0.909090909
190517JW1_32	220.4	381	1240	0.5975	1.908	0.03	0.1766	0.0021	0.07831	0.00096	1083.1	10	1048.1	12	1149	24	1149	24	FinalAge207_206	3.231465239	8.781549173
190517JW1_33	702	346.3	2364	2.094	4.196	0.07	0.2125	0.0039	0.143	0.0013	1672	14	1242	21	2262	15	0	0	Discordant	25.71770335	45.0928382
190517JW1_34	238.4	223.1	1351	1.0961	6.638	0.08	0.3786	0.0046	0.12725	0.00098	2064.5	11	2069	21	2058	14	2058	14	FinalAge207_206	-0.217970453	-0.534499514
190517JW1_35	210.9	146.9	444	1.501	1.718	0.039	0.1699	0.0033	0.07339	0.00098	1015	14	1011	18	1021	26	1021	26	FinalAge207_206	0.39408867	0.979431929
190517JW1_36	332.5	180.8	523	1.864	1.815	0.033	0.1753	0.0026	0.075	0.0013	1050	12	1041	14	1062	35	1062	35	FinalAge207_206	0.857142857	1.97740113
190517JW1_37	163.8	150	949	1.108	18.33	0.44	0.526	0.012	0.252	0.0019	2999	24	2719	53	3197	11	3197	11	FinalAge207_206	9.336445482	14.95151705
190517JW1_38	62.6	75.6	800	0.8301	19.08	0.22	0.5853	0.0076	0.2356	0.002	3045.1	11	2970	31	3090	14	3090	14	FinalAge207_206	2.466257266	3.883495146
190517JW1_39	112	210.9	1735	0.533	19.9	0.3	0.6095	0.01	0.2375	0.0026	3085	15	3066	41	3101	17	3101	17	FinalAge207_206	0.615883306	1.128668172
190517JW1_40	136.3	200.4	337.4	0.6814	0.862	0.019	0.0915	0.0014	0.0684	0.0016	632	11	564.1	8.3	863	48	564.1	8.3	FinalAge206_238	10.74367089	34.63499421
190517JW1_41	642	444	506	1.458	0.5936	0.011	0.06685	0.001	0.06429	0.00081	472.6	6.9	417.1	6.2	744	27	417.1	6.2	FinalAge206_238	11.74354634	43.93817204
190517JW1_42	260	159	752	1.662	3.119	0.056	0.2207	0.0032	0.1023	0.0014	1435	14	1287	18	1660	25	0	0	Discordant	10.31358885	22.46987952
190517JW1_43	166.3	207.9	1538	0.8148	14.51	0.17	0.5341	0.0069	0.1975	0.0016	2784.5	12	2758	29	2804	13	2804	13	FinalAge207_206	0.951696894	1.640513552
190517JW1_44	1493	281.8	426	5.383	0.662	0.02	0.08143	0.0011	0.0595	0.001	515	13	504.6	6.6	579	36	504.6	6.6	FinalAge206_238	2.019417476	12.84974093
190517JW1_45	2010	19100	1199	0.1093	0.492	0.024	0.0257	0.0013	0.1393	0.0012	402	16	163.3	8.4	2215	16	0	0	Discordant	59.37810945	92.6275395
190517JW1_46	143.9	167.8	523	0.8793	2.154	0.034	0.1762	0.0022	0.089	0.0012	1165	11	1045.8	12	1397	26	0	0	Discordant	10.23175966	25.13958482
190517JW1_47	88.8	88.7	655	1.019	11.25	0.15	0.4839	0.0064	0.168	0.0019	2543.6	12	2544	28	2534	19	2534	19	FinalAge207_206	-0.015725743	-0.394632991
190517JW1_48	206.1	349	226.3	0.613	0.2846	0.0094	0.04023	0.00065	0.0513	0.0017	253.5	7.4	254.3	4	234	71	254.3	4	FinalAge206_238	-0.315581854	-8.675213675
190517JW1_49	100.6	104.2	777	0.954	9.71	0.13	0.4534	0.007	0.156	0.0022	2409	13	2410	31	2409	24	2409	24	FinalAge207_206	-0.041511	-0.041511
190517JW1_50	329.4	152.1	1497	2.24	18.16	0.22	0.5683	0.0074	0.2314	0.0013	2996.9	11	2900	30	3060.2	8.8	3060.2	8.8	FinalAge207_206	3.233341119	5.234951964
190517JW1_51	166.1	211.4	2101	0.783	19.55	0.38	0.556	0.011	0.2545	0.0016	3065	18	2844	46	3213.9	9.7	3213.9	9.7	FinalAge207_206	7.210440457	11.50938113

Table A2.1. U-Pb isotopic data for Rising Star cave and surface samples (Continued).

Sample #_Spot #	U (in ppm)	Th (in ppm)	Pb (in ppm)	Th/U	Pb207 /U235	± 2σ	Pb206 /U238	± 2σ	Pb207 /Pb206	± 2σ	Pb207 /U235	± Ma	Pb206 /U238	± Ma	Pb207 /Pb206	± Ma	Preferred Age	± Ma	Age System	U-Pb/U-Pb Discordance (%)	U-Pb/Pb-Pb Discordance (%)
190517JW1_52	227.7	239.3	1574	0.948	6.28	0.12	0.3529	0.006	0.1284	0.0017	2014	16	1948	29	2073	23	2073	23	FinalAge207_206	3.277060576	6.029908345
190517JW2_1	312.7	256	803	1.261	1.98	0.027	0.1875	0.0023	0.0765	0.001	1107.8	9.2	1108	12	1102	27	1102	27	FinalAge207_206	-0.0180538	-0.54446461
190517JW2_2	0.001	-8.25153E-05	2.06	no value	no value	NAN	no value	NAN	no value	NAN	no value	NAN	no value	NAN	no value	NAN	#VALUE!	#VALUE!	#VALUE!	#VALUE!	#VALUE!
190517JW2_3	475	336.7	334	1.391	0.4036	0.0082	0.0452	0.00056	0.0651	0.0013	343.7	5.9	285	3.5	757	42	0	0	Discordant	17.07884783	62.35138705
190517JW2_4	1049	1243	3193	0.8385	3.575	0.04	0.2061	0.0022	0.12615	0.0008	1543.2	8.8	1208	12	2043	11	0	0	Discordant	21.72109902	40.87126774
190517JW2_5	701.5	1226	3212	0.577	4.831	0.087	0.2571	0.0045	0.1365	0.001	1787	15	1474	23	2181	13	0	0	Discordant	17.51538892	32.41632279
190517JW2_6	436.5	259.2	363.6	1.652	0.682	0.012	0.0852	0.001	0.05814	0.00094	527.4	7.2	527.8	5.8	522	36	527.8	5.8	FinalAge206_238	-0.075843762	-1.111111111
190517JW2_7	65.2	66.6	102.3	0.96	0.702	0.026	0.0891	0.0015	0.0575	0.0022	538	16	550.1	8.8	464	83	550.1	8.8	FinalAge206_238	-2.249070632	-18.55603448
190517JW2_8	298	562	2048	0.535	2.691	0.033	0.2273	0.0024	0.08607	0.00092	1325.1	9.2	1320	13	1335	21	1335	21	FinalAge207_206	0.384876613	1.123595506
190517JW2_9	166	452	1280	0.365	7.49	0.22	0.31	0.011	0.1773	0.0026	2160	28	1733	55	2624	24	0	0	Discordant	19.76851852	33.95579268
190517JW2_10	0.0026	-8.22161E-05	6.1	no value	no value	NAN	no value	NAN	no value	NAN	no value	NAN	no value	NAN	no value	NAN	#VALUE!	#VALUE!	#VALUE!	#VALUE!	#VALUE!
190517JW2_11	234.7	215.2	1228	1.0684	6.589	0.068	0.375	0.0038	0.1279	0.0011	2057	9.2	2052	18	2066	15	2066	15	FinalAge207_206	0.243072436	0.677637948
190517JW2_12	300.9	560	1267	0.5315	1.437	0.025	0.1326	0.0015	0.0786	0.0011	902.8	10	802.5	8.6	1153	28	802.5	8.6	FinalAge206_238	11.10988037	30.39895924
190517JW2_13	568	338.3	1194	1.644	3.168	0.057	0.1561	0.003	0.147	0.0013	1447	14	935	17	2308	15	0	0	Discordant	35.38355218	59.48873484
190517JW2_14	328	563	1473	0.5739	1.707	0.029	0.1675	0.0023	0.074	0.0011	1011.6	10	998	13	1038	30	998	13	FinalAge206_238	1.344404903	3.853564547
190517JW2_15	140.4	157.1	903	0.884	6.35	0.11	0.3667	0.005	0.1259	0.0018	2024	15	2013	23	2038	25	2038	25	FinalAge207_206	0.543478261	1.226692836
190517JW2_16	89.69	95.1	764	0.929	14.37	0.17	0.5374	0.0056	0.1942	0.0017	2773.2	11	2771	23	2775	14	2775	14	FinalAge207_206	0.079330737	0.144144144
190517JW2_17	165.9	311	403	0.5321	0.603	0.013	0.07608	0.001	0.0577	0.0013	478	8.3	472.6	6.3	494	49	472.6	6.3	FinalAge206_238	1.129707113	4.331983806
190517JW2_18	1449	1782	2721	0.816	2.689	0.056	0.0858	0.0017	0.2278	0.0027	1324	15	531	10	3034	19	0	0	Discordant	59.89425982	82.49835201
190517JW2_19	226.7	208.9	1256	1.073	6.521	0.083	0.3782	0.0039	0.1249	0.0011	2047	11	2067	18	2025	15	2025	15	FinalAge207_206	-0.97703957	-2.074074074
190517JW2_20	254.3	428	298	0.593	0.2951	0.0099	0.04087	0.00059	0.0524	0.0019	262	7.8	258.2	3.7	284	79	258.2	3.7	FinalAge206_238	1.450381679	9.084507042
190517JW2_21	830	2100	4140	0.3909	4.09	0.13	0.1436	0.0045	0.2064	0.0018	1643	24	863	25	2875	14	0	0	Discordant	47.47413268	69.9826087
190517JW2_22	18.02	57	529	0.3128	15.41	0.32	0.5348	0.0088	0.2108	0.0044	2835	20	2759	37	2904	32	2904	32	FinalAge207_206	2.680776014	4.993112948
190517JW2_23	80	67.3	564	1.184	17.99	0.51	0.584	0.015	0.2241	0.0043	2985	27	2964	60	3006	31	3006	31	FinalAge207_206	0.703517588	1.397205589
190517JW2_24	575	656	4830	0.884	11.29	0.14	0.415	0.0045	0.197	0.0014	2546	11	2237	21	2799	11	0	0	Discordant	12.136685	20.0785995
190517JW2_25	185.3	253.5	347.5	0.7301	0.65	0.015	0.0824	0.0011	0.0573	0.0012	507.6	8.9	510.4	6.7	483	46	510.4	6.7	FinalAge206_238	-0.551615445	-5.672877847
190517JW2_26	224	357	1316	0.633	2.922	0.042	0.2415	0.003	0.0877	0.001	1386	11	1394	16	1368	23	1368	23	FinalAge207_206	-0.577200577	-1.900584795
190517JW2_27	326.3	375.5	322.9	0.8711	0.3836	0.0081	0.04779	0.00059	0.0585	0.0012	330.7	6.3	300.9	3.6	530	47	300.9	3.6	FinalAge206_238	9.011188388	43.22641509
190517JW2_28	274.3	238.5	335	1.147	0.717	0.019	0.07371	0.001	0.0705	0.0016	548	11	458.4	6.3	926	49	0	0	Discordant	16.35036496	50.49676026
190517JW2_29	90.2	79.6	452.1	1.133	6.5	0.11	0.374	0.005	0.1261	0.0015	2043	14	2047	23	2038	21	2038	21	FinalAge207_206	-0.195790504	-0.441609421
190517JW2_30	366	248.7	307	1.491	0.583	0.012	0.07402	0.0011	0.0572	0.0011	465.9	7.7	460.2	6.4	491	43	460.2	6.4	FinalAge206_238	1.223438506	6.272912424
190517JW2_31	521	328	294	3.2	1.058	0.044	0.1074	0.0038	0.0714	0.001	726	21	657	22	960	30	657	22	FinalAge206_238	9.504132231	31.5625
190517JW2_32	180.7	118.3	934	1.518	15.4	0.16	0.5531	0.007	0.2018	0.0017	2840.3	10	2836	29	2838	14	2838	14	FinalAge207_206	0.151392459	0.070472163
190517JW2_33	56.28	94.2	805	0.596	18.25	0.47	0.585	0.012	0.2268	0.0042	3001	25	2966	48	3026	30	3026	30	FinalAge207_206	1.166277907	1.982815598
190517JW2_34	0.0012	-0.000088558	1.28	no value	no value	NAN	no value	NAN	no value	NAN	no value	NAN	no value	NAN	no value	NAN	#VALUE!	#VALUE!	#VALUE!	#VALUE!	#VALUE!
190517JW2_35	572	214.7	1192	2.626	2.796	0.059	0.1578	0.0035	0.1285	0.0012	1351	16	944	19	2076	17	0	0	Discordant	30.12583272	54.52793834
190517JW2_36	194.5	186.3	1057	1.038	6.553	0.081	0.3756	0.0043	0.1262	0.0012	2051.7	11	2055	20	2043	16	2043	16	FinalAge207_206	-0.160842228	-0.587371512
190517JW2_37	178.2	175.7	1297	1.016	14.2	0.2	0.5328	0.0079	0.1932	0.002	2764	13	2752	33	2767	17	2767	17	FinalAge207_206	0.434153401	0.542103361
190517JW2_38	505.5	434.7	534	1.162	0.5814	0.0099	0.07464	0.00098	0.05626	0.00087	464.9	6.4	464.8	6.1	452	34	464.8	6.1	FinalAge206_238	0.021510002	-2.831858407
190517JW2_39	427	666	958	0.747	1.35	0.024	0.1344	0.0021	0.07251	0.00093	865.9	10	813	12	996	27	813	12	FinalAge206_238	6.109250491	18.37349398
190517JW2_40	144	132.1	827	1.083	6.628	0.083	0.3632	0.0044	0.1319	0.0013	2061.5	11	1996	21	2119	17	2119	17	FinalAge207_206	3.177298084	5.804624823
190517JW2_41	58.8	100.9	328	0.579	2.538	0.07	0.217	0.0045	0.0851	0.0028	1280	20	1265	24	1298	63	1298	63	FinalAge207_206	1.171875	2.542372881
190517JW2_42	59.4	51.3	578	1.15	16.02	0.23	0.5485	0.0072	0.2119	0.0026	2876	14	2817	30	2915	20	2915	20	FinalAge207_206	2.051460362	3.361921098
190517JW2_43	278.7	338.6	1946	0.823	6.628	0.077	0.3758	0.004	0.1275	0.0011	2061.7	10	2056	19	2060	15	2060	15	FinalAge207_206	0.276470874	0.194174757
190517JW2_44	0.00104	-9.26038E-05	6.1	no value	no value	NAN	no value	NAN	no value	NAN	no value	NAN	no value	NAN	no value	NAN	#VALUE!	#VALUE!	#VALUE!	#VALUE!	#VALUE!
190517JW2_45	186.3	375.7	2683	0.4954	14.72	0.17	0.5138	0.0065	0.2076	0.0021	2796.1	11	2671	28	2884	16	2884	16	FinalAge207_206	4.47408891	7.385575589
190517JW2_46	195.7	331	527	0.578	0.816	0.02	0.0969	0.0014	0.0606	0.0012	604	11	596.3	7.9	615	45	596.3	7.9	FinalAge206_238	1.274834437	3.040650407
190517JW2_47	285.3	222.2	1221	1.29	6.421	0.088	0.369	0.0049	0.1255	0.0017	2034	12	2024	23	2031	24	2031	24	FinalAge207_206	0.491642085	0.344657804
190517JW2_48	177.5	119.6	639	1.5	5.496	0.08	0.3178	0.0043	0.1247	0.0011	1898	12	1778	21	2021	16	2021	16	FinalAge207_206	6.322444679	12.02375062
190517JW2_49	377.7	636	839	0.606	0.68	0.014	0.0785	0.00095	0.0628	0.0013	525.6	8.3	487.1	5.7	688	42	487.1	5.7	FinalAge206_238	7.324961948	29.2005814
190517JW2_50	607	829	2127	0.729	1.921	0.029	0.164	0.002	0.0847	0.0011	1087.2	9.8	978.8	11	1303	23	978.8	11	FinalAge206_238	9.970566593	24.88104375
190517JW2_51	143.2	187.8	1449	0.766	14.34	0.21	0.5368	0.0071	0.1924	0.0022	2770	14	2773	31	2759	19	2759	19	FinalAge207_206	-0.108303249	-0.507430228
190517JW2_52	148.5	196.8	709	0.7571	2.495	0.075	0.1865	0.0031	0.0968	0.0029	1265	22	1102	17	1536	56	0	0	Discordant	12.88537549	28.25520833

Table A2.1. U-Pb isotopic data for Rising Star cave and surface samples (Continued).

Sample #_Spot #	U (in ppm)	Th (in ppm)	Pb (in ppm)	Th/U	Pb207 /U235	± 2σ	Pb206 /U238	± 2σ	Pb207 /Pb206	± 2σ	Pb207 /U235	± Ma	Pb206 /U238	± Ma	Pb207 /Pb206	± Ma	Preferred Age	± Ma	Age System	U-Pb/U-Pb Discordance (%)	U-Pb/Pb-Pb Discordance (%)
190517JW2_53	304.5	334.4	1755	0.916	6.253	0.085	0.3534	0.0045	0.1278	0.0011	2010	12	1950	21	2068	14	2068	14	FinalAge207_206	2.985074627	5.705996132
190517JW2_54	384	712	672	0.5356	0.519	0.016	0.0569	0.0017	0.0657	0.0018	424	10	356	10	787	56	0	0	Discordant	16.03773585	54.76493011
190517JW2_55	304.8	706	2386	0.4354	7.899	0.097	0.3633	0.0042	0.1575	0.0014	2219.4	11	1997	20	2425	15	0	0	Discordant	10.02072632	17.64948454
190517JW2_56	228.5	526.7	2747	0.4309	6.93	0.13	0.3655	0.0061	0.1376	0.0022	2103	17	2007	29	2191	28	2191	28	FinalAge207_206	4.564907275	8.397991785
190517JW2_57	151.1	157.6	822	0.975	8.64	0.12	0.4264	0.0059	0.1465	0.0015	2299	12	2288	27	2301	18	2301	18	FinalAge207_206	0.4784689	0.564971751
190517JW2_58	217.8	193.7	1147	1.123	6.781	0.1	0.378	0.0064	0.1294	0.0016	2084	13	2066	30	2086	22	2086	22	FinalAge207_206	0.863723608	0.958772771
190517JW2_59	601.7	630	502.5	0.9558	0.3395	0.0069	0.0471	0.00063	0.05217	0.00099	296.4	5.2	296.7	3.9	277	43	296.7	3.9	FinalAge206_238	-0.101214575	-7.111913357
190517JW2_60	670.1	219	517	3.55	1.907	0.033	0.1781	0.0031	0.0774	0.001	1082	12	1056	17	1125	26	1125	26	FinalAge207_206	2.402957486	6.133333333
190517JW2_61	62.4	151.7	302	0.458	1.012	0.036	0.1088	0.002	0.0667	0.0022	705	18	665	12	791	71	665	12	FinalAge206_238	5.673758865	15.92920354
190517JW2_62	257.5	258.3	1451	0.992	6.102	0.079	0.3346	0.0044	0.1317	0.0013	1989	11	1860	21	2118	17	2118	17	FinalAge207_206	6.485671192	12.18130312
190517JW2_63	207.1	16.44	38.4	12.67	1.22	0.031	0.1332	0.0022	0.0662	0.0014	809	14	806	12	802	46	806	12	FinalAge206_238	0.370828183	-0.498753117
190517JW2_64	139.8	182.6	1280	0.764	14.31	0.25	0.5368	0.0091	0.1918	0.0022	2769	16	2768	38	2754	19	2754	19	FinalAge207_206	0.036114121	-0.508351489
190517JW2_65	106.6	171.6	1135	0.6178	9.59	0.15	0.448	0.0065	0.1551	0.0016	2396	15	2385	29	2401	19	2401	19	FinalAge207_206	0.459098497	0.666389005
190517JW2_66	177.8	173.1	607	1.015	2.184	0.038	0.185	0.0027	0.0854	0.0012	1175	12	1094	15	1319	29	0	0	Discordant	6.893617021	17.05837756
190517JW2_67	244.9	197.8	1125	1.24	6.53	0.11	0.3705	0.0072	0.1278	0.0017	2052	16	2030	34	2063	23	2063	23	FinalAge207_206	1.072124756	1.599612215
190517JW2_68	711	2780	1134	0.273	1.1	0.017	0.0967	0.002	0.0828	0.0018	752.3	8.4	595	12	1247	41	0	0	Discordant	20.90921175	52.28548516
190517JW2_69	355	831	1296	0.419	9.52	0.21	0.3045	0.0074	0.2266	0.0019	2383	21	1711	36	3026	13	0	0	Discordant	28.19974822	43.45670853
190517JW2_70	93.8	176.4	112.3	0.5284	0.269	0.014	0.03768	0.00087	0.052	0.0027	240	11	238.4	5.4	240	110	238.4	5.4	FinalAge206_238	0.666666667	0.666666667
190517JW3_1	137.8	239.4	340.1	0.5736	0.7	0.019	0.0879	0.0013	0.0578	0.0016	537	12	542.9	7.5	493	61	542.9	7.5	FinalAge206_238	-1.098696462	-10.12170385
190517JW3_2	285.4	279.3	800	1.025	1.754	0.035	0.1562	0.0018	0.0809	0.0013	1028	13	935.4	9.9	1210	30	935.4	9.9	FinalAge206_238	9.007782101	22.69421488
190517JW3_3	293	273	1204	1.06	5.108	0.065	0.2935	0.0039	0.1267	0.0011	1837.2	11	1658	19	2049	16	0	0	Discordant	9.753973438	19.08247926
190517JW3_4	90.8	114.3	639	0.801	6.363	0.1	0.3602	0.0058	0.128	0.002	2025	14	1982	27	2065	28	2065	28	FinalAge207_206	2.12345679	4.01937046
190517JW3_5	171.6	179.1	872	0.972	5.951	0.082	0.3393	0.004	0.1273	0.0013	1967	12	1883	19	2058	18	2058	18	FinalAge207_206	4.270462633	8.503401361
190517JW3_6	154.8	59.8	360.1	2.606	7.057	0.11	0.3856	0.0056	0.1327	0.0016	2117	13	2102	26	2131	22	2131	22	FinalAge207_206	0.708549835	1.360863444
190517JW3_7	440.6	101.9	395	4.86	1.769	0.023	0.1621	0.0022	0.07935	0.00097	1033.2	8.4	968	12	1174	24	968	12	FinalAge206_238	6.310491676	17.54684838
190517JW3_8	114.6	152.9	1202	0.748	22.35	0.29	0.6312	0.0083	0.2562	0.0024	3198	12	3153	33	3223	15	3223	15	FinalAge207_206	1.407129456	2.171889544
190517JW3_9	48.9	89.9	611	0.5454	11.97	0.19	0.4567	0.0071	0.1898	0.0025	2601	15	2423	31	2738	22	2738	22	FinalAge207_206	6.843521722	11.50474799
190517JW3_10	208.3	272.1	376.5	0.759	0.699	0.014	0.0869	0.0012	0.0586	0.0013	537.3	8.6	538.1	7.6	531	47	538.1	7.6	FinalAge206_238	-0.148892611	-1.337099812
190517JW3_11	482.7	227.7	608	2.109	1.542	0.023	0.1545	0.0021	0.0723	0.00086	945.9	9.1	926	12	990	25	926	12	FinalAge206_238	2.103816471	6.464646465
190517JW3_12	413	976	4620	0.4174	4.898	0.059	0.308	0.0041	0.1154	0.0012	1800.7	10	1730	20	1882	19	1882	19	FinalAge207_206	3.926250902	8.076514346
190517JW3_13	130	196.1	147.2	0.657	0.31	0.013	0.04316	0.00085	0.0524	0.002	273.1	9.6	272.3	5.2	267	83	272.3	5.2	FinalAge206_238	0.292932992	-1.985018727
190517JW3_14	185.6	387	310	0.4778	0.455	0.016	0.04157	0.00071	0.0791	0.0026	381	11	262.5	4.4	1159	68	0	0	Discordant	31.1023622	77.3511648
190517JW3_15	765	1073	1115	0.72	0.757	0.015	0.0725	0.0012	0.0758	0.0019	571.2	8.8	451.2	7.4	1067	49	0	0	Discordant	21.00840336	57.71321462
190517JW3_16	127.5	209.7	293.3	0.6064	0.688	0.019	0.0843	0.0013	0.0596	0.0016	531	12	521.8	7.8	552	61	521.8	7.8	FinalAge206_238	1.732580038	5.471014493
190517JW3_17	286.3	556.2	2874	0.5083	5.161	0.069	0.3185	0.0044	0.1178	0.0012	1846	11	1781	21	1923	17	1923	17	FinalAge207_206	3.521126761	7.384295372
190517JW3_18	-0.000148843	0.0027	69.6	no value	no value	NAN	no value	NAN	no value	NAN	no value	NAN	no value	NAN	no value	NAN	#VALUE!	#VALUE!	#VALUE!	#VALUE!	#VALUE!
190517JW3_19	332	273	1410	1.206	4.422	0.076	0.2513	0.0042	0.1281	0.0014	1716	15	1444	22	2067	19	0	0	Discordant	15.85081585	30.14029995
190517JW3_20	122.1	222	370	0.572	0.841	0.023	0.1001	0.0015	0.0611	0.0016	620	13	614.8	8.9	628	53	614.8	8.9	FinalAge206_238	0.838709677	2.101910828
190517JW3_21	530	329	493	1.623	0.715	0.013	0.08203	0.0009	0.06301	0.00099	548.3	7.8	508.2	5.4	704	35	508.2	5.4	FinalAge206_238	7.313514499	27.8125
190517JW3_22	247.5	103.2	160.5	2.371	0.799	0.019	0.0955	0.0017	0.0606	0.0015	595	11	588	10	606	52	588	10	FinalAge206_238	1.176470588	2.97029703
190517JW3_23	390.4	275.5	470	1.402	0.837	0.023	0.0988	0.0017	0.0615	0.0015	616	12	607.2	9.8	646	52	607.2	9.8	FinalAge206_238	1.428571429	6.00619195
190517JW3_24	254.3	222.1	1212	1.131	10.68	0.45	0.341	0.014	0.2266	0.0019	2470	40	1880	65	3025	14	0	0	Discordant	23.88663968	37.85123967
190517JW3_25	157.2	169.5	989	0.933	6.39	0.15	0.3666	0.0079	0.1271	0.0023	2029	20	2012	37	2054	31	2054	31	FinalAge207_206	0.837851158	2.044790652
190517JW3_26	853	1391	1683	0.6048	2.13	0.038	0.102	0.0019	0.1513	0.0012	1157	12	626	11	2360	14	0	0	Discordant	45.89455488	73.47457627
190517JW3_27	433.2	263.7	1480	1.64	5.798	0.098	0.3489	0.006	0.1208	0.0015	1945	15	1929	29	1965	22	1965	22	FinalAge207_206	0.822622108	1.832061069
190517JW3_28	545	124	71	8.3	0.832	0.017	0.0924	0.0013	0.0652	0.0011	613.7	9.2	569.5	7.7	770	35	569.5	7.7	FinalAge206_238	7.202216066	26.03896104
190517JW3_29	1728	829	1460	2.074	1.035	0.018	0.05828	0.00092	0.1289	0.001	721.4	9	365.1	5.6	2080	14	0	0	Discordant	49.39007485	82.44711538
190517JW3_30	284.2	351.5	1785	0.8063	6.075	0.076	0.3451	0.0038	0.1272	0.0011	1985.5	11	1910	18	2057	16	2057	16	FinalAge207_206	3.802568623	7.146329606
190517JW3_31	524	679	622	0.769	0.431	0.011	0.04487	0.00061	0.0694	0.0017	363.5	8	282.9	3.7	902	49	0	0	Discordant	22.17331499	68.63636364
190517JW3_32	83.1	131.6	186	0.6312	0.665	0.028	0.0832	0.0019	0.0584	0.0028	516	17	515	11	500	100	515	11	FinalAge206_238	0.19379845	-3
190517JW3_33	79.7	183.4	245.9	0.4268	0.686	0.022	0.0825	0.0012	0.0606	0.0021	528	13	510.8	7.1	580	76	510.8	7.1	FinalAge206_238	3.257575758	11.93103448
190517JW3_34	356.2	331.6	970	1.07	1.82	0.025	0.168	0.0018	0.07844	0.00099	1051.6	8.8	1001	10	1151	25	1151	25	FinalAge207_206	4.811715481	13.03214596
190517JW3_35	71.35	124	203.3	0.5764	0.917	0.037	0.0918	0.0015	0.0721	0.0028	657	20	567.2	9.4	940	84	567.2	9.4	FinalAge206_238	13.66818874	39.65957447

Table A2.1. U-Pb isotopic data for Rising Star cave and surface samples (Continued).

Sample #_Spot #	U (in ppm)	Th (in ppm)	Pb (in ppm)	Th/U	Pb207 /U235	± 2σ	Pb206 /U238	± 2σ	Pb207 /Pb206	± 2σ	Pb207 /U235	± Ma	Pb206 /U238	± Ma	Pb207 /Pb206	± Ma	Preferred Age	± Ma	Age System	U-Pb/U-Pb Discordance (%)	U-Pb/Pb-Pb Discordance (%)
190517JW3_36	175.4	177.1	696	1.005	17.2	0.31	0.4998	0.0094	0.2495	0.0022	2942	17	2609	40	3179	14	0	0	Discordant	11.31883073	17.93016672
190517JW3_37	54.2	228.7	1635	0.2346	13.36	0.27	0.5185	0.009	0.1867	0.0029	2702	19	2691	38	2708	25	2708	25	FinalAge207_206	0.407105848	0.627769572
190517JW3_38	260.4	309	670	0.864	14.05	0.2	0.5004	0.0075	0.2031	0.0018	2751	14	2614	32	2849	15	2849	15	FinalAge207_206	4.98000727	8.248508249
190517JW3_39	276.4	261.3	877	1.049	2.156	0.036	0.1846	0.0023	0.0844	0.0012	1165	12	1092	13	1298	29	0	0	Discordant	6.266094421	15.87057011
190517JW3_40	189.5	297	814	0.645	6.943	0.092	0.3507	0.0043	0.143	0.0013	2103	12	1937	21	2260	16	2260	16	FinalAge207_206	7.893485497	14.2920354
190517JW3_41	188	34.2	74.6	5.66	0.875	0.02	0.0956	0.0014	0.0663	0.0014	636	11	588.4	8	800	44	588.4	8	FinalAge206_238	7.48427673	26.45
190517JW3_42	799	1191	796	0.6672	0.2979	0.0079	0.041	0.0008	0.0525	0.0013	264.4	6.1	259	4.9	301	58	259	4.9	FinalAge206_238	2.042360061	13.95348837
190517JW3_43	253.2	329	1336	0.801	13.39	0.21	0.4568	0.0063	0.2124	0.0018	2705	14	2424	28	2921	13	0	0	Discordant	10.38817006	17.01472099
190517JW3_44	273.2	360.3	1969	0.752	5.82	0.11	0.3426	0.0054	0.1231	0.0018	1951	16	1899	26	1999	26	1999	26	FinalAge207_206	2.665299846	5.002501251
190517JW3_45	193.7	194.1	292.8	0.989	0.757	0.015	0.0923	0.0013	0.0597	0.0013	571.1	8.7	569.1	7.9	582	46	569.1	7.9	FinalAge206_238	0.350201366	2.216494845
190517JW3_46	312.7	295	779	1.057	1.741	0.026	0.1684	0.002	0.07501	0.00094	1022.7	9.5	1003	11	1061	25	1061	25	FinalAge207_206	1.92627359	5.466540999
190517JW3_47	64.6	138.2	172.7	0.462	0.621	0.026	0.0799	0.0014	0.0565	0.0023	487	16	495.3	8.4	410	90	495.3	8.4	FinalAge206_238	-1.704312115	-20.80487805
190517JW3_48	202.6	107.5	955	1.878	21.88	0.3	0.6349	0.0086	0.2497	0.0023	3177	13	3168	34	3181	14	3181	14	FinalAge207_206	0.283286119	0.408676517
190517JW3_49	259.2	165.1	203	1.567	0.462	0.028	0.04168	0.0009	0.0805	0.0046	384	19	263.2	5.6	1170	110	0	0	Discordant	31.45833333	77.5042735
190517JW3_50	35.14	55.6	151.8	0.6297	1.76	0.055	0.171	0.0032	0.0752	0.0025	1027	21	1017	17	1026	69	1026	69	FinalAge207_206	0.973709834	0.877192982
190517JW3_51	1094	126.8	173.5	8.565	0.6488	0.0085	0.08167	0.00094	0.05763	0.00067	507.4	5.2	506	5.6	512	25	506	5.6	FinalAge206_238	0.275916437	1.171875
190517JW3_52	0.0026	-6.03038E-05	0.47	no value	no value	NAN	no value	NAN	no value	NAN	no value	NAN	no value	NAN	no value	NAN	#VALUE!	#VALUE!	#VALUE!	#VALUE!	#VALUE!
190517JW3_53	246.4	273.5	1432	0.905	7.74	0.17	0.2637	0.0062	0.2127	0.0019	2196	20	1507	31	2924	14	0	0	Discordant	31.37522769	48.46101231
190517JW3_54	497.7	782.9	577	0.634	0.3844	0.0081	0.04309	0.00069	0.0647	0.0015	329.8	5.9	271.9	4.3	750	47	0	0	Discordant	17.5560946	63.74666667
190517JW3_55	76.8	95.6	805	0.796	19.71	0.25	0.6073	0.0077	0.2356	0.0025	3076	12	3058	31	3091	16	3091	16	FinalAge207_206	0.585175553	1.067615658
190517JW3_56	407	527	1378	0.7686	1.628	0.028	0.1632	0.0027	0.07224	0.00087	980	11	974	15	988	24	974	15	FinalAge206_238	0.612244898	1.417004049
190517JW3_57	341.6	218.3	1104	1.553	5.173	0.094	0.3303	0.0048	0.114	0.0017	1847	16	1840	23	1861	27	1861	27	FinalAge207_206	0.378992962	1.128425578
190517JW3_58	602	680	2590	0.964	8.63	0.15	0.3451	0.005	0.1815	0.0015	2296	16	1910	24	2664	14	0	0	Discordant	16.81184669	28.3033033
190517JW3_59	235	377.7	1188	0.619	6.048	0.072	0.3453	0.004	0.1267	0.0013	1981.4	10	1911	19	2051	18	2051	18	FinalAge207_206	3.553043303	6.825938567
190517JW3_60	103.9	104.9	909	0.984	18.1	0.21	0.5876	0.008	0.2235	0.0022	2994.1	11	2978	33	3004	16	3004	16	FinalAge207_206	0.537724191	0.86551265
190517JW3_61	62.3	36.6	187	1.69	2.466	0.077	0.1813	0.0027	0.0987	0.0029	1263	24	1074	15	1596	58	0	0	Discordant	14.96437055	32.70676692
190517JW3_62	698	1111	6420	0.6189	6.699	0.1	0.3045	0.0036	0.1595	0.0029	2070	13	1713	18	2439	31	0	0	Discordant	17.24637681	29.76629766
190517JW3_63	175.3	37.61	91	4.574	0.828	0.018	0.09166	0.0011	0.0657	0.0014	611.2	9.9	565.3	6.5	773	46	565.3	6.5	FinalAge206_238	7.509816754	26.86934023
190517JW3_64	124.5	223.6	2019	0.5522	21.6	0.24	0.6302	0.0068	0.2482	0.0021	3164.8	11	3150	27	3171	13	3171	13	FinalAge207_206	0.467644085	0.662251656
190517JW3_65	121.7	240.9	699	0.5015	1.719	0.049	0.1703	0.0033	0.073	0.0014	1013	18	1013	18	1012	43	1012	43	FinalAge207_206	0	-0.098814229
190517JW3_66	175.7	182.2	849	0.962	5.823	0.082	0.3277	0.0042	0.129	0.0011	1948	12	1827	20	2082	15	2082	15	FinalAge207_206	6.211498973	12.24783862
190517JW3_67	111.2	188.1	1162	0.5848	6.971	0.1	0.3842	0.0045	0.1318	0.0017	2110	12	2095	21	2117	23	2117	23	FinalAge207_206	0.710900474	1.039206424
190517JW3_68	145.7	273.8	3180	0.521	9.8	0.62	0.195	0.0067	0.354	0.011	2371	53	1150	37	3702	45	0	0	Discordant	51.49725854	68.93571043
190517JW3_69	238.4	155.1	379.7	1.521	1.451	0.023	0.1481	0.0016	0.07122	0.00096	909.2	9.4	890.4	8.8	955	28	890.4	8.8	FinalAge206_238	2.06775187	6.764397906
190517JW3_70	279.9	604	3141	0.466	15.08	0.22	0.4254	0.0066	0.257	0.0019	2818	14	2283	30	3227	12	0	0	Discordant	18.98509581	29.25317632
190517JW3_71	203.1	301.7	859	0.6698	1.839	0.029	0.1685	0.0019	0.079	0.0011	1058.2	10	1003.9	11	1168	29	1168	29	FinalAge207_206	5.131355131	14.04965753
190517JW3_72	15.12	64.2	99.9	0.2326	0.802	0.06	0.094	0.0028	0.0626	0.0046	581	34	578	16	550	160	578	16	FinalAge206_238	0.516351119	-5.090909091
190517JW3_73	464	276	844	1.723	2.058	0.028	0.1851	0.002	0.08043	0.00081	1133.9	9.1	1094.7	11	1203	20	1203	20	FinalAge207_206	3.457094982	9.002493766
190517JW3_74	92.61	225.8	1939	0.4097	16.44	0.25	0.5666	0.007	0.2104	0.0027	2902	15	2893	29	2913	23	2913	23	FinalAge207_206	0.310130944	0.686577412
190517JW3_75	401	462	2280	0.883	5.4	0.23	0.261	0.013	0.1525	0.0019	1864	37	1481	68	2368	22	0	0	Discordant	20.5472103	37.45777027
190517JW3_76	131.4	158.4	1436	0.827	22.48	0.27	0.6461	0.0076	0.252	0.002	3203	12	3211	30	3195	12	3195	12	FinalAge207_206	-0.249765845	-0.500782473
190517JW3_77	402.7	198.7	472.9	2.019	1.46	0.019	0.1482	0.0019	0.07164	0.00079	913.4	7.9	890.4	11	969	22	890.4	11	FinalAge206_238	2.518064375	8.111455108
190517JW3_78	339.1	193.7	378	1.85	0.681	0.023	0.06156	0.00097	0.0792	0.0022	524	14	385	5.9	1144	54	0	0	Discordant	26.52671756	66.34615385
190517JW3_79	236.7	340	2674	0.698	17.81	0.21	0.5483	0.0073	0.2368	0.0019	2980.1	11	2817	30	3096	13	3096	13	FinalAge207_206	5.472970706	9.011627907
190517JW3_80	21.61	40.3	351.8	0.5337	19.34	0.37	0.6032	0.0091	0.2329	0.004	3055	18	3040	36	3068	26	3068	26	FinalAge207_206	0.490998363	0.912646675
190517JW3_81	76.3	76.3	125	0.983	0.875	0.03	0.1024	0.0015	0.062	0.002	635	16	628.2	8.9	649	68	628.2	8.9	FinalAge206_238	1.070866142	3.204930663
190517JW3_82	354	144.4	173.2	2.452	0.558	0.012	0.07043	0.00089	0.0576	0.0012	449.4	7.7	439.4	5.5	493	45	439.4	5.5	FinalAge206_238	2.225189141	10.87221095
190517JW3_83	109.5	344.2	222.2	0.3156	0.2706	0.01	0.03761	0.00059	0.0524	0.0021	242.1	8	238	3.7	256	83	238	3.7	FinalAge206_238	1.693515076	7.03125
190517JW3_84	88.1	151.9	1049	0.5713	9.54	0.13	0.4481	0.0047	0.1549	0.0016	2389	12	2386	21	2396	18	2396	18	FinalAge207_206	0.125575555	0.41736227
190517JW3_85	317.9	562	1437	0.563	6.89	0.13	0.2394	0.0044	0.2094	0.0026	2096	16	1383	23	2898	20	0	0	Discordant	34.01717557	52.27743271
190517JW3_86	185.7	158.2	1470	1.167	22.52	0.23	0.6432	0.007	0.2543	0.0018	3205.5	9.6	3200	27	3210	11	3210	11	FinalAge207_206	0.171580097	0.31152648
190517JW3_87	225.5	282	1485	0.792	6.442	0.099	0.3709	0.0052	0.1264	0.0016	2037	14	2033	25	2045	23	2045	23	FinalAge207_206	0.196367207	0.586797066
190517JW3_88	193.1	263.4	424.2	0.7277	0.792	0.016	0.0905	0.0011	0.0636	0.0013	591.2	9.1	558.1	6.6	711	45	558.1	6.6	FinalAge206_238	5.598782138	21.50492264
190517JW3_89	209.9	187.6	1061	1.106	6.394	0.074	0.3694	0.0038	0.1259	0.0011	2030.2	10	2026	18	2038	15	2038	15	FinalAge207_206	0.20687617	0.588812561

Table A2.1. U-Pb isotopic data for Rising Star cave and surface samples (Continued).

Sample #_Spot #	U (in ppm)	Th (in ppm)	Pb (in ppm)	Th/U	Pb207 /U235	± 2σ	Pb206 /U238	± 2σ	Pb207 /Pb206	± 2σ	Pb207 /U235	± Ma	Pb206 /U238	± Ma	Pb207 /Pb206	± Ma	Preferred Age	± Ma	Age System	U-Pb/U-Pb Discordance (%)	U-Pb/Pb-Pb Discordance (%)
190517JW3_90	161.2	164.1	863	0.984	6.365	0.078	0.3635	0.004	0.127	0.0012	2027.7	10	1998	19	2053	16	2053	16	FinalAge207_206	1.464713715	2.679006332
190517JW3_91	124.8	221.4	1588	0.5678	13.56	0.25	0.4436	0.009	0.2222	0.0022	2718	17	2369	39	2994	16	0	0	Discordant	12.84032377	20.8750835
190517JW3_92	310	361	1971	0.873	6.424	0.072	0.3697	0.0038	0.12669	0.00098	2034.4	9.9	2028	18	2052	13	2052	13	FinalAge207_206	0.314589068	1.169590643
190517JW3_93	345.6	363.5	604	0.951	0.819	0.014	0.08336	0.00092	0.0711	0.0011	606.5	7.6	516.1	5.5	953	32	516.1	5.5	FinalAge206_238	14.90519373	45.84470094
190517JW3_94	371	609	539	0.6025	0.4162	0.0095	0.04585	0.00057	0.0662	0.0015	352.7	6.8	288.9	3.5	799	46	0	0	Discordant	18.0890275	63.84230288
190517JW3_95	127.8	238.4	1375	0.5349	6.473	0.082	0.3683	0.0038	0.1281	0.0015	2040.6	11	2021	18	2066	20	2066	20	FinalAge207_206	0.960501813	2.178121975
190517JW3_96	180.1	385.2	2229	0.4679	6.696	0.08	0.3725	0.0038	0.1307	0.0011	2070.7	11	2040	18	2106	16	2106	16	FinalAge207_206	1.482590428	3.133903134
190517JW3_97	510	870	470	1.06	6.7	1.4	0.28	0.051	0.1637	0.0082	1780	170	1490	240	2478	84	0	0	Discordant	16.29213483	39.8708636
190517JW3_98	160.3	230.5	655	0.6967	1.846	0.028	0.1788	0.002	0.0751	0.0011	1060.6	10	1060.3	11	1062	29	1062	29	FinalAge207_206	0.028285876	0.16007533
190517JW3_99	94.7	103.9	574	0.917	6	0.12	0.3278	0.0048	0.1329	0.0019	1973	17	1827	23	2132	25	2132	25	FinalAge207_206	7.399898632	14.30581614
190517JW3_100	614	1178	4470	0.5277	4.309	0.062	0.236	0.004	0.133	0.0011	1693	12	1365	21	2137	14	0	0	Discordant	19.3738925	36.12540945
190517JW3_101	343.5	276.4	798	1.25	1.86	0.025	0.1772	0.002	0.07633	0.00074	1066	8.8	1051.5	11	1099	19	1099	19	FinalAge207_206	1.360225141	4.32211101
190517JW3_102	110.9	188	263.5	0.595	0.711	0.03	0.0825	0.0017	0.0624	0.0026	543	18	511.2	9.9	655	91	511.2	9.9	FinalAge206_238	5.856353591	21.95419847
190517JW3_103	189.7	188.2	1239	1.01	6.87	0.078	0.3837	0.0045	0.13	0.0013	2094.1	10	2093	21	2095	18	2095	18	FinalAge207_206	0.052528533	0.095465394
190517JW3_104	166.4	158.9	928	1.048	6.461	0.098	0.3704	0.0068	0.1273	0.0016	2042	14	2030	31	2058	22	2058	22	FinalAge207_206	0.587659158	1.360544218
190517JW3_105	214.1	377	2494	0.5684	9.26	0.15	0.4399	0.0065	0.1532	0.0017	2363	14	2350	29	2380	19	2380	19	FinalAge207_206	0.550148117	1.260504202
190517JW3_106	774	893	1577	0.884	4.285	0.071	0.2688	0.0043	0.116	0.0014	1689	14	1534	22	1892	21	0	0	Discordant	9.177027827	18.9217759
190517JW3_107	144.8	260.6	904	0.557	2.559	0.042	0.2184	0.0024	0.085	0.0013	1287	12	1273	13	1307	29	1307	29	FinalAge207_206	1.087801088	2.6013772
190517JW3_108	191.3	206.3	643	0.9269	2.114	0.033	0.1975	0.0025	0.078	0.0011	1152	11	1162	13	1141	30	1141	30	FinalAge207_206	-0.868055556	-1.840490798
190517JW3_109	50.2	180.7	519	0.2779	1.787	0.061	0.1727	0.0029	0.0755	0.0027	1036	22	1029	15	1051	71	1051	71	FinalAge207_206	0.675675676	2.093244529
190517JW3_110	153.1	125.7	172.7	1.257	0.702	0.016	0.08718	0.001	0.0584	0.0013	538.7	9.7	538.8	6.1	529	49	538.8	6.1	FinalAge206_238	-0.018563208	-1.852551985
190517JW3_111	390.4	415	650	0.947	0.961	0.015	0.10182	0.0011	0.06851	0.00089	684	7.9	625	6.3	880	26	625	6.3	FinalAge206_238	8.625730994	28.97727273
190517JW3_112	156.8	110.4	890	1.425	19.68	0.3	0.6089	0.0097	0.2358	0.0025	3075	15	3065	39	3090	17	3090	17	FinalAge207_206	0.325203252	0.809061489
190517JW3_113	172	150.7	198.7	1.142	0.706	0.022	0.0862	0.0013	0.0593	0.0019	540	13	533.1	7.9	559	74	533.1	7.9	FinalAge206_238	1.277777778	4.633273703
190517JW3_114	60.6	114.2	221	0.5385	1.108	0.037	0.1242	0.0019	0.0648	0.0023	752	18	755	11	724	76	755	11	FinalAge206_238	-0.39893617	-4.281767956
190517JW3_115	410	494	1627	0.903	7.64	0.29	0.2358	0.0095	0.2362	0.0019	2172	34	1359	49	3092	13	0	0	Discordant	37.43093923	56.04786546
190517JW3_116	276.6	442	296.1	0.6296	0.3061	0.0081	0.04235	0.00059	0.0527	0.0013	270.6	6.3	267.4	3.6	289	56	267.4	3.6	FinalAge206_238	1.18255728	7.474048443
190517JW3_117	414	1121	5380	0.3689	7.88	0.12	0.2999	0.0051	0.1907	0.0016	2215	14	1690	25	2748	14	0	0	Discordant	23.7020316	38.5007278
190517JW3_118	858.5	881	3230	0.985	2.864	0.073	0.1064	0.0025	0.1955	0.0017	1367	19	651	14	2786	14	0	0	Discordant	52.37746891	76.63316583
190517JW3_119	173.9	218.4	292.2	0.7974	0.655	0.018	0.082	0.0012	0.0581	0.0016	510	11	507.8	7	509	59	507.8	7	FinalAge206_238	0.431372549	0.235756385
190517JW3_120	145.9	125	692	1.168	6.542	0.084	0.3732	0.0041	0.1273	0.0014	2050	11	2044	19	2058	20	2058	20	FinalAge207_206	0.292682927	0.680272109
190517JW3_121	322.1	257.8	1386	1.2506	6.371	0.065	0.3671	0.0036	0.1263	0.00099	2027.4	9	2015	17	2044	14	2044	14	FinalAge207_206	0.611620795	1.418786693
190517JW3_122	203.6	186	1006	1.131	5.834	0.077	0.3359	0.0046	0.1265	0.0011	1951	12	1866	22	2048	16	2048	16	FinalAge207_206	4.356740133	8.88671875
190517JW3_123	109.8	85.9	194.3	1.277	1.11	0.028	0.1021	0.0012	0.0789	0.0019	756	13	626.7	7.3	1150	49	0	0	Discordant	17.1031746	45.50434783
190517JW4_1	121.8	105.2	550	1.165	6.526	0.4	0.3723	0.025	0.127	0.0021	2048	53	2039	120	2053	29	2053	29	FinalAge207_206	0.439453125	0.681928885
190517JW4_2	155.9	110.2	142.8	1.427	0.689	0.046	0.0854	0.0058	0.0593	0.002	532	28	528	34	539	74	528	34	FinalAge206_238	0.751879699	2.040816327
190517JW4_3	76.7	66.7	355	1.165	6.53	0.4	0.3748	0.025	0.1263	0.0021	2046	54	2050	120	2039	30	2039	30	FinalAge207_206	-0.195503421	-0.539480137
190517JW4_4	192	268	1880	0.777	14.25	0.86	0.5332	0.035	0.1939	0.0024	2764.1	57	2753	150	2771	20	2771	20	FinalAge207_206	0.401577367	0.649584987
190517JW4_5	172.7	191.9	1014	0.915	16.51	1	0.5593	0.037	0.214	0.003	2905	58	2862	150	2932	22	2932	22	FinalAge207_206	1.48020654	2.38744884
190517JW4_6	248.4	215.6	1234	1.176	8.215	0.49	0.4209	0.028	0.1418	0.0018	2253.6	55	2264	130	2245	21	2245	21	FinalAge207_206	-0.461483848	-0.846325167
190517JW4_7	62	125.1	958	0.5107	20.84	1.3	0.6533	0.043	0.2313	0.0033	3127	58	3238	170	3056	23	3056	23	FinalAge207_206	-3.549728174	-5.955497382
190517JW4_8	143.5	114.8	263	1.265	1.545	0.097	0.1528	0.01	0.0731	0.0016	945	39	916	57	990	46	916	57	FinalAge206_238	3.068783069	7.474747475
190517JW4_9	161.2	221.3	365	0.721	0.939	0.061	0.1087	0.0072	0.0626	0.0016	672	30	666	43	671	55	666	43	FinalAge206_238	0.892857143	0.745156483
190517JW4_10	57.95	9.27	13.1	6.65	0.744	0.055	0.0922	0.0063	0.0592	0.0029	559	32	568	37	480	100	568	37	FinalAge206_238	-1.610017889	-18.33333333
190517JW4_11	53	43.38	461	1.222	16.85	1	0.5829	0.039	0.2098	0.0034	2922	59	2958	160	2899	26	2899	26	FinalAge207_206	-1.232032854	-2.035184546
190517JW4_12	72.3	82.4	284	0.872	1.772	0.12	0.1701	0.011	0.0756	0.0024	1029	43	1012	63	1046	64	1046	64	FinalAge207_206	1.652089407	3.250478011
190517JW4_13	58.7	60.1	336	0.994	10.96	1	0.343	0.035	0.235	0.0044	2424	84	1850	160	3078	30	0	0	Discordant	23.67986799	39.89603639
190517JW4_14	187.5	142.8	998	1.297	6.538	0.39	0.3727	0.025	0.127	0.0017	2051.6	50	2042	120	2054	23	2054	23	FinalAge207_206	0.467927471	0.584225901
190517JW4_15	183.2	184.1	1260	0.988	6.517	0.39	0.3754	0.025	0.1261	0.0017	2048.4	54	2054	120	2038	24	2038	24	FinalAge207_206	-0.273384105	-0.785083415
190517JW4_16	352	130.3	352	2.74	1.054	0.067	0.1194	0.008	0.0639	0.0013	728	33	727	46	732	42	727	46	FinalAge206_238	0.137362637	0.683060109
190517JW4_17	51.09	92.9	812	0.5466	13.13	0.8	0.5172	0.034	0.1844	0.0032	2685	58	2685	150	2683	28	2683	28	FinalAge207_206	0	-0.074543422
190517JW4_18	238	254	1623	0.953	6.362	0.39	0.3711	0.025	0.1252	0.002	2025	54	2034	120	2026	28	2026	28	FinalAge207_206	-0.444444444	-0.394866732
190517JW4_19	190.1	287.4	2263	0.643	8.69	0.55	0.4074	0.028	0.1546	0.0021	2299	57	2198	130	2394	23	2394	23	FinalAge207_206	4.393214441	8.187134503

Table A2.1. U-Pb isotopic data for Rising Star cave and surface samples (Continued).

Sample #_Spot #	U (in ppm)	Th (in ppm)	Pb (in ppm)	Th/U	Pb207 /U235	± 2σ	Pb206 /U238	± 2σ	Pb207 /Pb206	± 2σ	Pb207 /U235	± Ma	Pb206 /U238	± Ma	Pb207 /Pb206	± Ma	Preferred Age	± Ma	Age System	U-Pb/U-Pb Discordance (%)	U-Pb/Pb-Pb Discordance (%)
190517JW4_20	226.9	43.89	116.9	5.115	1.434	0.089	0.1512	0.01	0.0689	0.0013	902	36	907.4	56	890	37	907.4	56	FinalAge206_238	-0.598669623	-1.95505618
190517JW4_21	231.9	262	1639	0.8678	6.887	0.42	0.3928	0.026	0.127	0.0016	2095	54	2135	120	2053	22	2053	22	FinalAge207_206	-1.909307876	-3.994154895
190517JW4_22	278	344	2640	0.841	11.78	0.71	0.4988	0.033	0.1709	0.002	2586.6	57	2612	140	2563	19	2563	19	FinalAge207_206	-0.981984072	-1.911822083
190517JW4_23	485	49.3	185	9.55	1.871	0.12	0.1731	0.011	0.0783	0.0016	1072	44	1029	63	1145	41	1145	41	FinalAge207_206	4.01119403	10.13100437
190517JW4_24	183	428.8	2540	0.4137	5.452	0.33	0.3438	0.023	0.1152	0.0017	1891	52	1904	110	1876	26	1876	26	FinalAge207_206	-0.687466949	-1.492537313
190517JW4_25	351.2	249.5	1837	1.356	8.274	0.5	0.4195	0.028	0.1424	0.0017	2260.3	55	2258	130	2253	20	2253	20	FinalAge207_206	0.101756404	-0.22192632
190517JW4_26	86.2	110.9	1126	0.7503	19.29	1.2	0.6017	0.04	0.2313	0.0033	3054	59	3035	160	3056	23	3056	23	FinalAge207_206	0.622134905	0.687172775
190517JW4_27	101.5	166.2	1690	0.583	19.87	1.2	0.6092	0.04	0.2361	0.003	3083.2	59	3065	160	3092	20	3092	20	FinalAge207_206	0.590295797	0.873221216
190517JW4_28	97.7	81.1	526	1.154	6.416	0.39	0.3691	0.024	0.1262	0.002	2031	54	2024	110	2037	29	2037	29	FinalAge207_206	0.344657804	0.638193422
190517JW4_29	496	380.2	753	1.241	0.92	0.057	0.1091	0.0072	0.0614	0.0011	661.2	30	667.2	42	644	39	667.2	42	FinalAge206_238	-0.907441016	-3.602484472
190517JW4_30	136.1	191	1765	0.69	20	1.2	0.621	0.041	0.2336	0.0029	3090.6	57	3112	160	3075	19	3075	19	FinalAge207_206	-0.692422183	-1.203252033
190517JW4_31	144.1	71.4	133.6	1.912	2.132	0.13	0.1974	0.013	0.0781	0.0016	1156	43	1161	70	1135	40	1135	40	FinalAge207_206	-0.432525952	-2.290748899
190517JW4_32	126.5	13.32	71.4	9.12	19.67	1.2	0.5991	0.04	0.2354	0.0031	3075	56	3025	160	3086	21	3086	21	FinalAge207_206	1.62601626	1.976668827
190517JW4_33	401	388	1375	0.9887	8.274	0.5	0.418	0.027	0.1432	0.0016	2260.6	54	2251	130	2263	20	2263	20	FinalAge207_206	0.424666018	0.530269554
190517JW4_34	422.7	143.2	121.6	2.95	0.742	0.046	0.09114	0.006	0.059	0.0012	562.4	27	562.2	36	545	45	562.2	36	FinalAge206_238	0.035561878	-3.155963303
190517JW4_35	326	572	989	0.5526	2.901	0.18	0.2306	0.015	0.0911	0.0015	1380	46	1337	80	1446	31	1446	31	FinalAge207_206	3.115942029	7.538035961
190517JW4_36	80.5	154.9	121.5	0.5111	0.702	0.054	0.0864	0.0058	0.0592	0.003	531	33	534.1	35	470	110	534.1	35	FinalAge206_238	-0.583804143	-13.63829787
190517JW4_37	223.4	251.2	351.9	0.888	1.514	0.094	0.1562	0.01	0.0703	0.0015	935	37	935.4	58	919	44	935.4	58	FinalAge206_238	-0.042780749	-1.784548422
190517JW4_38	243.1	412.6	1430	0.5978	6.92	0.42	0.3758	0.025	0.1333	0.0018	2099.4	54	2056	120	2137	23	2137	23	FinalAge207_206	2.067257312	3.790360318
190517JW4_39	627	196	291	3.453	0.862	0.053	0.09884	0.0065	0.0626	0.0011	630.2	29	607.5	38	681	40	607.5	38	FinalAge206_238	3.602031101	10.79295154
190517JW4_40	207.6	191	813	1.146	8.38	0.51	0.4241	0.028	0.1428	0.0017	2271	57	2280	130	2260	21	2260	21	FinalAge207_206	-0.396301189	-0.884955752
190517JW4_41	142.3	338	1858	0.4998	0.896	0.061	0.1041	0.0069	0.0627	0.0022	646	34	638.4	41	636	77	638.4	41	FinalAge206_238	1.176470588	-0.377358491
190517JW4_42	171.5	320	965	0.93	8.34	0.56	0.386	0.028	0.157	0.0023	2257	61	2099	130	2419	25	2419	25	FinalAge207_206	7.000443066	13.22860686
190517JW4_43	179.1	380	4040	0.545	8.24	0.53	0.3863	0.027	0.1538	0.0027	2252	59	2103	120	2382	30	2382	30	FinalAge207_206	6.61634103	11.71284635
190517JW4_44	687	441	1389	1.781	0.81	0.05	0.09749	0.0064	0.06021	0.001	602.3	27	599.6	38	596	37	599.6	38	FinalAge206_238	0.448281587	-0.604026846
190517JW4_45	68.13	77.6	225	0.965	0.919	0.067	0.1007	0.0068	0.0665	0.003	657	35	618	40	739	95	618	40	FinalAge206_238	5.936073059	16.37347767
190517JW4_46	365.6	259	2166	1.509	6.665	0.4	0.3793	0.025	0.1271	0.0015	2066.9	53	2073	120	2054	21	2054	21	FinalAge207_206	-0.295127969	-0.925024343
190517JW4_47	74.1	46.7	156	3.6	1.014	0.075	0.1138	0.008	0.0652	0.0028	703	39	694	46	702	92	694	46	FinalAge206_238	1.280227596	1.13960114
190517JW4_48	80.87	104.1	1095	0.7919	19.82	1.2	0.6129	0.041	0.2342	0.003	3081	58	3079	160	3077	20	3077	20	FinalAge207_206	0.064913989	-0.064998375
190517JW4_49	27.73	20.93	61.2	1.356	1.702	0.13	0.1665	0.011	0.0744	0.0037	996	50	992	63	940	100	992	63	FinalAge206_238	0.401606426	-5.531914894
190517JW4_50	554	858	1352	0.6319	0.772	0.048	0.09342	0.0062	0.0598	0.0011	579.9	27	575.6	36	578	41	575.6	36	FinalAge206_238	0.741507156	0.415224913
190517JW4_51	476	415	816	0.95	2.704	0.18	0.1288	0.0092	0.1523	0.0024	1320	48	780	53	2364	27	0	0	Discordant	40.90909091	67.00507614
190517JW4_52	336.9	769	1798	0.395	4.336	0.27	0.2749	0.019	0.1144	0.0016	1697	51	1564	95	1866	25	0	0	Discordant	7.837360047	16.18435155
190517JW4_53	136.9	204	655	0.599	15.94	1	0.457	0.031	0.2524	0.0032	2866	60	2421	140	3197	20	0	0	Discordant	15.52686671	24.27275571
190517JW4_54	437	183	788	2.351	6.12	0.41	0.333	0.024	0.1337	0.0019	1984	61	1849	120	2145	26	2145	26	FinalAge207_206	6.804435484	13.7995338
190517JW4_55	86	160.5	423	0.4869	2.288	0.15	0.2045	0.014	0.0809	0.0021	1203	45	1199	73	1204	50	1204	50	FinalAge207_206	0.332502078	0.415282392
190517JW4_56	34.77	34.15	43.2	0.931	0.853	0.064	0.0999	0.0068	0.0628	0.0032	619	36	615	41	590	110	615	41	FinalAge206_238	0.646203554	-4.237288136
190517JW4_57	45.2	76.5	215.4	0.5376	2.533	0.17	0.2182	0.015	0.084	0.0028	1276	49	1271	77	1247	69	1247	69	FinalAge207_206	0.39184953	-1.924619086
190517JW4_58	211.5	30.5	40.8	6.5	0.717	0.047	0.0888	0.0059	0.0581	0.0018	548	28	548.2	35	505	69	548.2	35	FinalAge206_238	-0.03649635	-8.554455446
190517JW4_59	298.3	104.8	113.8	3.16	0.659	0.042	0.08293	0.0055	0.0577	0.0014	512.7	25	513.5	33	485	54	513.5	33	FinalAge206_238	-0.156036669	-5.87628866
190517JW4_60	482	695	1585	0.6458	1.811	0.11	0.1749	0.012	0.07534	0.0011	1049.5	39	1038.9	63	1071	30	1071	30	FinalAge207_206	1.010004764	2.99719888
190517JW4_61	83.9	106.6	1071	0.6959	22.27	0.33	0.6415	0.007	0.2507	0.0038	3194	14	3194	28	3186	24	3186	24	FinalAge207_206	0	-0.251098556
190517JW4_62	226.5	214	1359	0.9377	6.717	0.086	0.3825	0.0039	0.1277	0.0019	2074.6	12	2087	18	2061	26	2061	26	FinalAge207_206	-0.597705582	-1.261523532
190517JW4_63	181.2	78.3	275	2.119	2.156	0.049	0.1994	0.0029	0.0783	0.0016	1162	16	1171	15	1138	41	1138	41	FinalAge207_206	-0.774526678	-2.899824253
190517JW4_64	180	104.2	716	1.503	5.87	0.12	0.334	0.0059	0.1273	0.002	1950	18	1855	29	2056	29	2056	29	FinalAge207_206	4.871794872	9.776264591
190517JW4_65	162	97	855	1.446	13.64	0.33	0.469	0.011	0.2103	0.0028	2715	24	2472	47	2904	21	2904	21	FinalAge207_206	8.950276243	14.87603306
190517JW4_66	45.58	46.87	386.5	0.885	14.49	0.23	0.5382	0.0068	0.1951	0.0032	2779	15	2777	29	2780	28	2780	28	FinalAge207_206	0.071968334	0.107913669
190517JW4_67	431	392	350	1.016	0.3469	0.0091	0.04743	0.00062	0.0531	0.0015	301.5	6.8	298.7	3.8	299	63	298.7	3.8	FinalAge206_238	0.928689884	0.100334448
190517JW4_68	142.6	54.9	89.1	2.435	0.706	0.022	0.0875	0.0014	0.059	0.0019	542	13	540.4	8.4	528	70	540.4	8.4	FinalAge206_238	0.295202952	-2.348484848
190517JW4_69	608	543	814	1.063	0.684	0.013	0.08533	0.00087	0.05829	0.0011	528.1	8	527.8	5.2	522	43	527.8	5.2	FinalAge206_238	0.056807423	-1.111111111
190517JW4_70	334.2	195.2	413	1.665	1.127	0.021	0.1262	0.0015	0.0646	0.0013	764.7	10	766.2	8.5	747	42	766.2	8.5	FinalAge206_238	-0.196155355	-2.570281124
190517JW4_71	65.6	81.4	830	0.85	19.58	0.35	0.61	0.011	0.2327	0.004	3068	18	3065	42	3065	27	3065	27	FinalAge207_206	0.097783572	0
190517JW4_72	167	377	900	0.4623	4.67	0.11	0.2746	0.0062	0.1229	0.0021	1759	20	1561	32	1995	30	0	0	Discordant	11.25639568	21.75438596
190517JW4_73	178.5	279.4	814	0.649	1.892	0.039	0.183	0.0025	0.0754	0.0015	1077	14	1083	14	1064	40	1064	40	FinalAge207_206	-0.557103064	-1.785714286

Table A2.1. U-Pb isotopic data for Rising Star cave and surface samples (Continued).

Sample #_Spot #	U (in ppm)	Th (in ppm)	Pb (in ppm)	Th/U	Pb207 /U235	± 2σ	Pb206 /U238	± 2σ	Pb207 /Pb206	± 2σ	Pb207 /U235	± Ma	Pb206 /U238	± Ma	Pb207 /Pb206	± Ma	Preferred Age	± Ma	Age System	U-Pb/U-Pb Discordance (%)	U-Pb/Pb-Pb Discordance (%)
190517JW4_74	633	520	898	1.239	0.902	0.016	0.1066	0.0012	0.06099	0.0011	651.4	8.7	652.7	7.1	635	39	652.7	7.1	FinalAge206_238	-0.199570157	-2.787401575
190517JW4_75	130.6	97.1	884	1.355	18.05	0.36	0.58	0.011	0.2252	0.0032	2989	19	2946	44	3014	23	3014	23	FinalAge207_206	1.43860823	2.256138023
190517JW4_76	20	34.2	58.6	0.598	0.847	0.069	0.1003	0.0029	0.0628	0.0052	600	40	615	17	480	170	615	17	FinalAge206_238	-2.5	-28.125
190517JW4_77	78.1	81.6	663	0.962	15.29	0.22	0.5681	0.0071	0.1949	0.0029	2831	14	2898	29	2778	24	2778	24	FinalAge207_206	-2.366654892	-4.319654428
190517JW4_78	90.3	28.8	15.3	3.41	0.863	0.037	0.0978	0.0017	0.0646	0.003	628	21	601.5	10	694	97	601.5	10	FinalAge206_238	4.219745223	13.32853026
190517JW4_79	108.9	66.7	114.8	1.607	0.868	0.029	0.1024	0.0016	0.0614	0.0021	629	16	628	9.2	595	71	628	9.2	FinalAge206_238	0.158982512	-5.546218487
190517JW4_80	25.64	0.735	3.1	-750	0.84	0.064	0.0962	0.0026	0.0652	0.0052	596	37	591	15	520	170	591	15	FinalAge206_238	0.838926174	-13.65384615
190517JW4_81	16.66	177.2	1102	0.0947	6.98	0.24	0.3933	0.0084	0.1288	0.0045	2095	30	2138	40	2047	62	2047	62	FinalAge207_206	-2.052505967	-4.445530044
190517JW4_82	43.8	47.9	147	0.992	1.784	0.065	0.1768	0.0031	0.0743	0.003	1033	25	1049	17	992	81	992	81	FinalAge207_206	-1.548886738	-5.745967742
190517JW4_83	82.7	144.3	633	0.5733	3.537	0.077	0.2727	0.0035	0.0939	0.0021	1530	17	1554	18	1488	45	1488	45	FinalAge207_206	-1.568627451	-4.435483871
190517JW4_84	138.7	84.9	210.1	1.639	1.498	0.037	0.1523	0.0019	0.0713	0.0019	925	15	913.6	11	931	54	913.6	11	FinalAge206_238	1.232432432	1.86895811
190517JW4_85	147.1	147.5	1076	1.001	8.623	0.12	0.4515	0.0055	0.1385	0.002	2297	13	2400	24	2202	25	2202	25	FinalAge207_206	-4.484109708	-8.991825613
190517JW4_86	183	192.7	1093	0.944	5.553	0.08	0.352	0.0044	0.1143	0.0018	1907	13	1943	21	1865	28	1865	28	FinalAge207_206	-1.887781856	-4.18230563
190517JW4_87	76.3	131.5	1243	0.5712	18.39	0.48	0.566	0.015	0.2352	0.0036	2997	26	2881	60	3082	25	3082	25	FinalAge207_206	3.870537204	6.52173913
190517JW4_88	142	112	221	1.385	1.524	0.048	0.1355	0.0023	0.0816	0.0027	935	19	820	14	1212	66	820	14	FinalAge206_238	12.29946524	32.34323432
190517JW4_89	224	711	593	0.3268	0.363	0.013	0.04725	0.00073	0.0562	0.0022	314	10	297.6	4.5	393	85	297.6	4.5	FinalAge206_238	5.222929936	24.27480916
190517JW4_90	86.9	81.9	732	1.054	15.61	0.25	0.5774	0.007	0.1958	0.0029	2850	15	2936	29	2786	25	2786	25	FinalAge207_206	-3.01754386	-5.384063173
190517JW4_91	25.7	2.65	19.8	10.66	12.89	0.3	0.464	0.0083	0.2013	0.0047	2666	23	2459	38	2832	37	2832	37	FinalAge207_206	7.76444111	13.17090395
190517JW4_92	118.3	242	1050	0.606	10.49	0.31	0.343	0.011	0.222	0.0036	2462	29	1893	52	2991	26	0	0	Discordant	23.11129163	36.71013039
190517JW4_93	33.7	53.8	553	0.623	20.45	0.37	0.6435	0.009	0.2317	0.0044	3109	18	3199	35	3059	30	3059	30	FinalAge207_206	-2.894821486	-4.576659039
190517JW4_94	93.8	64.8	200	1.424	1.898	0.048	0.1857	0.0027	0.0744	0.002	1077	17	1098	14	1023	56	1023	56	FinalAge207_206	-1.949860724	-7.331378299
190517JW4_95	157	171	1050	0.967	7.26	0.13	0.4198	0.0064	0.1254	0.0019	2140	15	2257	29	2029	27	2029	27	FinalAge207_206	-5.46728972	-11.23706259
190517JW5_1	83.78	77.2	430.1	1.081	6.456	0.1	0.3689	0.0045	0.1269	0.0022	2037	14	2023	21	2045	30	2045	30	FinalAge207_206	0.687285223	1.075794621
190517JW5_2	81.8	71.1	149	1.145	1.121	0.037	0.1245	0.0017	0.0653	0.0023	759	18	756.3	9.7	725	78	756.3	9.7	FinalAge206_238	0.355731225	-4.317241379
190517JW5_3	83.5	46.51	139.1	1.789	1.961	0.047	0.1859	0.0025	0.0763	0.002	1099	17	1100	14	1085	55	1085	55	FinalAge207_206	-0.090991811	-1.382488479
190517JW5_4	178	112.3	320.9	1.57	1.891	0.037	0.1824	0.002	0.0748	0.0015	1075	13	1079.7	11	1051	40	1051	40	FinalAge207_206	-0.437209302	-2.730732636
190517JW5_5	145	181.8	544	0.803	1.936	0.044	0.1844	0.0023	0.0762	0.0018	1091	15	1091	12	1077	49	1077	49	FinalAge207_206	0	-1.299907149
190517JW5_6	42.65	95.8	739	0.4224	14.74	0.27	0.529	0.007	0.2021	0.0036	2796	17	2738	30	2836	29	2836	29	FinalAge207_206	2.074391989	3.455571227
190517JW5_7	247.5	118	398	1.982	2.283	0.036	0.2068	0.0021	0.0801	0.0014	1206.1	11	1211.3	11	1188	34	1188	34	FinalAge207_206	-0.431141696	-1.961279461
190517JW5_8	243.2	199	319	1.245	0.699	0.018	0.08738	0.0011	0.0577	0.0016	536	11	539.9	6.3	494	61	539.9	6.3	FinalAge206_238	-0.72761194	-9.291497976
190517JW5_9	160.8	216.7	1764	0.6937	16.54	0.2	0.5747	0.0063	0.2085	0.0028	2906.6	12	2925	26	2891	21	2891	21	FinalAge207_206	-0.633042042	-1.176063646
190517JW5_10	66.7	45.7	147.7	1.403	1.943	0.06	0.1856	0.003	0.0764	0.0024	1092	21	1097	16	1070	61	1070	61	FinalAge207_206	-0.457875458	-2.523364486
190517JW5_11	51.5	105.6	747	0.46	21.47	0.38	0.6174	0.0099	0.2517	0.0046	3158	18	3096	39	3191	30	3191	30	FinalAge207_206	1.963267891	2.977123159
190517JW5_12	104.8	280.6	465	0.3523	0.786	0.029	0.0975	0.0014	0.0586	0.0022	587	16	599.4	8.3	494	80	599.4	8.3	FinalAge206_238	-2.112436116	-21.33603239
190517JW5_13	154.4	216.7	329	0.6809	0.676	0.023	0.0837	0.0013	0.0586	0.002	522	14	518.1	7.8	504	77	518.1	7.8	FinalAge206_238	0.747126437	-2.797619048
190517JW5_14	198	181	1250	1.042	6.81	0.15	0.3934	0.0077	0.1249	0.0019	2080	19	2139	37	2023	28	2023	28	FinalAge207_206	-2.836538462	-5.734058329
190517JW5_15	159.8	181.1	121.1	0.85	0.296	0.015	0.04013	0.00072	0.0539	0.0028	261	12	253.6	4.5	280	110	253.6	4.5	FinalAge206_238	2.835249042	9.428571429
190517JW5_16	164.3	213.9	322	0.854	0.792	0.022	0.097	0.0013	0.059	0.0017	592	12	596.8	7.6	549	63	596.8	7.6	FinalAge206_238	-0.810810811	-8.706739526
190517JW5_17	204.4	289.6	682	0.777	1.885	0.035	0.1803	0.0022	0.0758	0.0015	1073	12	1068	12	1085	40	1085	40	FinalAge207_206	0.465983225	1.566820276
190517JW5_18	172.3	236.1	320	0.8135	0.68	0.021	0.0859	0.0012	0.0574	0.0018	524	12	531.2	7.2	460	70	531.2	7.2	FinalAge206_238	-1.374045802	-15.47826087
190517JW5_19	127	129.8	869	1.127	18.95	0.28	0.5902	0.0074	0.2324	0.003	3036	14	2988	30	3065	21	3065	21	FinalAge207_206	1.581027668	2.51223491
190517JW5_20	67.7	25.5	115	3.89	1.475	0.095	0.1252	0.0052	0.0835	0.0035	887	41	757	30	1193	90	757	30	FinalAge206_238	14.65614431	36.54652137
190517JW5_21	165.7	399	452	0.47	0.621	0.022	0.0759	0.0015	0.059	0.002	489	14	471.5	9.2	529	75	471.5	9.2	FinalAge206_238	3.578732106	10.86956522
190517JW5_22	203.4	236	1337	0.94	6.914	0.1	0.3909	0.0045	0.1284	0.002	2098	13	2126	21	2073	26	2073	26	FinalAge207_206	-1.334604385	-2.556681138
190517JW5_23	-0.000255657	-0.00055202	1.2	no value	no value	NAN	no value	NAN	no value	NAN	no value	NAN	no value	NAN	no value	NAN	#VALUE!	#VALUE!	#VALUE!	#VALUE!	#VALUE!
190517JW5_24	77.3	152.1	669	0.5375	10.44	0.29	0.3323	0.0088	0.2279	0.0039	2464	26	1844	43	3029	28	0	0	Discordant	25.16233766	39.12182238
190517JW5_25	200.4	213.4	1222	0.966	6.6	0.086	0.3767	0.0039	0.1268	0.0019	2057.5	11	2062	19	2048	26	2048	26	FinalAge207_206	-0.218712029	-0.68359375
190517JW5_26	143.2	87.8	285	1.486	1.988	0.041	0.187	0.0022	0.0768	0.0018	1109	14	1105	12	1103	45	1103	45	FinalAge207_206	0.360685302	-0.181323663
190517JW5_27	94.2	85.6	539	0.996	6.6	0.11	0.377	0.0049	0.1273	0.0022	2059	14	2063	23	2054	30	2054	30	FinalAge207_206	-0.194269063	-0.438169426
190517JW5_28	35.15	38.33	63.5	0.835	0.74	0.046	0.0927	0.0022	0.0584	0.0038	548	26	571	13	410	130	571	13	FinalAge206_238	-4.197080292	-39.26829268
190517JW5_29	281.9	284	445	0.974	0.716	0.018	0.08753	0.00098	0.059	0.0015	546	11	540.8	5.8	543	58	540.8	5.8	FinalAge206_238	0.952380952	0.405156538
190517JW5_30	64.2	61.45	529	0.958	13.46	0.21	0.5034	0.0065	0.1939	0.0031	2709	14	2626	28	2771	26	2771	26	FinalAge207_206	3.063861203	5.232767954
190517JW5_31	91.1	81	458	1.051	6.17	0.11	0.3536	0.0047	0.126	0.0021	1996	16	1951	22	2039	31	2039	31	FinalAge207_206	2.254509018	4.315841099

Table A2.1. U-Pb isotopic data for Rising Star cave and surface samples (Continued).

Sample #_Spot #	U (in ppm)	Th (in ppm)	Pb (in ppm)	Th/U	Pb207 /U235	± 2σ	Pb206 /U238	± 2σ	Pb207 /Pb206	± 2σ	Pb207 /U235	± Ma	Pb206 /U238	± Ma	Pb207 /Pb206	± Ma	Preferred Age	± Ma	Age System	U-Pb/U-Pb Discordance (%)	U-Pb/Pb-Pb Discordance (%)
190517JW5_32	498	530	3630	0.876	7.42	0.13	0.398	0.0065	0.1346	0.0018	2159	15	2157	30	2154	24	2154	24	FinalAge207_206	0.092635479	-0.139275766
190517JW5_33	205	79.8	294	2.379	7.53	0.25	0.2435	0.0081	0.2248	0.0035	2164	32	1399	42	3011	26	0	0	Discordant	35.35120148	53.53703089
190517JW5_34	70.8	149.2	1103	0.4516	12.3	0.18	0.5009	0.0055	0.1776	0.0028	2626	14	2616	24	2626	27	2626	27	FinalAge207_206	0.380807312	0.380807312
190517JW5_35	51.6	74.7	641	0.6662	19.39	0.32	0.6068	0.0074	0.2318	0.0038	3059	17	3055	30	3061	26	3061	26	FinalAge207_206	0.130761687	0.196014374
190517JW5_36	121.1	253	178.5	0.4776	0.358	0.018	0.04064	0.00077	0.0641	0.0033	309	14	256.7	4.8	640	110	0	0	Discordant	16.92556634	59.890625
190517JW5_37	243.4	225.2	173.4	1.078	0.316	0.012	0.04441	0.00069	0.0519	0.0021	276.8	9	280.1	4.3	232	82	280.1	4.3	FinalAge206_238	-1.192196532	-20.73275862
190517JW5_38	107.1	94.7	545	1.148	6.824	0.11	0.3937	0.0048	0.1254	0.0022	2085	14	2139	22	2030	31	2030	31	FinalAge207_206	-2.589928058	-5.369458128
190517JW5_39	110	236	707	0.573	1.729	0.046	0.1689	0.0023	0.0743	0.002	1018	17	1005	13	1023	55	1023	55	FinalAge207_206	1.277013752	1.759530792
190517JW5_40	241.2	62.2	172.8	3.894	1.843	0.032	0.1803	0.0022	0.0741	0.0014	1059	12	1068	12	1032	39	1032	39	FinalAge207_206	-0.849858357	-3.488372093
190517JW5_41	118.1	154.2	1538	0.769	22.83	0.36	0.6617	0.0099	0.2503	0.0033	3217	15	3270	39	3183	21	3183	21	FinalAge207_206	-1.647497669	-2.7332705
190517JW5_42	185.2	174	1322	1.122	14.46	0.17	0.5402	0.0059	0.1939	0.0025	2779	11	2783	25	2775	21	2775	21	FinalAge207_206	-0.143936668	-0.288288288
190517JW5_43	138.8	207.1	1322	0.6706	9.56	0.13	0.4481	0.0053	0.1547	0.0021	2393	13	2385	23	2396	24	2396	24	FinalAge207_206	0.334308399	0.459098497
190517JW5_44	231	223.9	1239	1.035	6.605	0.091	0.3752	0.004	0.1276	0.0018	2059	12	2053	19	2060	25	2060	25	FinalAge207_206	0.291403594	0.339805825
190517JW5_45	137.4	136.3	181.8	1.015	0.709	0.025	0.0865	0.0013	0.0593	0.0023	541	15	534.5	7.5	529	83	534.5	7.5	FinalAge206_238	1.201478743	-1.039697543
190517JW5_46	103.9	168	281	0.616	0.839	0.031	0.1013	0.0015	0.0601	0.0022	613	17	621.6	8.9	547	85	621.6	8.9	FinalAge206_238	-1.402936378	-13.63802559
190517JW5_47	55.94	73.69	486	0.729	10.49	0.19	0.4649	0.0063	0.1631	0.0029	2474	17	2459	28	2478	30	2478	30	FinalAge207_206	0.606305578	0.766747377
190517JW5_48	97.6	117.5	950	0.786	16.68	0.37	0.537	0.011	0.225	0.0035	2908	22	2769	48	3013	25	3013	25	FinalAge207_206	4.779917469	8.098240956
190517JW5_49	122.8	103.5	365.5	1.129	2.616	0.056	0.2241	0.0029	0.0846	0.0019	1301	16	1303	15	1284	43	1284	43	FinalAge207_206	-0.153727902	-1.479750779
190517JW5_50	242.7	433	774	0.54	0.917	0.024	0.1066	0.0014	0.0624	0.0017	658	12	652.9	8.4	667	59	652.9	8.4	FinalAge206_238	0.775075988	2.113943028
190517JW5_51	182.2	198	1139	0.867	6.649	0.097	0.3762	0.0044	0.128	0.0021	2065	13	2057	21	2067	28	2067	28	FinalAge207_206	0.387409201	0.483792937
190517JW5_52	383	557	404	0.6483	0.304	0.0088	0.04265	0.00057	0.0519	0.0016	269.4	7	269.2	3.5	254	66	269.2	3.5	FinalAge206_238	0.07423905	-5.984251969
190517JW5_53	759	545.5	1232	1.298	1.304	0.019	0.141	0.0014	0.06691	0.001	846.2	8.5	850.2	8	826	32	850.2	8	FinalAge206_238	-0.472701489	-2.929782082
190517JW5_54	123.4	113.6	627	1.027	6.594	0.11	0.3782	0.0046	0.1264	0.0021	2055	14	2066	22	2045	30	2045	30	FinalAge207_206	-0.535279805	-1.026894866
190517JW5_55	708.3	316.6	506	2.133	0.814	0.014	0.09793	0.0011	0.06004	0.001	603.4	7.8	602.2	6.3	592	37	602.2	6.3	FinalAge206_238	0.198873053	-1.722972973
190517JW5_56	165.7	238.3	145.5	0.724	0.281	0.014	0.03881	0.00066	0.0533	0.0028	249	11	245.4	4.1	250	100	245.4	4.1	FinalAge206_238	1.445783133	1.84
190517JW5_57	200.8	212.1	592	0.984	2.078	0.041	0.1954	0.0021	0.0771	0.0016	1139	13	1150	12	1105	41	1105	41	FinalAge207_206	-0.965759438	-4.07239819
190517JW5_58	80.04	65.44	473	1.264	14.4	0.22	0.5345	0.0063	0.195	0.003	2773	14	2759	27	2781	25	2781	25	FinalAge207_206	0.504868374	0.791082344
190517JW5_59	71.74	74.4	586	0.993	18.14	0.27	0.5888	0.0072	0.2229	0.0034	2996	14	2982	29	2996	24	2996	24	FinalAge207_206	0.46728972	0.46728972
190517JW5_60	150.8	231.1	801	0.6642	2.628	0.046	0.2305	0.0027	0.0827	0.0016	1307	13	1337	14	1251	38	1251	38	FinalAge207_206	-2.295332823	-6.8745004
190517JW5_61	371.2	294.9	405	1.27	0.7	0.017	0.08651	0.001	0.0585	0.0015	536.7	10	534.7	6.2	524	59	534.7	6.2	FinalAge206_238	0.372647662	-2.041984733
190517JW5_62	330.4	430	294	0.792	0.326	0.011	0.04453	0.00058	0.053	0.0018	285.1	8.3	280.8	3.6	288	73	280.8	3.6	FinalAge206_238	1.508242722	2.5
190517JW5_63	465	354	1460	1.32	4.3	0.13	0.1431	0.0041	0.2179	0.0036	1685	24	860	23	2958	26	0	0	Discordant	48.96142433	70.92630156
190517JW5_64	177.9	201.2	1105	0.8788	6.59	0.088	0.3745	0.0045	0.1275	0.0019	2056	12	2049	21	2057	26	2057	26	FinalAge207_206	0.340466926	0.388915897
190517JW5_65	304.1	152.3	247	2.002	0.846	0.02	0.1012	0.0012	0.0603	0.0014	620	11	621.4	7.2	591	53	621.4	7.2	FinalAge206_238	-0.225806452	-5.143824027
190517JW5_66	334	257	203	1.364	0.351	0.011	0.04961	0.00061	0.0518	0.0017	305.4	8.5	312.1	3.8	242	71	312.1	3.8	FinalAge206_238	-2.193844139	-28.96694215
190517JW5_67	429	102.8	156.4	4.281	0.778	0.015	0.09361	0.001	0.0602	0.0012	582.8	8.6	576.8	5.9	588	45	576.8	5.9	FinalAge206_238	1.029512697	1.904761905
190517JW5_68	200.2	258.2	194.5	0.7931	0.371	0.015	0.04342	0.00071	0.0625	0.0027	318	11	273.9	4.4	595	93	273.9	4.4	FinalAge206_238	13.86792453	53.96638655
190517JW5_69	194.1	187.3	1002	1.062	6.627	0.09	0.3778	0.0041	0.1269	0.0018	2062	12	2065	19	2056	26	2056	26	FinalAge207_206	-0.145489816	-0.437743191
190517JW5_70	98.7	70.13	371.4	1.441	6.61	0.11	0.378	0.0046	0.1267	0.0021	2057	15	2065	21	2046	30	2046	30	FinalAge207_206	-0.388915897	-0.928641251
190517JW5_71	45.07	117.6	324.1	0.3907	1.944	0.072	0.182	0.003	0.0776	0.003	1083	25	1077	16	1075	78	1075	78	FinalAge207_206	0.55401662	-0.186046512
190517JW5_72	233.6	191.6	263.4	1.246	0.699	0.02	0.0881	0.0012	0.0571	0.0016	538	11	544.4	6.9	464	63	544.4	6.9	FinalAge206_238	-1.189591078	-17.32758621
190517JW5_73	91.4	72.3	198.8	1.282	1.903	0.046	0.1812	0.0026	0.0765	0.0021	1079	17	1073	14	1086	53	1086	53	FinalAge207_206	0.556070436	1.197053407
190517JW5_74	601	118.3	164.8	5.22	0.698	0.013	0.08596	0.00097	0.05857	0.0011	536.5	8.1	531.5	5.8	534	42	531.5	5.8	FinalAge206_238	0.931966449	0.468164794
190517JW5_75	81.5	107.6	777	0.7549	14.29	0.2	0.5291	0.0061	0.195	0.0029	2767	13	2736	26	2781	25	2781	25	FinalAge207_206	1.120346946	1.618122977
190517JW5_76	121	127.7	111.5	0.914	0.36	0.016	0.04844	0.00093	0.0539	0.0025	309	12	304.8	5.7	305	97	304.8	5.7	FinalAge206_238	1.359223301	0.06557377
190517JW5_77	378.5	258.1	444	1.413	0.88	0.019	0.1037	0.0015	0.0617	0.0013	639.1	10	635.6	8.6	642	47	635.6	8.6	FinalAge206_238	0.547645126	0.996884735
190517JW5_78	109.2	147.8	1179	0.7159	16.29	0.2	0.5637	0.0061	0.2091	0.0027	2893.2	12	2880	25	2895	21	2895	21	FinalAge207_206	0.456242223	0.518134715
190517JW5_79	270.8	236	420	1.209	0.816	0.019	0.0971	0.0013	0.0609	0.0015	604	11	597.3	7.8	602	55	597.3	7.8	FinalAge206_238	1.109271523	0.780730897
190517JW5_80	155	221	1033	0.709	6.48	0.12	0.3736	0.006	0.1262	0.002	2039	16	2044	28	2038	28	2038	28	FinalAge207_206	-0.245218244	-0.294406281
190517JW5_81	90.8	100.6	569	0.881	6.543	0.11	0.3752	0.0047	0.1265	0.0021	2051	15	2052	22	2041	29	2041	29	FinalAge207_206	-0.048756704	-0.538951494
190517JW5_82	195.7	221.9	608	0.871	1.729	0.036	0.1684	0.0019	0.0741	0.0017	1017	13	1003	10	1034	46	1034	46	FinalAge207_206	1.376597837	2.998065764
190517JW5_83	231.6	68.6	97	3.374	0.699	0.018	0.08583	0.0011	0.0593	0.0017	536	11	530.7	6.4	545	63	530.7	6.4	FinalAge206_238	0.98880597	2.623853211
190517JW5_84	151.5	156.5	919	0.962	6.631	0.099	0.3786	0.0041	0.1267	0.0019	2061	13	2069	19	2045	27	2045	27	FinalAge207_206	-0.388161087	-1.173594132
190517JW5_85	307.9	159.5	508	1.903	2.112	0.034	0.1961	0.0023	0.0779	0.0013	1152	12	1154	12	1133	33	1133	33	FinalAge207_206	-0.173611111	-1.85348632

Table A2.1. U-Pb isotopic data for Rising Star cave and surface samples (Continued).

Sample #_Spot #	U (in ppm)	Th (in ppm)	Pb (in ppm)	Th/U	Pb207 /U235	± 2σ	Pb206 /U238	± 2σ	Pb207 /Pb206	± 2σ	Pb207 /U235	± Ma	Pb206 /U238	± Ma	Pb207 /Pb206	± Ma	Preferred Age	± Ma	Age System	U-Pb/U-Pb Discordance (%)	U-Pb/Pb-Pb Discordance (%)
190517JW5_86	52.7	12	84.9	4.58	14.62	0.33	0.5359	0.0096	0.1965	0.0043	2792	23	2763	40	2789	35	2789	35	FinalAge207_206	1.038681948	0.932233776
190517JW5_87	169.1	141.3	249.7	1.227	0.903	0.022	0.1072	0.0014	0.0613	0.0016	651	12	656	8.1	613	56	656	8.1	FinalAge206_238	-0.768049155	-7.014681892
190517JW5_88	351.9	244.3	325.8	1.49	0.656	0.015	0.08247	0.001	0.0578	0.0015	511.7	9.3	510.8	5.9	489	56	510.8	5.9	FinalAge206_238	0.175884307	-4.45807771
190517JW5_89	266	319.9	1796	0.8702	6.545	0.083	0.3761	0.004	0.1261	0.0018	2050.3	11	2057	19	2042	25	2042	25	FinalAge207_206	-0.326781447	-0.734573947
190517JW5_90	262	424	1140	0.611	8.46	0.25	0.2507	0.0078	0.2471	0.0041	2274	27	1437	40	3159	26	0	0	Discordant	36.80738786	54.51092118
190517JW5_91	258.6	263.9	317	1.041	0.594	0.019	0.0747	0.0011	0.0575	0.0019	471	12	464.2	6.6	481	70	464.2	6.6	FinalAge206_238	1.44373673	3.492723493
190517JW5_92	359.5	412.2	266.5	0.9271	0.2777	0.0092	0.03858	0.00049	0.0525	0.0018	249.9	7.8	244	3	290	76	244	3	FinalAge206_238	2.360944378	15.86206897
190517JW5_93	67.03	74.8	720	0.959	24.23	0.34	0.6834	0.0087	0.2568	0.0037	3275	14	3354	33	3222	23	3222	23	FinalAge207_206	-2.41221374	-4.096834264
190517JW5_94	320.2	496.5	3311	0.6809	11.77	0.14	0.4774	0.0052	0.1782	0.0023	2584.3	11	2515	23	2634	21	2634	21	FinalAge207_206	2.681577216	4.517843584
190517JW5_95	459	381	310	1.256	0.3746	0.0097	0.04906	0.00059	0.0552	0.0015	322.1	7.2	308.7	3.6	395	60	308.7	3.6	FinalAge206_238	4.160198696	21.84810127
190517JW5_96	126.6	254.7	2597	0.4438	22.14	0.3	0.635	0.007	0.2525	0.0035	3188	13	3170	28	3196	22	3196	22	FinalAge207_206	0.564617315	0.813516896
190517JW5_97	302	393	2280	0.631	5.6	0.13	0.2493	0.0053	0.163	0.0029	1909	20	1432	27	2477	30	0	0	Discordant	24.98690414	42.1881308
190517JW5_98	142.6	132.3	885	0.962	6.776	0.1	0.3829	0.0044	0.1281	0.002	2081	13	2089	21	2065	28	2065	28	FinalAge207_206	-0.384430562	-1.162227603
190517JW5_99	262.9	202	676	1.192	1.79	0.035	0.1736	0.0025	0.0743	0.0014	1039	13	1031	14	1045	40	1045	40	FinalAge207_206	0.769971126	1.339712919
190517JW5_100	125.5	279.4	231	0.4068	0.34	0.02	0.0429	0.001	0.0582	0.0037	295	16	270.9	6.5	420	130	270.9	6.5	FinalAge206_238	8.169491525	35.5
190517JW5_101	369	283	1591	1.181	4.941	0.085	0.3221	0.005	0.1112	0.0019	1809	15	1799	25	1813	30	1813	30	FinalAge207_206	0.552791598	0.772200772
190517JW6_1	66	62.7	615	0.96	22.46	0.32	0.6408	0.0077	0.2538	0.0038	3201	14	3190	30	3203	24	3203	24	FinalAge207_206	0.343642612	0.405869497
190517JW6_2	105.8	125.1	289.1	0.782	0.978	0.032	0.1072	0.0017	0.0659	0.0021	689	16	655.9	10	773	67	655.9	10	FinalAge206_238	4.804063861	15.14877102
190517JW6_3	315.3	287.6	774	1.015	1.574	0.032	0.1555	0.002	0.0732	0.0014	957	13	931	11	1003	38	931	11	FinalAge206_238	2.716823406	7.178464606
190517JW6_4	253.4	209.2	1228	1.1534	6.542	0.085	0.3719	0.0033	0.1272	0.0017	2049.9	11	2039	15	2055	24	2055	24	FinalAge207_206	0.531733255	0.778588808
190517JW6_5	44.35	52.6	134.9	0.922	1.788	0.071	0.1726	0.003	0.0752	0.003	1029	26	1026	17	1008	79	1008	79	FinalAge207_206	0.29154519	-1.785714286
190517JW6_6	117.3	138.6	693	0.925	6.507	0.099	0.3741	0.0041	0.1262	0.0021	2047	14	2048	19	2037	29	2037	29	FinalAge207_206	-0.048851979	-0.540009818
190517JW6_7	69.1	89.2	477	0.873	7.03	0.12	0.3889	0.005	0.1306	0.0026	2112	15	2116	23	2099	36	2099	36	FinalAge207_206	-0.189393939	-0.809909481
190517JW6_8	188.1	202	991	1.001	6.541	0.088	0.3774	0.0037	0.1257	0.0019	2051	12	2063	17	2033	26	2033	26	FinalAge207_206	-0.585080449	-1.475651746
190517JW6_9	65.1	209	268.8	0.3422	6.88	0.16	0.3181	0.0065	0.157	0.0033	2088	21	1777	32	2408	35	0	0	Discordant	14.89463602	26.20431894
190517JW6_10	189	423.2	595	0.489	0.786	0.023	0.0956	0.0012	0.0594	0.0018	585	13	588.4	7.1	540	68	588.4	7.1	FinalAge206_238	-0.581196581	-8.962962963
190517JW6_11	428	435	1510	1.025	5.53	0.14	0.1803	0.0043	0.2221	0.0033	1898	21	1067	24	2990	24	0	0	Discordant	43.7829294	64.31438127
190517JW6_12	115.07	229.1	1835	0.5265	19.73	0.23	0.6114	0.0062	0.2331	0.0031	3077	11	3074	25	3070	21	3070	21	FinalAge207_206	0.097497563	-0.13029316
190517JW6_13	219	184.1	964	1.235	6.538	0.077	0.3722	0.0038	0.1269	0.0018	2049.8	10	2041	18	2052	25	2052	25	FinalAge207_206	0.429310177	0.536062378
190517JW6_14	191	194	1124	1.024	7.37	0.14	0.4202	0.0071	0.1269	0.0019	2152	17	2258	32	2049	26	2049	26	FinalAge207_206	-4.925650558	-10.20009761
190517JW6_15	158.2	272.6	1352	0.585	5.456	0.078	0.3461	0.0037	0.1138	0.0018	1891	12	1915	18	1859	28	1859	28	FinalAge207_206	-1.269169751	-3.012372243
190517JW6_16	390.3	256.4	679	1.532	1.861	0.029	0.1789	0.0017	0.0751	0.0012	1065.7	10	1060.9	9.6	1067	33	1067	33	FinalAge207_206	0.450408182	0.571696345
190517JW6_17	182	237.5	639	0.687	1.578	0.035	0.1529	0.002	0.0748	0.0018	959	14	917	11	1042	50	917	11	FinalAge206_238	4.379562044	11.99616123
190517JW6_18	604	436	789	1.198	1.664	0.044	0.1593	0.0038	0.0758	0.0014	991	17	952	21	1080	36	952	21	FinalAge206_238	3.935418769	11.85185185
190517JW6_19	312.6	108.5	276.5	2.445	1.451	0.027	0.1477	0.0019	0.0711	0.0013	909	11	887.9	11	957	36	887.9	11	FinalAge206_238	2.321232123	7.220480669
190517JW6_20	140.2	298.7	2312	0.3902	9.39	0.13	0.4384	0.0047	0.1549	0.0023	2375	13	2342	21	2396	26	2396	26	FinalAge207_206	1.389473684	2.25375626
190517JW6_21	198	126.4	201	1.298	0.689	0.02	0.0853	0.0012	0.0588	0.0018	530	12	527.3	7.1	510	67	527.3	7.1	FinalAge206_238	0.509433962	-3.392156863
190517JW6_22	320.7	278.6	471	0.9358	0.711	0.015	0.08719	0.001	0.0591	0.0014	544.1	9.2	538.8	6	541	54	538.8	6	FinalAge206_238	0.974085646	0.406654344
190517JW6_23	220.5	225.2	370	0.7806	0.66	0.018	0.0841	0.001	0.0567	0.0017	512	11	520.4	6.1	440	64	520.4	6.1	FinalAge206_238	-1.640625	-18.27272727
190517JW6_24	64.2	93.4	906	0.5498	16.79	0.24	0.5714	0.0068	0.2121	0.0032	2920	14	2912	28	2915	25	2915	25	FinalAge207_206	0.273972603	0.102915952
190517JW6_25	783	252.5	855	2.419	1.765	0.022	0.1736	0.0016	0.07359	0.00099	1032.5	8.1	1031.8	9	1024	27	1024	27	FinalAge207_206	0.06779661	-0.76171875
190517JW6_26	169.5	133.7	936	0.991	6.541	0.094	0.3705	0.0041	0.1276	0.0019	2049	13	2031	19	2062	26	2062	26	FinalAge207_206	0.878477306	1.503394762
190517JW6_27	466.8	126.1	265.7	2.875	0.878	0.017	0.1039	0.0011	0.061	0.0013	638.7	9.1	637	6.7	625	45	637	6.7	FinalAge206_238	0.266165649	-1.92
190517JW6_28	176.8	131.7	936	1.04	6.625	0.091	0.3792	0.0038	0.1265	0.0019	2060.7	12	2074	18	2043	26	2043	26	FinalAge207_206	-0.645411753	-1.517376407
190517JW6_29	201.5	206	680	0.758	6.34	0.24	0.305	0.012	0.1509	0.0022	2002	32	1702	58	2354	26	0	0	Discordant	14.98501499	27.69753611
190517JW6_30	322.6	189.2	1079	1.324	4.4	0.059	0.2988	0.003	0.1067	0.0016	1711.7	11	1685	15	1737	27	1737	27	FinalAge207_206	1.559852778	2.993667242
190517JW6_31	484.8	75.1	155.5	5.074	0.875	0.016	0.10189	0.001	0.0621	0.0012	636.7	8.7	625.4	6.1	659	43	625.4	6.1	FinalAge206_238	1.77477619	5.098634294
190517JW6_32	397.8	77.5	142.2	5.097	0.914	0.026	0.1089	0.0021	0.06085	0.00088	658.5	14	666.4	12	628	32	666.4	12	FinalAge206_238	-1.199696279	-6.114649682
190517JW6_33	211.1	201.4	257	1.055	0.583	0.021	0.0762	0.0015	0.0555	0.0015	464.5	13	473.3	8.8	399	61	473.3	8.8	FinalAge206_238	-1.894510226	-18.62155388
190517JW6_34	140.7	152.8	871	0.92	6.666	0.18	0.381	0.0073	0.1269	0.0015	2067	24	2080	34	2051	21	2051	21	FinalAge207_206	-0.628930818	-1.413944417
190517JW6_35	111.4	110.4	645	1.019	6.64	0.18	0.3747	0.0069	0.1288	0.0016	2062.7	24	2051	32	2074	23	2074	23	FinalAge207_206	0.567217724	1.108968177
190517JW6_36	160.5	651	1930	0.28	1.855	0.056	0.1757	0.0034	0.0766	0.0014	1063	20	1043	19	1101	36	1101	36	FinalAge207_206	1.881467545	5.267938238
190517JW6_37	291.9	926	673	0.316	0.3138	0.011	0.04354	0.00084	0.0523	0.0013	277.8	8	274.7	5.2	278	55	274.7	5.2	FinalAge206_238	1.115910727	1.18705036

Table A2.1. U-Pb isotopic data for Rising Star cave and surface samples (Continued).

Sample #_Spot #	U (in ppm)	Th (in ppm)	Pb (in ppm)	Th/U	Pb207 /U235	± 2σ	Pb206 /U238	± 2σ	Pb207 /Pb206	± 2σ	Pb207 /U235	± Ma	Pb206 /U238	± Ma	Pb207 /Pb206	± Ma	Preferred Age	± Ma	Age System	U-Pb/U-Pb Discordance (%)	U-Pb/Pb-Pb Discordance (%)
190517JW6_38	201.2	245	368	0.857	0.76	0.025	0.0923	0.0018	0.0594	0.0013	572.1	14	569.1	11	565	49	569.1	11	FinalAge206_238	0.524383849	-0.725663717
190517JW6_39	94.4	115.5	232.1	0.8049	1.072	0.04	0.1215	0.0024	0.0641	0.0018	735	20	739	14	705	61	739	14	FinalAge206_238	-0.544217687	-4.822695035
190517JW6_40	142.4	165.8	401	0.85	1.335	0.042	0.1418	0.0027	0.0681	0.0014	859	18	854.4	15	851	43	854.4	15	FinalAge206_238	0.535506403	-0.399529965
190517JW6_41	104.2	129.9	237.6	0.805	0.844	0.033	0.0998	0.0021	0.0614	0.002	620	18	613	13	633	66	613	13	FinalAge206_238	1.129032258	3.159557662
190517JW6_42	216.7	191.2	1042	1.128	6.168	0.16	0.3551	0.0065	0.1261	0.0013	2000.8	23	1958	31	2040	18	2040	18	FinalAge207_206	2.139144342	4.019607843
190517JW6_43	215	209.6	1040	1.009	6.122	0.17	0.3371	0.0065	0.1316	0.0015	1992	25	1872	31	2115	19	2115	19	FinalAge207_206	6.024096386	11.4893617
190517JW6_44	138.8	120.3	328.2	1.1512	1.802	0.052	0.176	0.0032	0.0744	0.0012	1046	19	1044.7	18	1036	34	1036	34	FinalAge207_206	0.124282983	-0.83976834
190517JW6_45	82.4	88	598	0.938	16.57	0.43	0.5499	0.01	0.219	0.0023	2908.8	25	2823	42	2969	17	2969	17	FinalAge207_206	2.949669967	4.917480633
190517JW6_46	159.8	296	1693	0.5362	8.94	0.24	0.4187	0.0077	0.1546	0.0015	2330	24	2256	36	2394	17	2394	17	FinalAge207_206	3.175965665	5.764411028
190517JW6_47	412.8	164.7	266	2.558	0.719	0.021	0.08811	0.0016	0.0592	0.0011	549.4	12	544.3	9.7	564	41	544.3	9.7	FinalAge206_238	0.928285402	3.492907801
190517JW6_48	137.2	110.7	992	1.248	18.33	0.47	0.5653	0.01	0.2344	0.0019	3006.1	25	2887	42	3081	13	3081	13	FinalAge207_206	3.961944047	6.29665693
190517JW6_49	87.9	112.4	739	0.7823	9.463	0.25	0.4474	0.008	0.153	0.0017	2382.1	24	2383	36	2376	19	2376	19	FinalAge207_206	-0.037781789	-0.294612795
190517JW6_50	162	306	411	0.5238	0.653	0.023	0.08199	0.0016	0.0578	0.0015	511	14	507.9	9.7	490	57	507.9	9.7	FinalAge206_238	0.60665362	-3.653061224
190517JW6_51	116.5	110.4	575	1.0488	6.14	0.19	0.3491	0.0086	0.1276	0.0015	1990	28	1927	41	2062	20	2062	20	FinalAge207_206	3.165829146	6.547041707
190517JW6_52	280.6	482.4	696	0.5828	0.719	0.021	0.08824	0.0016	0.0591	0.0011	548.8	13	545.1	9.3	553	41	545.1	9.3	FinalAge206_238	0.674198251	1.428571429
190517JW6_53	122.7	135.8	452	1.098	5.98	0.2	0.3423	0.0089	0.1265	0.0014	1965	30	1894	43	2045	20	2045	20	FinalAge207_206	3.613231552	7.383863081
190517JW6_54	160.3	435.1	3268	0.3695	13.66	0.35	0.5244	0.0091	0.1885	0.0016	2725.7	24	2717	39	2727	15	2727	15	FinalAge207_206	0.319184063	0.366703337
190517JW6_55	57.6	228	273.1	0.253	0.553	0.028	0.0729	0.0016	0.0555	0.0027	441	19	453.5	9.7	347	100	453.5	9.7	FinalAge206_238	-2.83446712	-30.69164265
190517JW6_56	204.1	437	1378	0.507	5.12	0.14	0.3213	0.0064	0.1157	0.0012	1837	23	1795	31	1885	19	1885	19	FinalAge207_206	2.286336418	4.774535809
190517JW7_1	122	147	401	0.8378	1.901	0.061	0.1815	0.0035	0.076	0.0017	1079	22	1076	19	1077	45	1077	45	FinalAge207_206	0.278035218	0.092850511
190517JW7_2	126	281.2	2345	0.449	19.77	0.51	0.6107	0.011	0.2342	0.0024	3079	25	3072	45	3080	16	3080	16	FinalAge207_206	0.227346541	0.25974026
190517JW7_3	83	83.3	144	0.999	0.956	0.041	0.1088	0.0024	0.0643	0.0025	682	21	665.3	14	706	78	665.3	14	FinalAge206_238	2.448680352	5.764872521
190517JW7_4	649	324	1525	1.985	3.523	0.099	0.2693	0.0054	0.09502	0.00099	1532	23	1536	27	1525	20	1525	20	FinalAge207_206	-0.261096606	-0.721311475
190517JW7_5	263.1	293.2	1492	0.8979	5.419	0.14	0.3404	0.006	0.11517	0.001	1887.7	23	1888	29	1881	16	1881	16	FinalAge207_206	-0.015892356	-0.372142477
190517JW7_6	167	158.9	1457	1.039	20.16	0.56	0.6172	0.013	0.2363	0.0022	3097	27	3097	51	3093	15	3093	15	FinalAge207_206	0	-0.129324281
190517JW7_7	65.1	54.8	158.8	1.193	1.802	0.061	0.1776	0.0035	0.0738	0.0019	1045	22	1054	19	1002	52	1002	52	FinalAge207_206	-0.861244019	-5.189620758
190517JW7_8	443.4	546.8	480.5	0.8026	0.3989	0.012	0.05402	0.00099	0.0535	0.0011	340.8	8.8	339.2	6	336	45	339.2	6	FinalAge206_238	0.469483568	-0.952380952
190517JW7_9	256.1	421	2605	0.6056	9.22	0.26	0.431	0.0088	0.1548	0.0015	2358	26	2309	40	2397	17	2397	17	FinalAge207_206	2.078032231	3.671255736
190517JW7_10	295	670	481	0.4422	0.299	0.011	0.04308	0.00081	0.0504	0.0014	264.8	8.5	271.9	5	184	60	271.9	5	FinalAge206_238	-2.681268882	-47.77173913
190517JW7_11	47.91	61.4	443.7	0.7762	10.26	0.28	0.4833	0.0089	0.1539	0.002	2456	25	2540	39	2383	22	2383	22	FinalAge207_206	-3.42019544	-6.588334033
190517JW7_12	94.2	182.6	253	0.5093	0.7	0.032	0.0848	0.0019	0.0596	0.0025	535	19	524.7	11	539	91	524.7	11	FinalAge206_238	1.925233645	2.653061224
190517JW7_13	531	138.4	203.7	3.77	0.6943	0.019	0.08713	0.0015	0.05766	0.0008	535.3	12	538.5	9.1	507	32	538.5	9.1	FinalAge206_238	-0.597795629	-6.213017751
190517JW7_14	92.4	102.9	967	0.8851	22.23	0.57	0.6433	0.012	0.25	0.0025	3193.8	26	3201	46	3182	16	3182	16	FinalAge207_206	-0.225436784	-0.597108737
190517JW7_15	171	239	887	0.745	2.909	0.082	0.2403	0.0045	0.0876	0.0013	1382	21	1388	23	1369	27	1369	27	FinalAge207_206	-0.434153401	-1.387874361
190517JW7_16	180.7	152.6	1006	1.1695	8.579	0.22	0.4349	0.0076	0.1427	0.0014	2293.1	24	2327	34	2256	17	2256	17	FinalAge207_206	-1.478348088	-3.147163121
190517JW7_17	124.6	87.1	162	1.45	0.934	0.031	0.1098	0.0021	0.0613	0.0014	667	16	671.3	12	622	51	671.3	12	FinalAge206_238	-0.644677661	-7.926045016
190517JW7_18	328.4	164.3	468	1.97	1.671	0.048	0.1664	0.0031	0.0725	0.001	996.2	18	992.1	17	996	27	992.1	17	FinalAge206_238	0.411563943	0.391566265
190517JW7_19	147	139.8	840	1.039	6.749	0.18	0.3813	0.0069	0.1278	0.0015	2077.7	24	2082	32	2064	21	2064	21	FinalAge207_206	-0.206959619	-0.872093023
190517JW7_20	87.8	169.7	254.8	0.514	0.807	0.041	0.0974	0.0022	0.0607	0.0031	604	23	598.8	13	580	110	598.8	13	FinalAge206_238	0.860927152	-3.24137931
190517JW7_21	226.3	355.9	1717	0.6306	4.677	0.12	0.3155	0.0055	0.10733	0.0011	1762.1	22	1767.5	27	1750	18	1750	18	FinalAge207_206	-0.306452528	-1
190517JW7_22	419	418	1483	0.993	5.057	0.13	0.2468	0.0048	0.1484	0.0013	1828.2	23	1421	25	2325	15	0	0	Discordant	22.27327426	38.88172043
190517JW7_23	34.3	67.4	352	0.5021	5.44	0.17	0.3448	0.0071	0.1148	0.0024	1890	29	1911	35	1866	37	1866	37	FinalAge207_206	-1.111111111	-2.411575563
190517JW7_24	388.6	190	282.9	2.04	1.279	0.038	0.1322	0.0026	0.0702	0.0011	835.1	17	800.3	15	925	34	800.3	15	FinalAge206_238	4.167165609	13.48108108
190517JW7_25	280.7	298.3	1763	0.9429	6.689	0.17	0.38	0.0066	0.12745	0.0011	2070	23	2076	31	2060	15	2060	15	FinalAge207_206	-0.289855072	-0.776699029
190517JW7_26	63.2	67.1	217	0.927	2.215	0.087	0.1988	0.0043	0.0813	0.0026	1183	28	1169	23	1194	64	1194	64	FinalAge207_206	1.183431953	2.093802345
190517JW7_27	285	454	315	0.6348	0.2825	0.011	0.04046	0.00078	0.0504	0.0016	252.4	8.9	255.6	4.8	188	68	255.6	4.8	FinalAge206_238	-1.267828843	-35.95744681
190517JW7_28	468	697	1104	0.706	0.789	0.023	0.09503	0.0018	0.06008	0.00098	589.7	13	585.2	11	595	35	585.2	11	FinalAge206_238	0.763099881	1.647058824
190517JW7_29	433	524	3063	0.8245	6.56	0.17	0.3802	0.0066	0.12488	0.001	2053.1	22	2077	31	2024	15	2024	15	FinalAge207_206	-1.164093322	-2.618577075
190517JW7_30	309	1024	3460	0.2992	12.29	0.37	0.4015	0.0093	0.2216	0.0017	2622	28	2173	43	2990	13	0	0	Discordant	17.12433257	27.32441472
190517JW7_31	274.1	228.8	1505	1.1854	8.448	0.21	0.4315	0.0074	0.14171	0.0011	2279.7	23	2312	33	2246	14	2246	14	FinalAge207_206	-1.416853095	-2.938557435
190517JW7_32	51.4	31.1	293	1.707	21.4	0.56	0.6383	0.012	0.2426	0.0025	3155.1	25	3181	46	3133	17	3133	17	FinalAge207_206	-0.820893157	-1.532077881
190517JW7_33	87	90.1	777	0.965	18.03	0.47	0.591	0.011	0.2209	0.0022	2990.5	25	2992	44	2983	16	2983	16	FinalAge207_206	-0.050158836	-0.301709688
190517JW7_34	332.2	355.3	2118	0.928	6.884	0.19	0.3819	0.0072	0.1304	0.0013	2095	24	2085	34	2100	18	2100	18	FinalAge207_206	0.477326969	0.714285714

Table A2.1. U-Pb isotopic data for Rising Star cave and surface samples (Continued).

Sample #_Spot #	U (in ppm)	Th (in ppm)	Pb (in ppm)	Th/U	Pb207 /U235	± 2σ	Pb206 /U238	± 2σ	Pb207 /Pb206	± 2σ	Pb207 /U235	± Ma	Pb206 /U238	± Ma	Pb207 /Pb206	± Ma	Preferred Age	± Ma	Age System	U-Pb/U-Pb Discordance (%)	U-Pb/Pb-Pb Discordance (%)
190517JW7_35	257.9	229.6	2381	1.1149	20.84	0.54	0.5945	0.011	0.2537	0.0019	3130.7	26	3009	45	3206.1	12	3206.1	12	FinalAge207_206	3.887309547	6.147656031
190517JW7_36	98.6	89.9	180	1.083	1.098	0.036	0.1235	0.0024	0.0647	0.0016	753	19	750.6	14	738	56	750.6	14	FinalAge206_238	0.3187251	-1.707317073
190517JW7_37	611.9	169.1	214.8	3.587	0.5865	0.016	0.07515	0.0013	0.05665	0.00088	468.7	11	467.1	8	467	33	467.1	8	FinalAge206_238	0.341369746	-0.021413276
190517JW7_38	80.2	156.3	480	0.5064	2.387	0.063	0.215	0.0033	0.081	0.0019	1236	19	1255	17	1203	47	1203	47	FinalAge207_206	-1.537216828	-4.322527016
190517JW7_39	422	711	3310	0.631	5.237	0.093	0.3331	0.0044	0.1143	0.001	1857.4	15	1853	21	1870	16	1870	16	FinalAge207_206	0.236890277	0.909090909
190517JW7_40	206.4	280.8	2076	0.7276	18.53	0.31	0.5759	0.0073	0.2346	0.0019	3017.4	16	2931	30	3081	13	3081	13	FinalAge207_206	2.863392325	4.868549172
190517JW7_41	165.3	116.8	335.4	1.393	2.06	0.044	0.1948	0.0027	0.0769	0.0012	1133	14	1147	14	1103	31	1103	31	FinalAge207_206	-1.235657546	-3.98912058
190517JW7_42	319.5	112.1	368	2.911	2.508	0.049	0.2189	0.0027	0.08348	0.00096	1272	14	1276	15	1272	23	1272	23	FinalAge207_206	-0.314465409	-0.314465409
190517JW7_43	176.2	262.5	1064	0.6787	6.02	0.13	0.2846	0.0051	0.1543	0.0015	1974	19	1613	25	2389	17	0	0	Discordant	18.28774063	32.48221013
190517JW7_44	493	905	1754	0.5463	3.81	0.09	0.1902	0.0042	0.1465	0.0012	1592	20	1121	23	2302	14	0	0	Discordant	29.58542714	51.3032146
190517JW7_45	193.8	150.7	846	1.269	8.353	0.14	0.4248	0.0054	0.1428	0.0011	2269.8	16	2286	26	2259	14	2259	14	FinalAge207_206	-0.71371927	-1.195219124
190517JW7_46	179	160.5	797	1.086	6.314	0.12	0.366	0.0065	0.1261	0.0015	2018	17	2008	30	2043	22	2043	22	FinalAge207_206	0.495540139	1.713166911
190517JW7_47	618	437	291	1.44	0.3258	0.0083	0.04572	0.00063	0.0521	0.001	286.4	6.4	288.1	3.9	267	43	288.1	3.9	FinalAge206_238	-0.593575419	-7.902621723
190517JW7_48	468	440	906	1.021	3.144	0.1	0.1416	0.0034	0.1617	0.0027	1437	24	853	19	2462	27	0	0	Discordant	40.64022269	65.35337124
190517JW7_49	173.3	288.1	305.7	0.5931	0.59	0.017	0.07663	0.0011	0.0561	0.0015	468.5	11	475.9	6.6	414	58	475.9	6.6	FinalAge206_238	-1.579509072	-14.95169082
190517JW7_50	99.4	199.7	473.8	0.49	1.996	0.052	0.189	0.0028	0.0769	0.0017	1110	18	1115	15	1095	45	1095	45	FinalAge207_206	-0.45045045	-1.826484018
190517JW7_51	485	205.1	483	2.338	1.805	0.035	0.1761	0.0024	0.07453	0.00084	1045.7	13	1045	13	1047	23	1047	23	FinalAge207_206	0.066940805	0.191021968
190517JW7_52	94.6	144	511	0.681	13.21	0.3	0.5144	0.0094	0.1866	0.0022	2693	22	2672	40	2708	20	2708	20	FinalAge207_206	0.77979948	1.329394387
190517JW7_53	158	94.6	115.6	1.681	0.703	0.02	0.0874	0.0014	0.0585	0.0015	541	13	540.1	8.2	527	57	540.1	8.2	FinalAge206_238	0.166358595	-2.485768501
190517JW7_54	264.8	227.1	1044	1.151	6.294	0.12	0.3682	0.005	0.1245	0.0012	2017	16	2020	24	2017	17	2017	17	FinalAge207_206	-0.148735746	-0.148735746
190517JW7_55	309.5	120.9	160.5	2.598	0.663	0.016	0.07845	0.0012	0.0615	0.0013	514.8	9.8	486.8	7	632	46	486.8	7	FinalAge206_238	5.439005439	22.97468354
190517JW7_56	132.6	68.7	83.9	2.1	0.683	0.022	0.0846	0.0014	0.059	0.0017	526	13	523.4	8.3	518	66	523.4	8.3	FinalAge206_238	0.494296578	-1.042471042
190517JW7_57	131.7	108.1	272	1.211	1.992	0.051	0.1867	0.0029	0.0779	0.0016	1110	17	1103	16	1126	41	1126	41	FinalAge207_206	0.630630631	2.042628774
190517JW7_58	550	552	331	1.046	0.2918	0.0082	0.04193	0.00055	0.0505	0.0013	259.3	6.5	264.8	3.4	196	54	264.8	3.4	FinalAge206_238	-2.121095256	-35.10204082
190517JW7_59	5950	140500	174100	0.04309	0.7321	0.013	0.0897	0.0013	0.05961	0.00049	558.6	7.6	553.5	7.7	587	17	553.5	7.7	FinalAge206_238	0.912996778	5.706984668
190517JW7_60	53.89	42.67	57.3	1.255	0.731	0.041	0.0905	0.0018	0.0589	0.0033	551	25	557.9	11	480	120	557.9	11	FinalAge206_238	-1.252268603	-16.22916667
190517JW7_61	508	614	883	0.803	1.446	0.035	0.1452	0.0028	0.0725	0.001	906	15	873	16	994	28	873	16	FinalAge206_238	3.642384106	12.17303823
190517JW7_62	316	310	356.7	1.028	0.671	0.038	0.05415	0.0009	0.0888	0.0044	510	23	339.9	5.5	1250	100	0	0	Discordant	33.35294118	72.808
190517JW7_63	532	1530	1134	0.3579	1.309	0.029	0.1041	0.0019	0.0919	0.0015	849	13	638	11	1454	32	0	0	Discordant	24.85276796	56.12104539
190517JW7_64	166.1	86.5	202.3	1.909	1.182	0.03	0.1315	0.0018	0.0657	0.0014	792	15	796	10	773	45	796	10	FinalAge206_238	-0.505050505	-2.97542044
190517JW7_65	228.7	397.5	872	0.5697	1.423	0.03	0.1447	0.0019	0.0714	0.0012	897.7	13	871.1	11	963	33	871.1	11	FinalAge206_238	2.963127994	9.543094496
190517JW7_66	127	124.2	500	1.0085	4.137	0.08	0.2927	0.0039	0.1026	0.0013	1659	16	1654	20	1664	23	1664	23	FinalAge207_206	0.301386377	0.600961538
190517JW7_67	193.4	157.8	237	1.214	0.865	0.022	0.1038	0.0014	0.0604	0.0013	632.1	11	636.6	8.3	595	48	636.6	8.3	FinalAge206_238	-0.711912672	-6.991596639
190517JW7_68	265.9	64.4	131.7	4.6	1.217	0.028	0.1287	0.0019	0.0686	0.0011	806	13	780.1	11	873	34	780.1	11	FinalAge206_238	3.213399504	10.64146621
190517JW7_69	384.8	407.7	1247	0.9361	2.357	0.043	0.2076	0.0025	0.08238	0.00087	1228.3	13	1216	13	1253	22	1253	22	FinalAge207_206	1.001384027	2.952913009
190517JW7_70	46.8	44.7	108.1	1.035	1.79	0.064	0.1722	0.0036	0.0767	0.0027	1034	23	1023	20	1048	73	1048	73	FinalAge207_206	1.063829787	2.385496183
190517JW7_71	381	411	1075	0.931	9.28	0.27	0.351	0.01	0.192	0.0016	2354	26	1937	49	2756	14	0	0	Discordant	17.71452846	29.71698113
190517JW7_72	14.87	40.2	290.8	0.368	13.53	0.36	0.5202	0.01	0.1884	0.0041	2707	26	2695	43	2712	37	2712	37	FinalAge207_206	0.443295161	0.626843658
190517JW7_73	143.4	167.6	277.7	0.903	1.802	0.045	0.1753	0.0024	0.0743	0.0015	1046	16	1041	13	1039	42	1039	42	FinalAge207_206	0.478011472	-0.192492782
190517JW7_74	520	500	783	1.071	0.839	0.017	0.10092	0.0013	0.06027	0.00083	617.8	9.3	619.7	7.7	600	30	619.7	7.7	FinalAge206_238	-0.307542894	-3.283333333
190517JW7_75	240	401	608	0.624	0.795	0.025	0.0871	0.0013	0.0663	0.0019	591	14	538.5	7.5	771	60	538.5	7.5	FinalAge206_238	8.883248731	30.15564202
190517JW7_76	239.5	180.6	306.5	1.313	0.882	0.021	0.106	0.0014	0.0603	0.0012	641.4	12	649.3	8.2	601	43	649.3	8.2	FinalAge206_238	-1.231680698	-8.036605657
190517JW7_77	436	394	865	1.059	1.868	0.038	0.1798	0.0028	0.0751	0.001	1067.6	13	1065	15	1083	24	1083	24	FinalAge207_206	0.243536905	1.662049861
190517JW7_78	332.4	632	876	0.5232	0.688	0.016	0.08605	0.0011	0.0579	0.0011	530.3	9.9	532	6.7	505	44	532	6.7	FinalAge206_238	-0.32057326	-5.346534653
190517JW7_79	241.6	156.9	485	1.53	2.121	0.044	0.198	0.0025	0.0774	0.0011	1154	14	1165	14	1122	28	1122	28	FinalAge207_206	-0.953206239	-3.832442068
190517JW7_80	536	61.9	109.6	8.88	0.903	0.018	0.10692	0.0013	0.0613	0.00085	653.4	9.9	654.8	7.8	637	30	654.8	7.8	FinalAge206_238	-0.214263851	-2.794348509
190517JW7_81	227.5	131.8	945	1.73	15.28	0.25	0.5536	0.0068	0.1996	0.0014	2831.9	16	2839	28	2821	12	2821	12	FinalAge207_206	-0.250715068	-0.638071606
190517JW7_82	342.2	204.5	1363	1.663	10.381	0.17	0.4645	0.0056	0.1613	0.0012	2468.2	15	2460	25	2467	12	2467	12	FinalAge207_206	0.332225914	0.28374544
190517JW7_83	378	339	479	1.082	0.73	0.019	0.0912	0.0014	0.0577	0.0012	554.8	11	562.4	8.2	505	47	562.4	8.2	FinalAge206_238	-1.369863014	-11.36633663
190517JW7_84	107.6	115.1	91.5	0.936	0.363	0.017	0.04471	0.00084	0.0583	0.0026	311	13	281.9	5.2	461	98	281.9	5.2	FinalAge206_238	9.356913183	38.85032538
190517JW7_85	91.2	43.43	69.4	2.093	0.782	0.026	0.0979	0.0016	0.0578	0.0017	583	15	601.7	9.5	488	61	601.7	9.5	FinalAge206_238	-3.20754717	-23.29918033
190517JW7_86	183.3	183.5	1001	0.9972	6.54	0.12	0.377	0.0048	0.1252	0.0012	2049.5	16	2061	22	2031	17	2031	17	FinalAge207_206	-0.561112466	-1.477104874
190517JW7_87	33.1	71	542	0.4617	15.92	0.36	0.5616	0.0099	0.2054	0.0032	2870	21	2870	41	2864	26	2864	26	FinalAge207_206	0	-0.209497207
190517JW7_88	152.9	273.2	759	0.5542	1.911	0.043	0.1838	0.0023	0.0751	0.0012	1082	15	1087.4	13	1069	31	1069	31	FinalAge207_206	-0.499075786	-1.721234799

Table A2.1. U-Pb isotopic data for Rising Star cave and surface samples (Continued).

Sample #_Spot #	U (in ppm)	Th (in ppm)	Pb (in ppm)	Th/U	Pb207 /U235	± 2σ	Pb206 /U238	± 2σ	Pb207 /Pb206	± 2σ	Pb207 /U235	± Ma	Pb206 /U238	± Ma	Pb207 /Pb206	± Ma	Preferred Age	± Ma	Age System	U-Pb/U-Pb Discordance (%)	U-Pb/Pb-Pb Discordance (%)
190517JW7_89	312	300.8	832	1.027	1.877	0.036	0.1814	0.0023	0.07458	0.00087	1072.7	12	1074.1	12	1054	25	1054	25	FinalAge207_206	-0.130511793	-1.907020873
190517JW7_90	139.4	125.9	656	1.105	6.485	0.12	0.3747	0.0046	0.125	0.0014	2042	16	2051	22	2022	21	2022	21	FinalAge207_206	-0.440744368	-1.434223541
190517JW7_91	327.3	256.8	595	1.269	1.51	0.032	0.1557	0.0022	0.0703	0.001	932.3	13	932.6	12	923	31	932.6	12	FinalAge206_238	-0.032178483	-1.040086674
190517JW7_92	234.4	199.4	384	1.161	1.108	0.025	0.1242	0.0016	0.0646	0.0012	757.4	12	754.8	9.4	741	39	754.8	9.4	FinalAge206_238	0.343279641	-1.862348178
190517JW7_93	73.7	290.8	180	0.2513	0.288	0.028	0.0393	0.0018	0.0527	0.0051	254	22	248	11	260	200	248	11	FinalAge206_238	2.362204724	4.615384615
190517JW7_94	429	1120	859	0.4113	3.89	0.12	0.2027	0.0055	0.1383	0.0014	1601	26	1187	30	2201	17	0	0	Discordant	25.85883823	46.0699682
190517JW7_95	201.7	122.1	318	1.679	1.82	0.037	0.1757	0.0023	0.0747	0.0012	1050.7	14	1043.1	13	1048	33	1048	33	FinalAge207_206	0.723327306	0.467557252
190517JW7_96	128	238	296	0.608	0.684	0.023	0.0849	0.0015	0.0587	0.002	527	14	524.9	8.6	492	73	524.9	8.6	FinalAge206_238	0.398481973	-6.68699187
190517JW7_97	322.8	329	1390	0.979	4.24	0.074	0.2969	0.0036	0.10314	0.0009	1680.3	14	1675	18	1679	16	1679	16	FinalAge207_206	0.315419866	0.238237046
190517JW7_98	246.4	152.4	161.5	1.628	0.54	0.014	0.0709	0.001	0.0553	0.0013	438.2	9.7	442.1	6.3	399	54	442.1	6.3	FinalAge206_238	-0.890004564	-10.80200501
190517JW7_99	306.4	978	803	0.319	8.02	0.23	0.3509	0.0075	0.1644	0.0018	2223	26	1935	36	2495	19	0	0	Discordant	12.95546559	22.44488978
190517JW7_100	521	103.2	148.5	5.28	0.802	0.016	0.09783	0.0012	0.05901	0.00082	597.9	9.1	601.6	7.2	557	30	601.6	7.2	FinalAge206_238	-0.618832581	-8.007181329
190517JW7_101	756	814	1647	0.9192	1.272	0.022	0.1388	0.0017	0.06589	0.0008	832.8	10	837.7	9.8	794	25	837.7	9.8	FinalAge206_238	-0.588376561	-5.503778338
190517JW7_102	184.6	223	1451	0.826	14.09	0.25	0.5305	0.0073	0.1916	0.0018	2754.5	17	2742	31	2754	15	2754	15	FinalAge207_206	0.453802868	0.435729847
190517JW7_103	117.1	119.1	294	1.024	1.768	0.043	0.1674	0.0024	0.0762	0.0015	1032	16	998	13	1084	40	998	13	FinalAge206_238	3.294573643	7.933579336
190517JW7_104	91.4	117.3	457	0.75	4.975	0.11	0.2848	0.0043	0.1267	0.002	1812	19	1615	22	2040	27	0	0	Discordant	10.87196468	20.83333333
190517JW7_105	177.8	162.7	847	1.09	8.184	0.15	0.4179	0.0054	0.1409	0.0016	2250	17	2250	24	2234	19	2234	19	FinalAge207_206	0	-0.716204118
190517JW7_106	157.8	164.4	826	0.9626	6.486	0.11	0.3738	0.0048	0.1252	0.0013	2042.2	16	2046	23	2026	19	2026	19	FinalAge207_206	-0.186073842	-0.987166831
190517JW7_107	197	189	140	0.988	0.624	0.023	0.0682	0.0012	0.0662	0.0022	490	14	425.2	7.1	753	74	425.2	7.1	FinalAge206_238	13.2244898	43.53253652
190517JW7_108	428	771	461	0.5541	0.316	0.016	0.04241	0.00088	0.0539	0.0026	280	13	267.7	5.4	340	110	267.7	5.4	FinalAge206_238	4.392857143	21.26470588
190517JW7_109	278.2	210	1163	1.388	11.79	0.25	0.4698	0.0081	0.1812	0.0015	2583	20	2479	36	2662	14	2662	14	FinalAge207_206	4.026325978	6.874530428
190517JW7_110	60.08	62.8	113.2	0.953	1.109	0.041	0.1274	0.0023	0.0633	0.0022	754	20	773	13	678	70	773	13	FinalAge206_238	-2.519893899	-14.01179941
190517JW7_111	234	154.2	221	1.524	0.829	0.021	0.0991	0.0015	0.0603	0.0012	611.3	12	609.1	8.7	600	42	609.1	8.7	FinalAge206_238	0.359888762	-1.516666667
190517JW7_112	139.9	276.2	728	0.4993	1.936	0.045	0.1849	0.0026	0.0759	0.0014	1092	16	1093	14	1081	37	1081	37	FinalAge207_206	-0.091575092	-1.110083256
100517JW3_1	151.8	180.1	1030	0.8511	6.469	0.068	0.3701	0.0034	0.1273	0.0011	2040.7	9.2	2029	16	2060	15	2060	15	FinalAge207_206	0.57333268	1.504854369
100517JW3_2	264.9	283.3	670	0.955	1.325	0.028	0.1414	0.0025	0.0684	0.0013	856	12	852	14	876	39	852	14	FinalAge206_238	0.46728972	2.739726027
100517JW3_3	241.9	470	2861	0.5176	8.617	0.087	0.4279	0.0045	0.1465	0.0012	2297.8	9.3	2296	20	2303	14	2303	14	FinalAge207_206	0.078335799	0.303951368
100517JW3_4	147.9	152.5	857	0.9816	6.545	0.078	0.3743	0.0039	0.1272	0.0011	2053.3	9.9	2051	18	2056	15	2056	15	FinalAge207_206	0.112014805	0.243190661
100517JW3_5	78.1	139.9	1210	0.571	22.4	0.22	0.625	0.006	0.261	0.0021	3200.2	9.7	3129	24	3252	13	3252	13	FinalAge207_206	2.224860946	3.782287823
100517JW3_6	203.8	202.1	956	1.0223	3.993	0.049	0.2794	0.0025	0.1038	0.0011	1631.6	9.9	1588	13	1690	19	1690	19	FinalAge207_206	2.672223584	6.035502959
100517JW3_7	4.42	67.6	362	0.0658	18.12	0.54	0.3385	0.0096	0.396	0.014	2984	29	1875	46	3861	54	0	0	Discordant	37.16487936	51.43745144
100517JW3_8	109.2	160	217	0.728	0.693	0.029	0.0858	0.0013	0.059	0.0025	533	17	530.3	8	529	94	530.3	8	FinalAge206_238	0.506566604	-0.245746692
100517JW3_9	11.77	187.4	772	0.06322	8.6	0.19	0.2601	0.0046	0.2416	0.0053	2291	20	1489	23	3120	36	0	0	Discordant	35.00654736	52.27564103
100517JW3_10	0.0008	0.027	2.92	no value	no value	NAN	no value	NAN	no value	NAN	no value	NAN	no value	NAN	no value	NAN	#VALUE!	#VALUE!	#VALUE!	#VALUE!	#VALUE!
100517JW3_11	61.8	98.1	608	0.647	7.743	0.1	0.4061	0.0047	0.1391	0.0015	2202	11	2196	22	2214	20	2214	20	FinalAge207_206	0.272479564	0.81300813
100517JW3_12	186	364	271	0.5186	0.3032	0.0086	0.04243	0.00055	0.0519	0.0015	268.3	6.7	267.9	3.4	263	64	267.9	3.4	FinalAge206_238	0.149086843	-1.863117871
100517JW3_13	602	813	631	0.774	0.3519	0.0081	0.04472	0.00053	0.0573	0.0014	305.8	6	282	3.3	484	53	282	3.3	FinalAge206_238	7.782864617	41.73553719
100517JW3_14	469.1	572	2031	0.826	4.469	0.06	0.1509	0.0018	0.2147	0.002	1725	11	906.1	10	2940	15	0	0	Discordant	47.47246377	69.18027211
100517JW3_15	135.8	263	165.2	0.5197	0.272	0.011	0.03815	0.00059	0.0523	0.0021	244.5	9	241.3	3.7	254	86	241.3	3.7	FinalAge206_238	1.308793456	5
100517JW3_16	331.7	266.4	375.4	1.252	0.692	0.011	0.08601	0.00083	0.05852	0.00086	533.6	6.5	531.8	4.9	538	32	531.8	4.9	FinalAge206_238	0.337331334	1.152416357
100517JW3_17	152	522.6	2986	0.2913	6.728	0.075	0.38	0.0034	0.1287	0.0011	2075.2	9.8	2076	16	2077	15	2077	15	FinalAge207_206	-0.038550501	0.048146365
100517JW3_18	790	373.3	870	2.111	1.555	0.021	0.1518	0.0018	0.07434	0.00067	952	8.3	910.9	10	1047	18	910.9	10	FinalAge206_238	4.317226891	12.99904489
100517JW3_19	385	980	1330	0.506	3.82	0.2	0.216	0.011	0.1276	0.0011	1572	39	1251	59	2067	15	0	0	Discordant	20.41984733	39.47750363
100517JW3_20	233.4	253.4	1377	0.929	6.564	0.075	0.3757	0.0039	0.1268	0.0011	2054.7	9.8	2056	18	2052	15	2052	15	FinalAge207_206	-0.063269577	-0.194931774
100517JW3_21	174.3	173.1	239.7	1.012	0.691	0.015	0.08625	0.001	0.0584	0.0012	532.1	8.8	533.3	6.2	524	45	533.3	6.2	FinalAge206_238	-0.225521519	-1.77480916
100517JW3_22	159.3	175.1	979	0.9099	6.532	0.076	0.3751	0.0038	0.1266	0.0011	2049	10	2053	18	2048	15	2048	15	FinalAge207_206	-0.195217179	-0.244140625
100517JW3_23	52.17	92.1	214	0.5653	1.379	0.04	0.1455	0.002	0.0689	0.0019	876	17	875	11	871	57	875	11	FinalAge206_238	0.114155251	-0.45924225
100517JW3_24	7.12	89.5	451	0.0792	14.65	0.38	0.3084	0.0077	0.3487	0.0096	2784	25	1730	38	3687	41	0	0	Discordant	37.8591954	53.07838351
100517JW3_25	1086	1612	2104	0.6801	1.892	0.024	0.08047	0.0008	0.1708	0.0014	1078.5	8.3	498.9	4.8	2564	14	0	0	Discordant	53.74130737	80.54212168
100517JW3_26	10.49	218.7	980	0.04811	16.04	0.34	0.3201	0.0058	0.3661	0.0083	2873	21	1788	28	3761	35	0	0	Discordant	37.76540202	52.45945227
100517JW3_27	83.5	66.3	518	1.269	14.46	0.16	0.538	0.0058	0.195	0.0018	2778.8	11	2774	24	2781	15	2781	15	FinalAge207_206	0.172736433	0.251708019
100517JW3_28	129.7	101.7	565	1.29	6.513	0.075	0.3725	0.0034	0.127	0.0012	2046.4	10	2041	16	2053	17	2053	17	FinalAge207_206	0.26387803	0.584510472

Table A2.1. U-Pb isotopic data for Rising Star cave and surface samples (Continued).

Sample #_Spot #	U (in ppm)	Th (in ppm)	Pb (in ppm)	Th/U	Pb207 /U235	± 2σ	Pb206 /U238	± 2σ	Pb207 /Pb206	± 2σ	Pb207 /U235	± Ma	Pb206 /U238	± Ma	Pb207 /Pb206	± Ma	Preferred Age	± Ma	Age System	U-Pb/U-Pb Discordance (%)	U-Pb/Pb-Pb Discordance (%)
100517JW5_1	32.98	32.9	305	1.039	22.98	0.49	0.651	0.012	0.2566	0.0034	3224	21	3229	45	3222	21	3222	21	FinalAge207_206	-0.155086849	-0.217256363
100517JW5_2	171.9	197.5	1618	0.868	19.45	0.36	0.6094	0.0095	0.2323	0.0021	3062	18	3064	38	3066	14	3066	14	FinalAge207_206	-0.065316786	0.065231572
100517JW5_3	682	540	819	1.243	0.77	0.017	0.0918	0.0015	0.06092	0.00096	578.4	9.6	565.7	8.6	624	35	565.7	8.6	FinalAge206_238	2.19571231	9.342948718
100517JW5_4	646	1622	2451	0.3881	5.539	0.12	0.1826	0.0034	0.2203	0.0023	1902	18	1080	18	2978	17	0	0	Discordant	43.21766562	63.7340497
100517JW5_5	181.8	153.2	365	1.171	1.424	0.044	0.1487	0.0034	0.0693	0.0012	893	18	892	19	892	37	892	19	FinalAge206_238	0.111982083	0
100517JW5_6	666	622	1315	1.061	4.27	0.12	0.1314	0.0033	0.2367	0.0025	1683	23	795	19	3096	16	0	0	Discordant	52.76292335	74.32170543
100517JW5_7	75	57.3	462	1.288	14.57	0.29	0.5445	0.01	0.1949	0.0026	2784	19	2798	42	2777	22	2777	22	FinalAge207_206	-0.502873563	-0.756211739
100517JW5_8	335.6	210.2	290	1.599	0.691	0.018	0.086	0.0015	0.0585	0.0011	531.9	11	531.5	8.9	532	43	531.5	8.9	FinalAge206_238	0.075202106	0.093984962
100517JW5_9	535	113	568	4.88	2.68	0.1	0.1763	0.0044	0.1093	0.0018	1309	28	1045	24	1780	31	0	0	Discordant	20.16806723	41.29213483
100517JW5_10	333.6	283.5	758	1.18	1.719	0.039	0.1707	0.0032	0.0733	0.001	1013	14	1015	17	1009	28	1009	28	FinalAge207_206	-0.197433366	-0.594648167
100517JW5_11	330.9	730	3282	0.4568	13.12	0.24	0.4929	0.008	0.1937	0.0016	2685	18	2580	35	2772	14	2772	14	FinalAge207_206	3.910614525	6.926406926
100517JW5_12	185.1	232.8	1120	0.791	6.736	0.13	0.382	0.006	0.1281	0.0015	2075	17	2084	28	2067	22	2067	22	FinalAge207_206	-0.43373494	-0.822447992
100517JW5_13	88.6	172.8	1598	0.507	22.27	0.42	0.6452	0.011	0.2508	0.0031	3195	19	3207	41	3185	20	3185	20	FinalAge207_206	-0.375586854	-0.690737834
100517JW5_14	90.3	130.7	160.5	0.6845	0.567	0.023	0.073	0.0015	0.0564	0.0022	452	15	454	8.9	405	83	454	8.9	FinalAge206_238	-0.442477876	-12.09876543
100517JW5_15	298.5	291.8	410.3	1.012	0.635	0.018	0.0808	0.0014	0.0569	0.0013	497	11	500.8	8.4	464	53	500.8	8.4	FinalAge206_238	-0.764587525	-7.931034483
100517JW5_16	371	416	1614	0.874	3.633	0.077	0.2585	0.0048	0.1024	0.0012	1553	17	1481	25	1664	22	1664	22	FinalAge207_206	4.636188023	10.99759615
100517JW5_17	94.9	75.6	234	1.251	1.884	0.054	0.1818	0.0034	0.0744	0.0015	1070	19	1076	19	1053	43	1053	43	FinalAge207_206	-0.560747664	-2.184235518
100517JW5_18	818	548	747	1.494	0.776	0.018	0.0884	0.0018	0.06367	0.00094	581.8	10	547	11	718	31	547	11	FinalAge206_238	5.98143692	23.81615599
100517JW5_19	303.7	390.3	2472	0.767	8.116	0.15	0.4218	0.0061	0.14	0.0013	2242	17	2267	28	2222	16	2222	16	FinalAge207_206	-1.115075825	-2.02520252
100517JW5_20	125.4	135.3	236	0.911	0.847	0.026	0.1052	0.0019	0.0588	0.0016	621	14	644.8	11	521	61	644.8	11	FinalAge206_238	-3.83252818	-23.76199616
100517JW5_21	227.1	284.9	1459	0.7885	4.713	0.094	0.3185	0.005	0.1077	0.0015	1767	17	1781	25	1752	26	1752	26	FinalAge207_206	-0.792303339	-1.655251142
100517JW5_22	93.1	86.1	721	1.065	14.92	0.29	0.5541	0.0087	0.1957	0.0022	2807	19	2839	36	2787	19	2787	19	FinalAge207_206	-1.140007125	-1.865805526
100517JW5_23	232	305	2780	0.789	20.99	0.43	0.624	0.012	0.2449	0.0029	3139	19	3125	47	3150	18	3150	18	FinalAge207_206	0.446001911	0.793650794
100517JW5_24	318	506	2506	0.629	4.572	0.095	0.3131	0.0053	0.106	0.0012	1741	17	1755	26	1726	21	1726	21	FinalAge207_206	-0.804135554	-1.6801854
100517JW5_25	794	234.3	714	3.411	1.949	0.04	0.1861	0.003	0.07603	0.00086	1097	14	1099	16	1088	23	1088	23	FinalAge207_206	-0.182315406	-1.011029412
100517JW5_26	184.8	139.7	952	1.297	8.53	0.18	0.4308	0.0077	0.1432	0.002	2286	19	2312	36	2263	25	2263	25	FinalAge207_206	-1.13735783	-2.165267344
100517JW5_27	312	856	4210	0.421	4.761	0.093	0.3156	0.0048	0.1099	0.0013	1776	16	1767	23	1791	22	1791	22	FinalAge207_206	0.506756757	1.340033501
100517JW5_28	99.2	160.3	507	0.6123	1.982	0.054	0.191	0.0036	0.0758	0.0019	1107	19	1126	19	1059	50	1059	50	FinalAge207_206	-1.716350497	-6.326723324
100517JW5_29	384	496	2282	0.771	7.51	0.17	0.3296	0.0065	0.1652	0.0018	2169	21	1834	31	2503	18	0	0	Discordant	15.44490549	26.72792649
100517JW5_30	180	341	2040	0.5167	15.47	0.29	0.5395	0.0084	0.2084	0.0022	2843	18	2782	36	2890	17	2890	17	FinalAge207_206	2.145620823	3.737024221
100517JW5_31	10.28	23.41	86.9	0.438	2.55	0.14	0.223	0.0066	0.0846	0.005	1256	43	1298	35	1130	130	1130	130	FinalAge207_206	-3.343949045	-14.86725664
100517JW5_32	389	349	501	1.098	0.809	0.018	0.0975	0.0016	0.06035	0.00099	601.5	10	599.4	9.4	602	37	599.4	9.4	FinalAge206_238	0.349127182	0.431893688
100517JW5_33	90.7	218.8	149.6	0.4094	0.28	0.019	0.03812	0.00089	0.0532	0.0035	247	15	241.1	5.5	240	130	241.1	5.5	FinalAge206_238	2.388663968	-0.458333333
100517JW5_34	55.28	52.4	330.7	1.05	7.69	0.17	0.4078	0.0069	0.1373	0.0022	2192	20	2203	31	2185	27	2185	27	FinalAge207_206	-0.501824818	-0.823798627
100517JW5_35	81.9	127	400	0.6319	1.974	0.053	0.1893	0.0032	0.0759	0.0016	1102	18	1117	17	1072	43	1072	43	FinalAge207_206	-1.361161525	-4.197761194
100517JW5_36	239.6	141.3	251.2	1.676	0.855	0.02	0.1028	0.0016	0.0608	0.0012	627	11	630.3	9.5	606	44	630.3	9.5	FinalAge206_238	-0.526315789	-4.00990099
100517JW5_37	369.3	508.3	722	0.719	0.692	0.018	0.0854	0.0014	0.0589	0.0012	532.2	11	528.4	8.6	549	42	528.4	8.6	FinalAge206_238	0.714017287	3.752276867
100517JW5_38	120.3	287.5	205	0.4169	0.284	0.015	0.04138	0.00089	0.0504	0.0026	251	12	261.3	5.5	150	110	261.3	5.5	FinalAge206_238	-4.103585657	-74.2
100517JW5_39	349.4	493	1405	0.707	10.38	0.31	0.392	0.011	0.1928	0.0018	2457	27	2123	50	2762	15	0	0	Discordant	13.59381359	23.13540912
100517JW5_40	214	129	355	1.635	1.63	0.042	0.1668	0.0029	0.0709	0.0014	980	16	994	16	938	41	994	16	FinalAge206_238	-1.428571429	-5.970149254
100517JW5_41	550	1135	856	0.484	0.3218	0.011	0.04475	0.00077	0.0528	0.0016	282.2	8	282.1	4.7	282	60	282.1	4.7	FinalAge206_238	0.035435861	-0.035460993
100517JW5_42	140.3	131.5	381	1.056	1.807	0.049	0.176	0.0033	0.0747	0.0018	1044	18	1044	18	1036	49	1036	49	FinalAge207_206	0	-0.772200772
100517JW5_43	159.8	136.5	456	1.152	2.175	0.051	0.2015	0.0035	0.0782	0.0013	1170	16	1185	19	1137	34	1137	34	FinalAge207_206	-1.282051282	-4.221635884
100517JW5_44	191.5	184.6	1032	1.062	6.635	0.13	0.378	0.0055	0.1274	0.0014	2061	17	2068	26	2056	19	2056	19	FinalAge207_206	-0.339640951	-0.583657588
100517JW5_45	332.9	270.5	1555	1.208	7.017	0.14	0.3444	0.0057	0.148	0.0014	2111	17	1906	27	2323	15	0	0	Discordant	9.711037423	17.95092553
100517JW5_46	131.2	191.2	154.2	0.6765	0.327	0.016	0.04371	0.00098	0.0545	0.0026	284	12	275.7	6	320	100	275.7	6	FinalAge206_238	2.922535211	13.84375
100517JW5_47	658	395	1900	1.9	5.098	0.12	0.3043	0.0052	0.1214	0.0015	1832	20	1712	26	1970	23	1970	23	FinalAge207_206	6.550218341	13.0964467
100517JW5_48	251.9	175.7	279.3	1.5	0.791	0.021	0.0965	0.0015	0.0593	0.0012	590	12	593.4	8.8	555	48	593.4	8.8	FinalAge206_238	-0.576271186	-6.918918919
100517JW5_49	187.5	215.9	1279	0.8591	6.537	0.13	0.3785	0.0064	0.1252	0.0015	2049	18	2068	30	2026	22	2026	22	FinalAge207_206	-0.927281601	-2.073050346
100517JW5_50	58.1	92.1	315.6	0.6253	2.321	0.068	0.2092	0.0036	0.0807	0.0022	1212	21	1224	19	1198	53	1198	53	FinalAge207_206	-0.99009901	-2.170283806
100517JW5_51	260.1	297	1669	0.865	6.668	0.13	0.3819	0.0062	0.1269	0.0016	2066	17	2084	29	2050	22	2050	22	FinalAge207_206	-0.87124879	-1.658536585
100517JW5_52	400	39.6	59.2	10.16	0.768	0.016	0.0942	0.0014	0.05946	0.00097	577.8	9.4	580.1	8.2	571	35	580.1	8.2	FinalAge206_238	-0.398061613	-1.593695271
100517JW5_53	98.2	176.5	1172	0.5487	8.51	0.17	0.4341	0.0068	0.1422	0.0019	2284	18	2322	31	2248	24	2248	24	FinalAge207_206	-1.663747811	-3.291814947
100517JW5_54	127.7	78.8	513	1.62	13.8	0.93	0.412	0.026	0.2412	0.0032	2635	74	2180	120	3126	22	0	0	Discordant	17.26755218	30.26231606

Table A2.1. U-Pb isotopic data for Rising Star cave and surface samples (Continued).

Sample #_Spot #	U (in ppm)	Th (in ppm)	Pb (in ppm)	Th/U	Pb207 /U235	± 2σ	Pb206 /U238	± 2σ	Pb207 /Pb206	± 2σ	Pb207 /U235	± Ma	Pb206 /U238	± Ma	Pb207 /Pb206	± Ma	Preferred Age	± Ma	Age System	U-Pb/U-Pb Discordance (%)	U-Pb/Pb-Pb Discordance (%)
100517JW5_55	105.5	217.4	2069	0.4789	23	0.41	0.6655	0.01	0.2507	0.0024	3224	18	3285	39	3185	15	3185	15	FinalAge207_206	-1.892059553	-3.139717425
100517JW5_56	525.8	42.8	45.4	12.54	0.66	0.015	0.08295	0.0012	0.05761	0.00091	513.8	8.9	513.6	7	506	36	513.6	7	FinalAge206_238	0.038925652	-1.501976285
100517JW5_57	51.6	49.1	397	1.051	14.59	0.33	0.5434	0.0093	0.1948	0.0029	2784	22	2795	39	2775	24	2775	24	FinalAge207_206	-0.395114943	-0.720720721
100517JW5_58	125.9	103.3	598	1.202	6.625	0.14	0.3817	0.0062	0.1262	0.0017	2059	18	2082	29	2037	23	2037	23	FinalAge207_206	-1.11704711	-2.209131075
100517JW5_59	522	456	1294	1.161	5.22	0.13	0.2939	0.006	0.1283	0.0013	1851	22	1658	30	2070	18	0	0	Discordant	10.42679633	19.90338164
100517JW5_60	474	336	849	1.428	2.46	0.11	0.1911	0.0074	0.0928	0.0013	1239	32	1122	40	1474	28	0	0	Discordant	9.443099274	23.88059701
100517JW5_61	199.7	453	739	0.433	0.848	0.023	0.1017	0.0016	0.0607	0.0014	622	13	624.3	9.2	602	48	624.3	9.2	FinalAge206_238	-0.36977492	-3.704318937
100517JW5_62	120.7	217.5	317.7	0.5503	0.715	0.025	0.0891	0.0016	0.0582	0.0018	544	15	550	9.3	484	69	550	9.3	FinalAge206_238	-1.102941176	-13.63636364
100517JW5_63	21.4	5.13	8	4.95	0.906	0.061	0.105	0.0028	0.064	0.0044	650	32	645	17	610	130	645	17	FinalAge206_238	0.769230769	-5.737704918
100517JW5_64	216.6	237	1277	0.902	6.511	0.13	0.3762	0.0058	0.1255	0.0013	2046	18	2059	28	2029	19	2029	19	FinalAge207_206	-0.635386119	-1.478560867
100517JW5_65	207.1	208.5	1309	0.98	8.43	0.16	0.4312	0.0063	0.1415	0.0016	2276	17	2310	28	2243	20	2243	20	FinalAge207_206	-1.493848858	-2.987070887
100517JW5_66	72	206	1732	0.3632	18.78	0.41	0.6013	0.011	0.2261	0.0024	3025	21	3031	43	3022	18	3022	18	FinalAge207_206	-0.198347107	-0.297816016
100517JW5_67	149.8	160.5	1217	0.921	14.56	0.28	0.5421	0.0092	0.1945	0.002	2785	18	2790	38	2777	17	2777	17	FinalAge207_206	-0.179533214	-0.468131077
100517JW5_68	61.1	83.1	474	0.735	16.2	0.42	0.526	0.013	0.2241	0.0029	2880	24	2715	53	3005	20	3005	20	FinalAge207_206	5.729166667	9.650582363
100517JW5_69	172.3	413	1585	0.4109	7.51	0.15	0.3593	0.0059	0.1513	0.0022	2172	18	1978	28	2355	25	0	0	Discordant	8.931860037	16.00849257
100517JW5_70	212.9	108.1	179.8	1.943	0.866	0.023	0.1034	0.0016	0.0608	0.0014	631	12	634	9.3	610	50	634	9.3	FinalAge206_238	-0.475435816	-3.93442623
100517JW5_71	315	147.5	390	2.093	1.717	0.037	0.1708	0.0028	0.0729	0.0011	1013	14	1016	15	999	31	999	31	FinalAge207_206	-0.296150049	-1.701701702
100517JW5_72	66.1	96.6	818	0.6824	19.51	0.37	0.6197	0.0097	0.2281	0.0024	3066	19	3105	38	3034	17	3034	17	FinalAge207_206	-1.272015656	-2.340145023
100517JW5_73	215.8	163.6	290.9	1.307	0.98	0.025	0.115	0.0018	0.062	0.0013	692	13	701.5	11	655	46	701.5	11	FinalAge206_238	-1.37283237	-7.099236641
100517JW5_74	398.7	287	423	1.372	0.791	0.022	0.0953	0.0019	0.0601	0.0013	590	12	587	11	600	47	587	11	FinalAge206_238	0.508474576	2.166666667
100517JW5_75	405.5	102.1	127.7	3.941	0.594	0.015	0.07706	0.0012	0.0558	0.0011	473.2	9.7	478.4	7	426	45	478.4	7	FinalAge206_238	-1.098901099	-12.30046948
100517JW5_76	277	558	3100	0.531	13.75	0.33	0.4235	0.01	0.2336	0.0016	2728	22	2272	46	3075	11	0	0	Discordant	16.71554252	26.11382114
100517JW5_77	944	921	4087	1.013	6.22	0.12	0.3105	0.0054	0.1441	0.001	2003	17	1742	26	2274	12	0	0	Discordant	13.03045432	23.39489886
100517JW5_78	34.3	72.8	647	0.4659	20.05	0.29	0.6164	0.0078	0.2342	0.0031	3091	14	3094	31	3079	20	3079	20	FinalAge207_206	-0.097055969	-0.487171159
100517JW5_79	172.9	159.2	131.8	1.067	0.363	0.011	0.04901	0.00065	0.0534	0.0018	313.7	8.1	308.4	4	308	71	308.4	4	FinalAge206_238	1.689512273	-0.12987013
100517JW5_80	107.1	116.1	77.9	0.911	0.273	0.013	0.03884	0.00062	0.0511	0.0026	247	10	245.6	3.8	204	99	245.6	3.8	FinalAge206_238	0.566801619	-20.39215686
100517JW5_81	92.7	127.5	1246	0.709	19.94	0.24	0.5701	0.0072	0.2505	0.0024	3087	12	2907	29	3187	16	3187	16	FinalAge207_206	5.83090379	8.785691873
100517JW5_82	315	229.7	707	1.347	2.008	0.028	0.1912	0.0021	0.07555	0.00094	1117.3	9.3	1128	11	1078	25	1078	25	FinalAge207_206	-0.957665801	-4.638218924
100517JW5_83	153.6	309	398	0.4912	0.593	0.015	0.07623	0.001	0.0562	0.0015	471.6	9.7	473.5	6.1	430	60	473.5	6.1	FinalAge206_238	-0.4028838	-10.11627907
100517JW5_84	180.8	251.8	2263	0.7065	20.28	0.23	0.6223	0.0074	0.2343	0.002	3105.6	11	3118	29	3080	13	3080	13	FinalAge207_206	-0.399278722	-1.233766234
100517JW5_85	247	161	732	1.525	11.17	0.29	0.3553	0.0096	0.2265	0.0015	2528	25	1955	46	3026	11	0	0	Discordant	22.66613924	35.39325843
100517JW5_86	568	553	2337	1.0086	5.687	0.08	0.2494	0.0033	0.1643	0.0011	1928	12	1435	17	2500	12	0	0	Discordant	25.57053942	42.6
100517JW5_87	300.8	302.2	857	0.98	1.812	0.025	0.1758	0.0023	0.07427	0.00077	1048.8	9.2	1044	12	1046	22	1046	22	FinalAge207_206	0.457665904	0.191204589
100517JW5_88	111.2	142	1019	0.7725	10.72	0.13	0.4743	0.0057	0.1634	0.0017	2498	11	2501	25	2487	18	2487	18	FinalAge207_206	-0.120096077	-0.562927222
100517JW5_89	177.7	210.1	574	0.837	1.759	0.028	0.1729	0.0024	0.0737	0.0011	1030.6	11	1028	13	1028	29	1028	29	FinalAge207_206	0.252280225	0
100517JW5_90	614.2	176.7	414	3.44	2.259	0.038	0.2037	0.0036	0.0807	0.0012	1199	12	1195	19	1209	29	1209	29	FinalAge207_206	0.333611343	1.157981803
100517JW5_91	213	257.6	1464	0.82	6.619	0.074	0.3768	0.0037	0.1268	0.0013	2060.8	9.8	2061	17	2053	17	2053	17	FinalAge207_206	-0.009704969	-0.389673648
100517JW5_92	144.1	179.6	1244	0.796	18.08	0.37	0.54	0.012	0.2419	0.004	2993	20	2783	49	3130	27	3130	27	FinalAge207_206	7.016371534	11.08626198
100517JW5_93	133.3	321.2	943	0.4092	1.96	0.03	0.1857	0.0022	0.0763	0.0011	1100.4	10	1098	12	1098	29	1098	29	FinalAge207_206	0.218102508	0
100517JW5_94	108.8	64.4	193.2	1.675	1.855	0.039	0.1794	0.0027	0.0746	0.0018	1064	14	1063	15	1041	49	1041	49	FinalAge207_206	0.093984962	-2.113352546
100517JW5_95	132.4	303	268	0.4472	0.4	0.013	0.05358	0.00091	0.0541	0.0019	340.2	9.7	336.4	5.6	339	78	336.4	5.6	FinalAge206_238	1.116990006	0.766961652
100517JW5_96	120.8	102.4	150.2	1.159	0.747	0.016	0.0861	0.0012	0.0627	0.0015	565	9.4	532.2	6.8	704	46	532.2	6.8	FinalAge206_238	5.805309735	24.40340909
100517JW5_97	200.3	247.2	1372	0.8104	6.562	0.066	0.3742	0.0039	0.1269	0.0011	2053.4	8.9	2051	18	2053	15	2053	15	FinalAge207_206	0.116879322	0.097418412
100517JW5_98	226.7	179.5	1026	1.266	6.561	0.07	0.3747	0.0042	0.1267	0.0011	2053.2	9.5	2051	20	2049	16	2049	16	FinalAge207_206	0.107149815	-0.09760859
100517JW5_99	72.9	87.9	565	0.8	20.14	0.25	0.584	0.0068	0.2499	0.0026	3097	12	2964	28	3181	17	3181	17	FinalAge207_206	4.294478528	6.821754165
100517JW5_100	292	129.7	370	2.253	1.815	0.027	0.1762	0.0021	0.07455	0.00097	1049.9	9.9	1046	12	1051	27	1051	27	FinalAge207_206	0.371463949	0.475737393
100517JW5_101	169.9	318.7	220.2	0.5351	0.288	0.0087	0.04138	0.00058	0.0508	0.0017	257.3	7.1	261.3	3.6	200	70	261.3	3.6	FinalAge206_238	-1.554605519	-30.65
100517JW5_102	79.3	151.6	1320	0.5253	19.81	0.23	0.6125	0.0068	0.2339	0.0019	3080	11	3078	27	3076	13	3076	13	FinalAge207_206	0.064935065	-0.065019506
100517JW5_103	37.3	37.8	337	0.998	19.23	0.26	0.6016	0.0081	0.232	0.0029	3053	13	3034	33	3061	20	3061	20	FinalAge207_206	0.622338683	0.882064685
100517JW5_104	280	111.9	86	2.543	0.3592	0.0091	0.04927	0.00067	0.0528	0.0012	310.9	6.8	310	4.1	301	51	310	4.1	FinalAge206_238	0.289482149	-2.990033223
100517JW5_105	199.3	184.9	1032	1.0794	6.57	0.077	0.3748	0.0039	0.1271	0.0011	2054	10	2051	18	2054	16	2054	16	FinalAge207_206	0.146056475	0.146056475
100517JW5_106	81.5	103	913	0.8	20.67	0.31	0.6274	0.0084	0.2383	0.0027	3121	15	3138	33	3106	18	3106	18	FinalAge207_206	-0.544697212	-1.030264005
100517JW5_107	150	145.2	923	1.035	6.894	0.09	0.3755	0.005	0.1331	0.0013	2096	11	2054	23	2135	17	2135	17	FinalAge207_206	2.003816794	3.793911007
100517JW5_108	854	662	1034	1.293	1.629	0.022	0.1502	0.0018	0.07855	0.00064	980.7	8.3	902.1	10	1161	16	902.1	10	FinalAge206_238	8.014683389	22.2997416

Table A2.1. U-Pb isotopic data for Rising Star cave and surface samples (Continued).

Sample #_Spot #	U (in ppm)	Th (in ppm)	Pb (in ppm)	Th/U	Pb207 /U235	± 2σ	Pb206 /U238	± 2σ	Pb207 /Pb206	± 2σ	Pb207 /U235	± Ma	Pb206 /U238	± Ma	Pb207 /Pb206	± Ma	Preferred Age	± Ma	Age System	U-Pb/U-Pb Discordance (%)	U-Pb/Pb-Pb Discordance (%)
100517JW5_109	207.1	153.4	222.3	1.362	0.701	0.015	0.08711	0.0011	0.0584	0.0012	538.7	8.8	538.4	6.3	527	44	538.4	6.3	FinalAge206_238	0.055689623	-2.163187856
100517JW5_110	90.4	68.7	176.4	1.323	1.457	0.03	0.1447	0.0019	0.0732	0.0015	911	13	871	11	1002	42	871	11	FinalAge206_238	4.390779363	13.0738523
100517JW5_111	196.4	233.6	1335	0.8424	6.658	0.096	0.3789	0.0042	0.1269	0.0014	2066	13	2071	20	2052	19	2052	19	FinalAge207_206	-0.242013553	-0.925925926
100517JW5_112	496.2	544	392.2	0.913	0.2979	0.0054	0.04191	0.00054	0.05165	0.00085	264.5	4.2	264.7	3.3	264	38	264.7	3.3	FinalAge206_238	-0.075614367	-0.265151515
100517JW5_113	88.8	116.7	866	0.779	14.38	0.2	0.5372	0.0074	0.194	0.0023	2774	13	2771	31	2776	21	2776	21	FinalAge207_206	0.10814708	0.180115274
100517JW5_114	109.4	75.5	169.9	1.447	1.21	0.027	0.1328	0.0018	0.0663	0.0015	803	12	803.6	10	806	45	803.6	10	FinalAge206_238	-0.074719801	0.297766749
100517JW5_115	974	670	1843	1.434	2.274	0.062	0.1046	0.0029	0.158	0.0013	1199	20	640	17	2431	13	0	0	Discordant	46.62218515	73.67338544
100517JW5_116	163.4	135.1	872	1.207	8.46	0.098	0.4285	0.0047	0.1433	0.0012	2280.3	11	2298	21	2264	14	2264	14	FinalAge207_206	-0.776213656	-1.501766784
100517JW5_117	181.7	206.6	1164	0.8751	6.521	0.07	0.3749	0.004	0.1264	0.0011	2048.8	9.8	2052	19	2045	16	2045	16	FinalAge207_206	-0.156188989	-0.342298289
100517JW5_118	102.4	73.4	140.1	1.383	1.072	0.028	0.1208	0.0017	0.0645	0.0018	740	15	734.9	9.7	743	58	734.9	9.7	FinalAge206_238	0.689189189	1.090174966
100517JW5_119	365	410	1136	0.902	1.794	0.024	0.1743	0.0021	0.07504	0.00075	1042.5	8.8	1035	12	1065	20	1065	20	FinalAge207_206	0.71942446	2.816901408
100517JW5_120	171.5	189.8	490.3	0.893	1.763	0.029	0.1728	0.002	0.0744	0.0012	1031.9	11	1027	11	1041	33	1041	33	FinalAge207_206	0.474852214	1.344860711
100517JW5_121	65.5	59	81.7	1.106	0.646	0.024	0.0826	0.0013	0.0566	0.0022	503	15	511.6	8	432	86	511.6	8	FinalAge206_238	-1.709741551	-18.42592593
100517JW5_122	486	113	499.3	4.17	2.02	0.053	0.1633	0.0033	0.0897	0.0011	1119	18	975	18	1414	23	975	18	FinalAge206_238	12.86863271	31.0466761
100517JW5_123	209.8	185.8	1083	1.119	6.577	0.069	0.3765	0.0039	0.1268	0.0011	2055.5	9.3	2060	18	2052	15	2052	15	FinalAge207_206	-0.218924836	-0.389863548
100517JW5_124	224	237.8	724	0.932	1.987	0.039	0.1824	0.0025	0.0791	0.0012	1109	13	1080	13	1168	30	1168	30	FinalAge207_206	2.61496844	7.534246575
100517JW5_125	68.8	99.1	828	0.687	17.17	0.22	0.5325	0.006	0.2348	0.002	2943	12	2754	26	3082	14	3082	14	FinalAge207_206	6.422018349	10.64243997
100517JW5_126	166.5	263.5	376.3	0.6213	0.683	0.016	0.08616	0.001	0.0577	0.0013	527.2	9.4	532.7	5.9	503	49	532.7	5.9	FinalAge206_238	-1.043247344	-5.904572565
100517JW5_127	399	74	104.2	5.306	0.683	0.011	0.08592	0.001	0.05789	0.00096	528.2	6.8	531.3	6.1	512	37	531.3	6.1	FinalAge206_238	-0.586898902	-3.76953125
100517JW5_128	181.5	128.1	714.1	1.389	6.608	0.079	0.3772	0.004	0.1274	0.0013	2059.1	11	2062	19	2061	18	2061	18	FinalAge207_206	-0.14083823	-0.048520136
100517JW5_129	247.2	609	3762	0.3959	10.23	0.17	0.4539	0.0074	0.1641	0.0021	2454	15	2411	33	2495	21	2495	21	FinalAge207_206	1.752241239	3.366733467
100517JW5_130	248.3	199.6	1254	1.229	8.182	0.089	0.4195	0.0042	0.142	0.0011	2251.4	9.5	2257	19	2249	13	2249	13	FinalAge207_206	-0.248734121	-0.355713651
100517JW5_131	67.83	80.5	636	0.834	14.4	0.17	0.537	0.0064	0.1956	0.0022	2776	12	2770	27	2788	18	2788	18	FinalAge207_206	0.216138329	0.645624103
100517JW5_132	149.1	263.7	733	0.5571	1.747	0.028	0.172	0.002	0.0739	0.0012	1024.4	10	1024	11	1028	33	1028	33	FinalAge207_206	0.039047247	0.389105058
100517JW5_133	193	234.2	1335	0.8142	6.462	0.084	0.371	0.0044	0.1266	0.0012	2039	11	2033	21	2048	17	2048	17	FinalAge207_206	0.294261893	0.732421875
100517JW5_134	561	448	361	1.344	0.3526	0.0065	0.04844	0.00059	0.05308	0.00099	306.4	4.8	304.9	3.6	316	42	304.9	3.6	FinalAge206_238	0.489556136	3.512658228
100517JW5_135	133.2	109.7	682	1.198	8.328	0.098	0.4206	0.0043	0.1437	0.0012	2266	11	2262	20	2269	14	2269	14	FinalAge207_206	0.176522507	0.30850595
100517JW5_136	219	476.4	678	0.4548	0.686	0.014	0.08592	0.001	0.05768	0.00095	530.5	7.9	531.3	6.1	519	40	531.3	6.1	FinalAge206_238	-0.150801131	-2.369942197
100517JW5_137	130.2	147.3	835	0.8867	6.433	0.083	0.3723	0.004	0.1258	0.0012	2035	11	2040	19	2036	17	2036	17	FinalAge207_206	-0.245700246	-0.196463654
100517JW5_138	315	404	1706	0.7736	4.926	0.068	0.2726	0.0038	0.132	0.0012	1806	12	1553	19	2121	16	0	0	Discordant	14.00885936	26.77982084
100517JW5_139	365	1237	804	0.3024	0.2791	0.0067	0.03921	0.0005	0.0517	0.0013	249.5	5.3	247.9	3.1	257	56	247.9	3.1	FinalAge206_238	0.641282565	3.540856031
100517JW5_140	218.9	673	1879	0.332	1.898	0.032	0.1851	0.0028	0.07471	0.00095	1079	11	1094	15	1053	25	1053	25	FinalAge207_206	-1.390176089	-3.893637227
100517JW5_141	303.1	167.4	118.7	1.8	0.3073	0.0072	0.0432	0.00054	0.0519	0.0012	272.4	5.4	272.6	3.3	258	52	272.6	3.3	FinalAge206_238	-0.073421439	-5.658914729
100517JW5_142	194.5	377.1	256.7	0.5137	0.2894	0.0088	0.04003	0.00058	0.0525	0.0016	257.3	6.9	253	3.6	282	66	253	3.6	FinalAge206_238	1.671200933	10.28368794
100517JW5_143	55.6	88.6	331.4	0.6251	2.832	0.061	0.2367	0.0036	0.087	0.0018	1361	16	1369	19	1349	42	1349	42	FinalAge207_206	-0.587803086	-1.482579689
100517JW5_144	68.6	96.8	61.4	0.707	0.277	0.013	0.03875	0.00079	0.0519	0.0023	246	10	245	4.9	240	97	245	4.9	FinalAge206_238	0.406504065	-2.083333333
100517JW5_145	238	484	237	0.4901	0.1975	0.0074	0.02873	0.00044	0.0501	0.0017	182.5	6.2	182.6	2.8	169	73	182.6	2.8	FinalAge206_238	-0.054794521	-8.047337278
100517JW5_146	213.2	520	2800	0.4129	6.049	0.069	0.3483	0.0037	0.1263	0.0011	1981.8	9.9	1926	18	2044	15	2044	15	FinalAge207_206	2.815622162	5.772994129
100517JW5_147	107	262.2	2369	0.4109	22.13	0.24	0.6409	0.0072	0.2513	0.0018	3188	11	3191	28	3191	11	3191	11	FinalAge207_206	-0.094102886	0
100517JW5_148	69.1	59.5	162.7	1.169	1.601	0.037	0.1608	0.0022	0.0726	0.0017	967	15	961	12	979	49	961	12	FinalAge206_238	0.620475698	1.838610827
100517JW5_149	130.8	113.7	720	1.158	8.225	0.093	0.418	0.0043	0.1435	0.0013	2255.9	11	2251	20	2267	16	2267	16	FinalAge207_206	0.21720821	0.705778562
100517JW5_150	99.2	561	4340	0.1785	13.03	0.14	0.514	0.0057	0.1842	0.0016	2680.6	10	2673	24	2688	15	2688	15	FinalAge207_206	0.283518615	0.558035714
100517JW5_151	190.5	86.1	118.6	2.206	0.671	0.014	0.0838	0.0011	0.0582	0.0013	520.5	8.6	518.6	6.5	522	49	518.6	6.5	FinalAge206_238	0.365033622	0.651340996
100517JW6_1	44.5	54.3	426	0.816	17.99	0.38	0.5907	0.011	0.22	0.0033	2987	20	2990	44	2979	25	2979	25	FinalAge207_206	-0.100435219	-0.369251427
100517JW6_2	33.84	24.82	149.2	1.363	9.45	0.22	0.4437	0.0081	0.1535	0.0028	2379	22	2364	36	2374	31	2374	31	FinalAge207_206	0.630517024	0.421229992
100517JW6_3	194.2	58.7	426.8	3.253	18.71	0.35	0.6154	0.0097	0.2194	0.0021	3024	18	3092	40	2972	15	2972	15	FinalAge207_206	-2.248677249	-4.037685061
100517JW6_4	121.8	171.7	1347	0.7035	19.62	0.35	0.6231	0.009	0.2272	0.002	3071	17	3119	36	3032	14	3032	14	FinalAge207_206	-1.563008792	-2.86939314
100517JW6_5	81.1	167	1329	0.4861	19.93	0.36	0.626	0.0094	0.2302	0.0025	3085	17	3134	36	3048	18	3048	18	FinalAge207_206	-1.588330632	-2.82152231
100517JW6_6	47.7	30.4	75.4	1.634	1.546	0.061	0.1574	0.0032	0.0708	0.0025	940	24	942	18	907	74	942	18	FinalAge206_238	-0.212765957	-3.858875413
100517JW6_7	189.3	156.6	801	1.202	6.583	0.14	0.3777	0.006	0.1256	0.0018	2055	18	2064	28	2031	25	2031	25	FinalAge207_206	-0.437956204	-1.624815362
100517JW6_8	117.8	234.1	2017	0.4969	22.4	0.43	0.649	0.011	0.2488	0.0028	3199	19	3222	42	3173	18	3173	18	FinalAge207_206	-0.71897468	-1.544279861
100517JW6_9	104.3	80.2	344.5	1.301	6.05	0.14	0.3477	0.0065	0.126	0.0021	1981	20	1924	32	2030	29	2030	29	FinalAge207_206	2.877334679	5.221674877
100517JW6_10	71.5	100.1	737	0.717	14.91	0.31	0.5503	0.01	0.1958	0.0024	2806	20	2821	43	2787	21	2787	21	FinalAge207_206	-0.534568781	-1.219949767

Table A2.1. U-Pb isotopic data for Rising Star cave and surface samples (Continued).

Sample #_Spot #	U (in ppm)	Th (in ppm)	Pb (in ppm)	Th/U	Pb207 /U235	± 2σ	Pb206 /U238	± 2σ	Pb207 /Pb206	± 2σ	Pb207 /U235	± Ma	Pb206 /U238	± Ma	Pb207 /Pb206	± Ma	Preferred Age	± Ma	Age System	U-Pb/U-Pb Discordance (%)	U-Pb/Pb-Pb Discordance (%)
100517JW6_11	158.9	189.1	631	0.848	2.838	0.062	0.2363	0.0042	0.087	0.0015	1362	16	1366	22	1345	34	1345	34	FinalAge207_206	-0.293685756	-1.56133829
100517JW6_12	135.1	101.8	835	1.314	21.6	0.41	0.6464	0.01	0.242	0.0025	3163	18	3210	40	3128	16	3128	16	FinalAge207_206	-1.485931078	-2.621483376
100517JW6_13	268	345	1190	0.772	6.47	0.14	0.3727	0.0069	0.1252	0.0015	2041	18	2039	33	2029	22	2029	22	FinalAge207_206	0.097991181	-0.492853622
100517JW6_14	127.8	96.8	463	1.293	5.78	0.19	0.3479	0.0098	0.1191	0.0025	1936	30	1921	47	1938	40	1938	40	FinalAge207_206	0.774793388	0.877192982
100517JW6_15	292	361	1774	0.765	12.39	0.67	0.39	0.02	0.2281	0.0029	2598	58	2092	96	3032	21	0	0	Discordant	19.4765204	31.00263852
100517JW6_16	61.1	80.1	136.4	0.769	1.079	0.07	0.1181	0.0035	0.066	0.0036	735	34	719	20	740	120	719	20	FinalAge206_238	2.176870748	2.837837838
100517JW6_17	63.5	111.4	874	0.573	19.85	0.42	0.624	0.011	0.2295	0.0035	3079	20	3120	45	3042	24	3042	24	FinalAge207_206	-1.331601169	-2.564102564
100517JW6_18	221.3	240.2	1160	0.922	6.499	0.14	0.3732	0.0069	0.126	0.0017	2044	18	2042	32	2039	24	2039	24	FinalAge207_206	0.097847358	-0.147130947
100517JW6_19	101.2	141.8	163.2	0.7027	0.691	0.025	0.0849	0.0017	0.0589	0.002	529	15	525.3	9.9	502	75	525.3	9.9	FinalAge206_238	0.699432892	-4.641434263
100517JW6_20	184	471	2780	0.403	9.51	0.19	0.4513	0.0073	0.1517	0.0016	2385	18	2399	32	2363	17	2363	17	FinalAge207_206	-0.587002096	-1.523487093
100517JW6_21	299.1	33.2	69.4	9.67	0.865	0.026	0.0977	0.0021	0.0638	0.0013	630	14	600	12	713	44	600	12	FinalAge206_238	4.761904762	15.84852735
100517JW6_22	703	655	964	1.291	1.72	0.036	0.1624	0.0027	0.07658	0.00096	1014	14	970	15	1103	26	970	15	FinalAge206_238	4.339250493	12.05802357
100517JW6_23	359.9	234.9	287.2	1.505	0.66	0.016	0.0836	0.0014	0.057	0.0012	513.3	9.5	517.4	8.5	470	46	517.4	8.5	FinalAge206_238	-0.798753166	-10.08510638
100517JW6_24	101.7	134.1	198.8	0.7488	0.806	0.029	0.0996	0.002	0.0589	0.0019	597	16	612	11	517	68	612	11	FinalAge206_238	-2.512562814	-18.37524178
100517JW6_25	174.6	161.4	834	1.08	6.58	0.14	0.3782	0.0064	0.1252	0.0018	2054	19	2066	30	2025	25	2025	25	FinalAge207_206	-0.584225901	-2.024691358
100517JW6_26	95.2	122.9	843	0.774	14.45	0.29	0.5426	0.0091	0.1928	0.0028	2776	19	2795	39	2757	23	2757	23	FinalAge207_206	-0.68443804	-1.378309757
100517JW6_27	259.5	156.1	889	1.659	8.76	0.17	0.4339	0.0074	0.1459	0.0016	2311	18	2321	33	2293	20	2293	20	FinalAge207_206	-0.432713111	-1.221107719
100517JW6_28	142.7	286	2201	0.4973	19.59	0.38	0.6145	0.01	0.2298	0.0028	3068	19	3085	40	3045	19	3045	19	FinalAge207_206	-0.55410691	-1.3136289
100517JW6_29	167.2	104.2	645	1.538	18.59	0.41	0.595	0.012	0.2254	0.0031	3016	21	3014	47	3014	22	3014	22	FinalAge207_206	0.066312997	0
100517JW6_30	114.2	164.3	1299	0.6887	19.89	0.43	0.622	0.012	0.2304	0.003	3082	21	3115	48	3050	21	3050	21	FinalAge207_206	-1.07073329	-2.131147541
100517JW6_31	149.5	175.8	1279	0.839	16.08	0.38	0.523	0.012	0.2219	0.0026	2878	22	2707	49	2994	18	2994	18	FinalAge207_206	5.941626129	9.585838343
100517JW6_32	288.3	179	423.2	1.587	1.623	0.037	0.1646	0.0029	0.0707	0.0011	976	14	982	16	939	32	982	16	FinalAge206_238	-0.614754098	-4.579339723
100517JW6_33	113.4	114.3	675	0.994	15.97	0.47	0.498	0.014	0.2319	0.0028	2864	27	2594	61	3060	19	0	0	Discordant	9.427374302	15.22875817
100517JW6_34	67.7	68.2	165.2	0.984	1.759	0.049	0.1756	0.0036	0.0726	0.002	1025	18	1044	20	972	55	972	55	FinalAge207_206	-1.853658537	-7.407407407
100517JW6_35	89.2	156	1095	0.591	19.81	0.4	0.579	0.01	0.2482	0.0031	3080	19	2949	42	3166	20	3166	20	FinalAge207_206	4.253246753	6.854074542
100517JW6_36	191.8	251.2	639	0.754	1.94	0.051	0.1859	0.0037	0.0756	0.0014	1091	18	1098	20	1072	36	1072	36	FinalAge207_206	-0.641613199	-2.425373134
100517JW6_37	144.8	118.1	819	1.277	17.31	0.34	0.568	0.0099	0.2201	0.0024	2950	20	2896	40	2976	18	2976	18	FinalAge207_206	1.830508475	2.688172043
100517JW6_38	251.4	362	923	0.6865	1.894	0.044	0.1828	0.0033	0.0747	0.0012	1079	15	1082	18	1048	32	1048	32	FinalAge207_206	-0.278035218	-3.244274809
100517JW6_39	314.4	388	2472	0.8046	11.81	0.24	0.4929	0.009	0.1725	0.0019	2586	19	2580	39	2581	20	2581	20	FinalAge207_206	0.232018561	0.038744673
100517JW6_40	223	35.1	282	6.24	22.61	0.46	0.649	0.012	0.2505	0.0027	3207	20	3220	47	3184	17	3184	17	FinalAge207_206	-0.405363268	-1.130653266
100517JW6_41	450	448	540	0.994	0.643	0.016	0.0817	0.0015	0.0567	0.001	502.6	9.9	506	8.7	473	41	506	8.7	FinalAge206_238	-0.676482292	-6.976744186
100517JW6_42	121.4	285.7	366.3	0.4192	0.719	0.024	0.0899	0.0018	0.0584	0.0018	550	15	554.8	11	490	66	554.8	11	FinalAge206_238	-0.872727273	-13.2244898
100517JW6_43	87.1	258.3	1021	0.3354	3.84	0.091	0.2846	0.0055	0.0977	0.0018	1599	20	1613	28	1575	34	1575	34	FinalAge207_206	-0.875547217	-2.412698413
100517JW6_44	715	757	1405	0.941	1.193	0.03	0.1305	0.0026	0.0659	0.001	795	14	790	15	797	32	790	15	FinalAge206_238	0.628930818	0.878293601
100517JW6_45	171.4	166.5	1359	1.025	28.14	0.65	0.698	0.017	0.2932	0.0039	3420	23	3408	63	3431	21	3431	21	FinalAge207_206	0.350877193	0.670358496
100517JW6_46	264	322	2575	0.811	20.08	0.43	0.615	0.013	0.2357	0.0027	3092	21	3086	52	3089	19	3089	19	FinalAge207_206	0.194049159	0.097118809
100517JW6_47	89.4	106.7	777	0.837	17.72	0.37	0.5657	0.011	0.2268	0.0031	2974	20	2891	46	3025	22	3025	22	FinalAge207_206	2.790854069	4.429752066
100517JW6_48	258	563	357	0.4569	0.298	0.011	0.0429	0.00092	0.0505	0.0019	265.7	9.3	270.7	5.7	193	79	270.7	5.7	FinalAge206_238	-1.881821603	-40.25906736
100517JW6_49	87.5	119.4	1022	0.72	27.17	0.54	0.693	0.013	0.285	0.0033	3389	19	3389	48	3387	18	3387	18	FinalAge207_206	0	-0.059049306
100517JW6_50	149.6	142.8	360.1	1.057	1.547	0.043	0.1519	0.0035	0.0737	0.0015	946	17	911	19	1017	42	911	19	FinalAge206_238	3.699788584	10.42281219
100517JW6_51	145.3	163.3	1212	0.877	16.65	0.32	0.5826	0.0098	0.2071	0.0027	2912	18	2964	40	2878	22	2878	22	FinalAge207_206	-1.785714286	-2.98818624
100517JW6_52	475	885	2020	0.56	7.26	0.17	0.2322	0.0054	0.2267	0.0027	2139	21	1343	28	3024	20	0	0	Discordant	37.21365124	55.58862434
100517JW6_53	62.8	63.5	527	0.987	22.18	0.48	0.6492	0.011	0.2458	0.0035	3187	21	3221	44	3150	23	3150	23	FinalAge207_206	-1.066834013	-2.253968254
100517JW6_54	124.1	93.2	263.2	1.34	2.202	0.056	0.2017	0.004	0.079	0.0016	1178	18	1184	21	1153	41	1153	41	FinalAge207_206	-0.509337861	-2.688638335
100517JW6_55	188	219.8	353.1	0.841	1.036	0.027	0.1178	0.0026	0.0641	0.0014	719	14	717	15	721	46	717	15	FinalAge206_238	0.278164117	0.554785021
100517JW6_56	204.6	211.9	692	0.964	5.82	0.13	0.3356	0.0067	0.1252	0.0017	1944	19	1863	32	2022	25	2022	25	FinalAge207_206	4.166666667	7.863501484
100517JW6_57	124	335.8	2430	0.3644	16.89	0.35	0.5787	0.01	0.2116	0.0026	2926	21	2939	42	2916	20	2916	20	FinalAge207_206	-0.44429255	-0.788751715
100517JW6_58	48.8	42	317.3	1.156	22.53	0.5	0.643	0.012	0.2538	0.0035	3202	22	3193	49	3203	22	3203	22	FinalAge207_206	0.281074329	0.312207306
100517JW6_59	238.2	290	726	0.812	1.726	0.038	0.1699	0.0035	0.0737	0.0014	1017	15	1010	20	1020	39	1020	39	FinalAge207_206	0.688298918	0.980392157
100517JW6_60	180.1	307.2	1594	0.5815	6.611	0.14	0.3838	0.0063	0.1246	0.0017	2060	18	2092	29	2016	24	2016	24	FinalAge207_206	-1.553398058	-3.76984127
100517JW6_61	239	255	1209	0.949	6.28	0.14	0.365	0.0069	0.1248	0.0019	2012	20	2003	33	2018	26	2018	26	FinalAge207_206	0.447316103	0.743310208
100517JW6_62	104	58.6	374	1.759	16.45	0.35	0.5689	0.011	0.2107	0.0026	2901	21	2898	45	2904	20	2904	20	FinalAge207_206	0.103412616	0.20661157
100517JW6_63	908	1715	3304	0.5222	1.631	0.036	0.1506	0.0029	0.0785	0.00095	980	14	903	16	1151	24	903	16	FinalAge206_238	7.857142857	21.54648132
100517JW6_64	333.2	192.1	958	1.72	6.41	0.13	0.374	0.0066	0.1237	0.0016	2031	18	2046	31	2004	23	2004	23	FinalAge207_206	-0.738552437	-2.095808383

Table A2.1. U-Pb isotopic data for Rising Star cave and surface samples (Continued).

Sample #_Spot #	U (in ppm)	Th (in ppm)	Pb (in ppm)	Th/U	Pb207 /U235	± 2σ	Pb206 /U238	± 2σ	Pb207 /Pb206	± 2σ	Pb207 /U235	± Ma	Pb206 /U238	± Ma	Pb207 /Pb206	± Ma	Preferred Age	± Ma	Age System	U-Pb/U-Pb Discordance (%)	U-Pb/Pb-Pb Discordance (%)
100517JW6_65	251.2	394.6	571	0.6335	0.855	0.023	0.101	0.0021	0.0613	0.0012	625	12	620	12	633	44	620	12	FinalAge206_238	0.8	2.05371248
100517JW6_66	635	235.9	1074	2.751	4.52	0.21	0.1498	0.0067	0.2184	0.0026	1705	40	895	38	2967	20	0	0	Discordant	47.50733138	69.83485002
100517JW6_67	299	462	1688	0.639	6.46	0.15	0.3533	0.0071	0.1326	0.0019	2035	20	1951	35	2126	24	2126	24	FinalAge207_206	4.127764128	8.231420508
100517JW6_68	73.9	100.5	262	0.736	1.925	0.07	0.1872	0.0045	0.0747	0.0024	1085	25	1105	24	1026	69	1026	69	FinalAge207_206	-1.843317972	-7.699805068
100517JW6_69	242.2	344	1237	0.709	5.757	0.12	0.332	0.0068	0.1258	0.0015	1936	19	1845	33	2034	21	2034	21	FinalAge207_206	4.700413223	9.292035398
100517JW6_70	113.6	151.3	99.2	0.766	0.316	0.043	0.0402	0.0022	0.0578	0.0076	274	32	254	14	370	270	254	14	FinalAge206_238	7.299270073	31.35135135
100517JW6_71	299	415	279	0.777	0.314	0.012	0.04376	0.00099	0.0521	0.0018	277.6	9.6	276.1	6.1	257	74	276.1	6.1	FinalAge206_238	0.540345821	-7.431906615
100517JW6_72	53.7	112.2	775	0.4797	18.19	0.41	0.585	0.012	0.2259	0.0037	2997	22	2963	50	3014	26	3014	26	FinalAge207_206	1.134467801	1.692103517
100517JW6_73	164.7	140.4	865	1.168	8.41	0.18	0.4276	0.0082	0.1428	0.002	2273	20	2293	37	2259	24	2259	24	FinalAge207_206	-0.879894413	-1.505090748
100517JW6_74	160.8	225	1760	0.76	22.16	0.54	0.643	0.014	0.2508	0.0032	3187	24	3206	52	3183	20	3183	20	FinalAge207_206	-0.596171949	-0.722588753
100517JW6_75	173.8	112.5	178.5	1.513	0.868	0.029	0.1033	0.0021	0.0604	0.0018	631	16	634	12	581	64	634	12	FinalAge206_238	-0.475435816	-9.122203098
100517JW6_76	456	117.7	205.2	3.92	1.046	0.026	0.1182	0.0023	0.0644	0.0011	725	13	720	13	736	38	720	13	FinalAge206_238	0.689655172	2.173913043
100517JW6_77	147.5	164	311	0.903	1.069	0.034	0.1212	0.0024	0.0642	0.0017	733	17	737	14	712	57	737	14	FinalAge206_238	-0.545702592	-3.511235955
100517JW6_78	208.6	256.8	1395	0.803	6.79	0.15	0.3868	0.008	0.1272	0.0017	2085	19	2109	36	2054	23	2054	23	FinalAge207_206	-1.151079137	-2.677702045
100517JW6_79	229.6	185.2	1011	1.235	6.66	0.15	0.3796	0.0069	0.1269	0.0016	2065	20	2072	32	2050	23	2050	23	FinalAge207_206	-0.338983051	-1.073170732
100517JW6_80	636	622	1707	1.041	2.05	0.043	0.1907	0.0036	0.07832	0.00095	1130	15	1124	20	1147	24	1147	24	FinalAge207_206	0.530973451	2.005231037
100517JW6_81	290.5	621.9	5574	0.4634	23.59	0.48	0.635	0.012	0.2695	0.0028	3248	20	3166	46	3303	16	3303	16	FinalAge207_206	2.524630542	4.147744475
100517JW6_82	519	899	2241	0.568	1.431	0.034	0.1451	0.0026	0.0717	0.0012	900	14	873	15	962	34	873	15	FinalAge206_238	3	9.251559252
100517JW6_83	412	26.5	39.7	15.21	0.894	0.022	0.1054	0.0022	0.0618	0.0012	646.7	12	645	13	645	41	645	13	FinalAge206_238	0.262873048	0
100517JW6_84	249.4	498.8	1375	0.4937	1.738	0.042	0.1723	0.0031	0.0733	0.0013	1021	16	1024	17	1003	37	1003	37	FinalAge207_206	-0.293829579	-2.093718843
100517JW6_85	190.6	252.5	1511	0.7538	9.49	0.2	0.4445	0.0081	0.1553	0.0019	2384	19	2368	36	2399	21	2399	21	FinalAge207_206	0.67114094	1.292205085
100517JW6_86	597	1278	2051	0.453	1.557	0.034	0.1471	0.003	0.0771	0.0011	951	14	884	17	1111	29	884	17	FinalAge206_238	7.045215563	20.4320432
100517JW6_87	414.9	949	590	0.4298	0.2675	0.0088	0.03843	0.00079	0.0506	0.0015	240.6	7.1	243	4.9	200	61	243	4.9	FinalAge206_238	-0.997506234	-21.5
100517JW6_88	256	219.2	1237	1.163	6.675	0.13	0.3829	0.007	0.1272	0.0016	2066	18	2087	33	2052	23	2052	23	FinalAge207_206	-1.016456922	-1.705653021
100517JW6_89	154	222.9	1388	0.684	7.7	0.17	0.4101	0.0075	0.136	0.0018	2191	20	2216	33	2175	23	2175	23	FinalAge207_206	-1.141031492	-1.885057471
100517JW6_90	166.3	113.5	334	1.437	2.015	0.048	0.1921	0.0034	0.0764	0.0015	1117	16	1132	18	1083	40	1083	40	FinalAge207_206	-1.342882722	-4.524469067
100517JW6_91	252.4	364.4	2335	0.679	9.63	0.2	0.4572	0.0078	0.1535	0.0018	2397	18	2424	34	2383	20	2383	20	FinalAge207_206	-1.12640801	-1.720520352
100517JW6_92	432.3	388	487	1.214	0.921	0.024	0.1081	0.0022	0.0621	0.001	661	13	661	13	668	38	661	13	FinalAge206_238	0	1.047904192
100517JW6_93	705	726	2080	0.999	2.869	0.093	0.1264	0.0041	0.1658	0.0023	1364	24	766	23	2510	23	0	0	Discordant	43.84164223	69.48207171
100517JW6_94	481	412	1212	1.164	2.054	0.044	0.1943	0.0036	0.0769	0.001	1134	15	1146	20	1108	27	1108	27	FinalAge207_206	-1.058201058	-3.429602888
100517JW6_95	200	230.5	1252	0.86	6.537	0.13	0.3761	0.0065	0.1272	0.0018	2049	19	2056	30	2053	25	2053	25	FinalAge207_206	-0.341630063	-0.146127618
100517JW6_96	232	270.9	1394	0.853	6.45	0.14	0.3754	0.0068	0.1255	0.0017	2038	19	2052	32	2031	23	2031	23	FinalAge207_206	-0.686947988	-1.033973412
100517JW6_97	135.5	53.2	129	2.599	1.269	0.04	0.1368	0.0028	0.0671	0.0015	828	18	826	16	826	49	826	16	FinalAge206_238	0.241545894	0
100517JW6_98	216	258.1	211.6	0.821	0.369	0.014	0.0495	0.0012	0.0544	0.0018	316.7	10	311.4	7.3	345	70	311.4	7.3	FinalAge206_238	1.673508052	9.739130435
100517JW6_99	154.5	278.1	1305	0.5505	4.704	0.11	0.3167	0.0066	0.1081	0.0017	1763	19	1771	32	1755	28	1755	28	FinalAge207_206	-0.45377198	-0.911680912
100517JW6_100	250.6	280.5	2190	0.881	16.29	0.33	0.5818	0.01	0.203	0.0022	2891	19	2952	42	2852	17	2852	17	FinalAge207_206	-2.109996541	-3.50631136
100517JW6_101	89.1	152.2	739	0.582	4.99	0.13	0.3297	0.0071	0.1108	0.0021	1811	22	1834	35	1796	35	1796	35	FinalAge207_206	-1.270016565	-2.115812918
100517JW6_102	49.4	67	552	0.73	19.98	0.45	0.633	0.013	0.23	0.0034	3086	22	3161	51	3043	24	3043	24	FinalAge207_206	-2.430330525	-3.877752218
100517JW6_103	81	118.7	796	0.678	10.93	0.23	0.4822	0.008	0.1648	0.0023	2513	19	2534	35	2497	23	2497	23	FinalAge207_206	-0.835654596	-1.481778134
100517JW6_104	321.7	440.9	610	0.72	0.697	0.019	0.0861	0.0017	0.0588	0.0012	535.9	11	532.4	9.9	530	46	532.4	9.9	FinalAge206_238	0.653106923	-0.452830189
100517JW6_105	314.7	556	1525	0.57	2.01	0.046	0.1947	0.0036	0.075	0.0012	1117	15	1146	20	1057	33	1057	33	FinalAge207_206	-2.596239928	-8.420056764
100517JW6_106	137.9	408.6	275	0.3316	0.301	0.019	0.0417	0.0013	0.0533	0.0035	265	15	264.6	8.2	250	130	264.6	8.2	FinalAge206_238	0.150943396	-5.84
100517JW6_107	84.4	109.8	77.3	0.76	0.308	0.016	0.04249	0.0011	0.0536	0.003	269	13	268.1	6.5	250	110	268.1	6.5	FinalAge206_238	0.334572491	-7.24
100517JW6_108	133.4	108.9	150.9	1.215	0.663	0.024	0.0824	0.0017	0.059	0.0019	513	14	510.1	10	512	71	510.1	10	FinalAge206_238	0.565302144	0.37109375
100517JW6_109	226.7	137.3	207.6	1.644	0.802	0.021	0.0985	0.0019	0.0596	0.0014	597	12	605.4	11	558	52	605.4	11	FinalAge206_238	-1.407035176	-8.494623656
100517JW6_110	258.9	155.3	1093	1.717	13.46	0.36	0.4627	0.01	0.2102	0.0027	2703	25	2446	45	2900	20	0	0	Discordant	9.507954125	15.65517241
100517JW6_111	38.56	46.27	407	0.829	19.96	0.47	0.623	0.013	0.2331	0.0039	3084	22	3137	54	3064	27	3064	27	FinalAge207_206	-1.718547341	-2.382506527
100517JW6_112	59.7	94.6	597	0.638	7.85	0.2	0.4091	0.0087	0.1396	0.0028	2211	23	2208	40	2210	35	2210	35	FinalAge207_206	0.13568521	0.090497738

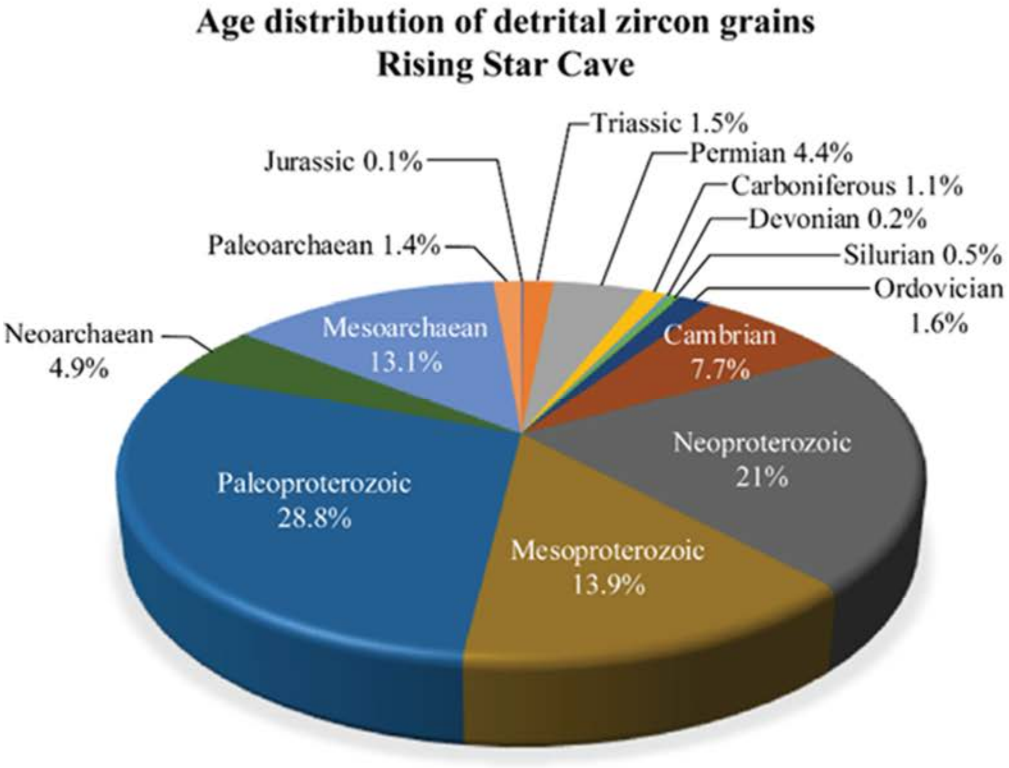

	Age (Ma)	Zircon grains	% of total zircon grains
🟦	182.6	1	0.1
🟧	238 - 248.2	13	1.5
⬜	253 - 298.7	39	4.4
🟨	300.9 - 339.2	10	1.1
🟦	407.6 - 417.1	2	0.2
🟩	425.2 - 442.1	4	0.5
🟦	447.5 - 478.4	14	1.6
🟫	486.8 - 540.8	68	7.7
⬛	542.9 - 999	186	21.0
🟫	1002 - 1575	123	13.9
🟦	1650 - 2497	255	28.8
🟩	2534 - 2795	43	4.9
🟦	2804 - 3197	116	13.1
🟧	3203 - 3431	12	1.4
	Total	**886**	**100.2%**

Figure A2.2. Age distribution of concordant Rising Star Cave detrital zircons. Pie chart overview of the age distributions and associated zircon quantity and percentages for each period.

Table A2.2. Cumulative probability data for Rising Star cave and surface samples (n=15).

	Rising Star Cave sediment samples						Rising Star Cave surface sediment samples						
Age (Ma)	**UW101-1783A, C, L**	**OSL-4**	**260517JW8**	**100517JW3**	**100517JW5**	**100517JW6**	**190517JW1**	**190517JW2**	**190517JW3**	**190517JW4**	**190517JW5**	**190517JW6**	**190517JW7**
170	0	0	0	0	0	0	0	0	0	0	0	0	0
203.46	1.44059E-08	1.49249E-18	0	6.32516E-34	0.00775248	2.70654E-07	0	6.12682E-16	4.33329E-30	1.2078E-23	2.42217E-31	9.49484E-27	2.57755E-08
236.92	1.70158E-07	0.000107871	0	0.000205472	0.008051875	0.000539202	1.11261E-10	0.001800425	0.000445319	1.06078E-19	3.81459E-06	6.34727E-19	0.000579064
270.38	3.44528E-05	0.046680525	0	0.059244439	0.057876807	0.02496063	0.023833286	0.037576336	0.023268348	1.93095E-15	0.035084188	0.000544054	0.025831223
303.84	0.037488293	0.081534982	0	0.149466306	0.08933907	0.056901943	0.024356496	0.055228546	0.044405036	0.009650849	0.086666673	0.018867336	0.06908334
337.3	0.042560313	0.081534989	0	0.149466842	0.112603128	0.065977529	0.024356496	0.079965897	0.044405065	0.022478858	0.117314532	0.018867772	0.070317574
370.76	0.042715728	0.081541225	2.62839E-32	0.149466842	0.118670836	0.066038191	0.024356496	0.079965897	0.044405065	0.02247891	0.117314644	0.018867772	0.079250447
404.22	0.043198209	0.082100146	0.000741956	0.149466842	0.118670844	0.066038191	0.02439384	0.079965897	0.044405065	0.0224829	0.117314644	0.018867772	0.079251826
437.68	0.044379823	0.089621201	0.082971141	0.149466842	0.118719108	0.066038191	0.048277102	0.079966024	0.045368731	0.022601871	0.117314748	0.019105233	0.087442279
471.14	0.046662882	0.1185892	0.082971141	0.149466842	0.125993744	0.066038251	0.054050688	0.106469378	0.055518858	0.024053698	0.125243783	0.03830231	0.103338927
504.6	0.051134396	0.125856116	0.082971141	0.149469256	0.144150585	0.069120467	0.081977844	0.159943774	0.06734518	0.031775035	0.13886863	0.059582755	0.12816833
538.06	0.098035872	0.142739013	0.085345246	0.220054045	0.194367602	0.104906544	0.145182356	0.194489315	0.1622096	0.061528869	0.185026973	0.112317368	0.161939844
571.52	0.143418521	0.142945975	0.166296691	0.299562037	0.240169644	0.120877706	0.172913283	0.218871817	0.227905333	0.104304448	0.248659521	0.175714642	0.220749348
604.98	0.197670072	0.155748367	0.166296691	0.299562842	0.266689867	0.130797565	0.213229269	0.23191835	0.287082762	0.149466574	0.285809606	0.208142728	0.249374121
638.44	0.256872356	0.170954302	0.166296691	0.299562842	0.289695501	0.163915887	0.222997189	0.242586762	0.327081054	0.203689456	0.331252933	0.245193779	0.289530069
671.9	0.264957845	0.204372764	0.166296691	0.299562842	0.310073912	0.184515327	0.240184888	0.262995005	0.333305568	0.243482247	0.359542668	0.288231969	0.323498636
705.36	0.27898258	0.234085202	0.166296691	0.299562842	0.314201653	0.191765487	0.263983548	0.279310405	0.333305895	0.261023849	0.362195015	0.301849604	0.336441785
738.82	0.281943709	0.27339077	0.166296691	0.299562842	0.321522474	0.214786634	0.268267214	0.279966325	0.333547324	0.271942735	0.364174962	0.307836592	0.337742478
772.28	0.296174347	0.285481274	0.166296691	0.299562842	0.326053798	0.226613462	0.268267393	0.279984593	0.342469305	0.283202946	0.377157509	0.32018739	0.357649028
805.74	0.303636074	0.285638362	0.167672008	0.299567819	0.328532189	0.233709782	0.268358737	0.295308232	0.344424754	0.29286772	0.382320523	0.320834398	0.386271298
839.2	0.303646445	0.285645843	0.247178659	0.303866923	0.333521307	0.24213846	0.280942738	0.338526517	0.344457537	0.303700358	0.383322299	0.322429359	0.399005055
872.66	0.303675979	0.286499828	0.24970077	0.352059126	0.33669433	0.250201285	0.292591244	0.339975357	0.344800651	0.310364217	0.393557876	0.336575717	0.412565798
906.12	0.303969204	0.298417747	0.25004831	0.405563951	0.348910123	0.269812822	0.292669982	0.339975506	0.363222092	0.31938982	0.394140929	0.358455062	0.425685287
939.58	0.305672228	0.316393107	0.252275109	0.448814869	0.356647879	0.287973911	0.292853981	0.339975983	0.380988628	0.339672446	0.395181209	0.393235087	0.432365865
973.04	0.312736362	0.327105135	0.260733694	0.449656516	0.367595017	0.305585593	0.294807553	0.342871219	0.402295262	0.352322072	0.398936629	0.416751802	0.440738797
1006.5	0.341000646	0.356817245	0.280051023	0.449656516	0.391484737	0.328323841	0.306879103	0.370422751	0.421645463	0.364872366	0.409755588	0.430211067	0.458847553
1039.96	0.359055638	0.372387588	0.307698607	0.449656516	0.422586679	0.345732152	0.338938117	0.380016357	0.432533115	0.378614813	0.431958377	0.451161057	0.484346688
1073.42	0.374270618	0.387811482	0.335704178	0.449656516	0.462158382	0.365313888	0.379440516	0.382174641	0.449047595	0.39536497	0.463310272	0.475427926	0.519259691
1106.88	0.39135325	0.401673198	0.361055911	0.449656516	0.493834198	0.38336733	0.407890379	0.392888218	0.467572093	0.413205236	0.495519012	0.493938267	0.55581969
1140.34	0.40513733	0.409577787	0.383985996	0.449656516	0.50997293	0.398229837	0.429150224	0.410225958	0.483750701	0.429701895	0.521578729	0.504469931	0.581765115
1173.8	0.410966903	0.416395009	0.401581913	0.449656516	0.520200133	0.409184933	0.455792218	0.419120818	0.499972165	0.444382519	0.53870368	0.508359909	0.595911264
1207.26	0.412263036	0.422061294	0.411413938	0.449656516	0.529234409	0.413729668	0.46837765	0.421160549	0.513854206	0.455124885	0.549137235	0.509238422	0.603584647
1240.72	0.412434995	0.425859421	0.415207416	0.449656516	0.535863519	0.414856583	0.479679763	0.423081845	0.521363676	0.461984545	0.556820929	0.509391665	0.611053944
1274.18	0.412449479	0.427757293	0.416205525	0.449656516	0.539065659	0.415176451	0.487974167	0.426277936	0.523147762	0.466418117	0.56397289	0.50942415	0.623318672
1307.64	0.412450224	0.429668993	0.416384131	0.449656516	0.540860593	0.416020334	0.49732849	0.431468099	0.526841164	0.469172567	0.569882572	0.509431899	0.631884336
1341.1	0.412450254	0.437211782	0.416405827	0.449656516	0.543051839	0.418661803	0.508366942	0.445589274	0.531387269	0.470712483	0.573165596	0.509433568	0.634479523
1374.56	0.412450314	0.446356446	0.416407615	0.449656516	0.545550048	0.422158301	0.511909783	0.466049433	0.533110499	0.471569002	0.574322701	0.509433866	0.638430536
1408.02	0.412452102	0.448786139	0.416407704	0.449656516	0.547297359	0.424063653	0.512173951	0.477448493	0.533307493	0.47292611	0.57457453	0.509433925	0.642418563
1441.48	0.412479699	0.448919535	0.416407704	0.449656516	0.548001707	0.42448923	0.512178302	0.479640752	0.533314109	0.477250725	0.574607015	0.509433925	0.643504143
1474.94	0.412723213	0.448920965	0.416407704	0.449656516	0.548174679	0.424535871	0.512178302	0.479911178	0.533314168	0.484190494	0.574609399	0.509433925	0.643603861
1508.4	0.413959265	0.448920965	0.416407704	0.449656516	0.54820931	0.424678326	0.512178302	0.479968339	0.533314168	0.489695996	0.574609518	0.509433925	0.644811451
1541.86	0.41759491	0.448920965	0.416407704	0.449656516	0.548219323	0.425674856	0.512178302	0.479979008	0.533314168	0.492702186	0.574609518	0.509433925	0.650439382

Table A2.2. Cumulative probability data for Rising Star cave and surface samples (Continued).

	Rising Star Cave sediment samples						Rising Star Cave surface sediment samples						
Age (Ma)	**UW101-1783A, C, L**	**OSL-4**	**260517JW8**	**100517JW3**	**100517JW5**	**100517JW6**	**190517JW1**	**190517JW2**	**190517JW3**	**190517JW4**	**190517JW5**	**190517JW6**	**190517JW7**
1575.32	0.424006969	0.448920965	0.416407704	0.449656516	0.548223436	0.428547055	0.512178302	0.479980528	0.533314168	0.49397099	0.574609518	0.509433925	0.653329849
1608.78	0.431844383	0.448920965	0.416407704	0.449656636	0.548244417	0.431948334	0.512178302	0.479980677	0.533314168	0.494321585	0.574609518	0.509433925	0.653517902
1642.24	0.440570742	0.448920965	0.416407704	0.449770153	0.548964143	0.433605254	0.512178302	0.479980677	0.533314168	0.49437958	0.574609518	0.509435654	0.65460366
1675.7	0.449025095	0.448920965	0.416407704	0.4565157	0.552622676	0.433947414	0.512178302	0.479980677	0.533314168	0.494385213	0.574609518	0.50954926	0.661943853
1709.16	0.454116434	0.448920965	0.416407704	0.486777753	0.556528449	0.434290349	0.512178302	0.479980677	0.533314168	0.49438554	0.574610829	0.511351109	0.672114193
1742.62	0.455708772	0.448920965	0.416407734	0.499269843	0.562709868	0.436721951	0.512178302	0.479980677	0.533314168	0.49438557	0.574665368	0.518570781	0.67544961
1776.08	0.455953628	0.448920965	0.4164083	0.499686837	0.569641709	0.44263941	0.512178659	0.479980677	0.533318222	0.494389653	0.575394809	0.526120186	0.681807876
1809.54	0.455971777	0.448920965	0.416415989	0.499687701	0.575461745	0.44842726	0.512290418	0.479980677	0.533492804	0.494567424	0.578523755	0.528591573	0.683604181
1843	0.45597288	0.448920965	0.416488349	0.499687701	0.577694297	0.451682121	0.51590687	0.479980677	0.535426319	0.4968431	0.582909346	0.532366335	0.685496271
1876.46	0.455995321	0.448920965	0.416970432	0.499687701	0.577849329	0.453081548	0.52951467	0.479980677	0.543200076	0.505343139	0.584927857	0.544581473	0.695848823
1909.92	0.456472725	0.448920965	0.419460356	0.499687701	0.577865243	0.454640299	0.536170721	0.479980677	0.55480361	0.514321804	0.585230112	0.561713994	0.710274875
1943.38	0.461110145	0.448920965	0.430442899	0.499687701	0.578407764	0.45746845	0.536566973	0.479982197	0.565440416	0.517126739	0.585284889	0.565925062	0.712600946
1976.84	0.482297361	0.448921412	0.467085093	0.499687761	0.581640363	0.462244064	0.536569595	0.480202347	0.574739695	0.518823445	0.586479247	0.566495895	0.712989807
2010.3	0.536204875	0.449546516	0.539454579	0.499936372	0.587714255	0.483583182	0.536729217	0.49001497	0.585206687	0.529043317	0.599451363	0.575147748	0.720004141
2043.76	0.626281381	0.48166579	0.613282323	0.537510097	0.622216284	0.541583538	0.551862061	0.556062818	0.621517479	0.568283677	0.652506471	0.636189997	0.756073117
2077.22	0.746615171	0.607598782	0.651779175	0.729022324	0.694327652	0.591313422	0.637195647	0.651162088	0.717741013	0.624275625	0.730855048	0.74691844	0.785035312
2110.68	0.775731802	0.697869062	0.663424313	0.797720671	0.710842252	0.60480994	0.690864384	0.702648997	0.770915389	0.648835182	0.770257294	0.803342581	0.797555804
2144.14	0.781978548	0.731322408	0.66747427	0.799876988	0.715571821	0.610879898	0.706598818	0.734914422	0.79961437	0.660893857	0.778977871	0.825071454	0.801790297
2177.6	0.78655839	0.734510064	0.679514349	0.800694704	0.720678747	0.618220329	0.707306027	0.744693935	0.809914172	0.672507584	0.784726679	0.829716623	0.801993906
2211.06	0.796680987	0.734661937	0.718646049	0.815717459	0.725784779	0.625898302	0.707307041	0.753644049	0.81107831	0.680453241	0.787107646	0.830155551	0.802627861
2244.52	0.814036131	0.734665632	0.777294219	0.843955934	0.740694642	0.631851852	0.707307041	0.759036124	0.812058806	0.694036245	0.787301898	0.830187619	0.812653065
2277.98	0.84096092	0.734665632	0.817789972	0.850446641	0.771857262	0.639582276	0.707307041	0.760974884	0.819509506	0.719884455	0.78730464	0.830188751	0.837174654
2311.44	0.854041159	0.734665632	0.831032097	0.877359688	0.784650743	0.648119092	0.707315028	0.771621585	0.822183132	0.729901195	0.787305474	0.830195189	0.841562927
2344.9	0.86182332	0.734665632	0.833101809	0.899599671	0.785211205	0.652850926	0.70816493	0.779592872	0.822386742	0.731254101	0.78739357	0.83091706	0.841809154
2378.36	0.867589414	0.734800994	0.833254218	0.89993751	0.785222173	0.66555202	0.7185691	0.78125596	0.826913655	0.736667275	0.788975537	0.843096316	0.845306933
2411.82	0.871068597	0.747256339	0.833259344	0.89993757	0.785222352	0.682185471	0.740095079	0.791694582	0.839955807	0.750044823	0.794270575	0.873826683	0.856663942
2445.28	0.876055896	0.774743021	0.833259404	0.89993757	0.785279751	0.688238025	0.753354251	0.799490571	0.844318211	0.760953367	0.798539698	0.885717094	0.861357987
2478.74	0.883089364	0.775486231	0.833259404	0.89993757	0.787777662	0.689997017	0.755993903	0.799990475	0.844437838	0.763830543	0.802415311	0.886758268	0.867916346
2512.2	0.888517201	0.77548629	0.833259404	0.89993757	0.796593487	0.694749713	0.757768273	0.799992621	0.844438016	0.764058411	0.806653738	0.886792243	0.871284723
2545.66	0.89069289	0.77548629	0.833259404	0.89993757	0.799878418	0.6979599	0.770774722	0.799992621	0.844438016	0.765229881	0.808352828	0.886792481	0.871293187
2579.12	0.89114362	0.77548629	0.833259404	0.89993757	0.800033569	0.701274514	0.779928148	0.799992621	0.844438016	0.771780789	0.808841646	0.886792481	0.871294022
2612.58	0.891191721	0.77548629	0.833259404	0.89993757	0.800034523	0.706521451	0.78047812	0.799992621	0.844438314	0.775173962	0.811993361	0.886792481	0.871314526
2646.04	0.891194344	0.77548629	0.833259404	0.89993757	0.800039709	0.707529962	0.780480266	0.799992621	0.844473243	0.775960505	0.822274685	0.886792481	0.872100949
2679.5	0.891194403	0.77548629	0.833259404	0.89993757	0.801216722	0.707549334	0.780480266	0.799992919	0.845354676	0.779312372	0.8290447	0.886795998	0.880813301
2712.96	0.891194403	0.775500357	0.833259404	0.89993757	0.806610823	0.707683086	0.780480266	0.800185502	0.850535154	0.784310997	0.830030262	0.888433933	0.890147209
2746.42	0.891197145	0.776604831	0.833259404	0.900106311	0.808917224	0.709819138	0.78220427	0.80898571	0.860299885	0.788887084	0.83351481	0.901848733	0.899898648
2779.88	0.89654094	0.792331398	0.833259404	0.91516155	0.827722728	0.717122018	0.809344649	0.854016364	0.865983427	0.805951536	0.85214591	0.905637503	0.909370303
2813.34	0.912700355	0.833050013	0.833259404	0.94765389	0.854724407	0.724642754	0.842740834	0.879630685	0.866680086	0.828240395	0.876504362	0.90566051	0.912186563
2846.8	0.912955463	0.855950952	0.833262384	0.949966192	0.859208584	0.729088426	0.85659951	0.891706228	0.869781315	0.837782204	0.888040721	0.90568769	0.92198205
2880.26	0.912956297	0.890234351	0.833418369	0.949968755	0.860542417	0.739615679	0.872790456	0.908911586	0.877670228	0.843966186	0.896355331	0.906598687	0.927159727
2913.72	0.912983119	0.897356391	0.836144328	0.949968755	0.86549437	0.752777338	0.877967894	0.936133325	0.88219744	0.857145607	0.909420669	0.912750721	0.930202365
2947.18	0.913353562	0.897941589	0.852515638	0.949968755	0.86668247	0.763794243	0.878044486	0.95576489	0.887577355	0.871342838	0.914783597	0.922517836	0.930722773

Table A2.2. Cumulative probability data for Rising Star cave and surface samples (Continued).

	Rising Star Cave sediment samples						Rising Star Cave surface sediment samples						
Age (Ma)	**UW101-1783A, C, L**	**OSL-4**	**260517JW8**	**100517JW3**	**100517JW5**	**100517JW6**	**190517JW1**	**190517JW2**	**190517JW3**	**190517JW4**	**190517JW5**	**190517JW6**	**190517JW7**
2980.64	0.919700861	0.897948325	0.888321221	0.949968755	0.867181361	0.779940069	0.878044546	0.963540196	0.889194965	0.876553833	0.917486787	0.935915351	0.933553576
3014.1	0.943130851	0.897950888	0.925407469	0.949968755	0.872795105	0.809927762	0.878044546	0.975718379	0.895477116	0.881865323	0.92680186	0.943181157	0.939940035
3047.56	0.9548558	0.901977241	0.960564971	0.949968755	0.88670969	0.853431284	0.878489554	0.99115777	0.901566088	0.898862243	0.938130796	0.945013165	0.940688908
3081.02	0.991992116	0.946959436	0.9880265	0.949968755	0.911153257	0.890499294	0.905704439	0.998632252	0.910892963	0.94034493	0.950624645	0.960167229	0.948339939
3114.48	0.999850988	0.966071188	0.998301029	0.949968755	0.937827885	0.904854119	0.940168142	0.99992305	0.938297153	0.98018229	0.956871748	0.98001945	0.968716025
3147.94	0.999994338	0.994811714	0.999897122	0.949968755	0.947999358	0.918105841	0.950977683	0.999998569	0.944551885	0.988808692	0.958305418	0.981224477	0.977121353
3181.4	0.999999881	0.999956608	0.999997497	0.949968755	0.963620782	0.941468298	0.951816976	1	0.955450773	0.99235791	0.966298878	0.983410478	0.983409882
3214.86	1	0.99999994	1	0.949992359	0.991452157	0.965610623	0.978603423	1	0.982531488	0.99798429	0.984919012	0.992164135	0.995180011
3248.32	1	1	1	0.960857928	0.998665094	0.971292675	0.999929428	1	0.998737633	0.999880433	0.997156203	0.99896425	0.999979973
3281.78	1	1	1	0.997943938	0.999954939	0.972097039	1	1	0.999996543	0.999998689	0.999853671	0.999973238	1
3315.24	1	1	1	0.999999523	0.999999881	0.977677464	1	1	1	1	0.99999845	0.999999881	1
3348.7	1	1	1	1	1	0.981120169	1	1	1	1	1	1	1
3382.16	1	1	1	1	1	0.983658016	1	1	1	1	1	1	1
3415.62	1	1	1	1	1	0.990891814	1	1	1	1	1	1	1
3449.08	1	1	1	1	1	0.997203231	1	1	1	1	1	1	1
3482.54	1	1	1	1	1	0.999839783	1	1	1	1	1	1	1
3516	1	1	1	1	1	1	1	1	1	1	1	1	1

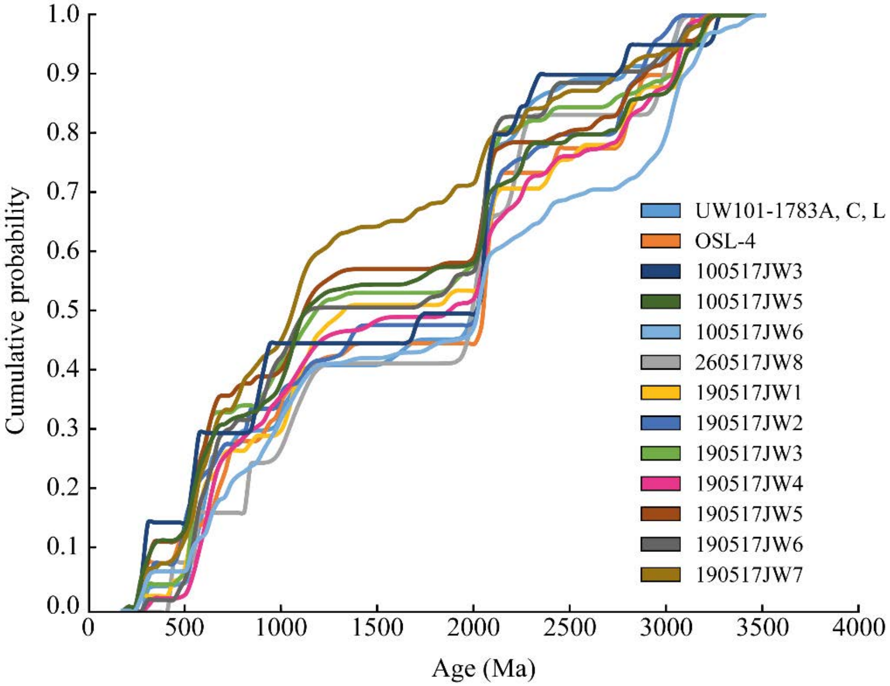

Figure A2.3. Cumulative frequency distribution plot for Rising Star Cave sediments.

Table A2.3. Age data for the Kolmogorov-Smirnov statistical test (n=15).

Rising Star Cave sediment samples												Rising Star Cave surface sediment samples													
UW101-1783A, C, L		**260517JW8**		**OSL-4**		**100517JW3**		**100517JW5**		**100517JW6**		**190517JW1**		**190517JW2**		**190517JW3**		**190517JW4**		**190517JW5**		**190517JW6**		**190517JW7**	
Age	*Error (2σ)*	*Age*	*Error (2σ)*	*Age*	*Error (2σ)*	*Age*	*Error (2σ)*	*Age*	*Error (2σ)*	*Age*	*Error (2σ)*	*Age*	*Error (2σ)*	*Age*	*Error (2σ)*	*Age*	*Error (2σ)*	*Age*	*Error (2σ)*	*Age*	*Error (2σ)*	*Age*	*Error (2σ)*	*Age*	*Error (2σ)*
273.8	3	407.6	3.7	246.6	5.9	241	3.7	182.6	2.8	243	4.9	254.3	4	238	5.4	238	3.7	298	4.5	244	3	275	5.2	248	11
293.5	3.5	539.9	3.8	248.2	4.8	268	3.4	241.1	5.5	254	14	417.1	6.2	258	3.7	259	4.9	299	3.8	245	4.1	454	9.7	255.6	4.8
511.9	7.6	816.8	7.9	268	3.5	282	3.3	245	4.9	265	8.2	470.3	6.9	297	3.9	267	3.6	514	33	254	4.5	473	8.8	264.8	3.4
514.2	5.7	1017	45	270.2	4.4	530	8	245.6	3.8	268	6.5	504.6	6.6	301	3.6	272	5.2	528	5.2	269	3.5	508	9.7	267.7	5.4
524	68	1118	53	440	22	532	4.9	247.9	3.1	271	5.7	504.8	7.1	460	6.4	439	5.5	528	34	271	6.5	520	6.1	271.9	5
557	12	2002	37	447.5	9.9	533	6.2	253	3.6	276	6.1	519.2	6.7	465	6.1	495	8.4	534	35	274	4.4	527	7.1	281.9	5.2
562.8	7	2004	54	505.9	8.1	852	14	261.3	5.5	311	7.3	563.7	7.2	473	6.3	506	5.6	540	8.4	280	4.3	539	6	288.1	3.9
569	8.5	2007	35	594	12	875	11	261.3	3.6	506	8.7	564.1	8.3	487	5.7	508	7	548	35	281	3.6	544	9.7	339.2	6
570	7	2212	34	638.3	9	911	10	264.7	3.3	510	10	593.4	6.9	510	6.7	508	5.4	562	36	305	5.7	545	9.3	425.2	7.1
604.8	9.2	2233	36	641.7	8.7	1690	19	272.6	3.3	517	8.5	649	16	528	5.8	511	7.1	568	37	309	3.6	569	11	442.1	6.3
616.7	6	2964	31	691.8	9.5	2048	15	275.7	6	525	9.9	689.3	9.6	550	8.8	511	9.9	576	36	312	3.8	588	7.1	467.1	8
618.6	9.2	3038	34	703.4	9.9	2052	15	282.1	4.7	532	9.9	831.9	12	596	7.9	515	11	591	15	464	6.6	613	13	475.9	6.6
678	18			704	19	2053	17	304.9	3.6	555	11	1021	26	657	22	516	5.5	600	38	472	9.2	625	6.1	486.8	7
761	11			733	13	2056	15	308.4	4	600	12	1029	39	665	12	522	7.8	602	10	511	5.9	637	6.7	523.4	8.3
987	13			900	18	2060	15	310	4.1	605	11	1041	33	803	8.6	533	7.9	608	38	518	7.8	656	10	524.7	11
1006	45			930	28	2077	15	336.4	5.6	612	11	1062	35	806	12	538	7.6	615	41	531	6.4	666	12	524.9	8.6
1008	43			986	16	2214	20	454	8.9	620	12	1071	24	813	12	539	6.1	615	17	531	7.2	739	14	532	6.7
1096	43			995.1	12	2303	14	473.5	6.1	634	12	1141	21	979	11	543	7.5	618	40	532	5.8	854	15	538.5	9.1
1098	33			1060	21	2781	15	478.4	7	645	13	1149	24	998	13	558	6.6	628	9.2	535	7.5	888	11	538.5	7.5
1567	44			1084	48	3252	13	500.8	8.4	661	13	1222	28	1102	27	565	6.5	638	41	535	6.2	917	11	540.1	8.2
1650	38			1174	53			511.6	8	717	15	1308	26	1125	26	567	9.4	653	7.1	540	6.3	931	11	553.5	7.7
1989	35			1339	25			513.6	7	719	20	1858	21	1298	63	569	7.9	666	43	541	5.8	952	21	557.9	11
1991	36			2034	14			518.6	6.5	720	13	2051	17	1335	21	570	7.7	667	42	544	6.9	1008	79	562.4	8.2
2008	37			2038	14			528.4	8.6	737	14	2055	17	1368	23	578	16	694	46	571	13	1024	27	585.2	11
2009	8			2054	14			531.3	6.1	790	15	2055	16	2021	16	588	10	727	46	577	5.9	1036	34	598.8	13
2010	36			2057	19			531.3	6.1	826	16	2058	14	2025	15	588	8	766	8.5	597	7.6	1067	33	601.6	7.2
2011	38			2058	19			531.5	8.9	873	15	2073	23	2031	24	607	9.8	820	14	597	7.8	1101	36	601.7	9.5
2013	37			2062	13			532.2	6.8	884	17	2077	14	2038	25	615	8.9	907	56	599	8.3	1737	27	609.1	8.7
2026	36			2062	13			532.7	5.9	903	16	2106	16	2038	21	625	6.3	914	11	602	6.3	1859	28	619.7	7.7
2048	18			2066	14			538.4	6.3	911	19	2377	21	2043	16	628	8.9	916	57	621	7.2	1885	19	636.6	8.3
2049	12			2069	15			547	11	942	18	2409	24	2060	15	755	11	935	58	622	8.9	2033	26	649.3	8.2
2052	15			2077	18			550	9.3	970	15	2534	19	2063	23	890	8.8	992	63	636	8.6	2037	29	654.8	7.8
2053	11			2088	18			565.7	8.6	972	55	2755	10	2066	15	890	11	992	81	653	8.4	2040	18	665.3	14
2055	16			2097	30			580.1	8.2	982	16	2783	12	2068	14	926	12	1023	56	656	8.1	2043	26	671.3	12
2059	35			2105	20			587	11	1003	37	2804	13	2086	22	935	9.9	1046	64	756	9.7	2045	20	750.6	14
2064	41			2107	14			593.4	8.8	1020	39	2860	17	2118	17	968	12	1064	40	757	30	2049	26	754.8	9.4
2202	35			2407	14			599.4	9.4	1026	69	3060	8.8	2119	17	974	15	1071	30	850	8	2051	21	773	13
2235	27			2416	11			624.3	9.2	1048	32	3090	14	2191	28	1012	43	1135	40	1023	55	2052	25	780.1	11
2262	15			2774	21			630.3	9.5	1057	33	3101	17	2301	18	1026	69	1138	41	1032	39	2055	24	796	10
2324	37			2782	9.9			634	9.3	1072	36	3197	11	2401	19	1051	71	1145	41	1034	46	2062	26	800.3	15
2459	40			2795	19			644.8	11	1083	40	3214	9.7	2754	19	1061	25	1204	50	1045	40	2062	20	837.7	9.8
2781	11			2826	19			645	17	1108	27			2759	19	1062	29	1247	69	1051	40	2074	23	871.1	11
2984	11			2855	8.8			701.5	11	1147	24			2767	17	1099	19	1446	31	1070	61	2099	36	873	16
3016	36			2865	22			734.9	9.7	1153	41			2775	14	1141	30	1488	45	1075	78	2115	19	932.6	12
3055	12			3056	13			803.6	10	1345	34			2838	14	1151	25	1865	28	1077	49	2376	19	992.1	17
3065	14			3058	11			871	11	1575	34			2884	16	1168	29	1876	26	1085	55	2394	17	998	13
				3073	12			892	19	1755	28			2904	32	1203	20	2026	28	1085	40	2396	26	1002	52

Table A2.3. Age data for the Kolmogorov-Smirnov statistical test (Continued).

Rising Star Cave sediment samples												Rising Star Cave surface sediment samples													
UW101-1783A, C, L		**260517JW8**		**OSL-4**		**100517JW3**		**100517JW5**		**100517JW6**		**190517JW1**		**190517JW2**		**190517JW3**		**190517JW4**		**190517JW5**		**190517JW6**		**190517JW7**	
Age	*Error (2σ)*	*Age*	*Error (2σ)*	*Age*	*Error (2σ)*	*Age*	*Error (2σ)*	*Age*	*Error (2σ)*	*Age*	*Error (2σ)*	*Age*	*Error (2σ)*	*Age*	*Error (2σ)*	*Age*	*Error (2σ)*	*Age*	*Error (2σ)*	*Age*	*Error (2σ)*	*Age*	*Error (2σ)*	*Age*	*Error (2σ)*
				3117	20			902.1	10	1796	35			2915	20	1307	29	2029	27	1086	53	2727	15	1039	42
				3130	10			961	12	1938	40			3006	31	1861	27	2037	29	1103	45	2915	25	1047	23
								975	18	2004	23			3026	30	1882	19	2038	24	1105	41	2969	17	1048	73
								994	16	2016	24					1923	17	2039	30	1133	33	3070	21	1048	33
								999	31	2018	26					1965	22	2047	62	1188	34	3081	13	1054	25
								1009	28	2022	25					1999	26	2053	29	1251	38	3203	24	1069	31
								1028	29	2025	25					2038	15	2053	22	1284	43			1077	45
								1028	33	2029	22					2044	14	2054	23	1813	30			1081	37
								1036	49	2030	29					2045	23	2054	21	2023	28			1083	24
								1041	49	2031	25					2048	16	2056	29	2030	31			1095	45
								1041	33	2031	23					2051	18	2061	26	2038	28			1103	31
								1046	22	2034	21					2052	13	2137	23	2039	31			1122	28
								1051	27	2039	24					2053	16	2145	26	2041	29			1126	41
								1053	43	2050	23					2054	31	2202	25	2042	25			1194	64
								1053	25	2052	23					2057	16	2245	21	2045	30			1203	47
								1059	50	2053	25					2058	18	2253	20	2045	30			1253	22
								1065	20	2054	23					2058	22	2260	21	2045	27			1272	23
								1072	43	2126	24					2058	20	2263	20	2046	30			1369	27
								1078	25	2175	23					2065	28	2382	30	2048	26			1525	20
								1088	23	2210	35					2066	20	2394	23	2054	30			1664	23
								1098	29	2259	24					2082	15	2419	25	2056	26			1679	16
								1130	130	2293	20					2095	18	2563	19	2057	26			1750	18
								1137	34	2363	17					2106	16	2683	28	2060	25			1866	37
								1168	30	2374	31					2117	23	2771	20	2065	28			1870	16
								1198	53	2383	20					2131	22	2778	24	2067	28			1881	16
								1209	29	2399	21					2132	25	2780	28	2073	26			2017	17
								1349	42	2497	23					2260	16	2786	25	2154	24			2022	21
								1664	22	2581	20					2380	19	2832	37	2396	24			2024	15
								1726	21	2757	23					2396	18	2899	26	2478	30			2026	19
								1752	26	2787	21					2708	25	2904	21	2626	27			2031	17
								1791	22	2852	17					2738	22	2932	22	2634	21			2043	22
								1970	23	2878	22					2849	15	3014	23	2771	26			2060	15
								2026	22	2904	20					2913	23	3056	23	2775	21			2064	21
								2029	19	2916	20					3004	16	3056	23	2781	25			2100	18
								2036	17	2972	15					3068	26	3059	30	2781	25			2234	19
								2037	23	2976	18					3090	17	3065	27	2789	35			2246	14
								2044	15	2979	25					3091	16	3075	19	2836	29			2256	17
								2045	16	2994	18					3096	13	3077	20	2891	21			2259	14
								2048	17	3014	22					3171	13	3082	25	2895	21			2383	22
								2049	16	3014	26					3181	14	3086	21	2996	24			2397	17
								2050	22	3025	22					3195	12	3092	20	3013	25			2467	12
								2052	19	3032	14					3210	11	3186	24	3061	26			2662	14
								2052	15	3042	24					3223	15			3065	21			2708	20
								2053	17	3043	24									3183	21			2712	37
								2053	15	3045	19									3191	30			2754	15
								2054	16	3048	18									3196	22			2821	12
								2056	19	3050	21									3222	23			2864	26

Table A2.3. Age data for the Kolmogorov-Smirnov statistical test (Continued).

Rising Star Cave sediment samples												Rising Star Cave surface sediment samples													
UW101-1783A, C, L		**260517JW8**		**OSL-4**		**100517JW3**		**100517JW5**		**100517JW6**		**190517JW1**		**190517JW2**		**190517JW3**		**190517JW4**		**190517JW5**		**190517JW6**		**190517JW7**	
Age	*Error (2σ)*	*Age*	*Error (2σ)*	*Age*	*Error (2σ)*	*Age*	*Error (2σ)*	*Age*	*Error (2σ)*	*Age*	*Error (2σ)*	*Age*	*Error (2σ)*	*Age*	*Error (2σ)*	*Age*	*Error (2σ)*	*Age*	*Error (2σ)*	*Age*	*Error (2σ)*	*Age*	*Error (2σ)*	*Age*	*Error (2σ)*
								2061	18	3064	27													2983	16
								2067	22	3089	19													3080	16
								2135	17	3128	16													3081	13
								2185	27	3150	23													3093	15
								2222	16	3166	20													3133	17
								2243	20	3173	18													3182	16
								2248	24	3183	20													3206	12
								2249	13	3184	17														
								2263	25	3203	22														
								2264	14	3303	16														
								2267	16	3387	18														
								2269	14	3431	21														
								2487	18																
								2495	21																
								2688	15																
								2772	14																
								2775	24																
								2776	21																
								2777	22																
								2777	17																
								2787	19																
								2788	18																
								2890	17																
								3005	20																
								3022	18																
								3034	17																
								3061	20																
								3066	14																
								3076	13																
								3079	20																
								3080	13																
								3082	14																
								3106	18																
								3130	27																
								3150	18																
								3181	17																
								3185	20																
								3185	15																
								3187	16																
								3191	11																
								3222	21																

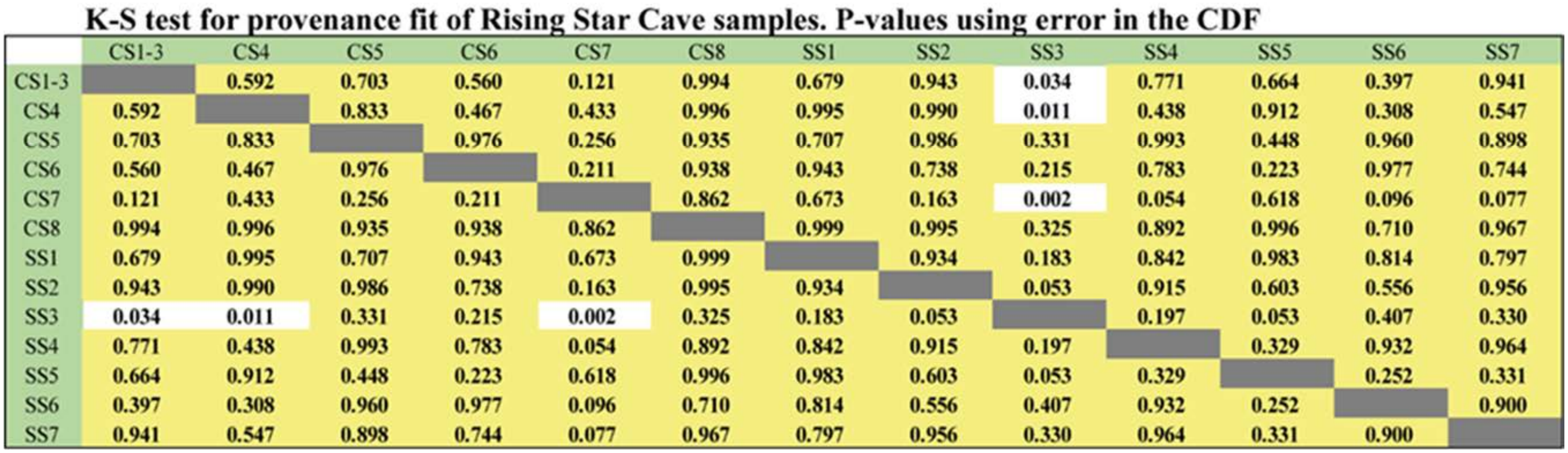

K-S test for provenance fit of Rising Star Cave samples. P-values using error in the CDF

	CS1-3	CS4	CS5	CS6	CS7	CS8	SS1	SS2	SS3	SS4	SS5	SS6	SS7
CS1-3		0.592	0.703	0.560	0.121	0.994	0.679	0.943	0.034	0.771	0.664	0.397	0.941
CS4	0.592		0.833	0.467	0.433	0.996	0.995	0.990	0.011	0.438	0.912	0.308	0.547
CS5	0.703	0.833		0.976	0.256	0.935	0.707	0.986	0.331	0.993	0.448	0.960	0.898
CS6	0.560	0.467	0.976		0.211	0.938	0.943	0.738	0.215	0.783	0.223	0.977	0.744
CS7	0.121	0.433	0.256	0.211		0.862	0.673	0.163	0.002	0.054	0.618	0.096	0.077
CS8	0.994	0.996	0.935	0.938	0.862		0.999	0.995	0.325	0.892	0.996	0.710	0.967
SS1	0.679	0.995	0.707	0.943	0.673	0.999		0.934	0.183	0.842	0.983	0.814	0.797
SS2	0.943	0.990	0.986	0.738	0.163	0.995	0.934		0.053	0.915	0.603	0.556	0.956
SS3	0.034	0.011	0.331	0.215	0.002	0.325	0.183	0.053		0.197	0.053	0.407	0.330
SS4	0.771	0.438	0.993	0.783	0.054	0.892	0.842	0.915	0.197		0.329	0.932	0.964
SS5	0.664	0.912	0.448	0.223	0.618	0.996	0.983	0.603	0.053	0.329		0.252	0.331
SS6	0.397	0.308	0.960	0.977	0.096	0.710	0.814	0.556	0.407	0.932	0.252		0.900
SS7	0.941	0.547	0.898	0.744	0.077	0.967	0.797	0.956	0.330	0.964	0.331	0.900	

Figure A2.4. K-S test for Rising Star sediment provenance. Kolmogorov-Smirnov statistical test results from detrital zircon data for provenance fit of the Rising Star Cave and surface sediments. P-values in yellow are ≥ 0.05 and in support of strong provenance fit. P-values in white are ≤ 0.05 and represent a poor statistical fit (highlighted in white).

Appendix 3

The age of *Homo naledi* and associated sediments in the Rising Star cave, South Africa

eLife

Dirks, P.H.G.M., Roberts, E.M., Hilbert-Wolf, H., Kramers, J.D., Hawks, J., Dossetto, A., Duval, M., Elliott, M., Evans, M., Grün, R., Hellstrom, J., Herries, A.I.R., Joannes-Boyau, R., Makhubela, T.V., Placzek, C.J., Robbins, J., Spandler, C., **Wiersma, J.**, Woodhead, J. and Berger, L.R. (2017).

The age of *Homo naledi* and associated sediments in the Rising Star Cave, South Africa

Paul HGM Dirks[1,2*], Eric M Roberts[1,2], Hannah Hilbert-Wolf[1], Jan D Kramers[3], John Hawks[2,4], Anthony Dosseto[5], Mathieu Duval[6,7], Marina Elliott[2], Mary Evans[8], Rainer Grün[6,9], John Hellstrom[10], Andy IR Herries[11], Renaud Joannes-Boyau[12], Tebogo V Makhubela[3], Christa J Placzek[1], Jessie Robbins[1], Carl Spandler[1], Jelle Wiersma[1], Jon Woodhead[10], Lee R Berger[2]

[1]Department of Geoscience, James Cook University, Townsville, Australia; [2]Evolutionary Studies Institute and the National Centre for Excellence in PalaeoSciences, University of the Witwatersrand, Wits, South Africa; [3]Department of Geology, University of Johannesburg, Johannesburg, South Africa; [4]Department of Anthropology, University of Wisconsin-Madison, Madison, United States; [5]School of Earth and Environmental Sciences, University of Wollongong, Wollongong, Australia; [6]Australian Research Centre for Human Evolution, Environmental Futures Research Institute, Griffith University, Nathan, Australia; [7]Geochronology, Centro Nacional de Investigación sobre la Evolución Humana (CENIEH), Burgos, Spain; [8]School of Geosciences, University of the Witwatersrand, Wits, South Africa; [9]Research School of Earth Sciences, The Australian National University, Canberra, Australia; [10]School of Earth Sciences, The University of Melbourne, Parkville, Australia; [11]The Australian Archaeomagnetism Laboratory, Department of Archaeology and History, La Trobe University, Melbourne, Australia; [12]Geoarchaeology and Archaeometry Research Group, Department of GeoScience, Southern Cross University, Lismore, Australia

***For correspondence:** paul.dirks@jcu.edu.au

Competing interests: The authors declare that no competing interests exist.

Funding: See page 55

Received: 13 December 2016
Accepted: 25 April 2017
Published: 09 May 2017

Reviewing editor: George H Perry, Pennsylvania State University, United States

Abstract New ages for flowstone, sediments and fossil bones from the Dinaledi Chamber are presented. We combined optically stimulated luminescence dating of sediments with U-Th and palaeomagnetic analyses of flowstones to establish that all sediments containing *Homo naledi* fossils can be allocated to a single stratigraphic entity (sub-unit 3b), interpreted to be deposited between 236 ka and 414 ka. This result has been confirmed independently by dating three *H. naledi* teeth with combined U-series and electron spin resonance (US-ESR) dating. Two dating scenarios for the fossils were tested by varying the assumed levels of ^{222}Rn loss in the encasing sediments: a maximum age scenario provides an average age for the two least altered fossil teeth of 253 +82/–70 ka, whilst a minimum age scenario yields an average age of 200 +70/–61 ka. We consider the maximum age scenario to more closely reflect conditions in the cave, and therefore, the true age of the fossils. By combining the US-ESR maximum age estimate obtained from the teeth, with the U-Th age for the oldest flowstone overlying *Homo naledi* fossils, we have constrained the depositional age of *Homo naledi* to a period between 236 ka and 335 ka. These age results demonstrate that a morphologically primitive hominin, *Homo naledi*, survived into the later parts of the Pleistocene in Africa, and indicate a much younger age for the *Homo naledi* fossils than have previously been hypothesized based on their morphology.

DOI: 10.7554/eLife.24231.001

Appendix 4

Formation of mud clast breccias and the process of sedimentary autobrecciation in the hominin-bearing (*Homo naledi*) Rising Star Cave system, South Africa

Sedimentology

Wiersma, J.P., Roberts, E.M. and Dirks, P.H.G.M. (2020)

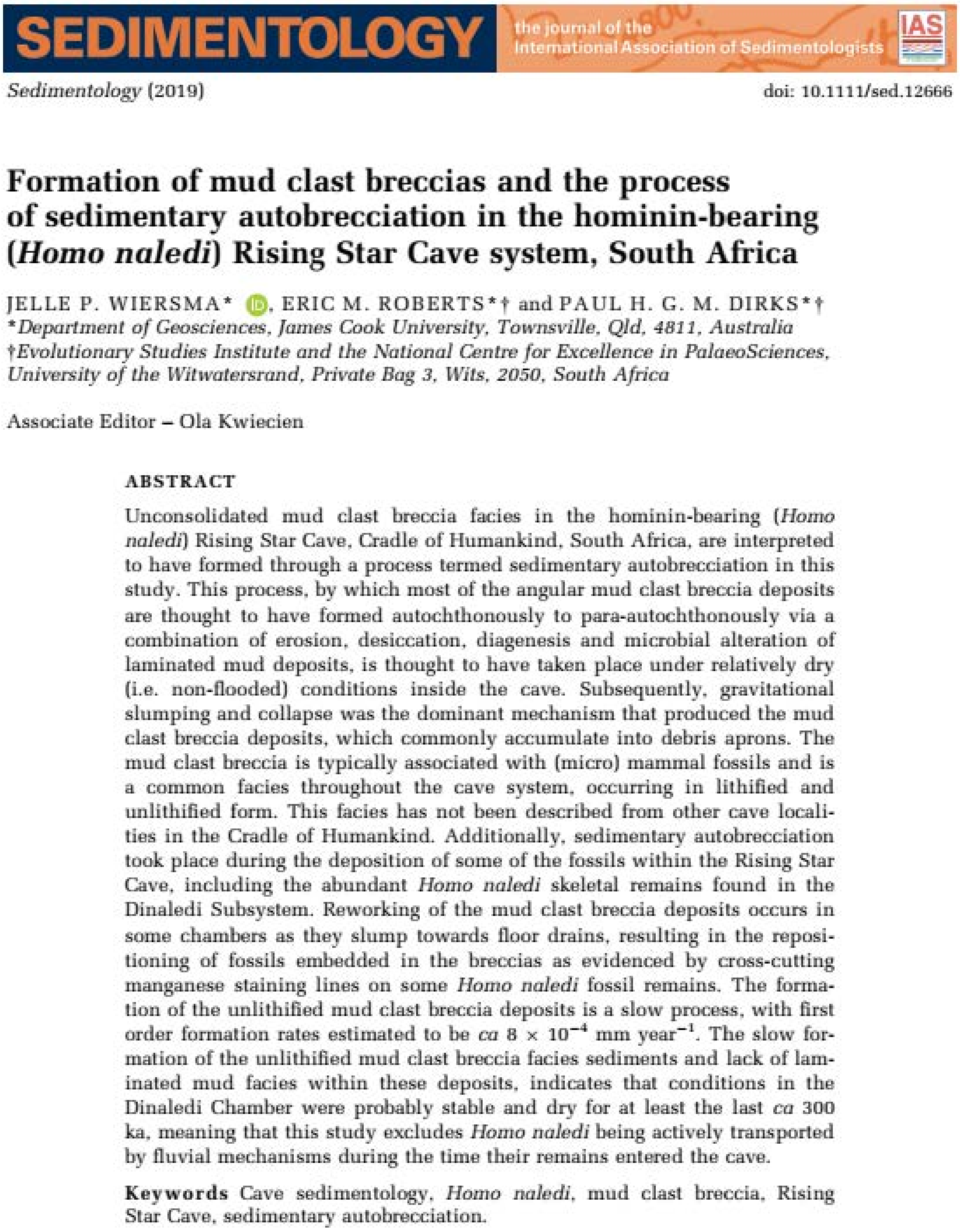

SEDIMENTOLOGY the journal of the International Association of Sedimentologists IAS

Sedimentology (2019) doi: 10.1111/sed.12666

Formation of mud clast breccias and the process of sedimentary autobrecciation in the hominin-bearing (*Homo naledi*) Rising Star Cave system, South Africa

JELLE P. WIERSMA*, ERIC M. ROBERTS*† and PAUL H. G. M. DIRKS*†
**Department of Geosciences, James Cook University, Townsville, Qld, 4811, Australia*
†Evolutionary Studies Institute and the National Centre for Excellence in PalaeoSciences, University of the Witwatersrand, Private Bag 3, Wits, 2050, South Africa

Associate Editor – Ola Kwiecien

ABSTRACT

Unconsolidated mud clast breccia facies in the hominin-bearing (*Homo naledi*) Rising Star Cave, Cradle of Humankind, South Africa, are interpreted to have formed through a process termed sedimentary autobrecciation in this study. This process, by which most of the angular mud clast breccia deposits are thought to have formed autochthonously to para-autochthonously via a combination of erosion, desiccation, diagenesis and microbial alteration of laminated mud deposits, is thought to have taken place under relatively dry (i.e. non-flooded) conditions inside the cave. Subsequently, gravitational slumping and collapse was the dominant mechanism that produced the mud clast breccia deposits, which commonly accumulate into debris aprons. The mud clast breccia is typically associated with (micro) mammal fossils and is a common facies throughout the cave system, occurring in lithified and unlithified form. This facies has not been described from other cave localities in the Cradle of Humankind. Additionally, sedimentary autobrecciation took place during the deposition of some of the fossils within the Rising Star Cave, including the abundant *Homo naledi* skeletal remains found in the Dinaledi Subsystem. Reworking of the mud clast breccia deposits occurs in some chambers as they slump towards floor drains, resulting in the repositioning of fossils embedded in the breccias as evidenced by cross-cutting manganese staining lines on some *Homo naledi* fossil remains. The formation of the unlithified mud clast breccia deposits is a slow process, with first order formation rates estimated to be *ca* 8×10^{-4} mm year^{-1}. The slow formation of the unlithified mud clast breccia facies sediments and lack of laminated mud facies within these deposits, indicates that conditions in the Dinaledi Chamber were probably stable and dry for at least the last *ca* 300 ka, meaning that this study excludes *Homo naledi* being actively transported by fluvial mechanisms during the time their remains entered the cave.

Keywords Cave sedimentology, *Homo naledi*, mud clast breccia, Rising Star Cave, sedimentary autobrecciation.

Appendix 5

Providing context to the *Homo naledi* fossils: Constraints from flowstones on the age of sediment deposits in Rising Star Cave, South Africa

Chemical Geology

Robbins, J.L., Dirks, P.H.G.M., Roberts, E.M., Kramers, J.D., Makhubela, T.V., Hilbert-Wolf, H.L., Elliott, M., **Wiersma, J.P.**, Placzek, C., Evans, M. and Berger, L. (2021)

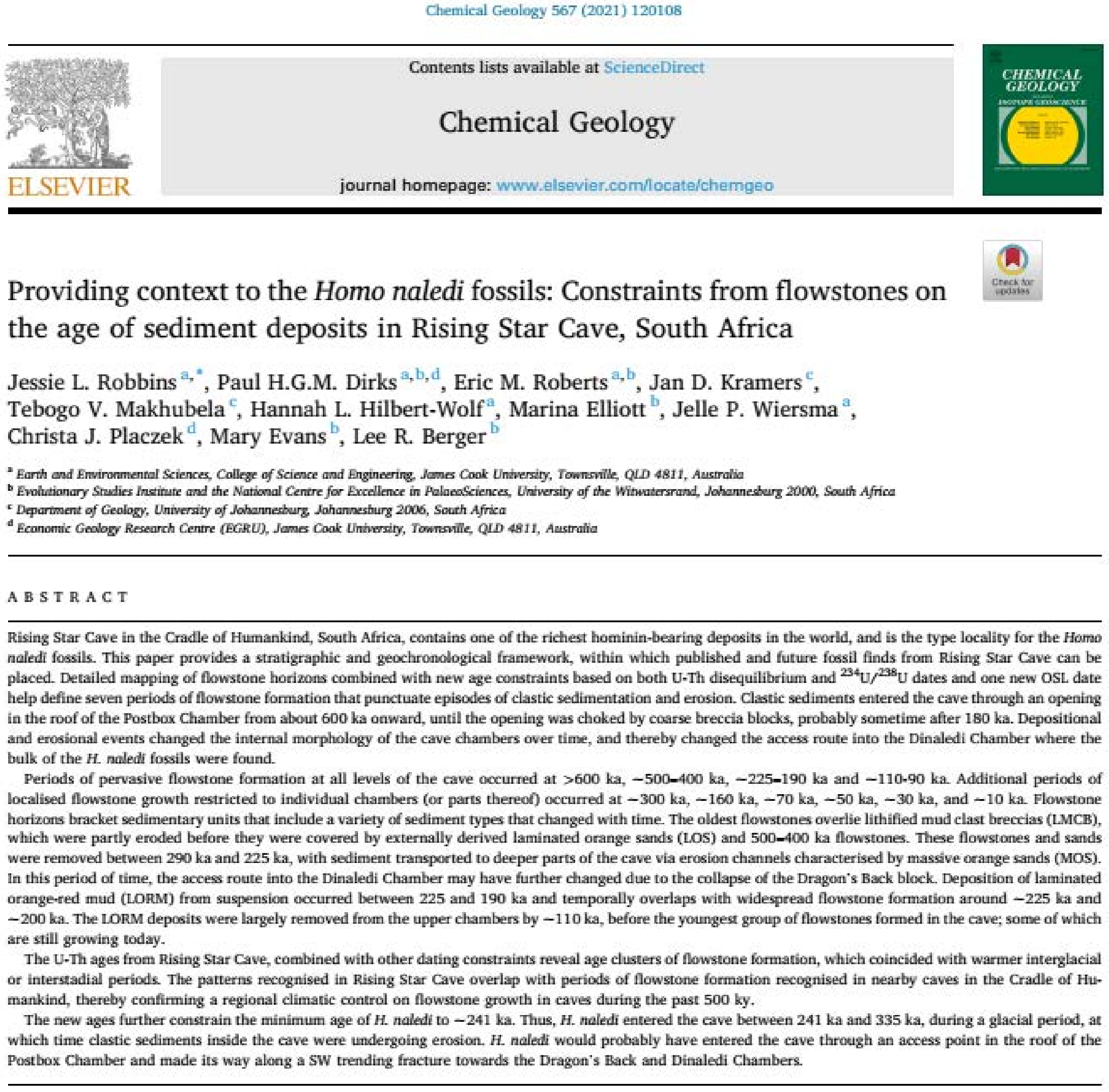

Chemical Geology 567 (2021) 120108

Contents lists available at ScienceDirect

Chemical Geology

journal homepage: www.elsevier.com/locate/chemgeo

Providing context to the *Homo naledi* fossils: Constraints from flowstones on the age of sediment deposits in Rising Star Cave, South Africa

Jessie L. Robbins [a,*], Paul H.G.M. Dirks [a,b,d], Eric M. Roberts [a,b], Jan D. Kramers [c], Tebogo V. Makhubela [c], Hannah L. Hilbert-Wolf [a], Marina Elliott [b], Jelle P. Wiersma [a], Christa J. Placzek [d], Mary Evans [b], Lee R. Berger [b]

[a] *Earth and Environmental Sciences, College of Science and Engineering, James Cook University, Townsville, QLD 4811, Australia*
[b] *Evolutionary Studies Institute and the National Centre for Excellence in PalaeoSciences, University of the Witwatersrand, Johannesburg 2000, South Africa*
[c] *Department of Geology, University of Johannesburg, Johannesburg 2006, South Africa*
[d] *Economic Geology Research Centre (EGRU), James Cook University, Townsville, QLD 4811, Australia*

ABSTRACT

Rising Star Cave in the Cradle of Humankind, South Africa, contains one of the richest hominin-bearing deposits in the world, and is the type locality for the *Homo naledi* fossils. This paper provides a stratigraphic and geochronological framework, within which published and future fossil finds from Rising Star Cave can be placed. Detailed mapping of flowstone horizons combined with new age constraints based on both U-Th disequilibrium and $^{234}U/^{238}U$ dates and one new OSL date help define seven periods of flowstone formation that punctuate episodes of clastic sedimentation and erosion. Clastic sediments entered the cave through an opening in the roof of the Postbox Chamber from about 600 ka onward, until the opening was choked by coarse breccia blocks, probably sometime after 180 ka. Depositional and erosional events changed the internal morphology of the cave chambers over time, and thereby changed the access route into the Dinaledi Chamber where the bulk of the *H. naledi* fossils were found.

Periods of pervasive flowstone formation at all levels of the cave occurred at >600 ka, −500–400 ka, −225–190 ka and −110-90 ka. Additional periods of localised flowstone growth restricted to individual chambers (or parts thereof) occurred at −300 ka, −160 ka, −70 ka, −50 ka, −30 ka, and −10 ka. Flowstone horizons bracket sedimentary units that include a variety of sediment types that changed with time. The oldest flowstones overlie lithified mud clast breccias (LMCB), which were partly eroded before they were covered by externally derived laminated orange sands (LOS) and 500–400 ka flowstones. These flowstones and sands were removed between 290 ka and 225 ka, with sediment transported to deeper parts of the cave via erosion channels characterised by massive orange sands (MOS). In this period of time, the access route into the Dinaledi Chamber may have further changed due to the collapse of the Dragon's Back block. Deposition of laminated orange-red mud (LORM) from suspension occurred between 225 and 190 ka and temporally overlaps with widespread flowstone formation around −225 ka and −200 ka. The LORM deposits were largely removed from the upper chambers by −110 ka, before the youngest group of flowstones formed in the cave; some of which are still growing today.

The U-Th ages from Rising Star Cave, combined with other dating constraints reveal age clusters of flowstone formation, which coincided with warmer interglacial or interstadial periods. The patterns recognised in Rising Star Cave overlap with periods of flowstone formation recognised in nearby caves in the Cradle of Humankind, thereby confirming a regional climatic control on flowstone growth in caves during the past 500 ky.

The new ages further constrain the minimum age of *H. naledi* to −241 ka. Thus, *H. naledi* entered the cave between 241 ka and 335 ka, during a glacial period, at which time clastic sediments inside the cave were undergoing erosion. *H. naledi* would probably have entered the cave through an access point in the roof of the Postbox Chamber and made its way along a SW trending fracture towards the Dragon's Back and Dinaledi Chambers.